NASA Technical Memorandum 78119

(NASA-TM-78119) SPACE AND PLANETARY ENVIRONMENT CRITERIA GUIDELINES FOR USE IN SPACE VEHICLE DEVELOPMENT 1977 REVISION (NASA) 451 p HC A20/MF A01 CSCL 22B

N78-15146

Unclas
G3/15 57782

Space and Planetary Environment Criteria Guidelines for Use in Space Vehicle Development, 1977 Revision

Edited by G. S. West, Jr.,
J. J. Wright, and H. C. Euler

NOVEMBER 1977

NASA

TECHNICAL REPORT STANDARD TITLE PAGE

1. REPORT NO.	2. GOVERNMENT ACCESSION NO.	3. RECIPIENT'S CATALOG NO.
NASA TM-78119		

4. TITLE AND SUBTITLE	5. REPORT DATE
Space and Planetary Environment Criteria Guidelines for Use in Space Vehicle Development, 1977 Revision	November 1977
	6. PERFORMING ORGANIZATION CODE
7. AUTHOR(S)	8. PERFORMING ORGANIZATION REPORT #
Edited by G. S. West, Jr., J. J. Wright, and H. C. Euler	M-233
9. PERFORMING ORGANIZATION NAME AND ADDRESS	10. WORK UNIT NO.
George C. Marshall Space Flight Center Marshall Space Flight Center, Alabama 35812	11. CONTRACT OR GRANT NO.
	13. TYPE OF REPORT & PERIOD COVERED
12. SPONSORING AGENCY NAME AND ADDRESS	Technical Memorandum
National Aeronautics and Space Administration Washington, D.C. 20546	14. SPONSORING AGENCY CODE

15. SUPPLEMENTARY NOTES

Prepared by Atmospheric Sciences Division, Space Sciences Laboratory, Science and Engineering Directorate

16. ABSTRACT

This document provides a consolidated presentation of space and planetary natural environment data for use as design criteria guidelines in space vehicle development programs.

Specifically, information is provided in the disciplinary areas of atmospheric and ionospheric properties, radiation, solar cycle predictions, geomagnetic field, astrodynamic constants, and meteoroids for the Earth's atmosphere above 90 km, interplanetary space, and the atmospheres and surfaces (when available) of the moon and the planets (other than earth) of this solar system. The current MSFC upper atmosphere model and solar cycle prediction routines are described in detail.

This document succeeds NASA TM X-64627 entitled "Space and Planetary Environment Criteria Guidelines for Use in Space Vehicle Development, 1971 Revision." The information in this new edition is recommended for use in the development of space vehicle and associated subsystem design and operational criteria unless otherwise stated in a given project's engineering specifications.

For regions of the earth's atmosphere below 90 km, terrestrial environment criteria are documented in NASA Technical Memorandum TM-78118 entitled "Terrestrial Environment (Climatic) Criteria Guidelines for Use in Aerospace Vehicle Development, 1977 Revision."

17. KEY WORDS	18. DISTRIBUTION STATEMENT
Environment criteria Space environment Solar radiation Atmospheric models Astrodynamics constants Planetary environments	Cat. 15

19. SECURITY CLASSIF. (of this report)	20. SECURITY CLASSIF. (of this page)	21. NO. OF PAGES	22. PRICE
Unclassified	Unclassified	450	$11.75

* For sale by the National Technical Information Service, Springfield, Virginia 22161

*U.S. GOVERNMENT PRINTING OFFICE: 1977 - 735-078/52

APPROVAL

SPACE AND PLANETARY ENVIRONMENT CRITERIA GUIDELINES FOR USE IN SPACE VEHICLE DEVELOPMENT, 1977 REVISION

The information in this report has been reviewed for security classification. Review of any information concerning Department of Defense or Atomic Energy Commission programs has been made by the MSFC Security Classification Officer. This report, in its entirety, has been determined to be unclassified.

This document has also been reviewed and approved for technical accuracy.

W. W. VAUGHAN
Chief, Atmospheric Sciences Division

CHARLES A. LUNDQUIST
Director, Space Sciences Laboratory

NASA Technical Memorandum 78119

Space and Planetary Environment Criteria Guidelines for Use in Space Vehicle Development, 1977 Revision

Edited by G. S. West, Jr.,
J. J. Wright, and H. C. Euler
George C. Marshall Space Flight Center
Marshall Space Flight Center, Alabama

National Aeronautics
and Space Administration

**Scientific and Technical
Information Office**

1977

FOREWORD

This document provides information relative to the natural environment for altitudes greater than 90 km above the surface of the earth. NASA Technical Memorandum TM-78118, entitled "Terrestrial Environment (Climatic) Criteria Guidelines for Use in Space Vehicle Development, 1977 Revision," dated 1977, provides natural environment information for altitudes below 90 km.

There is no intent to automatically change any references to previous documents in contract scopes of work by the issuance of the 1977 revision of this document.

This document, which succeeds all editions of TM X-64627, entitled "Space and Planetary Environment Criteria Guidelines for Use in Space Vehicle Development, 1971 Revision," is recommended for use in the development of space vehicles and associated equipment.

The information presented in this document is based on data and models considered to be accurate. However, in those design applications which indicate a critical environment interface the user should consult an environmental specialist to insure application of the most current information and scientific engineering interpretation.

Various programs of NASA's Office of Space Flight, Office of Aeronautics and Space Technology, Office of Applications, and Office of Space Science provided resources required for the preparation of this document.

TABLE OF CONTENTS

TABLE OF CONTENTS (Continued)

TABLE OF CONTENTS (Continued)

TABLE OF CONTENTS (Continued)

TABLE OF CONTENTS (Continued)

TABLE OF CONTENTS (Continued)

TABLE OF CONTENTS (Continued)

TABLE OF CONTENTS (Continued)

TABLE OF CONTENTS (Concluded)

SUMMARY

This document provides a consolidated presentation of space and planetary natural environment data for use as design criteria guidelines in space vehicle development programs.

Specifically, information is provided in the disciplinary areas of atmospheric and ionospheric properties, radiation, solar cycle predictions, geomagnetic field, astrodynamic constants, and meteoroids for the earth's atmosphere above 90 km, interplanetary space, and the atmospheres and surfaces (when available) of the moon and the planets (other than earth) of this solar system. The current MSFC upper atmosphere model and solar cycle prediction routines are described in detail.

In compiling this document, extensive use has been made of the technical contributions and review comments furnished by Space Sciences Laboratory personnel at the Marshall Space Flight Center. NASA publications and open literature were also used extensively in preparing this document.

INTRODUCTION

A knowledge of environment parameters is necessary for the establishment of design requirements for space vehicles and associated equipment. Such data are required to define the design condition for fabrication, storage, transportation, test, preflight, in-flight, and on-orbit design conditions and should be considered for both the whole system and the components which make up the system. The purpose of this document is to provide guideline data on space and planetary environmental conditions relative to various disciplinary areas which are applicable to the design of space vehicles and associated equipment for NASA.

Good engineering judgment must be exercised in the application of the environment data to space vehicle design analysis. Consideration must be given to the overall vehicle mission and performance requirements. Knowledge still is lacking on the relationships between some of the environment variates which are required as inputs to the design of space vehicles. Also, interrelationships between space vehicle parameters and environment variables cannot always be clearly defined. Therefore, a close working relationship and team philosophy should exist between the design/operational engineer and the respective organization's environment scientists. Although a space vehicle design should accommodate all expected operational environment conditions, it is neither economically

nor technically feasible to design space vehicles to withstand all extremes. For this reason, consideration should be given to protection of space vehicles or critical subsystem for some extremes. This document does not specify how the designer should use the data in regard to a specific space vehicle design. Such specifications may be established only through analysis and study of a particular design problem.

Assessment of the natural environment in early stages of a space vehicle development program will be advantageous in developing a space vehicle with a minimum operational sensitivity to the environment. For those areas of the environment that need to be monitored prior to and during tests and operations, this early planning will permit development of the required measuring and communication systems for accurate and timely monitoring of the environment.

The environment criteria data presented in this document were formulated based on discussions and requests from engineers involved in space vehicle development and operations; therefore, they represent responses to actual engineering problems and are not just a general compilation of environmental data. This report is used extensively by various government and private space vehicle development organizations in design and operational studies. Inquiries may be directed through appropriate organizational channels for subsequent communications to the Atmospheric Sciences Division, Space Sciences Laboratory, MSFC.

Based on known and projected user requirements, it was decided that it is more advantageous to present the natural environment parameters grouped according to spatial regions rather than scientific disciplinary areas. These spatial areas are interplanetary space and those surrounding the individual planets and the earth's moon. The outer limits depends upon the component of the environment being discussed. For clarity in discussion, limits have been arbitrarily taken to be 10 radii above the surface of the planet or moon. In the discussion of the meteoroid environment, however, the limits extend to a point where the gravitational attraction of the planet or moon becomes negligible.

Some of the space and planetary environmental data available today are speculative and will remain so until additional satellites, planetary probes, and manned space flights provide more information. Therefore, care must be used in the interpretation and use of available space environment data for a specific design decision. Although the data in this document provide valuable guides for preliminary design studies and analyses, their use for final program decisions depends upon the specific design problem involved. This report was prepared

primarily for use in NASA space vehicle development and advanced study projects. The data contained in this document are reviewed on a continuing basis, and revision or amendments will be published as necessary. The numbers given in brackets refer to references given at the end of each section.

ACKNOWLEDGMENTS

The following personnel of the MSFC Space Sciences Laboratory have read parts of this document and have offered comments, corrections, and suggestions in their various fields of expertise. This assistance contributed to the value of this publication and is greatly appreciated.

The MSFC Space Sciences Laboratory organizational name and symbol (Division) precedes each grouping of names:

ES51 Solar-Terrestrial Physics Division
- Mr. Bernard Blake
- Dr. Charles Chappell
- Dr. Anthony deLoach
- Dr. Mona Hagyard
- Mr. E. J. Reichmann
- Mr. William Snoddy
- Dr. Gary Swenson
- Dr. Einar Tandberg-Hanssen

ES61 Space Physics Division
- Mr. Stuart Clifton
- Dr. Rudolf Decher
- Mr. Edgar Miller
- Dr. Thomas Parnell
- Dr. Eugene Urban

ES71 Space Processing Division
- Dr. Roger Kroes
- Dr. Robert Naumann

ES81 Atmospheric Sciences Division
- Dr. Nicholas Costes
- Dr. Robert Smith
- Mr. O. H. Vaughan
- Dr. William Vaughan

University of Texas San Antonio and Southwest Research Institute
- Dr. James Burch

SPACE AND PLANETARY ENVIRONMENT CRITERIA GUIDELINES FOR USE IN SPACE VEHICLE DEVELOPMENT, 1977 REVISION

SECTION I. INTERPLANETARY SPACE ENVIRONMENT

1.1 Definition

Interplanetary space is defined as the region from the sun to the outer limits of the solar system, exclusive of those regions under the predominant influence of the individual planetary systems.

1.2 Gas Properties

The sun is coupled to the environments of the planets through the interplanetary medium. The sun's varying input to this medium and its impact on solar wind particle radiation and plasma flow is of primary importance. For design purposes, the following nominal gas properties should be employed. For additional information, see Table 1 in Xanthakis [I-1].

1.2.1 Kinetic Gas Temperature

Approximately 2×10^5 K.

1.2.2 Gas Pressure

Approximately 10^{-15} N/cm^2.

1.2.3 Density

Approximately 10^{-23} g/cm^3.

1.2.4 Composition

The composition of interplanetary space is primarily hydrogen, protons, helium, and alpha particles.

1.3 Radiation Environment

A spacecraft on an interplanetary trajectory is constantly exposed to charged and uncharged particles and to photons. When an encounter occurs,

a charge transfer to or from the body will occur. This mechanism of charge transfer can be classified as either charge collection or charge emission. The most important processes are the collection of environmental electrons and ions, and photoionization. There are other, less important charging mechanisms, such as cosmic rays and collisions with dust grains.

A distinction should be made in the charge buildup process between highly energetic particles and lower energy, thermal particles in that the latter are influenced by the spacecraft charge present whereas the former are essentially unaffected by spacecraft charge. It is also noted that the production of electrons by photoionization is dependent on the target material and perhaps even the cleanliness of the material (presence of oxides).

1.3.1 Galactic Cosmic Radiation

Composition:

~ 85 percent proton (H^+)

~ 13 percent alpha particles (He^{++})

~ 2 percent nuclei of elements Li → Fe

(in approximate cosmic abundance) .

Flux at sunspot minimum: ~4 protons/cm^2 s (isotropic) .

Integrated yearly rate: ~ 1.3×10^8 protons/cm^2 .

Flux at sunspot maximum: ~2.0 protons/cm^2 s (isotropic) .

Integrated yearly rate: ~ 7×10^7 protons/cm^2 .

Energy range: 40 MeV to 10^{13} MeV .

Integrated dose (without shielding): ~4 to 10 rad/year.

1.3.2 Solar Activity

Changes of the interplanetary radiation environment is dominated by solar activity. Characteristics of this environment are found in the following sections. Considerable additional discussions of this subject exist in the literature. A classic treatise of this subject was given by Tandberg-Hanssen [I-2].

1.3.2.1 Solar High Energy Particle Radiation

Composition: Predominantly of protons (H^+) and alpha particles (He^{++}).

Integrated yearly flux at 1 AU:

Energy > 30 MeV, $N \approx 8 \times 10^9$ protons/cm^2 near solar maximum.

$N \approx 5 \times 10^5$ protons/cm^2 near solar minimum.

Energy > 100 MeV, $N \approx 6 \times 10^8$ protons/cm^2 near solar maximum.

$N \approx 5 \times 10^4$ protons/cm^2 near solar minimum.

Maximum dosage with shielding of 5 g/cm^2 (equivalent thickness):

~ 200 rad per week (three flares), skin dose at a point detector.

This radiation environment applies for a solar distance of 1.0 AU. Since the dispersion processes acting upon this environmental parameter have not yet been defined, an accurate description of the radiation environment for solar distances of 0.5 and 1.75 AU cannot be provided. A rough estimate may be to scale by R^{-2} for implied spatial continuity.

1.3.2.1.1 Solar Flare Particle Events

A solar flare is a bright eruption of the sun's chromosphere associated with the release of large amounts of energy into the interplanetary medium. For particle emission from solar flares, see Svestka, Chapter V [I-3].

1.3.2.1.2 Particle Flux Spectrum

The time-integrated spectrum describing the particle flux for a given solar flare particle event is given by

$$J(>P) = N_o \exp(-P/P_o),$$

4070

where

$J(>P)$ = particles/cm^2-flare having rigidity greater than P.

N_o = constant determined from P_o and $J(>P)$.

P_o = characteristic rigidity in units of MV.

P = magnetic rigidity in MV, which is related to the particle kinetic energy (E) in MeV by

$$P(E) = \frac{\sqrt{E^2 + 2ME}}{q}$$

q = total electron charge (1 for protons, 2 for alpha particles)

M = particle rest mass energy (MeV) .

For protons and alpha particles,

$$P \approx \frac{\sqrt{2ME}}{q} = 43.5\sqrt{E}$$

when

$$E \leq 100 \text{ MeV},$$

and

$$P \approx \frac{E}{q}$$

when

$$E \geq 10^5 \text{ MeV} .$$

1.3.2.1.3 Free Space Dose Rates

The free space dose rates associated with 20 of the more energetic solar flare particle events that have occurred in the past are given in Table I-1 [I-4].

TABLE I-1. TOTAL ESTIMATED SOLAR FLARE DOSES BY EVENT FOR 10 SHIELDING CONFIGURATIONS

Date	Shielding Configuration									
	1/0[a]	2/0	5/0	10/0	20/0	1/5	2/5	5/5	10/5	20/5
2/23/56	280.00	181.00	91.80	50.20	24.80	64.78	58.00	43.75	30.40	17.90
8/3/56	8.50	5.00	2.20	1.00	0.40	1.39	1.21	0.85	0.53	0.27
1/20/57	122.00	43.50	8.30	1.80	0.30	3.42	2.57	1.23	0.46	0.11
8/29/57	77.00	25.10	4.20	0.80	0.10	1.63	1.20	0.54	0.19	0.04
10/20/57	18.50	10.30	4.10	1.80	0.70	2.53	2.17	1.46	0.88	0.41
3/23/58	148.00	53.60	10.90	2.50	0.40	4.67	3.55	1.75	0.69	0.17
7/7/58	150.00	53.70	10.50	2.30	0.40	4.38	3.30	1.60	0.61	0.15
8/16/58	23.70	8.60	1.80	0.40	0.10	0.75	0.57	0.28	0.11	0.03
8/22/58	45.00	14.90	2.50	0.50	0.10	0.96	0.71	0.32	0.11	0.02
8/26/58	75.00	23.10	3.40	0.50	0.10	1.19	0.85	0.36	0.11	0.02
5/10/59	470.00	211.10	59.30	18.30	4.40	30.18	24.28	13.60	6.70	2.10
7/10/59	420.00	214.00	73.20	27.40	8.40	41.56	34.65	21.76	11.84	4.80
7/14/59	650.00	284.50	75.90	22.30	5.00	37.56	30.00	16.75	7.80	2.50
7/16/59	382.00	194.80	67.20	25.30	7.80	38.30	31.98	20.16	11.03	4.50
9/3/60	13.00	7.20	2.90	1.20	0.50	1.77	1.52	0.10	0.06	0.03
11/12/60	484.00	269.60	105.50	44.90	16.20	64.53	55.12	36.87	21.83	10.05
11/15/60	288.00	151.90	55.90	22.40	7.50	30.04	7.91	18.14	10.33	4.49
11/20/60	17.30	9.50	3.60	1.50	0.05	2.14	1.82	1.20	0.69	0.31
7/12/61	25.70	8.40	1.40	0.30	0.03	0.54	0.40	0.18	0.06	0.01
7/18/61	128.00	64.20	21.60	8.00	2.40	12.16	10.11	6.30	3.39	1.35

a. Shielding configurations are given as X/Y where X is the shielding thickness in g/cm^2 of aluminum and Y is the shielding thickness in g/cm^2 of tissue.

1.3.3 Radiation Properties of the Sun (Thermal)

1.3.3.1 Solar Radiation [I-5]

The solar constant refers to the rate at which energy is received upon a unit surface, oriented perpendicular to the sun's direction, in free space at some mean distance from the sun. The magnitude of the solar constant is determined by integrating the measured spectral irradiance over all wavelengths (see Table I-2 [I-6] for solar spectral irradiance data). The solar radiation spectrum is plotted in Figure I-1 as a function of wavelength.

Solar constant at 1.0 AU: 1353 ± 13.5 W/m^2; 1.94 ± 0.02 cal/cm^2 min; this thermal radiation varies with distance from sun following the R^{-2} relation.

Perihelion to aphelion variation of the solar constant is 3.43 to -3.26 percent. For example, solar constant in space equals solar constant at 1 AU/R^2 where R is the distance from the sun in AUs.

Solar Irradiance at the Distance of Semi-Major Axis for the Nine Planets

Planet	Solar Constant Relative to Earth	W m^{-2}
Mercury	6.6735	9029
Venus	1.9113	2586
Earth	1.000	1353
Mars	0.4307	582.8
Jupiter	0.03695	49.9
Saturn	0.01099	14.87
Uranus	0.002718	3.678
Neptune	0.001106	1.496
Pluto	0.000643	0.870

TABLE I-2. SOLAR SPECTRAL IRRADIANCE (OUTSIDE ATMOSPHERE) AND SOLAR RADIATION AFTER ABSORPTION BY CLEAR ATMOSPHERE [I-6]

Wavelength (μm) λ	Solar Spectral Irradiance ($W\,cm^{-2}\,\mu m^{-1}$)	Area Under Solar Spectral Irradiance Curve ($W\,cm^{-2}$)	Solar Radiation After One Atmosphere Absorption ($W\,cm^{-2}\,\mu m^{-1}$)	Area Under One Atmosphere Solar Radiation Curve ($W\,cm^{-2}$)	Percentage of Solar Radiation After One Atmosphere Absorption for Wavelengths Shorter than λ (%)
0.120	0.000010	0.00000060	0.000000	0.000000	0.00
0.140	0.000003	0.00000073	0.000000	0.000000	0.00
0.150	0.000007	0.00000078	0.000000	0.000000	0.00
0.160	0.000023	0.00000093	0.000000	0.000000	0.00
0.170	0.000063	0.00000136	0.000000	0.000000	0.00
0.180	0.000125	0.00000230	0.000000	0.000000	0.00
0.190	0.000271	0.00000428	0.000000	0.000000	0.00
0.200	0.00107	0.000010	0.000001	0.000000	0.00
0.210	0.00229	0.000027	0.000003	0.000000	0.00
0.220	0.00575	0.000067	0.000007	0.000000	0.00
0.225	0.00649	0.000098	0.000007	0.000000	0.00
0.230	0.00667	0.000131	0.000008	0.000000	0.00
0.235	0.00593	0.000162	0.000007	0.000000	0.00
0.240	0.00630	0.000193	0.000007	0.000000	0.00
0.245	0.00723	0.000227	0.000008	0.000000	0.00
0.250	0.00704	0.000263	0.000008	0.000000	0.00
0.255	0.0104	0.000306	0.000012	0.000000	0.00
0.260	0.0130	0.000365	0.000015	0.000000	0.00
0.265	0.0185	0.000443	0.000021	0.000000	0.00
0.270	0.0232	0.000548	0.000026	0.000000	0.00
0.275	0.0204	0.000657	0.000023	0.000000	0.00
0.280	0.0222	0.000763	0.000025	0.000000	0.00
0.285	0.0315	0.000897	0.000036	0.000001	0.00
0.290	0.0482	0.001097	0.000055	0.000001	0.00
0.295	0.0584	0.001363	0.000066	0.000001	0.00
0.300	0.0514	0.001638	0.006677	0.000035	0.03
0.305	0.0603	0.001917	0.019830	0.000134	0.12
0.310	0.0689	0.002240	0.029084	0.000279	0.25
0.315	0.0764	0.002603	0.038941	0.000474	0.42
0.320	0.0830	0.003002	0.047684	0.000712	0.64
0.325	0.0975	0.003453	0.062018	0.001022	0.92
0.330	0.1059	0.003961	0.073829	0.001392	1.25
0.335	0.1081	0.004496	0.080896	0.001796	1.61
0.340	0.1074	0.005035	0.084636	0.002219	1.99
0.345	0.1069	0.005571	0.087080	0.002655	2.39
0.350	0.1093	0.006111	0.091327	0.003111	2.80
0.355	0.1083	0.006655	0.092186	0.003572	3.40
0.360	0.1068	0.007193	0.092857	0.004036	3.63
0.365	0.1132	0.007743	0.099873	0.004536	4.08
0.370	0.1181	0.008321	0.105507	0.005063	4.55
0.375	0.1157	0.008906	0.104596	0.005586	5.03
0.380	0.1120	0.009475	0.102971	0.006101	5.49
0.385	0.1098	0.010030	0.102273	0.006613	5.95
0.390	0.1098	0.010579	0.103977	0.007132	6.42
0.395	0.1189	0.011150	0.114309	0.007704	6.93
0.400	0.1429	0.011805	0.137403	0.008391	7.55
0.405	0.1644	0.012573	0.158076	0.009181	8.26
0.410	0.1751	0.013422	0.168365	0.010023	9.02
0.415	0.1774	0.014303	0.170576	0.010876	9.79
0.420	0.1747	0.015183	0.167980	0.011716	10.54
0.425	0.1693	0.016043	0.162788	0.012530	11.28
0.430	0.1639	0.016876	0.157596	0.013318	11.99
0.435	0.1663	0.017702	0.159903	0.014117	12.71
0.440	0.1810	0.018570	0.174038	0.014988	13.40
0.445	0.1922	0.019503	0.184807	0.015912	14.30
0.450	0.2006	0.020485	0.192884	0.016876	15.19
0.455	0.2057	0.021501	0.195904	0.017656	16.07
0.460	0.2066	0.022532	0.196761	0.018839	16.96
0.465	0.2048	0.023560	0.196923	0.019824	17.84
0.470	0.2033	0.024580	0.195480	0.020801	18.72

TABLE I-2. (Continued)

Wavelength (μm) λ	Solar Spectral Irradiance ($W\ cm^{-2}\ \mu m^{-1}$)	Area Under Solar Spectral Irradiance Curve ($W\ cm^{-2}$)	Solar Radiation After One Atmosphere Absorption ($W\ cm^{-2}\ \mu m^{-1}$)	Area Under One Atmosphere Solar Radiation Curve ($W\ cm^{-2}$)	Percentage of Solar Radiation After One Atmosphere Absorption for Wavelengths Shorter than λ (%)
0.475	0.2044	0.025600	0.196538	0.021784	19.61
0.480	0.2074	0.026629	0.197523	0.022772	20.50
0.485	0.1976	0.027642	0.186415	0.023704	21.34
0.490	0.1950	0.028623	0.183962	0.024624	22.17
0.495	0.1960	0.029601	0.183177	0.025539	22.99
0.500	0.1942	0.030576	0.179814	0.026439	23.80
0.505	0.1920	0.031542	0.176146	0.027319	24.60
0.510	0.1882	0.032492	0.172660	0.028183	25.37
0.515	0.1833	0.033421	0.168165	0.029023	26.13
0.520	0.1833	0.034337	0.168165	0.029864	26.88
0.525	0.1852	0.035259	0.169908	0.030714	27.65
0.530	0.1842	0.036182	0.168990	0.031559	28.41
0.535	0.1818	0.037097	0.166788	0.032393	29.16
0.540	0.1783	0.037997	0.163977	0.033211	29.90
0.545	0.1754	0.038882	0.160917	0.034015	30.62
0.550	0.1725	0.039751	0.158256	0.034806	31.33
0.555	0.1720	0.040613	0.157798	0.035595	32.05
0.560	0.1695	0.041466	0.155504	0.036373	32.75
0.565	0.1705	0.042316	0.156422	0.037155	33.45
0.570	0.1712	0.043171	0.157064	0.037940	34.16
0.575	0.1719	0.044028	0.157726	0.038729	34.87
0.580	0.1715	0.044887	0.157339	0.039516	35.57
0.585	0.1712	0.045744	0.157064	0.040301	36.28
0.590	0.1700	0.046597	0.155963	0.041081	36.98
0.595	0.1682	0.047442	0.154311	0.041852	37.68
0.600	0.1666	0.048279	0.152844	0.042616	38.37
0.605	0.1647	0.049107	0.151100	0.043372	39.05
0.610	0.1635	0.049928	0.150000	0.044122	39.72
0.620	0.1602	0.051546	0.146972	0.045592	41.05
0.630	0.1570	0.053132	0.145370	0.047045	42.30
0.640	0.1544	0.054689	0.144299	0.048488	43.66
0.650	0.1511	0.056217	0.142547	0.049914	44.94
0.660	0.1486	0.057715	0.141523	0.051329	46.22
0.670	0.1456	0.059186	0.140000	0.052729	47.48
0.680	0.1427	0.060628	0.137211	0.054101	48.71
0.690	0.1402	0.062042	0.134807	0.055449	49.93
0.700	0.1369	0.063428	0.131634	0.056766	51.11
0.710	0.1344	0.064784	0.129230	0.058058	52.27
0.720	0.1314	0.066113	0.126346	0.059321	53.41
0.730	0.1290	0.067415	0.124038	0.060562	54.53
0.740	0.1260	0.068690	0.121153	0.061773	55.62
0.750	0.1235	0.069938	0.118750	0.062961	56.69
0.800	0.1107	0.075793	0.106442	0.068283	61.48
0.850	0.0988	0.081030	0.095000	0.073033	65.76
0.900	0.0889	0.085723	0.080090	0.077037	69.36
0.950	0.0835	0.090033	0.077314	0.080903	72.84
1.000	0.0746	0.093985	0.071730	0.084490	76.07
1.100	0.0592	0.100675	0.056923	0.090182	81.20
1.200	0.0484	0.106055	0.046538	0.094836	85.39
1.300	0.0396	0.110455	0.036000	0.098436	88.63
1.400	0.0336	0.114115	0.002240	0.098660	88.83
1.500	0.0287	0.117230	0.027333	0.101393	91.29
1.600	0.0244	0.119885	0.023461	0.103739	93.40
1.700	0.0202	0.122115	0.019423	0.105681	95.15
1.800	0.0159	0.123920	0.013826	0.107064	96.40
1.900	0.0126	0.125345	0.000126	0.107077	96.41
2.000	0.0103	0.126490	0.009809	0.108057	97.29
2.100	0.0090	0.127455	0.008653	0.108923	98.07
2.200	0.0079	0.128300	0.007596	0.109682	98.76
2.300	0.0068	0.129035	0.006538	0.110336	99.34

TABLE I-2. (Concluded)

Wavelength (μm) λ	Solar Spectral Irradiance ($W\ cm^{-2}\ \mu m^{-1}$)	Area Under Solar Spectral Irradiance Curve ($W\ cm^{-2}$)	Solar Radiation After One Atmosphere Absorption ($W\ cm^{-2}\ \mu m^{-1}$)	Area Under One Atmosphere Solar Radiation Curve ($W\ cm^{-2}$)	Percentage of Solar Radiation After One Atmosphere Absorption for Wavelengths Shorter than λ (%)
2.4	0.0064	0.129695	0.006153	0.110951	99.90
2.5	0.0054	0.130285	0.001080	0.111059	100.00
2.6	0.0048	0.130795	0.000005	0.111060	100.00
2.7	0.0043	0.131250	0.000004	0.111060	100.00
2.8	0.00390	0.131660	0.000004	0.111061	100.00
2.9	0.00350	0.132030	0.000004	0.111061	100.00
3.0	0.00310	0.132360	0.000003	0.111061	100.00
3.1	0.00260	0.132645	0.000002	0.111062	100.00
3.2	0.00226	0.132888	0.000002	0.111062	100.00
3.3	0.00192	0.133097	0.000002	0.111062	100.00
3.4	0.00166	0.133276	0.000001	0.111062	100.00
3.5	0.00146	0.133432	0.000001	0.111062	100.00
3.6	0.00135	0.133573	0.000001	0.111062	100.00
3.7	0.00123	0.133702	0.000001	0.111062	100.00
3.8	0.00111	0.133819	0.000001	0.111063	100.00
3.9	0.00103	0.133926	0.000001	0.111063	100.00
4.0	0.00095	0.134025	0.000001	0.111063	100.00
4.1	0.00087	0.134116	0.000001	0.111063	100.00
4.2	0.00078	0.134198	0.000000	0.111063	100.00
4.3	0.00071	0.134273	0.000000	0.111063	100.00
4.4	0.00065	0.134341	0.000000	0.111063	100.00
4.5	0.00059	0.134403	0.000000	0.111063	100.00
4.6	0.00053	0.134459	0.000000	0.111063	100.00
4.7	0.00048	0.134509	0.000000	0.111063	100.00
4.8	0.00045	0.134556	0.000000	0.111063	100.00
4.9	0.00041	0.134599	0.000000	0.111063	100.00
5.0	0.0003830	0.13463906	0.000000	0.111063	100.00
6.0	0.0001750	0.13491806	0.000000	0.111063	100.00
7.0	0.0000990	0.13505506	0.000000	0.111063	100.00
8.0	0.0000600	0.13513456	0.000000	0.111063	100.00
9.0	0.0000380	0.13518356	0.000000	0.111063	100.00
10.0	0.0000250	0.13521506	0.000000	0.111063	100.00
11.0	0.0000170	0.13523606	0.000000	0.111063	100.00
12.0	0.0000120	0.13525056	0.000000	0.111063	100.00
13.0	0.0000087	0.13526091	0.000000	0.111063	100.00
14.0	0.0000055	0.13526801	0.000000	0.111063	100.00
15.0	0.0000049	0.13527321	0.000000	0.111063	100.00
16.0	0.0000038	0.13527756	0.000000	0.111063	100.00
17.0	0.0000031	0.13528101	0.000000	0.111063	100.00
18.0	0.0000024	0.13528376	0.000000	0.111063	100.00
19.0	0.0000020	0.13528596	0.000000	0.111063	100.00
20.0	0.0000016	0.13528776	0.000000	0.111063	100.00
25.0	0.000000610	0.13529328	0.000000	0.111063	100.00
30.0	0.000000300	0.13529556	0.000000	0.111063	100.00
35.0	0.000000160	0.13529671	0.000000	0.111063	100.00
40.0	0.000000094	0.13529734	0.000000	0.111063	100.00
50.0	0.000000038	0.13529800	0.000000	0.111063	100.00
60.0	0.000000019	0.13529829	0.000000	0.111063	100.00
80.0	0.000000007	0.13529855	0.000000	0.111063	100.00
100.0	0.000000003	0.13529865	0.000000	0.111063	100.00
1000.0	0.000000000	0.13530000	0.000000	0.111063	100.00

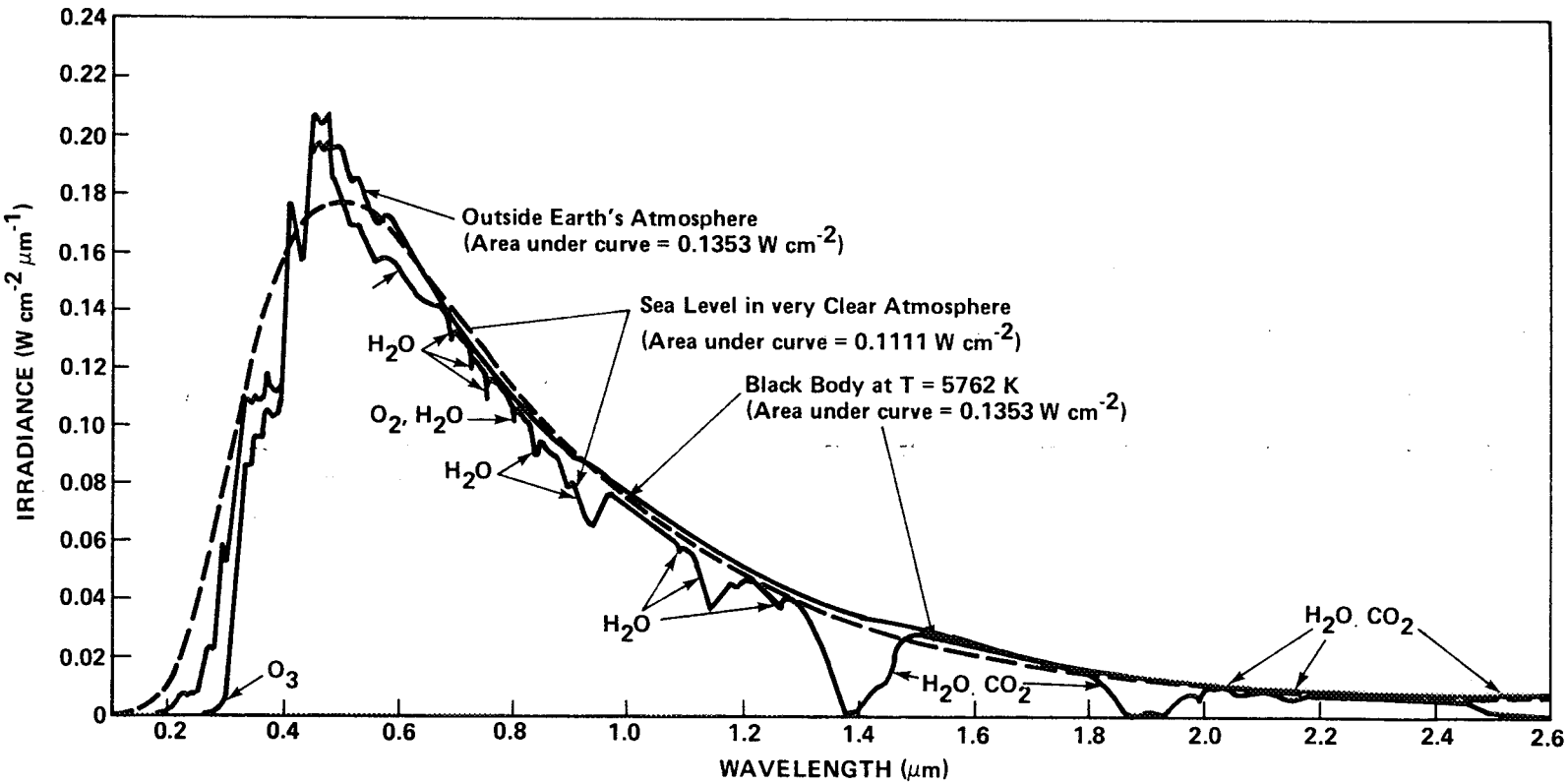

Figure I-1. Normally incident solar radiation at sea level on very clear days, solar spectral irradiance outside the earth's atmosphere at 1 AU, and black body spectral irradiance curve at T = 5762 K (normalized to 1 AU) [I-6].

The mean brightness of solar disk outside the atmosphere is 6.33×10^5 lamberts or 2.015×10^9 cd/m^2. Solar illumination is (1.37×10^5) R^{-2} lm/m^2 where R is the distance from the sun (AU).

1.3.3.1.1 Visible and Infrared Radiation [I-5, I-7]

Radiant energy distribution:

Approximated by that from a 5800 K blackbody.

Fraction of solar radiation:

Above 7000 Å = 53.12 percent.

Above 4000 Å ~ 91.28 percent.

3000 Å - 30 000 Å = 96.62 percent.

1.3.3.1.2 Ultraviolet and X-Ray Radiation [I-5]

Fraction of solar radiation:

Below 4000 Å = 8.72 percent.

Below 3000 Å = 1.21 percent.

Below 2000 Å = 0.008 percent (variable).

Below 1000 Å = 10^{-4} percent (variable).

Principle line emission fluxes at 1.0 AU:

Lyman Alpha HI (1215.67A): 51.0×10^{-4} W/m^2

HE II (303.8A): 2.5×10^{-4} W/m^2

HI (1025.72A): 0.60×10^{-4} W/m^2

C III (977A): 0.50×10^{-4} W/m^2.

X-ray flux:

	2 to 8 Å	8 to 20 Å	20 to 200 Å
Sunspot min (quiet sun)	3×10^{-9} W/m^2	4×10^{-7} W/m^2	1.3×10^{-4} W/m^2
Sunspot max (quiet sun)	2×10^{-6} W/m^2	2.3×10^{-5} W/m^2	1.0×10^{-3} W/m^2
Upper limit during flare activity	2.2×10^{-4} W/m^2	4.5×10^{-4} W/m^2	92×10^{-4} W/m^2

Strength of line emission flux varies as R^{-2}; e.g., flux in space is flux at 1.0 AU/R^2 where R is the solar distance (AU).

1.3.3.1.3 Solar Radiation Pressure

Pressure on a flat plate at 1.0 AU:

For 100 percent reflecting body = 9.02×10^{-6} N/m^2.

For blackbody = 4.51×10^{-6} N/m^2 .

Radiation pressure on a flat plate variation with solar distance follows the relation:

$P = S/c$ for blackbody

$P = 2\ S/c$ for 100 percent reflecting body

where

P = radiation pressure, N/m^2

S = solar constant at specified solar distance, Wm^{-2}

and

c = speed of light, m/s

1.3.3.1.4 Solar Wind

Mean Density:

0.5 AU = ~ 20 hydrogen atoms/cm^3

1.0 AU = ~ 5 hydrogen atoms/cm^3

1.75 AU = ~ 2 hydrogen atoms/cm^3

Mean Flux:

0.5 AU = ~ 8×10^8 hydrogen atoms/cm^2 s

1.0 AU = ~ 2×10^8 hydrogen atoms/cm^2 s

1.75 AU = ~ 10^8 hydrogen atoms/cm^2 s.

Mean velocity of solar wind from 0.5 to 1.75 AU is 450 to 500 km/s. (Mariner II results: protons 563-690 km/s, Explorer X: 300 km/s, IMP 6 results: Reference I-8).

1.3.4 Solar Radio Noise

Noise power flux = $\frac{(4.5 \times 10^{-31})\ (f)^{1.1}}{R^2}$ W/m^2 Hz, where f is frequency (Hz) and R is astronomical units distance from sun.

Approximate noise power at 1.0 AU, quiet sun: 10^{-19} W/m^2 Hz at 1.0 cm wavelength to 10^{-22} W/m^2 Hz at 400 cm wavelength.

During solar storms, noise power may increase from 1 to 8 orders of magnitude. The variation with sunspots is greatest between 6 to 200 cm wavelengths, with the spectral power showing a range of variation of 4 orders of magnitude.

1.3.4.1 Characteristics of Solar Radio Noise

Type	Identifying Characteristics	Source Characteristics	Frequency Characteristics
I	Noise storms usually lasting from hours to days; or bursts of ~ 1 s duration.	Assumed to be of a nonthermal origin, associated with sunspots, "R centers," and sometimes flares.	Less than ~ 250 MHz with bandwidth 1 to 10 MHz/s for bursts and 10 to 100 MHz/s for continuum. The intensity at 100 MHz/s, 10^{-21} to 10^{-19} W/m^2 (Hz/s).

Type	Identifying Characteristics	Source Characteristics	Frequency Characteristics
II	Bursts with slow drift of ~ 0.3 MHz/s^2 lasting from 5 to 10 min.	Source is due to plasma oscillations associated with flares. Occurrence begins about 7 min after flare. The source moves outward at ~ 1000 km/s.	Mainly less than 150 MHz/s with the bandwidth of about 2×10^{-1} of the observed frequency. Intensity usually at 100 MHz/s, 10^{-20} to 10^{-19} W/m^2 (Hz/s).
III	Bursts with fast drift of ~ 0.3 MHz/s^2 lasting singly 3-10 s or in groups of 1 to 5 min.	Assumed to be associated with plasma oscillation associated 50-60% of the time with flares. The source has an outward velocity of $\sim 10^5$ km/s.	Ranges from < 4000 MHz/s to > 10 MHz/s with a bandwidth almost equal to the frequency. The intensity usually is less than 10^{-20} W/m^2 (Hz/s).
IV	Smooth continuum lasting from minutes to hours.	Source is due to synchrotron radiation. Occurring 70 to 80% of the time with flares at ~ 15 min after start. Initial source velocity ranges from 1 to 5×10^3 km/s for about 10 min and then source becomes stationary.	Cover the complete radio band but vary from burst to burst. The bandwidth is frequently several octaves with intensities from 10^{-20} to 10^{-19} W/m^2 (Hz/s).
V	Smooth continuum lasting from 1 to 2 min.	Synchrotron radiation occurring before the maximum of solar flares. The velocity of the source is $\sim 5 \times 10^3$ km/s.	Frequencies less than 200 MHz/s with a bandwidth of several MHz/s at 50 to 100 MHz/s. Intensities, 10^{-20} to 10^{-19} W/m^2 (Hz/s).

Type	Identifying Characteristics	Source Characteristics	Frequency Characteristics
Micro-wave	Continuum and bursts lasting 0.5 to 20 min.	Assumed to be of synchrotron and possibly thermal origin associated about 80% of the time with flares.	The frequency range is ~1000 to 20 000 MHz/s with a bandwidth of several octaves. The intensity is usually $\sim 5 \times 10^{-22}$ to 5×10^{-20} W/m^2 (Hz/s) at 3000 MHz/s.

1.3.5 Additional Information

Additional information relative to the interplanetary radiation environment is given in References I-4, I-6, I-9, and I-10.

1.4 Meteoroids, Asteroids, and Comets

Major meteor streams, asteroids, and comets are listed in Tables I-3, I-4, and I-5; for additional detailed information on comets, consult References I-11, I-12, I-13, I-14, and I-15.

1.4.1 Cometary Meteoroids

1.4.1.1 Spatial Density

The spatial density (gm/m^3) of cometary meteoroids is expressed mathematically as follows: For $10^{-6} \leq m \leq 10^{-2}$,

$$\log S_c = -18.173 - 1.213 \log m - 1.5 \log R - 0.869 \left|\sin \beta\right| ,$$

and for $10^{-12} \leq m \leq 10^{-6}$,

$$\log S_c = -18.142 - 1.584 \log m - 0.063 (\log m)^2 - 1.5 \log R - 0.869 \sin \beta .$$

Spatial density is related to flux on a randomly tumbling surface by

$$F_c = \frac{1}{4} S_c V_c$$

TABLE I-3. ORBITAL ELEMENTS FOR MAJOR METEOR STREAMS [I-16]

Name	Period of Activity	Date Max.	F_{max}	Ω (deg)	π (deg)	ω (deg)	i (deg)	ϵ	q (AU)	a (AU)	Velocity		Period (Years)
											Geocentric (km/s)	Heliocentric (km/s)	
Quadrantids[a]	Jan. 2-4	Jan 3	8.0	282	92	166	67	0.46	0.97	1.7	42	39	13
Lyrid	April 19-22	April 21	0.85	30.5	--	210	81	0.88	0.90	---	48	40	19.8
η - Aquarid	May 1-8	May 4-6	2.2	45	152	108	162	0.96	0.66	17.95	64	41	11
0 - Cetid	May 14-23	May 14-23	2.0	238	89	211	34	0.91	0.11	1.3	37	33	1.5
Arietid	May 29-June 19	June 6	4.5	77	106	29	21	0.94	0.09	1.6	38	34	1.8
ζ - Perseid	June 1-16	June 6	3.0	78	--	59	4 ± 2	0.79	0.35	1.6	29	35	2.2
β - Taurids	June 24-July 5	June 28	2.0	276	162 ± 4	246 ± 4	9 ± 4	0.86	0.36	2.5	31	37	3.3
δ - Aquarid	July 26-Aug. 5	July 28	1.5	305	101 ± 2	156 ± 2	24 ± 5	0.96	0.08	1.8	40	35	3.6
Perseid	July 15-Aug. 18	Aug. 10-14	5.0	142	--	155	114	0.96	0.97	23.0	60	42	109.5
Giacobinid[a]	Oct. 9-10	Oct. 10	20.0	196	--	172	30.8	0.72	0.99	3.5	23	41	6.57
Orionid	Oct. 15-25	Oct. 20-23	1.2	29.3	103	87.8	163	0.92	0.54	6.32	66	41.5	--
Arietid, Southern	Oct. - Nov.	Nov. 5	1.1	27	150	122	6	0.85	0.30	1.91	28	36	2.64
Taurids, Northern	Oct. 26-Nov. 22	Nov. 10	0.4	221	160	308	2.5	0.86	0.31	2.16	29	37	3.2
Taurids, Night	Nov.		1.0	220	160	300	3	0.86	0.3	2.1	37	37	3.3
Taurids, Southern	Oct. 26-Nov. 22	Nov. 5	0.9	45	157	112	5.1	0.85	0.36	2.39	28	38	3.69
Leonid[a]	Nov. 15-20	Nov. 16-17	0.9	234	49	179	162	0.92	0.99	12.8	72	41	33.25
Bielids[a]	Nov. 15-Dec. 6		2.5	250	109	223	13	0.76	0.88	3.6	16	39.5	6.6
Geminid	Nov. 25-Dec. 17	Dec. 12-13	4.0	261	--	324	24	0.90	0.14	1.4	35	35	1.7
Ursids	Dec. 20-24	Dec. 22	2.5	270	--	210	5 ± 3	1.0	0.92	---	37	42	--

a. Periodic streams

TABLE I-4. ORBITAL ELEMENTS FOR SOME ASTEROIDS [I-16, I-17]

Cat. No.	Name	Year of Discovery	Diameter (miles)	Opposition Magnitude	Semi-Major Axis of Orbit (AU)	Orbital Period (years)	Eccentricity	Inclination of Orbit (deg)
1	Ceres	1801	478.5	7.4	2.767	4.6	0.0802	10.60
2	Pallas	1802	304.5	8.0	2.770	4.61	0.2394	34.82
3	Juno	1804	118	8.7	2.670	4.36	0.2574	13.02
4	Vesta	1807	236	6.5	2.361	3.63	0.0889	7.14
5	Astræa	1845	49.7	9.9	2.577	4.13	0.1862	5.33
6	Hebe	1847	69.6	7.0	2.42	3.77	0.2019	11.65
7	Iris	1847	77.7	6.7	2.386	3.69	0.2309	5.47
8	Flora	1847	56	7.8	2.201	3.27	0.1567	5.88
9	Metis	1848	77.7	8.1	2.387	3.69	0.1233	5.60
12	Victoria	1850	37.3	8.1	2.334	3.57	0.2190	8.38
15	Eunomia	1851	?	7.4	2.644	4.30	0.1870	11.76
18	Melpomene	1852	59	7.7	2.296	3.48	0.2176	10.15
20	Massalia	1852	65.9	8.2	2.409	3.74	0.1426	0.68
192	Nausicaa	1879	46.6	7.5	2.403	3.72	0.2445	6.87
324	Bamberga	1892	59	7.3	2.68	4.39	0.3346	11.30
387	Aquitania	1894	66.5	8.2	2.74	4.53	0.2383	17.97
433	Eros	1898	15.5	7.2	1.458	1.76	0.2230	10.83
719	Albert	1911	2.5	12.0	2.58	4.16	0.54	10.82
851	Wladilena	1920	?	12.7	2.362	3.63	0.274	23.0
944	Hidalgo	1920	21.7	11.0	5.71	13.7	0.65	43.06
1036	Ganymede	1924	?	12.5	2.665	4.35	0.54	26.2
1221	Amor	1932	1.6	16.0	1.973	2.77	0.45	----
----	Apollo	1932	1.2	17.0	1.486	1.81	0.566	6.4
----	Adonis	1936	0.6	19.0	1.969	2.76	0.78	1.5
----	Hermes	1937	0.9	18.0	1.290	1.47	0.474	4.7
1566	Icarus	1949	0.9	12.6	1.078	1.12	0.827	23.0

TABLE I-5. COMETS [I-7]

Comet[a]	Recent Perihelion Date, and Return Number		Mean Orbital Elements[b]						
			P (year)	ω	Ω	i	e	q (AU)	a (AU)
Encke	1961.10	46	3.30	185	335	12.4	0.847	0.339	2.21
Grigg-Skjellerup	1957.09	9	4.90	356	215	17.6	0.704	0.855	2.89
Temple	1957.10	12	5.28	191	119	12.5	0.545	1.38	3.0
Kopff	1958.05	8	6.3	160	120	5	0.556	1.51	3.4
Giacobini-Zenner	1959.82	7	6.5	172	196	30.8	0.72	0.94	3.5
Schwass.-W.[c]	1961.68	6	6.53	358	126	3.7	0.384	2.155	3.50
Wirtanen	1961.29	3	6.67	343	86	13.4	0.543	1.62	3.55
Reinmuth	1960.90	3	6.7	45	296	7.0	0.46	1.93	3.6
Brooks	1960.46	10	6.75	197	177	5.6	0.50	1.76	3.6
Finlay	1960.67	7	6.85	321	42	3.5	0.705	1.07	3.6
Borrelly	1960.45	7	7.01	351	76	31.1	0.604	1.450	3.67
Faye	1955.17	14	7.42	201	206	10.6	0.565	1.655	3.80
Whipple	1955.91	4	7.42	190	189	10.2	0.356	2.450	3.80
Reinmuth	1958.23	4	7.67	13	124	8.4	0.478	2.03	3.90
Oterma	1958.44	Annual	7.89	355	155	4.0	0.144	3.39	3.96
Schaumasse	1960.29	6	8.18	52	86	12.0	0.705	1.195	4.05
Wolf	1959.22	10	8.42	161	204	27.3	0.396	2.505	4.15
Comas Sola	1961.26	5	8.57	40	63	13.5	0.577	1.775	4.19
Vaisala	1960.35	3	10.5	44	135	11.3	0.635	1.745	4.79
Schwass.-W.	1957.36	Annual	16.1	356	322	9.5	0.132	5.53	6.4
Neujmin	1948.96	3	17.9	347	347	15.0	0.774	1.54	6.8
Crommelin	1956.80	6	27.9	196	250	28.9	0.919	0.744	9.2
Olbers	1956.45	3	69.6	65	85	44.6	0.930	1.18	16.8
Pons-Brooks	1954.39	3	70.9	199	255	74.1	0.955	0.775	17.2
Halley	1910.30	29	76.2	112	57	162.3	0.967	0.587	17.8

a. These comets have appeared at least three times and are expected to reappear as predicted.

b. Orbital elements equinox 1950.

c. Schwassmann-Wachmann.

Note: This table is used with the permission of Oxford University Press (C. W. Allen's, Astrophysical Quantities).

(For Comet Kohoutek data, see Reference I-15)

where

S_c = number of cometary meteoroids of mass m or greater per m^3.

m = mass of the meteoroid in grams.

F_c = number of cometary meteoroids of mass m or greater per m^2/s.

R = distance from the sun in AUs.

V_c = average cometary velocity relative to the spacecraft (paragraph 1.4.1.2), m/s.

β = heliocentric latitude.

1.4.1.2 Cometary Meteoroid Velocity

The average velocity (m/s) of cometary meteoroids relative to the spacecraft, V_c, is expressed as follows:

$$V_c (R, \sigma, \theta) = R^{-1/2} U_c (\sigma, \theta)$$

where

R = distance from the sun in AUs.

U_c = cometary velocity parameter (Fig. I-2) as a function of σ and θ, km $(AU)^{1/2}/s$.

σ = ratio of the spacecraft's heliocentric speed at R to the speed of a circular orbit of radius R.

θ = angle between the spacecraft velocity vector and the surface of an imaginary sphere of radius R (deg).

1.4.2 Asteroidal Meteoroids

Asteroidal meteoroids need not be considered inside the orbit of Mars.

1.4.2.1 Asteroidal Flux-Mass Model

The model given here is an approximation of that given in Reference I-10. For $10^{-9} \leqq m \leqq 10^{9}$, $1.5 \leqq R \leqq 2.2$,

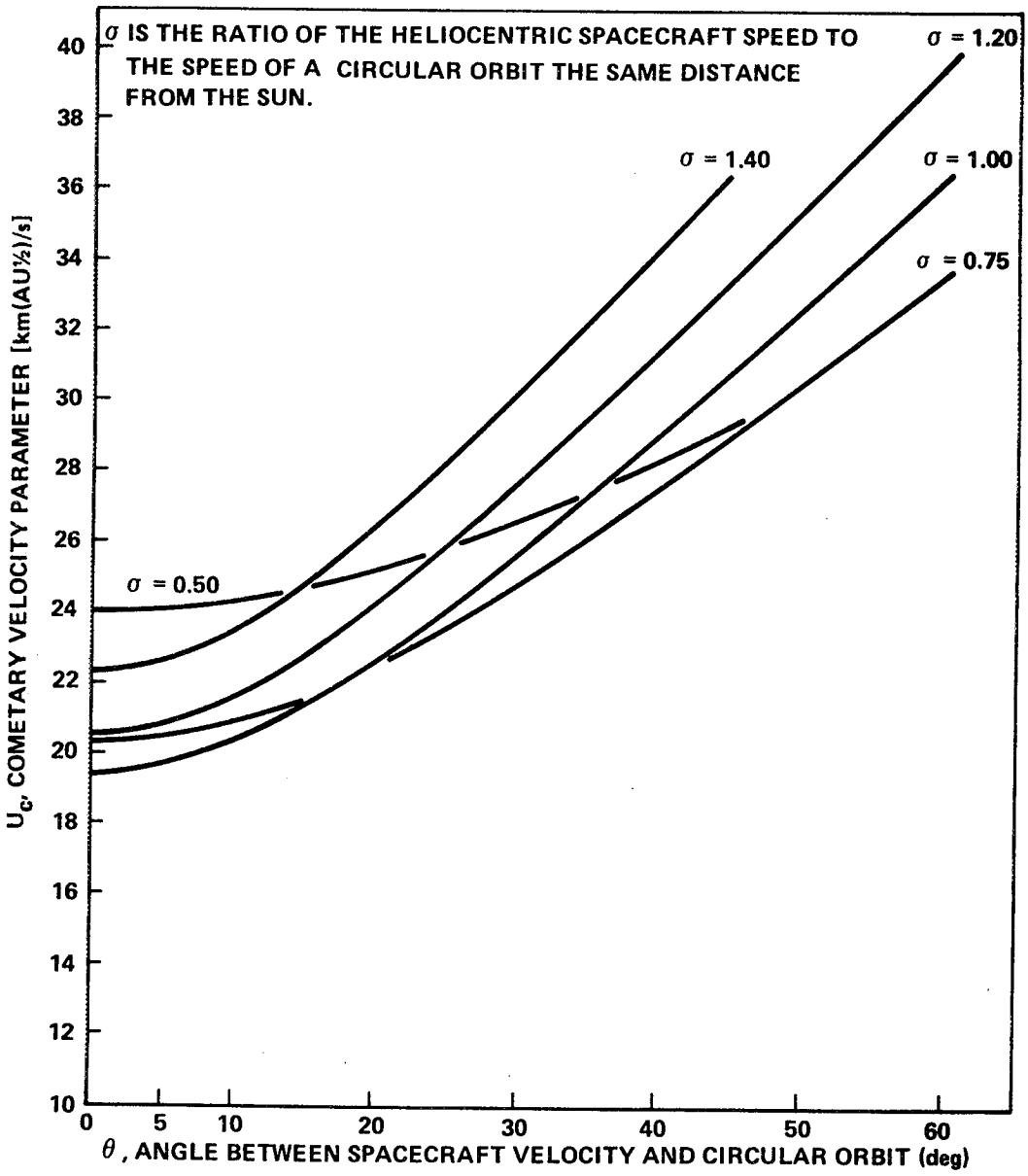

Figure I-2. Average relative velocity, cometary particles.

$$\log F_a = -15.89 - 0.84 \log m + 2.92 (R - 1),$$

where

F_a = number of asteroidal impacts/m^2 s of mass m or greater.

m = mass in grams.

R = distance from the sun in AUs.

1.4.2.2 Asteroidal Meteoroid Velocity

The average asteroidal velocity in this region of space is approximately 10 km/s.

1.4.2.3 Asteroidal Mass Density

The average asteroidal mass density is approximately 3.5 g/cm^3 .

1.4.3 Additional Information

Detailed information relative to asteroidal meteoroids and the interplanetary meteoroid environment is given in References I-18, I-19, and I-20.

1.5 Geomagnetic Environment

1.5.1 Magnetic Field

The principal magnetic field in space from 1.0 to 1.5 AU solar distance is that of the sun as carried by the solar plasma. The strength of the solar interplanetary magnetic field at 1.0 AU is about 5 γ, (5×10^{-5} Gauss). The strength of the field depends upon solar activity, with maximum field strength at maximum solar activity. Fluctuations of one or two orders of magnitude may occur depending upon solar activity.

The interplanetary field appears to be directed along the classical Archimedean spiral from the sun as described by Parker, but the remote possibility of a distorted solar dipole field should not be excluded.

1.6 Astrodynamic Constants

1.6.1 General Constants [I-21]

Astronomical Unit [I-13]: AU = 1.495978930×10^8 km.

Ephemeris-Universal Time reduction: The relationship between Ephemeris Time and Universal Time is given in "The American Ephemeris and Nautical Almanac," U. S. Government Printing Office. For example, the difference $\Delta T = ET - UT$ is approximated by $\Delta T(A)$

$\Delta T(A)$	= +46.7 s	for Jan. 1, 1976
	= +47.0 s	for Apr. 1, 1976
	= +47.3 s	for July 1, 1976
	= +47.5 s	for Oct. 1, 1976
	= +47.8 s	for Jan. 1, 1977

(For international atomic time formally introduced on 1 January 1972, see page vii of Reference I-21.)

1.6.2 Gravitational Constants and Mass Ratios [I-22]

Body	Mass Ratio M_{sun}/M_{planet}	Gravitational Constant (km^3/s^2)
Sun	1	$1.32712499 \times 10^{11}$
Mercury	5 987 000 ± 32 000	2.218159×10^{4}
Venus	408 522 ± 3	3.24860×10^{5}
Earth and Moon	328 900.1 ± 0.3	4.035040×10^{5}
Mars	3 098 709 ± 100	4.282832×10^{4}
Jupiter	1047.39 ± 0.04	1.267076×10^{8}
Saturn	3499.3 ± 1.5	$(3.7925 \pm 0.0016) \times 10^{7}$
Uranus	22 930 ± 6	5.787722×10^{6}
Neptune	19 260 ± 100	6.890574×10^{6}
Pluto	1 812 000 ± 40 000	7.324088×10^{5}
Earth	332 945.6	3.986012×10^{5}
Moon		4.90278×10^{3}

REFERENCES

I-1. Solar Activity and Related Interplanetary and Terrestrial Phenomena. J. Xanthakis (editor), Springer Verlag, 1973.

I-2. Tandberg-Hanssen, Einar: Solar Activity. Blaisdell Publishing Co., 1967.

I-3. Svestka, Z.: Solar Flares. D. Reidel Publishing Co., 1976.

I-4. Burrell, M. O., Wright, J. J., and Watts, J. W.: An Analysis of Energetic Space Radiation and Dose Rates, NASA TN D-4404, February, 1968.

I-5. Johnson, F. S.: Satellite Environment Handbook. Second Edition, Stanford University Press, Stanford, California, 1965.

I-6. Solar Electromagnetic Radiation. NASA SP-8005, May 1971.

I-7. Allen, C. W.: Astrophysical Quantities. Athlone Press, University of London, 1963.

I-8. Feldman, W. C., Asbridge, J. R., Bame, S. J., Gary, S. P., Montgomery, M. D., and Zink, S. M.: Evidence for the Regulation of Solar Wind Heat Flux at 1 AU. Journal of Geophysical Research, vol. 81, no. 28, October 1, 1976.

I-9. Brandli, H. W.: The Natural Environment of a Satellite in a Synchronous Circular Orbit. Technical Report 192, Air Weather Service, USAF, June 1967.

I-10. Thekaekara, M. P., Editor: The Solar Constant and the Solar Spectrum Measured from a Research Aircraft. NASA TR R-351, Washington, D.C., October 1970.

I-11. The Study of Comets, Part 1 and Part 2. NASA SP-393, 1976.

I-12. Delsemme, A. H.: Physical Study of Comets, Minor Planets and Meteorites. Proceedings of IAU Commission 15, 1976.

I-13. O'Dell, C. R.: A New Model for Cometary Nuclei. Icarus 19, 1973, pp. 137-146.

REFERENCES (Concluded)

I-14. Marsden, B. G.: Comets and Nongravitational Forces III. The Astronomical Journal, vol. 75, no. 1, February 1970.

I-15. Gary, G. A.: Comet Kohoutek. A Workshop Held at Marshall Space Flight Center, June 13-14, 1974.

I-16. Burbank, P. B., Cour-Palais, B. G., and McAllum, W. E.: A Meteoroid Environment for Near-Earth Cislunar and Near Lunar Operations. NASA TN D-2747, Manned Spacecraft Center, Houston, Texas, April 1965.

I-17. Special Icarus "EROS" Issue. Icarus, International Journal of Solar System Studies, vol. 28, no. 1, May 1976.

I-18. Meteoroid Environment Model - 1970. NASA SP-8038, Interplanetary and Planetary, October 1970.

I-19. Kessler, D. J.: Spatial Density of the Known Asteroids in the Ecliptic Plane. NASA TM X-538026, Manned Spacecraft Center, March 1969.

I-20. Kessler, D. J.: Average Relative Velocity of Sporadic Meteoroids in Interplanetary Space. AIAA Journal, vol. 7, no. 12, December 1969.

I-21. The American Ephemeris and Nautical Almanac for the Year 1976. U.S. Government Printing Office, Washington, D.C.

I-22. Melbourne, W. G., Mulholland, J. D., Sjogren, W. L., and Sturms, F. M., Jr.: Constants and Related Information for Astrodynamic Calculations, 1968. Jet Propulsion Lab., Technical Report 32-1306, July 15, 1968.

BIBLIOGRAPHY

Gibson, Ed: The Quiet Sun. NASA SP-303, 1973.

Intercorrelated Satellite Observations Related to Solar Events. V. Manno and D. E. Page (editors), Springer Verlag, 1970.

High Energy Phenomena on the Sun. NASA SP-342, 1973.

McCrosky, R. E.: Cometary Debris, The Dusty Universe. Proc. of a Symposium Honoring Fred Lawerence Whipple on his retirement as Director of the Smithsonian Astrophysical Observatory, October 17-19, 1973, pp. 169-183.

Physics of the Solar System. NASA SP-300, 1972.

Space for Mankind's Benefit. NASA SP-313, 1972.

Solar Flares and Space Research. C. DeJager and Z. Svestka (editors), North-Holland Publishing Co., 1969.

Solar Wind. NASA SP-308, 1972.

SECTION II. TERRESTRIAL SPACE

2.1 Definition

"Terrestrial space" is defined in this document as the region between 90 and 65 000 km above the surface of the earth for all environment components except meteoroids, where the outer limit of the earth's influence extends into space until the gravitational attraction becomes negligible.

2.2 Neutral Gas Properties[1]

Atmospheric conditions encountered by a spacecraft in orbit about the earth are important factors in space vehicle design, mission planning, and mission operations. Density is the primary atmospheric property that affects the spacecraft' s orbital altitude, lifetime, and motion in the altitude range of 90 to 1000 km. Near the lower limit of this range where density is greatest, a spacecraft will generally remain in orbit for a very short time; near the upper limit, the density effect on orbital lifetime is almost negligible. Density directly affects the torques which result from aerodynamic interaction between the space vehicle and the atmosphere; such torques must be considered in design of spacecraft attitude control systems. Density scale height is required in heating calculations for space vehicles re-entering the earth' s upper atmosphere. Density, as well as chemical compostion and temperature, is needed in calculating a spacecraft' s drag coefficient. Chemical composition and temperature are also required in the design of experiment sensors to be flown in this altitude range.

Because of variability of atmospheric conditions with spatial location and solar condition, invariant models of the earth's atmosphere (90 to 2500 km) are not useful for most engineering applications. Therefore, a computerized version of a prediction method to provide models of the earth' s atmosphere which vary with solar condition and geographic location is required. The resulting atmospheric models, which are predicted for particular times and locations, provide atmospheric density, chemical composition, temperature, molecular mass, and density scale height between 90 and 2500 km altitude.

Most of the density values for the atmosphere between 90 and 2500 km have been derived from the analysis of changes in the periods of orbiting

1. Appendix B contains a complete discussion.

satellites. Temperature and chemical composition may be inferred from the drag determined densities under the assumption of static diffusion. Since mass density, temperature, and chemical composition at these altitudes vary with solar and geomagnetic activity, the level of such activity must be considered to estimate these parameters for a given time.

2.2.1 Variations

2.2.1.1 Chemical Composition

In the earth's homosphere, extending from the surface to an altitude of near 90 to 100 km, the atmospheric gases mix thoroughly so the constituent gas distribution of N_2/O_2 does not vary. However, above 90 km and primarily near 105 km, extreme ultraviolet (EUV) solar radiation causes molecular oxygen to dissociate. The resulting production of atomic oxygen combined with diffusive transport processes results in a changing atmosphere. Accordingly, the chemical composition above the 90 to 100 km altitude level is a function of the variable amounts of EUV radiation received from the sun.

2.2.1.2 Temperature

The temperature lapse rate is influenced by solar radiation. In the lower thermosphere (100 to 300 km), solar radiation in the EUV band (40 to 2000Å) is absorbed and causes the temperature to increase steadily with altitude. Above 300 km, where little or no solar radiation is absorbed, the temperature increases very little with altitude and becomes isothermal as shown in Figure II-1. The isothermal temperature, which is designated as the "exospheric temperature," varies diurnally, seasonally, and with solar and geomagnetic activity from about 650 to 2100 K.

2.2.1.3 Density

Variation in density has been found to be related closely to the amount of EUV received from the sun. Although EUV cannot be measured at the earth's surface, early investigators assumed that there was correlation between EUV and radiation at about 10 cm wavelength which can be measured at the earth's surface. Data from the first Orbiting Solar Observatory (OSO-1) confirmed this assumption, showing close correlation between EUV and radiation at 10.7 cm. Therefore, the mean daily solar flux at 10.7 cm which is measured by the National Research Council, Ottawa, Canada, has been accepted as an indicator of the amount of EUV radiation that reaches the top of the earth's atmosphere.

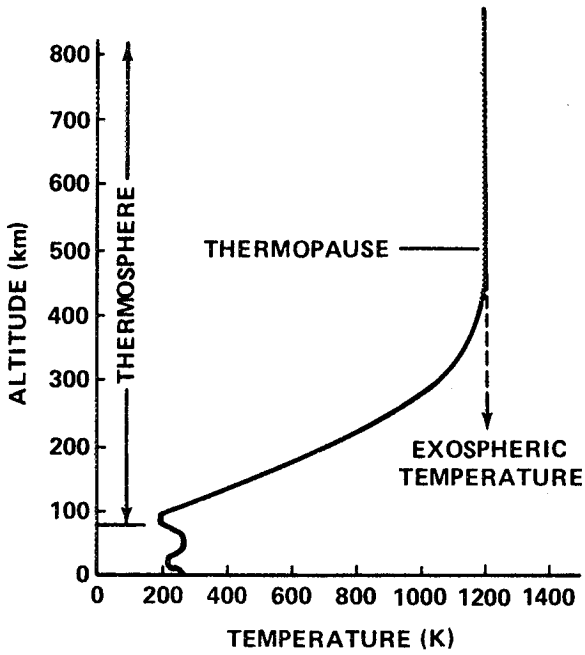

Figure II-1. Typical plot of temperature versus altitude and exospheric temperature.

The principal periodic variability found in the solar flux at 10.7 cm occurs at a cycle of 27 days, corresponding to the 27 day solar rotation. The same periodicity is reflected in atmospheric density. Semiannual, diurnal, and solar cycle variations have also been identified to occur in the upper atmospheric temperature.

Density variation also can be related to fluctuations in the three-hourly geomagnetic index of magnetic activity at the earth's surface. The geomagnetic variations are strongly correlated with the extent and magnitude of precipitating electrons and protons in the polar regions. This energy source heats the lower thermosphere in the polar regions. This condition results from changes in the global thermospheric temperature and density. The correlation between changes in geomagnetic activity and density variation is useful in density prediction.

Density also varies between the winter and summer hemispheres in the 60 to 80 deg latitude range. Some investigators attribute the higher density in the winter hemisphere to increased concentration of helium.

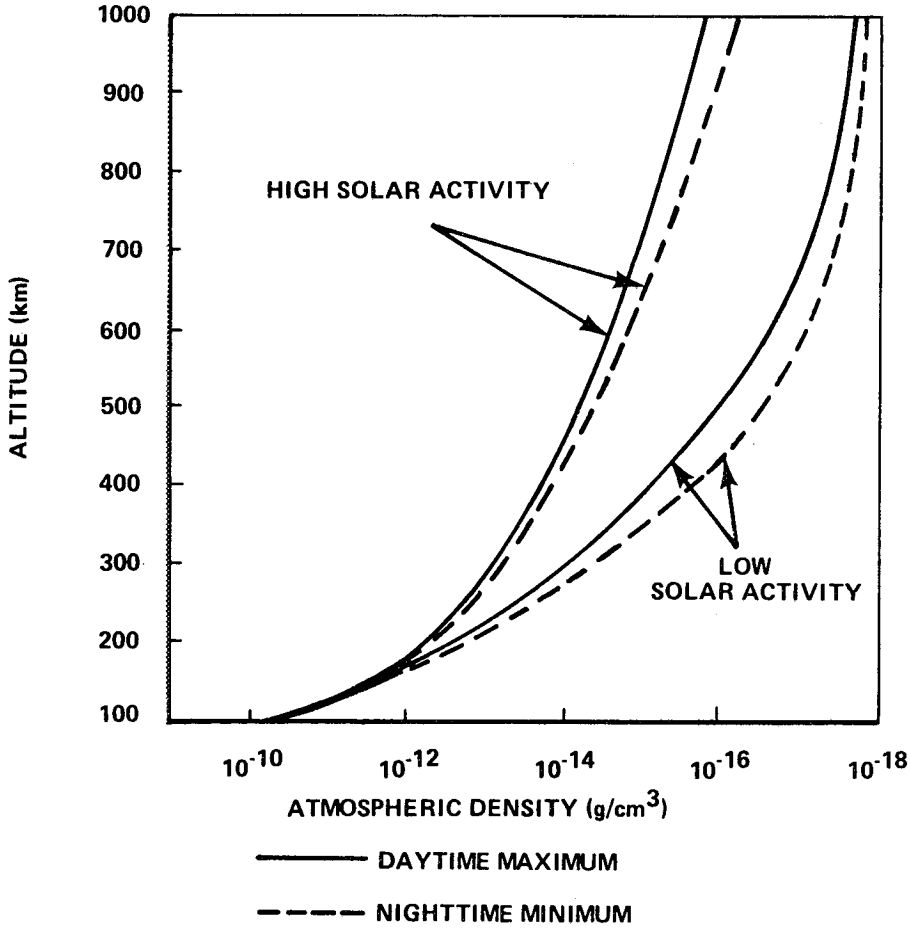

Figure II-2. Typical daytime maximum and nighttime minimum atmospheric density profiles for high and low solar activity.

2.2.1.4 Criteria

The upper atmosphere model used by MSFC is described in Appendix B and should be used to predict the neutral gas properties of the atmosphere between 90 and 2500 km altitude for orbital dynamics, lifetime, and control and guidance analyses. The model should be used for reentry and analyses from orbital altitudes down to 25 km above the earth's surface. This model provides only nominal atmospheric density data below ~ 90 km. Solar activity data required for input to this model are described in Section 2.4.7 and Appendix A. The Global Reference Atmosphere Model is used with the MSFC Lifetime Prediction Computer Routine for calculating orbital lifetime. This model is a combination of the 4-D Model Atmosphere, the Groves Model, and the Jacchia 1970 Atmosphere Model [II-1].

2.2.2 2500 to 65 000 km Altitude

Gas pressure decreases exponentially with increasing altitude above 2500 km until it reaches the interplanetary value of 10^{-15} N/cm^2 near 20 000 km. It then remains relatively constant with increasing altitude.

Gas density decreases exponentially above 2500 km altitude to the interplanetary value of approximately 10^{-23} g/cm^3 near 20 000 km and then remains relatively constant with altitude.

Kinetic temperature increases linearly above 2500 km to the interplanetary value of about 2×10^5 K at 20 000 km and then remains relatively constant with increasing altitude.

2.2.3 Additional Information

Additional information relative to the structure and variability of the atmosphere is given in References II-2 and II-3.

2.3 Ionosphere[2]

The ionosphere is that region of the upper atmosphere where an appreciable amount of atmospheric ionization exists. This region extends outward from altitudes of approximately 60 km until it merges with the plasma of interplanetary space.

The ionosphere is of concern to space vehicle designers because of the effects of spacecraft interaction (spacecraft charging) with the electrically active medium and because of the influence of the ionosphere on mission communications, guidance, and tracking. Specifically, the ionosphere may affect frequency selection and design of receivers, transmitters, and antennas. In addition, the flow of charge between the plasma and the spacecraft represents a leakage current to exposed conductors which may lead to electrical breakdown of normally nonconducting paths.

The interaction of the spacecraft and medium must be considered in the design of experiments having the purpose of taking measurements within the ionosphere. These interactions include formation of wakes by passage of the spacecraft through the medium, generation of large electrical potentials by long antennas and booms, and formation of plasma sheaths around the

2. These data were extracted from NASA SP-8049 [II-4] which contains additional information.

spacecraft which can isolate it from the ambient medium. Sheaths can affect results of direct measurement experiments such as Langmuir probes and experiments mounted on booms. In addition, the electric potential acquired by the spacecraft usually serves as a reference for onboard experiments of this type.

2.3.1 Basic Concepts

The ionization of the upper atmosphere is the result of solar radiation and cosmic rays interacting with the atmosphere to produce a plasma consisting of (usually) equal concentrations of positively and negatively charged particles. The plasma remains in a state of dynamic equilibrium because the loss of charged particles through recombination is balanced by the creation of new particles. Because the prime source of energy for the ionosphere is the sun, the parameters defining the ionosphere vary diurnally, seasonally, and with the solar cycle. Geographical variations from anomalies in the earth's magnetic field also exist.

2.3.2 Ionospheric Parameters

2.3.2.1 The Ionosphere Below 1000 km

Three regions have been identified as prominent features of the structure of the lower ionosphere during the daytime. In order of increasing altitude and increasing ion concentration they are the D, E, and F regions. Large diurnal effects exist which occur in this part of the ionosphere. At nighttime, the D region virtually disappears and a depression in electron concentration occurs between the E and F regions.

The D region is the lowest ionospheric region and has an approximate altitude range from 60 to 85 km. The predominant ionizing agent is Lyman alpha radiation with cosmic rays contributing in the lower altitudes. Nitric oxide (NO^+) and oxygen (O_2^+) are the principal ionic constituents together with heavy ion complexes involving water vapor. The D region has the lowest electron density concentration of the three regions with a maximum of 10^3 electrons/cm^3 near 80 km.

The approximate altitude range of the E region is from 85 to 140 km. Ultraviolet and soft x-radiation are the principal ionizing agents in this region. The predominant ionic constituents are NO^+ and O_2^+. The electron concentration in the E region ranges from approximately 10^5 electrons/cm^3 during solar minimum to a value approximately 50 percent larger during solar maximum.

The F region has an approximate altitude range from 140 to 1000 km and in daytime has two divisions: F_1 and F_2. The solar spectrum in the wavelength range from 200 to 900 Å is the principal ionizing agent in this region. The two divisions or density peaks occur because the degree of ionization and recombination falls off with decreasing altitude at different rates. The F_1 region is associated with the ion production peak occurring in the vicinity of 150 km. The F_1 region disappears at night as the concentration of electrons decreases above the E region. The F_2 region is associated with the peak in the electron density distribution which varies with time of day, season, solar cycle, and latitude. It usually lies within the region from 200 to 400 km. The predominant ions near the low altitude boundary are mainly NO^+ and O_2^+; with increasing altitude, a gradual transition occurs until at the upper boundary O^+ becomes the principal ion.

The section of ionosphere above the peak of the F_2 region commonly is referred to as the topside ionosphere. Information on the topside ionosphere is obtained mainly through satellite measurements and the incoherent backscatter radar technique.

2.3.2.2 The Ionosphere Above 1000 km

The ionosphere above 1000 km includes the upper portion of the topside ionosphere and the region of the near-earth plasma (or outer ionosphere) extending to altitudes of the order of 3 to 4.5 earth's radii (R_o). From this altitude to about 10 R_o is the region of transition to the interplanetary medium.

Most information on the outer ionosphere has come through experimental research with the aid of whistlers (RF electromagnetic signals generated by some lightning discharges) although in situ measurements by satellites also have provided useful results. The data indicate a steady decrease in electron concentration with increasing altitude until a rapid and abrupt decrease occurs at altitudes of 15 000 to 25 000 km above the magnetic equator. This decrease in electron concentration is called the "knee" or plasmapause.

The predominant ions in the outer ionosphere vary with altitude. In the lowest part of the region, atomic oxygen (O^+) predominates, whereas atomic hydrogen (H^+) is the main constituent above 1000 km (protonosphere).

2.3.2.3 Electron Densities

The density of electrons in the ionosphere varies geographically, diurnally, seasonally, and with solar activity. It is not yet possible, however, to produce models of the electron density distribution which show all these variations because of the limited number of observations. Available information is provided mainly by vertical incidence sounders and rockets and by satellites.

Below the peak of the F_2 region, the electron density increases with altitude. Above this region, measurements (made primarily with topside sounders and incoherent backscatter radars) indicate a rather smooth and slow decrease in electron concentration with increasing altitude. In the region of the knee (where measurements have been made by whistlers and satellites), a rapid decrease in electron concentration occurs. This decrease occurs even during the periods of relatively weak magnetic disturbances.

Typical mid-latitude electron density profiles for the ionosphere below 1000 km are presented in Figures II-3 and II-4. Variations with latitude are shown in Figure II-5. If greater accuracy is required, the tabulated values of electron density in Reference II-5 should be consulted; this reference covers both the mid-latitude and polar ionosphere.

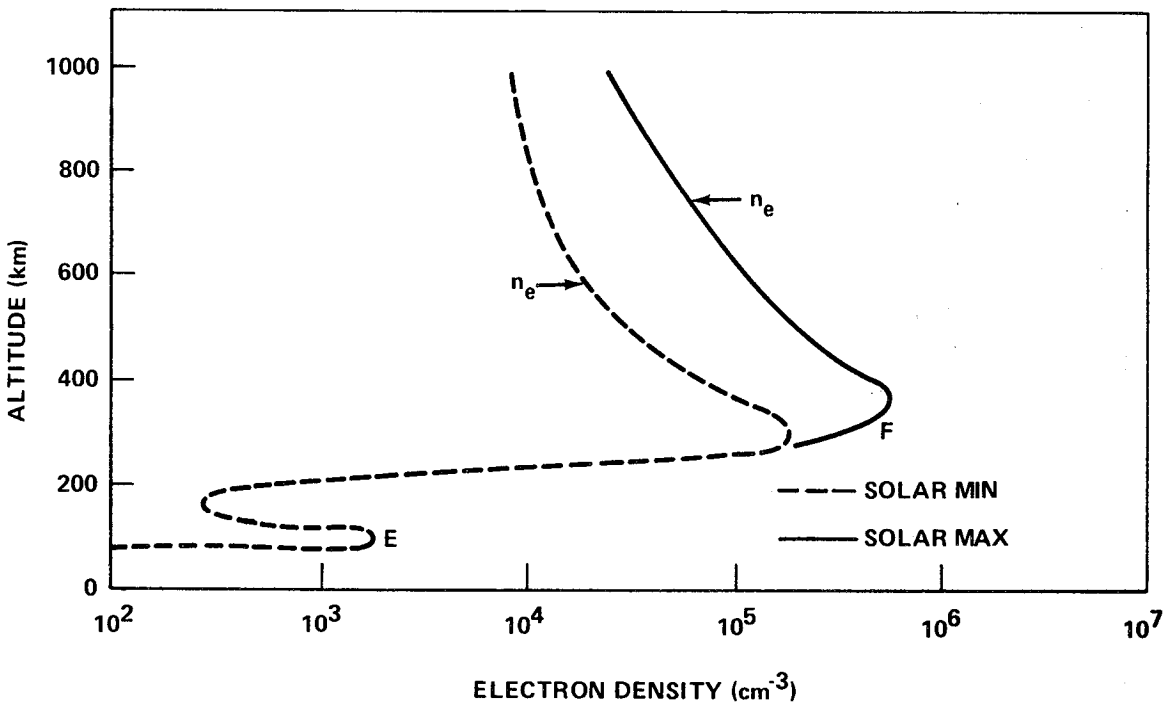

Figure II-3. Ionospheric electron concentration - nighttime.

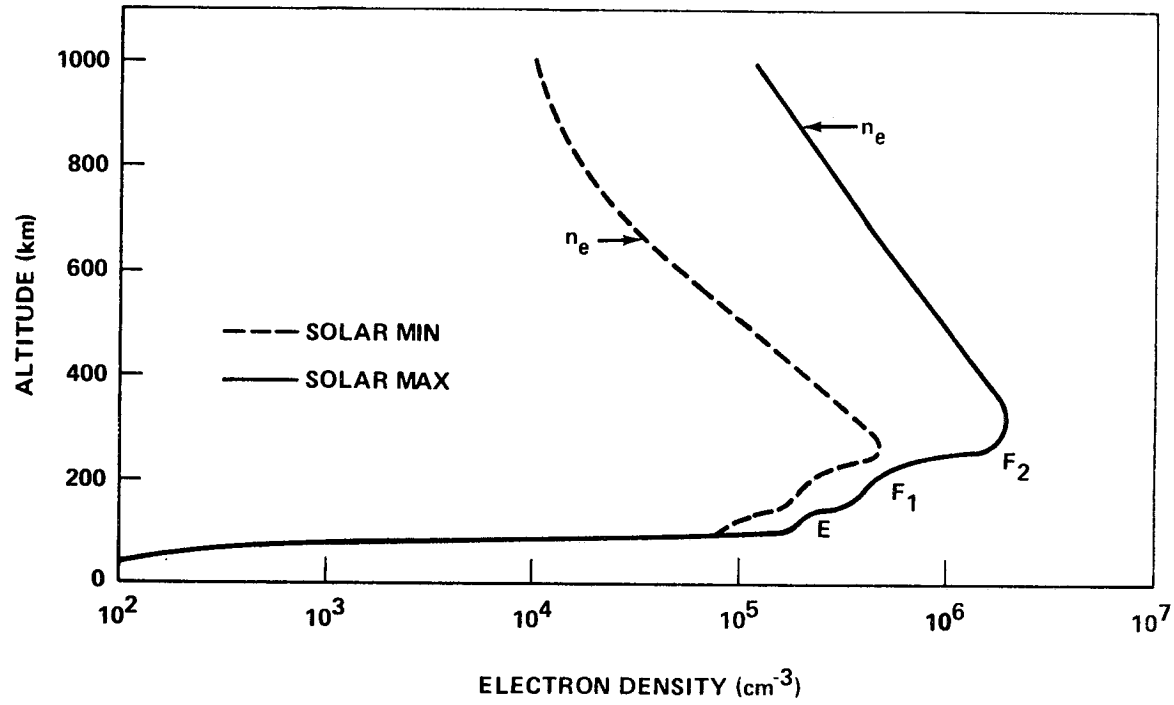

Figure II-4. Ionospheric electron concentration - daytime.

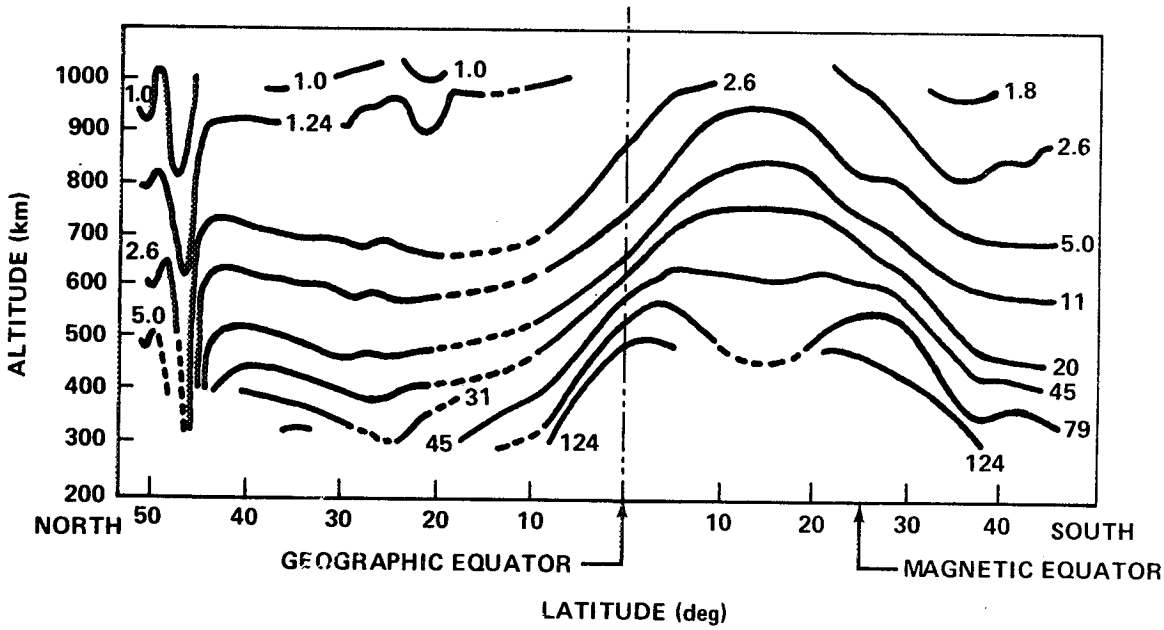

Figure II-5. Daytime contours of equal electron density in the orbital plane of an Alouette Satellite. (Density units of 10^4 electrons cm^{-3}.)

2.3.2.4 Ionic Composition

In the lower regions of the ionosphere, NO^+ and O_2^+ predominate with O^+ becoming the main ionic constituent in the higher part of the F region. A transition between a predominantly O^+ ionosphere to one predominantly of H^+ occurs in moving upward in the topside ionosphere. Helium is never a predominant ion species. It is, however, a minor constituent at all times; its maximum density is 15 percent of the total at about 450 km.

Above 1000 km, the ionic composition is predominantly H^+; it becomes 90 percent H^+ above 2800 km. The only other component of interest is approximately 10 percent He^+ with a concentration of about 1 to 4 percent of the hydrogen concentration. The concentration of hydrogen ions is deduced from proton whistler observations by the Alouette 1 and Injun 3 satellites. Concentrations of ions other than hydrogen are derived from incoherent backscatter data. Observations indicated that the concentration of hydrogen ions increases in winter and that the nighttime summer results may be applied to daytime winter conditions. The values then merge with those below 1000 km.

The number variation of ionic composition in the lower ionosphere in daytime is presented in Figure II-6. The percentage variation of ionic composition is presented in Figure II-7. This information was deduced from proton whistler observations on the Alouette 1 and Injun 3 satellites and from incoherent backscatter data. Averaging the various percentage concentrations with respect to mass yields night and day profiles of average ion mass.

2.3.2.5 Ionospheric Temperature

The temperature profile of the ionosphere above the E region has been obtained with measurements by sounding rockets and satellites and backscatter sounders. The temperature of the ionosphere depends on the balance between the various heating and cooling processes in the ionosphere and the diurnal and seasonal variation of this balance. The daytime temperature of the ionospheric electrons in the F_1 region is generally larger than the ambient gas temperature by a factor of two. This results from the relative efficiency of the ambient electrons in removing the excess kinetic energy from the continually released energetic photoelectrons and the relatively small number of electrons to share such energy. The resulting hot electron gas is cooled mainly by collisions with neutral particles at altitudes below about 250 km and by collision with ions at higher altitudes. The temperature of the ions approaches that of the electrons above 600 km with both exceeding the neutral gas temperature.

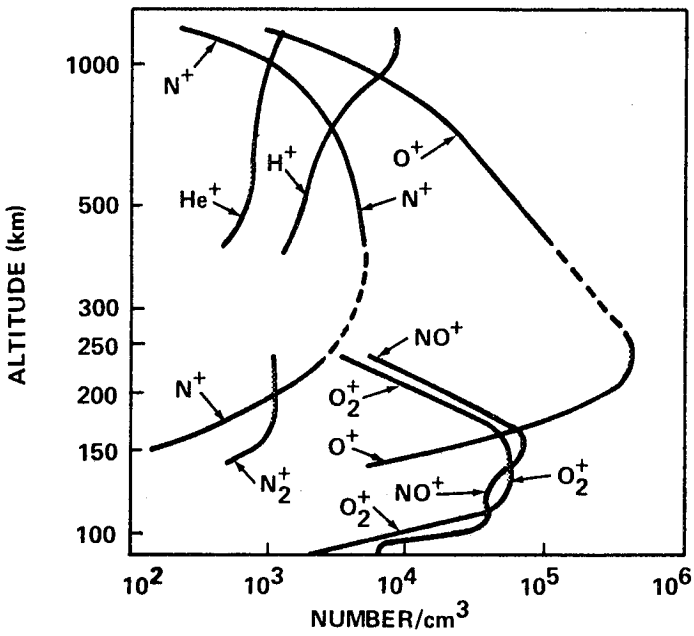

Figure II-6. Ionic composition of solar minimum daytime winter ionosphere.

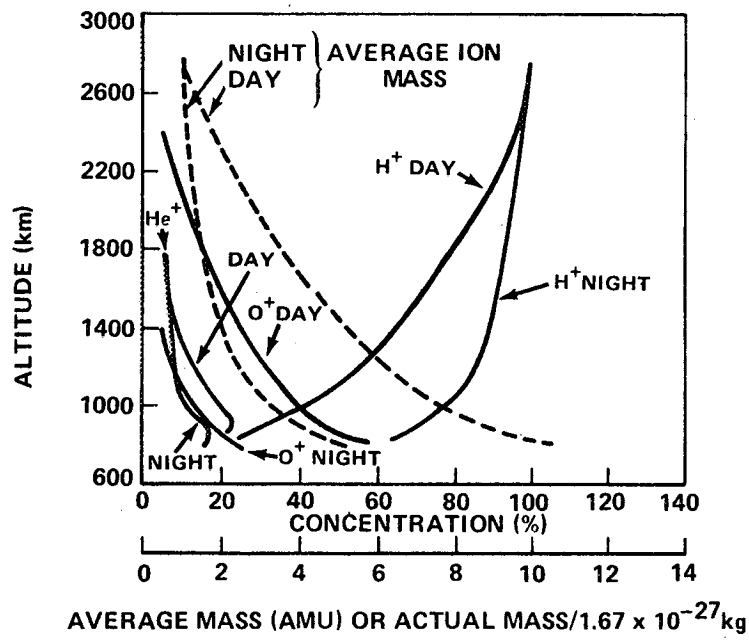

Figure II-7. Relative concentration of H^+, O^+, and He^+ and their average mass for solar minimum and a quiet summer time. (Nighttime summer profiles are also appropriate for winter daytime.)

The model presented herein is based on experimental results for altitudes below 1000 km.

Temperature measurements made by the IMP 1 spacecraft in the region from 2 to 5 R_E show that the electron temperature, T_e, is approximately proportional to the square of the radial distance, L, from the earth. Here, the value of 2.4 for the power of L is used to join lower altitude daytime temperature to data obtained from the OGO-1 satellite. The value of 1.9 was used as the power of L to match nighttime values of T_e with the low temperature readings.

The electron temperature profiles for daytime summer solar minimum conditions at altitudes below 1000 km are presented in Figure II-8, the ion temperature profiles are presented in Figure II-9.

Above 1000 km, the ion temperature is taken as equal to the electron temperature because the ion temperatures theoretically approach the electron temperature values. Figure II-10.gives the electron temperature profiles during periods of minimum and maximum solar activity.

2.3.3 Spacecraft Interaction with the Ionosphere

2.3.3.1 Spacecraft Potential

A spacecraft moving through the ionospheric plasma will gather charge as a result of its contact with both positive and negative charges. In a state of equilibrium, the spacecraft will assume a potential sufficiently negative to equalize the flow of ions and electrons. This potential depends upon the temperature of the ambient plasma, the relative spacecraft motion, the electron density, the electrostatic fields surrounding electrically active surfaces, the incident flux of ultraviolet radiation and energetic particles, and the intentional ejection of charge by onboard equipment.

The spacecraft potential is important because it generally is used as a potential reference for onboard experiments. In this case, the spacecraft vehicle potential is assumed to be constant, and any variation in its value appears as an inaccuracy in the final experimental result.

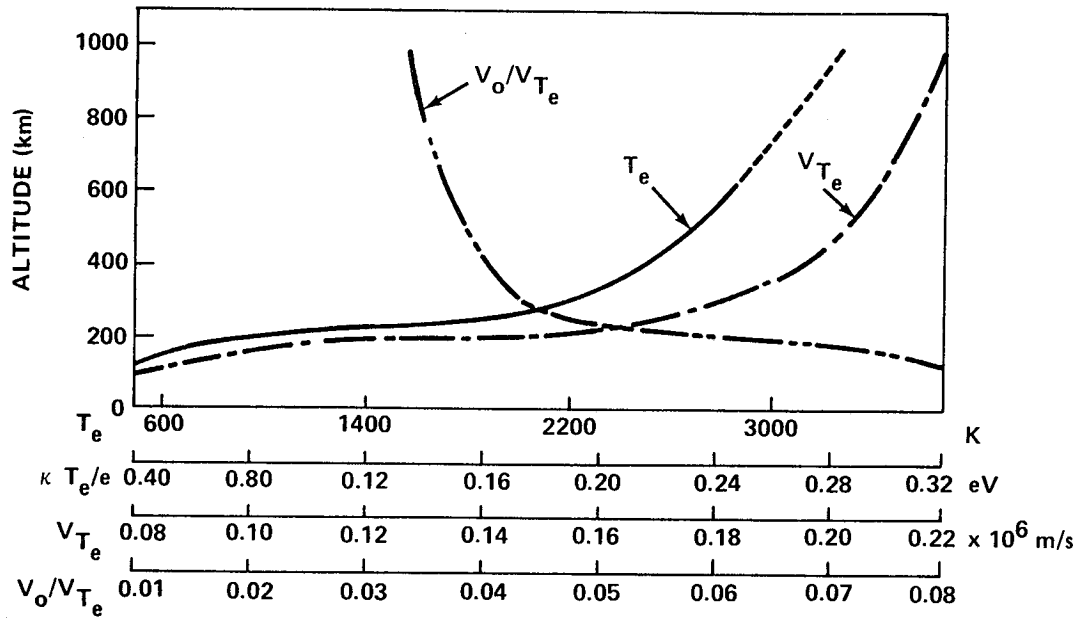

Figure II-8. Electron temperature, thermal velocity, and satellite/thermal velocity ratio.

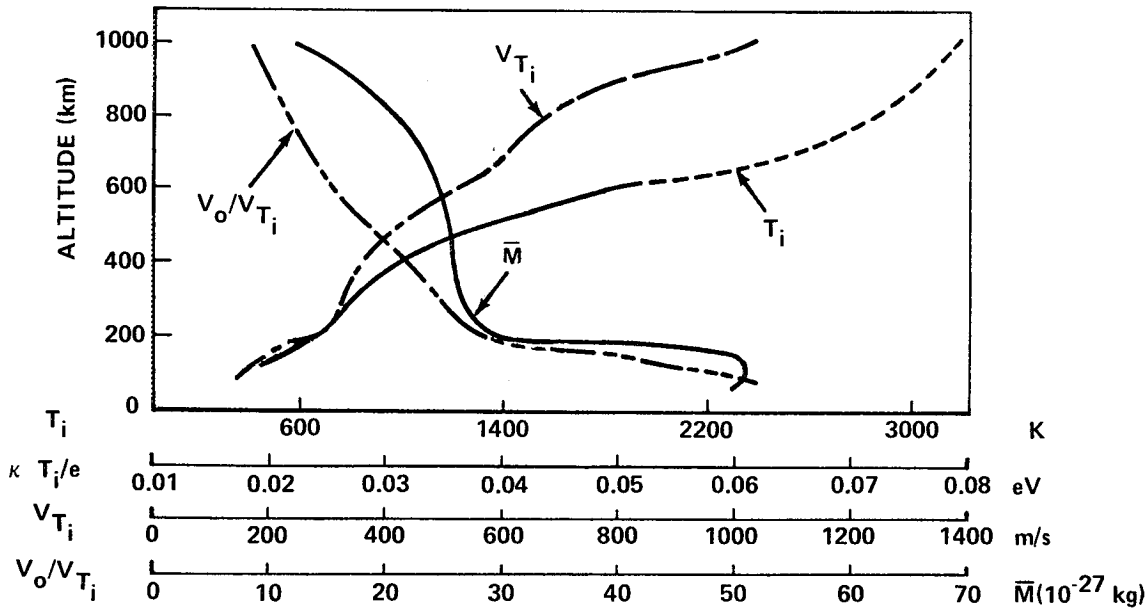

Figure II-9. Ion,temperature, thermal velocity, and satellite/thermal velocity ratio.

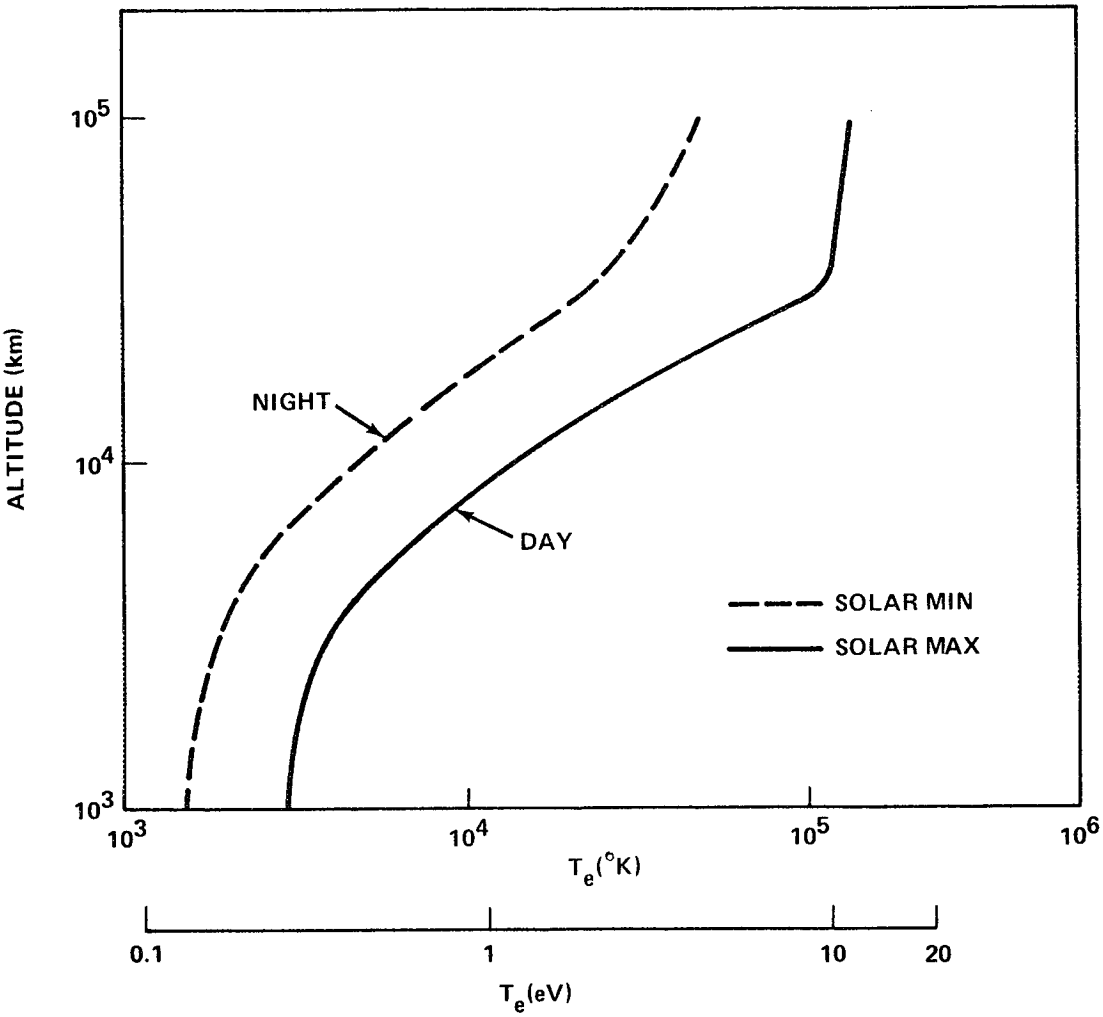

Figure II-10. Models of electron temperature profiles in K or in eV(viz., $\kappa T_e/e$).

2.3.3.2 Plasma Sheaths

The potential of the spacecraft is usually different from that of the ambient plasma and, as a result, the spacecraft tends to be surrounded by a plasma sheath. Three different classes of plasma sheaths exist: (a) the stationary sheath, (b) the wake, and (c) the specialized sheaths formed by exposure to direct voltages induced by RF or $\vec{V} \times \vec{B}$. It should be noted, however, that the spacecraft plasma sheath usually is a compound of all three forms unless special measures have been taken to eliminate certain of them.

The stationary sheath is formed around a body placed in a plasma. Theoretical analyses usually assume that the body is spherical and the sheath is of the dimension considerably larger than the plasma Debye length, λ_D (defined as $6.9\,[T_e/N_e]^{1/2}$ where T_e is the electron temperature in K and N_e the electron density in cm^{-3}). However, the sheath is considered smaller than the mean free path of the particles. These conditions permit collisionless treatment of the plasma in such analyses.

The sheath effects associated with the presence of an RF signal on an antenna strongly depend on the relationship between its frequency and the local plasma frequency. In general, an RF signal can cause the formation of quite extensive sheaths around an antenna which may disturb direct measurement experiments.

2.3.3.3 $\overline{V} \times \overline{B}$ Effects

When a conductor moves through a magnetic field, an electric field is developed across the conductor according to the relationship,

$$\overline{E} = \overline{V} \times \overline{B}$$

where

$\overline{E}$ = the electric field produced

$\overline{V}$ = the velocity vector of the conductor

$\overline{B}$ = the magnetic field.

In the case of the spacecraft's interaction with the environment, the magnetic field is that of the earth, and the conductor is the metallic skin or appendages of the spacecraft.

If good coupling exists between the spacecraft and the plasma, an appreciable current will flow under the influence of the induced field. The energy of the spacecraft can be radiated away by resistive heating, and the net effect is equivalent to a loss of energy by a drag mechanism. This drag effect of the $\overline{V} \times \overline{B}$ mechanism is proportional to the cube of the spacecraft's characteristic dimension and may exceed the mass drag for spacecraft larger than 50 m in diameter above an altitude of 1200 km. Small spacecraft may have

very large booms or antennas so that the total potential difference induced may be considerable (this potential is $(\bar{V} \times \bar{B}) \cdot \bar{L}$ where L is the vector length of a boom or antenna).

Another $\bar{V} \times \bar{B}$ effect is the formation of an induced plasma sheath associated with a large potential of perhaps tens of volts. This sheath varies as the spacecraft spins and thus changes orientation with respect to the magnetic field. Therefore, it can have unfortunate effects on experiments mounted on the spacecraft such as Langmuir probes measuring ambient densities and temperatures.

2.3.3.4 The Spacecraft Wake

The wake, which is a distorted sheath formed by the relative motion between the spacecraft and the plasma, extends many spacecraft diameters downstream. Immediately behind the spacecraft there is a region of high negative potential followed by an ion-focusing or concentration. Indications are that from this concentration an ion density enhancement extends downstream as a V wave analogous to a Mach cone. This enhancement is not attached to the spacecraft but commences at a number of body radii downstream equal to the Mach number.

2.3.3.5 Thermal Particle Flux to a Spacecraft at Plasma Potential

Particle fluxes for electrons and ions at altitudes below 1000 km are presented in Figure II-11 and fluxes above 1000 km are presented in Figure II-12. For electrons, the number of particles flowing through unit area is based on the electron thermal velocity, V_{T_e} ; for ions, the number is based on the satellite orbital velocity, V_o (circular orbit). The orbital velocity is used as a basis for the ion flux because it is generally greater than the ion thermal velocity, V_{T_i} .

2.3.4 Communications

Attenuation of radio waves is a function of the refractive index, μ, which in turn is a function of electron density N_e, where

$$\mu^2 = 1 - \frac{4\pi N_e e^2}{\epsilon_o m_e \omega^2}$$

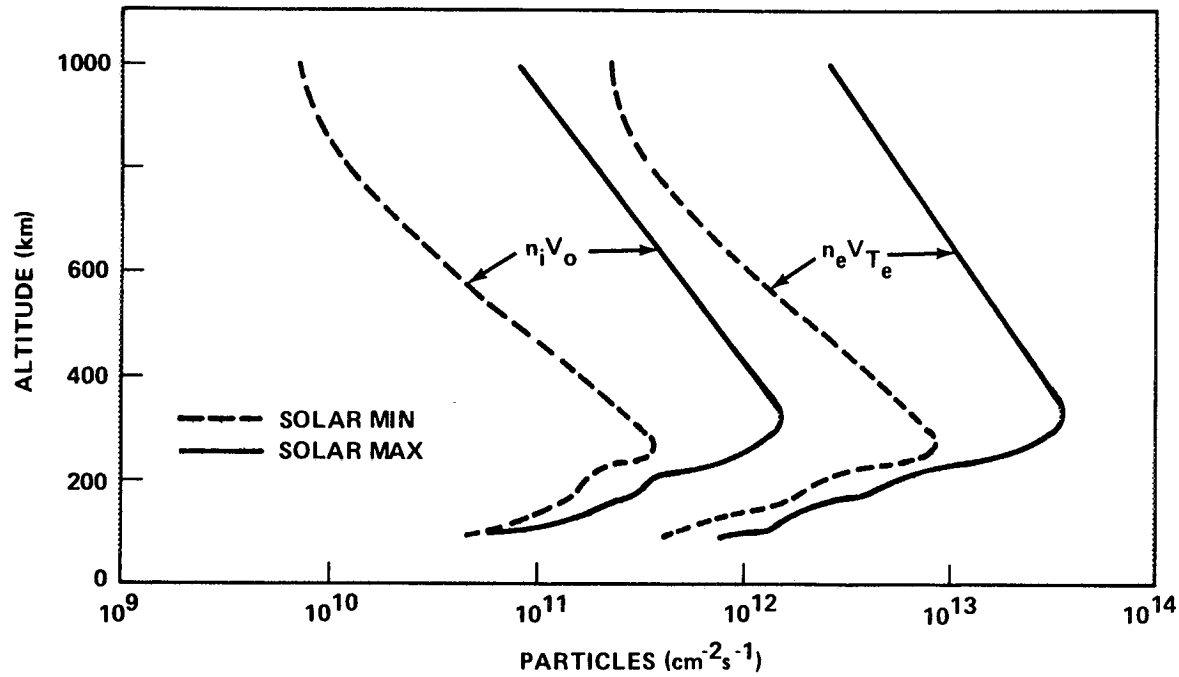

Figure II-11. Thermal particle flux — daytime.

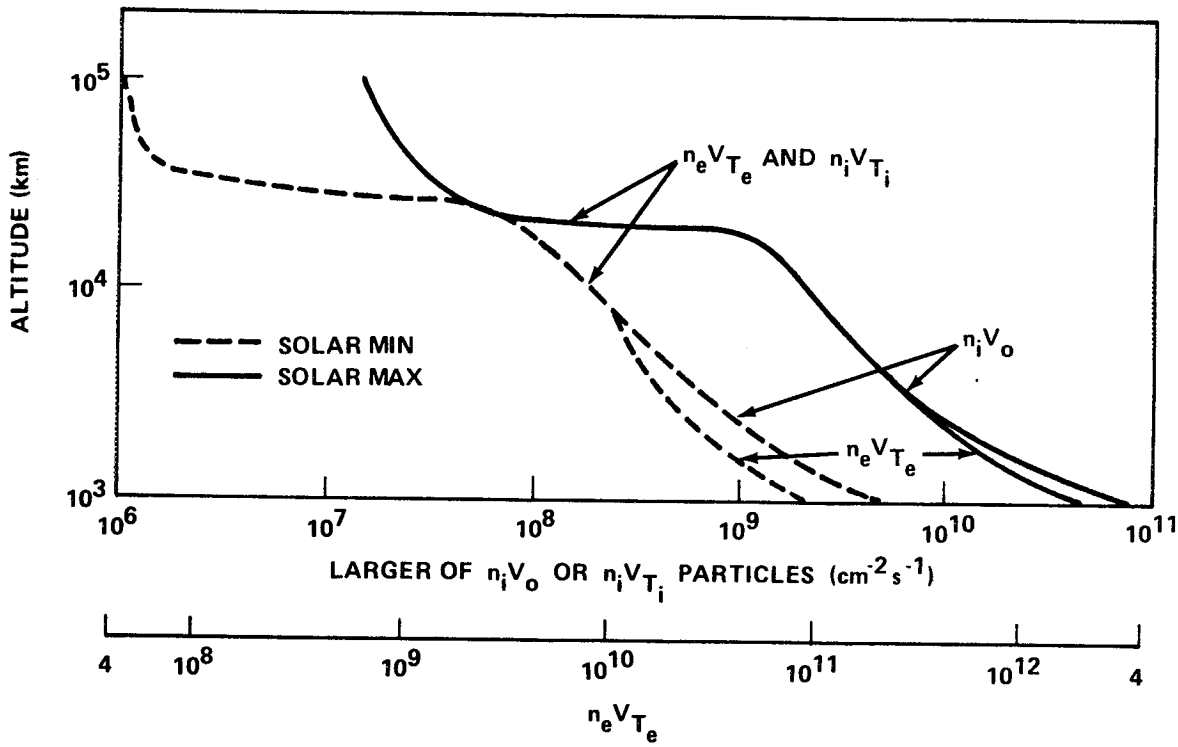

Figure II-12. Thermal electron and ion particle fluxes.

and

e_e = electron charge (coulombs)

m_e = electron mass (kg)

ω = angular frequency of the wave (rad/s)

ϵ_o = permittivity of free space (assuming the effects of ions are negligible).

At the F_2 peak (point of maximum electron density) of the ionosphere, the frequency of the radio wave which will penetrate is called the critical frequency, f_c. For satellite communications, a frequency higher than f_c must be selected, and for the best signal strength possible, frequencies considerably higher than f_c(max) should be chosen. However, some investigations have indicated that the ionosphere may have resonance modes which could interfere significantly with even much higher frequency signals.

2.4 Radiation Environment

The natural radiation environment in terrestrial space consists of galactic cosmic radiation, geomagnetically trapped radiation, and solar flare particle events. This environment may be defined by establishing a description of the particle flux as a function of energy, species, and location (time and space).

Radiation dose rates should be calculated as specified in Paragraph 2.4.8.

2.4.1 Galactic Cosmic Radiation

Galactic cosmic radiation consists of low intensity, extremely high-energy particles. These particles, about 85 percent protons, 13 percent alphas, and the remainder heavier nuclei, bombard the solar system from all directions. They have energies from 10^8 to 10^{19} eV per particle and are encountered essentially everywhere in space. The intensity of this environment in "free-space" (e.g., outside the influence of the earth's

magnetic field) is relatively constant (0.2 to 0.4 particles/cm^2 steradian s) except during periods of enhanced solar activity when the fluxes of cosmic rays have been observed to decrease. This decrease is caused by an increase in the strength of the interplanetary magnetic field which acts as a shield to incoming particles. Near the earth, cosmic rays are similarly influenced by the earth's magnetic field resulting in a spatial variation in their dose rate (Fig. II-13) and intensity (Fig. II-14).

Composition: ~ 85 percent protons (H^+)

~ 13 percent alpha particles (He^{++})

~ 2 percent nuclei of elements Li → Fe in approximate cosmic abundance.

Flux at sunspot minimum: ~ 4 protons/cm^2 s (isotropic)

Integrated yearly rates: ~ 1.3×10^8 protons/cm^2

Flux at sunspot maximum: ~ 2.0 ± 0.3 protons/cm^2

Integrated yearly rates: ~ 7×10^7 protons/cm^2

Energy range: 10^2 to 10^{13} MeV; most particles having $10^3 < E < 10^7$ MeV.

Integrated dose: ~ 4 to 10 rads/year.

Energy spectrum - illustrated in Figure II-15:

1 BeV = 10^9 eV

1 MeV = 10^6 eV

1 keV = 10^3 eV.

2.4.2 Trapped Radiation

The earth's magnetic field provides the mechanism which traps charged particles in belts about the earth. Electrons and protons are trapped in a region about the equator extending in geomagnetic latitude to about ±50 deg and in altitude from the top of the atmosphere to the outer limits of the magnetosphere. Figures II-15 and II-16 show the spatial distribution of electrons and protons, respectively.

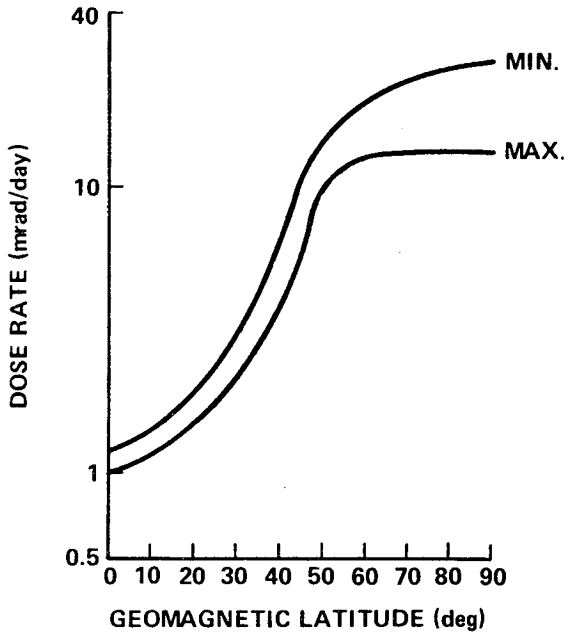

Figure II-13. Cosmic ray dose rate as a function of latitude at solar minimum and solar maximum.

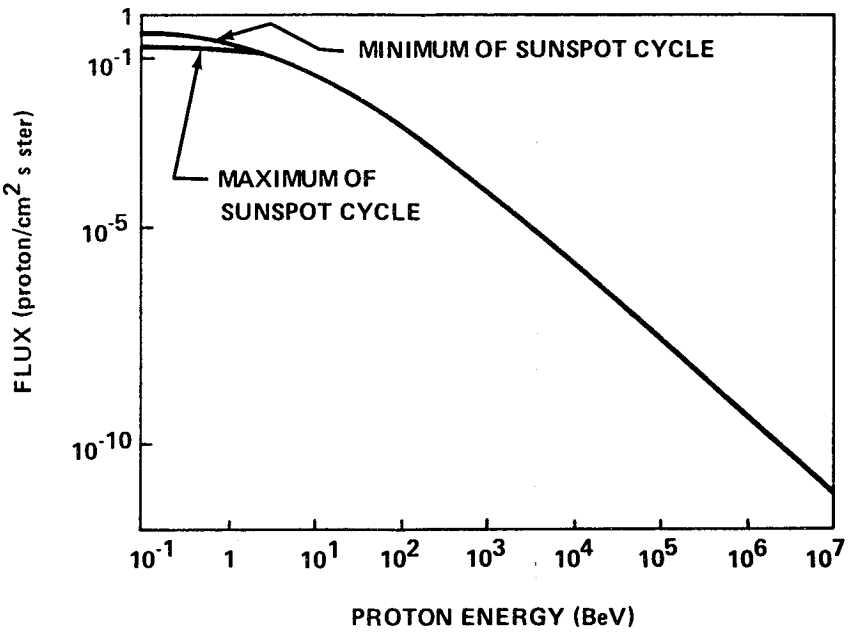

Figure II-14. Galactic radiation energy spectrum.

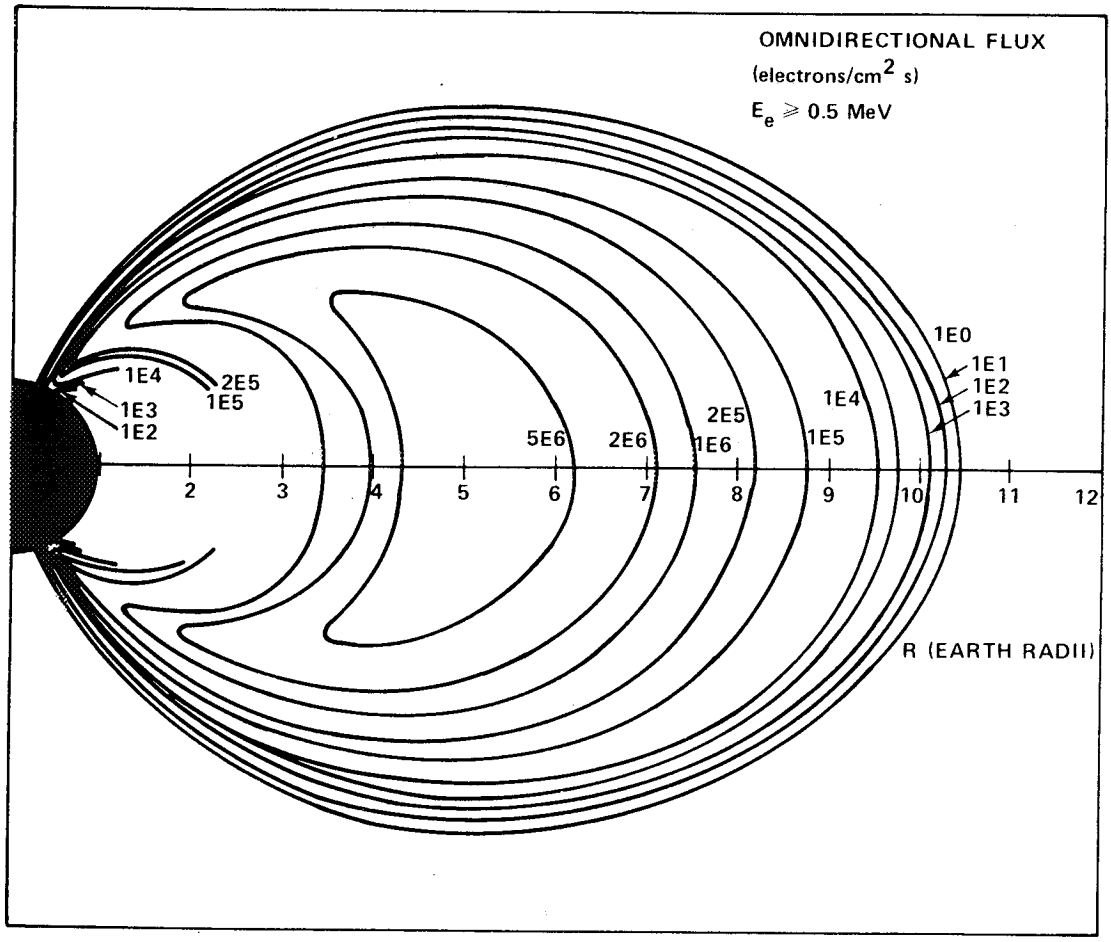

Figure II-15. Electron distribution in the earth's field.

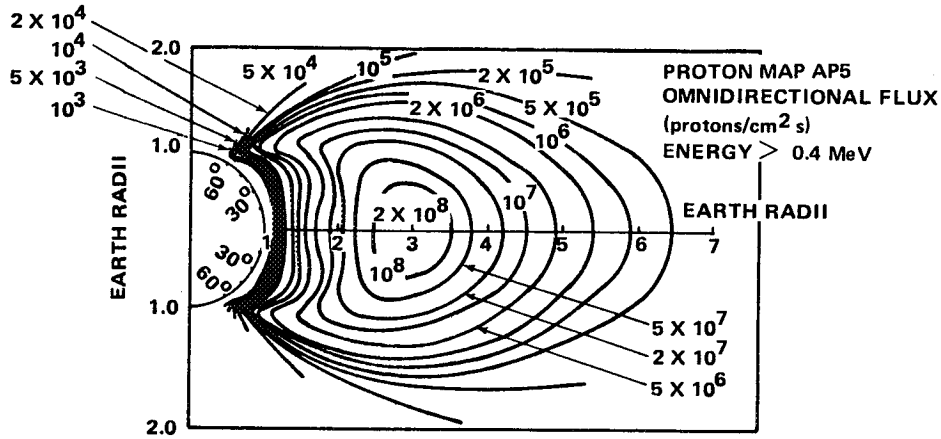

Figure II-16. Proton distribution in the earth's field.

2.4.2.1 Near-Earth Environment

The radiation belts trapped near the earth are approximately azimuthally symmetric, with the exception of the South Atlantic Anomaly. The earth's magnetic field can be approximated by a magnetic dipole whose axis is displaced 450 km from the center of the earth and tilted 10 deg with respect to the spin axis of the earth. In addition, the magnetic field is anomalously low in the region over the South Atlantic, which allows the radiation belts to reach their lowest altitude (Fig. II-17). Figure II-18 reflects the presence of the anomaly in the area where proton fluxes are encountered at an altitude of 296 km. The natural occurring trapped radiation environment in the anomaly region remains fairly constant with time although it fluctuates with solar activity. In addition to the electrons in the anomaly region at low altitudes, electrons will also be encountered in the auroral zones [II-6].

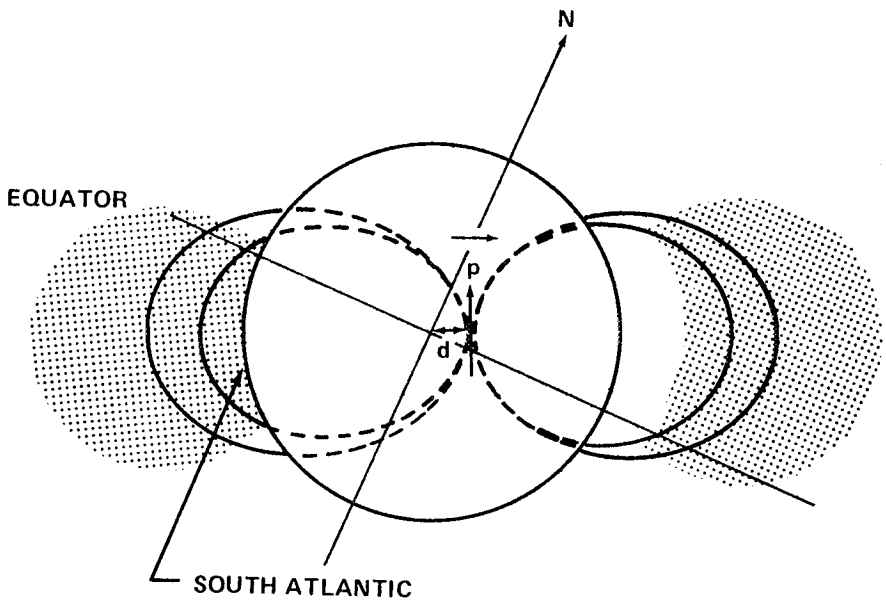

Figure II-17. South Atlantic Anomaly diagram.

The trapped radiation to be encountered in a 400 km polar orbit and in a 500 km, 57 deg inclination orbit has been determined. The electron and proton energy spectra design values are shown in Figures II-19 and II-20, respectively.

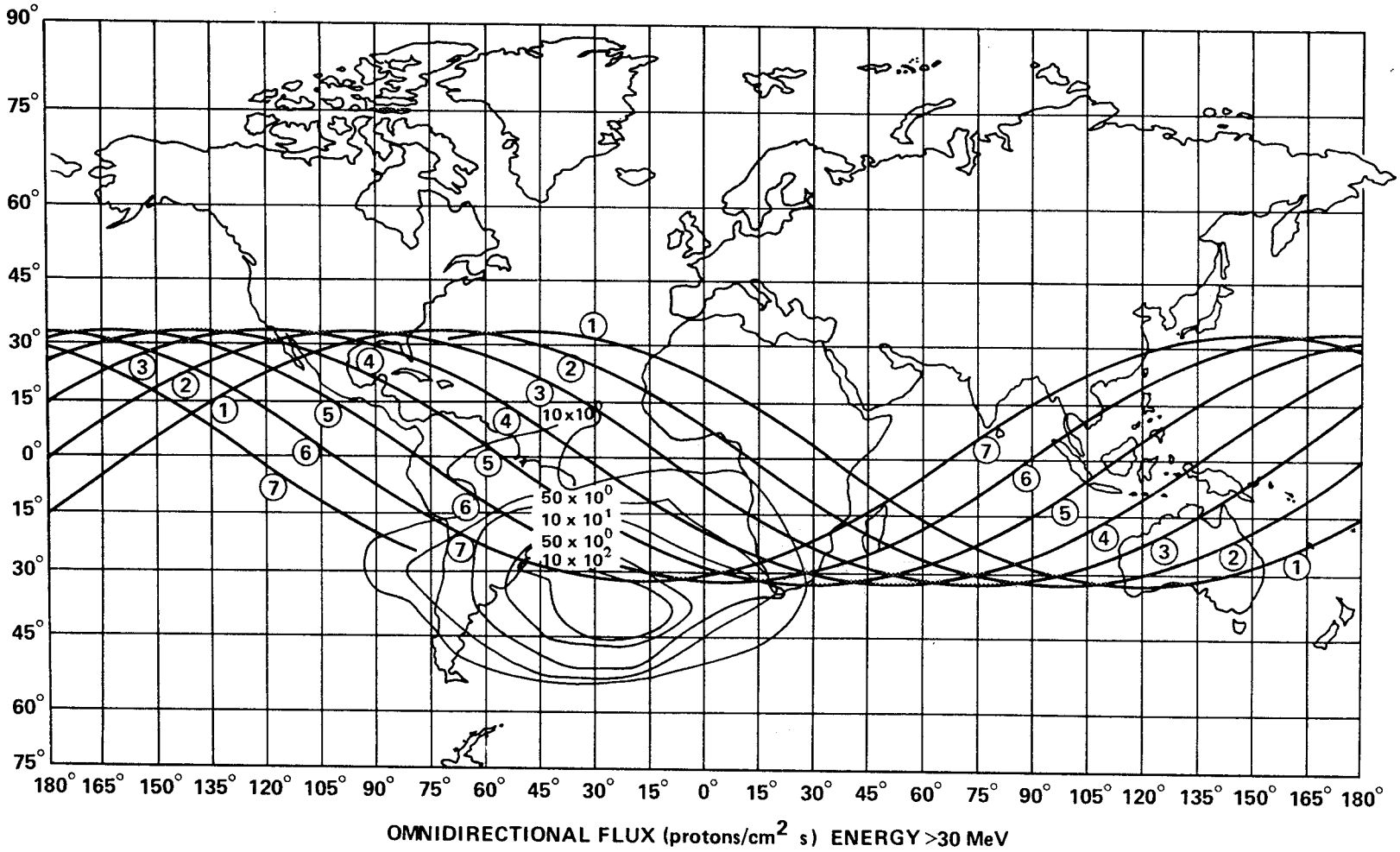

Figure II-18. Proton flux densities at an altitude of 296 km.

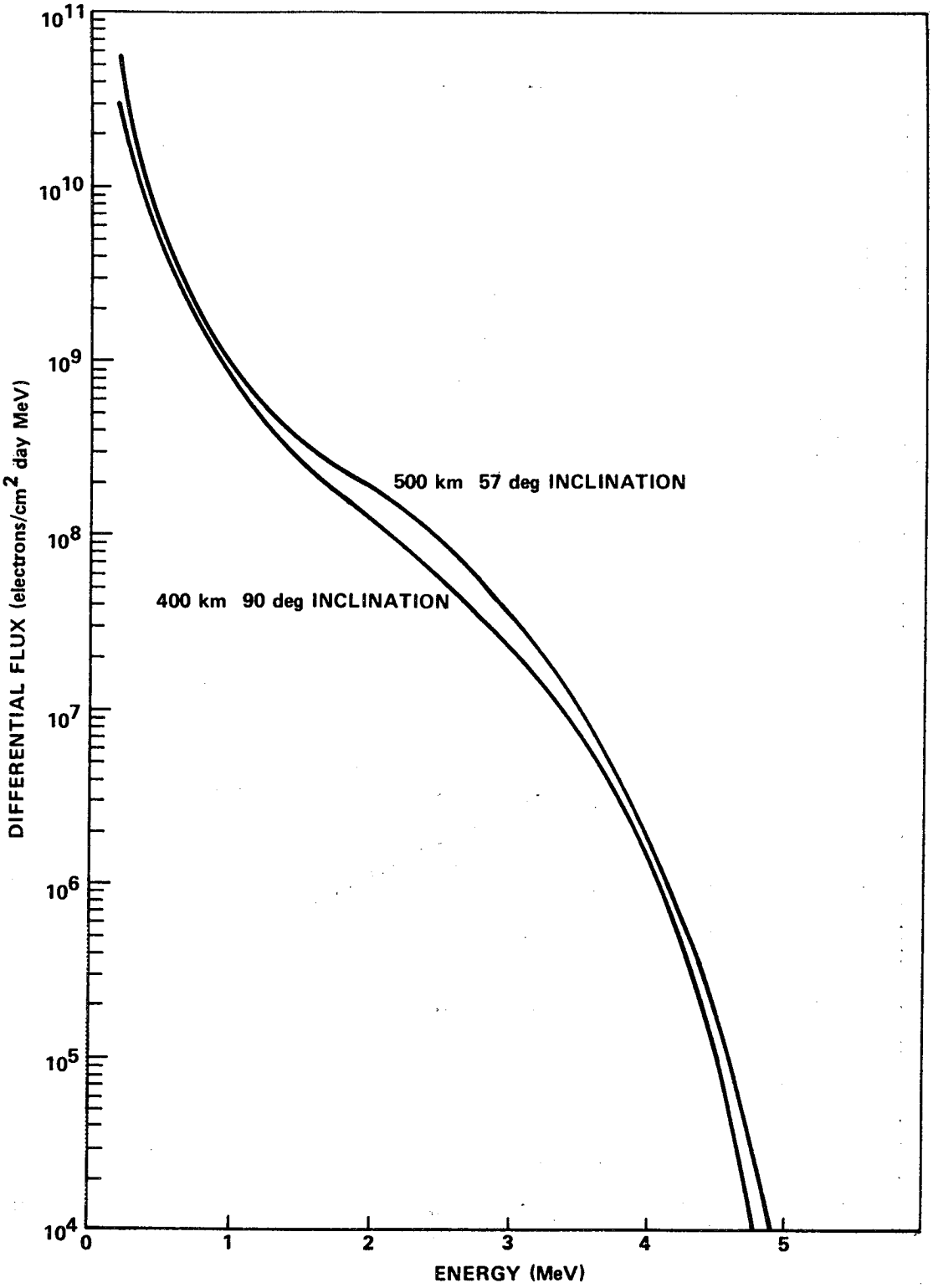

Figure II-19. Electron differential energy spectra.

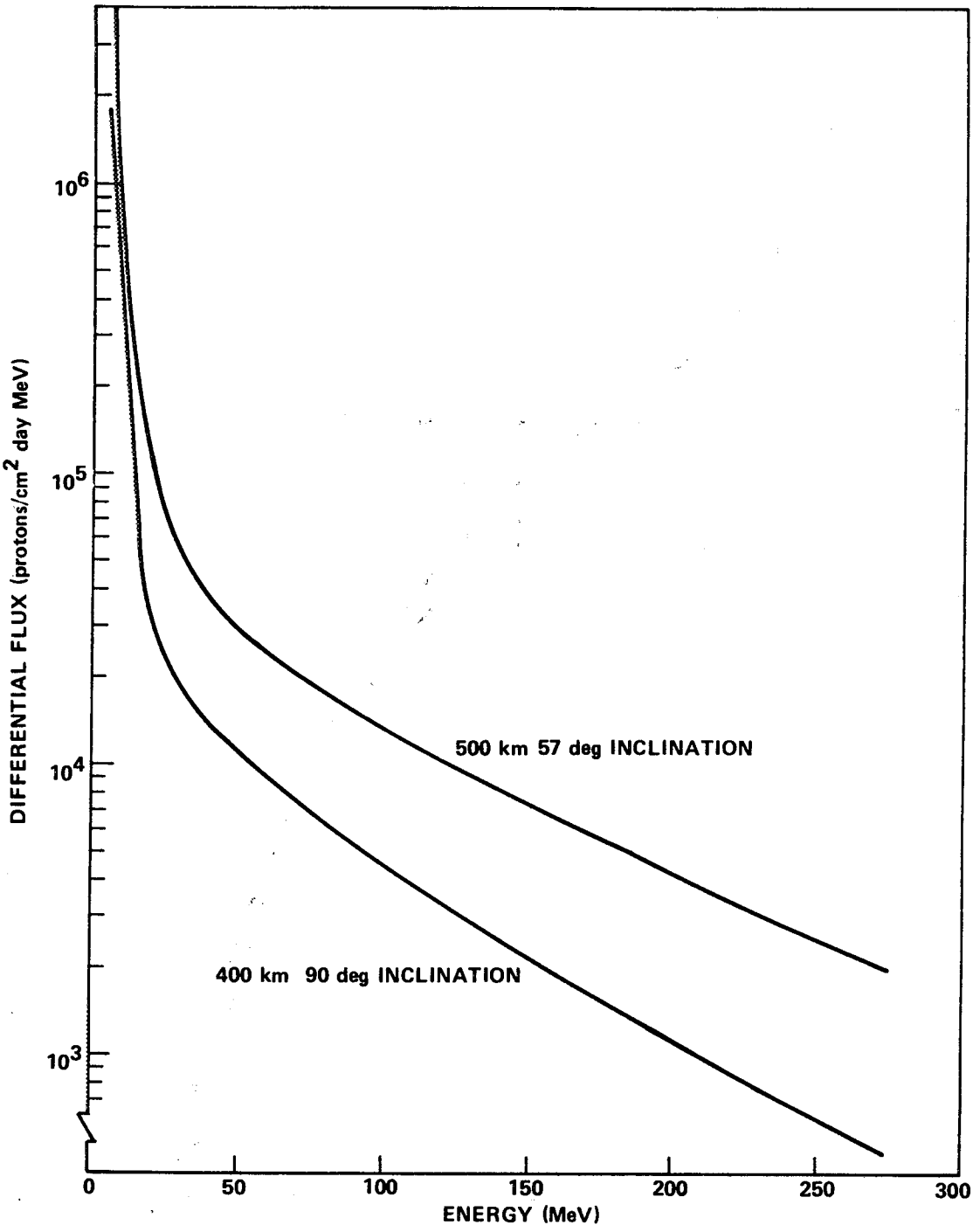

Figure II-20. Proton differential energy spectra.

2.4.2.2 Synchronous Orbit Altitude Environment

The trapped proton environment at synchronous orbit altitude is of no direct biological significance, but may cause deterioration of material surfaces over long exposure times. The proton flux at this altitude is composed of only low energy protons (less than 4 MeV) and is on the order of 10^5 protons/cm^2 s. A detailed description of this environment is given in Reference II-7. The local time-averaged proton energy spectrum for an equatorial synchronous orbit is shown in Figure II-21.

The trapped electron environment at synchronous altitude is characterized by variations in particle intensity of several orders of magnitude over periods as short as a few hours. However, for extended synchronous altitude missions, a local time-averaged environment can be used. The local time-averaged electron energy spectrum for an equatorial synchronous orbit is shown in Figure II-21. The environment encountered by synchronous orbit missions having different inclinations will be less than the equatorial environment [II-7, II-8, II-9].

2.4.3 Solar Particle Events

Solar particle events are the emission of charged particles from disturbed regions on the sun during solar flares. They are composed of energetic protons and alpha particles that occur sporadically and last for several days.

2.4.3.1 Particle Event Model

The free-space particle event model which should be used for spacecraft studies is given below.

$$\text{Protons: } N_p(>T) = \begin{cases} 7.25 \times 10^{11}\, T^{-1.2}\,; & 1\ \text{MeV} \leqq T \leqq 10\ \text{MeV} \\ 3.54 \times 10^{11}\, e^{-P(T)/67}\,; & 10\ \text{MeV} \leqq T \leqq 30\ \text{MeV} \\ 2.64 \times 10^{11}\, e^{-P(T)/73}\,; & T \geqq 30\ \text{MeV}. \end{cases}$$

$$\text{Alphas: } N_\alpha(>T) = \begin{cases} N_p(>T)\,; & T < 30\ \text{MeV} \\ 7.07 \times 10^{12}\, T^{-2.14}\,; & T \geqq 30\ \text{MeV}. \end{cases}$$

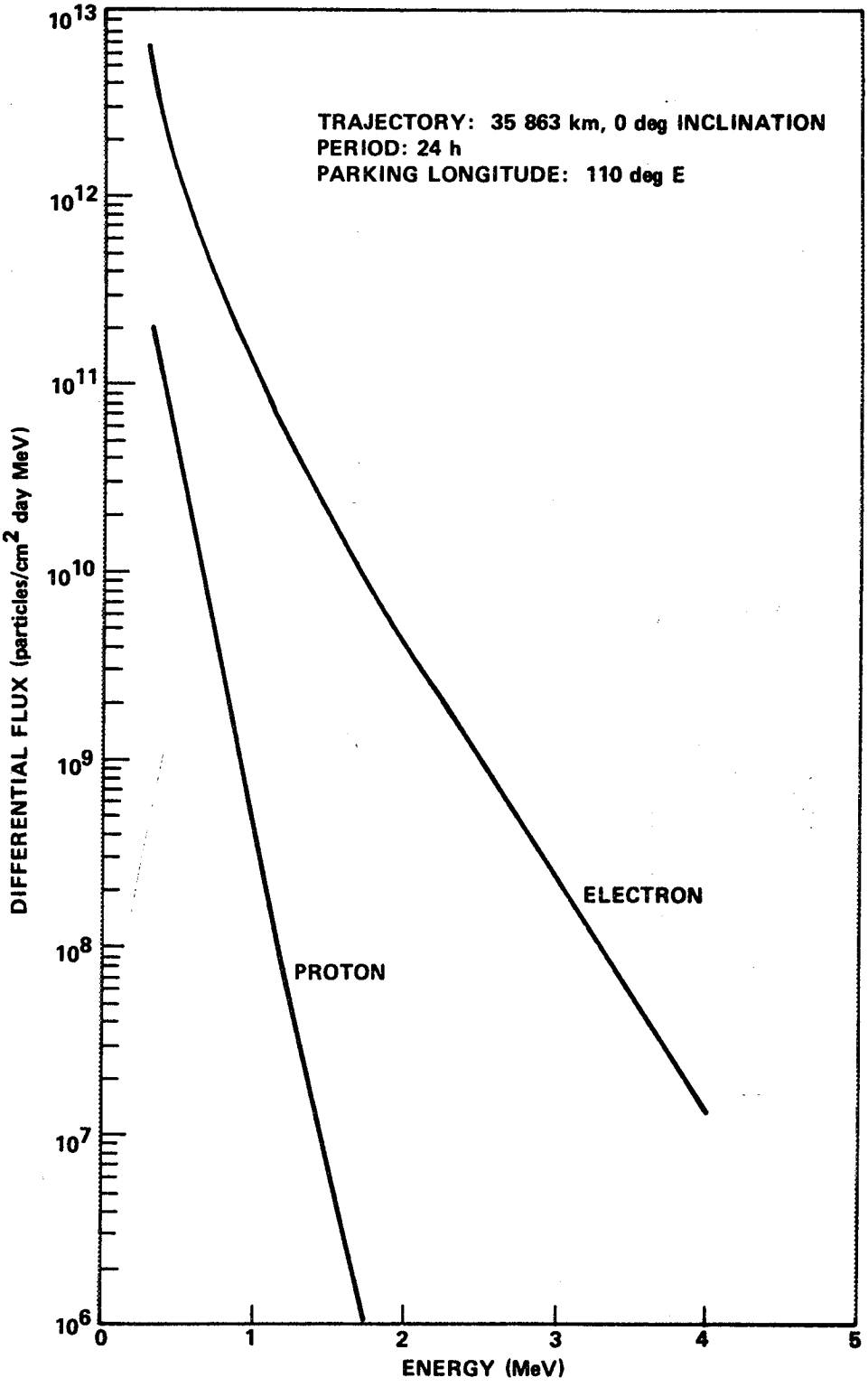

Figure II-21. Electron and proton differential energy spectra.

The terms $N_p(>T)$ and $N_\alpha(>T)$ are the integral fluxes in units of protons/cm^2 and alphas/cm^2, respectively. T is the particle's kinetic energy in units MeV and P (T) is the particle's magnetic rigidity in units mV given by

$$P(T) = \frac{1}{Ze}\sqrt{T\,(T + 2m_oC^2)}$$

where the quantity Ze is the magnitude of the particle's charge in units of electron charge; i.e., Ze = 1 for protons and Ze = 2 alphas. The rest mass energy for the particle is given by m_oC^2; i.e., m_oC^2 = 938 MeV for protons and 3728 MeV for alpha particles.

For synchronous orbit altitudes, the free-space solar particle event model described above should be used. For near-earth orbital altitudes, however, the free-space event model must be modified to account for the fact that the earth's magnetic field deflects some of the low-energy particles that would enter the atmosphere at low latitudes to the poles.

Solar particle events are more likely to occur at times of the solar maximum than at solar minimum.

2.4.4 Solar Cosmic Radiation

2.4.4.1 Particle Flux Spectrum

The particle flux spectrum is the same as in interplanetary space (see Paragraph 1.3.2.1.2).

2.4.4.2 Cutoff Rigidity

The magnetic field alters the penetration of charged particles in the vicinity of the earth. The minimum rigidity (cutoff rigidity) necessary to reach some geomagnetic latitude (L) and geocentric radius (R), in units of earth radii, is given by

$$P_c = \frac{60\cos^4 L}{R^2\,(1 + \sqrt{1 - \cos^3 L\cos\gamma})^2}\ ,$$

where P_c is the cutoff rigidity in mV units and γ is the half angle of the allowed cone about the normal to the meridian plane.

For vertical arrival, $\gamma = 90$ deg,

$$P_c = \frac{15 \cos^4 L}{R^2} .$$

2.4.4.3 Additional Information

Additional information relative to the terrestrial radiation environment is given in Reference II-7.

2.4.5 Thermal and Albedo Radiation (Earth)

The radiation of the earth consists of the sum of the earth-emitted thermal radiation and the reflected (albedo) radiation. The visual earth radiation, for the purpose of this section, consists entirely of visual albedo.

2.4.5.1 Earth Radiation [II-10, II-11]

Between 8 and 12 μm, the thermal spectral radiation emitted by the earth's atmosphere system is approximately the same as that emitted from a blackbody at 288 K. For longer wavelengths, it is approximated by a blackbody at 218 K (Fig. II-22).

The emitted thermal radiation is not a constant over the globe. It is principally influenced by the temperature of the earth's surface, the amount of cloud cover, the temperature of the air and the moisture content of the air.

2.4.5.2 Earth Albedo Radiation [II-10, II-11]

The global earth albedo is the ratio of the total radiation reflected from the earth to the solar radiation incident on the earth. The spectral

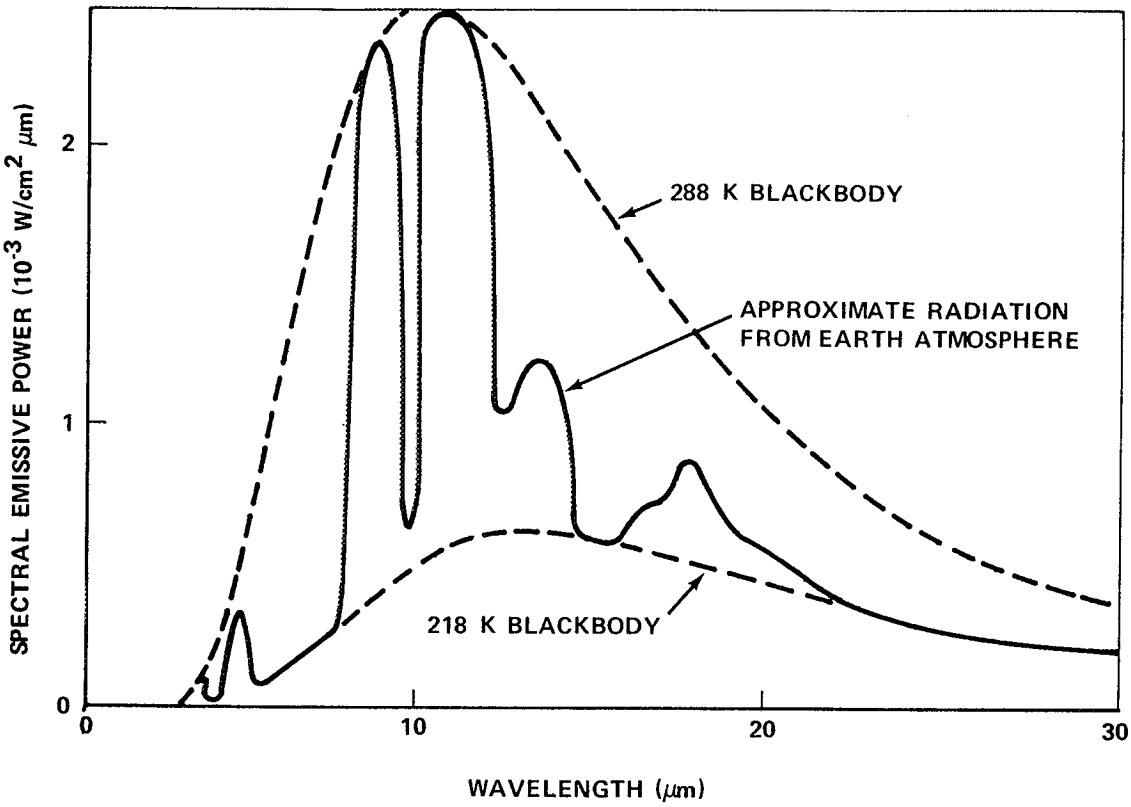

NOTE: THE 288 K BLACKBODY CURVE APPROXIMATES THE RADIATION FROM THE EARTH'S SURFACE, AND THE 218 K BLACKBODY CURVE APPROXIMATES THE RADIATION FROM THE ATMOSPHERE IN THOSE SPECTRAL REGIONS WHERE THE ATMOSPHERE IS OPAQUE

Figure II-22. A typical spectral emissive power curve for the thermal radiation leaving the earth.

distribution can be approximated by a blackbody at 5760 K. Approximate total ($\sim$0.2 to 4.0 μm) global is 0.39. Visual albedo (0.4 to 0.7 μm) is approximately 0.40. Visual albedo is somewhat higher than total albedo since less solar radiation in the visual wavelengths is absorbed in the earth's atmosphere system [II-12].

Local albedo for a wavelength region is defined by

$$\frac{\int_0^{2\pi}\int_0^{\pi/2} I(\theta,\phi)\cos\theta\sin\theta\,d\theta\,d\phi}{F\cos z}$$

where I is the emergent intensity, F is the incident flux and z the solar zenith angle. θ and ϕ are the geocentric latitude and longitude, respectively. Local albedo is highly variable, depending on the spatial position of the observer and the time of the observation.

Local albedo values range from 0.10 to 0.80 for clouds, 0.05 to 0.45 for land, and 0.03 to 0.20 for water. To date, there is no precise theoretical or empirical model for the albedo which includes:

a. The geometrical-physical aspects of the surface, scattering by the clear atmosphere and clouds.

b. The geographical-meteorological aspects as a function of time and position.

2.4.5.3 Thermal Environment Parameters [II-10, II-11]

Variation of the Time Average Effective Values about Their Global Values

Time Increment	Albedo Variation	Earth Emitted Thermal Radiation Variation W/m^2
$\Delta t < 0.3$ h	+0.30 +0.30 -0.15	+28 237 -97
$0.3 < \Delta t < 3$ h	0.30 ± 0.10	+24 237 -48
$\Delta t > 3$ h	0.30 ± 0.05	237 ± 21

The time average effective value is defined to be the average value of the albedo (or earth thermal radiation), taken over a time increment Δt, to which a satellite in near-earth orbit (period $\lesssim$ 3 h) is exposed. The range of the time average effective value decreases with increasing Δt and for large Δt (i.e., $\approx$ 3 h) approaches the range because of the seasonal variation.

See Paragraph 1.3.1.1 for the value of the solar constant.

2.4.5.4 Mean Visual Illumination of Earth by Sun (Day Outside Atmosphere)

1.37×10^5 lm/m^2.

2.4.5.5 Mean Brightness of Full Earth at Subsolar Point [II-11]

1.7×10^4 cd/m^2.

2.4.6 Radiation Properties of the Sun (Thermal)

See Paragraph 1.3.3.

2.4.7 Solar Cycle Predictions

A description of the MSFC Solar Cycle Prediction Program is given in Appendix A.

2.4.8 Dose Rate Calculation

The radiation dose contributed by electron and protons trapped in the earth's magnetic field should be determined for a given shielding configuration and trajectory by Burrell and Watt's dose codes [II-13, II-14]. The electron energy spectra should be obtained from the Vette 1980 [II-9] electron environment. The proton energy spectra should be obtained from Vette [II-8]. Reference II-15 uses the Vette environment, in B-L flux coordinates with a selection of the latest geomagnetic coordinate models [II-6] to obtain the desired electron and proton spectra used in the dose calculation.

2.4.9 Additional Information

Additional information relative to radiation and thermal properties is given in Reference II-11.

2.5 Meteoroid Environment

The meteoroid environment model [II-17, II-18] encompasses particles of only cometary origin and is composed of sporadic meteoroids in the mass range between 1 and 10^{-12} g and stream meteoroids in the mass range from 1 to 10^{-6} g.

2.5.1 Average Total Meteoroid Environment

The average total meteoroid (average sporadic plus a derived average stream) environment is to be used for preliminary design and for mission periods that cannot be rigidly specified. When the mission launch date and duration are specified later in the design, the probability of stream damage should be evaluated.

2.5.1.1 Particle Density

The mass density is 0.5 g/cm^3 for all meteoroid particle sizes.

2.5.1.2 Particle Velocity

The average meteoroid particle velocity is 20 km/s with the distribution as given in Figure II-23.

2.5.1.3 Flux-Mass Model

The average annual cumulative meteoroid flux-mass model in logarithmic plot is described mathematically as follows:

$$10^{-6} \leqq m \leqq 10^{0},\ \log N_t = -14.37 - 1.213 \log m$$

$$10^{-12} \leqq m \leqq 10^{-6},\ \log N_t = -14.339 - 1.584 \log m - 0.063 (\log m)^2$$

where N_t is the number of particles/m^2 s of mass m or greater and m is the mass in g.

The gravitationally focused, unshielded flux, N_t, must be multiplied by an appropriate defocusing factor for earth, G_e, and, if applicable, by the shielding factor. The G_e factor applies to all missions and is to be obtained from the equation given below. The body shielding factor for randomly oriented spacecraft, ζ, is calculated by the method given in Figure II-24 and applies to all missions. For oriented spacecraft, the effects of body shielding on the number of impacts as seen by parts of the spacecraft must be determined on a unique basis. The defocusing factor (G_e) may be calculated by

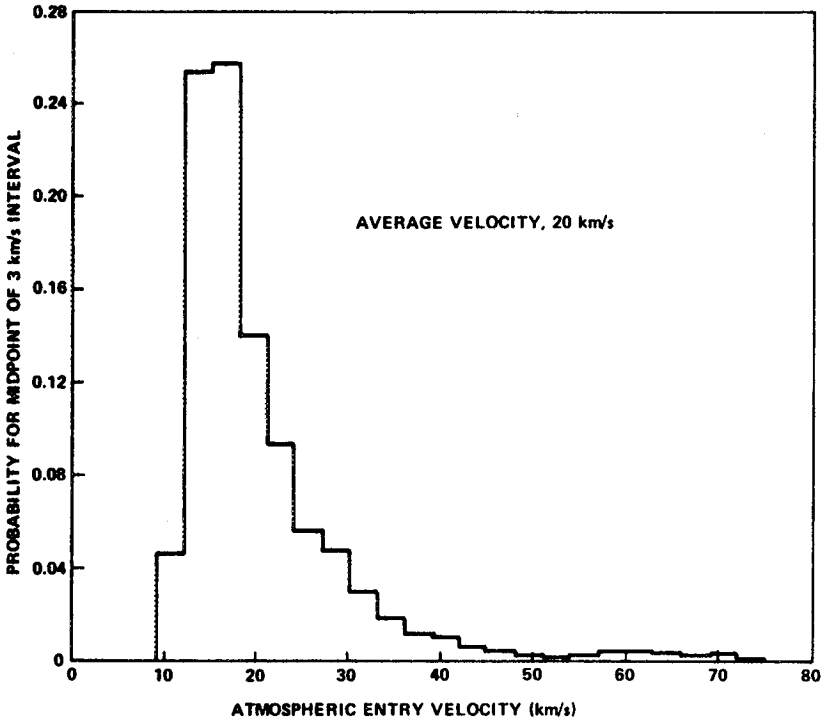

Figure II-23. Probability velocity distribution for sporadic meteoroids.

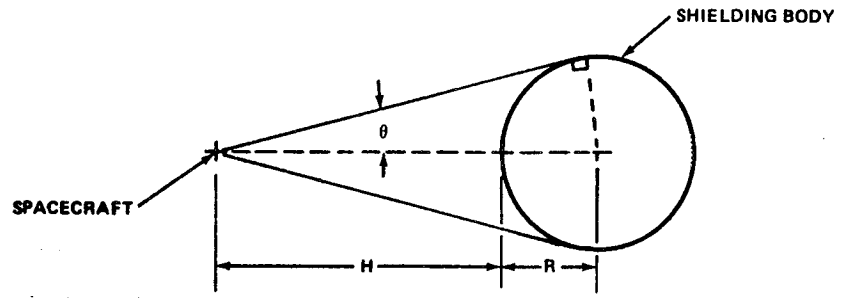

BODY SHIELDING FACTOR, ζ (DEFINED AS RATIO OF THE SHIELDED TO UNSHIELDED FLUX)

$$\zeta = \frac{1 + \cos\theta}{2}$$

WHERE: $\sin\theta = \frac{R}{R + H}$

R = RADIUS OF SHIELDING BODY

H = ALTITUDE ABOVE SURFACE

Figure II-24. Method for determining body shielding factor for randomly oriented spacecraft.

$$G_e = 0.568 + \frac{0.432}{r}$$

where r is the distance from the center of the earth in units of the earth's radius.

2.5.2 Sporadic Meteoroids

The average sporadic meteoroid environment is to be used in conjunction with the specific stream meteoroid environment for the design of a vehicle with a specified mission period (launch date and duration).

2.5.2.1 Particle Density

The mass density is 0.5 g/cm^3 for all sporadic particle sizes.

2.5.2.2 Particle Velocity

The average sporadic particle velocity is 20 km/s with the distribution as given in Figure II-23.

2.5.2.3 Flux-Mass Model

The flux-mass model for sporadic meteoroids is described mathematically as follows: For $10^{-6} \leqq m \leqq 10^{0}$,

$$\log N_{sp} = -14.41 - 1.22 \log m + \log G_e + \log \frac{1 + \sqrt{1 - 1/r^2}}{2} + \log F_{seasonal},$$

for $10^{-12} \leqq m \leqq 10^{-6}$,

$$\log N_{sp} = -14.339 - 1.584 \log m - 0.063 (\log m)^2 + \log G_e + \log \frac{1 + \sqrt{1 - 1/r^2}}{2} + \log F_{seasonal},$$

where

N_{sp} = number of particles/m^2 s of mass m or greater encountered by a randomly oriented surface

m = mass in g

G_e = the defocusing factor for the earth, which is applicable to all missions and is equal to $0.568 + 0.432/r$

r = the distance from the center of the earth in units of the earth's radius

$F_{seasonal}$ = a seasonal factor obtained from the table below. (The factor is obtained by taking the average of monthly factors listed for the months of the mission duration.)

Monthly Factors

January	0.6
February	0.4
March	0.5
April	0.6
May	1.1
June	1.6
July	1.8
August	1.6
September	1.1
October	1.1
November	0.9
December	0.7

2.5.3 Stream Meteoroids

The specific stream environment is to be used in conjunction with the sporadic meteoroid environment in the design of a vehicle with a specified mission period (launch date and duration).

2.5.3.1 Particle Density

The mass density is 0.5 g/cm^3 for all stream particle sizes.

2.5.3.2 Particle Velocity

The particle velocity of each stream is that given in Table II-1.

TABLE II-1. MAJOR METEOROID STREAMS

Name	Period of Activity	Date of Maximum	F_{max} [a]	Geocentric Velocity (km/s)
Quadrantids	Jan. 2 to 4	Jan. 3	8.0	42
Lyrids	Apr. 19 to 22	Apr. 21	0.85	48
η-Aquarids	May 1 to 8	May 4 to 6	2.2	64
O-Cetids	May 14 to 23	May 14 to 23	2.0	37
Arietids	May 29 to June 19	June 6	4.5	38
ζ-Perseids	June 1 to 16	June 6	3.0	29
β-Taurids	June 24 to July 5	June 28	2.0	31
δ -Aquarids	July 26 to Aug. 5	July 8	1.5	40
Perseids	July 15 to Aug. 18	Aug. 10 to 14	5.0	60
Orionids	Oct. 15 to 25	Oct. 20 to 23	1.2	66
Arietids, southern	Oct. through Nov.	Nov. 5	1.1	28
Taurids, northern	Oct. 26 to Nov. 22	Nov. 10	0.4	29
Taurids, night	Nov.		1.0	37
Taurids, southern	Oct. 26 to Nov. 22	Nov. 5	0.9	28
Leonids, southern	Nov. 15 to 20	Nov. 16 to 17	0.9	72
Bielids	Nov. 12 to 16	Nov. 14	0.4	16
Geminids	Nov. 25 to Dec. 17	Dec. 12 to 13	4.0	35
Ursids	Dec. 20 to 24	Dec. 22	2.5	37

a. F_{max} is the ratio of average maximum cumulative stream to average sporadic flux for a mass of 1 g and a velocity of 20 km/s.

2.5.3.3 Flux-Mass Model

The cumulative flux-mass model applicable to each individual stream is described mathematically as follows: For $10^{-6} \leqq m \leqq 10^{0}$,

$$\log N_{st} = -14.41 - \log m - 4.0 \log (V_{st}/20) + \log F$$

where

N_{st} = number of particles/m^2 s of mass m or greater

m = mass in g

V_{st} = geocentric velocity of each stream in km/s

F = ratio of cumulative flux of stream to the average cumulative sporadic flux as calculated from Figures II-25 and II-26. for the portion of the stream's duration within the mission period.

No gravitational factor is to be applied to the flux of a specific stream. Similarly, no shielding effect exists unless a shielding body eclipses the spacecraft relative to the radiant of a stream. When an eclipse occurs, the flux of that specific stream is zero.

2.5.4 Additional Information

Additional information relative to the meteoroid environment is given in References II-17 and II-18.

2.6 Geomagnetic Environment

2.6.1 Magnetic Field

The earth is surrounded by a magnetic field, often called the geomagnetic or terrestrial magnetic field, originating in its interior. The axis of the hypothetical magnet does not coincide with the north-south poles, and is displaced from the center by a distance of about 450 km. Consequently, the geomagnetic field is not exactly symmetrical to the earth's surface.

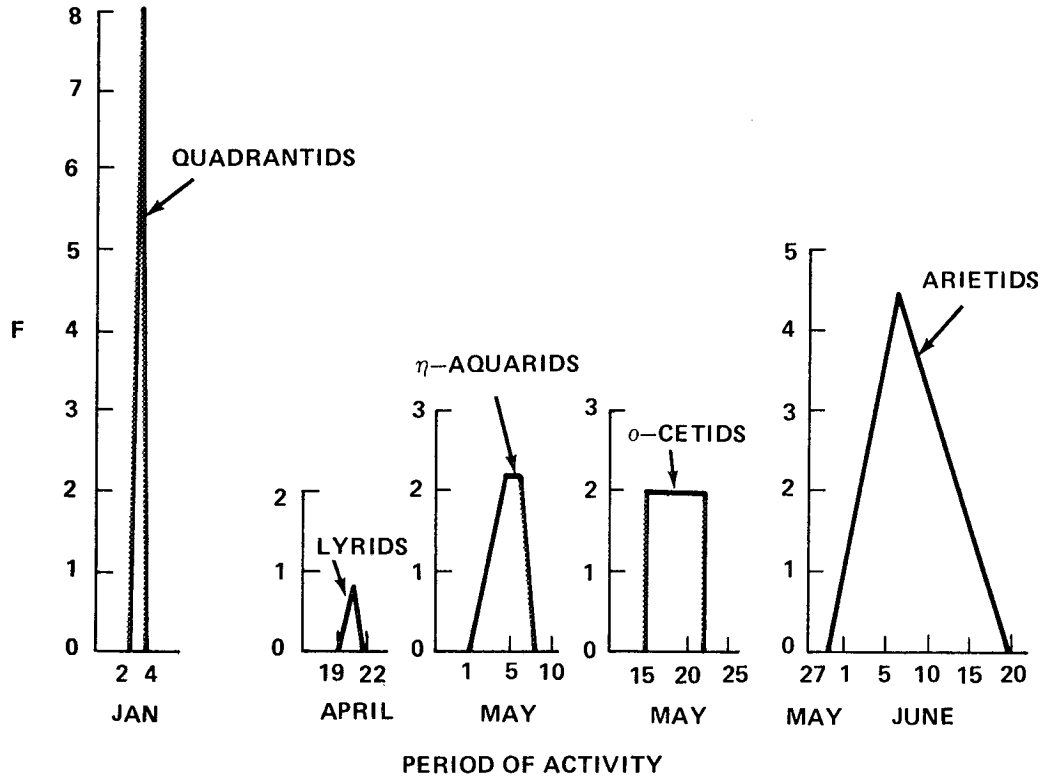

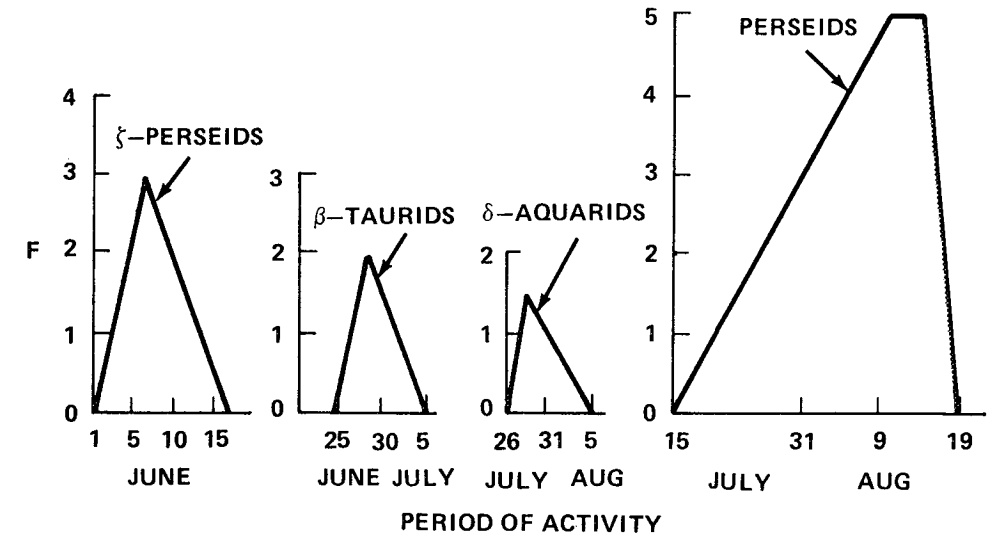

$$F = \frac{\text{CUMULATIVE FLUX OF STREAM}}{\text{AVERAGE CUMULATIVE SPORADIC FLUX}}$$

Figure II-25. Activity ratio factor versus period of activity (Jan.-Aug.) for major streams based on photographic meteors (mass = 1 g, velocity = 20 km/s).

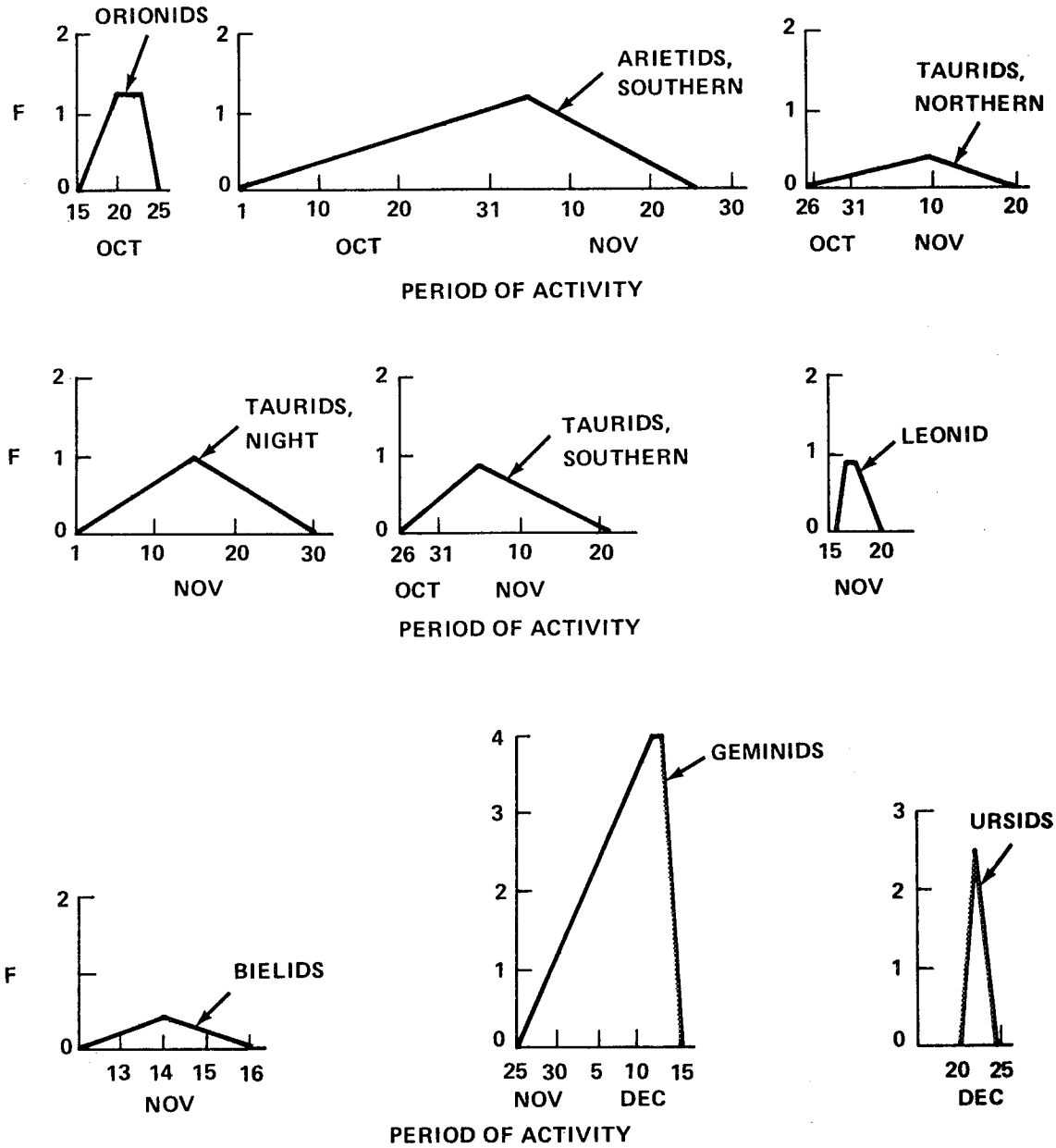

Figure II-26. Activity ratio factor versus period of activity (Sept. - Dec.) for major streams based on photographic meteors (mass = 1 g, velocity = 20 km/s).

The magnetic poles on the surface are the locations that, for all practical purposes, have the lines of force perpendicular to the surface.

The geomagnetic axis is a line joining the two magnetic poles. At the magnetic equator the lines of force are parallel everywhere to the earth's surface; i.e., horizontal. From about 170 deg W eastward to about 30 deg E, the geomagnetic equator is south, but at other longitudes it is north of the geographic equator.

The total strength of the earth's magnetic field varies over the surface of the earth from 0.65 to 0.70 gauss near the magnetic poles; it is weakest toward the equatorial region where its value is 0.30 to 0.35 gauss. Its variation with latitude is by no means uniform — an exceptionally low value of 0.25 gauss has been recorded in southeast Brazil.

At some distance from the earth, the intensity variation may be taken to be inversely proportional to the cube of the distance from the center of the dipole. The average total magnetic field is given in the following tabulation.

Average Total Magnetic Field in Gauss

Altitude (km)	Geodetic Colatitude (deg)			
	0	30	60	90
200	0.52243	0.50782	0.40338	0.31406
400	0.48121	0.46403	0.36670	0.28630
1000	0.37978	0.35841	0.28088	0.21778
2000	0.26428	0.24682	0.18904	0.14629
3000	0.19052	0.17608	0.13343	0.10330
4000	0.14158	0.12988	0.09773	0.07571
6371	0.07693	0.07001	0.05217	0.04044

From measurements of the strength of the geomagnetic field, it is clear that the field is not steady, but has secular and transient variations. It takes many years for the effect of the secular variations to become significant. The transient variation, however, occur within days or less and are caused by external factors, some of which are of solar origin.

2.6.2 Temporal Variations

Temporal variations are short-duration disturbances in the geomagnetic field resulting from solar activity and changing relative positions of the sun and earth. These variations typically have durations ranging from a few seconds to several days and amplitudes from a few hundredths to several hundred gammas.

The sun's emission of a solar plasma (i.e., the solar wind) influences the earth's magnetic field. When the solar plasma enters the earth's magnetic field, the interaction produces a sheath of current in the plasma which opposes, by Lenz's law, the earth's field. At the subpolar point, the earth's magnetic field is compressed until its magnetic pressure (i.e., its magnetic energy density) balances the kinetic pressure of the solar plasma. This balance is reached at about 10 earth radii, and therefore the earth's magnetic field is to be limited to such a finite distance in a direction toward the sun. In directions that make an appreciable angle with the sun, the influence of the earth's magnetic field will be extended considerably.

2.6.3 Magnetic Field at Geosynchronous Altitudes

At synchronous altitude, an average magnetic field of about 138 γ (138 nT) is to be expected; however, this value can vary considerably. Approximations to the magnetic field in this region may be obtained from the spherical harmonic expansion model [II-19], but expansion beyond the first 8 terms in this model is not warranted because contributions from external sources are not included.

2.6.4 Models of the Earth's Magnetic Environment

For design studies requiring a detailed description of the earth's magnetic field the current International Geomagnetic Reference Field corrected to the proper epoch should be used [II-6, II-19, II-20, II-21].

2.6.5 Additional Information

More detailed information relative to the geomagnetic environment is given in the two NASA design criteria monographs [II-22, II-23].

2.7 Astrodynamics Constants

2.7.1 Earth Constants (Epoch 1960.0) [II-24, II-25, II-26]

Distance from sun (average)	1.495978930×10^8 km
Eccentricity of orbit	0.0167295
Orbital period (sidereal)[3]	365.25636 days
Radius (equatorial)	6378.140 km
Mass ratio (sun/planet)	332945.6
Flattening (dynamic)	1:298.256
Average density[3]	5.517 g/m^3
Rotation rate $\dot{\theta}$	0.7292115085×10^4 s^{-1}
Gravitational parameter	3.986012×10^5 km^3/s^2

2.7.2 Gravitational Potential Function for the Earth [II-24]

One of the environmental forces which exerts a torque on a large spacecraft in earth orbit is the gravity gradient. This force acts in a direction tangent to a contour line of the geopotential surface. When a spacecraft attitude is locked into a particular coordinate system (e.g., solar-fixed), the gravity gradient forces vary with time as the spacecraft's main moments of inertia axes have varying inclinations to the geopotential contour lines. Stable equilibrium may be reached by producing correcting forces of the proper magnitude and direction. The energy required for the main spacecraft attitude hold control over a period of months against gravity gradient torques can be quite large for certain spacecraft configurations.

$$U = \frac{GE}{r}\left[1 - \sum_{n=2}^{\infty} (a_e/r)^n J_n P_n(\sin \phi') + \sum_{n=2}^{\infty} \sum_{m=1}^{\infty} (a_e/r)^n P_{nm}(\sin \phi') (C_{nm} \cos m\lambda + S_{nm} \sin m\lambda)\right]$$

where

r = radius from center of the earth

ϕ' = geocentric latitude

λ = geographic longitude

P_{nm} = associated Legendre functions

GE = gravitational constant of Earth

a_e = equatorial radius of the earth.

Values for the zonal harmonics (J_n) are as follows:

$$J_2 = (1082.7 \pm 0.1) \times 10^{-6}$$

$$J_3 = (-2.56 \pm 0.1) \times 10^{-6}$$

$$J_4 = (-1.58 \pm 0.2) \times 10^{-6}$$

$$J_5 = (-0.15 \pm 0.2) \times 10^{-6}$$

$$J_6 = (0.59 \pm 0.2) \times 10^{-6}$$

$$J_7 = (-0.44 \pm 0.2) \times 10^{-6} .$$

Values for the tesseral harmonics (C_{nm}, S_{nm}) are given in the following tablulation:

n	m	C_{nm}	S_{nm}
2	1	0 $\times 10^{-6}$	0 $\times 10^{-6}$
2	2	1.57 $\times 10^{-6}$	-0.897 $\times 10^{-6}$
3	1	2.10 $\times 10^{-6}$	0.16 $\times 10^{-6}$

n	m	C_{nm}	S_{nm}
3	2	0.25×10^{-6}	-0.27×10^{-6}
3	3	0.077×10^{-6}	0.173×10^{-6}
4	1	-0.58×10^{-6}	-0.46×10^{-6}
4	2	0.074×10^{-6}	0.16×10^{-6}
4	3	0.053×10^{-6}	0.004×10^{-6}
4	4	-0.0065×10^{-6}	0.0023×10^{-6}

The zonal harmonics (J_2, J_3, J_4 . . .) have a greater effect on the orbit of a satellite than the tesseral harmonics. The tesseral harmonics cause oscillatory disturbances that change sign rapidly, but the zonal harmonic effect is cumulative. The even coefficients, J_2, J_4, . . . , can well be determined from the regression of the node, and the rotation of perigee. Reliable gravitational coefficients have been obtained from low altitude artificial satellites. Perhaps the most significant result obtained from artificial satellites is the reliable determination of J_2, and hence the flattening f. Presently accepted values of 1/f range from 298.2 to 298.3. This flattening of the earth's surface causes the largest but not the only deviation of the gravitational field of the earth from that of a homogeneous sphere. Numerous higher-order spherical harmonic expansions derived from analysis of artificial satellite motions present different sets of coefficients with each analysis. Since the data still yield divergent results, only the first few terms have been used for these approximation calculations since they make the largest contribution with additional terms giving diminishing returns.

During the Apollo mission, the gravitational function was approximated using the first three zonal harmonic coefficients (J_2, J_3, and J_4) and the main tesseral harmonic coefficients (C_{22} and S_{22}). The following expressions for the gravitational potential function of the earth was recommended for space vehicle design studies; however, recent improvements and greater accuracy are available if needed [II-26].

$$U = \frac{GE}{r}\left[1 - \frac{J_2}{2}(a_e/r)^2(3\sin^2\phi' - 1) - \frac{J_3}{2}(a_e/r)^3(5\sin^3\phi' - 3\sin\phi')\right.$$

$$- \frac{J_4}{8} (a_e/r)^4 \ (35 \sin^4 \phi' - 30 \sin^2 \phi' + 3)$$

$$+ 3(C_{22} \cos 2\lambda + S_{22} \sin 2\lambda) \ (a_e/r)^2 \cos^2 \phi' \Big]$$

where

r = radial distance from center of the earth

ϕ' = geocentric latitude

$J_2 = 1082.7 \ (\pm 0.1) \times 10^{-6}$

$J_3 = -2.56 \ (\pm 0.1) \times 10^{-6}$

$J_4 = -1.58 \ (\pm 0.2) \times 10^{-6}$

$C_{22} = 1.57 \ (\pm 0.01) \times 10^{-6}$

$S_{22} = -0.897 \ (\pm 0.01) \times 10^{-6}$

a_e = equatorial radius of the earth

λ = geographic longitude.

If a more accurate gravity model is needed or desired, then the gravity model of the 1973 Smithsonian Standard Earth [III] should be used [II-24].

2.7.3 Geodetic Models

If accurate geodetic positions are required, the geodetic model given in the Smithsonian Astrophysical Observatory Special Report 353 should be used [II-24].

2.8 Winds

2.8.1 Theoretical Models of the Wind Field

Geisler [II-27] and Kohl and King [II-28] have computed wind fields from Jacchia's [II-29] static diffusion model, J64, of the thermosphere, and

Geisler [II-30] has computed winds using Jacchia and Slowey's [II-31] modifications to J64. In these studies, the temperature, density, and mean molecular weight fields are used to derive pressure gradients which then are combined with ion drag forces in the form of models of the electron density distribution and simple vertical profiles of the kinematic viscosity to generate wind fields. Figures II-27 and II-28 [II-30] depict the distribution of winds as a function of time and latitude, respectively. The meridional winds become large at night, approaching 225 m/s above 300 km at 0200 LT, and then decrease to about 100 m/s above 300 km at 1400 LT because of the increase in ion drag (electron number density). Figures II-29 and II-30 [II-29] show that the change in electron number density changes both the wind speed and the direction. Figure II-31 shows the height distribution of the meridional and zonal wind components for the low electron number density case [II-29]. These models provide an estimate of the distribution of both the direction and speed of the winds on a global basis. They are useful first approximations; however, they should not be expected to be quantitatively accurate.

2.8.2 Winds in the Lower Thermosphere — 90 to 150 km

Winds in the lower thermosphere are principally deduced from direct measurements of motions of chemiluminescent clouds, although measurements of meteor drifts, distortions of the geomagnetic currents, and measurements of charged particle drifts have contributed. Tidal and gravity waves contribute significantly to motions observed below 200 km. Kochanski [II-32] indicates that internal gravity waves contribute to all observed wind profiles between 80 and 120 km. The energy of the internal gravity waves decreases exponentially [II-33] from 80 to 180 km so that at approximately 180 km only about 20 percent of the wind data include a wave portion.

Figure II-32 shows the resultant components of the wind (the internal gravity wave motions have been removed) obtained from 25 sodium cloud experiments. Figure II-33 shows the annual, summer, and winter mean wind velocities and the frequency of occurrence of wind speeds above specific values. One of the principal features is the persistently high speeds observed between 100 and 105 km. Figure II-34 shows that intense wind shears are also observed in the region just above 100 km.

Figures II-35 and II-36 show the meridional and zonal components of winds measured at Sardinia from nine sodium cloud experiments [II-33]. These figures show the autumn to spring variations in the vertical wind profile. The zone of strong vertical shear found above 100 km by Kochanski [II-32] and shown in Figure II-34 is easily recognizable.

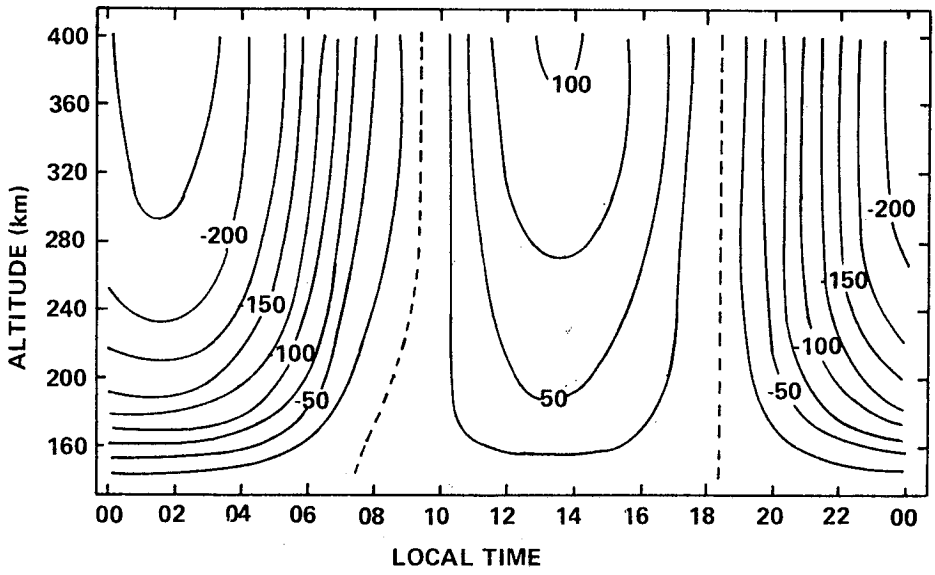

Figure II-27. Contours of meridional wind speed at 45 deg north latitude in units of ms^{-1}, positive values directed toward the north. [Results are obtained with equinox transition times and the Jacchia and Slowey (1967) model.]

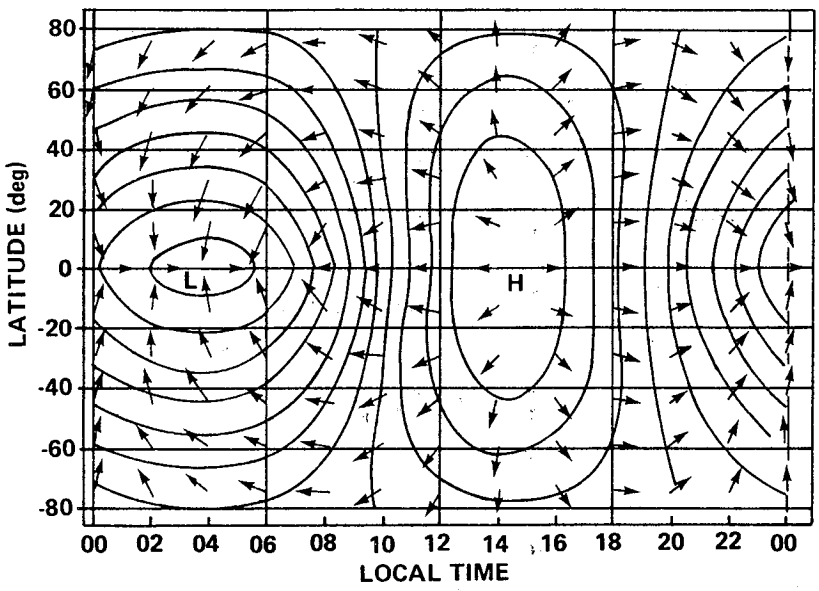

Figure II-28. Wind vectors at the 300 km level are shown against a background of isobars at this level, the longest arrow representing a wind speed of about 225 ms^{-1}. (The pressure and wind fields are symmetric about the equator.)

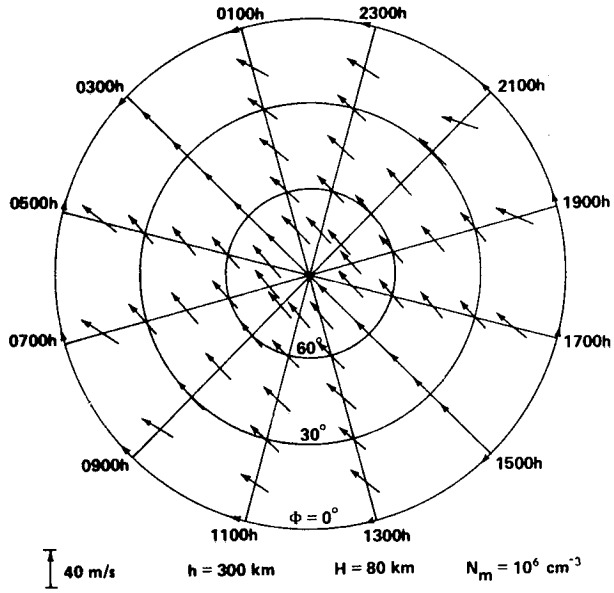

Figure II-29. The atmospheric wind system in the northern hemisphere calculated for an altitude of 300 km when the peak electron density is 10^6 cm^{-3}.

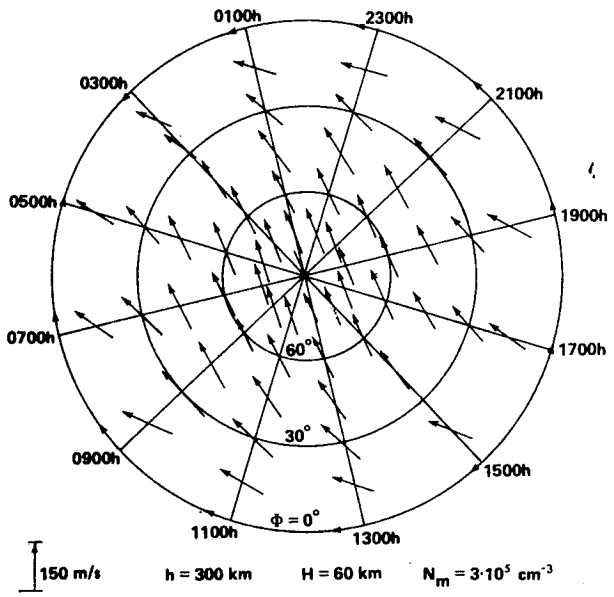

Figure II-30. The atmospheric wind system in the northern hemisphere calculated for an altitude of 300 km when the peak electron density is 3×10^5 cm^{-3}.

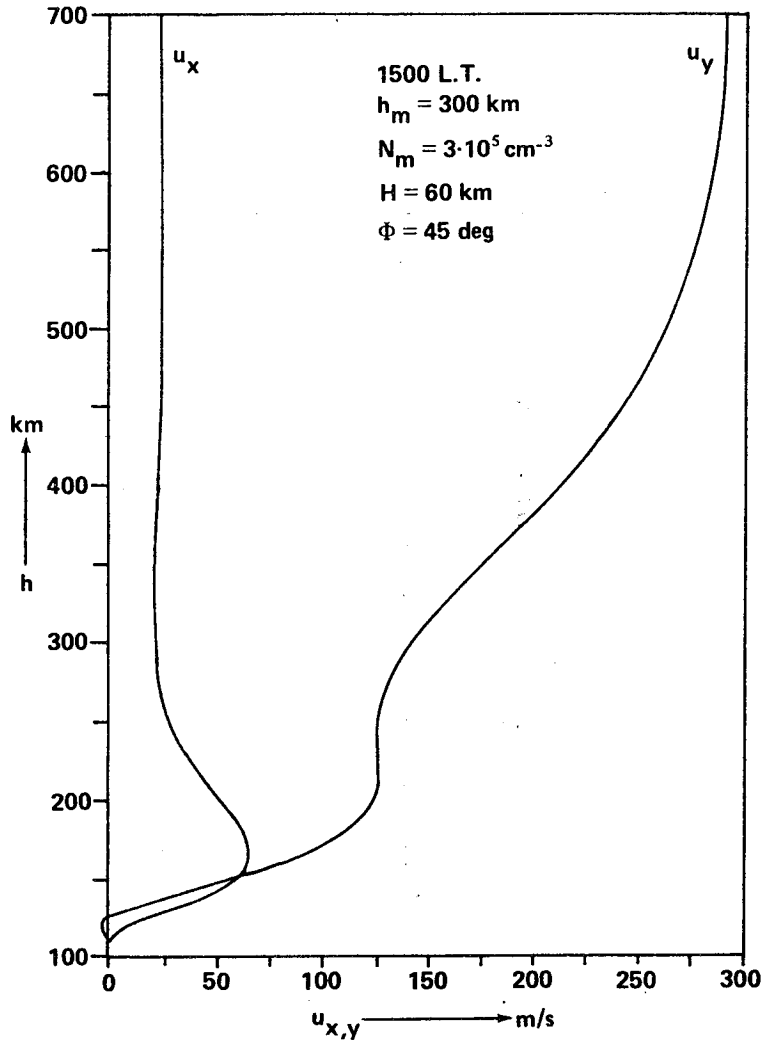

Figure II-31. The variation with height of the horizontal velocity components at 15.00 L.M.T. at a latitude of 45 deg.

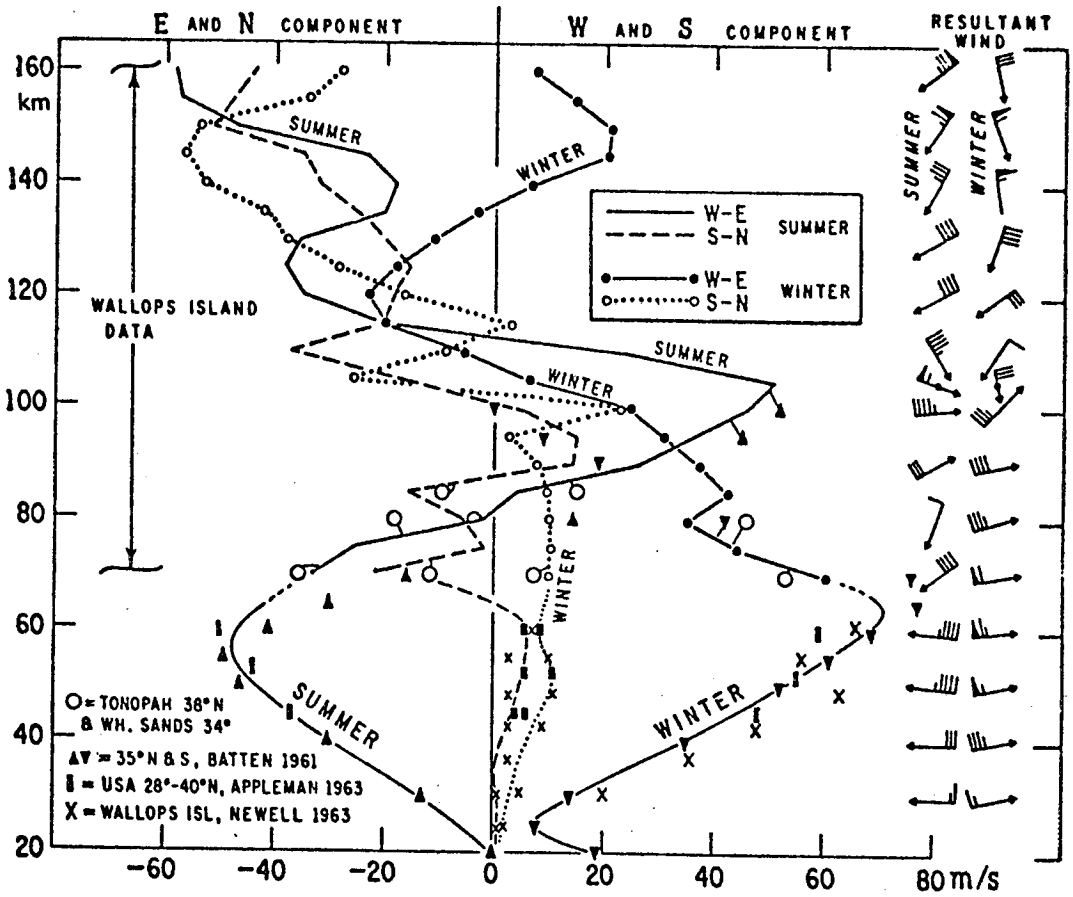

Figure II-32. Resultant components of the wind near latitude 38 deg N (The upper part is based on 25 sodium cloud experiments from Wallops Island. Arrows indicate the resultant wind.)

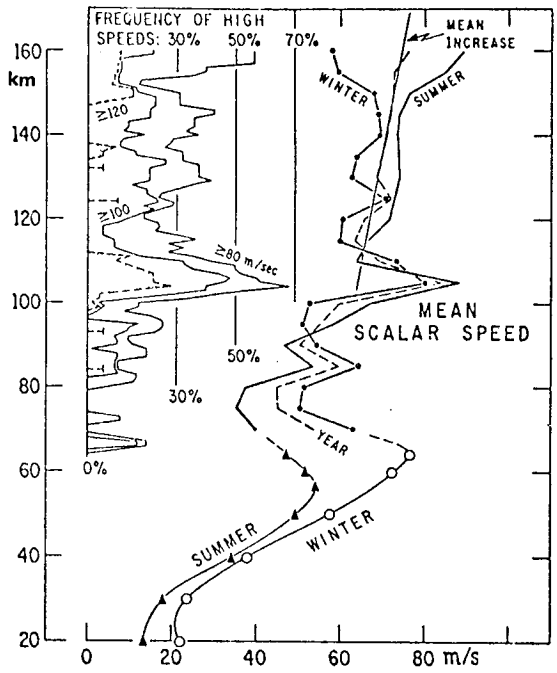

Figure II-33. Averages of the absolute value of wind velocity regardless of direction (i.e. the mean scalar speed), based on the same data as Figure II-32. (Inset: frequency of occurrence of speeds over 80, 100, and 120 m/s.)

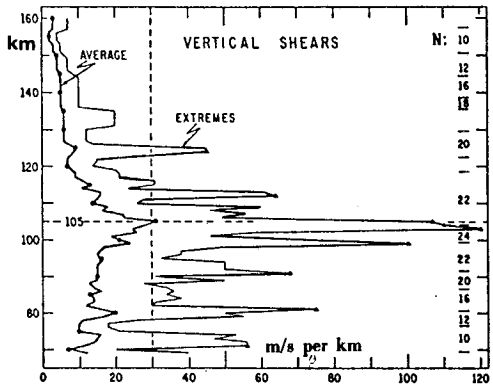

Figure II-34. Magnitude of vertical wind shears based on sodium cloud data from Wallops Island. (The shears were computed for $\Delta Z = 1$ km and plotted for each kilometer of elevation. N is the number of observations.)

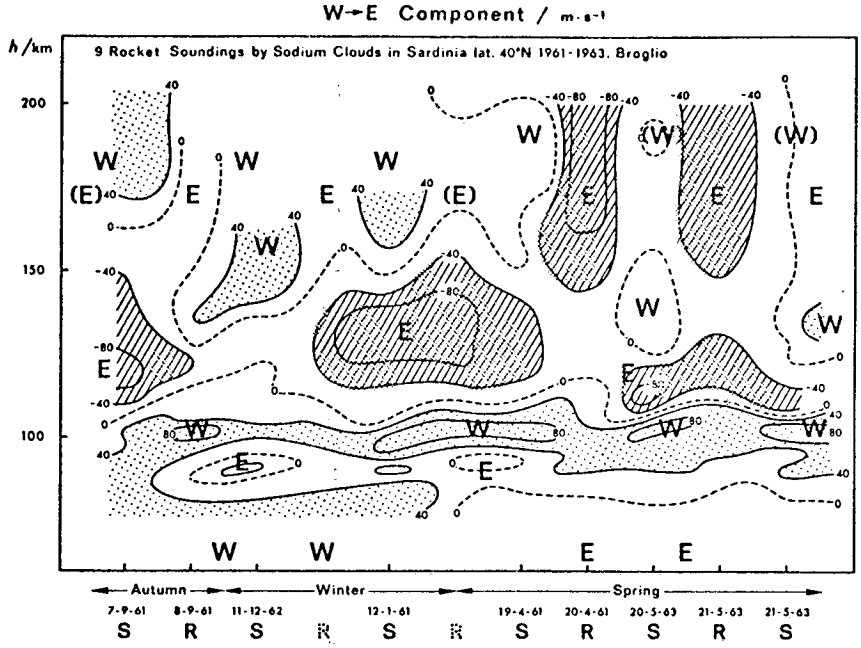

Figure II-35. Results of rocket soundings by sodium clouds in Sardinia 1961-1963, east-west. (Numerical indications give speed in m/s.)

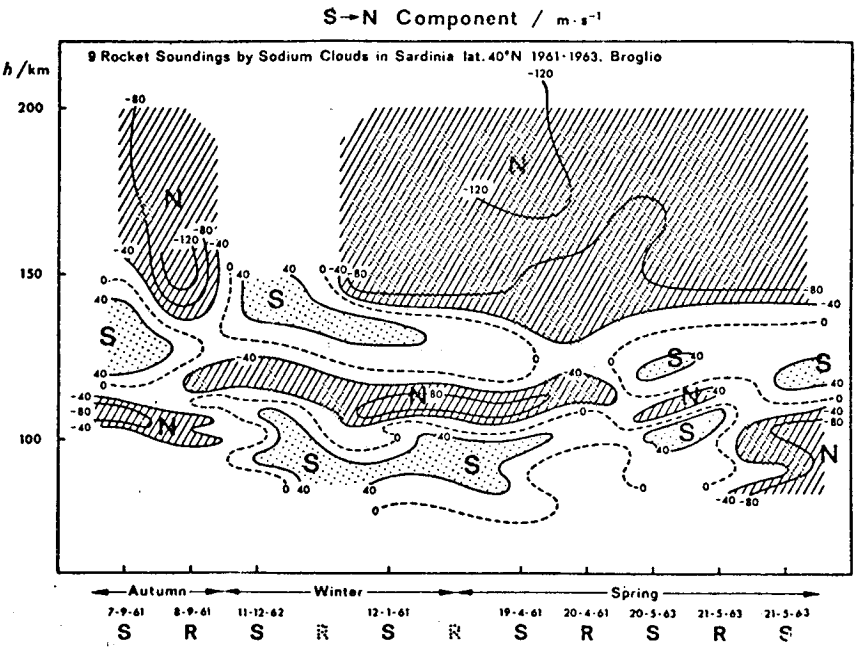

Figure II-36. Result of rocket soundings by sodium clouds in Sardinia 1961-1963, north-south. (Numerical indications give speed in m/s.)

Figures II-32, II-35, and II-36 show that above 150 km a rather persistent equatorward flow is observed and that a weak westward flow observed in the winter gives way to a stronger eastward flow in spring and summer. Kochanski [II-32] indicates that a general equatorward flow occurs for both summer and winter in the region above 100 km, whereas Fedele and Zanela (Fig. II-36) indicate that some seasonal variation is observed in the meridional winds between 100 and 150 km. In addition, Kochanski in Figure II-32 indicates that the zonal component changes from westward (90 to 115 km) to eastward (115 to 140 km) with increasing altitude for both seasons, whereas Fedele and Zanela indicate a more complicated seasonal variation.

Data from chemiluminescent cloud experiments give instantaneous wind profiles at specific locations. The data are complicated by the fact that many dynamic processes contribute to the observed profile. Data from these experiments are obtained at widely separated locations and times. Consequently, the data give little indication of global fields or processes. Neither do the data give good measure of mesoscale variability of the winds. Thus, these data give a general indication of the types of magnitudes of motion one should expect to find in probing the lower thermosphere, but no information on the general distribution of the winds as do those studies using the global distribution of density to derive horizontal winds.

2.8.3 Winds Above 150 km

Above 150 km, the principal source of wind data is observation of variations of the inclination angle of satellites in orbit. King-Hele has studied these variations over the past 8 years to determine the eastward rotation rate of the upper atmosphere. Figure II-37 summarizes the results of these studies [II-34].

In Figure II-37, Λ is the rotation rate of the atmosphere, where $\Lambda = 1$ is the rotation rate of the earth. To determine the zonal velocity u_x relative to the earth at an altitude z and latitude ϕ we have

$$u_x = \omega(\Lambda - 1)\ (r_E + z)\ \cos\phi\ ,$$

where r_E is the radius of earth and ω is the rotation rate,

$$\omega = 7.292116 \times 10^{-5}\ \text{rad/s}.$$

ORIGINAL PAGE IS
OF POOR QUALITY

Figure II-37. Mean upper-atmosphere rotation rate, derived from analysis of 29 satellite orbits.

With these definitions, Figure II-37 indicates that the atmosphere is rotating faster than the earth above 140 km to about 450 km. The average eastward winds are indicated to increase from a band 40 m/s at 200 km to 160 m/s at 350 km at 30 deg latitude. Above 450 km, a reversal exists of the wind direction as $\Lambda < 1$.

Challinor [II-35] believes that the apparent mean rotation of the upper atmosphere is caused by an eastward daytime motion which is primarily confined to equatorial latitudes. The satellite observations are weighted toward low latitude and daytime conditions. A number of other explanations have been offered for these observations of the super-rotation of the upper atmosphere [II-37].

2.8.4 Vertical Winds

The vertical velocities are about two orders of magnitude less than the horizontal velocities. Dickinson and Geisler [II-36] in a study based on Geisler's [II-27] earlier work find the vertical velocities generally to be less than 10 m/s.

2.8.5 Anomalous Strong Winds

Increases in the density of the upper atmosphere during geomagnetic storms have been observed many times. On one occasion near the auroral oval a horizontal wind speed on the order of 1.5 km s^{-1} was observed to occur at approximately 150 km altitude simultaneously with a large increase in the ambient density during a very large geomagnetic storm. Theoretical calculations support this observation and also postulate the possibility of vertical wind speeds on the order of 50 to 75 ms^{-1}. Large changes in the composition of the neutral upper atmosphere have been observed during geomagnetic storms. Users should contact the Atmospheric Sciences Division of the Space Sciences Laboratory if a specific design problem arises which might be affected by these anomalous occurrences.

2.8.6 Design Criteria

For design purposes, the following scalar wind speeds (ms^{-1}) should be used:

Altitude (km)	Speed (ms^{-1}) Mean	Maximum
90 to 150	200	325
150 to 200	200	250
200 to 300	150	200
300 to 400	150	200

These wind speeds are referenced to a coordinate system fixed to and rotating with the earth's surface.

Satellites other than those at geosynchronous altitude will be affected by a combination of these winds and the winds caused by the rotation of the earth which can be calculated from:

$$u_x = \omega(R_E + z) \cos \varphi \quad ms^{-1}$$

where

$\omega = 7.292116 \times 10^{-5}$ rad s^{-1}

$R_E = 6378.1$ km

z = geometric altitude (km) above the earth

φ = geocentric latitude.

These winds will always be from the west and at the equator they will have the following values:

z(km)	Speed (ms^{-1})
100	472
200	480
300	488
400	495

These wind speeds are referenced to a nonrotating coordinate system fixed at the center of the earth.

The winds driven by the pressure gradients are influenced strongly by the electron density profiles distributions; therefore, for problem areas requiring directional wind inputs or detailed information of the winds at these altitudes, users should contact the Atmospheric Sciences Division, Space Sciences Laboratory, Marshall Space Flight Center, Alabama.

REFERENCES

II-1. Justus, C. G., Woodrum, A. W., Roper, R. G., and Smith, O. E.: Four-D Global Reference Atmosphere: Technical Description. Part I, NASA TM X-64871, September 1974.

II-2. Model of Earth's Atmosphere (90 to 2500 km). NASA SP-8021, March 1973.

II-3. Weidner, D. K., and Swenson, G. R.: Diurnal Variations in the Thermosphere from a Series of Marshall-University of Michigan Probes. Journal of Geophysical Research, vol. 74, 1969, pp. 4755-4763.

II-4. The Earth's Ionosphere. NASA SP-8049, March 1971.

II-5. Chan, K. L., and Colin, L.: Global Electron Density Distribution from Topside Soundings, Proceedings of IEEE, vol. 57, no. 6, June 1969, pp. 990-1004.

II-6. Stassinopoulos, E. G., and Mead, G. D.: ALLMAG, GDALMG, LINTRA: Computer Programs for Geomagnetic Field and Field-line Calculations. National Space Science Data Center, February 1972.

II-7. Stassinopoulos, E. G.: Radiation Hazards to Synchronous Satellites. NASA Report X-601-73-330, Goddard Space Flight Center, September 1973.

II-8. Vette, J. I. and Sawyer, D. J.: AP8 Trapped Proton Environment for Solar Maximum and Solar Minimum, National Space Science Data Center, December 1976.

II-9. Vette, J. I., AE6: A Model Environment of Trapped Electrons for Solar Maximum. National Space Science Data Center 76-04, May 1976.

II-10. Raschke, E., and Bandeen, W. R.: The Radiation Balance of the Planet Earth from Radiation Measurements of the Satellite Nimbus II. Journal of Applied Meteorology, vol. 9, April 1970, pp. 215-238.

REFERENCES (Continued)

II-11. Earth Albedo and Emitted Radiation. NASA SP 8067, July 1971.

II-12. Anon: Meteorological Glossary. American Meteorological Society.

II-13. Burrell, M. O.: The Calculation of Proton Penetration and Dose Rates. NASA TM X-53063, August 19, 1964.

II-14. Watts, J. W., Jr., and Burrell, M. O.: Electron and Bremstrahlung Penetration and Dose Calculation. NASA TN D-6385, June 1971.

II-15. Burrell, M. O., and Wright, J. J.: Orbital Calculation and Trapped Radiation Mapping. NASA TM X-53406, March 8, 1966.

II-16. U.S. Standard Atmosphere, 1976, U.S. Government Printing Office, Washington, D.C., October 1976.

II-17. Meteoroid Environment Model - 1969 (Near-Earth to Lunar Surface). NASA SP-8013, March 1969.

II-18. McCrosky, R. E.: Cometary Debris, the Dusty Universe. Proc. of a Symposium Honoring Fred Lawrence Whipple on his retirement as Director of the Smithsonian Astrophysical Observatory, October 17-19, 1973, pp. 169-183.

II-19. International Geomagnetic Reference Field 1975. EOS, vol. 57, no. 3, March 1976.

II-20. IAGA Division 1 Study Group: International Geomagnetic Reference Field 1975. Journal of Geophysical Research, vol. 81, no. 28, October 1, 1976.

II-21. Zmuda, A. J. (Editor): World Magnetic Survey 1957-1969. Bulletin 28, Int. Assn. Geomagn. and Aeron., 1971.

II-22. Magnetic Fields Earth and Extraterrestrial. NASA SP-8017, March 1969.

II-23. Spacecraft Magnetic Torques. NASA SP-8018, March 1969.

REFERENCES (Continued)

II-24. 1973 Smithsonian Standard Earth (III) Smithsonian Astrophysical Observatory Special Report 353, E. M. Gaposchkin (editor), 1973.

II-25. The American Ephemeris and Nautical Almanac for the Year 1976. U.S. Government Printing Office, Washington, D.C.

II-26. Gaposchkin, E. M.: Gravity-Field Determination Using Laser Observations. Smithsonian Astrophysical Observatory, Center for Astrophysics, preprint series no. 548, February 1976.

II-27. Geisler, J. E.: Atmospheric Winds in the Middle Latitude F-Region. J. Atmos. Terr. Phys., vol. 28, 1966, pp. 703-720.

II-28. Kohl, H., and King, J. W.: Atmospheric Winds Between 100 and 700 km and Their Effects on the Ionosphere. J. Atmos. Terr. Phys., vol. 29, 1967, pp. 1045-1062.

II-29. Jacchia, L. G.: The Temperature Above the Thermopause. Space Res., vol. 5, 1965, pp. 1152-1174.

II-30. Geisler, J. E.: A Numerical Study of the Wind System in the Middle Thermosphere. J. Atmos. Terr. Phys., vol. 29, 1967, pp. 1469-1482.

II-31. Jacchia, L. G., and Slowey, J.: The Shape and Location of the Diurnal Bulge in the Upper Atmosphere. Space Res., vol. 7, 1967, pp. 1077-1090.

II-32. Kochanski, A.: Atmospheric Phenomena in the Height Region from 70 to 160 km. WMO Tech. Note No. 70, World Meteorological Organization, Geneva, 1965, pp. 140-169.

II-33. Kochanski, A.: Atmospheric Motions from Sodium Cloud Drifts of Four Locations. Monthly Weather Rev., vol. 94, 1966, pp. 199-212.

II-34. King-Hele, D. G.: Measurement of Upper-Atmospheric Rotational Speed from Changes in Satellite Orbits. Space Res., vol. 14, 1971.

REFERENCES (Concluded)

II-35. Challinor, R. A.: The Apparent Rotation of the Upper Atmosphere. Planet. Space Sci., vol. 16, 1968, pp. 557-566.

II-36. Dickinson, R. E., and Geisler, J. E.: Vertical Motion Fields in the Middle Thermosphere from Satellite Drag Densities. Monthly Weather Rev., vol. 94, 1968, pp. 606-616.

II-37. King-Hele, D. G., and Walker, D. M. C.: Upper-Atmosphere Zonal Winds: Variation with Height and Local Time. Planet. Space Sci., vol. 25, 1977, pp. 313-336.

SECTION III. CISLUNAR SPACE

3.1 Definition

Cislunar space is defined as that region between the earth and moon that extends from 65 000 to 344 400 km. The outer limit of this region is 40 000 km inside the mean lunar orbital distance and is considered to be the outer limit (from the moon) of the moon's sphere of influence.

3.2 Gas Properties

Same as Interplanetary Space (see Paragraph 1.2).

3.3 Radiation Environment

Same as Interplanetary Space (see Paragraph 1.3).

3.4 Meteoroid Environment

The meteoroid environment model is composed of sporadic meteoroids in the mass range between 1 and 10^{-12} g and stream meteoroids in the mass range from 1 to 10^{-6} g.

3.4.1 Average Total Meteoroid Environment

Same as Terrestrial Space (see Paragraph 2.5.1).

3.4.2 Sporadic Meteoroids

The average sporadic meteoroid environment is to be used in conjunction with the specific stream meteoroid environment in design of a vehicle with a specified mission period (launch date and duration).

3.4.2.1 Particle Density

The mass density is 0.5 g/cm^3 for all sporadic particle sizes.

3.4.2.2 Particle Velocity

The average sporadic particle velocity is 20 km/s with the distribution as given in Figure III-1.

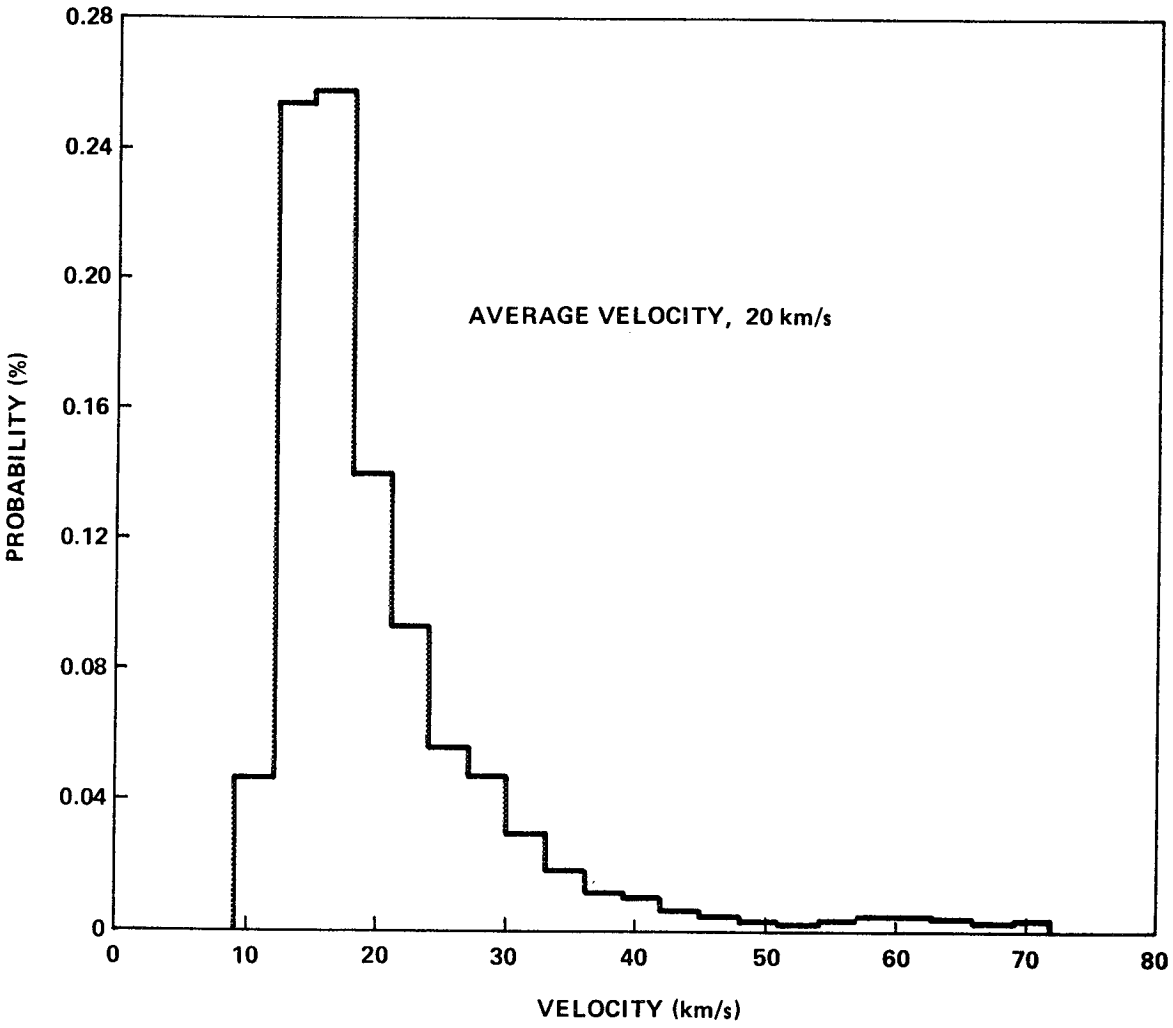

Figure III-1. Probability velocity distribution for sporadic meteoroids.

3.4.2.3 Flux-Mass Model

The flux (N_{sp}), in number/m^2 s, of sporadic cometary meteoroids of mass m or greater on a randomly tumbling surface is: For $10^{-6} \leqq m \leqq 10^{0}$

$$\log N_{sp} = -14.41 - 1.22 \log m + \log \left(1 + \frac{0.035}{r}\right) + \log G_E$$

$$+ \log \left[\frac{1 + \sqrt{1 - 1/r_e^2}}{2}\right] + \log \left[\frac{1 + \sqrt{1 - 1/r_m^2}}{2}\right]$$

$$+ \log F_{seasonal}.$$

For $10^{-12} \leqq m \leqq 10^{-6}$,

$$\log N_{sp} = -14.339 - 1.584 \log m - 0.063 (\log m)^2 + \log G_E$$

$$+ \log \left[\frac{1 + \sqrt{1 - 1/r_e^2}}{2}\right] + \log \left[1 + \frac{0.035}{r}\right]$$

$$+ \log \left[\frac{1 + \sqrt{1 - 1/r_m^2}}{2}\right] + \log F_{seasonal}$$

where

G_E = the defocusing factor for the earth and is applicable to all missions

$$G_E = 0.568 + \frac{0.432}{r_e}$$

r_e = the distance from the center of the earth in units of the earth's radius

r_m = the distance from the center of the moon in units of the moon's radius

m = mass in g

$F_{seasonal}$ = a seasonal factor obtained from the tabulation below. (The factor is obtained by taking the average of monthly factors listed for the months of the mission duration.)

Monthly Factors

January	0.6
February	0.4
March	0.5
April	0.6
May	1.1
June	1.6
July	1.8
August	1.6
September	1.1
October	1.1
November	0.9
December	0.7

3.4.3 Stream Meteoroids

Same as Terrestrial Space (see Paragraph 2.5.3).

3.4.4 Additional Information

For additional information relative to the cislunar meteoroid environment, see References III-1 and III-2.

3.5 Magnetic Environment

Same as Interplanetary Space (see Paragraph 1.5).

REFERENCES

III-1. Meteroid Environment Model - 1970. NASA SP-8038, Interplanetary and Planetary, October 1970.

III-2. McCrosky, R. E.: Cometary Debris, the Dusty Universe. Proc. of a Symposium Honoring Fred Lawrence Whipple on his retirement as Director of the Smithsonian Astrophysical Observatory, October 17-19, 1973, pp. 169-183.

SECTION IV. MOON

4.1 Atmospheric Environment

4.1.1 Gas Properties

The moon has a tenuous atmosphere that will have a negligible effect on spacecraft except for problems associated with the effects of vacuum on components and materials.

4.1.1.1 Pressure

Pressure at the lunar surface was observed to be less than 8×10^{-9} torr during the Apollo 12 mission [IV-1].

4.1.1.2 Density

Based on measurements involving radio star occulations, the density is estimated to be less than 10^{-13} times the mean density of the atmosphere at the earth's surface. Minimum density at very small solar flux excluding SO_2 and CO_2 is 5.5×10^4 particles/cm^3.

4.1.1.3 Composition [IV-2]

Gas	Mass Spectrometer Data, molecules/cm^3		Cold Cathode Gage Data, molecules/cm^3		Predicted Data, molecules/cm^3	
	Day	Night	Day	Night	Day	Night
Hydrogen (H_2)	1×10^8	1×10^5			3.6×10^3	2.3×10^4
Helium	2×10^3	4×10^4			3×10^3	
Neon		7×10^4			1.7×10^3	4.1×10^4
^{36}Ar		2×10^3			5×10^4	1.3×10^6
^{40}Ar		2×10^3			3×10^2	8×10^3
Total	4×10^8	4.6×10^5	1×10^7	2×10^5		

4.1.2 Radiation Environment

4.1.2.1 Galactic Radiation

Use criteria given in Paragraph 1.3.1.

4.1.2.2 Trapped Radiation

None.

4.1.2.3 Solar Proton Events

Use criteria given in Paragraph 1.3.2.

4.1.2.4 Thermal Radiation [IV-2]

The thermal radiation from the lunar surface varied from 565 W/m^2 at 200 km to about 5 W/m^2 at 20 000 km.

$$Q = FAI \quad ,$$

where

Q = thermal radiation flux incident upon vehicle

F = view factor (varies with altitude above the planet and vehicle shape)

A = cross-sectional area of exposed spherical surface

I = lunar thermal radiation flux (324.35 W/m^2).

4.1.2.5 Albedo Radiation [IV-3]

This varies from 151 W/m^2 at 200 km to 1 W/m^2 at 20 000 km. The albedo radiation is determined from the general equation for albedo radiation flux:

$$Q = FASa \quad ,$$

where

Q = incident radiation flux

F = view factor

A = cross-sectional area of exposed spherical surface

S = solar constant at the moon

a = lunar albedo.

4.1.3 Meteoroid Environment

4.1.3.1 Average Total Meteoroid Environment

The average annual cumulative meteoroid model on the lunar surface is described mathematically as follows: For $10^{-6} \leqq m \leqq 10^{0}$,

$$\log N_t = -14.597 - 1.213 \log m.$$

For $10^{-12} \leqq m \leqq 10^{-6}$,

$$\log N_t = -14.566 - 1.584 \log m - 0.063 (\log m)^2,$$

where

N_t = number of particles/m^2 s of mass m or greater

m = mass in g.

The gravitationally focused unshielded flux, N_t, must be multiplied by an appropriate defocusing factor for the moon, G_m, and, if applicable, by the shielding factor (Fig. IV-1). The G_m factor applies to all missions and may be obtained from the equation given below. The body-shielding factor for randomly oriented spacecraft may be calculated by the method given in Figure IV-1 and applied to all missions. For oriented spacecraft, the effects of body shielding on the number of impacts as seen by the parts of the spacecraft must be determined on a unique basis.

The defocusing factor for the moon, G_m, may be calculated by

$$G_m = 0.966 + \frac{0.034}{r} ,$$

where r is the distance from the center of the moon in units of lunar radius.

4.1.3.2 Sporadic Meteoroids

4.1.3.2.1 Particle Density

The mass density is 0.5 g/cm^3 for all sporadic particle sizes.

4.1.3.2.2 Particle Velocity

The average sporadic particle velocity is 20 km/s with the distribution as given in Figure IV-2.

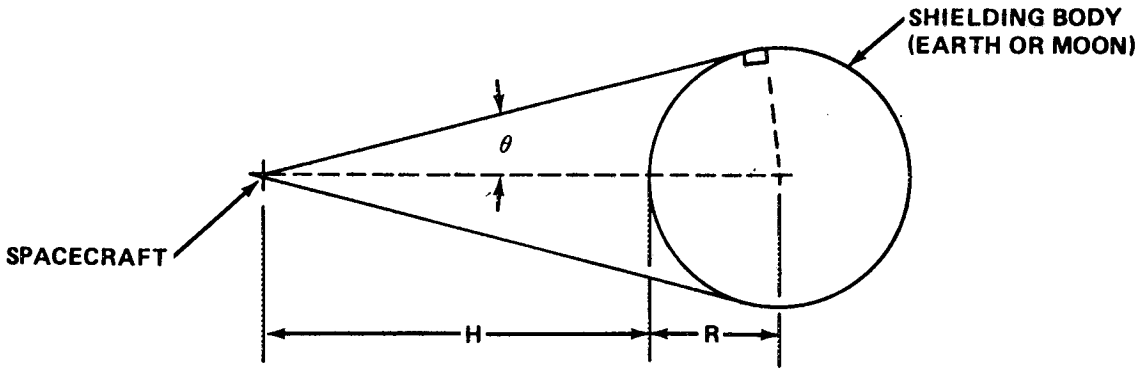

BODY SHIELDING FACTOR, ζ (DEFINED AS RATIO OF THE SHIELDED TO UNSHIELDED FLUX)

$$\zeta = \frac{1 + \cos\theta}{2}$$

WHERE:

$$\sin\theta = \frac{R}{R + H}$$

R = RADIUS OF SHIELDING BODY

H = ALTITUDE ABOVE SURFACE

Figure IV-1. Method for determining body shielding factor for randomly oriented spacecraft.

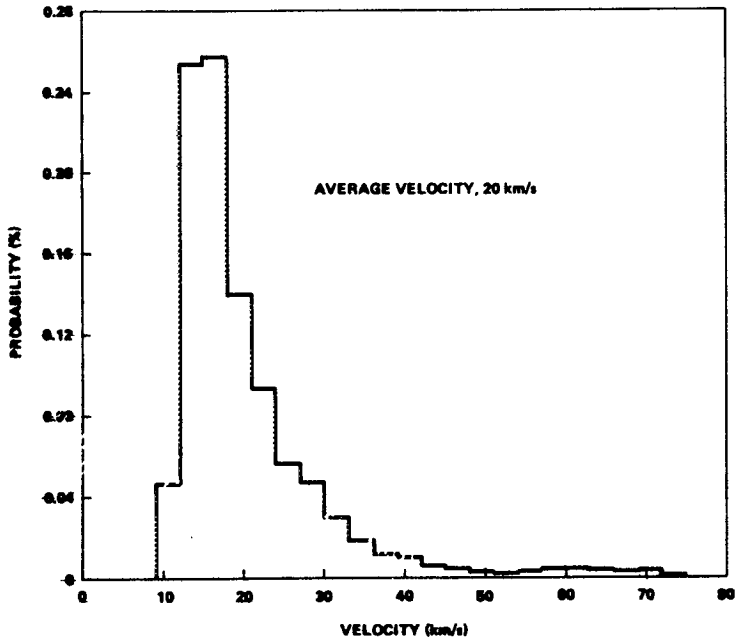

Figure IV-2. Probability velocity distribution for sporadic meteoroids.

4.1.3.2.3 Flux-Mass Model

The flux-mass model for sporadic meteoroids is described mathematically as follows: For $10^{-6} \leqq m \leqq 10^{0}$,

$$\log N_{sp} = -14.41 - 1.22 \log m + \log \left(1 + \frac{0.035}{r}\right) + \log \left(\frac{1 + \sqrt{1 - 1/r^2}}{2}\right) + \log F_{seasonal} .$$

For $10^{-12} \leqq m \leqq 10^{-6}$,

$$\log N_{sp} = -14.339 - 1.584 \log m - 0.063 (\log m)^2 + \log \left(1 + \frac{0.035}{r}\right) + \log \left(\frac{1 + \sqrt{1 - 1/r^2}}{2}\right) + \log F_{seasonal} ,$$

where

N_{sp} = number of particles/m^2 s of mass m or greater encountered by a randomly oriented surface

m = mass in g

r = distance from the center of the moon in units of the lunar radius

$F_{seasonal}$ = seasonal factor obtained from the table below. (The factor is obtained by taking the average of monthly factors listed for the months of the mission duration.)

Monthly Factors

January	0.6
February	0.4
March	0.5
April	0.6
May	1.1
June	1.6
July	1.8
August	1.6
September	1.1
October	1.1
November	0.9
December	0.7

4.1.3.3 Stream Meteoroids

Same as given in Paragraph 2.5.3.

4.1.3.4 Lunar Ejecta Environment

The lunar ejecta environment encompasses the lunar particles ejected from impacts of meteoroids on the lunar surface. In addition to the hazard of meteoroids in extravehicular activities and other operations on or near the lunar surface, lunar ejecta must be considered. The lunar ejecta environment given herein is to be used from the lunar surface to an altitude of 30 km. The effects of the ejecta environment must be considered separately from meteoroids because of their different velocity regimes.

4.1.3.4.1 Particle Density

The mass density is 2.5 g/cm^3 for all ejecta particle sizes.

4.1.3.4.2 Particle Velocity

The average ejecta velocity is 0.1 km/s for all ejecta particle sizes.

4.1.3.4.3 Flux-Mass Models

4.1.3.4.3.1 Average Total Ejecta Flux-Mass Model

An average annual total cumulative flux-mass model for the lunar ejecta is to be used in preliminary design and is described as follows:

$$0 \leqq V_{ej} \leqq 1.0, \quad \log_{10} N_{ej_t} = -10.75 - 1.2 \log_{10} m$$

where

N_{ej_t} = number of particles/m^2 s of mass m or greater

m = mass in g.

The average ejecta velocity, 0.1 km/s, is to be used with this distribution model.

4.1.3.4.3.2 Individual Ejecta Flux-Mass Models

An average annual individual cumulative lunar ejecta flux-mass distribution for each of three velocity intervals should be used in detailed consideration of the ejecta hazard. These three distributions are:

$$0 \leqq V_{ej} \leqq 0.1 \quad (V_{ej} = 0.1 \text{ km/s}); \quad \log_{10} N_{ej} = -10.79 - 1.2 \log_{10} m$$

$$0.1 \leqq V_{ej} \leqq 0.25 \quad (V_{ej} = 0.25 \text{ km/s}); \quad \log_{10} N_{ej} = -11.88 - 1.2 \log_{10} m$$

$$0.25 \leqq V_{ej} \leqq 1.0 \quad (V_{ej} = 1.0 \text{ km/s}); \quad \log_{10} N_{ej} = -13.41 - 1.2 \log_{10} m$$

4.1.3.5 Additional Information

Additional information relative to the meteoroid environment is given in References IV-4 and IV-5.

4.1.4 Magnetic Environment

4.1.4.1 Magnetic Field

The lunar total magnetic field strength at the equator is considered to be approximately 35 γ. Apollo 15 data have revealed differences in the far-side field strength.

4.1.5 Astrodynamic Constants [IV-6]

4.1.5.1 Lunar Constants

Mean lunar radius:[1]

$$R_m = 1738.09\ (\pm 0.07)\ \text{km}.$$

Inertial rotational rate of the moon:

$$\omega_m = 0.00015250437\ \text{deg/s}.$$

4.1.5.1.1 Principal Axes

$$a = 1738.57\ (\pm 0.07)\ \text{km}$$

$$b = 1738.21\ (\pm 0.07)\ \text{km}$$

$$c = 1737.49\ (\pm 0.07)\ \text{km}$$

where a is directed toward the mean center of the lunar disk, c is coincident with the moon's rotational axis, and b is perpendicular to a and c.

1. Apollo 15 data show that on the average the back-side elevation of the moon is 2 to 4 km above the mean lunar radius [IV-7].

4.1.5.1.2 Gravitational Parameter

$$\mu_m = GM_m = 4902.78\ (\pm 0.06)\ km^3/s^2.$$

4.1.5.1.3 Earth-Moon Mass Ratio

$$M_e/M_m = 81.3010\ (\pm 0.001) \quad .$$

4.1.5.1.4 Sidereal Period, True Period of Rotation and Revolution

27.322 days.

4.1.5.1.5 Synodic Period, New Moon to New Moon

29.531 days.

4.1.5.2 Gravitational Potential Function of Moon

$$U(r,\phi,\theta) = \frac{\mu_m}{r}\left[1 - \frac{J_2}{2}\left(\frac{R_m}{r}\right)^2 (3\sin^2\phi - 1) + 3C_{22}\left(\frac{R_m}{4}\right)^2 \cos^2\phi \cos 2\theta\right],$$

where

r = magnitude of selenocentric radius vector, km

ϕ = selenocentric latitude

θ = selenocentric longitude (positive eastward)

R_m = mean lunar radius = 1738.09 (±0.07) km

$J_2 = 2.07108\ (\pm 0.05) \times 10^{-4}$

$C_{22} = 0.20716\ (\pm 0.05) \times 10^{-4}$.

(Additional information on the previously mentioned subject is found in Reference IV-8.)

4.1.5.3 Gravitational Acceleration

The mean equatorial gravitational acceleration on the surface of the moon has been estimated to be 162.3 cm/s^2.

4.2 Surface Environment

Data and interpretation of Apollo samples is found in References IV-9 through IV-19.

Engineering models of the lunar surface are needed in mission planning and in the design of landing and exploration vehicles and lunar bases. Models of terrain and soil mechanical properties assist in the evaluation of vehicle landing performance, descent engine plume-surface interactions, and exploration vehicle performance and power requirements. Crater and block (rock) models aid in assessing hazardous landing conditions and obstacles encountered in typical traverse missions. Optical models help in establishing camera design parameters and in determining visual capabilities of astronauts. Dielectric models aid in radar system design. Chemical, bearing strength, density, and thermal models are used in design of surface and subsurface base structures and surface vehicles.

The lunar surface models presented here are based on state of the art; they upgrade and extend the earlier engineering models developed by Vaughan [IV-20] and Vaughan and Costes.[2] They are founded on a review and interpretation of available literature and lunar data as well as discussions with scientists familiar with data provided by the Ranger,

2. Vaughan, O. H. and Costes, N. C.: Document Exhibit 1 to Lunar Roving Vehicle Request for Proposals entitled "MSFC Natural Environment Design Criteria Guidelines for use in the Design of Lunar Exploration Vehicles." December 11, 1969.

Surveyor, Orbiter programs, the Russian Luna probes, and the Apollo program in addition, these engineering models reflect, where possible, the consensus of the NASA Lunar Trafficability Model Working Group which is composed of members of NASA centers and other government agencies working on lunar exploration programs.

4.2.1 Physical Properties

Many physical properties of the moon have been known for years; Apollo results have provided much additional information and refinement [IV-1, IV-3, IV-22, IV-23, IV-24, and IV-25].

4.2.2 Morphologic Subdivisions [IV-8 - IV-25]

Two fundamental large-scale morphologic types of lunar terrain are clearly evident — Mare and Upland regions. Well-formed young craters are superimposed on both of these surface types and constitute a widely distributed third basic surface.

The Mare surface is characterized by relatively gentle topography with low normal albedo and features, such as craters, ridges, rilles, domes, ray systems, and scarps. In contrast, the Uplands have higher albedo and are rugged with complex superimposed craters.

Besides Mare and Upland, more detailed terms (smooth Mare, rough Mare, hummocky Upland, and rough Upland) are used.

Since most lunar regions are composite, the morphologic term applied to any region describes the predominant type of terrain. Hence, a smooth Mare may contain subregions that are rougher than some subregions in a rough Mare.

The topographies of lunar surfaces are characterized by craters of various sizes and ages. Ideally, the surfaces can be grouped into two types:[3] (1) the young surface where the frequency distribution directly reflects the rate of crater production, and (2) the steady state surface which is the result of the combined effects of crater production and erosion-infilling produced by extensive cratering (crater saturation). Crater frequencies can be expressed approximately by equations of the form $N_o = K D^n$ where N_o is the cumulative number of craters per unit area greater than diameter D, and K and n are constants. The exponent, n, is about -3 for

3. Moore, H.J.: Some Observations of the Lunar Trafficability Problem. U.S. Geological Survey, Nov. 1968 (Working Paper).

the young surface in which the craters are fresh and uneroded. For the steady-state surface (ranging from fresh, well-preserved craters to those so eroded and filled that they are barely discernible), the exponent, n, is about -2 and the coefficient K is 10^{-1}.

4.2.3 Topography

McCauley and Rowan demonstrated with earth-based photography that the median slope was related to the slope length[4] for both terrestrial and Mare topography (a linear relation on a log-log plot). The relationship thus obtained from earth-based lunar observations predicted the mean slope which was later measured from Ranger 7 photographs (when the 0.75 km resolution was extrapolated to 1 m). With Orbiter data, Pike[5] extended the work of Rowan and McCauley and developed relations between the mean lunar slope and slope length for the smooth Mare, rough Mare, hummocky Upland, and rough Upland [IV-23].

In addition, Pike's study of terrestrial slope distributions indicated identical cumulative distributions when normalized to the mean slope, regardless of the gentleness or steepness of the mean slope. By assuming that lunar slopes have the same characteristic distributions, Pike developed a basic distribution model using photoclinometry data obtained from 7 lunar regions (data read to 0.6 m resolution, but most likely are valid only above 1 m). The slope distribution model presented herein is a current estimate from a continuing investigation by Pike and others at the Center of Astrogeology, U.S. Geological Survey.

Lunar topography studies were conducted in support of the Apollo Program, primarily for the landing sites in the Mare regions. Cumulative slope distributions are presented[6] for slope lengths of about 1 and 10 m for various locations in the Mare region. The data demonstrate that the slope distributions, for a single slope length, vary from site to site, even though, within the context of the morphological subdivisions, the region might be

---

4. The slope length is the incremental horizontal distance between two elevations over which the slope is to be determined. It is also referred to as sample cell length by Rowan and McCauley.

5. Pike, R. J.: Preliminary Models of Slope Distributions on the Moon. U.S. Geological Survey, Branch of Astrogeologic Studies, Oct. 29, 1968.

6. Anon.: A Preliminary Analysis of Photometric/Computer Terrain Data for Lunar Trafficability Models. Mapping Sciences Laboratory, NASA Manned Spacecraft Center, Oct. 4, 1968.

termed a smooth Mare region. Therefore, within a given morphologic region, a distribution exists for the mean lunar slope for any single slope length. The nominal lunar surface model presented in this document provides an estimate of the most likely value of the mean slope for a given slope length.

Variations in the distribution of the average slope for a single base length have been inferred from data; these data consisted of about 50 lunar slope cumulative frequency distributions for Apollo landing site II P-8 in Sinus Medii. From the data, the mean slope and standard deviation were computed to be 4.5 and 1.2 deg, respectively, for the lunar module base length of about 8.5 m (distance between foot pads). These results were used in establishing the relation between slope standard deviation and mean slope [IV-23].

The United States Air Force Aeronautical Chart and Information Center used photometric techniques to determine lunar topography.

Figures IV-3 through IV-6 show the mean lunar slope for various slope lengths. The standard deviation of the mean slope distribution for a single slope length is approximately 0.3 times the mean slope.

The lunar surface roughness models are described in terms of power spectral density (PSD). Similar data have been concerned primarily with the smooth Mare regions in the Apollo belt [IV-26].

The Mare regions contain both the smoothest and roughest regions on the moon with the Upland roughness falling in between two extremes. Even though the Mare has rougher regions than the Uplands, the steepest slopes are found in the Upland regions. Figures IV-7 through IV-10 present lunar surface roughness in terms of power spectral density (m^2/cycle m). Table IV-1 presents data on lunar surface features which are representative of large-scale slopes and should be considered in the design of lunar roving vehicles.

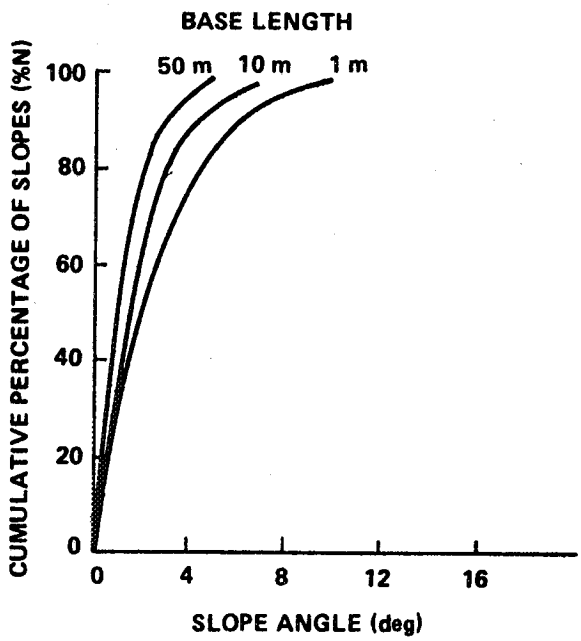

Figure IV-3. Smooth Mare cumulative slope frequency distribution for three base lengths.

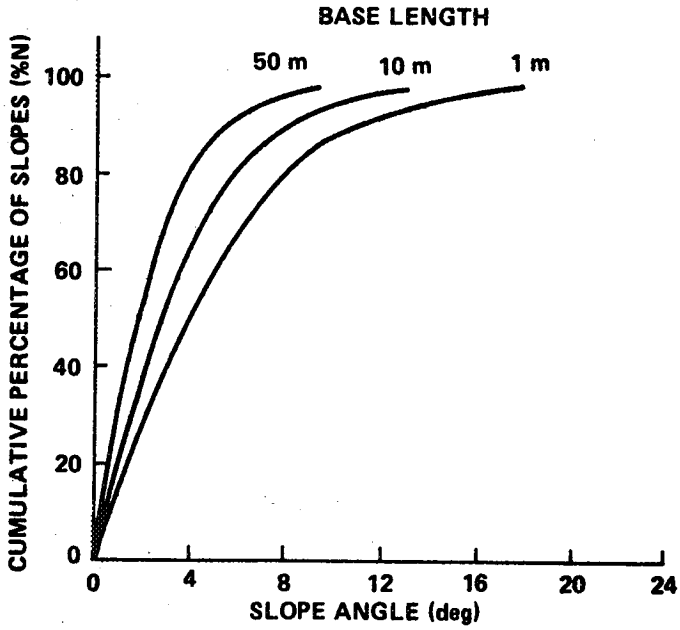

Figure IV-4. Rough Mare cumulative slope frequency distributions for three base lengths.

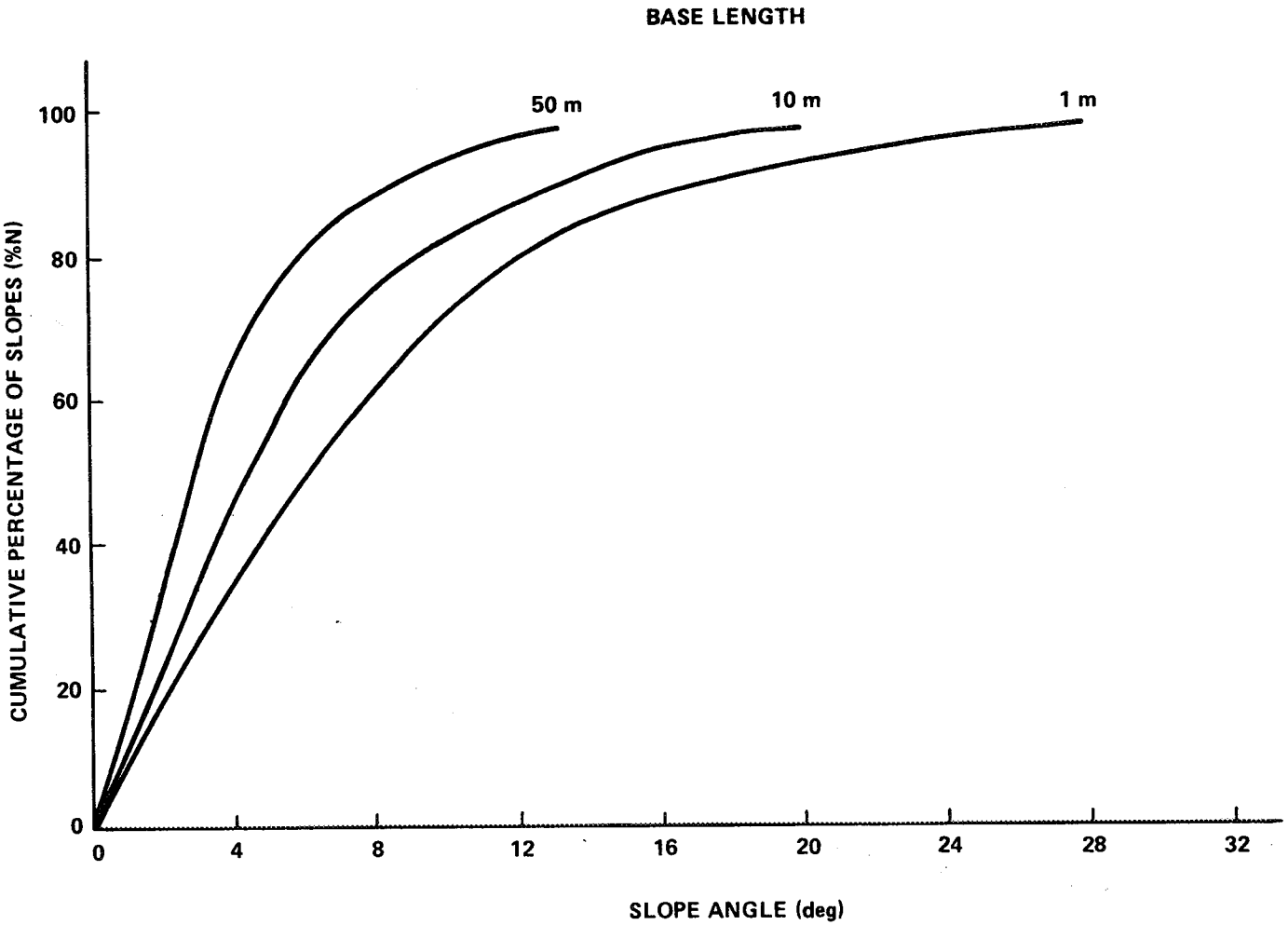

Figure IV-5. Hummocky Uplands cumulative slope frequency distributions for three base lengths.

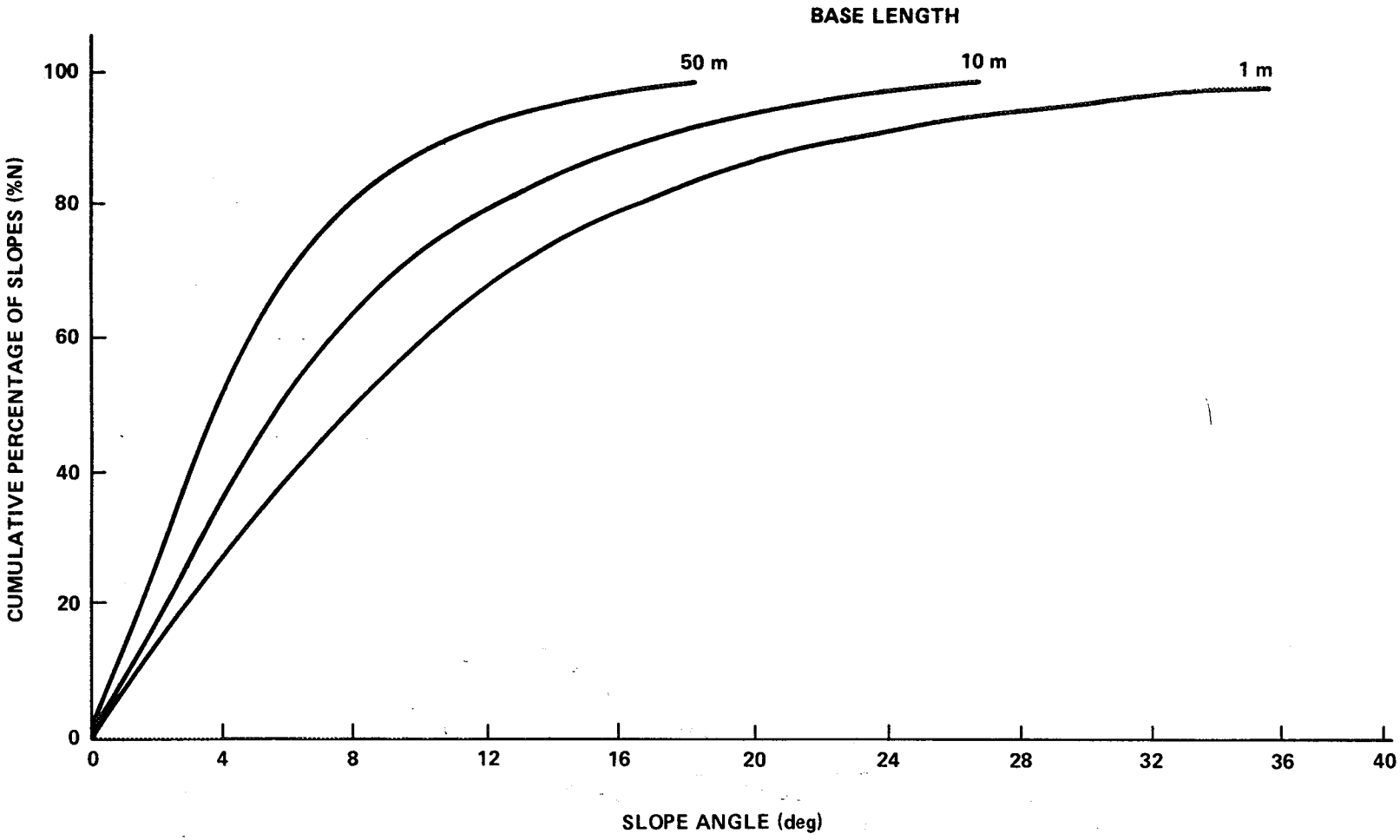

Figure IV-6. Rough Uplands cumulative slope frequency distributions for three base lengths.

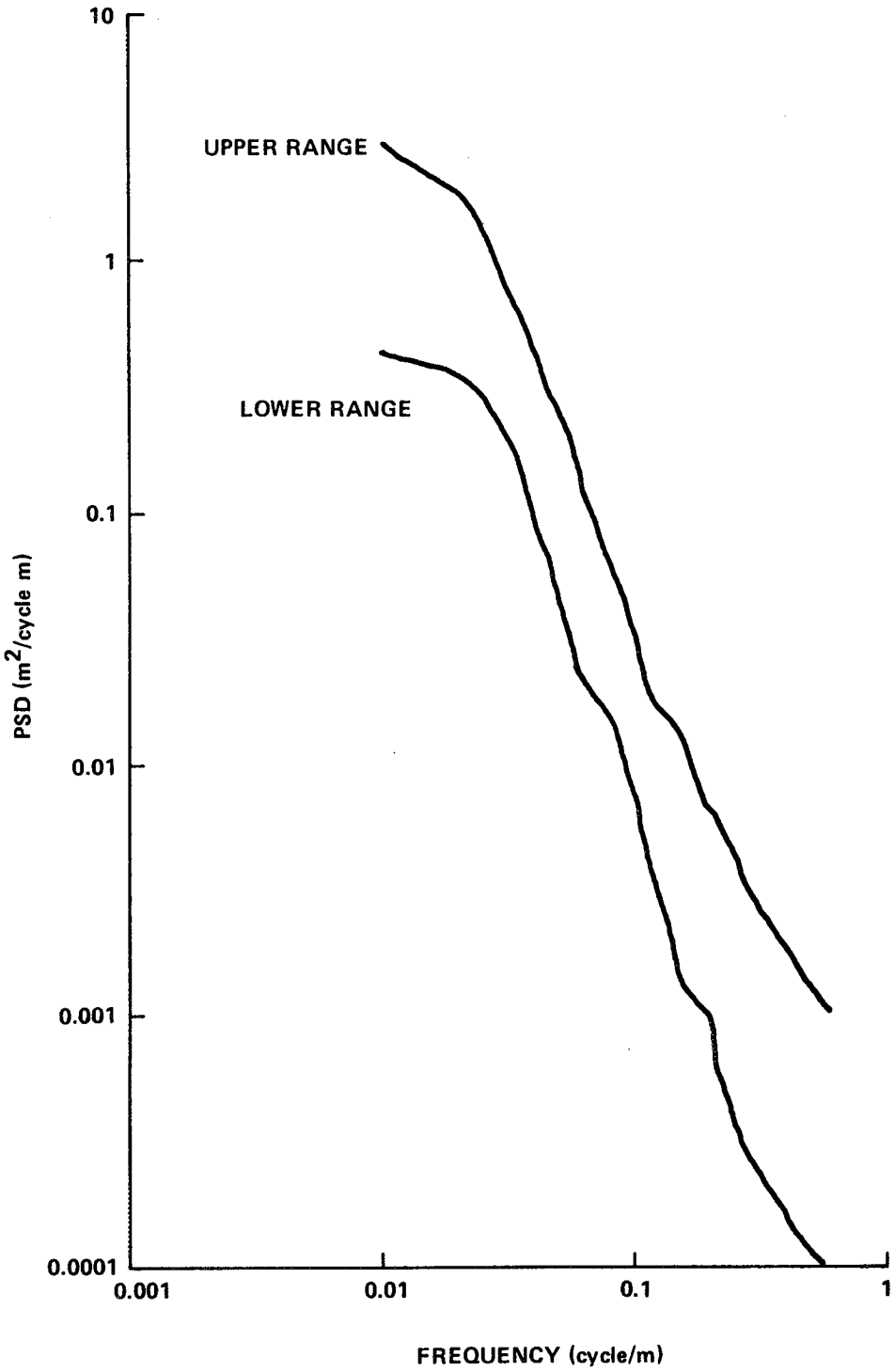

Figure IV-7. Smooth Mare power spectral density versus frequency.

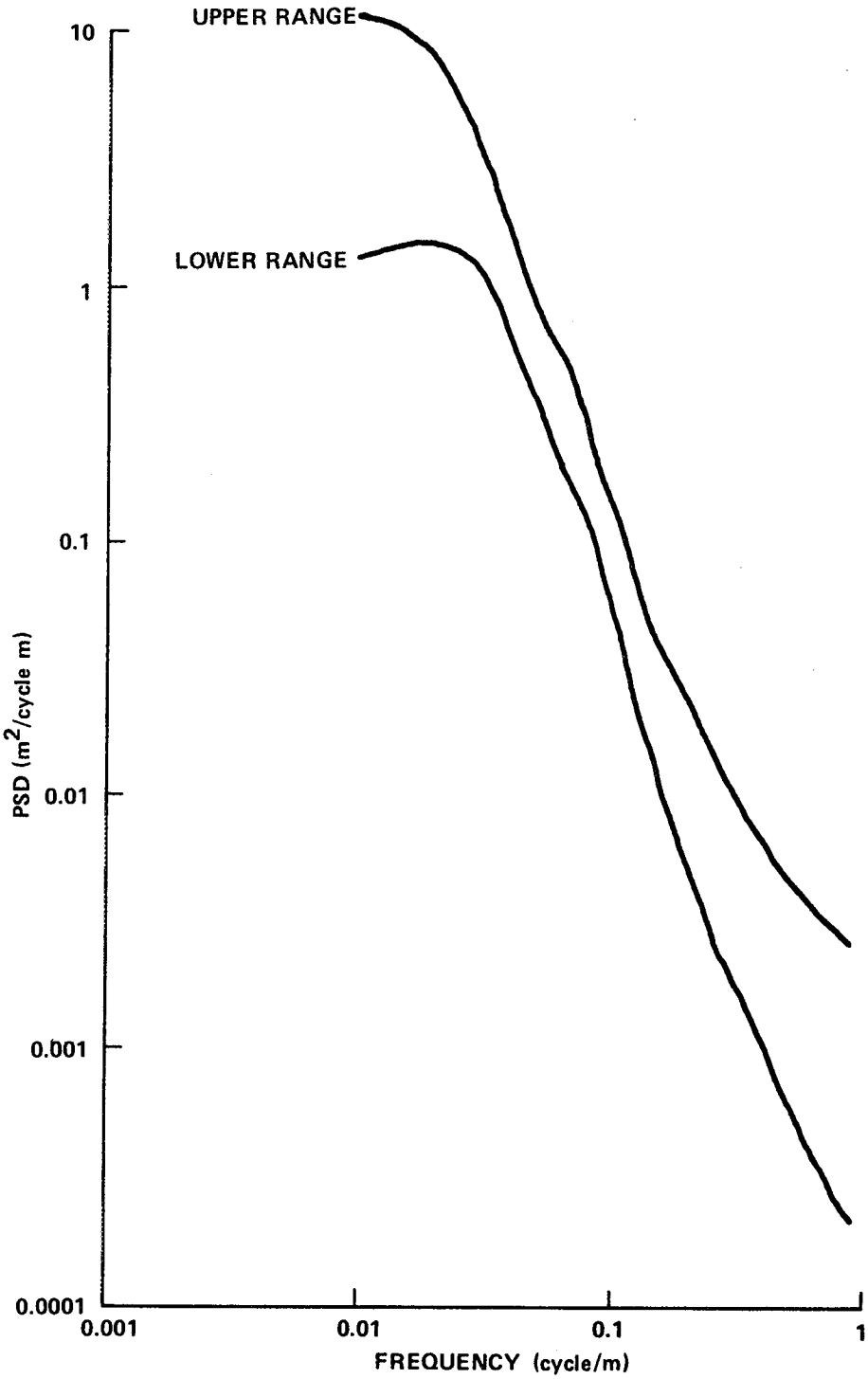

Figure IV-8. Rough Mare power spectral density versus frequency.

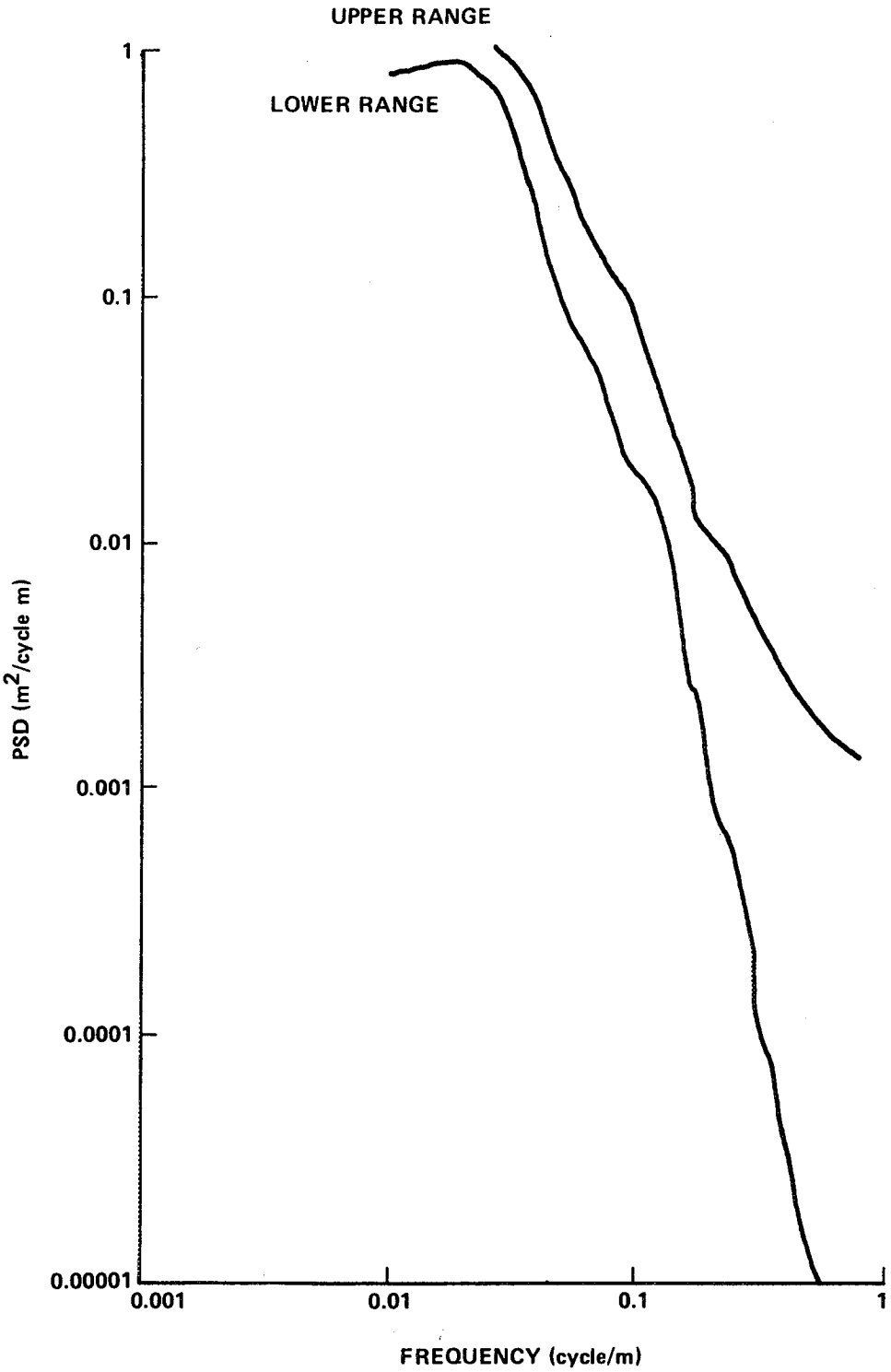

Figure IV-9. Hummocky Upland power spectral density versus frequency.

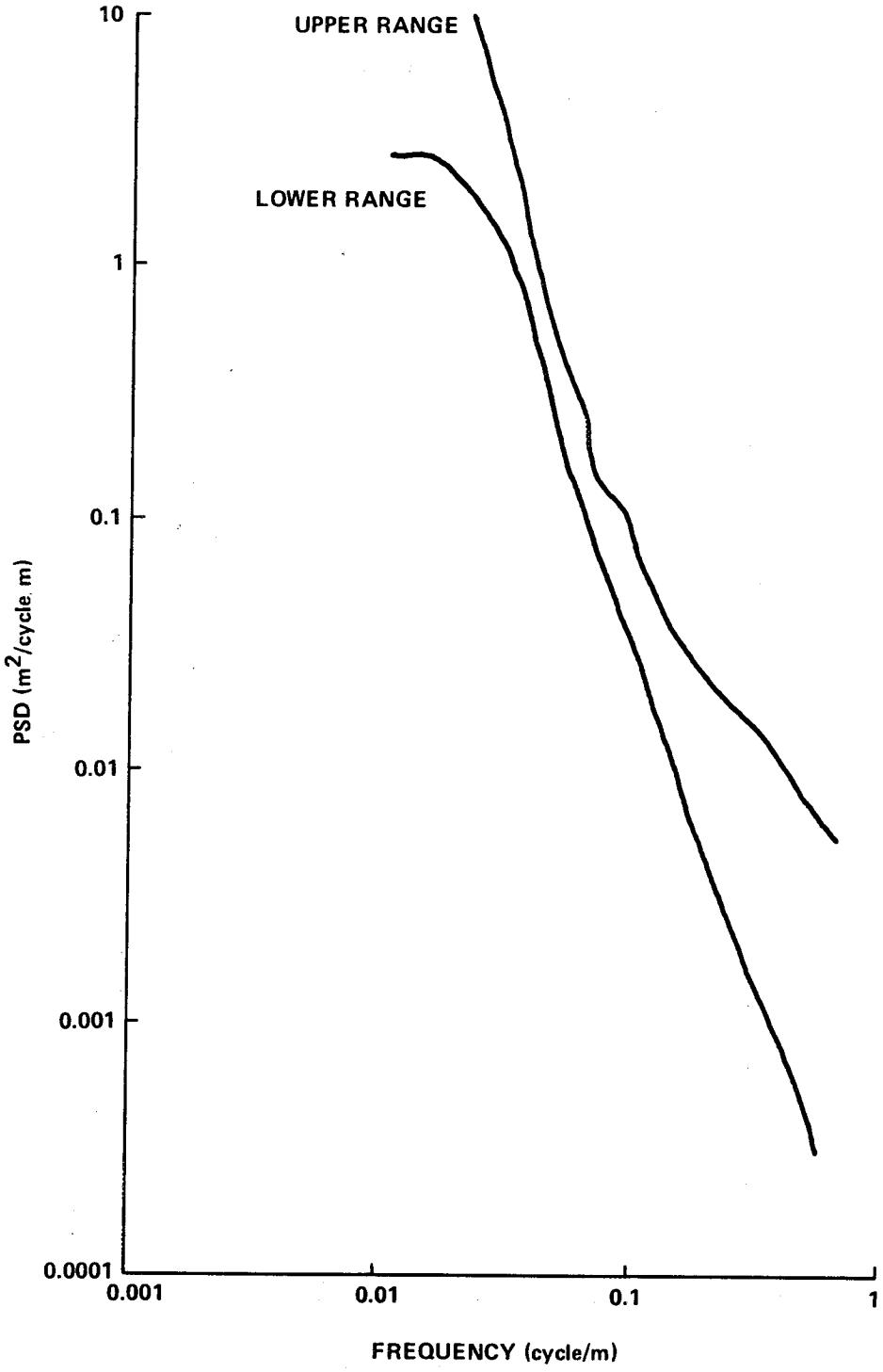

Figure IV-10. Rough Upland power spectral density versus frequency.

TABLE IV-1. LARGE-SCALE SLOPES AND OTHER DATA FOR LUNAR FEATURES[a]

Harbinger Mountains Local Slopes on Rille Wall, 39 deg Long Slopes of Rille Wall, 22 deg Long Slope on Upland Ridge, 13 to 19 deg Relief of Ridges, 200 to 400 m Slopes on Small Rille Walls, 15 deg Relief of Small Rilles, 200 to 400 m
Schröters Valley Long Slope of Rille Wall, 31 deg for 1 km Relief, 663 m
Near Aristarchus (Slope of Upper to Lower Plateau) Long Slope, 22.5 deg for 3 km
Small Crater (180 m dia) in Schröters Valley Relief, 26 m Slopes of Upper Walls near 29 to 31 deg
Domical Hill Width of Crest, 4 km Typical Relief 850 m Drop in 2.5 km 850 m Rise in 3.5 km Comment — Most hills are hummocky at 1 to 10 m wavelengths and many of the dome-type features and ridges and/or rills will be strewn with block fields and small craters with blocky ejecta.

a. Moore, H. J.: Some Observations of the Lunar Trafficability Problem. U.S. Geological Survey, Nov. 1968 (Working Paper).

4.2.4 Block and Crater Frequencies

Most of the block (protuberance) and crater data models given here were derived from data furnished by H.J. Moore. These models also included results obtained by E. Shoemaker and E. Morris of USGS and R. Choate of JPL. Often, the block counts by various investigators differed substantially, probably because different lunar regions and different sizes were used in making the counts. Block frequency data here reflect a compromise between the two block frequency curves in Figures III-42 and IV-34 of Reference IV-27.

4.2.4.1 Craters

Table IV-2 illustrates idealized crater shapes with depth and rim height data for various age groups. Figure IV-11 shows the cumulative crater frequency distribution for the "steady-state" surface for various age groups. The lower line indicates the cumulative frequency for only fresh craters. The next higher line indicates the cumulative frequency for both fresh and young craters. The highest line shows the frequency for all crater types. The figure also indicates the percent of original relief remaining for each age group. Figure IV-12 shows the range of crater cumulative frequency distributions for the smooth Mare, rough Mare, and Upland terrains.

4.2.4.2 Blocks

For mobility studies, the obstacle height should be considered equal to one-half the block diameter.

4.2.4.2.1 Block Properties

The dimension and shapes of blocks encompass a wide range. A standard lunar block is considered as one having a ratio of its longest dimension to its shortest dimension in the range of 1/1 to 1/5. Surfaces may be rounded or rectangular, and may be pitted, eroded, or vesiculated. The standard height is considered to be equal to one-half the block diameter.

The blocks are gray in color. Most are brighter than the fine soil material and have a normal albedo of 14 to 22 percent. Light reflected from some rocks showed polarization up to 30 percent at phase angles near 120 deg.

TABLE IV-2. IDEALIZED CRATER SHAPES IN RELATION TO THEIR MORPHOLOGY[a]

Crater Type	Typical Profile	Depth to Dia Ratio	Rim Height to Dia Ratio
Fresh	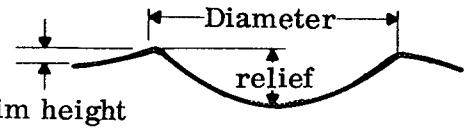	0.23 to 0.25	0.022 to 0.06
Young		0.17 to 0.19	0.016 to 0.045
Mature		0.11 to 0.13	0.008 to 0.03
Old			

a. Moore, H. J.: Some Observations of the Lunar Trafficability Problem. U.S. Geological Survey, Nov. 1968 (Working Paper).

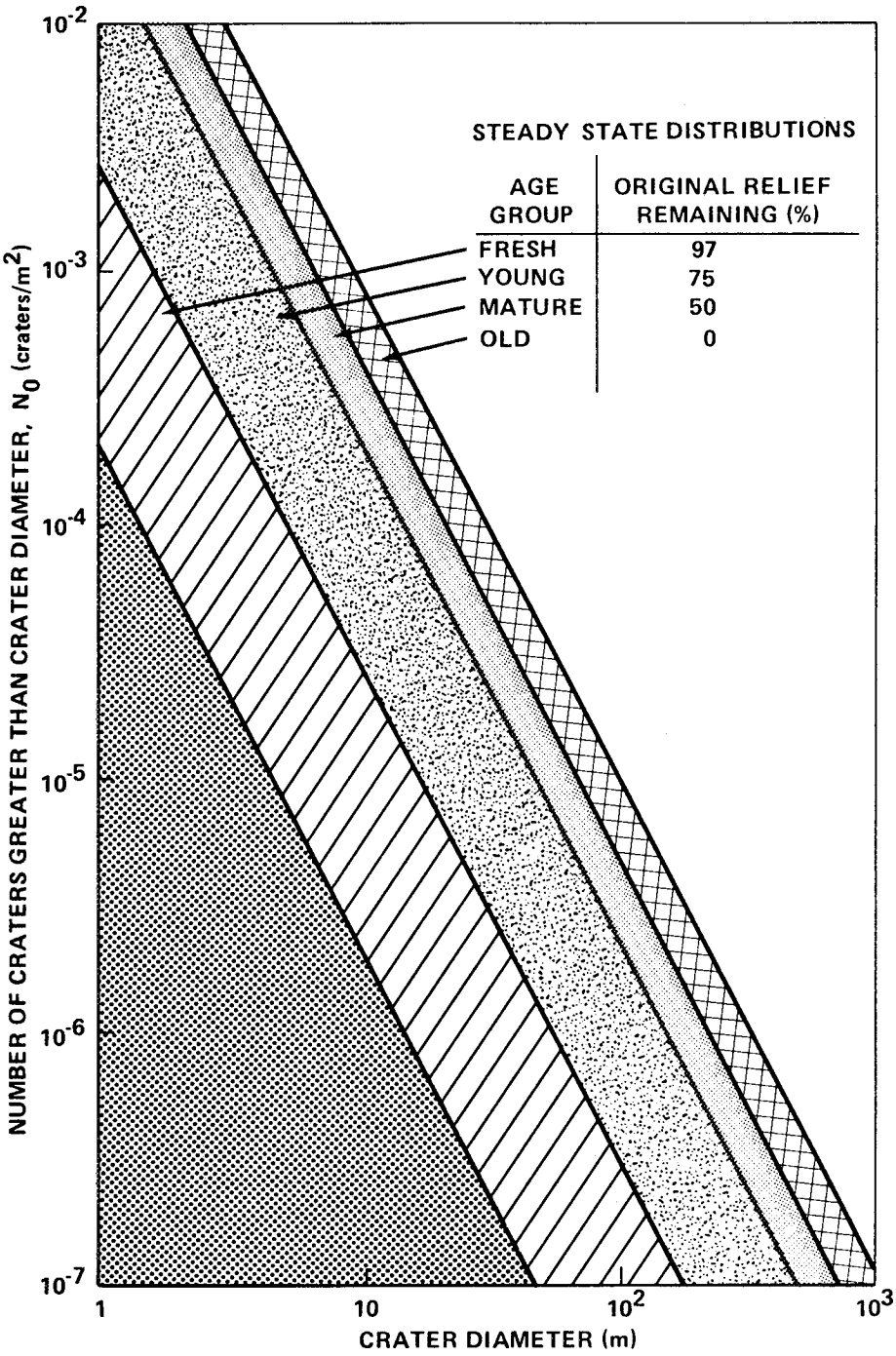

Figure IV-11. Cumulative frequency and relief of craters for various age groups that occur on the smooth Mare, rough Mare, and Upland terrains.

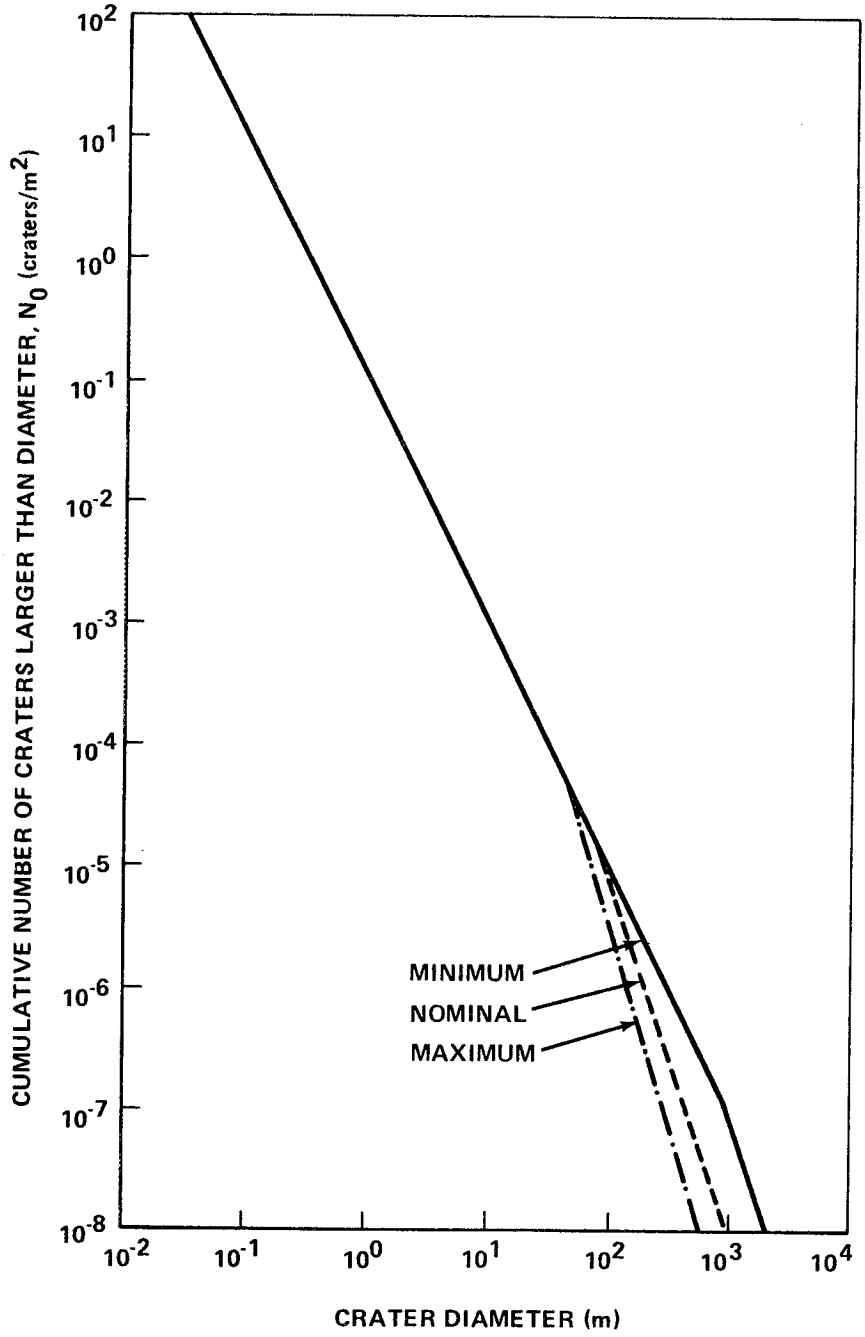

Figure IV-12. Cumulative crater distribution for smooth Mare, rough Mare, and Upland terrains.

It is estimated that a typical lunar block has a density of 2.8 to 2.9 g/cm^3 and a shearing strength of about 200 N/cm^2.

4.2.4.2.2 Block Distributions in the Intercrater Region

Figure IV-13 shows the cumulative distribution of blocks in the intercrater regions, while Figure IV-14 shows the percent of area covered by blocks of a given diameter/m^2.

4.2.4.2.3 Block Distributions Around Craters

Block distributions around craters vary from crater to crater. For interim design purposes the models shown in Figures IV-15 and IV-16 are considered representative of blocky craters.

Figure IV-15 shows typical cumulative frequency distribution of blocks in the annular region between the crater rim and a distance two radii from the crater center (between R and 2R for a fresh crater). Figure IV-16 shows the corresponding percent of this area covered by blocks of a given diameter.

4.2.4.2.4 Block Fields

Studies by H.J. Moore of dense block fields indicate the distributions may be higher than those shown in Figure IV-15. However, Moore's data also show that there are often paths 50 m or wider through even dense block fields which are relatively free of blocks.

4.2.5 Soil Characteristics

Cameras on the Surveyor spacecraft with about 1 mm resolution [IV-2 and IV-27 through IV-31] and Luna spacecraft with a resolution of several mm [IV-35] have provided detailed information on the lunar surface material in both Mare and Upland regions. Surveyors 1 and 3 and Lunas 9 and 13 landed in a rough Mare region (Oceanus Procellarum, Western limb), Surveyor 5 landed in a smooth Mare region (Mare Tranquillitatis, Eastern limb), Surveyor 6 landed between the rough and smooth Mare regions (Sinus Mefii, middle region), and Surveyor 7 landed in the Uplands near Tycho. Data from both U.S. and U.S.S.R. spacecraft indicate the surface material to be a matrix of fine, partially cohesive particles less than 1 mm in diameter with a few rocks scattered in and on the matrix. The data from the Apollo program show that the lunar soil is characterized by a brownish, medium-gray, slightly granular soil largely composed of bulky grains in the silt-to-fine-sand range and exhibiting adhesive characteristics. In general the

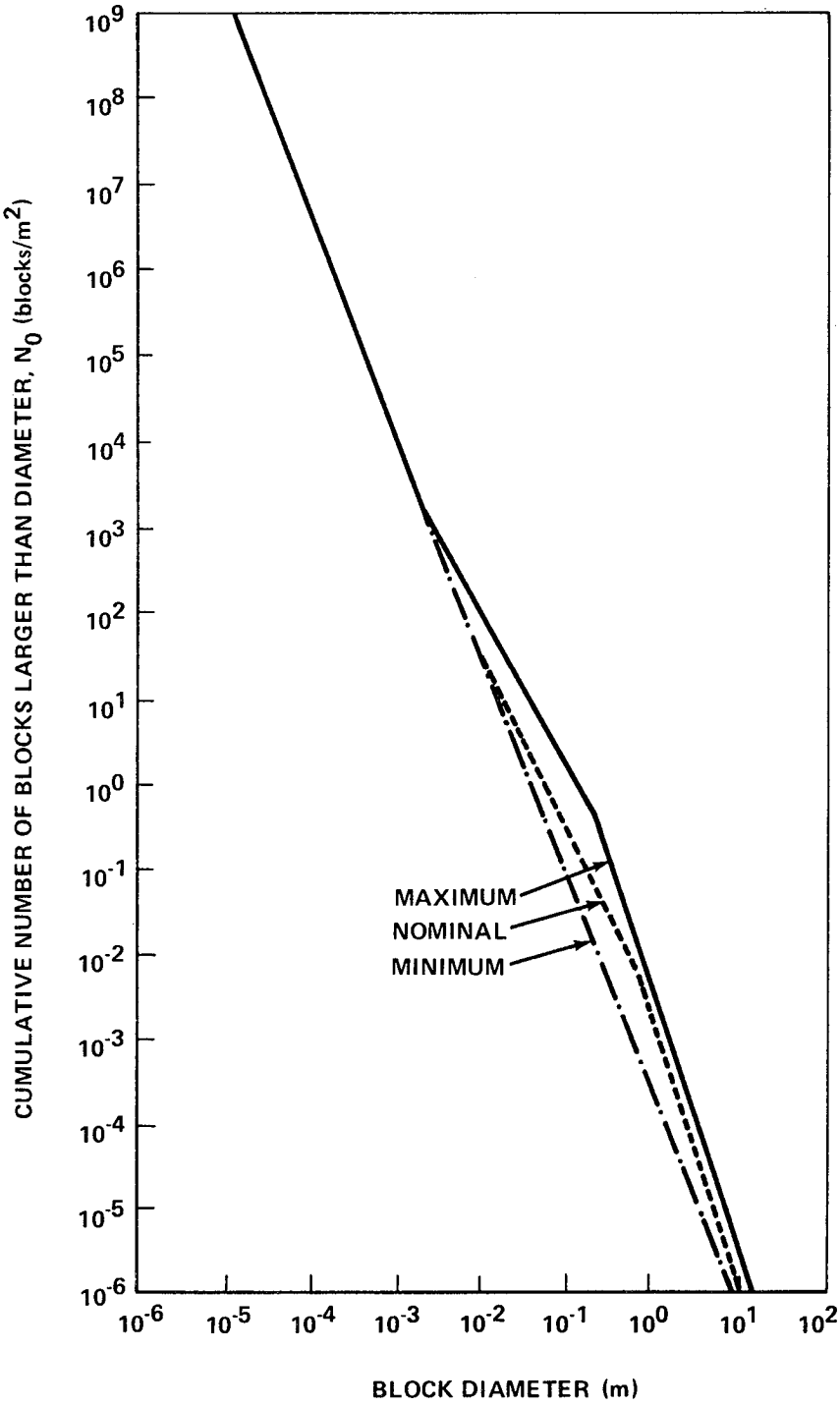

Figure IV-13. Cumulative number of blocks in intercrater region of smooth Mare, rough Mare, and Upland terrains.

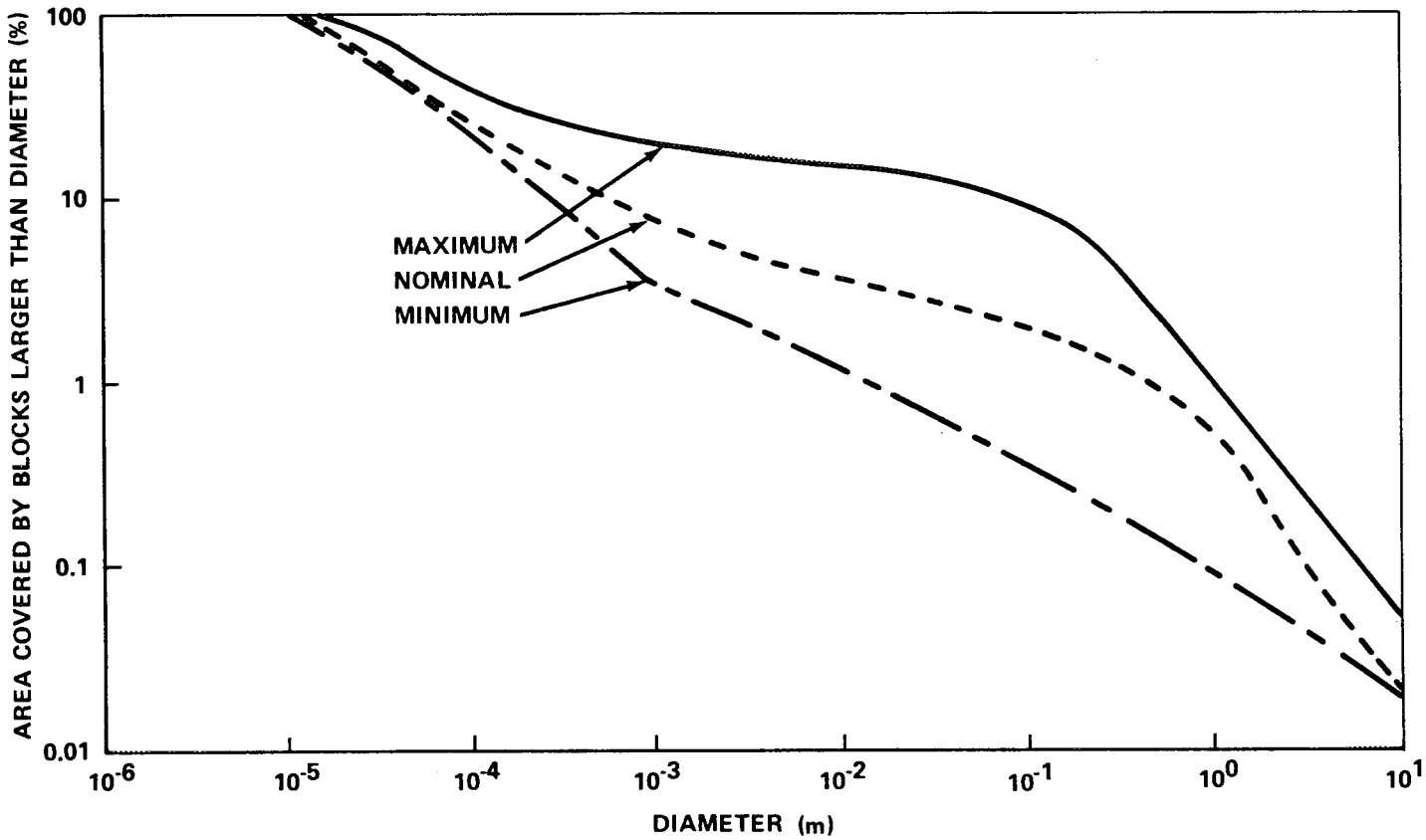

Figure IV-14. Percent of intercrater area of smooth Mare, rough Mare, and Upland terrains which are covered by blocks.

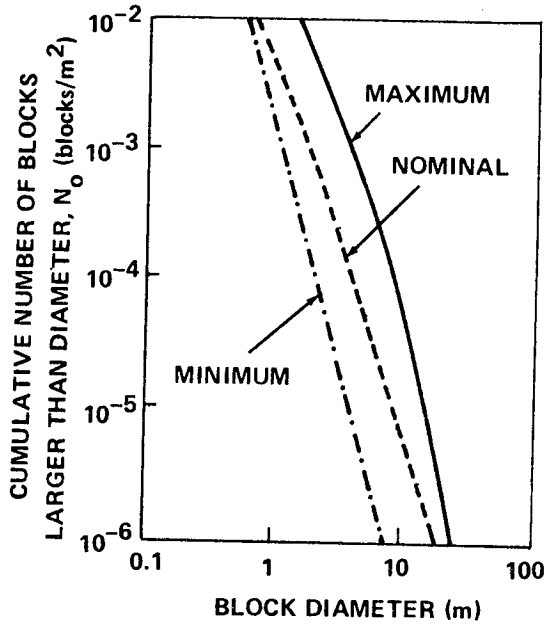

Figure IV-15. Cumulative distribution of blocks between crater rim and two crater radii as seen around craters in smooth Mare, rough Mare, and Upland terrains.

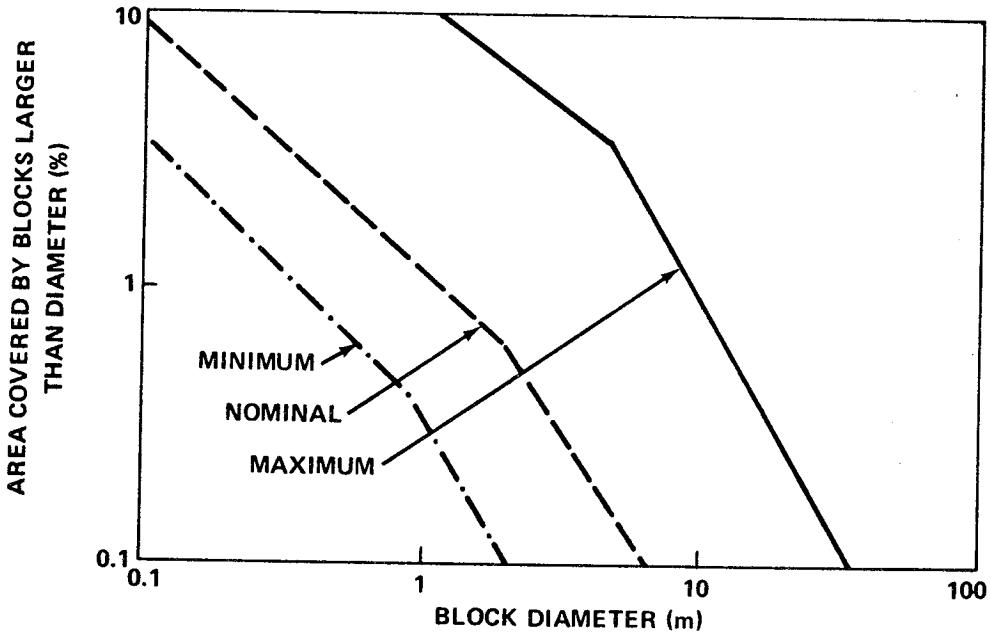

Figure IV-16. Percent of area covered by blocks between crater rim and two crater radii as seen around craters in smooth Mare, rough Mare, and Upland terrains.

particle size range from 0.01 to 5 mm and the density and porosity are the most important characteristics controlling the physical behaviors. Substantial regional and local density variations and changes in density with depth have been observed.

4.2.5.1 Soil Parameters

Table IV-3 presents the average soil parameters.

4.2.6 Thermal Properties

Infrared (10 to 12 μm) and photometric (0.45 μm) measurements were made by Saari and Shorthill from earth-based observations; their results are presented in the form of isothermal and isophotic charts for 23 phase angles. The infrared temperatures as measured are not independent of the observation angle (as they are for a Lambertian surface), but have a directional effect; these directional characteristics are one of the most anomalous characteristics of the surface. A mathematical expression relating infrared temperature to incident and observational directions has been developed from experimental data by Ashby and Burkhard.

Calvert [IV-32] fitted a Fourier series to the equatorial brightness temperature measurements of Murray and Wildey, Low, and Sinton over a complete lunation and presented the coefficients through the fiftieth order. Surface temperature anomalies[7] for local regions much hotter or cooler than the surrounding regions have been detected and closely examined by Shorthill and Saari. The brightness temperature differs from the actual surface temperature in three ways. First, the lunar surface is assumed to be a blackbody. Second, the thermal radiation is measured only over the 10 to 12 μm portion of the infrared band. Third, the thermal energy measured by the detector is an average of the radiation from distribution of temperatures over a region of the moon's surface. The size of the region changes with the location being viewed. The region is a circular area from 14 to 17 km in diameter when viewed at the center of the moon's disk. The Planck radiation equation is then used with the 10 to 12 μm band radiation and corrected for atmospheric absorption to determine the brightness temperature. The derived brightness temperature and actual surface temperature can be regarded as approximately equal [IV-33, IV-34].

7. Over 400 anomalies have been recorded. Mare Humoram typically showed 10 K enhancement above the surrounding Uplands.

TABLE IV-3. SOIL PARAMETERS

Parameter	Value
Composition (Atomic Percent)	
Oxygen	60
Silicon	20
Aluminum	7
Iron Content (Percent)	
Mare Terrain	5
Upland Terrain	2
Grain Size (μm)	2 to 60
Cohesion (N/cm^2)	0.02 to 0.2
Nominal	0.05
Internal Friction Angle (deg)	31 to 39
Effective Friction Coefficient (Nondimensional)	
Metal to Soil or Rock	0.4 to 0.8
Adhesive Strength (N/cm^2)	0.0025 to 0.01
Permeability (cm^2)	1×10^{-8} to 7×10^{-8}
Seismic Velocities (m/s)	
Compressional Wave	30 to 90
Shear Wave	15 to 35
Bulk Density (g/cm^3)	
at 5 cm	1.6
at 40 cm	2.0
Porosity (Nondimensional) at 5 cm Depth	0.465

4.2.6.1 Brightness Temperature

A Fourier series representation of measured equatorial brightness temperature (T_E) over a complete lunation period P is:

$$T_E = A_o + \sum_{n=1}^{50} A_n \cos \frac{2n\pi t}{P} + B_n \sin \frac{2n\pi t}{P}$$

The Fourier coefficients (A_n and B_n) are listed in Table IV-4. Below a depth of about 1 m, the temperature remains constant at about 230 K.

A first-order approximation for the variation of temperature with latitude (β) on the sunlit surface is given by

$$T = T_E \cos^{1/4} \beta$$

Lunar surface temperatures based on mathematical models for various values of the thermal inertia parameter (γ) are shown in Figure IV-17.

4.2.6.2 Brightness Temperature Directionality

An empirical expression, considering the directional aspects, has been developed for predicting the surface brightness temperature (T_B) of the sunlit portion in the infrared spectrum as follows:

$$T_B = \left(\frac{\pi I_o}{\sigma} \right)^{1/4}$$

where

TABLE IV-4. FOURIER SERIES BRIGHTNESS TEMPERATURE COEFFICIENTS

$A_o = 227.194$								
n	A_n	B_n	n	A_n	B_n	n	A_n	B_n
1	172.959	16.710	18	1.287	-0.2525	35	-0.6859	-1.395
2	30.978	-2.828	19	-2.292	-1.712	36	-0.6548	0.1242
3	-32.580	-5.861	20	-1.104	0.1936	37	0.5814	1.387
4	-11.958	1.437	21	1.990	1.620	38	0.6360	-0.1012
5	15.280	3.794	22	0.9928	-0.2003	39	-0.5067	-1.370
6	6.405	-0.8830	23	-1.707	-1.590	40	-0.6452	0.0698
7	-9.454	-2.819	24	-0.9227	0.1567	41	0.4118	1.351
8	-4.129	0.6055	25	1.486	1.522	42	0.6612	-0.0093
9	6.595	2.317	26	0.8615	-0.1585	43	-0.2845	-1.339
10	2.885	-0.5805	27	-1.235	-1.500	44	-0.6237	0.0645
11	-5.097	-2.161	28	-0.7767	0.1743	45	0.2027	1.369
12	-2.246	0.3976	29	1.063	1.499	46	0.5865	-0.01564
13	4.041	1.968	30	0.7044	-0.1354	47	-0.1762	-1.356
14	1.789	-0.3521	31	-0.9409	-1.457	48	-0.6448	-0.01454
15	-3.312	-1.921	32	-0.6887	0.1051	49	0.05244	1.329
16	-1.526	0.2377	33	0.8296	1.409	50	0.3160	0.000041
17	2.731	1.744	34	0.6733	-0.1237			

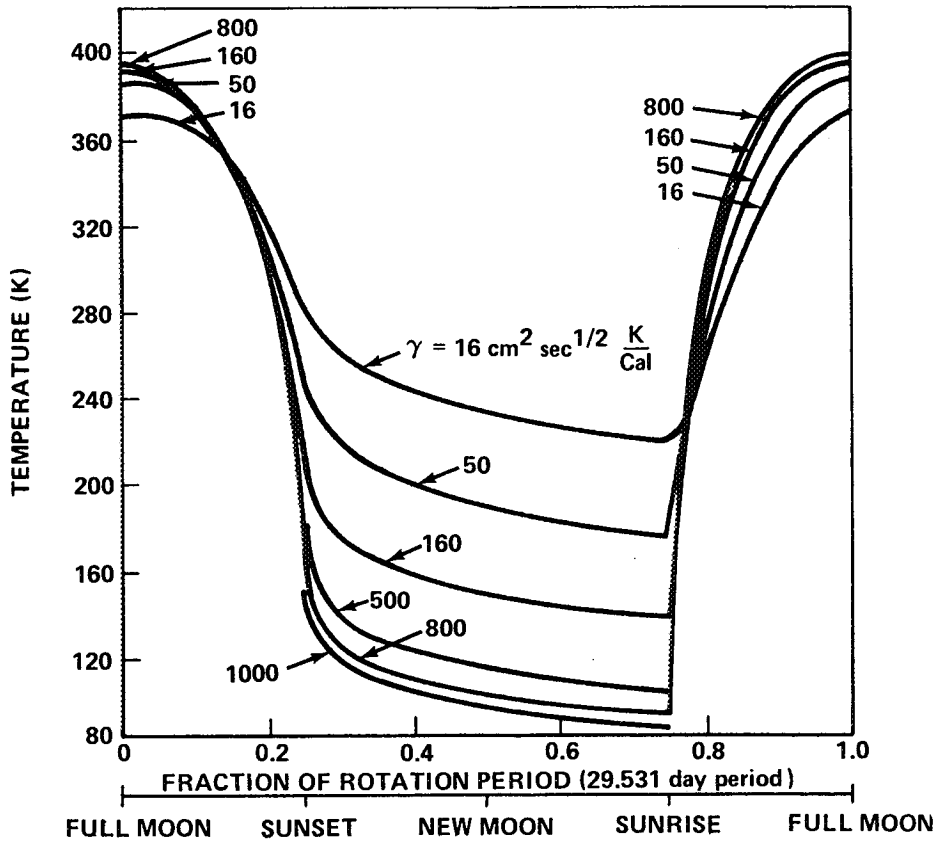

Figure IV-17. Temperatures nearest surface for different thermal parameter values.

$$I_o(i, \epsilon, g) = \frac{a_1 \cos i + a_2 \cos \alpha'}{1 + a_4 \frac{\sin \alpha'}{\cos i}} + \frac{a_3}{\pi} \left[(\pi - |g|) \cos |g| + \sin |g| \right]$$

and i, ϵ, ϕ_i, ϕ_ϵ, g are angles defined in Figure IV-18 and

$$\alpha = \frac{\pi}{2} \sqrt{\frac{i^2 + \epsilon^2 - 2i\epsilon \cos (\phi_i - \phi_\epsilon)}{\frac{\pi^2}{4} + \frac{4i^2 \epsilon^2}{\pi^2} - 2i\epsilon \cos (\phi_i - \phi_\epsilon)}}$$

where

$a_1 = 335 \text{ W/m}^2 \text{ sr}$
$a_2 = 97.6 \text{ W/m}^2 \text{ sr}$
$a_3 = 51.6 \text{ W/m}^2 \text{ sr}$
$a_4 = 0.121.$

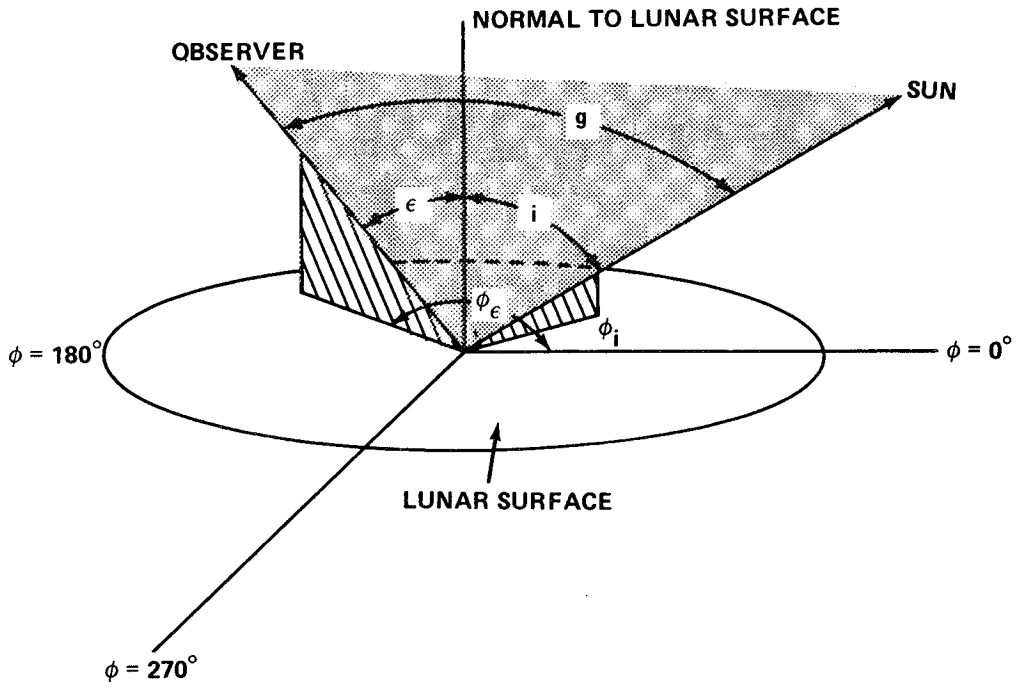

Figure IV-18. Angles used in directionality analysis.

The brightness directionality effect along the thermal meridian is shown graphically in Figure IV-19 as functions of sun angle and elevation angle of observation. In terms of an observer on the surface as shown below, the 90 deg observer elevation angle corresponds to his looking vertically downward at the surface, 0 deg elevation angle to his looking at the horizon with the sun on his back, and the 180 deg elevation angle to his looking at the horizon facing the sun.

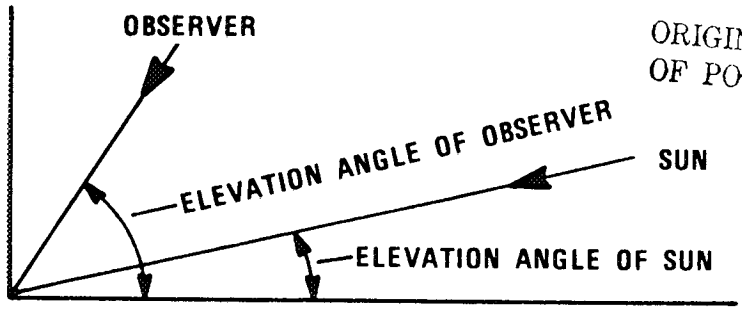

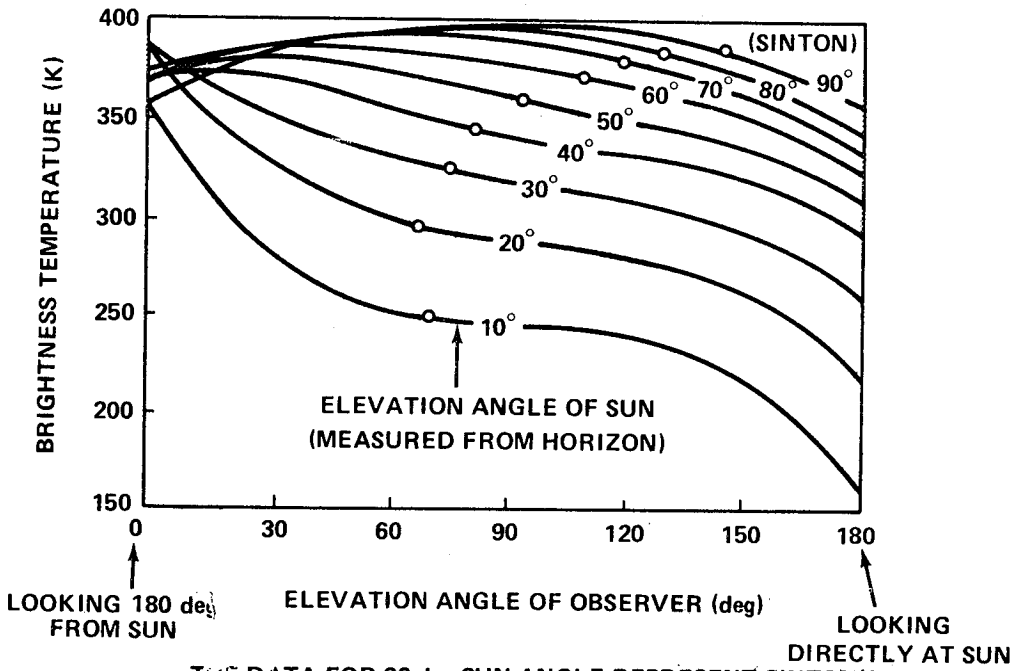

THE DATA FOR 90 deg SUN ANGLE REPRESENT SINTON'S (39) OBSERVATIONS OF THE SUBSOLAR POINT. THE LAMBERT TEMPERATURE IS INDICATED BY THE OPEN CIRCLES (33). (DATA (10 TO 80 deg) FITTED BY LEAST SQUARE POLYNOMIAL APPROXIMATIONS-SAARI AND SHORTHILL DATA)

Figure IV-19. Brightness temperature versus observer's elevation angle to the surface with the sun at different elevation angles.

4.2.6.3 Surface Thermal Properties

Thermal conductivity, k, should be considered temperature-dependent and can be expressed as

$$k = k_o + k_1 T^3$$

where T is the temperature, and k_o and k_1 are the conductive and reflectivity constants, respectively.

Laboratory data for powdered pumice and basalt are used for the estimates of the conductivity constant, k_o, and reflectivity constant, k_1, given here.

$$2.5 < k_o \times 10^6 < 21 \text{ W/cm K}$$

$$0.88 < k_1 \times 10^{13} < 3.57 \text{ W/cm K}^4.$$

These ranges should be considered as representative of the lunar soil.

The specific heat, c, is likely to be temperature dependent, and the density, ρ, is depth dependent. However, constant material thermal properties are useful as average properties for data comparison and environmental criteria.

Table IV-5 lists recommended ranges for the thermal inertia parameter, γ, specific heat, c, conductivity, k, and density, ρ.

4.2.6.4 Thermal Radiation

The thermal radiation from the lunar surface is about 310 W/m^2 at 1 AU with an average albedo of 0.110.

An attempt to determine effective constant material thermal properties for the Maria and Uplands with earth-based measurements has been unsuccessful because variations within a region (Maria or Upland) are as great as the average variation between regions. For this reason, the lunation cooling curves derived from experimental infrared measurements taken from

TABLE IV-5. LUNAR SURFACE THERMAL PROPERTIES

Surface Material	Parameter, γ $cm^1\ s^{1/2}$ K/joule ($cm^2\ s^{1/2}$ K/cal)	Density, ρ kg/m^3 (g/cm^3)	Specific Heat, c joule/kg K (cal/g K)	Conductivity, k W/m K (cal/cm s K)
Total Range	5.97 to 334 (25 to 1400)	500 to 3000 (0.5 to 3)	755 to 1007 (0.18 to 0.24)	2.14×10^{-3} to 1.13 (5.1×10^{-6} to 2.7×10^{-3})
Range for Particulate Material Heavily Mixed With Blocks	57.2 to 119 (240 to 500)	1200 to 2000 (1.2 to 2.0)	837 (0.20)	7.12×10^{-3} to 1.8×10^{-2} (1.7×10^{-5} to 4.3×10^{-5})
Blocks (Rocks)	7.2 (30)	2500 (2.5)	837 (0.20)	9.22×10^{-1} (2.2×10^{-3})
Range, Excluding Blocks	95.5 to 238 (400 to 1000)	500 to 1100 (0.5 to 1.1)	837 (0.20)	4.18×10^{-3} to 1.17×10^{-2} (1×10^{-5} to 2.8×10^{-5})
Average Maria	95.5 to 191 (400 to 800)	800 to 1500 (0.8 to 1.5)	837 (0.20)	4.18×10^{-3} to 8.8×10^{-2} (1×10^{-5} to 2.1×10^{-5})

the earth are not uniquely determined, but may be combined statistically to obtain an average cooling curve.

Surveyor spacecraft instrument compartment temperature data have been used to infer values of the soil thermal inertia, $\gamma = (k\rho c)^{-1/2}$, where k is thermal conductivity, ρ is density, and c is specific heat. The Surveyor data indicated a constant γ cannot adequately represent earth-based measurements during both eclipse and post-sunset. Winter and Saari developed a particulate lunar soil model which agrees with both eclipse and post-sunset cooling. Surveyor data [IV-2] indicated a value of γ of about 800 agreed best with the equatorial landing sites. Eclipse data, which give an estimate of γ for the insulating surface material, indicate a value for γ of about 1100 to 1400. Figure IV-14 in Reference IV-2 shows the directionality effect at a sun angle of 60 deg [IV-35].

4.2.7 Optical Properties

The parameter commonly used to express the diffuse reflectivity of the full moon is called the normal albedo. Published albedo values for various lunar surface features are not entirely in agreement. Errors in determining the normal albedo, for example, may arise because of uncertainty in the photometric function, extrapolations to zero phase angle, luminescence, and limitations or errors in recording and measuring instruments.

Pohn and Wildey obtained other normal albedo data by using a combined photographic and photoelectric technique with improved photo processing methods. (Pohn and Wildey's albedo measurements included the surge effect.) Gehrels et al. give the normal albedo of Mare Crisium as 0.082 to 0.092 in the ultraviolet region (3600 Å), 0.194 to 0.218 in the infrared region (9400 Å), and 0.08 to 0.15 over the visible region (3800 to 7800 Å).

Estimates of the average normal albedo values for the back side of the moon have been made by J. Dragg of NASA, from Orbiter photographs. He indicates the average normal albedo to be 0.217 for the back side of the moon.

4.2.7.1 Normal Albedo

Normal albedo values for the front and rear faces of the moon are listed in Table IV-6. Table IV-7 gives normal albedo values for some prominent features on the front face.

TABLE IV-6. NORMAL ALBEDO VALUES OF FRONT AND BACK FACES OF THE MOON

Regions	Normal Albedo		
	Minimum	Maximum	Average (peak value)
Front Side			
Mare	0.07	0.12	0.095
Upland	0.108	0.24	0.150
Entire face	0.07	0.24	0.110
Back Side			
Entire face			0.217

4.2.7.2 Photometric Model

The luminance, B, of the lunar surface is related to the photometric function, ϕ, the solar constant, E(1400 W/m^2 at 1 AU), and the normal albedo, ρ_o, by the equation

$$B = \frac{E}{\pi} \rho_o \phi$$

where the function, ϕ, depends on the phase angle, g, and surface orientation angle, α, as shown in Figure IV-20.

TABLE IV-7. NORMAL ALBEDO FOR SELECTED LUNAR FEATURES

Lunar Feature	After Thompson	After Tyler	After Tikhonova
Darkest Point	0.05	0.0516	0.070
Brightest Point	0.18	0.2190	0.240
Mare Crisium	0.062	0.0631 to 0.0784	0.085 to 0.096
Mare Fecunditatis	0.069	0.0655	0.090 to 0.108
Oceanus Procellarum	0.051 to 0.070	0.0533 to 0.0737	0.079 to 0.096
Sinus Iridum	0.065	0.0674	0.085 to 0.096
Mare Tranquillitatis	0.066	0.0571 to 0.0668	0.085 to 0.108
Mare Serenitatis	0.070	0.0585 to 0.0692	0.090 to 0.114
Mare Frigoris	0.089	0.0738	0.102 to 0.127
Mare Imbrium	0.054 to 0.074	0.0632	0.086 to 0.102
Mare Vaporum	0.060	0.0657	0.090 to 0.108
Mare Nubium	0.062 to 0.073	0.0627 to 0.0705	0.090 to 0.108
Tycho	0.154	0.0742 to 0.1737	0.150 to 0.169

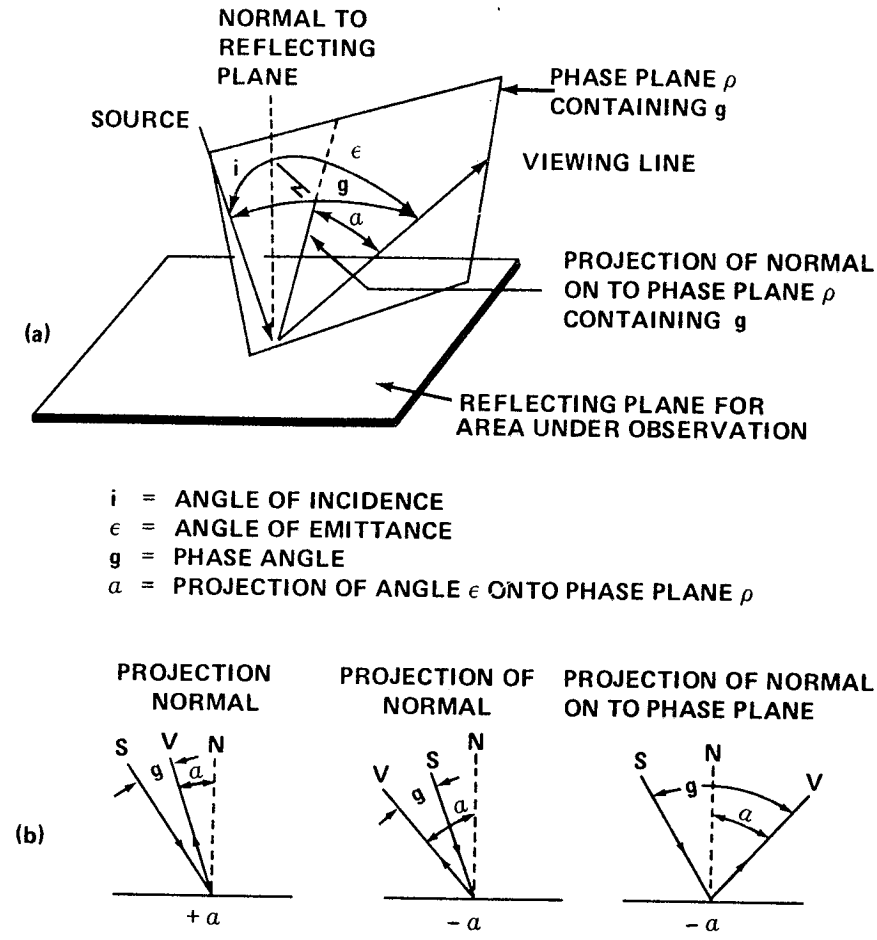

Figure IV-20. Photometric model geometry; (a) geometry, (b) positive and negative α .

Figure IV-20 (a) shows the location of a section of the lunar surface being observed along with the direction of the sunline and observation direction. The sunline and observation direction define a plane, called the phase plane, which is independent of the orientation of the lunar surface plane being observed. The phase angle is the angle in the phase plane (also independent of orientation of observed lunar surface area) between the sunline and line of observation. The angle, α, is an angle in the phase plane between the viewing direction and a line perpendicular to the line of intersection of the phase plane and lunar surface plane. The angle, α, is positive when the viewing line lies between the solar vector and the perpendicular line. Illustrations of positive and negative α are shown in Figure IV-20.

Figures IV-21 and IV-22 display the variation of the photometric function with angles g and α.

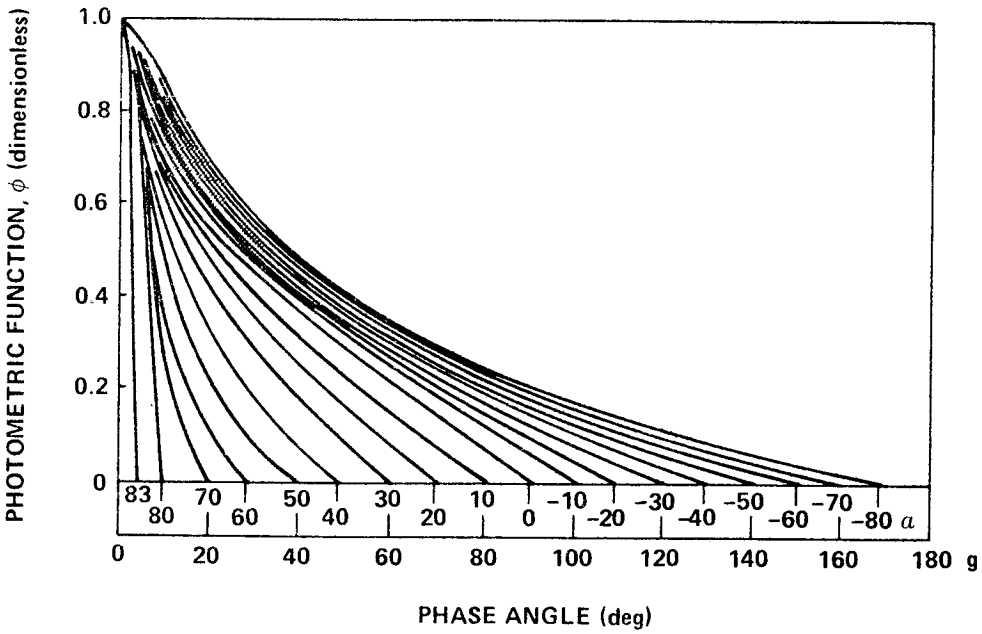

Figure IV-21. Variation of photometric function with phase angle g and angle α (after Fedoretz).

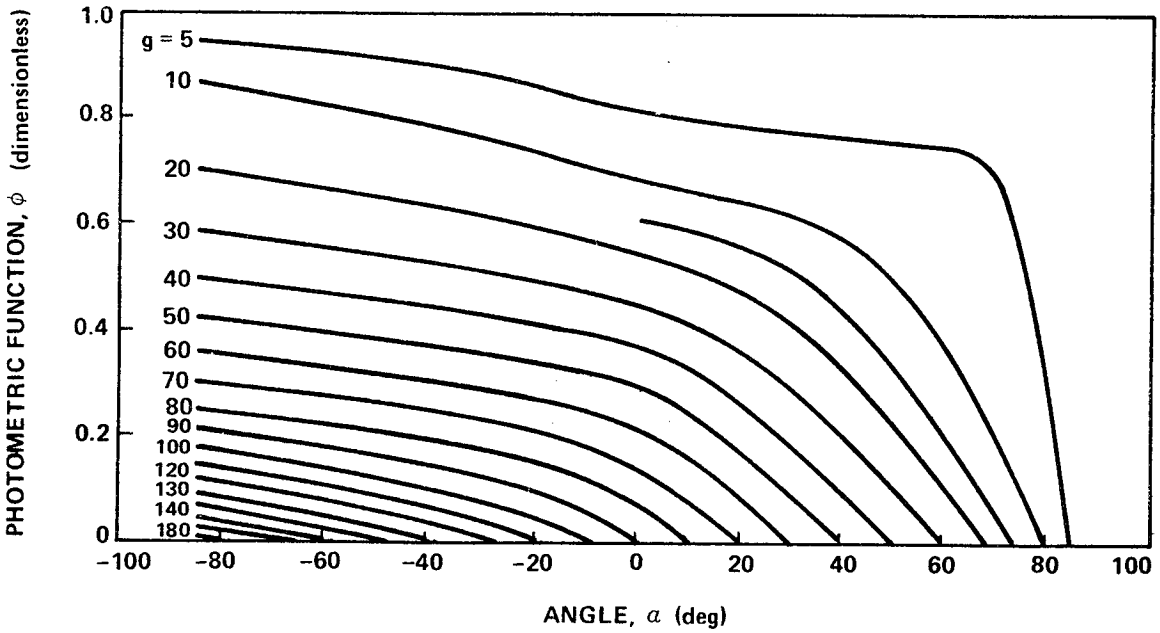

Figure IV-22. Variation of photometric function with angle α and phase angle g (after Fedoretz).

4.2.7.3 Polarization of Moonlight

Electromagnetic vibrations in the light emanating from the sun are distributed fairly equally in planes in all directions. After reflection from the moon, the intensities in different planes are no longer equal. The portion of polarized light is defined by

$$P_1 = \frac{I_1 - I_2}{I_1 + I_2}$$

where I_2 is the intensity of the reflected light in the plane defined by the incident and reflected light paths (phase plane) and I_1 is the intensity in the plane at right angles. The polarization curves for the moon shown in Figure IV-23 for both the waxing and waning moon were obtained by Lyot. The differences in polarization are attributed to the distributions of the Maria which have unusually large polarization and occupy about twice as much area at the last quarter as at the first quarter. The polarization changes in roughly inverse proportion to the albedo [IV-32].

For different areas of the moon, there are variations in the photometric function. This function relates the brightness of the lunar surface to the viewing angle and solar incidence angle. Two basic photometric functions (based on different assumptions) have been derived from earth-based observations. The first was derived by Hapke by fitting data to a theoretical scattering model of the lunar surface. The model was later revised in 1966. The second, based entirely on Fedoretz' lunar photographic data, was derived empirically by Herriman, Washburn, and Willingham in 1963. Since the data exhibited a large data scatter for small phase angles, Willingham developed a revised model with data from Sytinskaya and Sharanov in 1964. The function presented here is commonly called the Fedoretz function.

4.2.8 Dielectric Constant

The dielectric constant of lunar material has been estimated from the reflection at the surface of microwave emission and from radar return data.

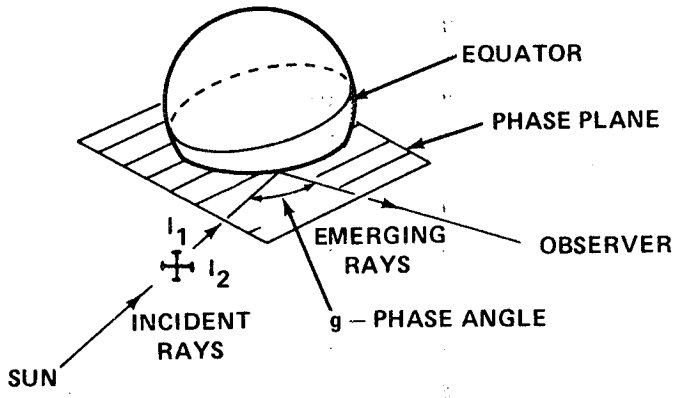

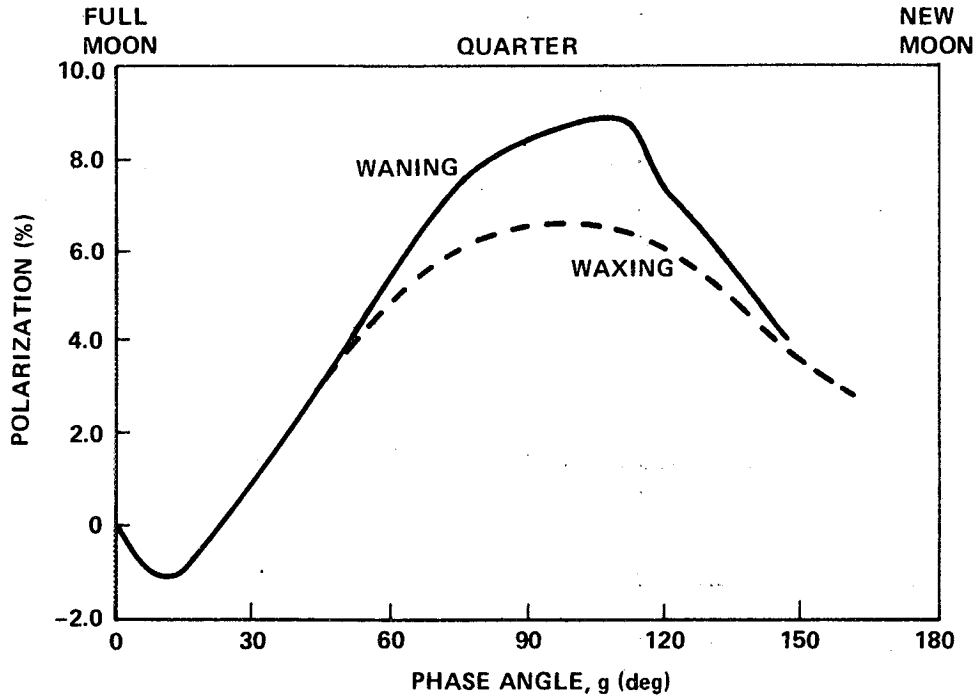

Figure IV-23. Polarization of lunar surface as a function of phase angle g (after Lyot).

On the basis of radar return data from the Surveyor spacecraft at a 2 to 3 cm wavelength (appropriate for surface estimates), Muhleman [VI-2] estimated the surface dielectric constant to be from 1.84 to 2.47 in the Mare (Surveyors 1, 3, 5, and 6) and from 2.88 to 3.68 in the Upland (Surveyor 7).

Estimates of the dielectric constant by Russian investigators do not differentiate between Mare and Upland regions. The dielectric constant estimate is about 3 at a 1.7 m wavelength. The dielectric constant is expressed as a function of wavelength and soil density. For a soil density of 1.5 to 2.5 g/cm^3, the corresponding dielectric constant lies in the range 2 to 3 at the Surveyor wavelength (2 to 3 cm) and in the range 3 to 4.9 at the Explorer wavelength (2.2 m).

4.2.8.1 Dielectric Constant and Loss Tangent

The complete range of values for the dielectric constant is about 1 to 8 where the high values are for solid material. The probable range is from 2 to 4 with the average value about 3. At a 2 to 3 cm wavelength, the value is about 2.4 ± 0.5 on the Mare and 3.3 ± 0.4 in the Upland [IV-2]. The relationship to the wavelength can be approximated by the equation:

$$\epsilon = [1 + \rho\xi(\lambda)]^2 \quad , \quad \xi(\lambda) = 0.5 + 0.045 \ell n\left(\frac{\lambda}{3}\right)$$

for $0.03 \text{ m} < \lambda < 200 \text{ m}$. The loss tangent, $\tan \phi$, lies in the range from 0.02 to 0.06, assuming a density of 1 to 2 g/cm^3 [IV-29].

4.2.9 Lunar Trafficability

One of the important problems in designing for or predicting vehicle mobility over lunar terrain involves consideration of the soil and vehicle interaction. Currently, designers of lunar roving vehicles have had to rely on approaches developed to predict terrestrial off-road performance capability or trafficability. A recent survey by Cornell Aeronautical Laboratories of the state of the art in terrestrial off-the-road locomotion [IV-36] concluded that there were two general approaches to assessing off-road mobility performance of wheel and track vehicles: one theory initially developed by Bekker [IV-37, IV-38] and modified by personnel at the Land Locomotion Laboratory (LLL), Army Tank Automotive Center; the other theory developed by the U.S. Army Engineering Waterways Experiment Station (WES). The latter approach gives a "go" or "no-go" prediction from an interpretation of cone penetrometer tests in a soil along with empirical formulas; it is primarily applicable to quick predictions of the trafficability of fine-grained soils and sands. Being based on

historical performance data of conventional vehicle designs, both methods have limited use for new and different vehicles incorporating unconventional design concepts for operation in a lunar environment.

The Bekker method examines mobility from a more fundamental viewpoint to obtain performance predictions and thrust requirements. The procedure assumes a combined frictional-cohesive soil and then develops wheel-soil equations describing wheel sinkage and tractive force (soil thrust). The relations involve several semi-empirical moduli for the soil. The Cornell survey [IV-36] mentions that there is no comparable work to match the Bekker-LLL approach in depth. Also, when it is applied with judgment to real problems, it often yields reasonable results. However, one major shortcoming of the Bekker-LLL theory is that it was only developed for mobility over flat terrains.

Soil cohesion is another factor affecting the mobility of a vehicle operating on the lunar surface. Halajean [IV-39] considers the influence of cohesion and gravity field on vehicle performance on level terrain. His results show cohesion has a negligible influence in low cohesive soils compared to the soil frictional contributions in earth's gravity field. However, in a lunar gravity field the relative importance of cohesion is much greater.

Soil cohesion takes on added importance in assessing vehicle performance of slopes. At high slope angles (approaching the angle of soil repose), the soil's strength and rigidity because of its frictional character tend to disappear, leaving mainly the cohesive component for load support.

Soil adhesion is an additional factor affecting the design and mobility of a lunar roving vehicle. The clogging of soil on wheels and tracks and the entrance of the soil into bearings that are not completely enclosed could cause problems in the lunar vacuum environment.

The design criteria for the lunar roving vehicle (LRV) were based on the data obtained from the Surveyor and Orbiter programs, and the vehicle performance estimates were based on data using simulated lunar materials (ground basalt).

REFERENCES

IV-1. Anon: Apollo 12 Preliminary Science Report. NASA SP-235, 1970.

IV-2. Anon: Surveyor Project Report. Jet Propulsion Lab., Tech. Rept. 32-1265.

IV-3. Anon: Apollo 16 Preliminary Science Report, NASA SP-315, 1972.

IV-4. Meteoroid Environment Model — 1970. NASA SP-8038 (Interplanetary and Planetary), October 1970.

IV-5. McCrosky, R. E.: Cometary Debris, the Dusty Universe. Proceedings of a Symposium Honoring Fred Lawrence Whipple on his retirement as Director of the Smithsonian Astrophysical Observatory, October 17-19, 1973, pp. 160-183.

IV-6. Apollo Missions and Navigation Systems Characteristics. Apollo Navigations Working Group Technical Report No. AN-1.3, Revision 2, October 1969.

IV-7. Anon: Collection of Papers on Apollo 15 Scientific Mission Results. Science, vol. 175, no. 4020, January 28, 1972, pp. 363-375, 407-443.

IV-8. Kaula, W. M.: Lunar Gravity Field, Rotational Dynamic and Surface Geometry. Reviews of Geophysics and Space Physics, vol. 13, July 1975, pp. 272-292.

IV-9. Wood, J. A.: Nature and Interpretation of the Apollo 11 Lunar Samples. Physics of the Solar System, NASA SP-300, Chapter 10, 1972.

IV-10. Adams, J. B.: Spectral Reflectance of Highland Rock Types at Apollo 17: Evidence from Boulder 1, Station 2, The Moon, vol. 14, 1975, pp. 483-489.

IV-11. Blanchard, D. P.: Major and Trace Element Chemistry of Boulder 1 at Station 2, Apollo 17, The Moon, vol. 14, 1975, pp. 359-371.

IV-12. Boynton, W. V.: Element Distribution in Size Fractions of Apollo 16 Soils: Evidence for Element Mobility During Regolith Processes. Earth and Planetary Science Letters, vol. 29, 1976, pp. 21-33.

REFERENCES (Continued)

IV-13. Casella, C. J.: Evolution of the Lunar Fracture Network. Geological Society of America Bulletin 87, 1976, pp. 226-234.

IV-14. Elachi, C.: Local Lunar Topography from the Apollo 17 ALSE Radar Imagery and Altimetry. The Moon, vol. 15, 1976, pp. 119-131.

IV-15. Grigoriev, D. P.: Morphology of Skeleton Crystals of Ovaline in a Fragment of Spinel Trocolite Delivered by Luna 20 Automatic Station. Doklady Akademii Nauk SSSR 225, 1975, pp. 403-405.

IV-16. Grogler, N. et al.: A Detailed Study of the ^{39}Ar-^{40}Ar Ages of Two Apollo 11 Basalts. Meteoritics, vol. 10, 1975, pp. 411-412.

IV-17. Meyer, H. O. A.: Lunar Glass Compositions: Apollo 16 Core Sections 60002 and 60004, Earth and Planetary Science Letters, vol. 28, 1975, pp. 234-240.

IV-18. Ryder, G.: Apollo 15 KREEP Basalt. Transactions of the American Geophysical Union, vol. 57, 1976, p. 278.

IV-19. Schmitt, H. H.: Evolution of the Moon: The 1974 Model. Space Science Reviews, vol. 18, 1975, pp. 259-279.

IV-20. Vaughan, O. H.: Lunar Environment: Design Criteria Models for Use in Lunar Surface Mobility Studies. NASA TM X-53661, September 28, 1967.

IV-21. Anon: Apollo 17 Preliminary Science Report. NASA SP-330, 1973.

IV-22. Anon: Apollo 14 Preliminary Science Report. NASA SP-272, 1971.

IV-23. Anon: A Study of Lunar Traverse Missions. Jet Propulsion Lab., Document 760-26, September, 1968.

IV-24. Anon: Apollo 11 Preliminary Science Report. NASA SP-214, 1969.

IV-25. McCroskey, R. E.: Cometary Debris, the Dusty Universe. Proceedings of a Symposium Honoring Fred Lawrence Whipple on his retirement as Director of the Smithsonian Astrophysical Observatory, October 17-19, 1973, pp. 169-183.

REFERENCES (Continued)

IV-26. Anon: Collection of Papers on Apollo 11 Lunar Science Conference. Science, Houston, Texas, vol. 167, no. 3918, January 5-8, 1970.

IV-27. Anon: Surveyor VII Mission Report, Part II: Scientific Results. Jet Propulsion Lab., Tech. Rept. 32-1264, March 15, 1968.

IV-28. Anon: Surveyor I Mission Report, Part II: Scientific Results. Jet Propulsion Lab., Tech. Rept. 32-1023, September 10, 1966.

IV-29. Anon: Surveyor III Mission Report, Part II: Scientific Results. Jet Propulsion Lab., Tech. Rept. 32-177, June 1, 1967.

IV-30. Anon: Surveyor V Mission Report, Part II: Scientific Results. Jet Propulsion Lab., Tech. Rept. 32-1246, November 1, 1967.

IV-31. Anon: Surveyor VI Mission Report, Part II: Scientific Results. Jet Propulsion Lab., Tech. Report. 32-1262, January 10, 1968.

IV-32. Calvert, T. A.: Thermal and Dielectric Properties of a Homogeneous Moon Based on Microwave and Infrared Temperature Observations. NASA TM X-1734, February 1969.

IV-33. Low, F. J.: Lunar Nighttime Temperatures Measured at 20 Microns. Astrophysical J., vol. 142, 1965, pp. 806-808.

IV-34. Sinton, W. M.: Temperatures on the Lunar Surface. Physics and Astronomy of the Moon, Z. Kopal, ed., Academic Press, 1962, pp. 407-427.

IV-35. Vingradov, A. P., Surkov, Yu. A., Cherkasov, I. I., and Shvarev, V. V.: Lunar Surface Explorations with Soviet Automatic Stations "Luna-9" to "Luna-13." Presented by the Government of the USSR to the U.N. Conf. on the Exploration and Peaceful Uses of Outer Space, May 1968.

IV-36. Anon: Survey and Program Definition for Off-Road Mobility Research. Cornell Aeronautical Laboratories, TR CAL VJ-2330-G-1, March 7, 1967.

REFERENCES (Concluded)

IV-37. Bekker, M. G.: Theory of Land Locomotion. The University of Michigan Press, Ann Arbor, Michigan, 1962.

IV-38. Bekker, M. G.: Mechanics of Off-the-Road Locomotion. James Clayton Lecture presented at an Ordinary Meeting of the Institution of Mechanical Engineers, London, November 13, 1962.

IV-39. Halajian, J.: Vehicle-Soil Mechanics on the Moon. Paper No. 63213 presented at the Automotive Engineering Congress, January 1963.

SECTION V. MERCURY

This section contains a summary of the most pertinent facts about Mercury's atmosphere and surface environments. Most of the information given herein appeared in NASA SP 8085 entitled "The Planet Mercury," or in the references cited.

5.1 Atmospheric Environment

5.1.1 Definition

The atmospheric environment of Mercury is considered to include the region of space between the surface of Mercury and ~20 000 km above the surface.

5.1.2 Gas Properties (Surface to ~1000 km Altitudes)

5.1.2.1 Temperature

Mercury is the smallest planet of the solar system and is also nearest to the sun. The combination of these two circumstances makes it a hot and gravitationally weak planet. Because of its small orbit and concomitant proximity to the sun, Mercury is a very difficult object to observe. It is now known that Mercury turns on its axis fast enough that no one side perpetually faces from the sun. Present estimates of the temperature on Mercury vary but it is generally agreed that any atmosphere on Mercury is expected to have a very high exospheric temperature because of its nearness to the sun. This characteristic combining with the weak gravitational field implies that all except the extremely heavy molecules should escape from the Mercurian atmosphere efficiently.

On earth, the exospheric temperature varies by about a factor of two over the solar cycle. Atmospheric escape occurs almost entirely at higher temperatures, and it appears that an effective mean temperature for escape is about 1500 K. Intuitively, one expects the exospheric

temperature on Mercury to vary over a wider range than on earth. At very low pressure ($\sim 10^{-6}$ mb) the exospheric temperatures depend strongly on the flux of solar ultraviolet radiation and thus vary diurnally and with the solar cycle. Temperatures suggested for the day-side exosphere with CO_2 being the major atmospheric constituent range between 980 and 2800 K [V-1].

Actually, the temperature structure of the Mercurian atmosphere has not been observed. Available information concerning the thermal structure on Mercury is based on various hypothetical atmospheric models. The temperature structure considers solar ultraviolet radiation, infrared radiative transfer, conduction, convection, dissociation, and escape of atmospheric constituents. In the lower atmosphere, for pressure > 0.1 mb, the surface temperature T_s forms the lower boundary condition, and the temperature gradient in the Mercurian atmosphere should be approximately adiabatic until the value $(0.5)^{1/4} T_s$ is reached. Higher temperature gradients that would be required for conductive or radiative heat transport are unstable against convection, which would re-establish a nearly adiabatic gradient. Figure V-1 shows the vertical temperature profiles for sunlit and dark cases for the upper density limit model [V-1].

5.1.2.2 Composition [V-1]

The search for atmospheric gases on Mercury was carried out by Antoniadi and later by Kuiper, but failed to give any positive results. It was therefore generally believed that if an atmosphere exists on Mercury, it must be composed of rare gases, such as argon, which are not observable by spectroscopic techniques. This was indeed proved by Dollfus who has produced evidence in the early 1960's that Mercury might be surrounded by a thin layer of argon. In 1965, Moroz reported data suggesting that the Mercurian atmosphere might contain some carbon dioxide. Both findings seemed reasonable.

In 1963, Kozyrev claimed that he had detected the presence of hydrogen through his spectroscopic studies and proposed an all-hydrogen atmosphere for Mercury. However, most other researchers conclude that the anomalies have solar, terrestrial, or instrumental origins since Mercury

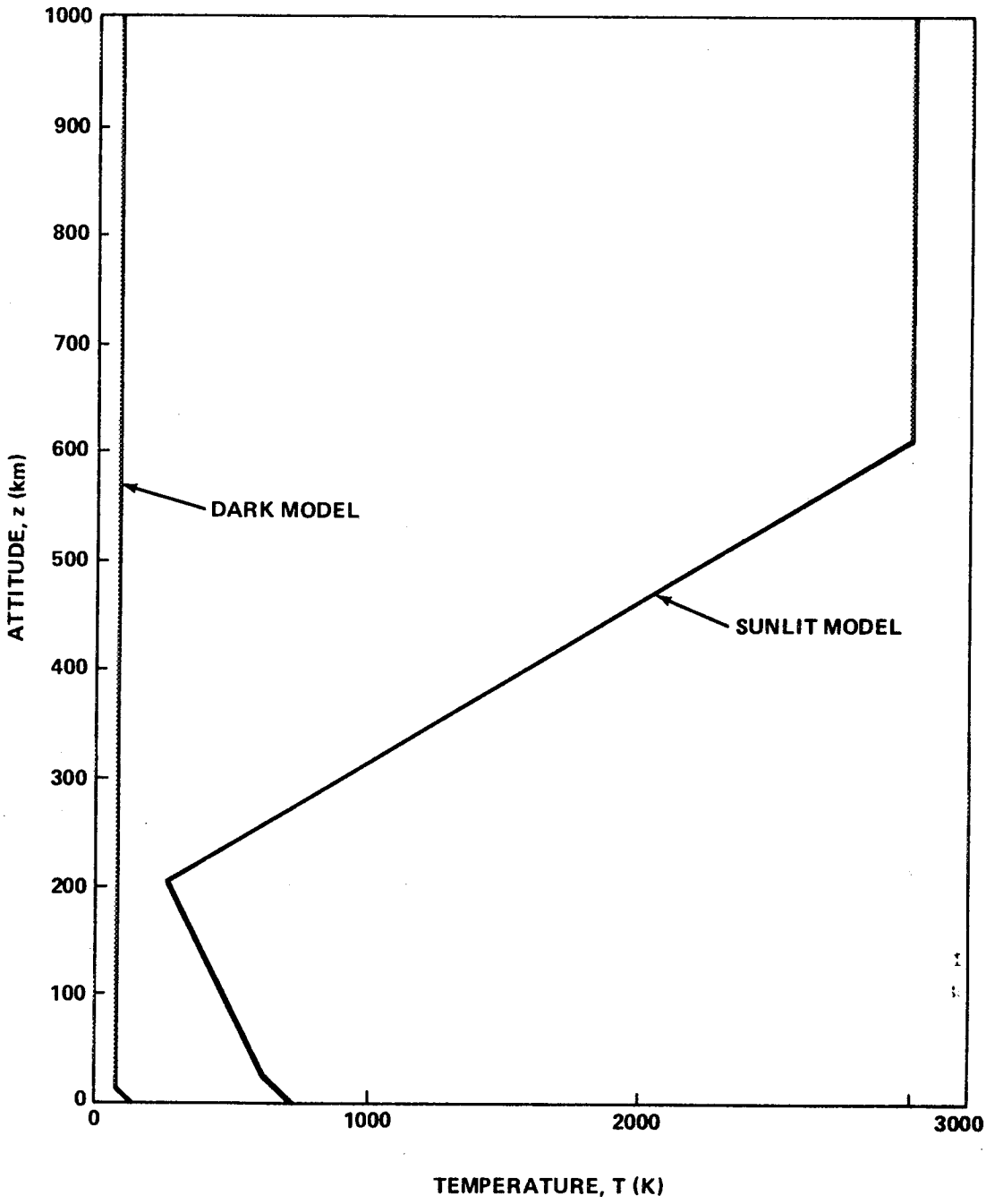

Figure V-1. Range of temperatures between dark and sunlit profiles versus altitude for the Mercury upper density limit model.

has a very high exospheric temperature, it is likely that hydrogen would escape quickly from Mercury. Kozyrev's arguments about the likelihood of a hydrogen atmosphere being cool and replenished from the solar wind are considered inconclusive.[1] Likewise, other lightweight molecules probably have escaped completely from the atmosphere. As a consequence, only those heavy gases such as neon, krypton, argon, and carbon dioxide could exist in the Mercurian atmosphere.

Table V-1 shows the spectroscopic results for Mercury.[2] Note that CO_2 is the only abundant gas presently in the atmospheres of Venus, Earth, and Mars whose molecular weight is equal to or greater than 44 g/mole. The spectroscopic evidence has shown that CO_2 is also existing in the Mercurian atmosphere with the smallest reliable upper limit on the CO_2 partial pressure being 0.04 mb, except for the controversial claim by Moroz.[3] The possibility of the presence of heavy gases in the atmosphere of Mercury other than carbon dioxide and argon has not been ruled out. One can predict that none of the other heavier gases such as oxygen, nitrogen, sulphur vapor, carbon disulphide, sulphur dioxide, neon, krypton or xenon could ever have reached the required escape velocity, with the possible exception of neon. If any of the gases were ever present on Mercury at any time past, they must still be there. Other gases which might be found would include chlorine, hydrogen bromide and iodine vapor [V-2].

Field, 1962, has noted that the terrestrial ratio of the mass of atmospheric argon to the mass of the planet is approximately 10^{-6} with the argon presumably of radiogenic origin. The assumption that this mass ratio corresponds to the terrestrial value results in the partial pressure of argon on Mercury of 1.9 mb. This result suggests that sufficient argon may exist to constitute the difference between the CO_2 partial pressure limit (0.1 mb). A thin atmosphere of 40 percent CO_2 and 60 percent argon probably could remain cool enough through infrared emission to avoid the high temperatures derived by Belton et al. That would cause the rapid loss of a mainly argon atmosphere.

1. NASA SP 8085, "The Planet Mercury (1971)." March 1972.

2. Ibid.

3. Ibid.

TABLE V-1. SUMMARY OF SPECTROSCOPIC RESULTS FOR MERCURY[a]

Wavelength (μm)	Molecule	Abundance (m-atm)	Pressure (mb)	Spectra	Reference	Remarks
0.4102(Hδ) 0.4861(Hβ)	H_2	0.8 to 80[b]	0.003 to 0.3[b]	Photographic	V-10 and V-11	Detection claimed,[b] abundance not estimated
0.4102(Hδ) 0.4861(Hβ)	H_2			Photographic		Reality of detection in references V-10, V-11
Blue ~0.8					V-13	No Mercury lines detected
~0.8 ~0.8 ~0.8	H_2O O_2 CO_2	<30μm[c] < 1.0 <57	<0.05 <4.2		V-14	
1.049	CO_2	< 5	<0.35	Photoelectric	V-5	
1.203	CO_2	< 1.0	<0.073	Photographic	V-15	
1.203 1.2177	CO_2 CO_2	< 0.2[d] < 0.58	<0.02[d] <0.04	Photographic	V-15	Band heads of CO_2 not detected
1.2177	CO_2	< 1.4	<0.10	Photographic	V-15	No Mercury lines detected
1.6	CO_2			IR Spectrometer	V-16	
1.6	CO_2	1.5-3.5[b]	0.11-0.26[b]	PbS Photocell	V-9	Detection claimed[b]
2.12, 2.26 2.26 to 2.32 2.35 3.3	N_2O NH_3 CO CH_4	< 0.02 < 0.01 < 0.1 < 0.003	<0.0015 <0.0003 <0.005 <0.0001	PbS Photocell	V-9	No Mercury lines detected

a. Adapted from NASA Monograph, "The Planet Mercury (1971)," March 1972.
b. Reality of detection questioned by other investigators listed at same wavelength.
c. μm of precipitable water.
d. Limit suspect because of nearby strong solar and terrestrial absorption lines.

5.1.2.3 Pressure

The evidence for an atmosphere on Mercury is based on two observations. Dollfus, 1961, reported an atmosphere of surface pressure $p_s \sim 1$ mb, from measurements of the polarization at the center and cusps of the planet in the red and green; Moroz, 1965, detected absorption in the 1.6 m CO_2 band in the infrared spectrum of Mercury. By re-analysis of Dollfus's data with laboratory and lunar data from the literature, O'Leary and Rea, 1967, found that the observer polarization properties of Mercury can be expected from laboratory data and are similar to those of the moon. They concluded that no reason exists to suggest any polarimetric evidence for an atmosphere on Mercury and estimate an upper limit of 1 mb for the surface pressure of Mercury from the sensitivity of the polarimetric method. O'Leary and Rea also reason that if the surface of Mercury has been weathered by solar wind and micrometeorite bombardment to produce its present albedo, color, polarization, and photometric properties, then the atmospheric pressure at the surface must be $\leq 10^{-5}$ mb for the solar protons to penetrate the atmosphere.

Since the spectroscopic measurement of the saturated CO_2 lines in the 1.6 μm band depends on both the effective pressure and the amount of CO_2, it is impossible to separate the two by observing only in one band. Therefore, Spinrad, Field, and Hodge, 1965, attempted to measure the intensity of the weak unsaturated lines of CO_2 at 8700 Å which are not pressure dependent. Combining these measurements with those of Moroz, they expected to get the amount of CO_2 and the total atmospheric pressure at the surface of the planet. Despite a low detection limit of 4 mÅ, they were unable to observe CO_2 lines in the 8700 Å region. Therefore, Spinrad, Field, and Hodge proposed an upper limit to the CO_2 content of 57 m-atm, which corresponds to a maximum possible partial pressure of 4.2 mb on the surface. Combining this upper limit on the amount of CO_2 with the Moroz observation of the equivalent width of the 1.6 μm CO_2 band, they conclude that the surface pressure on Mercury is near 4 mb if the atmosphere is pure CO_2.

Evidence of a tenuous atmosphere on Mercury is also supported by the comparison of Mercury's surface properties to the moon's. The apparent similarity of the surface properties of these two is consistent with the hypothesis that their histories and environments are similar because of direct impact by solar wind and solar ultraviolet radiation. If these radiations reach Mercury's surface, a negligible atmosphere is implied.[4] Also, the

4. Ibid.

discussion of the properties of the surface layers by Klein [V-3] concludes that the large value derived for the inverse thermal inertia from microwave observation requires that the surface pressure be less than 1 mb. All of these arguments are in good agreement with more recent precise polarimetric results cited by Dollfus [V-4] in which the upper limit total pressure on Mercury has been reduced to 0.1 mb.

5.1.2.4 Atmospheric Models

Based on the available information described in the preceding subsections, it is clear that Mercury has a tenuous atmosphere with carbon dioxide and argon as possible constituents, and a surface pressure being much less than 1 mb. Two model atmospheres are adopted[5] to illustrate the upper limit pressure and density that could exist on Mercury. The model applicable to sunlit condition uses the CO_2 partial pressure limit of 0.04 mb and the total surface pressure limit of 0.1 mb with argon accounting for the remaining pressure. The resulting composition is 60 percent argon and 40 percent CO_2 by number and implies a mean molecular weight of 41.6 and an adiabatic lapse rate of -4 K/km on Mercury. The appropriate extreme of surface temperature is 700 K and an exospheric temperature of 3000 K. At tropopause, the temperature is $(0.5)^{\frac{1}{4}} T_S$ which has a value of 590 K. In the upper atmosphere, the warmest temperatures cited in the theoretical literature are approximately 250 K at the mesopause and 3000 K at the critical level (pressure near 10^{-8} mb). To account for the night conditions, a model is specified which yields a still greater density in the first 8 km above the Mercurian surface. Note that the surface pressure of the dark model results from assumed pure argon atmosphere since CO_2 would be frozen out at the prevailing temperature.

Table V-2 shows the values of temperature, pressure, density, pressure scale height, and density scale height as a function of altitude for both sunlit and dark conditions. The table values are terminated at the level where the density has reached a value of approximately 10^{-16} g/cm^3. Vertical profiles of temperature, pressure, and density are given in Figures V-1 and V-2.

5.1.3 Gas Properties (1000 to 20 000 km Altitude)

Pressure and density decrease exponentially, and temperature increases linearly with increasing altitude to their respective interplanetary

5. Ibid.

TABLE V-2. MERCURY UPPER DENSITY LIMIT ATMOSPHERIC MODELS[a]

Sunlit (noon)						Dark			
z (km)	T (K)	P (mb)	ρ (g/cm^3)	H_p (km)	H_ρ (km)	T (K)	P (mb)	ρ (g/cm^3)	H_p or H_ρ (km)
0.0	700	0.1000	7.15×10^{-8}	37.4	47.6	100	600×10^{-2}	2.89×10^{-7}	5.56
5.0	680	0.0873	6.42×10^{-8}	36.4	46.2	84	2.26×10^{-2}	1.29×10^{-7}	4.67
10.0	660	0.0759	5.76×10^{-8}	35.3	44.9	84	7.05×10^{-3}	4.04×10^{-8}	4.67
15.0	640	0.0658	5.14×10^{-8}	34.2	43.5	84	2.42×10^{-3}	1.38×10^{-8}	4.67
20.0	620	0.0567	4.57×10^{-8}	33.1	42.2	84	8.28×10^{-4}	4.74×10^{-9}	4.67
25.0	600	0.0486	4.05×10^{-8}	32.1	40.8	84	2.84×10^{-4}	1.63×10^{-9}	4.67
27.5	590[b]	0.0450	3.81×10^{-8}	31.5	40.1	84	1.66×10^{-4}	9.52×10^{-10}	4.67
30.0	585	0.0415	3.55×10^{-8}	31.3	34.8	84	9.73×10^{-5}	5.58×10^{-10}	4.67
40.0	566	0.0300	2.65×10^{-8}	30.3	33.7	84	1.14×10^{-5}	6.55×10^{-11}	4.67
50.0	547	0.0214	1.96×10^{-8}	29.2	32.6	84	1.34×10^{-6}	7.70×10^{-12}	4.67
60.0	528	0.0151	1.43×10^{-8}	28.2	31.4	84	1.58×10^{-7}	9.04×10^{-13}	4.67
70.0	509	0.0105	1.04×10^{-8}	27.2	30.3	84	1.86×10^{-8}	1.06×10^{-13}	4.67
80.0	490	0.00725	7.41×10^{-9}	26.2	29.2	84	2.18×10^{-9}	1.25×10^{-14}	4.67
100.0	452	0.00327	3.62×10^{-9}	24.1	26.9	84	3.00×10^{-11}	1.72×10^{-16}	4.67
120.0	413	0.00138	1.67×10^{-9}	22.1	24.6				
140.0	375	0.000532	7.10×10^{-10}	20.1	22.3				
160.0	337	0.000186	2.76×10^{-10}	18.0	20.0				
180.0	299	5.72×10^{-5}	9.58×10^{-11}	16.0	17.8				
200.0	261	1.50×10^{-5}	2.87×10^{-11}	13.9	15.5				
205.5	250[b]	1.00×10^{-5}	2.00×10^{-11}	13.4	9.8				
210.0	280	7.29×10^{-6}	1.30×10^{-11}	15.0	11.0				
225.0	381	3.10×10^{-6}	4.07×10^{-12}	20.4	15.0				
250.0	549	1.12×10^{-6}	1.02×10^{-12}	29.4	21.6				
275.0	717	5.34×10^{-7}	3.72×10^{-13}	38.4	28.2				
300.0	886	2.97×10^{-7}	1.68×10^{-13}	47.3	34.8				
350.0	1222	1.21×10^{-7}	4.97×10^{-14}	65.3	48.0				
400.0	1559	6.17×10^{-8}	1.98×10^{-14}	83.3	61.3				
500.0	2232	2.28×10^{-8}	5.10×10^{-15}	119.3	87.7				
600.0	2905	1.09×10^{-8}	1.88×10^{-15}	155.3	114.2				
614.19	3000[b]	1.00×10^{-8}	1.67×10^{-15}	160.4	160.4				
700.0	3000	5.856×10^{-9}	9.76×10^{-16}	160.4	160.4				
800.0	3000	3.14×10^{-9}	5.23×10^{-16}	160.4	160.4				
900.0	3000	1.68×10^{-9}	2.81×10^{-16}	160.4	160.4				
1000.0	3000	9.02×10^{-10}	1.50×10^{-16}	160.4	160.4				

a. NASA SP-8085 "The Planet Mercury (1971)," March 1972.

b. At these levels the lapse rate dT/dz changes value.

Note: For an isothermal atmosphere $\frac{d \log T}{d \log P} = \beta = 0$, $H_p = H_\rho$ (App. B).

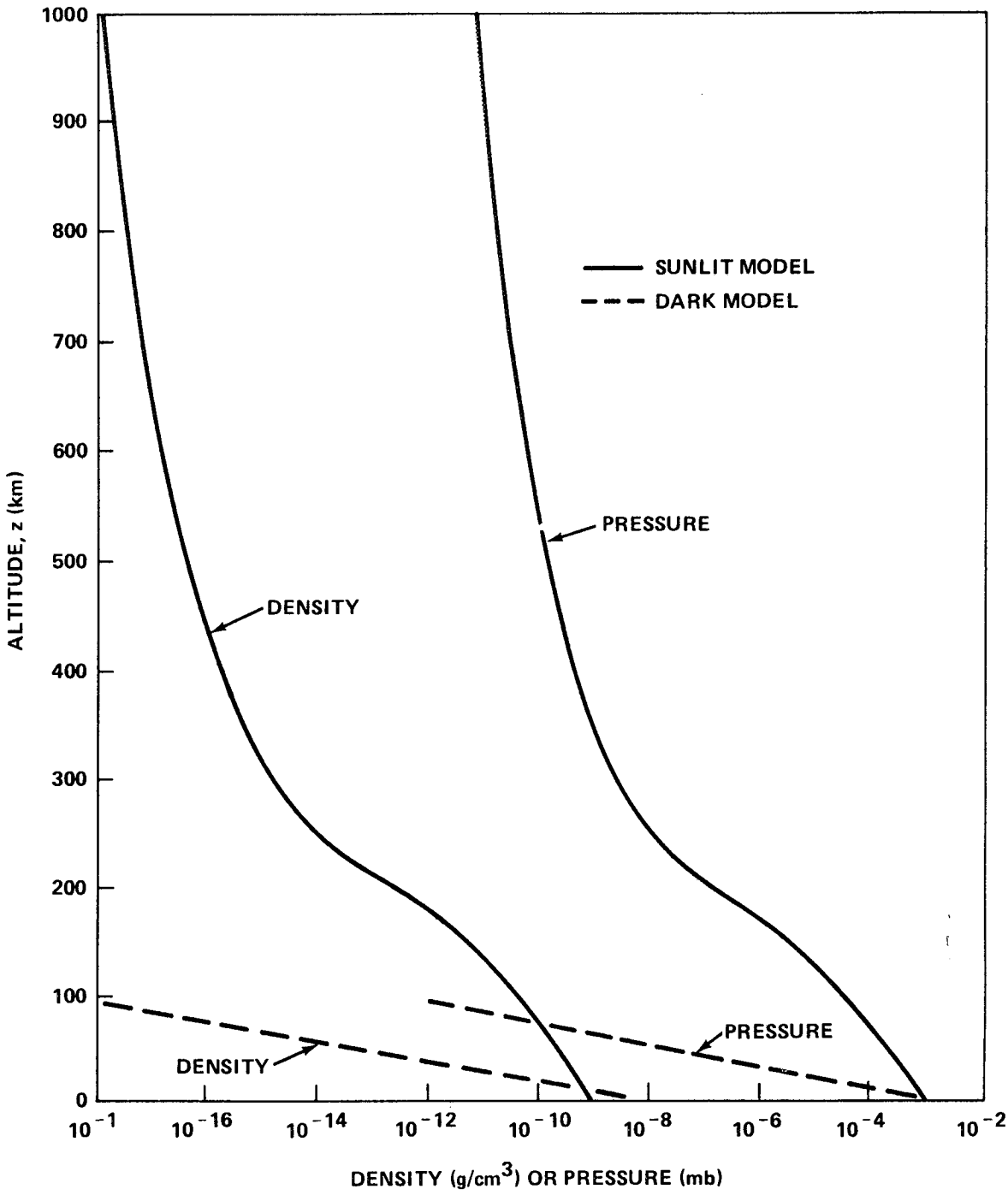

Figure V-2. Dark and sunlit model profiles of density and pressure versus altitude for upper density limit atmospheres.

space values of 10^{-15} N/cm^2, 10^{-23} g/cm^3, and 2×10^5 K near 20 000 km. Above 20 000 km altitude, all three quantities remain relatively constant with increasing altitude.

5.1.4 Ionosphere and Charged Particles [V-5 and V-6]

Mariner 10 observed a well developed bow shock and modest magnetosphere near the planet Mercury. Since Mercury has a magnetic field and a magnetosphere, some sort of ionosphere and trapped plasma belt about Mercury may exist.

5.1.5 Clouds

Some have been observed.

5.1.6 Circulation

Information is not available.

5.1.7 Electromagnetic Radiation

The electromagnetic radiation environment near Mercury includes the x-ray, ultraviolet, visible, infrared, and microwave portions of the spectrum.

5.1.7.1 Solar Radiation

The solar radiation environment at 1 AU from the sun is given in Reference V-7 which specifies the spectral irradiance P_λ (the received power per unit area and per unit wavelength interval) for all wavelengths between 1 Å and 100 cm. At the extremes of this range, i.e., the x-ray and microwave regions, the radiation is sporadic; but between 0.1 and 10 μm the radiation is steady with an integrated flux of $S = 0.1353 \pm 0.0021$ W/cm^2 at 1 AU from the sun; i.e., the solar constant [V-8]. These quantities, S and P_λ, multiplied by r^{-2} (where r is the distance of Mercury from the sun in AU) provide estimates of the radiation at Mercury. Because of the high eccentricity of Mercury's orbit, r^{-2} ranges between 4.6 and 10.6 AU and, accordingly, the integrated flux S/r^2 ranges between 0.623 and 1.435 W/cm^2 in the sunlight.

5.1.7.2 Mercury Reflected Radiation

Solar radiation reflected from Mercury has been measured visually and photographically by various observers whose results are discussed by Harris, 1961. The photoelectric measurements of Irvine et al., 1968, are generally in agreement with the foregoing results at the few angles for which data are published, and are intrinisically more precise. Therefore, they are adopted here.

Mercury's astronomical magnitudes, m, phase function, $\phi(\alpha)$, and geometric albedo, $p(\lambda)$, are satisfactorily approximated by the following expressions:

$$m = m_{\odot} - 2.5 \log [p(\lambda)\phi(\alpha)] + 5 \log (rR/R_M)$$

$$\log \phi(\alpha) = \frac{\alpha}{250} \frac{1}{2} \left[3.8 + \frac{\alpha}{100} \left(-2.73 + \frac{\alpha}{50}\right)\right]$$

$$\log p(\lambda) = (-0.94 \pm 0.07) + (0.25 \pm 0.05)(2 - \lambda^{-1}) \quad .$$

These expressions have been adapted from Harris, 1961, Irvine, 1968, and Allen, 1963. The distance r from the sun must be expressed in astronomical units, the phase angle α in degrees, and the wavelength λ in micrometers. The apparent magnitude $m_{\odot}$ of the sun is given at several wavelengths in Table V-3 [V-9].

The flux of reflected sunlight may be calculated directly from the foregoing values of the phase function, $\phi(\alpha)$, and the geometric albedo, $p(\lambda)$, by the formula

$$F_{\lambda} = \frac{p(\lambda)\phi(\alpha)}{r^2(R/R_M)^2} P_{\lambda} \quad .$$

Here, P_{λ} is the solar spectral irradiance specified in Reference V-7 and the distance r from the sun must be expressed in astronomical units. If the solid angle of the visible, sunlit portion of Mercury's disk is Ω_M, the intensity of the surface, I_{λ}, has the average value

$$I_{\lambda} = F_{\lambda}/\Omega_M \quad .$$

TABLE V-3. PHOTOMETRIC PARAMETERS FOR THE SUN, MOON, AND PLANETS[a]

	Photometric Passband Parameters[b]				
	U	B	V	R	I
Effective Wavelength (μm)	0.353	0.448	0.554	0.690	0.820
Apparent Magnitude of the Sun ($m_\odot$)	-28.04	-28.18	-28.81	-29.26	-29.55
Absolute Magnitude of —					
Mercury (m_o)	c	+0.57	-0.36	-1.21	-1.73
Venus (m_o)	-2.97	-3.47	-4.29	c	c
Earth (m_o)	c	-3.67	-3.87	c	c
Moon (m_o)	+1.59	+1.13	+0.21	-0.59	-1.05
Mars (m_o)	+0.42	-0.16	-1.52	-2.64	-3.02
Jupiter (m_o)	-7.94	-8.42	-9.25	-9.75	-9.72
Saturn (m_o)[d]	-7.26	-7.84	-8.88	c	c
Uranus (m_o)	-6.35	-6.63	-7.19	-7.04	-6.24
Neptune (m_o)	-6.25	-6.46	-6.87	-6.54	-5.74
Pluto (m_o)	+0.06	-0.21	-1.01	-1.64	-1.92

a. NASA SP-8085, "The Planet Mercury (1971)," March 1972 [V-1].
b. See Appendix A of Newburn, R. L., and Gulkis, S.: A Brief Survey of the Outer Planets Jupiter, Saturn, Uranus, Neptune, Pluto, and Their Satellites. Jet Propulsion Laboratory TR 32-1529, 1971.
c. Data not available.
d. Can vary with ring inclination up to one magnitude less, i.e., brighter, than specified.

The reflection properties of different portions of the disk imply that an uncertainty factor of 2 in either direction should be applied to the intensity on the basis of lunar analogy. The uncertainties specified for the albedo, $P(\lambda)$, are large enough so that the uncertainties from substitution of the albedo values into expressions for magnitude, m, and flux, F_λ, bracket the variations and uncertainties for all wavelengths and phase angles.

The polarization of the light reflected from Mercury varies with phase and position on the disk. The latest measurements reported by Dollfus [V-4] conclude that the polarization is similar to the moon's [V-10].

Although photometric observations of Mercury are not complete enough to permit a determination of the integrated or radiometric albedo, the similarity of the observed parameters to those of the moon suggests the adoption of lunar values for Mercury. For the moon, the range from 0.07 to 0.24 includes extremes based on differing surface terrains, and the average value is 0.12.

5.1.7.3 Mercury Thermal Emission

The observational data from which the characteristics of Mercury's thermal emission have been inferred are discussed in subsection 5.2.4 and summarized in Table V-4. In the wavelength range between 1 μm and 0.1 cm, thermal emission occurs within 100 wavelengths of the surface, and is therefore characteristic of the surface temperature and material properties. Although direct measurements of infrared emissivity are not available, it has been estimated as close to unity [V-11] and that value is adopted here. With the infrared emissivity taken as unity, the intensity and flux of thermal radiation are distributed in wavelength according to the Planck function $B_\lambda(T)$, which describes blackbody radiation, and the formulas in Table V-5 where T is the local surface temperature. The integrated flux incident on a spacecraft can be obtained only by integrating the intensities over wavelength and solid angle, but limiting values may be obtained in the form of σT^4 where the limiting values of T are taken as 90 and 700 K. These temperature limits imply limits on the integrated flux of 0.0004 and 1.4 W/cm^2 at Mercury's surface. At larger separations from Mercury ($R > R_M$), the flux limits are proportional to $(R/R_M)^{-2}$.

TABLE V-4. INFRARED OBSERVATIONS OF MERCURY INTERPRETED AS SURFACE TEMPERATURES[a]

Reference	Wavelength (μm)	Temperature (K)	Interpretation
V-12	8 to 14	600	Subsolar point at mean distance from sun
V-13	8 to 14	613	Same
V-14	8 to 14	180	Night quadrant, after sunset
V-15	8 to 13	<150	Night hemisphere
V-16	3.75 to 11.3	522	Sunlit surface, including subsolar point
V-16	8.6	205	Sunlit crescent near terminator
V-16	11.8	111 ± 3	Night hemisphere

a. NASA SP-8085, "The Planet Mercury (1971)," March 1972 [V-1].

TABLE V-5. ELECTROMAGNETIC RADIATION NEAR MERCURY[a]

	Direct Sunlight[b]	Sunlight Reflected from Mercury[c]	Mercury Thermal, and Radio Emission[d]
Intensity	$I_\lambda = \dfrac{P_\lambda}{(6.8 \times 10^{-5}\ \text{sterad})}$	$0 < I_\lambda < \dfrac{p(\lambda) P_\lambda}{r^2\ (\pi\ \text{sterad})}$	$I_\lambda = B_\lambda\ (T)$
Flux	$F_\lambda = P_\lambda / r^2$	$0 < F_\lambda < \dfrac{p(\lambda)\phi(\alpha)}{r^2\ (R/R_M)^2} P_\lambda$	$F_\lambda = \dfrac{\pi B_\lambda (T)}{(R/R_M)^2}$
Integrated Flux	$0.62 < F < 1.43\ \dfrac{W}{cm^2}$	$0 < F < \dfrac{0.35}{(R/R_M)^2}\ \dfrac{W}{cm^2}$ (average albedo = $0.12 \times 2 \pm 1$)	$\dfrac{0.0004}{(R/R_M)^2} < F < \dfrac{1.4}{(R/R_M)^2}\ \dfrac{W}{cm^2}$

a. NASA SP 8085, "The Planet Mercury (1971)." March 1972 [V-1].

b. Beyond shadow of Mercury, take solar spectral irradiance P_λ, given in NASA SP-8005 [V-7], and use the distance r from the sun in astronomical units.

c. Applicable except for conditions of specular reflection of sunlight; then the entries in column 1 are appropriate upper limits. Expressions for $p(\lambda)$ and $\phi(\alpha)$ are in footnote a., P_λ is from NASA SP-8005 Reference V-7 and r is the distance from the sun in astronomical units.

d. For $\lambda < 0.1$ cm, the range of T is that of the physical temperature of the observed surface; for $\lambda > 0.1$ cm the range of T is that of the brightness temperature T_B shown in Figure V-3.

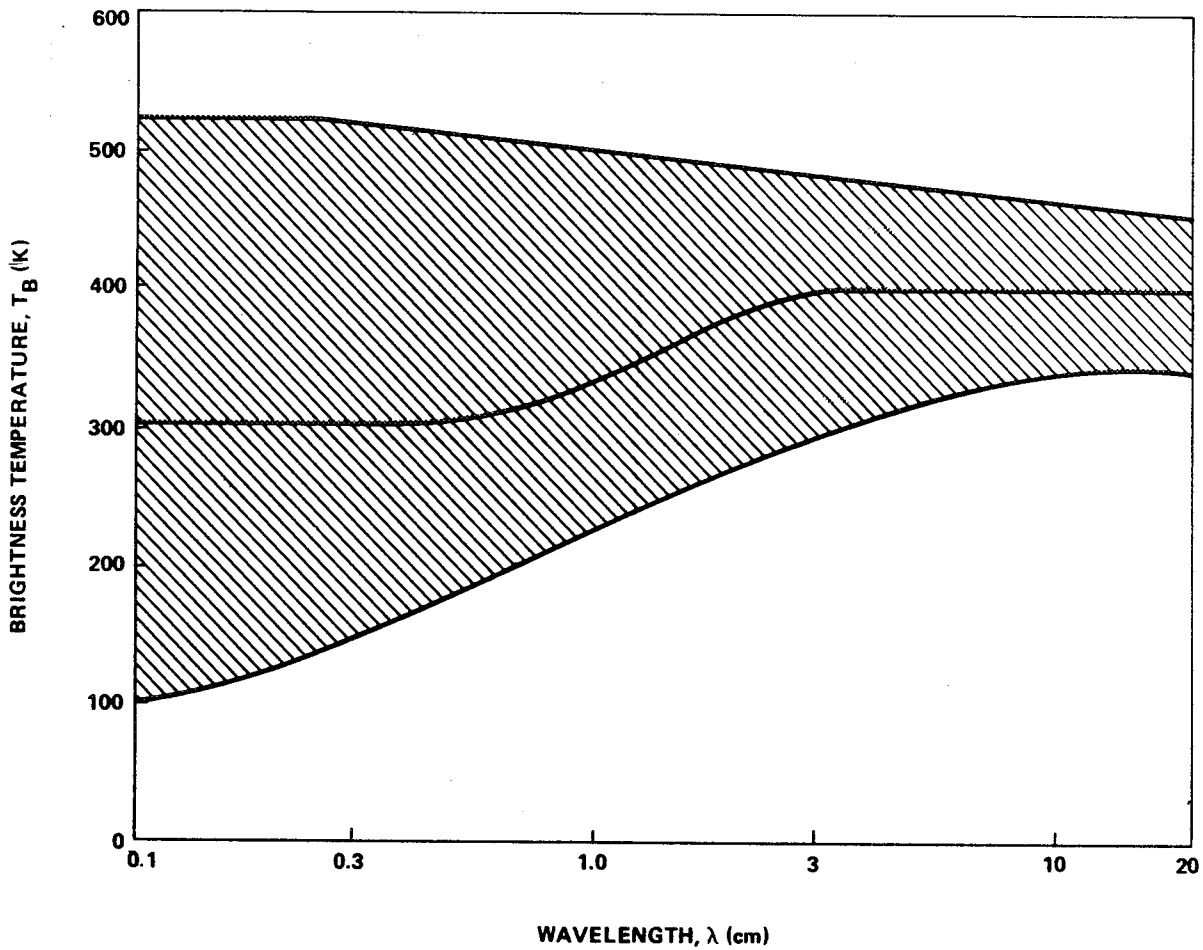

Figure V-3. The range of brightness temperature T_B for Mercury. (The central line represents the nominal dependence of T_B on wavelength λ, and the shaded area includes the uncertainties and time variations.)

5.1.7.4 Mercury Microwave Emission

At wavelengths between 0.33 and 11.3 cm, Mercury's radio emission has been detected by several observers, including those listed in Table V-6. The observational data have been interpreted in terms of effective brightness temperature T_B which is related to the observed flux F_ν by the modified Rayleigh-Jeans formula,

$$F_\nu = 2\pi k T_B (R_M/r\lambda)^2 \quad ,$$

where k is Boltzman's constant, R_M is the radius of Mercury, r is the distance from the sun, and λ is the wavelength of electromagnetic radiation. The brightness temperatures exhibit variations with wavelength and time of observation which exceed observational uncertainties and permit derivation of numerical values for physical, thermal, and electrical properties of Mercury's epilith or soil near the surface. The mean brightness temperatures, i.e., those averaged over a long interval of observation, derived at various wavelengths are shown in Table V-6 (adapted from Reference V-17).

At some wavelengths, the data reported in the references cited in Table V-6 indicate strong dependence of the brightness temperature on phase angle and its weaker dependence on heliocentric longitude. Because of the resonance between the periods of Mercury's orbit and rotation, these dependencies can be expressed in terms of the hermographic latitude, longitude, and the local time of that point on Mercury's surface directly beneath a nearby spacecraft.

These considerations are not pertinent to spacecraft design when the encounter circumstances are unspecified, but they do lead to a broad range of possible brightness temperatures at each wavelength. The range adopted here for design purposes is shown as a function of wavelength in Figure V-3. The adopted values are based on the references given in Table V-6. The tabulation of brightness temperatures versus wavelengths in Table V-6 indicates a probable increase of mean brightness temperature with wavelength between a few millimeters and several centimeters [V-17].

If the brightness temperature T_B is substituted for the physical temperature T in the formulas for the thermal emission given in subsection 5.1.7.3, the same formulas describe the microwave emission in the wavelengths from 0.1 to 20 cm.

TABLE V-6. SUMMARY OF MERCURY'S RADIO BRIGHTNESS TEMPERATURE MEASUREMENTS[a]

Wavelength (cm)	Mean Brightness Temperature, T_B (K)	Reference
0.33	296 ± 30[b]	V-18
0.34	277 ± 30	V-19
0.80	530 ± 50	V-20
1.53	450 ± 60	V-21
1.95	288 ± 30	V-22
1.95	350 ± 30	V-17
2.82	375 ± 40[c]	V-17
3.45, 3.75	400 ± 80	V-23
3.75	380 ± 20	V-24
6.00	385 ± 30	V-17
11.3	300 ± 40	V-25

a. NASA SP 8085, "The Planet Mercury (1971)," March 1972 [V-1].
b. Uncertainty estimates by Morrison and Klein [V-17] rather than Epstein et al. in most cases.
c. Unpublished results of Medd, cited by Morrison and Klein [V-17].

5.1.7.5 Other Radiation Sources

Harris, 1961, describes the light reflected from the moon and planets visible from Mercury. The magnitudes of these objects vary with relative positions (including phase angle) and orientations (including rotation and Saturn's ring inclination) which are specified in the "American Ephemeris and Nautical Almanac" [V-25]. Uncertainty broad enough to include these variations is implied by the expression for the apparent magnitude

$$m = (m_o \pm 0.3) + 5 \log (r\Delta) + (0.03 \pm 0.02)\alpha \quad .$$

where m_o is the absolute visual magnitude whose values are specified in Table V-3 and Δ is the distance from the reflecting surface to observer in astronomical units. Magnitudes and colors of bright stars may be obtained from standard star catalogs [V-26].

The integrated flux from the stars and planets is approximately $\sigma T^4 = 4.6 \times 10^{-10}$ W/cm^2 where T = 3 K, the equivalent blackbody temperature of space. This flux is an appropriate lower limit for all spacecraft surfaces when shadowed from both the sun and Mercury if Mercury is the nearest planet.

5.1.8 Meteoroid Environment

5.1.8.1 Cometary Meteoroid Flux

The flux (F_c), in number per square meter per second, of cometary meteoroids of mass m or greater on a randomly tumbling surface is: For $10^{-6} \leq m \leq 10^2$,

$$\log F_c = -13.669 - 1.213 \log m + \log \left(1 + 0.042 \frac{1}{r}\right) + \log \tfrac{1}{2} \left[1 + \left(1 - \frac{1}{r^2}\right)^{\frac{1}{2}}\right] \quad .$$

For $10^{-12} \leq m \leq 10^{-6}$,

$$\log F_c = -13.638 - 1.584 \log m - 0.063 (\log m)^2 + \log \left(1 + 0.042 \frac{1}{r}\right) + \log \tfrac{1}{2} \left[1 + \left(1 - \frac{1}{r^2}\right)^{\frac{1}{2}}\right] \quad ,$$

where r is the distance of the spacecraft from the center of Mercury (in units of the planet's radius).

5.1.8.2 Average Velocity of Cometary Meteoroids

The average velocity of cometary meteoroids relative to the spacecraft is 31.06×10^3 m/s.

5.1.8.3 Survival Mass

The survival mass for micrometeoroids can be calculated as a function of height in the atmosphere by using the following approximate expression

$$m^{1/3} - m_{\infty}^{1/3} = \frac{\Lambda A \rho_m^{-2/3} v^2}{6\xi \cos Z} \int_{\infty}^{h} \rho_a \, dh \quad ,$$

(does not hold for dust balls)

where

$$\text{columnar mass} = - \int_{h}^{\infty} \rho_a \, dh$$

Z = zenith angle

ρ_m = density of micrometeoroid $\left(3.5 > \rho_m > 0.5 \text{ g/cm}^3\right)$

v = velocity of micrometeoroid

$$\left(v_{\text{parabolic}} \text{ or } v_{\text{orbital}} > v > v_{\text{escape}}\right)$$

A = shape factor = 1.2 for sphere

$\Lambda/\xi = 10^{-11.449}$.

5.1.9 Magnetic Environment

5.1.9.1 Magnetic Field and Magnetosphere

There are no data that directly indicate existence of an intrinsic magnetic field of Mercury. Three apparently independent estimates of the

surface field strength are of the order of 10^{-2} gauss. Reiffel, 1966, assumed intrinsic magnetic field for Mercury because of its slow rotation. (Fast rotation is thought to be significant in the maintenance of the fields of the Earth and Jupiter.) The range of magnetic moments corresponding to the foregoing estimates is between zero and the upper limit $M_1 = 4 \times 10^{23}$ gauss-cm^3. The corresponding magnetic field strengths range from the lower limit of 10γ, a low interplanetary field estimate near Mercury, to $2M_1/R^3$ where $2M/R^3_M = 2800\gamma$.

The boundary of the magnetosphere is fixed by the interaction of the planetary field with the solar wind. For the minimum field estimates, the magnetosphere is nonexistent, but the maximum field estimates yield a magnetosphere boundary one planetary radius above the surface in the solar direction and slightly larger elsewhere. If a magnetosphere exists, its configuration is probably similar to the earth's [V-27], except that the distortions caused by the earth's rotation should be neglected. In these circumstances the simple expression adapted from Good, 1967, can be expected to describe the shape of the magnetosphere's outer boundary as follows:

$$R = R_1 (4-\cos\theta)/3 \quad .$$

Here, R_1 is the sunward extent (for Mercury $R_1 < 2R_M$) and θ is the angle from the solar direction.

5.1.10 Astrodynamic Constants [V-28]

Parameter	Value
Semi-major axis	a = 0.3871 AU
Inclination to ecliptic	i = 7 deg
Eccentricity	e = 0.2056
Perihelion distance	a(1-e) = 0.3075 AU
Aphelion distance	a(1+e) = 0.4667 AU
Sidereal period	T_o = 87.969 days
Synodic period	115.88 days

Parameter	Value
Mean motion (orbital angular velocity)	$n = 2\pi/T_o = 8.267 \times 10^{-7}$ rad/s
Maximum angular velocity	$n(1-e)^{-2} = 1.310 \times 10^{-6}$ rad/s
Minimum angular velocity	$n(1+e)^{-2} = 5.688 \times 10^{-7}$ rad/s
Gravitational parameter	2.1686×10^4 km^3/s^2
Gravitational potential	$\psi = -(9.10 \pm 0.07$ km^2/s$^2)$ (R_M/R)
Escape velocity at distance R	$V_e = (4.27 \pm 0.02$ km/s$)$ $(R_M/R)^{1/2}$
Period of Keplerian orbit of semi-major axis a	$T_a = (84.5 \pm 0.6$ min$)$ $(a/R_M)^{3/2}$
Surface acceleration of gravity	$g = 374 \pm 4$ cm/s^2
Mass	$M_M = (3.32 \pm 0.02) \times 10^{23}$ kg
Radius	$R_M = 2435 \pm 6$ km
Mean density	$\bar{\rho} = 5.5 \pm 0.1$ g/cm^3
Period of rotation	$T_r = 58.646 \pm 0.03$ days
Angular velocity of rotation	$\omega_r = (1.2400 \pm 0.0006) \times 10^{-6}$ rad/s
Inclination of rotational pole to normal of orbital plane	<10 deg

5.2 Surface Environment

Because of the lack of good observational evidence for an atmosphere on Mercury, there is now more reason to believe that the surfaces of Mercury and the moon have been conditioned by similar mechanisms. No need would exist to invoke hypotheses such as the presence of radiogenic argon with a low exospheric temperature, a buildup of a Mercury atmosphere after meteoric erosion, or a meteoric rain on a Mercurian surface after braking by an atmosphere [V-29]. Rather, support is lent to the hypothesis that bombardment of Mercury by the solar wind and by micrometeorites may have darkened and roughened its surface, and caused it to evolve to its present albedo, color, polarization, and photometric phase properties.

5.2.1 Surface Features — Observations of Mercury by Mariner 10 [V-30]

The morphology and optical properties of the surface of Mercury resemble that of the moon in remarkable detail, recording a very similar sequence of events; chemical and mineralogical similarity of the outer layers is implied. Mercury is probably a differentiated planet with an iron-rich core. Differentiation is inferred to have occurred very early. No evidence of atmospheric modification of any land form is found. Large-scale scares and ridges unlike lunar or Martian features may reflect a unique period of planetary compression near the end of heavy bombardment, perhaps related to contraction of the core.

Pre-Mariner 10 visual observations and radar measurement data are found in References V-31 through V-38, Figure V-4, and Table V-7.

5.2.2 Physical Conditions

Measurements which relate to Mercury's surface properties indicate marginal differences at most between Mercury and the moon. The photometry (including the absolute and relative albedo, colors, contrast, and polarization and their dependences on wavelength and phase) is almost indistinguishable from the moon's [V-4]. Reflected radar signals show that Mercury's roughness and the ratio of its cross-section to its geometrical area are also indistinguishable from the moon's [V-31 through V-38] (Table V-7). Analysis of the microwave observations indicates that Mercury's electrical properties are similar to the moon's [V-11]; microwave observations coupled with infrared observations indicate that the thermal response of Mercury's surface is similar to that expected for the moon if placed in Mercury's orbit with its rotation [V-12 through V-16].

Theoretically, similarity between Mercury and the moon is to be expected on the basis that the qualitative theoretical considerations about the surface histories are the same. These concern the lack of an appreciable atmosphere and the associated surface modification by meteorites, solar wind [V-29 and V-39], and solar ultraviolet radiation. The foregoing concept assumes that the original surface compositions and internally-generated orogenic processes were similar.

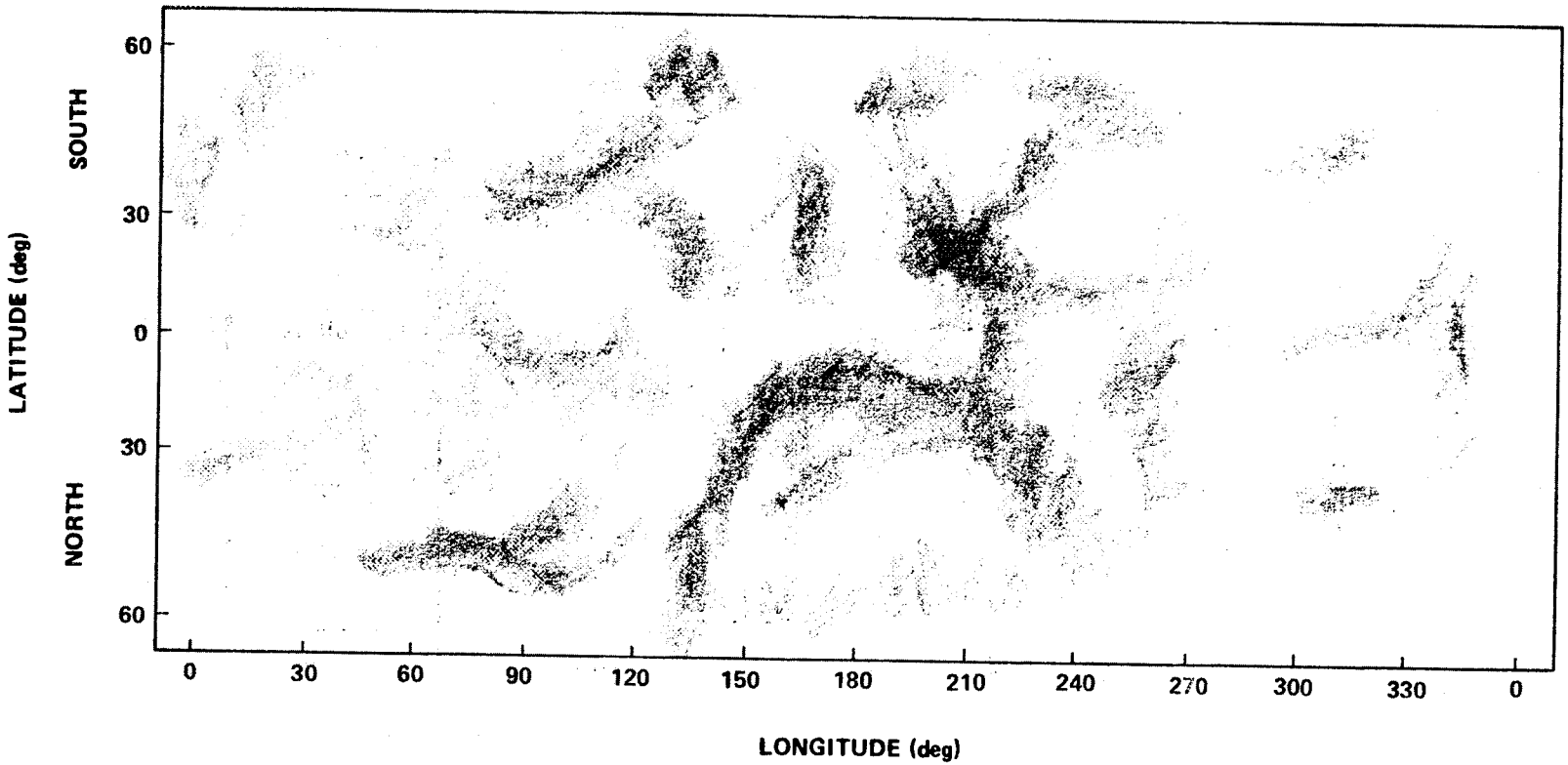

Figure V-4. Map of the surface features of Mercury from Camichel and Dollfus, 1968. (The Mercator projection is used, South is at the top, and the longitude system is that adopted by the IAU).

TABLE V-7. RADAR INVESTIGATIONS OF MERCURY[a]

Reference	Wavelength (cm)	Chief Subject of Report
V-65	12.5	Surface roughness
V-63	12.5	Surface features (large scale)
V-66	23	Surface roughness
V-67	23, 70	Mass, radius, and ephemeris values
V-68	43	Reflectivity
V-69	70	Rotation rate
V-70	70	Cross-section and reflectivity
V-64		Surface features (large scale)

a. NASA SP 8085, "The Planet Mercury, March 1972."

Therefore, the following sections assume that lunar values for the composition, mechanical properties, and topography can be applied directly to Mercury's surface. Much of material in these sections is taken from Reference V-10 which has been corroborated by NASA References V-40 and V-41 that report Apollo 11 and 12 results.

5.2.2.1 Surface Composition

From the foregoing assumption of similar surface values for the moon and Mercury, the study of Apollo samples [V-42] provided pertinent data on composition of Mercury's rocks and soil. The minerals which make up the bulk of these samples are very similar to those found in terrestrial basalts (namely, plagioclase, pyroxene, and ilmenite) and, less commonly, in anorthosites (primarily plagioclase). The minerals are primarily silicates and other oxides with the major differences from common terrestrial basalts being a larger fraction of ilmenite (containing iron and titanium oxides), the absence of ferric compounds, and the absence of moisture and hydrous minerals. Although Mercury's surface composition doubtless strongly depends on its local geological history, the absence of such data and photometric evidence makes it reasonable to accept the lunar surface composition as similar to Mercury's. One likely difference, however, would be an enhanced ratio of heavy metals, principally iron, in comparison to the earth or moon, to make Mercury's surface composition compatible with its overall high mean density. The magnitude of this difference is indicated by Reynolds and Summers [V-43] in terms of overall iron mass fractions for which representative values of 0.68 for Mercury and 0.13 for the moon are obtained. According to Khodak [V-44], the heavy metals could be present on the surface in the form of a higher fraction of ilmenite than for the moon or of metallic iron and nickel.

5.2.2.2 Soil Mechanical Properties

The mechanical properties of lunar soil have been measured remotely by Surveyor spacecraft, studied from the samples returned by the Apollo missions, and deduced from observations of astronauts and photographs of mobility and sinkage. The pre- and post-Apollo estimates agree in most important respects [V-10, V-45, V-46]. Because these properties are relatively numerous and complex, the lunar values are not discussed in detail here but simply tabulated in Table V-8 and adopted for Mercury's surface. The results of Morrison [V-11] support the tabulated values of density and porosity because loosely-packed rock powders duplicate many of

the properties required to explain the microwave data from Mercury. The other entries in Table V-8 are from Costes et al. [V-10, V-45].

TABLE V-8. SOIL MECHANICS PROPERTIES FOR MERCURY[a]

Properties	Symbols, Values, Units
Bulk density	1.8 ± 0.2 g/cm^3
Porosity	0.35 to 0.53
Specific gravity	3.1 to 3.4 g/cm^3
Grain size	2 to 60 μm
Cohesion	0.02 to 0.2 N/cm^2 (nominal 0.05 N/cm^2)
Adhesion	0.0025 to 0.01 N/cm^2
Static Bearing capacity (y = penetration depth in cm)	(1.0 ± 0.4)y N/cm^2
Angle of internal friction	31 to 39 deg
Effective coefficient of friction (metal to soil or rock)	0.4 to 0.8

a. NASA SP 8085, "The Planet Mercury, March 1972." [V-1].

5.2.2.3 Topography

The absence of shadows near the terminator, as observed from earth, indicates that large-scale elevation differences are not significantly greater than on the moon. The maximum elevation differences of about 12 km are reflected in the uncertainty ascribed to Mercury's radius (subsection 5.1.10). On smaller scales, relief or roughness is conventionally described in terms of the power spectral density function which is defined as the Fourier transform of the autocorrelation function of the surface elevation. Figure V-5, adapted from Reference V-10, shows the range of power spectral density versus wavenumber on the moon which is adopted here as the roughness description for Mercury. The similarity in roughness is supported on scales between 10 and 100 cm by the radar data (Table V-7). Slopes on the lunar surface are also specified in Reference V-10 from which Figures V-6 and V-7 are adapted for Mercury.

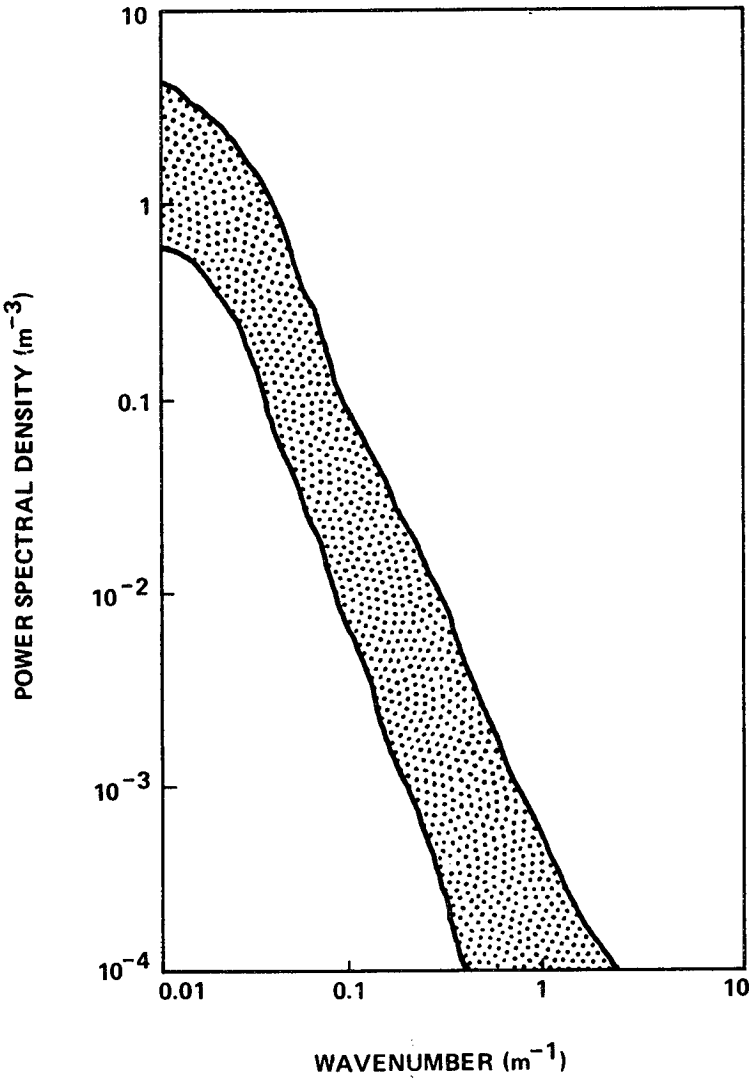

Figure V-5. Roughness of Mercury's surface, given by the power spectral density of the elevation as a function of the wavenumber [V-10].

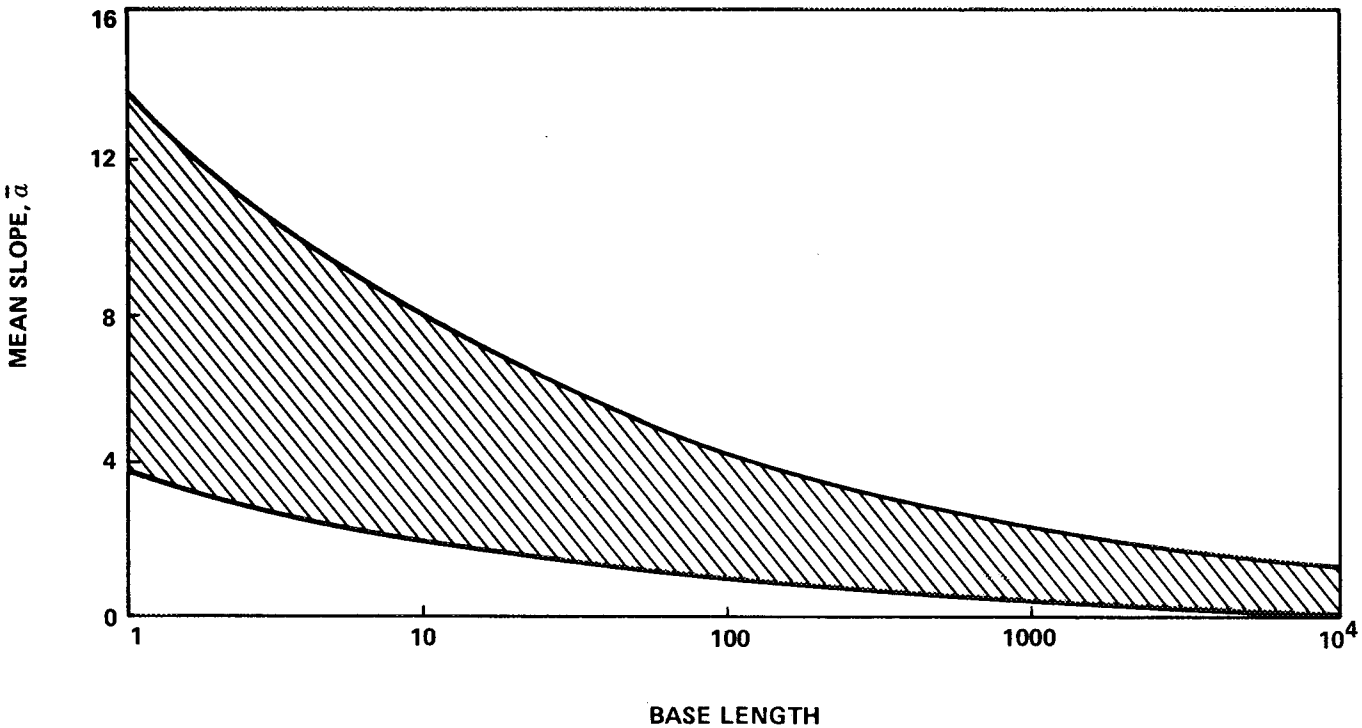

Figure V-6. Variation of mean slope of Mercury's surface with horizontal base length [V-10].

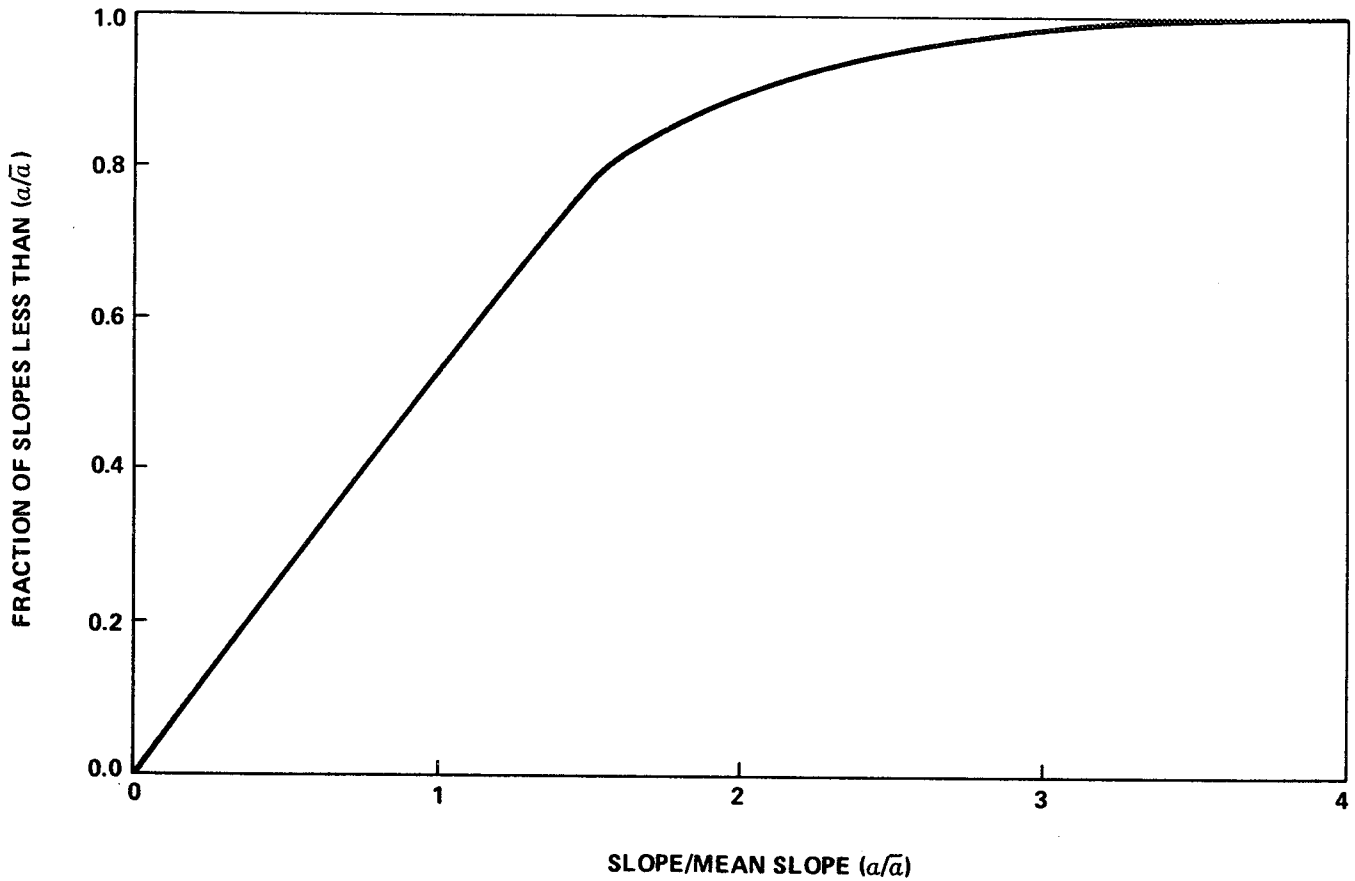

Figure V-7. Relative distribution of slopes on Mercury's surface for use with Figure 8 [V-10].

Crater and block distributions are also specified in Reference V-10 for the moon. The distributions shown in Figure V-8 are taken directly from Reference V-10 for adoption here for Mercury's crater and block frequencies; the Apollo 12 results [V-41] have confirmed these results and extended them to slightly smaller sizes for the craters. Craters outnumber blocks at all sizes shown for craters greater than 1 cm in diameter. For craters, the ratio of depth to diameter is less than 0.25, whereas for blocks the height is nominally 0.5 times the characteristic size [V-10]. For blocks and particles, Figure V-9 from Reference V-10 shows the fraction of the surface area covered and indicates that the entire surface is covered with dust particles greater than 10 μm in size.

5.2.3 Electromagnetic Properties

Several radar observations have provided data on the electrical properties of Mercury's surface and the interaction of the surface with electromagnetic radiation. The original articles describing these observations (Table V-7) indicate radar reflection properties for Mercury very similar to those for the moon. These properties include a low radar reflectivity [V-38] which implies a high microwave emissivity. The latter is supported by the analyses of the microwave data obtained by the investigators listed in Table V-6. On the basis of these data and appropriate theoretical considerations, several authors [V-3, V-11, V-17, V-18] have derived values for the electrical as well as thermal parameters of Mercury's surface layers (subsections 5.2.2.2 and 5.2.4). These results are based on the mean value and the amplitude and phase of the periodic variations of the brightness temperature as functions of wavelength and provide effective values for dielectic constant, solar wind flux, and ratio of electrical to thermal skin depths. The ranges adopted in Table V-9 for these parameters bracket not only the effective values cited in the literature but also variations likely to result from inhomogeneities. They are consistent with the composition and mechanical properties (subsection 5.2.2) and with corresponding ranges for the moon [V-11].

5.2.4 Temperature and Thermal Properties

Since Mercury has little atmosphere of any kind to diffuse or hold heat, the temperature of the surface in any given area will depend almost entirely upon how much direct sunlight is striking that area when the surface

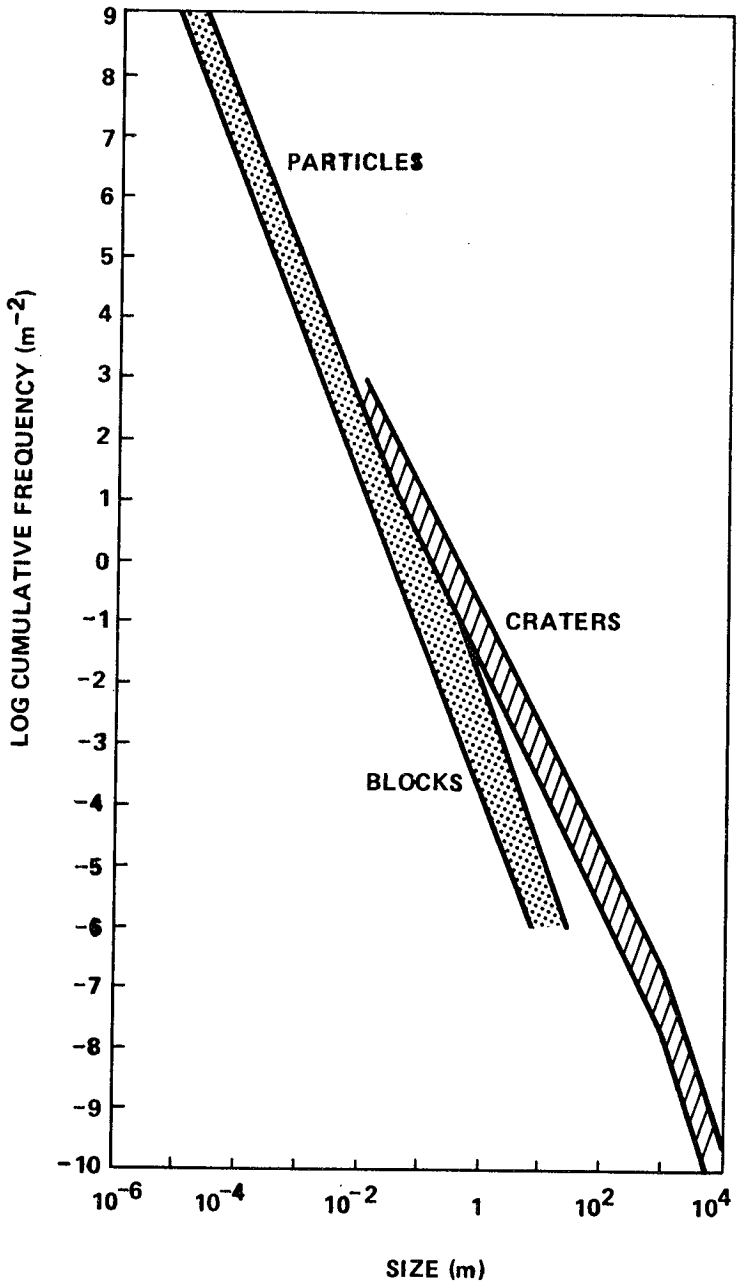

Figure V-8. Number per unit area of blocks, particles, and craters larger than specified characteristic size for the surface of Mercury [V-10, V-45, V-46].

C-3

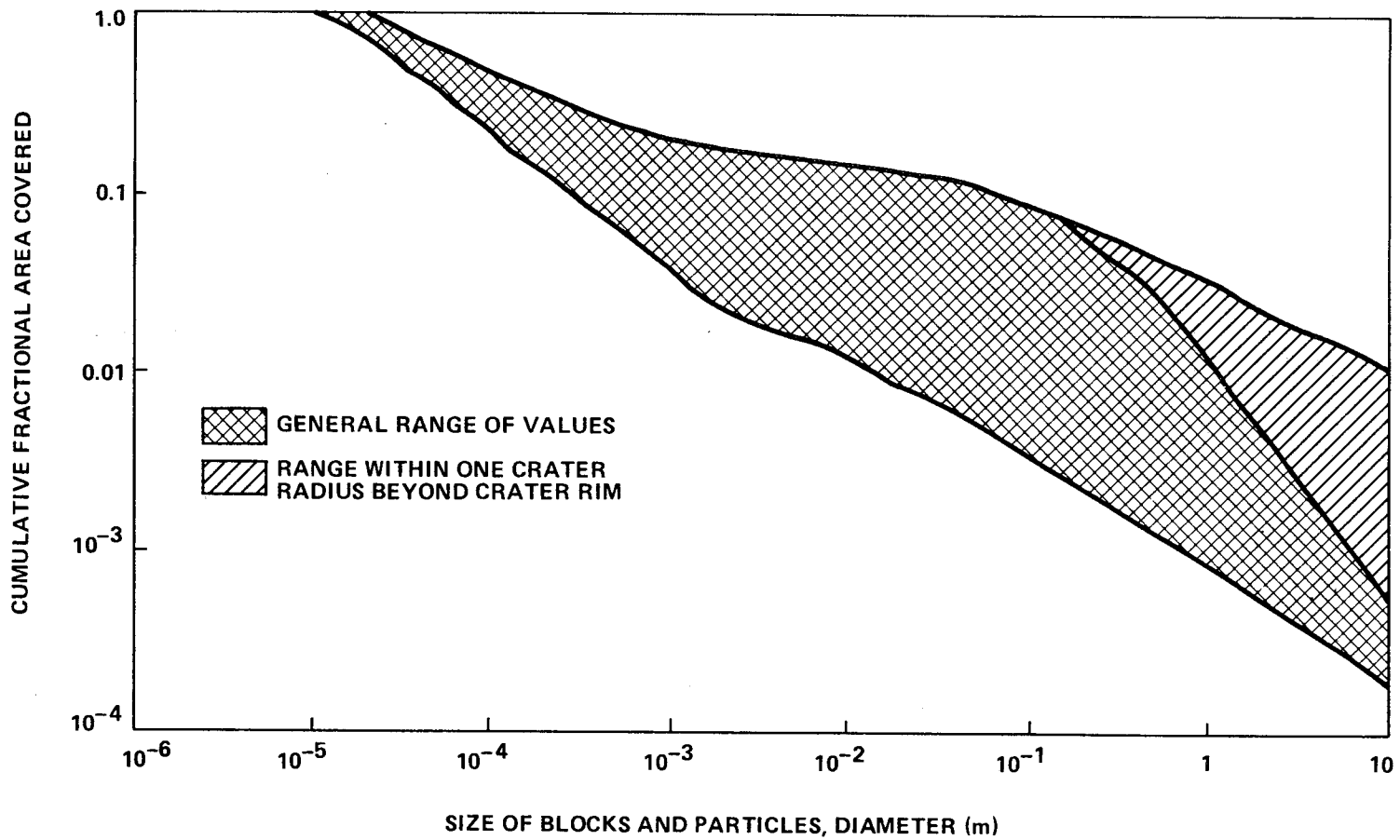

Figure V-9. Fraction of surface area covered by blocks and particles larger than specified characteristic size for the surface of Mercury [V-10].

TABLE V-9. ELECTROMAGNETIC PROPERTIES OF MERCURY'S SURFACE LAYERS

Property	Range of Values
Radar reflectivity	0.06 ± 0.03
Microwave emissivity	0.94 ± 0.03
Dielectric constant ϵ	$1.6 < \epsilon < 4$
Dielectric loss tangent	$0.0002 < (\tan \phi) < 0.013$
Ratios $\frac{\text{(electrical skin depth)}}{\text{(thermal skin depth) (wavelength)}}$	$0.5 < \frac{\delta}{\lambda} < 2.0\ \text{cm}^{-1}$

temperature is measured. To a much smaller degree it will depend upon how long the sunlight has been striking that area as the surface would take some time to heat, and how long the heat is held by the surface after the sunlight is gone.

Temperature measurements of Mercury have been made by recording the thermal emission of the planet in the infrared and microwave regions of the spectrum.

Measurements of Mercury's emission in the infrared, particularly in the 8 to 14 μm region, have been interpreted in terms of the planet's surface temperature. Table V-4 lists the temperature values so derived. All listed values are based on original observations except Soter's which is derived from Pettit and Nicholson's data. Night temperature values are difficult to obtain from the observations because the infrared energy received is susceptible to contamination by sunlight reflected from Mercury's illuminated crescent, the earth's atmosphere, and the observing telescope. Nevertheless, the observations clearly indicate night surfaces are warmer than a permanently dark surface.

The microwave measurements of Mercury discussed in subsection 5.1.7.4 (Table V-6) are also used to derive temperatures. The cited values depend on wavelength and are averages of physical temperatures at and below the surface and over the planet's disk. Thus, the microwave results have a smaller range of temperatures than the infrared ones.

The infrared and microwave temperature measurements have been supplemented by detailed theoretical analyses of the thermal and radio behavior of Mercury's surface layers of which only some highlights follow. Pettit and Nicholson [V-12] showed in calculations using the solar constant and Mercury's albedo that if the temperatures of sunlit surfaces are in equilibrium with the absorbed solar energy, they match the measured temperatures rather well. A detailed calculation is given by Soter and Ulrichs, 1967. They conclude that in thermal equilibrium, the daytime temperature T of the sunlit surface is given by

$$T = T_p \left(\frac{r_p}{r}\right)^{\frac{1}{2}} (\cos Z)^{\frac{1}{4}} \quad ,$$

Here, T_p equals 700 ± 25 K, r_p equals (Mercury's perihelion distance) 0.3075 AU, r is its actual distance from the sun, and Z (the zenith angle of the sun) is less than 90 deg. Both the infrared and microwave data are consistent with temperatures calculated from the above equation. The uncertainty in T_p is that given by Morrison [V-11].

Surface twilight and night temperatures may be calculated from the theory of heat conduction if appropriate boundary conditions and thermal parameter values are assumed. For materials as dry and porous as Mercury's soil, conduction may occur simultaneously by contact (phonon transport) and radiation (photon transport). Analyses of these phenomena have been applied to Mercury by Soter and Ulrichs, 1967, Morrison [V-11], Winter and Saari, 1969, and Ulrichs and Campbell, 1969. When the geometrical circumstances of the solar radiation are considered and lunar values for the thermal and electrical properties of the surface are employed, the variations of temperature theoretically predicted are consistent with the results of both the infrared and microwave observations which include part of Mercury's night hemisphere (Tables V-4 and V-6 and the references cited therein). Although some details of the variation of temperature with planetary latitude and longitude, depth below the surface, and time have been published [V-11], they are too complex to be practical for design criteria. Furthermore, although the foregoing results are reasonable for the planet as a whole, they may be unrealistic for particular locations because of surface inhomogenieties. The range from 90 to 200 K brackets the observed values and those derived from the theory and is adopted here for the temperature of all surface points for which the sun is invisible (night side or Z > 90 K)

or for which the predicted temperature T is less than 200 K (near the terminator). Within this range, the higher temperatures are appropriate just after sunset and the lower ones from Mercury's midnight to dawn.

Table V-10 lists ranges of thermal property values which include those ascribed to Mercury by the foregoing authors, and to the moon by References V-10, V-47, and V-48. Reference V-48 includes results for lunar samples returned by Apollo 11. The ranges cited include both uncertainty and variations of characteristics with temperature and materials; they are deliberately large as contrasted with the range of effective values for the whole disc derived by Klein [V-3] and Morrison [V-11].

TABLE V-10. THERMAL PARAMETER RANGES FOR MERCURY CITED IN LITERATURE[a]

Parameter	Range	Units
Specific Heat	$0.07 < C < 0.24$	cal/g K
Thermal Conductivity	$2.5 \times 10^{-6} < K < 4 \times 10^{-3}$	cal/cm sec K
Inverse Thermal Inertia	$20 < (K\rho c)^{-1/2} < 200$	$cm^2\ sec^{1/2}$ K/cal

a. NASA SP 8085, "The Planet Mercury [1971].", March 1972 [V-1].

5.3 Satellites

None.

REFERENCES

V-1. Anon: The Planet Mercury (1971). NASA SP-8085, March 1972.

V-2. Nourse, A. E.: Nine Planets. New York, Harper& Row, 1970.

V-3. Klein, M. J.: Mercury: Recent Observations at 3.75-cm Wavelength — Summary. Radio Science, vol. 5, no. 2, 1970, pp. 397-400.

V-4. Dollfus, A.: Résultats Récents sur les Planètes Mercure, Vénus et Mars, Obtenus par les Observations Astronomiques au Sol. La Recherche Spatiale, vol. 7, no. 1, 1968, pp. 1-12.

V-5. Ness, N. F., Behannon, K. W., Lepping, R. P., and Whang, Y. C.: Observations of Mercury's Magnetic Field. Icarus, vol. 28, no. 4, August 1976, pp. 479-488.

V-6. Ness, N. F., Behannon, K. W., Lepping, R. P., and Whang, Y. C.: Interaction of Solar Wind with Mercury and its Magnetic Field. NASA SP-397, November 1975.

V-7. Anon: Solar Electromagnetic Radiation. NASA SP-8005, Revised, May 1971.

V-8. Thekaekara, M. P.: Proposed Standard Values of the Solar Constant and the Solar Spectrum. J. Environmental Science, vol. 13, no. 4, 1970, pp. 6-9.

V-9. de Vaucouleurs, G.: Photomètrie des Surfaces Planétaires. Surfaces and Interiors of Planets and Satellites. A. Dollfus (editor), Academic Press, New York, Chap. 5, 1970, p. 226.

V-10. Anon: Lunar Surface Models. NASA SP-8023, May 1969.

V-11. Morrison, D.: Thermophysics of the Planet Mercury. Space Science Reviews, vol. 11, no. 2/3, 1970, pp. 271-307.

V-12. Pettit, E., and Nicholson, S. B.: Radiation from the Planet Mercury. Astrophys. J., vol. 83, 1936, p. 84-102.

V-13. Pettit, E.: Planetary Temperature Measurements, Planets and Satellites. Solar System, vol. 3, Univ. of Chicago Press, Chap. 10, 1961, pp. 400-428

REFERENCES (Continued)

V-14. Soter, S. L.: Mercury — Infrared Evidence for Nonsynchronous Rotation. Science, vol. 153, 1966, pp. 1112-1113.

V-15. Murray, B. C.: Infrared Radiation from the Daytime and Nighttime Surfaces of Mercury. American Geophysical Union Transactions, vol. 48, no. 1, 1967, pp. 148-149.

V-16. Murdock, T. L., and Ney, E. P.: Mercury: The Dark-Side Temperature. Science, vol. 170, no. 3957, 1970, pp. 535-537.

V-17. Morrison, D., and Klein, M. J.: The Microwave Spectrum of Mercury. Astrophys. J., vol. 160, no. 1, 1970, pp. 325-332.

V-18. Epstein, E. E., Dworetsky, M. M., Fogarty, W. G., Montgomery, J. W., and Cooley, R. C.: Mercury: Epileth Physical Parameters and a Hermocentric Longitude Dependence of its 3.3-mm Radiation. Radio Science., vol. 5, no. 2, 1970, pp. 401-409.

V-19. Epstein, E. E., Oliver, J. P, Schorn, R. A., Soter, S. L., and Wilson, W. J.: Mercury: Observations of the 3.4-Millimeter Radio Emission. Science, vol. 157, no. 3796, 1967, pp. 1550-1552.

V-20. Golovkov, V. K., and Losovskii, B. Ya.: Measurements of the Phase Dependence of the 0.8-cm Radio Emission of Mercury, and Some Properties of its Surface Layer. Soviet Astronomy-AJ, vol. 12, no. 2, 1968, pp. 229-302.

V-21. Welch, W. J., Thornton, D. D., and Lohman, R.: Observations of Jupiter, Saturn, and Mercury at 1.53 cm. Astrophys. J., vol. 146, no. 3, 1966, pp. 799-809.

V-22. Kaftan-Kassim, M. A., and Kellermann, K. I.: Measurements of the 1.9 cm Thermal Radio Emission from Mercury. Nature, vol. 213, no. 5073, 1967, pp. 272-273.

V-23. Howard, W. E., Barrett, A. H., and Haddock, F. T.: Measurements of Microwave Radiation from the Planet Mercury. Astrophys. J., vol. 136, 1962, pp. 995-1004.

REFERENCES (Continued)

V-24. Kellermann, K. I.: 11-cm Observations of the Temperature of Mercury. Nature, vol. 205, no. 4976, 1965, pp. 1091-1092.

V-25. American Ephemeris and Nautical Almanac. U.S. Government Printing Office.

V-26. Woolley, R. v. d. R.: Planetary Co-ordinates for the years 1960-1980. Her Majesty's Stationery Office, London, 1958.

V-27. Anon., Magnetic Fields — Earth and Extraterrestrial. NASA SP-8017, March 1969.

V-28. Melbourne, W. G., Mulholland, J. D., Sjogren, W. L, and Sturms, F. M.: Constants and Related Information for Astrodynamic Calculations, 1968. Technical Report 32-1306, Jet Propulsion Laboratory, Pasadena, 1968.

V-29. Sagan, C., and Morrison, D.: The Planet Mercury. Science J., vol. 4, no. 12, 1968, pp. 72-77.

V-30. Murray, B. C.: Television Observations of Mercury by Mariner 10. NASA, Ames Research Center, California, NTIS.

V-31. Goldstein, R. M.: Mercury: Surface Features Observed During Radar Studies. Science, vol. 168, no. 3930, 1970, pp. 467-469.

V-32. Smith, W. B., Ingalls, R. P., Shapiro, I. I., and Ash, M. E.: Surface-Height Variations on Venus and Mercury. Radio Science, vol. 5, no. 2, 1970, pp. 411-423.

V-33. Carpenter, R. L., and Goldstein, R. M.: Radar Observations of Mercury. Science, vol. 142, 1963, p. 381.

V-34. Evans, J. V., Brockelman, R. A., Henry, J. C., Hyde, G. M., Kraft, L. G., Reid, W. A, and Smith, W. W.: Radio Echo Observations of Venus and Mercury at 23 cm Wavelength, 1965. Astronom. J., vol. 70, no. 7, 1965, pp. 486-501.

V-35. Ash, M. E., Shapiro, I. I., and Smith, W. B.: Astronomical Constants and Planetary Ephemerides Deduced from Radar and Optical Observations. Astronom. J., vol. 72, no. 3, 1967, pp. 338-350.

REFERENCES (Continued)

V-36. Kotel'nikov, V. A.: Radar Probes of the Planet Mercury. Doklady Akad. Nauk SSSR, vol. 147, no. 6, 1962, pp. 1320-1323.

V-37. Pettengill, G. H., Dyce, R. B.: A Radar Determination of the Rotation of the Planet Mercury. Nature, vol. 206, no. 4990, 1965, p. 1240.

V-38. Pettengill, G. H., Dyce, R. B., and Campbell, D. B.: Radar Measurements at 70 cm of Venus and Mercury. Astron. J., vol. 72, no. 3, 1967, pp. 330-337.

V-39. Field, G. B.: The Atmosphere of Mercury. The Origin and Evolution of Atmospheres and Oceans. John Wiley & Sons, New York, 1964, pp. 269-278.

V-40. Anon.: Apollo 11 Preliminary Science Report. NASA SP-214, 1969.

V-41. Anon.: Apollo 12 Preliminary Science Report. NASA SP-235, 1970.

V-42. Wood, J. A.: The Lunar Soil. Scientific American, vol. 223, no. 2, 1970, pp. 14-23.

V-43. Reynolds, R. T., and Summers, A. L.: Calculations on the Composition of the Terrestrial Planets. J. Geophysical Research, vol. 74, no. 10, 1969, p. 2494.

V-44. Khodak, Yu. A.: Hermesology—Geology of Mercury. Izvestiya Akad. Nauk CCCP, Seriya Geologiya, no. 10, 1969, pp. 136-142 (U. S. Dept. of Commerce, Joint Publications Research Service 48346, No. 217, Nov. 28, 1969).

V-45. Costes, N. C., Carrier, W. D., Mitchell, J. K., and Scott, R. F.: Apollo 11 Soil Mechanics Investigation. NASA SP-214, 1969, pp. 85-122.

V-46. Scott, R. F., Carrier, W. D., Costes, N. C., and Mitchell, J. K.: Mechanical Properties of the Lunar Regolith. NASA SP-235, 1970, pp. 161-182.

REFERENCES (Concluded)

V-47. Horai, K., Simmons, G., Kanamori, H., and Wones, D.: Thermal Diffusivity and Conductivity of Lunar Material. Science, vol. 167, no. 3918, 1970, pp. 730-731.

V-48. Bastin, J. A., Clegg, P. E., and Fielder, G.: Infrared and Thermal Properties of Lunar Rock. Science, vol. 167, no. 3918, 1970, pp. 728-730.

SECTION VI. VENUS

6.1 Atmospheric Environment (Based on VI-1)

Quantitative data for the Venus atmosphere have been obtained from earth-based observations and from spacecraft which have entered the Venus atmosphere or passed within several planetary radii of the planet. These data have been used in conjunction with existing theories of planetary atmospheres to predict other characteristics of the Venus atmosphere [VI-2]. Because of limited observational data, extrapolation within the limits of applicable theory was necessary to establish reasonably complete model atmospheres for this report. Earth-based observations have generally provided information on the composition, temperature, and optical properties of Venus, whereas spacecraft measurements have yielded data on composition, temperature, pressure, density, and atmospheric structure.

The models herein provide the temperature, pressure, and density profiles required to perform basic aerodynamic analyses. The six model atmospheres developed herein include a nominal model and five other models that encompass reasonable extremes for molecular mass, solar activity, and exospheric temperature. The profiles are supplemented by computed values of viscosity, specific heat, and speed of sound. These ambient values and the calculated aerodynamic forces influence flight dynamics and space vehicle design, i.e., configuration, size, strength, and materials. Other characteristics are inferred from the measured data that influence the design of the space vehicle and its subsystems [VI-2]. For example, electron densities of the ionosphere and the plasma characteristics in the region of the solar wind may dictate requirements for electromagnetic shielding. Also, opacity of the atmosphere can constrain the design of landed solar power systems and influence the performance of communications equipment, and clouds may adversely affect performance of experiments. Section VI provides a set of engineering models [VI-1] for the Venus atmosphere on the basis of theory and measured data.

Knowledge of Venus has grown rapidly in recent years. The advance has proceeded on a variety of fronts. Radio and radar astronomy played a major role and provided the first indications that the surface temperature was

exceedingly large. The evidence, however, was not generally accepted prior to 1967 and the successful flights of Mariner 5 and Venera 4. It was difficult to account physically for the observed radio brightness and a variety of more or less esoteric models were devised to account for the radio data using non-thermal emission mechanisms. A variety of interpretations of the data led to widely differing atmospheric models [VI-1]. Even earlier models, which included data from Mariner 5 and Venera 4, reflected considerable uncertainty in values of the planetary radius, surface pressure, and surface temperatures. The uncertainties have been reduced significantly since 1967. Before presenting the models, the sources of data are reviewed for the various parameters which characterize the atmosphere of Venus. (Results of the Mariner 10 flyby of Venus are found in References VI-4 and VI-5.)

6.1.1 Earth-Based Measurements

6.1.1.1 Optical

Optical observations of Venus by ground-based telescopes established the existence of a dense atmosphere, identified its major constituents, established the existence of extensive cloud cover, and determined the optical size of the planet.

Photographs taken in ultraviolet light reveal variable patterns that are interpreted as high altitude clouds. In yellow or red light, markings are not discernible except on rare occasions. The cloud pattern appears to move across the planetary disc in retrograde motion, corresponding to a rotation period of 4 to 5 days (paragraph 6.1.3.5). The photographic evidence is interpreted as showing multiple cloud layers, that is, an upper cloud layer opaque to ultraviolet light and transparent to visible and near-infrared solar radiation which is reflected from a featureless lower cloud layer [VI-4].

Venus, viewed under visible or near-infrared light, presents a disc which is optically larger than the actual solid planet because of the opaque layer of clouds. Measurements taken during occultation of the star Regulus by Venus in 1959 [VI-14] resulted in a value of 6169 ± 2 km for the occultation height (about 40 km above the visible cloud layer). A mean value for the optical radius of 6120 ± 8 km was determined from the occultation result and the

results of numerous other studies [VI-1]. More recent measurements yielded 6100 km in red and near-infrared light and 6145 km in ultraviolet [VI-6] that indicated the existence of two distinct layers.

Spectroscopic measurements in the near-infrared hands have been used to determine the basic constituents of the Venus atmosphere [VI-1]. These measurements have affirmed that carbon dioxide (CO_2) is the dominant atmospheric constituent. Other gases identified include hydrogen chloride (HCl), hydrogen fluoride (HF), carbon monoxide (CO), and oxygen (O_2). Water vapor was tentatively identified by spectral observations but there is lack of agreement as to the amount [VI-7]. However, it is acknowledged that water is a minor constituent. Its abundance may be variable on the basis of earth-based spectroscopy.

High-altitude aircraft and balloons have been used to carry spectroscopic instrumentation above the bulk of the earth's atmosphere with resultant reduction in the errors and attenuation caused by the atmospheric constituents, particularly water vapor. Interferometer observations made from a Convair 990 jet aircraft at altitudes of 12 to 13 km revealed a very low but finite mixing ratio of H_2O/CO_2 [VI-6]. These data were confirmed by similar measurements obtained from balloon flights.

Results of interferometer spectrometer measurements of the reflection spectra of Venus are shown in Figure VI-1. Reflection spectra have been used to investigate the constituents of the Venus cloud layers. The variations in albedo, i.e., the measure of the radiation reflected by a given surface, at the various wavelengths were associated with known spectra of chemical elements, compounds, and gaseous mixtures. For example, comparison of spectra obtained for the Venus upper cloud layer and those obtained from laboratory experiments led to an identification of partially-hydrated ferrous chloride as a possible constituent of the Venus clouds [VI-6]. The identification is not generally accepted by planetary scientists, however.

Studies of the polarization of light reflected by Venus provide a valuable source of information on the properties of the cloud particles. Polarization measurements reported in Reference VI-1 were compared to theoretical

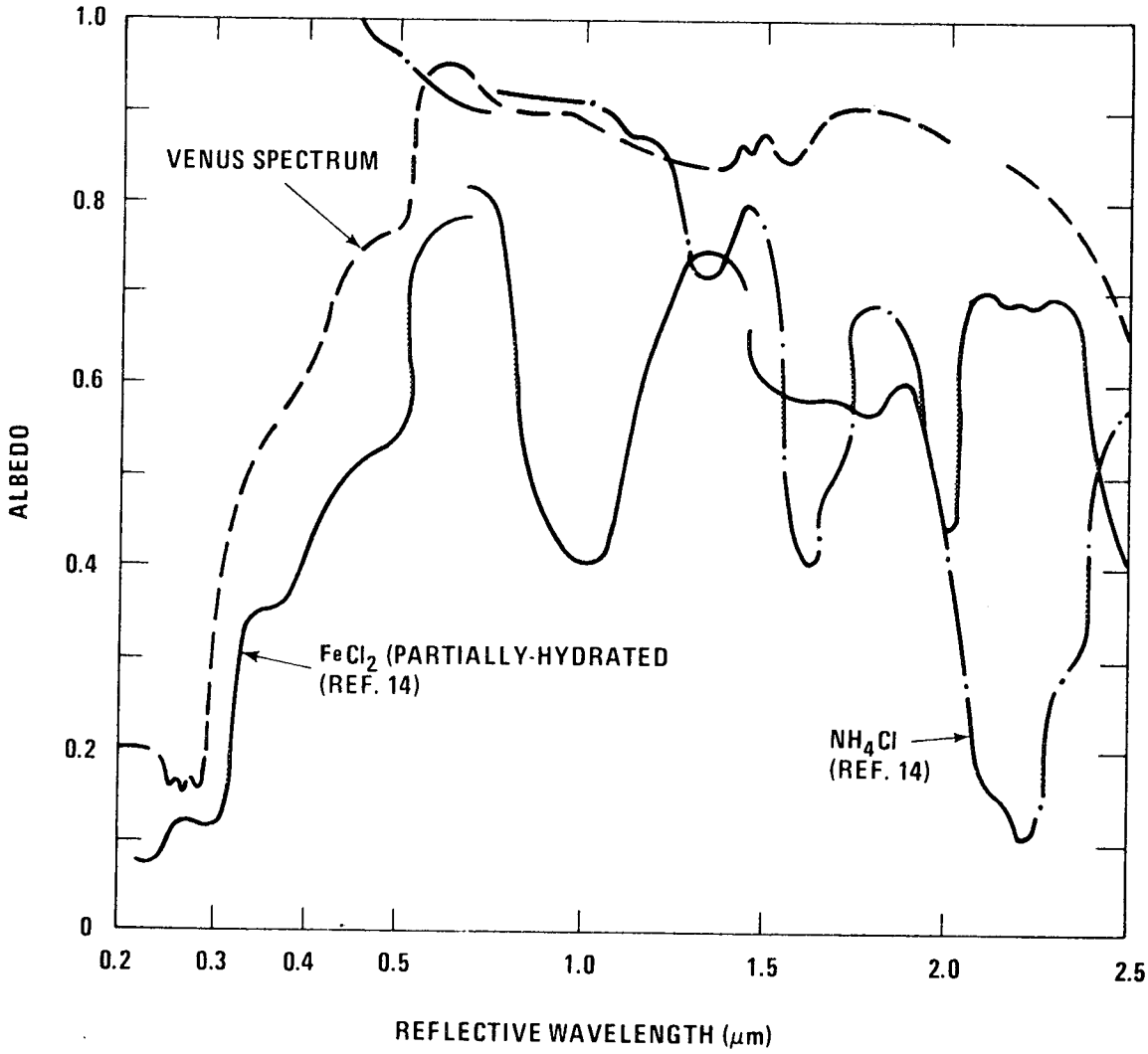

Figure VI-1. Reflective spectrum of Venus.

calculations in Reference VI-8. Particle shape and dispersion in the clouds were determined, and it was concluded that the cloud particles are most likely liquid. The refractive index of the cloud layer was found to be 1.46 ± 0.02 in ultraviolet light with a decrease to 1.43 ± 0.02 in the near-infrared region. The upper limit of the refractive index recently has been revised to 1.44 ± 0.02 in a wavelength of $0.55\,\mu m$. These results helped to eliminate a number of potential cloud constituents. In particular, pure water or ice, a mixture of dust and water, or a mixture of mercury compounds failed to satisfy constraints imposed by the polarization data.

Polarization measurements were also used to estimate the atmospheric pressure near the top of the reflecting cloud layer [VI-8, VI-9]. Computations for polarized light at ultraviolet wavelengths indicated pressures near the cloud top of about 0.05 cm [VI-7]. The analysis implied that either the reflecting cloud was located high in the stratosphere or that a second cloud layer was located in this region and the pressures derived from the ultraviolet studies referred to a region somewhere between the high-altitude cloud layer and the principal cloud layer.

6.1.1.2 Radio Astronomy

Measurements on the time delay of radar echoes from Venus can be analyzed in conjunction with astronomical and orbital data for Venus to obtain values for the mean equatorial radius [VI-1]. From the encounter of the Mariner 5 spacecraft with Venus it was possible to determine very accurately the position and velocity of the center of mass of Venus as well as its mass. The improved data were employed to compute a mean value for the planetary radius of 6053.7 ± 2.2 km [VI-1]. Most recent data indicate a mean equatorial radius of 6050 ± 0.5 with some evidence of topographic relief [VI-10]. Numerous values of radius are summarized in Table VI-1.

Radar measurements are used to define the shape of the planet and to investigate the topography. Results indicate that the equatorial cross section of the planet is an ellipse with the difference in semi-axes equal to 1.1 ± 0.35 km [VI-1]. Surface height variations, detected by radar measurements, did not exceed 3 to 4 km [VI-10].

TABLE VI-1. RADIUS OF VENUS

Radius (km)	Year of Publication	Reference
6057 ± 55	1965	VI-1
6056 ± 1.2	1967	VI-1
6048 ± 1	1968	VI-1
6052 ± 2.0	1968	VI-1
6053.7 ± 2.2	1968	VI-1
6050 ± 5	1968	VI-1
6050 ± 0.5	1972	VI-10

Radio telescopes have been used to study the microwave emission spectrum of Venus and the data have been analyzed to determine the brightness temperature as a function of wavelength. Data reported in Reference VI-1 indicate that Venus has a surface temperature of about 700 K. Measurements at short radio wavelengths indicate a cool atmosphere with high opacity. The most accurate data are in the wavelength range of 2 mm to 21 cm. Microwave emission results are shown in Figure VI-2. The opacity of the atmosphere is clearly indicated by the low brightness temperatures measured below 3 cm. Comparison of the observed spectra with analytic models shows that the opacity can be attributed to a high percentage of CO_2 in the atmosphere and 0.65 ± 0.35 percent water vapor. Other results of this model indicate that any possible isothermal layer near the surface cannot be thicker than 4 km, that the radius is 6049.5 ± 3 km, the surface temperature is 770 ± 25 K, and the surface pressure is 95 ± 20 atm [VI-1].

Radio interferometer measurements have been made to determine the temperature distribution of Venus [VI-11, VI-12]. Results indicate that no large-scale differences in the surface temperature greater than 25 K exist; in particular, the mean equatorial temperature is the same as that at the poles within 25 K.

6.1.2 Spacecraft

6.1.2.1 Mariner 2

Mariner 2 passed within 34 751 km of the center of Venus in December 1962. The spacecraft was equipped with a microwave radiometer and an infrared radiometer. The microwave radiometer used two channels, one to detect emissions at 1.35 cm which was sensitive to water vapor and the other at 1.9 cm which was relatively unaffected by water vapor so its detected emissions were expected to originate deeper in the atmosphere. Scans of the day and night sides and the terminator region showed no significant differences between the day and night sides of Venus. Highest temperatures were found along the terminator. Maximum brightness temperatures recorded along the terminator was 590 K ± 5 percent. The edges were observed to be cooler than the center of the planet; this was construed as a limb-darkening effect. Differences in the 1.35 and 1.9 cm data indicated the possibility of very low amounts of water vapor in the Venus atmosphere [VI-1].

The infrared radiometer was sensitive to wavelengths of 8.4 and 10.4 μm which penetrate water vapor but not clouds. A temperature gradient detected across the planet was interpreted as a limb-darkening effect. The

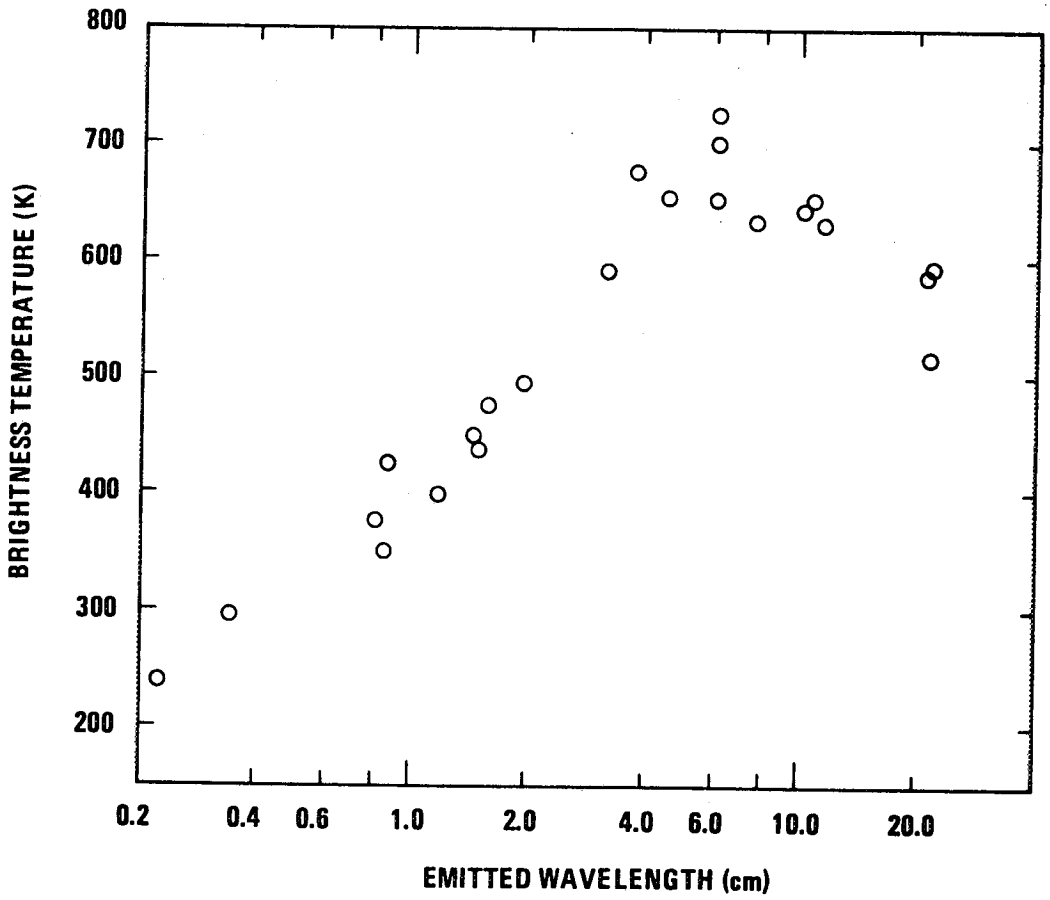

Figure VI-2. Microwave spectrum of Venus (radio brightness) [VI-1].

temperature was observed to decrease by approximately 20 K between the central region (estimated at 240 K) and the limbs [VI-12]. The similarity of the results at both wavelengths indicated that cloud temperatures had been measured and that the clouds were optically thick at both wavelengths.

6.1.2.2 Venera 4

The U.S.S.R. spacecraft Venera 4 entered the atmosphere on the night side of Venus on October 18, 1967, and performed measurements to determine composition, temperature, pressure, and density. Initial reports claimed that the spacecraft had landed on the surface of Venus because calculations of the descent distance based on the measured parameters was in agreement with a value of 28 km obtained from a radio altimeter at the time of parachute deployment. Thus, the final measured value of temperature was considered to be the surface value in subsequent investigations [VI-1 and VI-13]. However, comparison with Mariner 5 data revealed a serious discrepancy. It was shown that

transmission from Venera 4 ended when the spacecraft was still approximately 20 km above the mean planetary surface indicated by earth-based radar. Either the radar data were in error, or Venus had local elevations of 20 km, or Venera 4 did not in fact reach the planetary surface [VI-3, VI-14 — VI-15]. Subsequently, it was reported [VI-16, VI-17] that routine periodic modulation of the radio altimeter led to a faulty reading. An actual altitude reading in the 50 to 60 km range above the mean surface level was misconstrued as 28 km. Data transmission actually had been interrupted at about 26 km above the surface. The calculated rate of descent varied from 10 to 11 m/s after parachute deployment to 2.5 to 3 m/s at the interruption of data transmission.

Venera 4 was equipped with eleven gas analyzers to determine the composition of the Venus atmosphere. The analyzers were designed to detect CO_2, inert gases, O_2, and H_2O [VI-18, VI-19]. Measurements were taken immediately after parachute deployment at a pressure of 0.7 atm and again when the pressure had increased to 2 atm. The data revealed that the major constituent is CO_2, accounting for 90 ± 10 percent of the atmosphere and probably exceeding 90 percent. Other results reported included:

O_2	> 0.4 percent but < 1.6 percent (probably ~ 1 percent)
N_2 and other inert gases	< 7 percent (probably < 2.5 percent)
H_2O	from 1 to 8 mg/liter

Atmospheric temperature, pressure, and density were measured with a resistance thermometer, an aneroid manometer, and a gas densitometer, respectively. Temperature was measured throughout the flight until termination at an altitude of 26 km and ranged from 304 to 544 K [VI-1, VI-20, VI-21]. Pressure was measured until it went off scale at 35 km [VI-4, VI-13, VI-22]. Its range was from 0.7 atm to 7.5 atm. Density ranged between 1.4×10^{-3} and 1.2×10^{-2} g/cm^3. The densitometer went off scale at about 30 km [VI-4, VI-13, VI-20, VI-21]. The temperature, pressure, and density profiles are shown in Figure VI-3 as a function of altitude above the mean surface. The temperature profile was determined to be basically adiabatic and the corresponding pressure profile could be determined analytically with the equations for hydrostatics and for quasi-uniform parachute descent [VI-1, VI-13, VI-22]. The density profile (Fig. VI-3) was felt to be in error between 34 and 43 km because the measured temperature and pressure data gave no indication of the nonmonotonic nature of the profile in these altitudes [VI-20, VI-21]. Possible errors in the densitometer readings are discussed in Reference VI-21. As a result, a theoretical density profile was developed on the basis of the equation

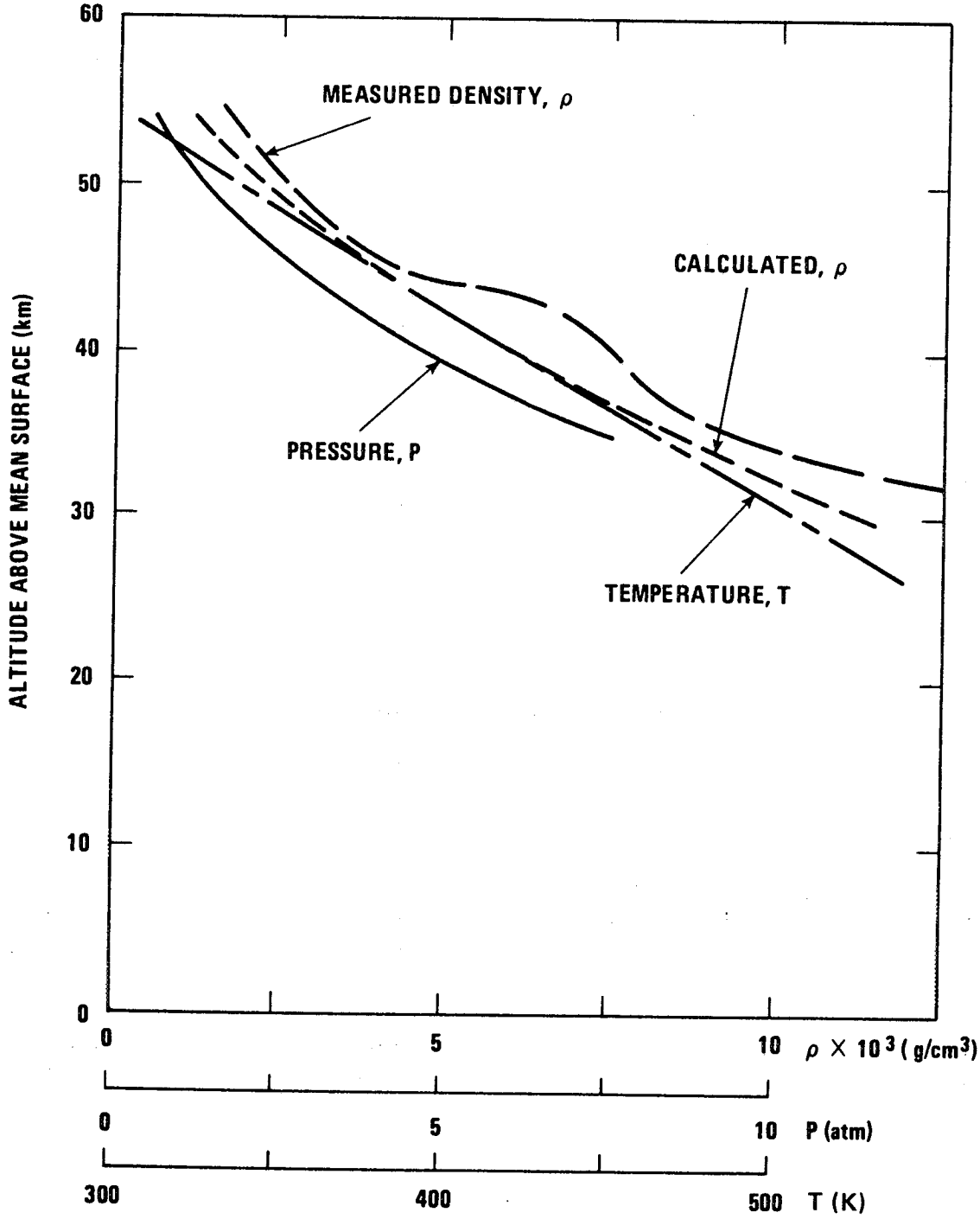

Figure VI-3. Venera 4 measured data [VI-1, VI-13, VI-22].

of state. This profile closely matched the measured profile except for the questionable region [VI-2, VI-13, VI-22]. Analyses of Venera 4 data revealed that the descent of the spacecraft was smooth and that the limiting value for convective currents in the atmosphere was 1.0 to 1.5 m/s.

Venera 4 measurements were compared to the equation of state and the variation of the partial water vapor pressure as a function of temperature. With the measured water vapor content of 0.5 percent and 1 percent as boundary values, it was determined that the lower boundary of a possible cloud layer was at an altitude of about 60 km. Also, if the clouds were formed by condensation, they consisted of ice crystals or supercooled water [VI-1, VI-13, VI-22]. The thickness of the cloud layer was calculated to be 5 to 10 km. However, the validity of both the H_2O and O_2 measurements has been challenged in the subsequent literature because the stated abundances are not consistent with values inferred from ground-based spectroscopy.

6.1.2.3 Mariner 5

On October 19, 1967, the day after the flight of Venera 4 terminated, the Mariner 5 spacecraft encountered Venus at an altitude of less than one planetary radius. The trajectory, as viewed from earth, passed almost diametrically behind the center of Venus. Two independent radio propagation experiments were conducted during the occultation of Mariner 5. One used a 2297 MHz (S-band) radio signal transmitted by the spacecraft [VI-23, VI-24]. The other employed two harmonically related frequencies, 49.8 and 423.3 MHz, which were transmitted from earth to the spacecraft [VI-24, VI-25]. The S-band experiment measured the refraction of the radio signal by the charged particles of the upper atmosphere and by the electrically-neutral gases that constitute the lower atmosphere. The refraction produced changes in the frequency phase and amplitude of the signal. In addition, the amplitude was affected by defocusing and absorption in the lower atmosphere. The dual frequency experiment provided Doppler and amplitude data of two harmonically related frequencies as the signals passed through the ionosphere and neutral atmosphere of Venus. The locations where the radio beams of the two experiments probed the atmosphere are shown in Figure VI-4. The spacecraft began occultation on the night side and emerged on the day side of the planet [VI-25].

Besides the radio experiments, an ultraviolet (UV) photometer produced Lyman-alpha measurements of the distribution of radiating hydrogen atoms in the upper atmosphere on both the day and night sides of Venus [VI-26, VI-27].

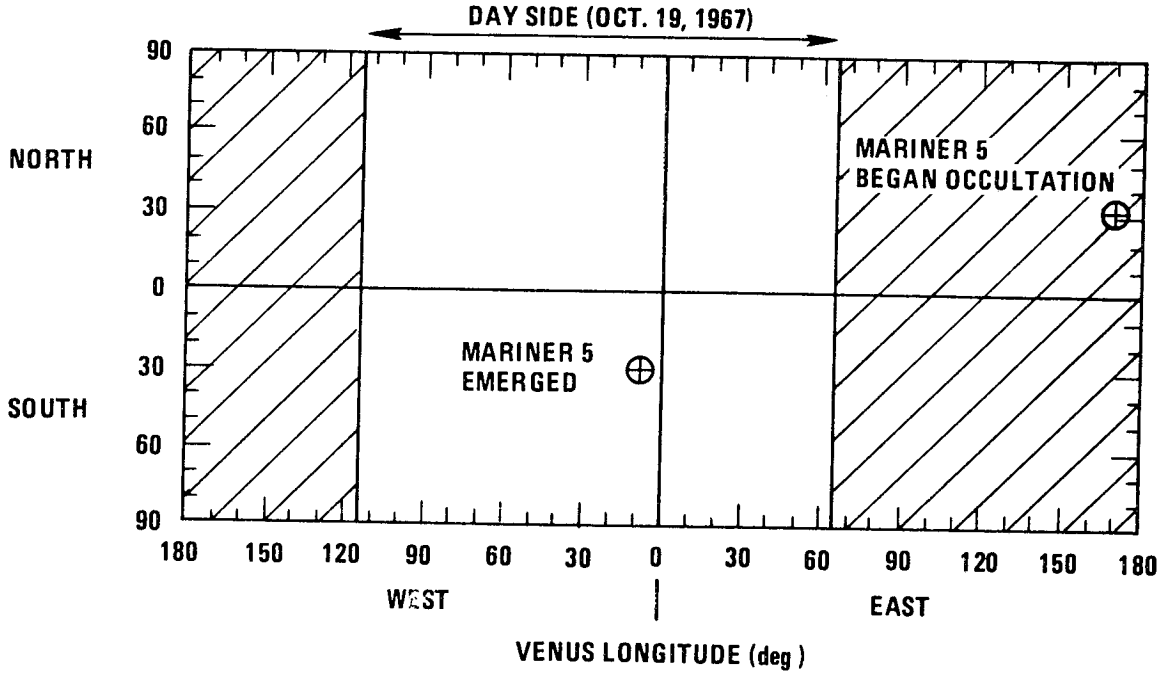

Figure VI-4. Mariner 5 occultation experiment.

High quality, two-way tracking data were used to calculate the orbital characteristics of Mariner 5. Perturbation analyses were conducted to determine the effects of Venus on the orbit so that the accuracy of the distance of the spacecraft from the center of Venus was known to high precision [VI-23]. Therefore, Mariner 5 data were determined relative to the planet center.

Data from the dual frequency experiments were converted to yield electron densities. Ionization profiles shown in Figure VI-5 extend beyond an altitude of 1000 km on the night side and terminate in a plasmapause near 500 km on the day side. Both day- and night-side profiles peaked at about 140 km with the day-side density reaching a peak value of about 5.5×10^5 electrons/cm^3. The maximum density on the night side was about 2×10^4 electrons/cm^3 [VI-25]. Differences between the day side and night side and residual electron-content data showed that the distribution of ionization was not symmetric and indicated the possible presence of a plasma tail. The average interplanetary electron number density determined during the occultation was about 5.06 electrons/cm^3. Evaluation of the Lyman-alpha measurements with theoretical models of the Venus thermosphere (< 9000 km) indicate that the temperature of the day-side thermosphere of Venus is about 650 K [VI-26].

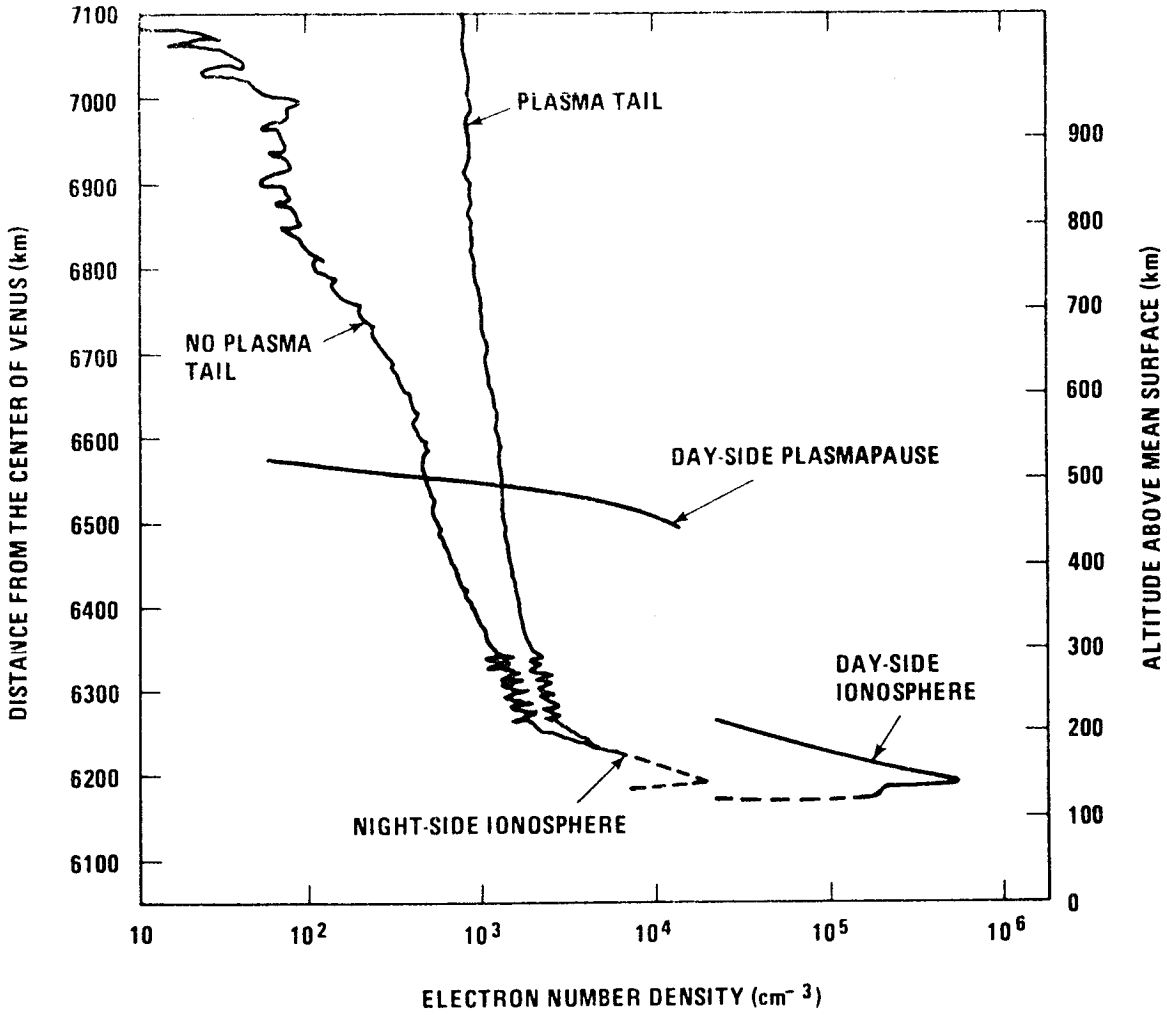

Figure VI-5. Mariner 5 ionization profiles [VI-25].

Measurements were made during the occultation from about 6140 to 6085 km from the center of Venus. At the lower altitude the radius of curvature of the radio signal path became comparable to the distance to the center of mass of Venus so the signal was extinguished by severe defocusing. Data obtained from the experiments were related to the refractivity of the atmosphere, and the refractivity profiles were used to compute pressure and temperature as a function of altitude. The temperature and pressure profiles shown in Figure VI-6 indicate little difference between the day side and the night side of Venus. [VI-24]. Boundary temperatures of 150 and 250 K for a 100 percent CO_2 atmosphere were used at an altitude of 90 km to represent extremes for computing the profiles. The fine structure in the temperature profiles between 60

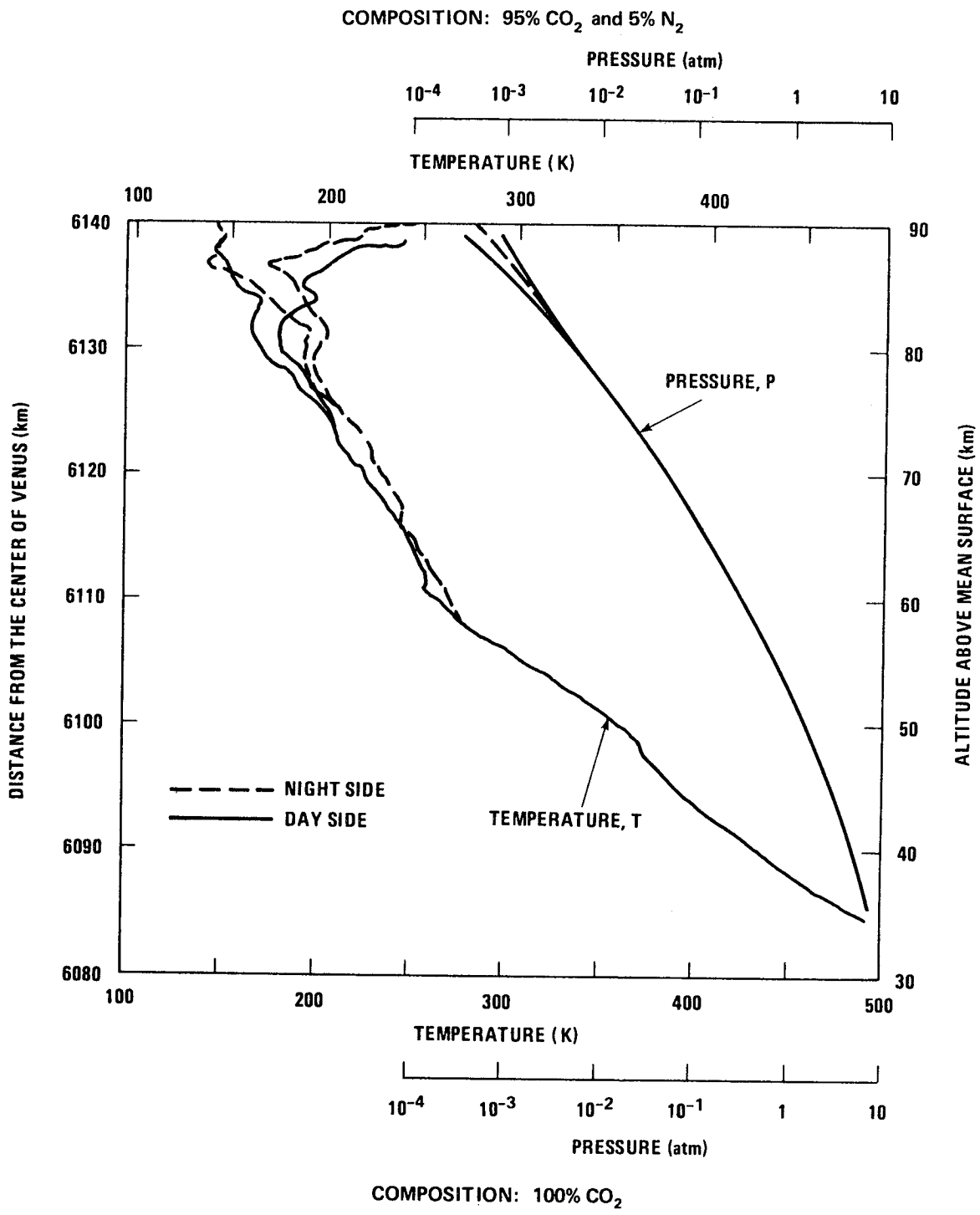

Figure VI-6. Mariner 5 temperature and pressure profiles for two compositions [VI-24].

and 90 km indicated a region with several relatively warm and cold layers. The average temperature lapse rate between 80 and 60 km was 4 K/km. The corresponding value between 60 and 50 km was 10 K/km. The change in lapse rate at about 60 km indicated the possible condensation of some vapor. Mass mixing ratios of water vapor between 10^{-3} and 10^{-2} were suggested as a possible explanation for the observed change in lapse rate.

It was determined that the S-band signal suffered a propagation loss because of absorption below 50 km. The loss profile suggested that the composition may vary with altitude [VI-24]. Accordingly, calculations were made using an atmosphere consisting of CO_2 and a microwave absorber below 50 km with the same refractivity as CO_2. The resulting profile reproduced the minimum temperature lapse rate between 50 and 45 km altitude (Fig. VI-6). This change in lapse rate and the S-band loss profile suggested the condensation of vapor, but H_2O is an unlikely candidate in view of the high temperatures at these altitudes. Therefore, the possibility was presented for two different cloud systems, one at 60 km altitude and the other at near 50 km altitude.

6.1.2.4 Venera 5 and 6

The U.S.S.R. spacecraft Venera 5 and 6 entered the atmosphere on the night side of Venus on May 16 and 17, 1969, at points separated by about 300 km. Venera 4 results had been used to improve the design of the spacecraft and the scientific equipment. Major changes in Venera 5 and 6 included a reduction of the main parachute area, an increase in the structural strength of the spacecraft, an improvement in radio altimeter operation, expansion of the range of pressure and temperature measurements, an increase in the accuracy of the gas analyzer, and installation of a different type of densitometer [VI-16].

Distance to the surface was determined by a radio altimeter which began operation after main parachute deployment and returned signals corresponding to altitude increments of 8 to 10 km. The altitude regions traversed by both spacecraft as determined by radio altimeter agreed satisfactorily with calculations made by the hydrostatic equation and the equation of state and by the equation for quasi-uniform descent of a vehicle on a parachute [VI-17]. The results of the calculations indicated that the descent velocities varied from 32 to 6 m/s. Both radio altimeters made initial readings where the pressure was about 6.6 atm. Because the difference in length of vertical travel by Venera 5 (36.7 km) and Venera 6 (34.2 km) was within the error limits of the altimeters, the readings at the 6.6 atm level were averaged to yield an altitude 36.1 km above the surface. Data transmission ended at 20 km above the mean surface.

Both Venera 5 and 6 were equipped with gas analyzers to determine the concentrations of CO_2, inert gases, O_2, and H_2O. Measurements by Venera 5 were made at pressure levels of 0.6 atm and 5 atm and by Venera 6 at 2 atm and 10 atm. Results of the gas analysis indicated the following composition [VI-19]:

CO_2	97 (+3, -4 percent)
O_2	not more than 0.1 percent
N_2 and other inert gases	not more than 2 percent
H_2O	from 6 to 11 mg/l (at 0.6 to 2 atm pressure)

Each spacecraft was equipped with six aneroid-type manometers for pressure measurement, three resistance thermometers to measure temperature, and a tuning-fork densimeter to measure density. During each descent, 70 readings of pressure and more than 50 measurements of temperature were made beginning at the 0.6 atm level at an altitude of 56 km and ending at 20 km. The temperature, pressure, and density profiles are shown in Figure VI-7 as a function of altitude above the mean surface. The data have been superposed so that the pressure of 6.6 atm is at 36.1 km, the average altitude. The temperature profile was near adiabatic [VI-16, VI-17]. The measured density values were not consistent with the measured pressure and temperature so the density profile was calculated with the equation of state on the basis of observed temperature and pressure [VI-13, VI-16].

Analysis of the measurements indicated that the descent was smooth and that vertical currents did not exceed 0.3 to 0.5 m/s [VI-17, VI-28]. An indirect estimate of horizontal wind velocity was made in Reference VI-28. Winds of 3 to 25 m/s were estimated with the lower value more probable.

The Venera 5 and 6 water vapor measurements were used to estimate the altitude of the condensation and the thickness of the resultant clouds. The lower boundary altitude was 60 km and the most probable thickness of the supercooled water vapor or ice crystal clouds was 8 to 10 km [VI-16, VI-17].

Microwave attenuation was computed for the Venus atmosphere based on Venera 5 and 6 data. Radiowave absorption was calculated taking into account the measured percentages of CO_2, H_2O, and O_2. It was concluded that wavelengths shorter than 5 cm should not be used for communication between earth and the spacecraft during its landing on the surface of Venus or for operation of radio equipment in the spacecraft landing system because of the necessity of increasing the power of the transmitters and the sensitivity of the receivers [VI-1]. A related study of radiowave attenuation showed that statistical

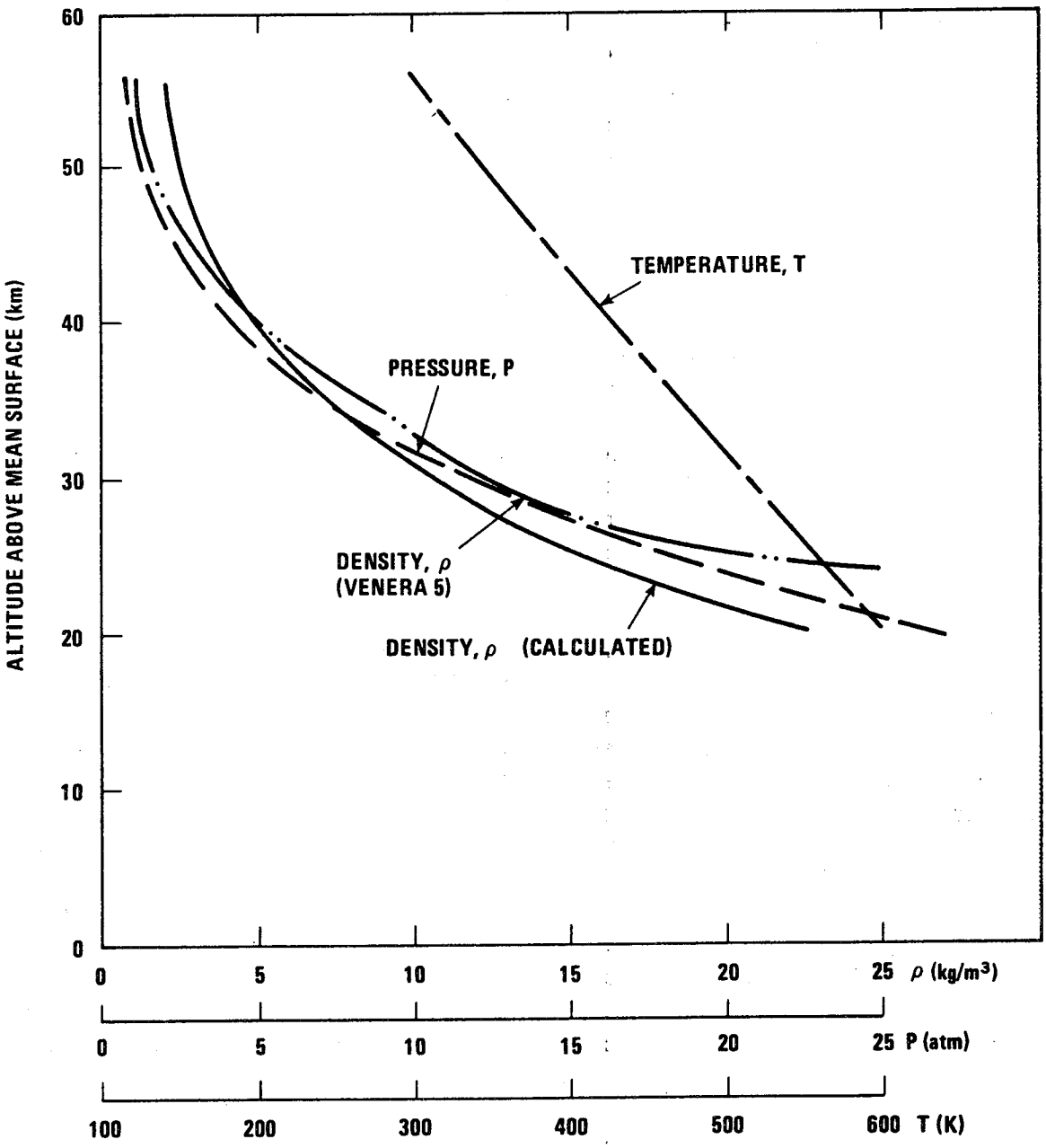

Figure VI-7. Venera 5 and 6 measured data [VI-16, VI-17].

inhomogeneities of the refractive index could be an indication of turbulence in the atmosphere. Also, a singularity at 47 km in the measured data for the refractive attenuation of radio waves can be explained by the presence of an inversion layer which increases the refractive attenuation. The inversion layer could be associated with the lower boundary of a cloud layer. The singularity is weaker on the day side of Venus where the inversion would be expected to be less stable because of higher turbulence in the atmosphere [VI-1].

6.1.2.5 Venera 7

A soft landing on the night side of Venus was made in December 1970 by the U.S.S.R. spacecraft Venera 7. Although the spacecraft had basically the same design and general structure as previous Veneras, it had been designed for a maximum of 800 K external temperature and 180 atm pressure. The descent spacecraft was protected by thermal insulation and by a heat protection system. The thermal insulation maintained a favorable heat balance inside the spacecraft during its operation in the hot atmosphere and on the surface of Venus and served as a damping device during landing. The heat protection system shielded the spacecraft from the high temperatures produced by aerodynamic drag of the atmosphere [VI-1].

Descent velocity in the Venus-earth direction was derived from Doppler shift of onboard radio frequencies. The time history of descent velocity was used to compute height increments above the surface. Velocity measurements showed that when the descent parachute opened at an altitude of about 30 km, descent velocity decreased from 27 to 19 m/s. At about 25 km the descent velocity unexpectedly increased from 15 to 26 m/s, then slowly returned to the previous levels at about 10 km. The spacecraft was descending at 16.5 m/s when it landed. Because of the recorded abrupt stop, it appeared that the surface was hard [VI-1]. Altitude was computed from the descent velocity and from the equations of an adiabatic gas on the basis of Venera 4, 5, and 6 experience. The adiabatic results indicated a descent path 2 km longer than measured by the descent velocity. The latter path deviated from the adiabatic path in the altitude region between 25 km and 5 km, which is the same region in which the descent velocity had changed abruptly.

Venera 7 was equipped with resistance thermometers and aneroid manometers to measure temperature and pressure. However, the onboard telemetry commutator remained in a fixed position and only ambient temperature information was transmitted. Measurements began at 55 km and continued to the surface where a temperature of 747 ± 20 K was measured. The

temperature profiles for the foregoing adiabatic and measured paths are shown in Figure VI-8. The adiabatic curve was computed for a surface temperature of 747 K [VI-1].

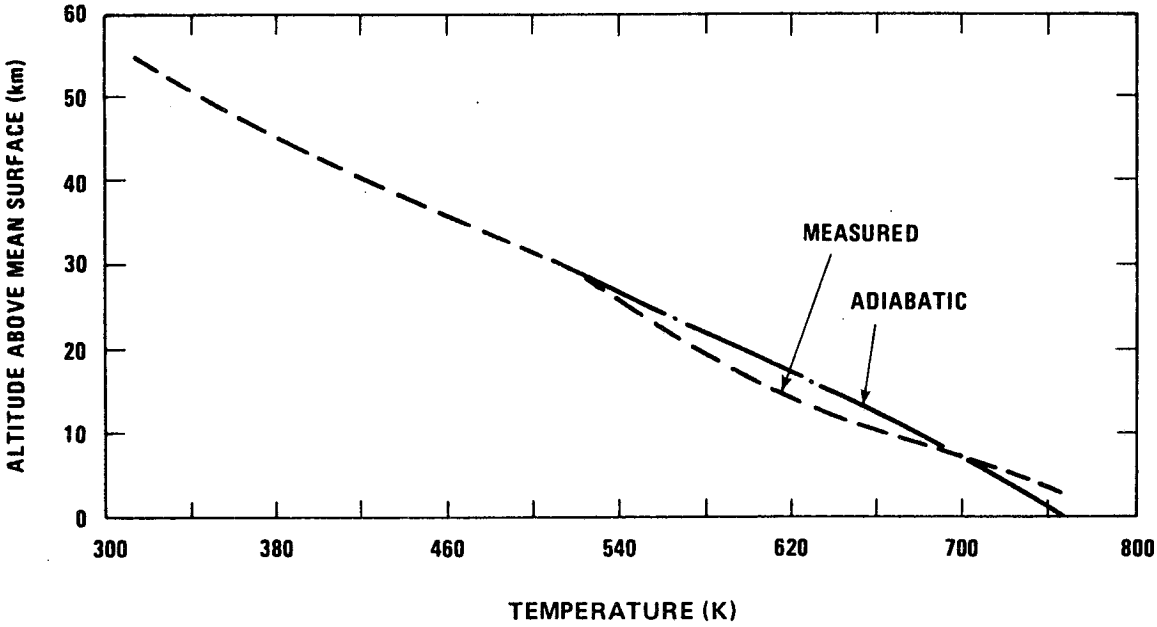

Figure VI-8. Venera 7 measured data [VI-1].

6.1.3 The Atmosphere

Discussion of the parameters applicable to the engineering models of the Venus atmosphere is divided into the lower and upper atmosphere as shown in Figure VI-9. These regions have been subdivided into regions bearing names associated with the earth atmosphere such as troposphere and exosphere. Planetary radius is discussed first because the value of the radius is critical to the determination of parameter values at the surface. Discussions are also included on atmospheric interaction with solar wind, clouds, and gravity; also see Reference VI-4 for Mariner 10 results.

Prior to the determination of the radius of Venus by radio astronomy, the only available measurements referred to the optical disc which had led to a mean value for the optical radius of 6120 ± 8 km (paragraph 6.1.1.1). Since then, however, radio astronomy techniques (Table VI-1) have provided numerous readings of the solid planetary sphere of which the value of 6050 ± 5 km is considered best.

As discussed in Paragraph 6.1.6, Venera altitude data were determined by radio altimeter readings to the planetary surface and Mariner 5 data were given as a function of Venus-centered distance, the accuracy of which depended on the Mariner 5 trajectory and the Venus orbit determinations [VI-14]. Comparison of the experimental results of Venera 5 and 6 to Mariner 5 results indicated that the mean surface level in the descent region was 6050 km [VI-16]. Mariner 5 data published in Reference VI-24 was also referenced to 6050 km in order to determine altitude. A radius of 6050 ± 5 km has been adopted for this monograph; the uncertainty is considered to be realistic.

Data published in Reference VI-10 indicated surface height variations over the entire equatorial region of Venus. The highest observed elevation was a 3 km peak with a slope of about 0.04 deg on one side and a steep slope of 0.5 deg on the other side. The general area of the elevated region extended about 500 km in latitude and 6000 km in longitude.

6.1.3.1 Composition — Lower Atmosphere

The components of the Venus lower atmosphere have been identified by gas analysis experiments onboard the Venera 4, 5, and 6 spacecraft and by spectroscopic measurements made from earth. Table VI-2 summarizes current estimates of percentages by volume of component gases in the Venus atmosphere. The major constituents are CO_2 and inert gases, principally N_2; values shown were obtained from Venera 5 and 6 measurements. The value of O_2 reflects an upper limit obtained from spectroscopic measurements. The content of oxygen as measured by Venera 5 and 6 did not exceed 0.1 percent, but the exact amount could not be determined because of limitations of the detector [VI-19].

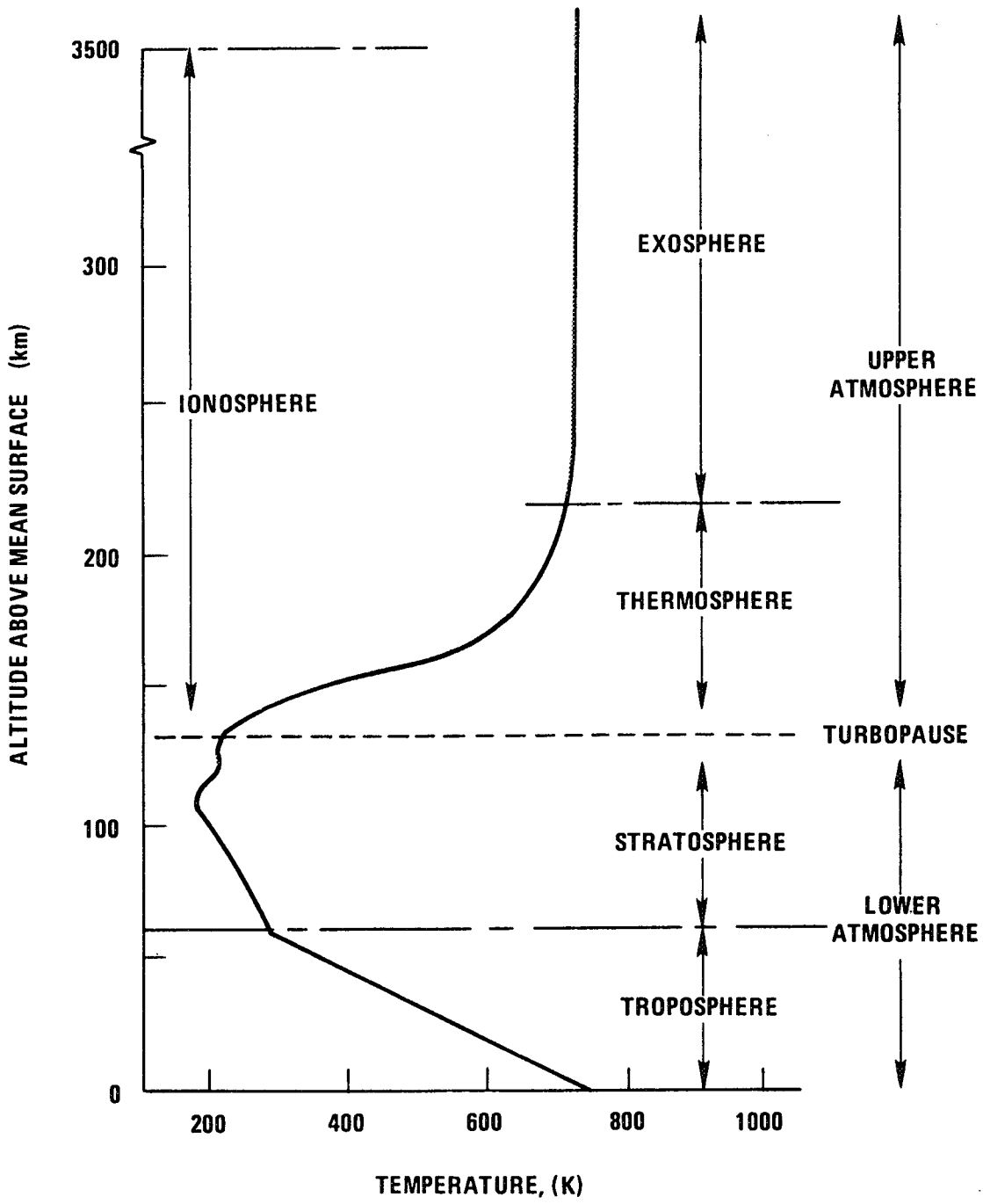

Figure VI-9. Atmospheric regions of Venus.
(See Fig. VI-16 for temperature profile.)

TABLE VI-2. COMPOSITION OF THE VENUS ATMOSPHERE

Component	Estimated Percent by Volume	Reference
CO_2	97, +3, -4	VI-19
N_2, A, Inert Gases	< 2	VI-19
O_2	$< 10^{-3}$	VI-4
H_2O	10^{-2} to 10^{-1} 10^{-4} to 10^{-2}	VI-19 VI-2
HCl	$10^{-4.2}$	VI-1
HF	$10^{-6.2}$	VI-1
CH_4	$< 10^{-4}$	VI-1
CO	$10^{-2.34}$	VI-1
COS	$< 10^{-6}$ to 10^{-4}	VI-6
NH_3	$< 10^{-5.5}$ [a]	VI-6
N_2O	$< 5 \times 10^{-5}$	VI-1
He	$\approx 10^{-2}$	VI-1
CH_3Cl	$< 10^{-4}$	VI-1
C_2H_2	$< 10^{-4}$	VI-1
HCN	$< 10^{-4}$	VI-1
O_3	$< 10^{-6}$	VI-1
C_3O_2	$< 10^{-4.3}$	VI-6
H_2S	$< 10^{-1.7}$	VI-6
SO_2	$< 10^{-5.5}$	VI-6
CH_3F	$< 10^{-4}$	VI-1

a. In contrast to the spectroscopic limit, the Venera 8 measured an NH_3 abundance between 0.01 and 0.1 percent at altitudes between 46 and 33 km.

The quantity of H_2O detected by the Venera spacecraft and spectroscopic measurements are shown in Table VI-2. The Venera values (which indicate water vapor mixing ratios of the order of 10^{-3} to 10^{-2}) are in disagreement with spectroscopic measurements which indicate water vapor mixing ratios of the order of 10^{-6} to 10^{-4} [VI-2, VI-6, VI-7]. The spectroscopic data would appear to eliminate H_2O as the major component of the observed visual cloud at 240 K. The amount of H_2O present has been widely discussed because of its importance in the theory of cloud formation, its effect on earth-based measurements such as brightness temperature, and its effect on radiowave absorption. The Venera value is supported by several arguments. It was noted in Reference VI-19 that the water vapor concentration decreased with a reduction in pressure. In References VI-1 and VI-3 it was indicated that the presence of a cloud layer, particularly ice clouds, could result in the moisture content above the clouds being significantly lower than that measured below the clouds. The Venera concentrations were used to show that clouds of either ice particles or supercooled water vapor could result at altitudes slightly higher than that at which Venera measurements were begun [VI-16, VI-22]. The Mariner 5 results reported in Reference VI-24 confirmed these conclusions. Comparison of theoretical studies and microwave spectrum measurements [VI-1] also indicated a water content of 0.65 ± 0.35 percent in agreement with the Venera values. A similar comparison in Reference VI-11 indicated a water vapor molar fraction of 0.4 ± 0.3 percent.

Radiowave absorption in the presence of water vapor content between 0.1 and 0.8 percent was studied in Reference VI-1. Other studies indicated that this amount of water might be sufficient to supply the infrared opacity needed to maintain the high surface temperatures of Venus [VI-1]. Studies based on thermochemical considerations suggest a water vapor content of 0.04 percent.

Polarization studies on the basis of refraction index, however, showed that the visual clouds could not be pure water or ice [VI-8]. In addition, numerous other cloud components such as ferrous chloride [VI-6] were dismissed on the basis of the measured refraction index as well as chemical properties [VI-8, VI-1]. Pure ice or water clouds were rejected in References VI-1 because liquid water present in the atmosphere would be in extremely concentrated aqueous HCl solution in the presence of the HCl that has been detected spectroscopically (Table VI-2). Furthermore, the HCl solution would have caused the Venera gas analysers to detect the conductivity of a strong solution of a strong electrolyte and caused an erroneous reading of water content. It was argued that the mole fraction of water vapor was overestimated and should have been on the order of 10^{-4} [VI-1, VI-2]. Thus, although H_2O has been identified as a constituent of the Venus atmosphere, the concentration is in question.

The Venera gas analyzers were designed to detect CO_2, inert gases, O_2, and H_2O. Other component gases listed in Table VI-2 are derived from spectroscopic measurements except the value for the He which is an estimated amount. Other possible components derived from chemical analysis considerations are given in Reference VI-1.

6.1.3.2 Temperature — Lower Atmosphere

Temperature profiles from about 90 km to the surface of Venus have been obtained by spacecraft (Figs. VI-3, VI-6, VI-7, and VI-8). These profiles are compared in Figure VI-10 with a mean planetary radius of 6050 km. The Venera 4, 5, and 6 data were adjusted to agree at a pressure of 6.6 atm and Venera 7 data was superposed at a temperature of 500 K because pressure data were not recorded [VI-1]. The variation in the Venera 7 data below 27 km was discussed in Paragraph 6.1.2.5.

The data agree well in the region in which they overlap and are within rms errors. Because the Mariner 5 data were calculated from refractivity profiles which used a composition of 95 percent CO_2 and 5 percent N_2, it has been suggested that these data could be adjusted to agree more closely with the Venera data by reducing the mean molecular weight. Improved correlation has been achieved by using less CO_2, e.g., 85 percent (which is in conflict with the Venera composition measurements), or relatively large percentages of light inert gases, e.g., 8 percent He. However, there is little evidence to support these values.

The lapse rate, i.e., the change in temperature with altitude, is close to adiabatic below 50 km. The curves in Figure VI-10 have been extrapolated to the surface with adiabatic gradients. The Venera curve was extrapolated by using the constant lapse rate that was determined from the final segment of the observed temperature data. This results in a surface temperature of 772 K [VI-17]. Mariner 5 data were extrapolated by using a variable lapse rate for a dry adiabatic atmosphere which included effects of compressibility [VI-1]. For the calculations, lapse rates were determined for an ideal, 95 percent CO_2 and 5 percent N_2, atmosphere. Changes in compressibility and molecular weight had little effect on the extrapolated value of surface temperature, 774 K. Extrapolation of the Venera data by the same method yielded 76 K at the surface. At 2 km above the mean surface, a temperature of 746 K was computed which corresponds to the surface value observed by Venera 7. A possible discrepancy of 2 km in measured altitude for Venera 7 is noted in Paragraph 6.1.2.5.

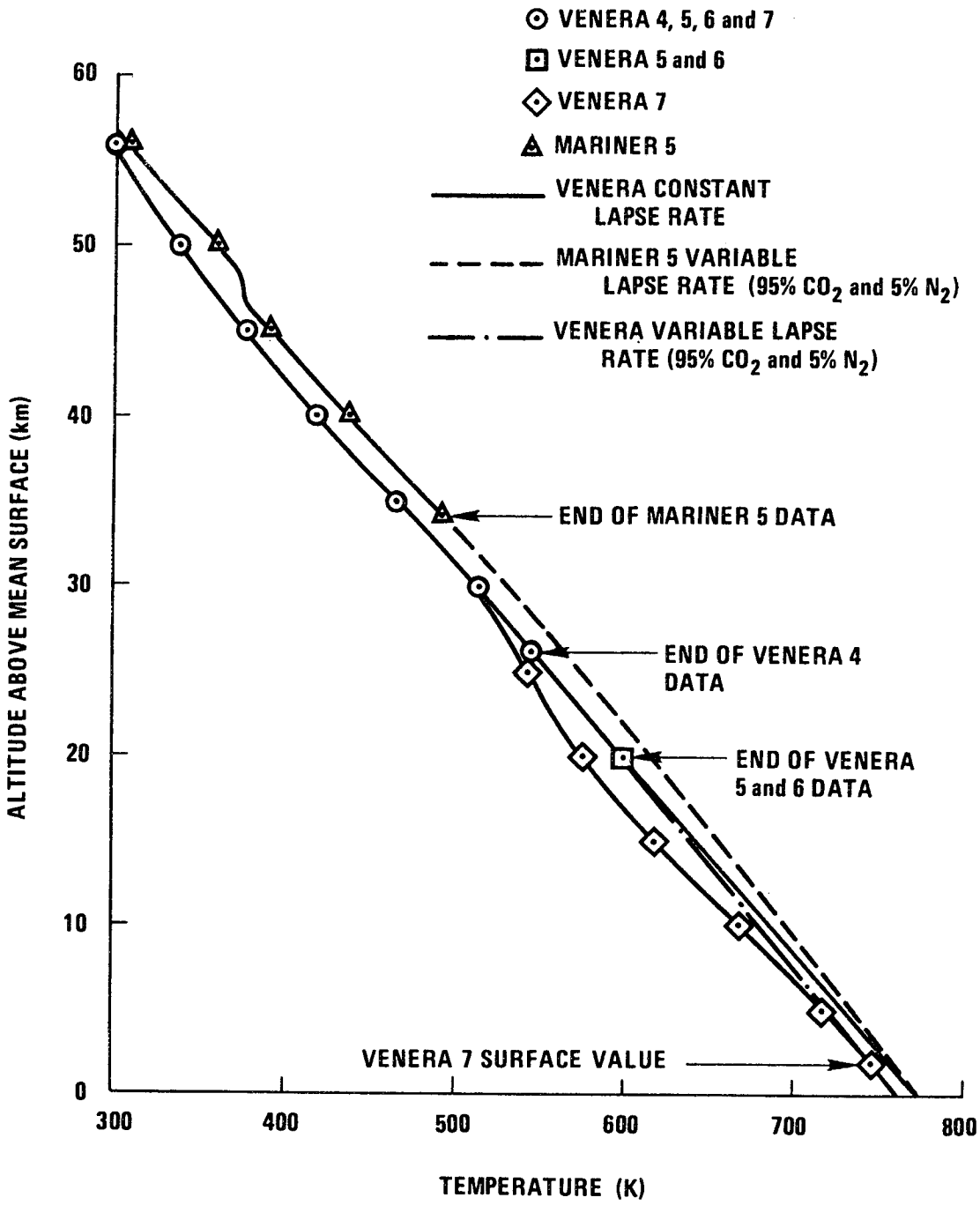

Figure VI-10. Venus lower atmosphere temperature profiles.

Extrapolations of Venera data were also made which assumed that the temperature gradient tends toward an isothermal condition at the surface [VI-1, VI-17]. A surface temperature of about 720 K was predicted for a 5 to 10 km isothermal layer. A parameter study was conducted on an adiabatic model with an isothermal layer at the surface in order to verify brightness temperature measurements of 700 ± 50 K at 6 cm [VI-1]. Results indicated that the surface temperature should be 770 ± 25 K and the isothermal layer less than 4 km in order for the model to predict the observed brightness temperature.

Large-scale differences in the surface temperature across the planetary disc have not been observed (Paragraph 6.1.1). Also, the Mariner 5 occultation experiment indicated only minor diurnal temperature changes in the lower atmosphere, as shown in Figure VI-6.

The temperature profile between 60 and 90 km obtained from Mariner 5 (Fig. VI-6) was correlated with results derived from earth-based measurements at altitudes where cloud layers are believed to exist. Emissions in the near-infrared wavelengths measured by Mariner 2 were interpreted to give a temperature at the top of the clouds of 240 K (Paragraph 6.1.2.1). These values agreed with similar earth-based measurements which yielded temperatures between 215 and 250 K [VI-2, VI-9]. In addition, spectroscopic studies have defined the effective cloud top temperature between 220 and 280 K [VI-2]. The marked change in lapse rate at about 60 km in the Mariner 5 data (Fig. VI-6) has been interpreted to indicate the presence of a cloud layer. The Mariner 5 temperature of 260 K at this altitude also supports this interpretation [VI-7]. The presence of a cloud layer at about 60 km was also inferred from Venera investigations (Paragraphs 6.1.2.2 and 6.1.2.4).

The upper cloud or haze layer has been identified by ultraviolet photographs [VI-6] and by observations made as Venus transits the Sun. Measurements taken during the more recent observations indicate that the temperature at this cloud level is 180 K which corresponds well with the temperature minimum of the Mariner 5 data at about 81 km [VI-7].

6.1.3.3 Surface Pressure — Lower Atmosphere

Direct measurements of atmospheric pressure on Venus were obtained by Venera 4, 5, and 6 (Figs. VI-3 and VI-7) and during the Mariner 5 occultation experiment (Fig. VI-6). The pressure profiles are compared in Figure VI-11 for a mean planetary radius of 6050 km. The Venera 4, 5, and 6 data were adjusted to agree at a pressure of 6.6 atm [VI-16]. The Venera and Mariner 5 profiles agree remarkably well.

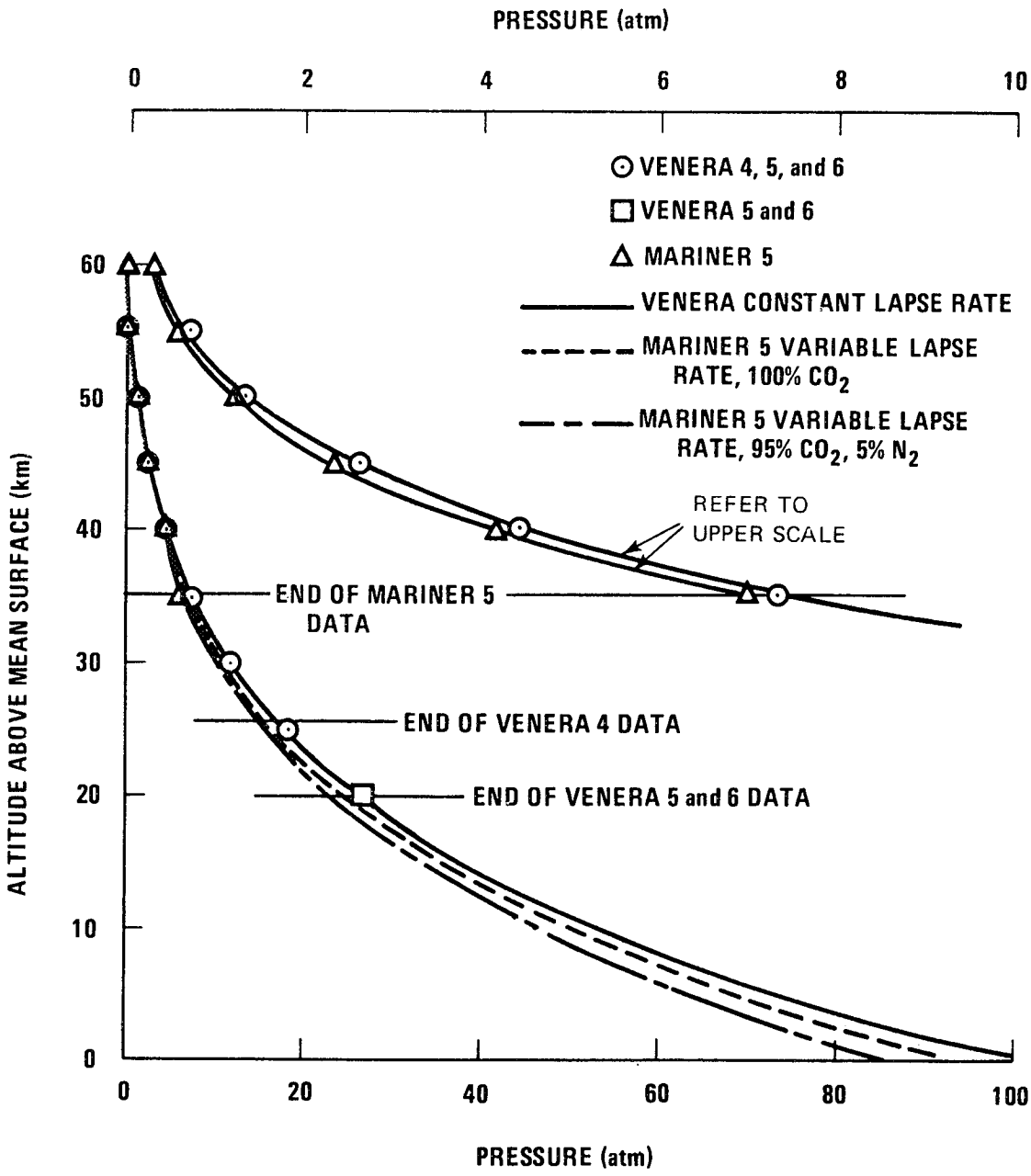

Figure VI-11. Venus lower atmosphere pressure profiles.

Because surface pressure was not measured, the profiles of Figure VI-11 have been extrapolated to the surface with the adiabatic gradients used for the temperature extrapolation (Paragraph 6.2.2.2). Extrapolation of the Venera data with a constant lapse rate results in a surface pressure of 102 atm [VI-17]. With a variable lapse rate [VI-1], a surface pressure of 94 atm was determined from Mariner 5 data for an atmospheric composition of 100 percent CO_2 and 86 atm for a composition of 95 percent CO_2 and 5 percent N_2. Extrapolation was begun at 35 km, the lowest value of pressure determined from the Mariner 5 data. A similar extrapolation of Venera data at 20 km results in a surface pressure of 100 atm for a 95 percent CO_2 and 5 percent N_2 atmosphere [VI-1].

Pressure profiles for Venera 7 were computed from the temperature profiles with the hydrostatic law and the equation of state. Surface values for the adiabatic and measured paths (Paragraph 6.1.2.5) were 86 and 97 atm [VI-1]. Surface pressure determined from Venera data with an assumed isothermal condition near the surface resulted in a predicted pressure of 107 atm [VI-17]. A value of 95 ± 20 atm has been deduced from a model used to correlate radio brightness measurements [VI-1].

The resolution of an appropriate uncertainty range for the mean surface pressure is a direct consequence of the planetary mean surface radius. As noted in Reference VI-2, surface pressure lies in the range of 70 to 120 atm which is considerably better than the 3 to 1000 atm range which existed prior to the accumulation of the spacecraft data [VI-1].

6.1.3.4 Density — Lower Atmosphere

Density values measured by Venera 4, 5, and 6 (Figs. VI-3 and VI-7) were not consistent with measured pressures and temperatures, so a density profile was calculated (Paragraph 6.1.2.4). Surface density values were 67 kg/m^3 for adiabatic and 78 kg/m^3 for isothermal extrapolation [VI-17].

Number density was calculated from refractivity data obtained during the Mariner 5 occultation experiment of planetocentric distances between about 6085 and 6140 km. These data are compared to calculated values in Figure VI-12 [VI-1]. The Regulus occultation density value at 6169 km [VI-15] is also given in Figure VI-12.

6.1.3.5 Winds — Lower Atmosphere

The nature and theory of general circulation of Venus' atmosphere remain uncertain although considerable progress has been reported in recent

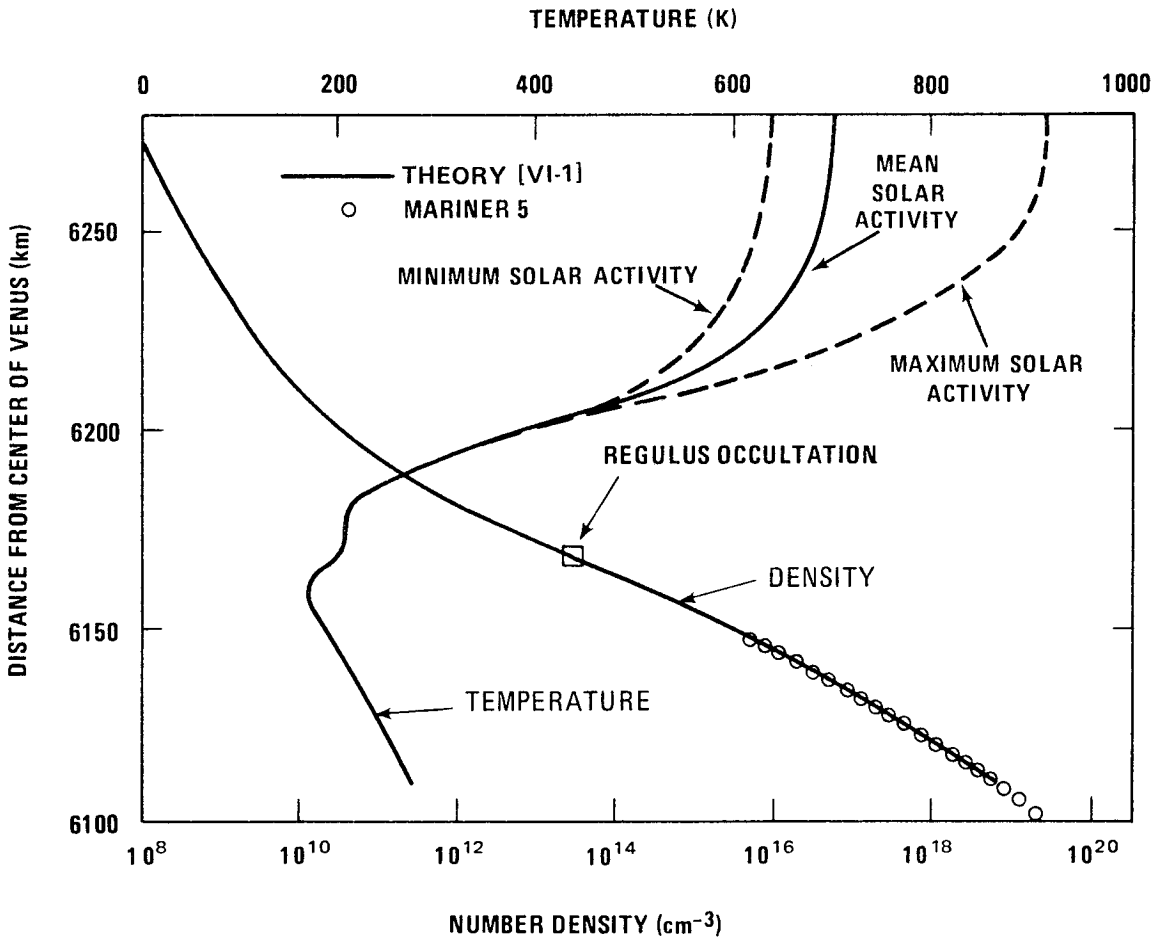

Figure VI-12. Model of Venus neutral atmosphere and measured density data [VI-1].

years. The only observational data relevant to the question of atmospheric winds refer to regions of the atmosphere above the visible clouds. The wind field at greater depths must be inferred on the basis of detailed theoretical models.

Pictures of Venus taken in ultraviolet revealed a variety of features. Ultraviolet markings traveled around the planet with an apparent period of 3.6 to 4.5 days: A rotation period of this magnitude implies zonal velocities of the order of 100 m/s, some 50 times larger than the rotation speed of the solid planet at the equator. More recent photographic data confirm the earlier work and strongly imply retrograde rotation of the Venus atmosphere with a period of 4 to 5 days in the vicinity of the ultraviolet clouds. Independent support for this

surprising result is provided by spectroscopic observations in which significant Doppler shifts were detected in the solar spectrum reflected by Venus. These shifts were interpreted to indicate retrograde velocities of about 100 m/s, equivalent to an estimated rotation period of 4.3 ± 0.4 days [VI-1].

The observed zonal wind speeds are unexpectedly large, comparable with zonal circulations in the earth's atmosphere at high latitudes. High zonal wind speeds can be understood for the earth in terms of the differential angular momentum available on a planet with a rapid rotation period, 24 hours. Evidently a different mechanism is operative for Venus. There is general agreement that zonal winds on Venus result from the apparent motion of the sun during the Venus solar day. The relative motion of the heat source (sun) and Venus sets up a typical convection cell. The convection cell is tilted because of the finite time required for diffusion of heat. Consequently, the cell develops an average Reynolds stress which acts to maintain a steady zonal flow. The magnitude of the flow is limited by the mean viscous stress [VI-1].

Strong support for the moving heat source mechanism is provided by laboratory experiments with mercury, a fluid characterized by an extremely low Prandtl number. In these experiments a moving flame was applied to an annulus; the result was a steady rotation of the liquid in a sense opposite to the motion of the flame. The magnitude of the observed flow velocity was approximately four times larger than the velocity associated with the flame. Various theoretical discussions confirm the applicability of the moving flame model to Venus and yield velocities which are typically in the order of 100 m/s. Although details of the models remain obscure, there are reasons to believe that an atmospheric probe entering the Venus atmosphere will encounter significant zonal winds ($\sim$100 m/s) at least above the visible cloud deck [VI-1].

The first comprehensive attempt to model atmospheric dynamics below the cloud deck used a two-dimensional Boussinesq model for the atmosphere which assumed that heat was applied and removed at the upper boundary (visible clouds) and that the Rossby number was small so that effects of rotation would be minor. Results indicated that the day-side mean temperature is several tens of degrees higher than that of the night side and that the typical wind speed is close to 5 m/s [VI-1].

Numerical models (one a Boussinesq model and another in which basic stratification of density was considered) were used to investigate circulation deep in the atmosphere. Two extreme cases were considered. First, rotation was neglected and the subsolar point was fixed. Second, solar heating was averaged over a Venus solar day and rotation was included. In order to account for the observed temperature profile in the deep atmosphere, it was necessary to assume significant penetration of sunlight to the near surface region, as much as 6 percent at the equator. The horizontal velocities are generally small below 30 km, less than 1 m/s, but may be significant at higher altitudes. The models yield meridional velocities as large as 30 m/s near 50 km. A typical pattern is shown in Figure VI-13. Vertical velocities are generally small except for a narrow region of descending air near the poles, at latitudes of about 75 to 85 deg. Here, vertical velocities may approach 1 m/s. Elsewhere, vertical velocities are expected to be of order of or less than 1 cm/s.

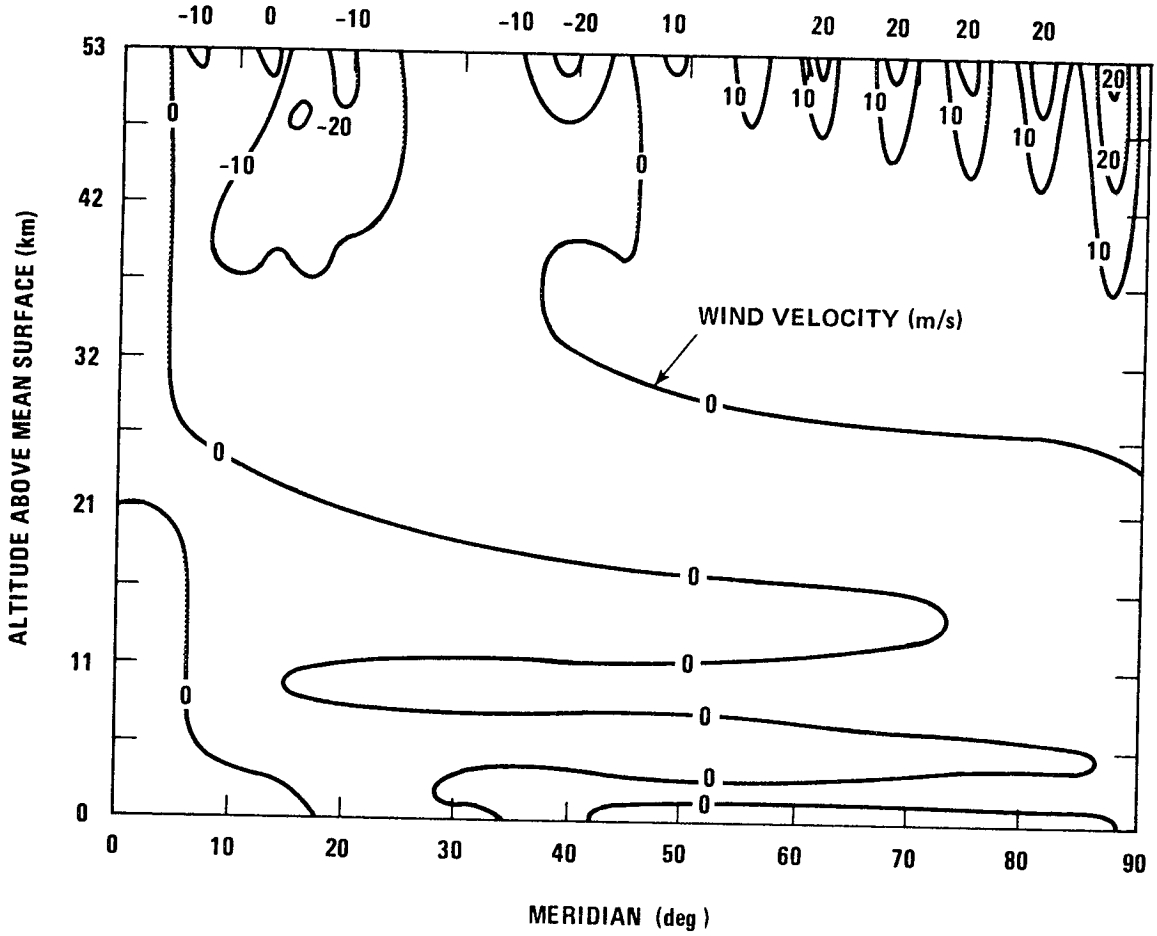

Figure VI-13. Typical horizontal wind patterns [VI-1].

Atmospheric winds determined for Venera 4, 5, and 6 correlate well with the theoretical winds. Vertical velocities of 1.0 to 1.5 m/s were obtained from Venera 4 and 0.3 to 0.5 m/s for Venera 5 and 6. Estimated horizontal winds of 3 to 25 m/s for Venera 5 and 6 were of the same order of magnitude as the winds measured during the last 18 to 20 km (< 50 km altitude) of the descent of Venera 4 [VI-28].

6.1.3.6 Ionosphere — Upper Atmosphere

The only measurements which pertain directly to conditions in the upper atmosphere of Venus are the electron density profiles obtained from Mariner 5 and the ultraviolet airglow data obtained from Mariner 5 and Venera 4. Therefore, engineering models for the upper atmosphere must rely on a variety of theoretical studies. The range in the models, however, has been limited by spacecraft results.

Mariner 5 observed an extensive ionosphere on both day and night sides of Venus [VI-25]. Occultation on the day side occurred at a solar zenith angle of 33 deg. The peak value for electron density was about $5 \times 10^5/cm^3$ at a planetocentric distance of 6190 km. The electron density, as indicated in Figure VI-5, remained high ($>10^4/cm^3$) to an approximate planetocentric distance of 6500 km. At greater distances, the electron density decreased rapidly to typical values for the undisturbed interplanetary medium. The peak value for electron density on the night side was about $2 \times 10^4/cm^3$, and the night-side ionosphere was surprisingly extensive. Significant electron density ($>10^2/cm^3$) was observed to a planetocentric distance of at least 6800 km. Some evidence exists that on the night side a plasma tail extends to planetocentric distances of at least 7200 km. The ionosphere at high altitudes is believed to be controlled in large measure by electromagnetic interactions with the solar wind.

Mariner 5 carried ultraviolet photometers sensitive to radiations emitted by atomic hydrogen and atomic oxygen. The resulting measurements provide data for the day and night sides of the planet. Venera 4 carried similar instrumentation, but the planetary data are limited to conditions during probe descent on the dark side of the planet. Neither experiment showed any evidence of significant abundances of atomic oxygen; both experiments revealed an extensive hydrogen corona. The Mariner results indicate a day-side exospheric temperature of about 650 K [VI-27], which is consistent with the plasma scale heights observed in the S-band occultation experiment. Other interpretations of the Mariner data suggested appreciable abundances of H_2 and deuterium in the upper atmosphere. The evidence is considered weak, however, so models requiring large concentrations of these elements are viewed as highly speculative [VI-1].

Models of the ionosphere already in the literature assume that CO_2^+ is the dominant positive ion. Increased understanding of Mars, however, has led to the expectation that O_2^+ is probably the important component. It is produced by reaction of CO_2^+ with O [VI-1].

6.1.3.7 Neutral Atmosphere — Upper Atmosphere

The major uncertainties in neutral densities of the upper atmosphere relate to the location of the turbopause and the abundance of light constituents, O, N_2, CO, and He, at the turbopause. The relative abundance of these gases is expected to increase rapidly with increasing altitude. The drag experienced by an orbiting spacecraft will be particularly sensitive to O and He, but knowledge concerning abundances of these constituents is minimal.

Atomic oxygen is produced copiously by photodissociation of CO_2. On theoretical grounds one might expect atomic oxygen to be a dominant species in the upper atmosphere. However, detailed theoretical analysis of the ionospheric profiles suggests that oxygen is a minor constituent (<10 percent) at the ionospheric peak, as is the case for Mars; Venus models are constructed subject to this constraint.

There is no positive evidence for helium, but it has been noted that apparent discrepancies between Mariner 5 and Venera data in the lower atmosphere may be removed if Venus' atmosphere includes a significant abundance of He (~5 percent). Moreover, the extended night-time ionosphere can be understood if helium is a major component of the upper atmosphere. Although the evidence is inconclusive, engineering models must allow at least for the possibility of a significant helium concentration. The lifetime of an orbiting spacecraft is affected by the assumed value for the mixing ratio of He at the turbopause [VI-1].

The neutral atmosphere of Venus is described by the theoretical thermal model shown in Figure VI-12. The model yielded an exospheric temperature of 700 K. This value compares favorably with the value of 650 K derived from Mariner 5 Lyman-alpha results. The model has also been applied to the ionosphere [VI-1].

The exospheric temperature varies with solar flux. Estimates for Venus exospheric temperatures at periods of minimum and maximum solar activity are shown in Figure VI-12. Table VI-3 shows estimates for the variation of solar ultraviolet (UV) flux below 1000 Å and the estimated exospheric temperatures for minimum, mean, and maximum solar activity. The values for mean solar activity are for the time of the Mariner 5 Venus flyby on October 19, 1967.

TABLE VI-3. VARIATION OF UV FLUX[a] AND EXOSPHERIC TEMPERATURE WITH SOLAR ACTIVITY

Solar Activity	Ratio of UV Flux to Solar Min UV Flux	Exospheric Temperature (K)
Minimum	1.0	625 ± 200
Mean	1.5	710 ± 200
Maximum	3.0	931 ± 300

a. Below 1000 Å wavelength.

6.1.3.8 Dynamics — Upper Atmosphere

Preliminary models for dynamics of the upper atmosphere suggest that the night side may be significantly colder than the day side. The night-side exospheric temperature could be as low as 250 K, compared to day-side values of about 750 K. If valid, the dynamic studies imply large lateral gradients in the neutral density from day to night. Lifetimes for orbital spacecraft would then depend critically on the position of the perigee because orbits with perigees on the dark side of the planet would encounter markedly less drag than orbits with perigees at similar heights on the sunlit side. To take into account the possibility of a low night-side exospheric temperature, an appropriate model has been developed [VI-1].

6.1.3.9 Interaction with Solar Wind — Upper Atmosphere

Analysis of Mariner 2 magnetometer measurements showed that the magnetic field of Venus is negligible. Thus, the planet apparently is not shielded by a magnetosphere as is the earth, so the solar wind can interact directly with the Venus upper atmosphere. A similar situation is found for Mars where a standing bow shock wave is believed to form as the solar wind impinges on the atmosphere with resulting sharp density gradients between the solar wind and the upper atmosphere [VI-1].

Such gradients were observed for Venus. The day-side electron density detected during the Mariner 5 occultation experiment terminated at an altitude of about 500 km (Fig. VI-5). This termination point, called the plasmapause (or ionopause), has been attributed to the presence of a bow shock as shown in Figure VI-14 and has been the subject of several papers [VI-1].

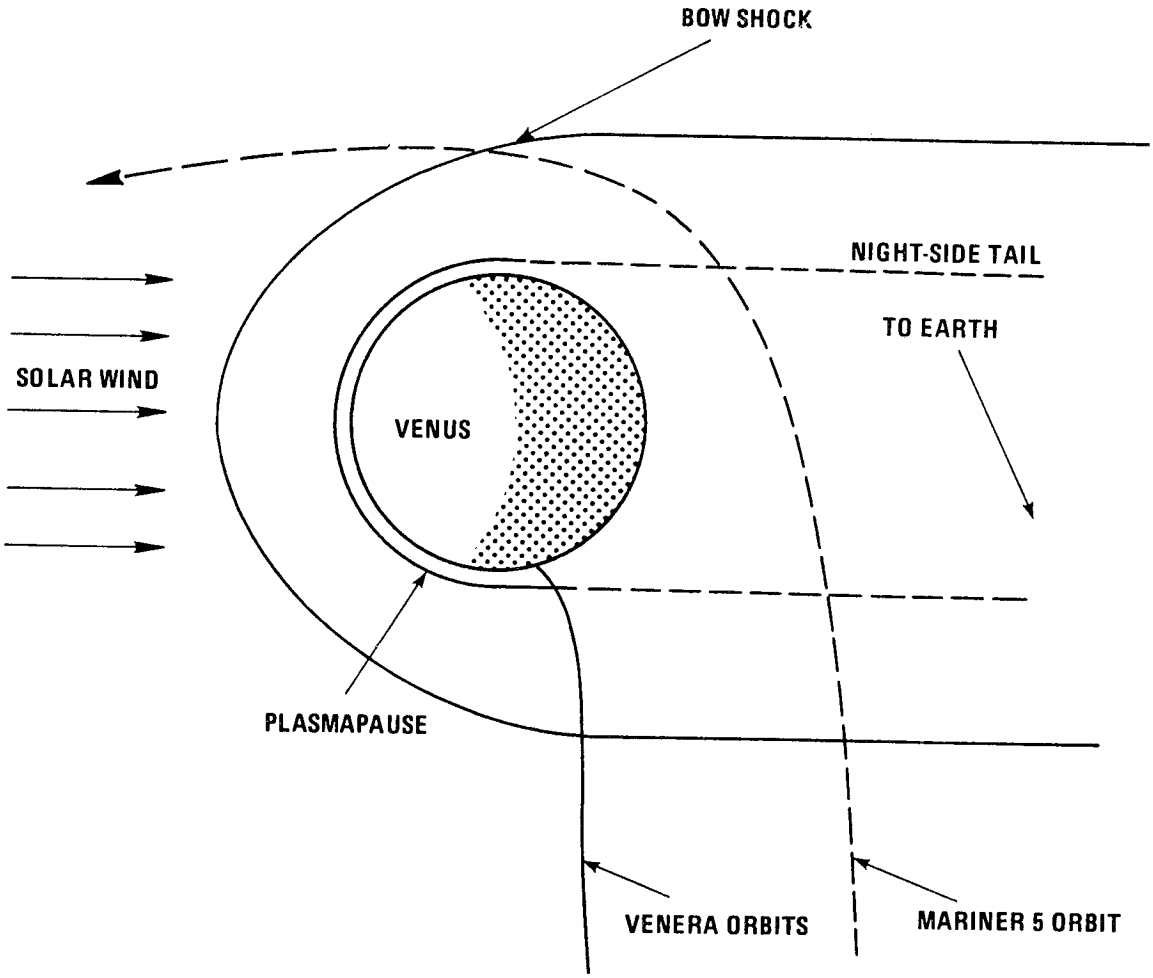

Figure VI-14. Bow shock formation for Venus [VI-1].

The most prevalent theory of the shock wave formation postulates that the magnetic field of the solar wind is compressed against the ionospheric plasma. This compression results in the formation of electromagnetic forces which deflect the solar wind around Venus. The pressure of the solar wind is balanced by the pressure of the ionosphere and the pressure of the compressed magnetic field. The plasmapause is identified as the sharp gradient between the uncompressed solar wind magnetic field and the compressed magnetic field which prevents intermixing of the solar wind and the ionospheric plasma.

It is proposed that a magnetohydrodynamic shock wave is formed as the magnetized supersonic plasma flow (solar wind) interacts with the planetary ionosphere. Most of the subsonic flow on the planetary side of the shock wave is deflected around Venus. Between the ionosphere and shock wave, the dynamics of the interaction of the solar wind and ionosphere indicates that the plasma is compressed more than the magnetic field. The result is a region called the plasmapause where there is a balance of pressure between the plasma and the solar wind [VI-1].

The presence of a bow shock wave has not been firmly established. Venus probe data do not include a sharp shock; in fact, flow density changed over a distance comparable to the radius of Venus. This suggests that the interaction may be similar to that between the outer regions of a comet and the solar wind which does not form a shock wave [VI-1].

6.1.4 Clouds

Knowledge of clouds is important for spacecraft design and the design and operation of instrumentation for observing the Venus atmosphere. Possible adverse effects include absorption or distortion of radio transmissions and microwave observations, distortion of optical observations, corrosive action by aerosol or other cloud particles, and undesirable chemical action. The existence of two cloud layers in the Venus atmosphere was revealed by photographs taken in infrared and ultraviolet wavelengths (Paragraph 6.1.1.1). The upper layer is opaque to ultraviolet but transparent to infrared, whereas the lower layer is opaque to both ultraviolet and infrared wavelengths.

Information on the clouds has been obtained from radio brightness measurements, polarization studies, spectroscopic and interferometer observations, and spacecraft experiments. The data generally agree that at least two cloud layers exist and that the temperature of the lower layer is approximately 240 K and at a level of about 60 km above the mean surface. However, there is disagreement about cloud composition and the nature of the upper clouds.

The composition, particularly the presence of water vapor, and temperature of the clouds have been discussed in Paragraphs 6.2.2.1 and 6.2.3.1. Data concerning the clouds indicates that [VI-7]:

a. The top of the upper layer is at an altitude of 81 km with a pressure of 0.003 atm and temperature of 175 K.

b. The top of the lower layer is at an altitude of 61 km with a pressure of 0.240 atm and temperature of 260 K.

Because the opacity of the atmosphere cannot be explained on the basis of pure CO_2, other constituents have been proposed. Dust has been suggested as a principal component of the clouds, but results of radio brightness studies and polarization observations [VI-8] indicate that dust cannot be a major component of the visible cloud decks. Other components such as H_2O, C_3O_2, $FeCl_2$, and NH_4 Cl (Fig. VI-1) have been proposed with little supporting evidence [VI-7].

The presence and importance of water vapor in cloud formation is still open to question (Paragraph 6.2.2.1). Water vapor may exist in the form of HCl solutions and an HCl-H_2O system is presently the leading contender as the major constituent of the upper cloud layer [VI-1].

The level and temperature of the lower cloud level have been established, but its composition is open to question. As noted in Paragraph 6.2.2.1, water in the amounts detected by the Venera spacecraft can be used to explain the clouds at about 60 km. These explanations are supported by Mariner 5 temperature measurements [VI-24]. However, analysis of the geochemistry of Venus suggests mercury compounds (specifically, a thin haze of Hg_2Cl_2 overlaying a deep cloud of mercury droplets) as more likely components of the lower cloud layer (Fig. VI-15). If these compounds are the main cloud constituent, they could cause the observed pale yellow tint of Venus observed from earth. Mercury compounds could complicate radio-wavelength studies of the phase effect and meridional temperature gradients [VI-1].

Possible cloud layers have been identified from Mariner 5 occultation data at temperatures of 402 K (corresponding to an altitude of 44 km) and of 371 K (corresponding to an altitude of 47 km). Figure VI-15 proposes a chemical model of the atmosphere with mercurious bromide (HG_2Br_2) at 44 km and mercurious iodide (HG_2I_2) at 47 km. Cloud layers in the 37 to 50 km region were postulated on the basis of the S-band loss coefficient observed by Mariner 5 (Paragraph 6.1.2.3). Also studies of the refractive index indicated the possible presence of an inversion layer on the night side of Venus at an altitude of 47 km which could be associated with the lower edge of a cloud layer. (For tentative data see Paragraph 6.1.7) [VI-4].

6.1.5 Gravity

The acceleration of gravity g_0 at the surface of Venus[2] with a radius of 6050 km is derived from the Venus gravitational constant of $GM_{\varphi} = 324\,873.5$ km^3/s^2 measured by Mariner 5 [VI-1].

---

2. $g_0 = \frac{GM_{\varphi}}{r_0^2}$ where r_0 is the planetary surface radius.

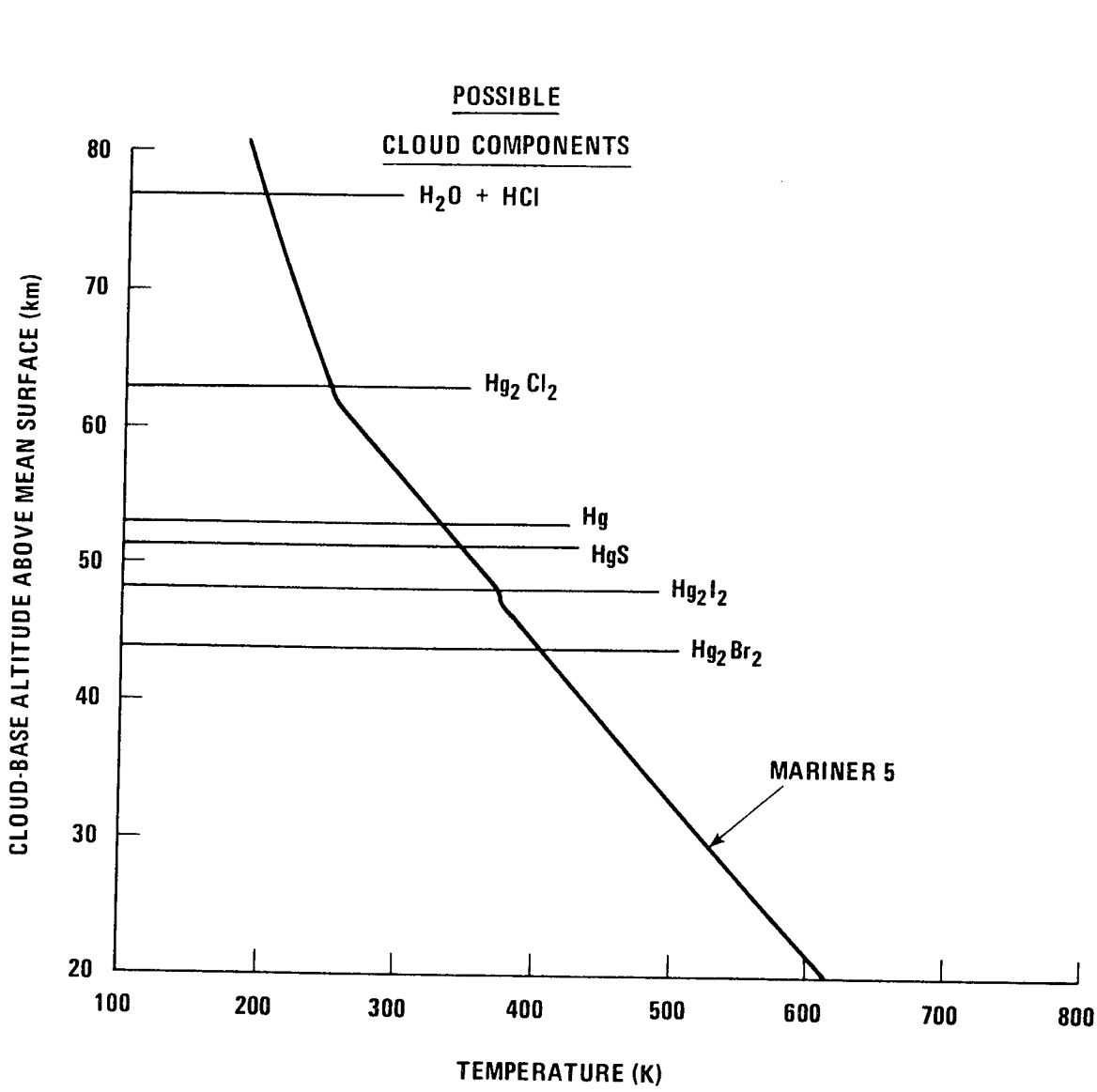

Figure VI-15. Cloud layers and proposed components on Venus [VI-1].

6.1.6 Atmospheric Models — Calculation and Parameters

The models presented in this monograph were generated by the computer program described in NASA TND-4292 [VI-29]. The program was modified to include a molecular mass subroutine (based on the molecular mass variation with altitude), an extended temperature range for the calculation of the specific heat and the reduced collision integral which appears in the viscosity relationship, an extended pressure range for the calculation of the specific heat, and thermochemical data which allow for the inclusion of atomic oxygen as a component gas [VI-1].

The basic inputs to the computer program are the temperature profile, the surface pressure, the near-surface atmospheric composition and corresponding molecular mass, the planetary radius, the acceleration of gravity at the planet's surface, and the atmospheric density at the turbopause. The values for density, pressure, speed of sound, molecular mass, density scale height, number density, mean free path, and viscosity as functions of altitude are calculated with the mathematical relationships given in Reference VI-1; additional mathematical operations are required to determine the mean molecular mass values above the turbopause. All operations satisfy the hydrostatic equation and equation of state.

Atmospheric models were computed for the lower and upper atmospheres to account for uncertainties in the atmospheric parameters. Table VI-4 shows the input parameters for the engineering models of the Venus atmosphere that have been developed. The lower atmosphere was based on temperature profiles determined from spacecraft measurements with surface values obtained by adiabatic extrapolation to the surface. Upper atmosphere models were calculated with the thermal model constrained at the lower boundary by values at the turbopause and at the upper boundary by exospheric temperatures. All models account for the variation of gravitational acceleration with altitude [VI-1].

6.1.6.1 Lower Atmosphere

The temperature profile for the lower atmosphere has been established by spacecraft measurements (Fig. VI-10). A mean profile based on Figure VI-10 is used for the most probable temperature profile and is shown in Figure VI-16. The most probable model is computed for a planetary radius of 6050 km and a molecular mass of 43.5 determined for a composition of 97 percent CO_2 and 3 percent N_2. For all models of the lower atmosphere, it is assumed that the molecular mass is constant up to the turbopause.

Uncertainties in surface temperature and pressure are associated with topographic differences and uncertainties in composition. A range of values for local radii of 6046 to 6054 km was used, and two atmospheric compositions were chosen to encompass a reasonable range for molecular mass. One composition is pure CO_2 which provides the maximum molecular mass, and the other composition has 93 percent CO_2 and 7 percent He which provides the minimum molecular mass.

TABLE VI-4. COMPUTER INPUTS FOR MODELS OF VENUS ATMOSPHERE (1972)

Parameters	Model I (Most Probable Molecular Mass)	Modeis II, III, and VI (Maximum Molecular Mass)	Models IV and V (Minimum Molecular Mass)
Planetary Radius (km)	6050	6050[a]	6050[b]
Surface Gravity (cm/s^2)	887.6	887.6	887.6
Surface Pressure (atm)	93.8	95.5[a]	86.7[b]
Surface Temperature (K)	767.5	772.5[a]	738.7[b]
Composition (% by volume)			
Below Turbopause			
CO_2	97	100	93
N_2	3	–	–
He	–	–	7
At Turbopause			
CO_2	95.99	100	93
N_2	3	–	–
He	0.01	–	5
O	1	–	2
Molecular Mass (g/g mole)			
Below Turbopause	43.52	44.00	41.20
At Turbopause	43.24	44.00	41.44
Density at Turbopause (g/cm^3)	1.44×10^{-11}	1.46×10^{-13}	1.37×10^{-9}
Exospheric Temperature (K) (Model Number)			
Minimum Solar Activity	–	625 (II)	625 (IV)
Mean Solar Activity	710 (I)	–	–
Maximum Solar Activity	–	931 (III)	931 (V)
Night-Side Temperature	–	250 (VI)	–

a. Extreme high values for surface pressure and temperature are obtained at a planetary radius of 6046 km (Paragraph 6.1.6.3).

b. Extreme low values for surface pressure and temperature are obtained at a planetary radius of 6054 km (Paragraph 6.1.6.3).

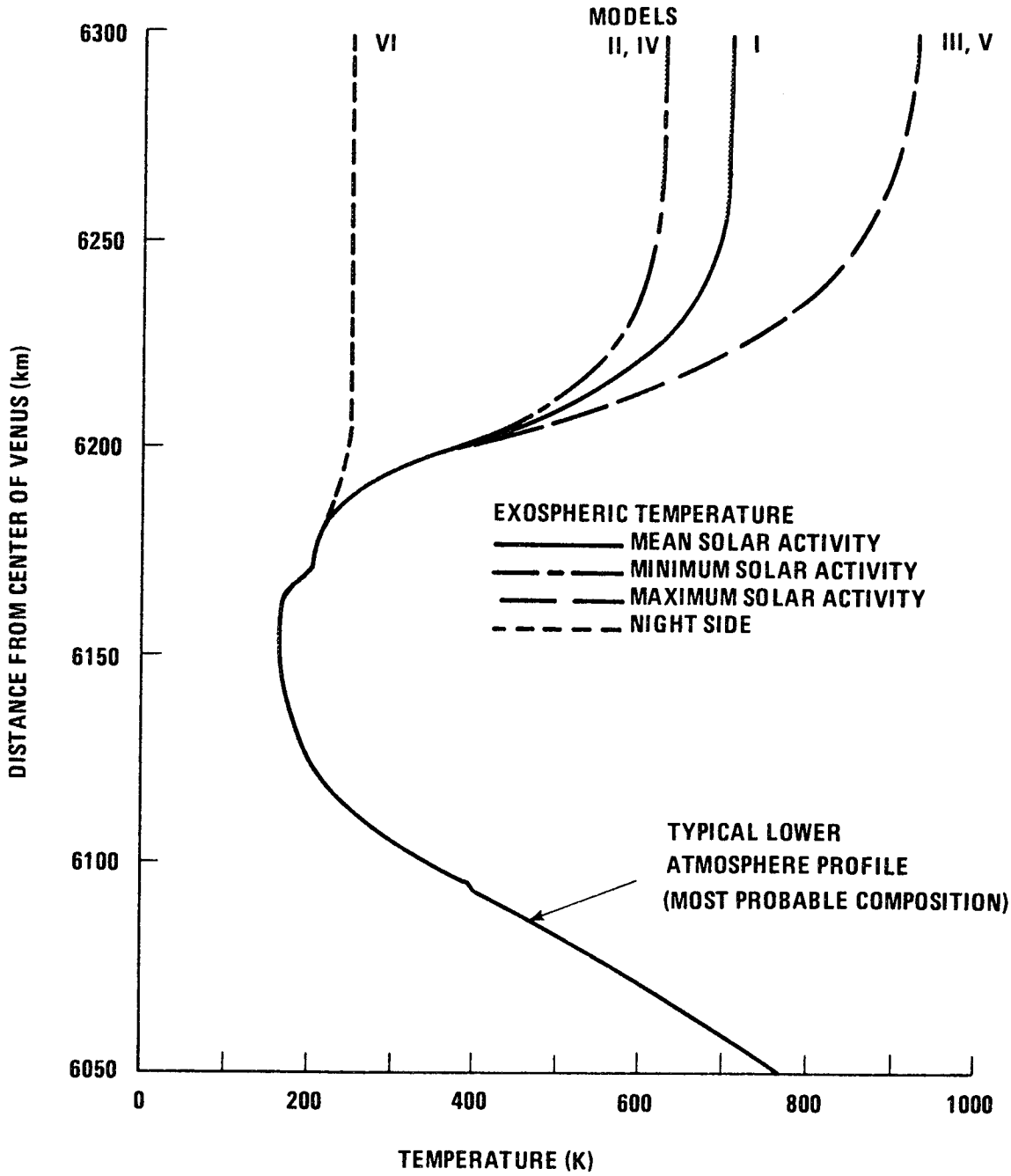

Figure VI-16. Temperature profile for models of Venus atmosphere.

6.1.6.2 Upper Atmosphere

The lower boundary for the theoretical upper atmosphere is the turbopause. The turbopause is the altitude below which the atmospheric gases mix in constant proportions; above this altitude each constituent gas is taken to be in diffusive equilibrium, with number density decreasing with altitude at a rate which depends upon the molecular mass of the gas and the ambient atmospheric temperature. The turbopause was estimated for three possible values of eddy diffusion coefficient, 10^5, 10^7, and 10^9 cm^2/s which were selected to span a reasonable range of values. The coefficients then were used to determine the associated density values at the turbopause. The model of maximum molecular mass is a pure CO_2 atmosphere, the model of minimum molecular mass assumes the highest mixing ratios for O and He at the turbopause, and the model of most probable molecular mass was selected to give the most likely values of mixing ratios for O and He. The upper atmosphere models are superposed on the lower atmosphere models at the turbopause.

The upper constraint on the upper atmosphere models is the exospheric temperature which is a function of both diurnal heating and solar cycle heating. A value of 250 K is for a night-side atmosphere with minimum solar activity. The temperatures presented in Table VI-3 for minimum, mean, and maximum solar activity are used for day-side exospheric temperatures. The upper atmosphere temperature profiles for the different exospheric temperatures are shown in Figure VI-16.

6.1.6.3 Models for Planning and Design

The engineering models of the Venus atmosphere presented herein should be used for mission planning and design of space vehicles which are to orbit Venus, descend through the atmosphere, maneuver in the atmosphere, land on the planetary surface, or conduct scientific investigations during a planetary flyby mission. The models should be used for all facets of space vehicle design including

Structure
Deceleration system
Propulsion system
Flight control system
Guidance system
Heat shield and thermal control system
Communication systems
Electronics
Power supply
Mechanical devices
Scientific experiments (equipment and measurement ranges)

The models should be regarded as approximations which are based on the best available data and which encompass current uncertainties in the atmospheric parameters. The most probable model should be used as the nominal design model; it is most accurate in the lower atmosphere below an altitude of 70 km.

The engineering models of the Venus atmosphere are given in Tables VI-5 through VI-10. Model I (Table VI-5) should be considered as the nominal model. Models II through VI (Tables VI-6 through VI-10) take into account possible extremes of molecular mass, solar activity, and exospheric temperature in appropriate combinations as shown in Table VI-4.

All models are based on the most probable planetary radius of 6050 km which corresponds to 0 km altitude in the tables. However, to encompass possible extremes of surface pressure and temperature, the tables have been extended downward to -4 km which corresponds to a planetary radius of 6046 km. Extreme high values for surface pressure and temperature should be read at -4 km in Models II, III, and VI (Tables VI-6, VI-7, and VI-10). On the other hand, extreme low values for surface pressure and temperature should be read at +4 km in Models IV and V (Tables VI-8 and VI-9) which corresponds to a planetary radius of 6054 km.

The six tables were terminated at altitudes where the density falls to 10^{-16} g/cm^3 because the hydrostatic equilibrium assumption upon which these models are based undoubtedly becomes invalid at greater altitudes.

An alternate model has been proposed in Reference VI-30 which is generally consistent with the nominal model given in Table VI-5. The alternate model is revised to reflect the surface temperature obtained from Venera 7. This model, however, does not incorporate the improved Mariner 5 results [VI-24] which affect the model above 50 km [VI-1].

6.1.6.4 Winds

Studies of the dynamics of the Venus atmosphere and limited data obtained from spacecraft indicate that the wind values presented in Reference VI-4 are valid. Accordingly, the following wind parameter values should be used:

Mean horizontal wind speed below 50 km	2 to 30 m/s
Mean horizontal wind speeds above 50 km	100 m/s
Maximum wind shear	0.05 m s^{-1} m^{-1}
Mean vertical wind speed	1 m/s

TABLE VI-5. 1972 VENUS ATMOSPHERE (MODEL I) (MOST PROBABLE MOLECULAR MASS AND MEAN SOLAR ACTIVITY)[a]

Altitude (km)	Temperature (K)	Pressure (mb)	Density (g/cm^3)	Speed of Sound (m/s)	Molecular Mass (g/g mole)	Density Scale Height (km)	Number Density (per cm^3)	Mean Free Path (m)	Viscosity (kg/m·s)
-4	798.1	1.20+05	7.89-02	426.	43.531	20.52	1.09+21	1.33-09	3.33-05
0[b]	767.5	9.49+04	6.47-02	418.	43.531	19.79	8.95+20	1.62-09	3.24-05
4	736.5	7.41+04	5.27-02	410.	43.531	19.06	7.29+20	1.99-09	3.15-05
8	705.2	5.73+04	4.25-02	402.	43.531	18.32	5.88+20	2.46-09	3.06-05
12	673.4	4.38+04	3.40-02	393.	43.531	17.57	4.71+20	3.07-09	2.96-05
16	641.2	3.30+04	2.70-02	384.	43.531	16.81	3.73+20	3.88-09	2.85-05
20	608.5	2.46+04	2.11-02	375.	43.531	16.03	2.93+20	4.95-09	2.74-05
24	575.3	1.80+04	1.64-02	365.	43.531	15.24	2.27+20	6.39-09	2.62-05
28	541.4	1.29+04	1.25-02	355.	43.531	14.43	1.73+20	8.36-09	2.51-05
32	506.8	9.10+03	9.40-03	345.	43.531	13.59	1.30+20	1.11-08	2.39-05
36	471.4	6.25+03	6.94-03	334.	43.531	12.74	9.61+19	1.51-08	2.25-05
40	433.0	4.16+03	5.03-03	321.	43.531	11.82	6.97+19	2.08-08	2.09-05
44	397.6	2.67+03	3.52-03	308.	43.531	10.51	4.87+19	2.97-08	1.95-05
48	371.4	1.66+03	2.34-03	299.	43.531	9.19	3.23+19	4.47-08	1.82-05
52	336.8	9.91+02	1.54-03	286.	43.531	9.36	2.13+19	6.79-08	1.65-05
56	299.6	5.57+02	9.74-04	271.	43.531	7.99	1.35+19	1.07-07	1.49-05
60	267.6	2.93+02	5.7 -04	258.	43.531	7.12	7.92+18	1.83-07	1.33-05
64	246.2	1.44+02	3.06-04	249.	43.531	6.13	4.24+18	3.42-07	1.23-05
68	231.9	6.71+01	1.51-04	242.	43.531	5.47	2.10+18	6.91-07	1.16-05
72	217.0	2.99+01	7.22-05	235.	43.531	5.30	9.99+17	1.45-06	1.10-05
76	200.4	1.25+01	3.27-05	227.	43.531	4.76	4.53+17	3.20-06	1.03-05
80	187.9	4.92+00	1.37-05	211.	43.531	4.46	1.90+17	7.63-06	.94-05
84	180.1	1.84+00	5.35-06	203.	43.531	4.16	7.40+16	1.95-05	.89-05
88	175.2	6.65-01	1.99-06	199.	43.531	3.97	2.75+16	5.27-05	.86-05
92	171.4	2.35-01	7.16-07	195.	43.531	3.88	9.91+15	1.46-04	.83-05
96	168.3	8.11-02	2.52-07	193.	43.531	3.77	3.49+15	4.15-04	.81-05
100	166.5	2.77-02	8.70-08	191.	43.531	3.74	1.20+15	1.20-03	.80-05
110	171.0	1.86-03	5.70-09	195.	43.531	3.70	7.88+13	1.84-02	.83-05
120	203.9	1.59-04	4.10-10	229.	43.531	4.09	5.67+12	2.55-01	1.04-05
130[c]	214.0	1.91-05	4.67-11	234.	43.531	4.75	6.46+11	2.24+00	1.09-05
140	268.0	3.01-06	5.81-12	261.	42.963	5.39	8.15+10	1.79+01	1.33-05
150	378.4	7.79-07	1.04-12	308.	42.015	6.92	1.49+10	9.76+01	1.85-05
160	502.4	2.98-07	2.91-13	355.	40.818	9.09	4.29+09	3.39+02	2.37-05
170	591.0	1.41-07	1.13-13	390.	39.404	11.62	1.73+09	8.40+02	2.67-05
180	641.4	7.51-08	5.32-14	414.	37.732	13.93	8.49+08	1.71+03	2.84-05
190	674.9	4.28-08	2.73-14	435.	35.781	15.66	4.60+08	3.16+03	2.96-05
200	691.5	2.58-08	1.50-14	455.	33.576	17.31	2.70+08	5.39+03	3.01-05
210	700.8	1.62-08	8.66-15	475.	31.179	18.70	1.67+08	8.70+03	3.04-05
220	705.5	1.06-08	5.18-15	496.	28.700	20.14	1.09+08	1.34+04	3.06-05
230	707.8	7.20-09	3.21-15	520.	26.266	21.71	7.37+07	1.97+04	3.06-05
240	709.0	5.07-09	2.06-15	544.	23.994	23.49	5.18+07	2.81+04	3.07-05
250	709.4	3.69-09	1.37-15	569.	21.963	25.54	3.76+07	3.87+04	3.07-05
260	709.4	2.75-09	9.43-16	593.	20.207	27.80	2.81+07	5.18+04	3.07-05
270	709.4	2.10-09	6.68-16	616.	18.719	30.21	2.15+07	6.77+04	3.07-05
280	709.4	1.64-09	4.86-16	638.	17.467	32.69	1.68+07	8.68+04	3.07-05
290	709.4	1.30-09	3.62-16	658.	16.409	35.15	1.33+07	1.10+05	3.07-05
300	709.4	1.05-09	2.75-16	677.	15.499	37.52	1.07+07	1.36+05	3.07-05
310	709.5	8.51-10	2.12-16	696.	14.699	39.74	8.69+06	1.67+05	3.07-05
320	709.5	7.01-10	1.66-16	713.	13.976	41.80	7.15+06	2.03+05	3.07-05
330	709.5	5.82-10	1.31-16	731.	13.306	43.71	5.95+06	2.45+05	3.07-05
340	709.5	4.89-10	1.05-16	749.	12.672	45.51	4.99+06	2.92+05	3.07-05
350	709.5	4.14-10	8.46-17	768.	12.063	47.24	4.22+06	3.44+05	3.07-05

a. A one- or two-digit number (preceded by a plus or minus sign) following an entry indicates the power of ten by which that entry should be multiplied.

b. Corresponds to planetary radius of 6050 km.

c. Density is 1.44×10^{-11} g/cm^3 at the turbopause (lower boundary of upper atmosphere).

TABLE VI-6. 1972 VENUS ATMOSPHERE (MODEL II) (MAXIMUM MOLECULAR MASS AND MINIMUM SOLAR ACTIVITY)[a]

Altitude (km)	Temperature (K)	Pressure (mb)	Density (g/cm^3)	Speed of Sound (m/s)	Molecular Mass (g/g mole)	Density Scale Height (km)	Number Density (per cm^3)	Mean Free Path (m)	Viscosity (kg/m·s)
-4	803.1	1.23+05	8.09-02	424.	44.010	20.39	1.11+21	1.30-09	3.34-05
0[b]	772.5	9.66+04	6.62-02	416.	44.011	19.65	9.06+20	1.59-09	3.25-05
4	741.5	7.54+04	5.38-02	408.	44.011	18.94	7.37+20	1.96-09	3.16-05
8	710.2	5.82+04	4.34-02	400.	44.011	18.21	5.94+20	2.43-09	3.07-05
12	678.5	4.45+04	3.47-02	392.	44.011	17.47	4.75+20	3.04-09	2.97-05
16	646.3	3.35+04	2.75-02	383.	44.011	16.72	3.76+20	3.84-09	2.86-05
20	613.7	2.49+04	2.15-02	374.	44.011	15.95	2.94+20	4.90-09	2.75-05
24	580.5	1.82+04	1.66-02	364.	44.011	15.17	2.28+20	6.34-09	2.64-05
28	546.7	1.31+04	1.27-02	355.	44.011	14.37	1.74+20	8.30-09	2.52-05
32	512.1	9.22+03	9.53-03	344.	44.011	13.54	1.30+20	1.11-08	2.40-05
36	476.6	6.33+03	7.03-03	333.	44.011	12.73	9.62+19	1.50-08	2.26-05
40	437.8	4.21+03	5.10-03	320.	44.011	11.82	6.97+19	2.07-08	2.10-05
44	402.0	2.71+03	3.56-03	308.	44.011	10.51	4.88+19	2.95-08	1.96-05
48	375.5	1.68+03	2.37-03	299.	44.011	9.20	3.24+19	4.45-08	1.83-05
52	340.5	1.00+03	1.56-03	286.	44.011	9.36	2.13+19	6.76-08	1.66-05
56	302.8	5.64+02	9.86-04	271.	44.011	8.00	1.35+19	1.07-07	1.49-05
60	270.3	2.96+02	5.80-04	258.	44.011	7.13	7.94+18	1.82-07	1.33-05
64	248.9	1.46+02	3.10-04	249.	44.011	6.12	4.24+18	3.40-07	1.23-05
68	234.5	6.79+01	1.53-04	242.	44.011	5.47	2.10+18	6.87-07	1.17-05
72	219.4	3.03+01	7.31-05	235.	44.011	5.31	1.00+18	1.44-06	1.10-05
76	202.6	1.27+01	3.31-05	227.	44.011	4.76	4.53+17	3.18-06	1.03-05
80	190.0	4.98+00	1.39-05	220.	44.011	4.46	1.90+17	7.59-06	.95-05
84	182.0	1.86+00	5.42-06	215.	44.011	4.16	7.41+16	1.94-05	.89-05
88	177.0	6.72-01	2.01-06	212.	44.011	3.96	2.75+16	5.24-05	.86-05
92	173.0	2.37-01	7.24-07	209.	44.011	3.88	9.91+15	1.45-04	.84-05
96	169.6	8.16-02	2.55-07	207.	44.011	3.76	3.49+15	4.14-04	.82-05
100	168.0	2.78-02	8.75-08	206.	44.011	3.73	1.20+15	1.20-03	.81-05
110	171.0	1.84-03	5.70-09	208.	44.011	3.68	7.79+13	1.85-02	.82-05
120	203.9	1.53-04	3.98-10	227.	44.011	4.05	5.45+12	2.64-01	1.04-05
130	214.0	1.79-05	4.44-11	232.	44.011	4.70	6.07+11	2.37+00	1.08-05
140	272.3	2.80-06	5.44-12	259.	44.011	5.37	7.45+10	1.93+01	1.34-05
150	399.3	7.26-07	9.62-13	307.	44.011	6.95	1.32+10	1.10+02	1.95-05
160[c]	555.8	2.82-07	2.69-13	358.	44.011	9.23	3.68+09	3.92+02	2.55-05
170	675.4	1.37-07	1.07-13	392.	44.011	11.98	1.47+09	9.83+02	2.96-05
180	760.0	7.36-08	5.13-14	414.	44.011	14.41	7.01+08	2.05+03	3.21-05
190	826.0	4.21-08	2.70-14	431.	44.011	16.27	3.69+08	3.90+03	3.40-05
200	862.3	2.50-08	1.53-14	440.	44.011	18.10	2.10+08	6.87+03	3.51-05
210	890.2	1.51-08	9.00-15	447.	44.011	19.08	1.23+08	1.17+04	3.59-05
220	905.9	9.29-09	5.43-15	451.	44.011	19.99	7.43+07	1.94+04	3.64-05
230	916.7	5.75-09	3.32-15	453.	44.011	20.52	4.54+07	3.17+04	3.67-05
240	922.8	3.58-09	2.06-15	455.	44.011	20.94	2.81+07	5.13+04	3.68-05
250	926.8	2.24-09	1.28-15	455.	44.011	21.20	1.75+07	8.23+04	3.70-05
260	926.9	1.41-09	8.02-16	455.	44.011	21.46	1.10+07	1.31+05	3.70-05
270	926.9	8.82-10	5.04-16	456.	44.011	21.53	6.90+06	2.09+05	3.70-05
280	927.0	5.55-10	3.17-16	456.	44.011	21.60	4.34+06	3.32+05	3.70-05
290	927.1	3.50-10	2.00-16	456.	44.011	21.67	2.73+06	5.28+05	3.70-05
300	927.1	2.21-10	1.26-16	456.	44.011	21.74	1.72+06	8.37+05	3.70-05
310	927.2	1.39-10	7.95-17	456.	44.011	21.81	1.09+06	1.32+06	3.70-05

a. A one- or two-digit number (preceded by a plus or minus sign) following an entry indicates the power of ten by which that entry should be multiplied.

b. Corresponds to planetary radius of 6050 km.

c. Density is 1.46×10^{-13} g/cm^3 at the turbopause (lower boundary of upper atmosphere).

TABLE VI-7. 1972 VENUS ATMOSPHERE (MODEL III) (MAXIMUM MOLECULAR MASS AND MAXIMUM SOLAR ACTIVITY)[a]

Altitude (km)	Temperature (K)	Pressure (mb)	Density (g/cm^3)	Speed of Sound (m/s)	Molecular Mass (g/g mole)	Density Scale Height (km)	Number Density (per cm^3)	Mean Free Path (m)	Viscosity (kg/m·s)
-4	803.1	1.23+05	8.09-02	424.	44.010	20.39	1.11+21	1.30-09	3.34-05
0[b]	772.5	9.66+04	6.62-02	416.	44.011	19.65	9.06+20	1.59-09	3.25-05
4	741.5	7.54+04	5.38-02	408.	44.011	18.94	7.37+20	1.96-09	3.16-05
8	710.2	5.82+04	4.34-02	400.	44.011	18.21	5.94+20	2.43-09	3.07-05
12	678.5	4.45+04	3.47-02	392.	44.011	17.47	4.75+20	3.04-09	2.97-05
16	646.3	3.35+04	2.75-02	383.	44.011	16.72	3.76+20	3.84-09	2.86-05
20	613.7	2.49+04	2.15-02	374.	44.011	15.95	2.94+20	4.90-09	2.75-05
24	580.5	1.82+04	1.66-02	364.	44.011	15.17	2.28+20	6.34-09	2.64-05
28	546.7	1.31+04	1.27-02	355.	44.011	14.37	1.74+20	8.30-09	2.52-05
32	512.1	9.22+03	9.53-03	344.	44.011	13.54	1.30+20	1.11-08	2.40-05
36	476.6	6.33+03	7.03-03	333.	44.011	12.73	9.62+19	1.50-08	2.26-05
40	437.8	4.21+03	5.10-03	320.	44.011	11.82	6.97+19	2.07-08	2.10-05
44	402.0	2.71+03	3.56-03	308.	44.011	10.51	4.88+19	2.95-08	1.96-05
48	375.5	1.68+03	2.37-03	299.	44.011	9.20	3.24+19	4.45-08	1.83-05
52	340.5	1.00+03	1.56-03	286.	44.011	9.36	2.13+19	6.76-08	1.66-05
56	302.8	5.64+02	9.86-04	271.	44.011	8.00	1.35+19	1.07-07	1.49-05
60	270.3	2.96+02	5.80-04	258.	44.011	7.13	7.94+18	1.82-07	1.33-05
64	248.9	1.46+02	3.10-04	249.	44.011	6.12	4.24+18	3.40-07	1.23-05
68	234.5	6.79+01	1.53-04	242.	44.011	5.47	2.10+18	6.87-07	1.17-05
72	219.4	3.03+01	7.31-05	235.	44.011	5.31	1.00+18	1.44-06	1.10-05
76	202.6	1.27+01	3.31-05	227.	44.011	4.76	4.53+17	3.18-06	1.03-05
80	190.0	4.98+00	1.39-05	220.	44.011	4.46	1.90+17	7.59-06	.95-05
84	182.0	1.86+00	5.42-06	215.	44.011	4.16	7.41+16	1.94-05	.89-05
88	177.0	6.72-01	2.01-06	212.	44.011	3.96	2.75+16	5.24-05	.86-05
92	173.0	2.37-01	7.24-07	209.	44.011	3.88	9.91+15	1.45-04	.84-05
96	169.6	8.16-02	2.55-07	207.	44.011	3.76	3.49+15	4.14-04	.82-05
100	168.0	2.78-02	8.75-08	206.	44.011	3.73	1.20+15	1.20-03	.81-05
110	171.0	1.84-03	5.70-09	208.	44.011	3.68	7.79+13	1.85-02	.82-05
120	203.9	1.53-04	3.98-10	227.	44.011	4.05	5.45+12	2.64-01	1.04-05
130	214.0	1.79-05	4.44-11	232.	44.011	4.70	6.07+11	2.37+00	1.08-05
140	272.3	2.80-06	5.44-12	259.	44.011	5.37	7.45+10	1.93+01	1.34-05
150	399.3	7.26-07	9.62-13	307.	44.011	6.95	1.32+10	1.10+02	1.95-05
160[c]	555.8	2.82-07	2.69-13	358.	44.011	9.23	3.68+09	3.92+02	2.55-05
170	675.4	1.37-07	1.07-13	392.	44.011	11.98	1.47+09	9.83+02	2.96-05
180	760.0	7.36-08	5.13-14	414.	44.011	14.41	7.01+08	2.05+03	3.21-05
190	826.0	4.21-08	2.70-14	431.	44.011	16.27	3.69+08	3.90+03	3.40-05
200	862.3	2.50-08	1.53-14	440.	44.011	18.10	2.10+08	6.87+03	3.51-05
210	890.2	1.51-08	9.00-15	447.	44.011	19.08	1.23+08	1.17+04	3.59-05
220	905.9	9.29-09	5.43-15	451.	44.011	19.99	7.43+07	1.94+04	3.64-05
230	916.7	5.75-09	3.32-15	453.	44.011	20.52	4.54+07	3.17+04	3.67-05
240	922.8	3.58-09	2.06-15	455.	44.011	20.94	2.81+07	5.13+04	3.68-05
250	926.8	2.24-09	1.28-15	455.	44.011	21.20	1.75+07	8.23+04	3.70-05
260	926.9	1.41-09	8.02-16	455.	44.011	21.46	1.10+07	1.31+05	3.70-05
270	926.9	8.82-10	5.04-16	456.	44.011	21.53	6.90+06	2.09+05	3.70-05
280	927.0	5.55-10	3.17-16	456.	44.011	21.60	4.34+06	3.32+05	3.70-05
290	927.1	3.50-10	2.00-16	456.	44.011	21.67	2.73+06	5.28+05	3.70-05
300	927.1	2.21-10	1.26-16	456.	44.011	21.74	1.72+06	8.37+05	3.70-05
310	927.2	1.39-10	7.95-17	456.	44.011	21.81	1.09+06	1.32+06	3.70-05

a. A one- or two-digit number (preceded by a plus or minus sign) following an entry indicates the power of ten by which that entry should be multiplied.

b. Corresponds to planetary radius of 6050 km.

c. Density is 1.46×10^{-13} g/cm^3 at the turbopause (lower boundary of upper atmosphere).

TABLE VI-8. 1972 VENUS ATMOSPHERE (MODEL IV) (MINIMUM MOLECULAR MASS AND MINIMUM SOLAR ACTIVITY)[a]

Altitude (km)	Temperature (K)	Pressure (mb)	Density (g/cm^3)	Speed of Sound (m/s)	Molecular Mass (g/g mole)	Density Scale Height (km)	Number Density (per cm^3)	Mean Free Path (m)	Viscosity (kg/m·s)
-4	768.9	1.11+05	7.14-02	431.	41.210	21.06	1.04+21	1.45-09	3.28-05
0[b]	738.7	8.77+04	5.89-02	423.	41.210	20.29	8.60+20	1.76-09	3.19-05
4	708.1	6.88+04	4.82-02	415.	41.210	19.53	7.04+20	2.15-09	3.10-05
8	677.1	5.34+04	3.91-02	406.	41.210	18.75	5.71+20	2.65-09	3.00-05
12	645.7	4.09+04	3.14-02	397.	41.210	17.96	4.59+20	3.30-09	2.89-05
16	613.9	3.10+04	2.50-02	388.	41.210	17.16	3.66+20	4.14-09	2.78-05
20	581.6	2.31+04	1.97-02	378.	41.210	16.34	2.88+20	5.25-09	2.67-05
24	548.7	1.70+04	1.53-02	368.	41.210	15.51	2.24+20	6.75-09	2.56-05
28	515.1	1.22+04	1.18-02	358.	41.210	14.65	1.72+20	8.80-09	2.44-05
32	480.9	8.62+03	8.89-03	347.	41.210	13.77	1.30+20	1.17-08	2.31-05
36	446.1	5.92+03	6.58-03	335.	41.210	12.81	9.61+19	1.58-08	2.16-05
40	409.8	3.94+03	4.77-03	322.	41.210	11.82	6.97+19	2.17-08	2.02-05
44	376.3	2.53+03	3.34-03	310.	41.210	10.51	4.87+19	3.11-08	1.86-05
48	351.5	1.57+03	2.21-03	301.	41.210	9.19	3.24+19	4.68-08	1.74-05
52	318.7	9.38+02	1.46-03	288.	41.210	9.36	2.13+19	7.10-08	1.58-05
56	283.5	5.27+02	9.22-04	273.	41.210	7.99	1.35+19	1.12-07	1.42-05
60	253.0	2.77+02	5.42-04	260.	41.210	7.12	7.92+18	1.91-07	1.27-05
64	233.0	1.36+02	2.90-04	251.	41.210	6.12	4.23+18	3.58-07	1.18-05
68	219.5	6.34+01	1.43-04	244.	41.210	5.46	2.09+18	7.24-07	1.12-05
72	206.4	2.83+01	6.80-05	237.	41.210	5.26	9.93+17	1.52-06	1.06-05
76	192.4	1.19+01	3.08-05	229.	41.210	4.81	4.50+17	3.37-06	.98-05
80	181.0	4.77+00	1.31-05	222.	41.210	4.52	1.91+17	7.94-06	.90-05
84	173.8	1.81+00	5.17-06	218.	41.210	4.24	7.56+16	2.00-05	.86-05
88	169.6	6.69-01	1.95-06	215.	41.210	4.04	2.86+16	5.30-05	.83-05
92	166.4	2.42-01	7.20-07	213.	41.210	3.97	1.05+16	1.44-04	.81-05
96	163.8	8.59-02	2.60-07	211.	41.210	3.86	3.80+15	3.99-04	.80-05
100	163.0	3.03-02	9.21-08	211.	41.210	3.85	1.35+15	1.13-03	.79-05
110[c]	171.0	2.27-03	6.57-09	216.	41.210	3.85	9.60+13	1.58-02	.84-05
120	203.9	2.24-04	5.23-10	241.	39.629	4.14	7.94+12	1.90-01	1.05-05
130	214.0	4.24-05	6.34-11	300.	26.595	5.24	1.44+12	1.05+00	1.10-05
140	263.0	1.88-05	1.06-11	483.	12.386	7.24	5.17+11	2.92+00	1.31-05
150	366.6	1.38-05	3.26-12	736.	7.179	11.82	2.73+11	5.52+00	1.80-05
160	471.9	1.19-05	1.69-12	937.	5.576	19.61	1.82+11	8.28+00	2.26-05
170	542.9	1.07-05	1.17-12	1062.	4.941	32.34	1.43+11	1.06+01	2.52-05
180	583.8	9.82-06	9.36-13	1134.	4.628	50.04	1.22+11	1.24+01	2.66-05
190	602.9	9.09-06	8.07-13	1174.	4.450	72.86	1.09+11	1.38+01	2.73-05
200	612.9	8.46-06	7.20-13	1198.	4.338	92.38	1.00+11	1.51+01	2.76-05
210	620.3	7.89-06	6.52-13	1216.	4.263	104.87	9.21+10	1.64+01	2.78-05
220	620.8	7.37-06	6.01-13	1224.	4.209	126.14	8.60+10	1.75+01	2.79-05
230	621.3	6.90-06	5.56-13	1230.	4.169	131.96	8.04+10	1.88+01	2.79-05
240	621.5	6.45-06	5.17-13	1235.	4.138	137.44	7.52+10	2.01+01	2.79-05
250	621.7	6.05-06	4.81-13	1239.	4.113	141.24	7.04+10	2.14+01	2.79-05
260	621.7	5.67-06	4.49-13	1242.	4.093	144.88	6.60+10	2.29+01	2.79-05
270	621.8	5.31-06	4.19-13	1244.	4.078	147.56	6.19+10	2.44+01	2.79-05
280	621.8	4.98-06	3.92-13	1246.	4.065	149.87	5.81+10	2.60+01	2.79-05
290	621.9	4.68-06	3.67-13	1248.	4.054	151.88	5.45+10	2.77+01	2.79-05
300	621.9	4.39-06	3.43-13	1249.	4.045	153.65	5.11+10	2.95+01	2.79-05
310	622.0	4.12-06	3.22-13	1251.	4.038	155.22	4.80+10	3.14+01	2.79-05
320	622.0	3.87-06	3.02-13	1252.	4.032	156.62	4.51+10	3.35+01	2.79-05
330	622.1	3.64-06	2.83-13	1252.	4.027	157.88	4.24+10	3.56+01	2.79-05

TABLE VI-8. (Concluded)

Altitude (km)	Temperature (K)	Pressure (mb)	Density (g/cm^3)	Speed of Sound (m/s)	Molecular Mass (g/g mole)	Density Scale Height (km)	Number Density (per cm^3)	Mean Free Path (m)	Viscosity (kg/m·s)
340	622.1	3.42-06	2.66-13	1253.	4.023	159.02	3.98+10	3.79+01	2.79-05
350	622.2	3.22-06	2.50-13	1254.	4.020	160.06	3.74+10	4.03+01	2.79-05
360	622.2	3.02-06	2.35-13	1254.	4.017	161.01	3.52+10	4.29+01	2.79-05
370	622.3	2.84-06	2.21-13	1254.	4.015	161.90	3.31+10	4.56+01	2.79-05
380	622.3	2.68-06	2.07-13	1255.	4.013	162.73	3.11+10	4.85+01	2.79-05
390	622.4	2.52-06	1.95-13	1255.	4.011	163.51	2.93+10	5.15+01	2.79-05
400	622.4	2.37-06	1.84-13	1255.	4.010	164.25	2.76+10	5.47+01	2.79-05
425	622.5	2.04-06	1.58-13	1256.	4.007	165.95	2.37+10	6.36+01	2.79-05
450	622.7	1.76-06	1.36-13	1256.	4.006	167.53	2.04+10	7.39+01	2.79-05
475	622.8	1.51-06	1.17-13	1256.	4.005	169.02	1.76+10	8.57+01	2.79-05
500	622.9	1.31-06	1.01-13	1257.	4.004	170.45	1.52+10	9.93+01	2.79-05
525	623.0	1.13-06	8.73-14	1257.	4.004	171.86	1.31+10	1.15+02	2.79-05
550	623.1	9.78-07	7.55-14	1257.	4.003	173.24	1.14+10	1.33+02	2.79-05
575	623.2	8.47-07	6.54-14	1257.	4.003	174.62	9.84+09	1.53+02	2.79-05
600	623.3	7.34-07	5.67-14	1257.	4.003	175.99	8.53+09	1.77+02	2.79-05
625	623.5	6.38-07	4.92-14	1257.	4.003	177.36	7.41+09	2.04+02	2.79-05
650	623.6	5.54-07	4.28-14	1257.	4.003	178.73	6.44+09	2.34+02	2.79-05
675	623.7	4.82-07	3.72-14	1258.	4.003	180.10	5.60+09	2.69+02	2.79-05
700	623.8	4.20-07	3.24-14	1258.	4.003	181.48	4.88+09	3.09+02	2.80-05
725	623.9	3.66-07	2.83-14	1258.	4.003	182.86	4.25+09	3.55+02	2.80-05
750	624.0	3.20-07	2.47-14	1258.	4.003	184.24	3.71+09	4.07+02	2.80-05
775	624.1	2.79-07	2.15-14	1258.	4.003	185.63	3.24+09	4.66+02	2.80-05
800	624.2	2.44-07	1.88-14	1258.	4.003	187.03	2.83+09	5.32+02	2.80-05
825	624.3	2.14-07	1.65-14	1258.	4.003	188.43	2.48+09	6.08+02	2.80-05
850	624.4	1.87-07	1.44-14	1258.	4.003	189.83	2.17+09	6.94+02	2.80-05
875	624.5	1.64-07	1.27-14	1258.	4.003	191.24	1.91+09	7.92+02	2.80-05
900	624.6	1.44-07	1.11-14	1259.	4.003	192.66	1.67+09	9.02+02	2.80-05
925	624.7	1.27-07	9.78-15	1259.	4.003	194.08	1.47+09	1.03+03	2.80-05
950	624.8	1.12-07	8.60-15	1259.	4.003	195.50	1.29+09	1.17+03	2.80-05
975	624.9	9.82-08	7.57-15	1259.	4.003	196.93	1.14+09	1.33+03	2.80-05
1000	627.1	8.66-08	6.65-15	1261.	4.003	170.30	1.00+09	1.51+03	2.81-05

a. A one- or two-digit number (preceded by a plus or minus sign) following an entry indicates the power of ten by which that entry should be multiplied.

b. Corresponds to planetary radius of 6050 km.

c. Density is 1.37×10^{-9} g/cm^3 at the turbopause (lower boundary of upper atmosphere).

TABLE VI-9. 1972 VENUS ATMOSPHERE (MODEL V) (MINIMUM MOLECULAR MASS AND MAXIMUM SOLAR ACTIVITY)[a]

Altitude (km)	Temperature (K)	Pressure (mb)	Density (g/cm^3)	Speed of Sound (m/s)	Molecular Mass (g/g mole)	Density Scale Height (km)	Number Density (per cm^3)	Mean Free Path (m)	Viscosity (kg/m·s)
-4	768.9	1.11+05	7.14-02	431.	41.210	21.06	1.04+21	1.45-09	3.28-05
0[b]	738.7	8.77+04	5.89-02	423.	41.210	20.29	8.60+20	1.76-09	3.19-05
4	708.1	6.88+04	4.82-02	415.	41.210	19.53	7.04+20	2.15-09	3.10-05
8	677.1	5.34+04	3.91-02	406.	41.210	18.75	5.71+20	2.65-09	3.00-05
12	645.7	4.09+04	3.14-02	397.	41.210	17.96	4.59+20	3.30-09	2.89-05
16	613.9	3.10+04	2.50-02	388.	41.210	17.16	3.66+20	4.14-09	2.78-05
20	581.6	2.31+04	1.97-02	378.	41.210	16.34	2.88+20	5.25-09	2.67-05
24	548.7	1.70+04	1.53-02	368.	41.210	15.51	2.24+20	6.75-09	2.56-05
28	515.1	1.22+04	1.18-02	358.	41.210	14.65	1.72+20	8.80-09	2.44-05
32	480.9	8.62+03	8.89-03	347.	41.210	13.77	1.30+20	1.17-08	2.31-05
36	446.1	5.92+03	6.58-03	335.	41.210	12.81	9.61+19	1.58-08	2.16-05
40	409.8	3.94+03	4.77-03	322.	41.210	11.82	6.97+19	2.17-08	2.02-05
44	376.3	2.53+03	3.34-03	310.	41.210	10.51	4.87+19	3.11-08	1.86-05
48	351.5	1.57+03	2.21-03	301.	41.210	9.19	3.24+19	4.68-08	1.74-05
52	318.7	9.38+02	1.46-03	288.	41.210	9.36	2.13+19	7.10-08	1.58-05
56	283.5	5.27+02	9.22-04	273.	41.210	7.99	1.35+19	1.12-07	1.42-05
60	253.0	2.77+02	5.42-04	260.	41.210	7.12	7.92+18	1.91-07	1.27-05
64	233.0	1.36+02	2.90-04	251.	41.210	6.12	4.23+18	3.58-07	1.18-05
68	219.5	6.34+01	1.43-04	244.	41.210	5.46	2.09+18	7.24-07	1.12-05
72	206.4	2.83+01	6.80-05	237.	41.210	5.26	9.93+17	1.52-06	1.06-05
76	192.4	1.19+01	3.08-05	229.	41.210	4.81	4.50+17	3.37-06	.98-05
80	181.0	4.77+00	1.31-05	222.	41.210	4.52	1.91+17	7.94-06	.90-05
84	173.8	1.81+00	5.17-06	218.	41.210	4.24	7.56+16	2.00-05	.86-05
88	169.6	6.69-01	1.95-06	215.	41.210	4.04	2.86+16	5.30-05	.83-05
92	166.4	2.42-01	7.20-07	213.	41.210	3.97	1.05+16	1.44-04	.81-05
96	163.8	8.59-02	2.60-07	211.	41.210	3.86	3.80+15	3.99-04	.80-05
100	163.0	3.03-02	9.21-08	211.	41.210	3.85	1.35+15	1.13-03	.79-05
110[c]	171.0	2.27-03	6.57-09	216.	41.210	3.85	9.60+13	1.58-02	.84-05
120	203.9	2.24-04	5.23-10	241.	39.629	4.14	7.94+12	1.90-01	1.05-05
130	214.0	4.24-05	6.34-11	300.	26.595	5.24	1.44+12	1.05+00	1.10-05
140	272.3	1.90-05	1.05-11	487.	12.570	7.27	5.05+11	2.99+00	1.36-05
150	399.3	1.41-05	3.17-12	750.	7.449	11.67	2.56+11	5.90+00	1.96-05
160	555.8	1.23-05	1.55-12	987.	5.841	18.20	1.60+11	9.45+00	2.57-05
170	675.4	1.12-05	1.03-12	1148.	5.180	29.21	1.20+11	1.26+01	2.97-05
180	760.0	1.04-05	7.99-13	1256.	4.836	43.66	9.95+10	1.52+01	3.23-05
190	826.0	9.83-06	6.63-13	1335.	4.631	58.36	8.62+10	1.75+01	3.41-05
200	862.3	9.31-06	5.84-13	1382.	4.497	83.96	7.82+10	1.93+01	3.52-05
210	890.2	8.85-06	5.27-13	1418.	4.403	101.14	7.20+10	2.09+01	3.60-05
220	905.9	8.44-06	4.85-13	1442.	4.334	126.91	6.74+10	2.24+01	3.64-05
230	916.7	8.05-06	4.52-13	1459.	4.281	144.98	6.36+10	2.37+01	3.68-05
240	922.8	7.69-06	4.25-13	1470.	4.240	164.51	6.04+10	2.50+01	3.69-05
250	926.8	7.35-06	4.01-13	1479.	4.207	177.86	5.74+10	2.63+01	3.70-05
260	926.9	7.03-06	3.81-13	1484.	4.179	198.55	5.49+10	2.75+01	3.70-05
270	926.9	6.73-06	3.63-13	1485.	4.156	203.38	5.26+10	2.87+01	3.70-05
280	927.0	6.44-06	3.46-13	1492.	4.137	208.52	5.03+10	3.00+01	3.70-05
290	927.1	6.17-06	3.30-13	1495.	4.120	212.61	4.82+10	3.13+01	3.71-05
300	927.1	5.91-06	3.15-13	1498.	4.106	216.26	4.61+10	3.27+01	3.71-05
310	927.2	5.66-06	3.00-13	1500.	4.093	219.53	4.42+10	3.41+01	3.71-05
320	927.2	5.42-06	2.87-13	1502.	4.082	222.51	4.24+10	3.56+01	3.71-05
330	927.3	5.20-06	2.75-13	1504.	4.073	225.22	4.06+10	3.72+01	3.71-05

TABLE VI-9. (Concluded)

Altitude (km)	Temperature (K)	Pressure (mb)	Density (g/cm^3)	Speed of Sound (m/s)	Molecular Mass (g/g mole)	Density Scale Height (km)	Number Density (per cm^3)	Mean Free Path (m)	Viscosity (kg m·s)
340	927.4	4.99-06	2.63-13	1505.	4.065	227.71	3.89-10	3.88-01	3.71-05
350	927.4	4.78-06	2.52-13	1507.	4.057	230.01	3.73-10	4.04+01	3.71-05
360	927.5	4.59-06	2.41-13	1508.	4.051	232.14	3.58-10	4.21+01	3.71-05
370	927.5	4.40-06	2.31-13	1509.	4.046	234.12	3.44-10	4.39-01	3.71-05
380	927.6	4.22-06	2.21-13	1510.	4.041	235.97	3.30-10	4.58-01	3.71-05
390	927.7	4.05-06	2.12-13	1511.	4.036	237.71	3.16-10	4.77-01	3.71-05
400	927.7	3.89-06	2.03-13	1512.	4.033	239.34	3.04-10	4.97-01	3.71-05
425	927.9	3.51-06	1.83-13	1513.	4.025	243.04	2.74-10	5.50-01	3.71-05
450	928.0	3.18-06	1.66-13	1514.	4.019	246.32	2.48-10	6.08+01	3.71-05
475	928.2	2.88-06	1.50-13	1515.	4.015	249.27	2.24-10	6.72-01	3.71-05
500	928.3	2.61-06	1.35-13	1516.	4.012	251.98	2.03+10	7.42-01	3.71-05
525	928.5	2.36-06	1.23-13	1517.	4.010	254.52	1.84-10	8.19-01	3.71-05
550	928.6	2.14-06	1.11-13	1517.	4.008	256.93	1.67+10	9.03+01	3.71-05
575	928.7	1.93-06	1.01-13	1517.	4.007	259.24	1.52-10	9.94+01	3.71-05
600	928.9	1.77-06	9.18-14	1518.	4.006	261.48	1.38+10	1.09+02	3.71-05
625	929.0	1.61-06	8.34-14	1518.	4.005	263.68	1.25+10	1.20+02	3.71-05
650	929.2	1.46-06	7.59-14	1518.	4.005	265.83	1.14+10	1.32+02	3.71-05
675	929.3	1.33-06	6.91-14	1518.	4.004	267.96	1.04+10	1.45-02	3.71-05
700	929.4	1.22-06	6.30-14	1518.	4.004	270.08	9.47+09	1.59+02	3.71-05
725	929.6	1.11-06	5.74-14	1519.	4.004	272.18	8.64+09	1.75+02	3.71-05
750	929.7	1.01-06	5.24-14	1519.	4.004	274.28	7.89-09	1.91+02	3.71-05
775	929.9	9.24-07	4.79-14	1519.	4.003	276.38	7.20+09	2.10+02	3.71-05
800	930.0	8.45-07	4.37-14	1519.	4.003	278.47	6.58+09	2.29+02	3.71-05
825	930.1	7.73-07	4.00-14	1519.	4.003	280.57	6.02+09	2.51+02	3.71-05
850	930.2	7.07-07	3.66-14	1519.	4.003	282.67	5.51+09	2.74+02	3.71-05
875	930.4	6.48-07	3.35-14	1519.	4.003	284.77	5.04+09	2.99+02	3.71-05
900	930.5	5.93-07	3.07-14	1519.	4.003	286.88	4.62-09	3.27+02	3.72-05
925	930.6	5.44-07	2.82-14	1519.	4.003	288.99	4.24+09	3.56-02	3.72-05
950	930.8	4.99-07	2.58-14	1520.	4.003	291.12	3.89+09	3.88+02	3.72-05
975	930.9	4.58-07	2.37-14	1520.	4.003	293.24	3.57-09	4.23+02	3.72-05
1000	934.2	4.21-07	2.17-14	1522.	4.003	236.80	3.27+09	4.62-02	3.73-05

a. A one- or two-digit number (preceded by a plus or minus sign) following an entry indicates the power of ten by which that entry should be multiplied.

b. Corresponds to planetary radius of 6050 km.

c. Density is 1.37×10^{-9} g/cm^3 at the turbopause (lower boundary of upper atmosphere).

TABLE VI-10. 1972 VENUS ATMOSPHERE (MODEL VI) (MAXIMUM MOLECULAR MASS AND NIGHT-SIDE EXOSPHERIC TEMPERATURE)[a]

Altitude (km)	Temperature (K)	Pressure (mb)	Density (g/cm^3)	Speed of Sound (m/s)	Molecular Mass (g/g mole)	Density Scale Height (km)	Number Density (per cm^3)	Mean Free Path (m)	Viscosity (kg/m·s)
-4	803.1	1.23+05	8.09-02	424.	44.010	20.39	1.11+21	1.30-09	3.34-05
0[b]	772.5	9.66+04	6.62-02	416.	44.011	19.65	9.06+20	1.59-09	3.25-05
4	741.5	7.54+04	5.38-02	408.	44.011	18.94	7.37+20	1.96-09	3.16-05
8	710.2	5.82+04	4.34-02	400.	44.011	18.21	5.94+20	2.43-09	3.07-05
12	678.5	4.45+04	3.47-02	392.	44.011	17.47	4.75+20	3.04-09	2.97-05
16	646.3	3.35+04	2.75-02	383.	44.011	16.72	3.76+20	3.84-09	2.86-05
20	613.7	2.49+04	2.15-02	374.	44.011	15.95	2.94+20	4.90-09	2.75-05
24	580.5	1.82+04	1.66-02	364.	44.011	15.17	2.28+20	6.34-09	2.64-05
28	546.7	1.31+04	1.27-02	355.	44.011	14.37	1.74+20	8.30-09	2.52-05
32	512.1	9.22+03	9.53-03	344.	44.011	13.54	1.30+20	1.11-08	2.40-05
36	476.6	6.33+03	7.03-03	333.	44.011	12.73	9.62+19	1.50-08	2.26-05
40	437.8	4.21+03	5.10-03	320.	44.011	11.82	6.97+19	2.07-08	2.10-05
44	402.0	2.71+03	3.56-03	308.	44.011	10.51	4.88+19	2.95-08	1.96-05
48	375.5	1.68+03	2.37-03	299.	44.011	9.20	3.24+19	4.45-08	1.83-05
52	340.5	1.00+03	1.56-03	286.	44.011	9.36	2.13+19	6.76-08	1.66-05
56	302.8	5.64+02	9.86-04	271.	44.011	8.00	1.35+19	1.07-07	1.49-05
60	270.3	2.96+02	5.80-04	258.	44.011	7.13	7.94+18	1.82-07	1.33-05
64	248.9	1.46+02	3.10-04	249.	44.011	6.12	4.24+18	3.40-07	1.23-05
68	234.5	6.79+01	1.53-04	242.	44.011	5.47	2.10+18	6.87-07	1.17-05
72	219.4	3.03+01	7.31-05	235.	44.011	5.31	1.00+18	1.44-06	1.10-05
76	202.6	1.27+01	3.31-05	227.	44.011	4.76	4.53+17	3.18-06	1.03-05
80	190.0	4.98+00	1.39-05	220.	44.011	4.46	1.90+17	7.59-06	.95-05
84	182.0	1.86+00	5.42-06	215.	44.011	4.16	7.41+16	1.94-05	.89-05
88	177.0	6.72-01	2.01-06	212.	44.011	3.96	2.75+16	5.24-05	.86-05
92	173.0	2.37-01	7.24-07	209.	44.011	3.88	9.91+15	1.45-04	.84-05
96	169.6	8.16-02	2.55-07	207.	44.011	3.76	3.49+15	4.14-04	.82-05
100	168.0	2.78-02	8.75-08	206.	44.011	3.73	1.20+15	1.20-03	.81-05
110	171.0	1.84-03	5.70-09	208.	44.011	3.68	7.79+13	1.85-02	.82-05
120	203.9	1.53-04	3.98-10	227.	44.011	4.05	5.45+12	2.64-01	1.04-05
130	214.0	1.79-05	4.44-11	232.	44.011	4.70	6.07+11	2.37+00	1.08-05
140	232.0	2.39-06	5.45-12	241.	44.011	4.97	7.46+10	1.93+01	1.16-05
150[c]	239.0	3.56-07	7.89-13	244.	44.011	5.26	1.08+10	1.34+02	1.19-05
160	242.0	5.56-08	1.22-13	246.	44.011	5.39	1.66+09	8.66+02	1.20-05
170	245.0	8.94-09	1.93-14	247.	44.011	5.48	2.64+08	5.46+03	1.22-05
180	248.0	1.48-09	3.15-15	248.	44.011	5.56	4.31+07	3.34+04	1.23-05
190	249.0	2.49-10	5.29-16	249.	44.011	5.63	7.24+06	1.99+05	1.23-05
200	249.0	4.24-11	9.01-17	249.	44.011	5.66	1.23+06	1.17+06	1.23-05

a. A one- or two-digit number (preceded by a plus or minus sign) following an entry indicates the power of ten by which that entry should be multiplied.

b. Corresponds to planetary radius of 6050 km.

c. Density is 1.46×10^{-13} g/cm^3 at the turbopause (lower boundary of upper atmosphere).

6.1.6.5 Ionosphere

The theoretical thermal model of Reference VI-1 should be used for computing the temperature and density of the ionosphere. The following peak values for electron density should be used:

Day Side	$5 \times 10^5/cm^3$
Night Side	$2 \times 10^4/cm^3$

6.1.7 Clouds — Tentative Data

Two cloud layers have been identified, but cloud models are speculative. The following data for clouds have been proposed but should be regarded as tentative

Cloud Layer	Altitude above Mean Surface (km)	Temperature (K)	Composition
Upper, or Haze	81 (top)	180	$HCl—H_2O$
Lower, Second, or Visible	60 (top)	260	Hg_2Cl_2
(not visible)	~ 53 (base)	~ 330	Hg
(not visible)	~ 51 (base)	~ 345	HgS
(not visible)	47 (base)	375	Hg_2I_2
(not visible)	44 (base)	400	Hg_2Br_2

Because wavelengths below 3 cm are severely attenuated, all communication wavelengths should be above 5 cm.

6.1.8 Circulation [VI-1]

Slow rotational speed will cause the atmosphere fluid to rise near the subsolar point and subside near the antisolar point in a symmetrical regime. However, at higher altitudes, a symmetric regime similar to that of a rotating planet may be predominant; i.e., where ascent occurs near the equator and descent occurs near the poles.

For design purposes the following should be used:

Mean horizontal wind speed at surface	30 ms^{-1}
Mean horizontal wind speed at cloud altitudes	100 ms^{-1}
Maximum wind shear	0.05 ms^{-1} m^{-1}

6.1.9 Radiation Environment

6.1.9.1 Galactic Radiation

Same as Interplanetary Space (see Section 1.3.1).

6.1.9.2 Solar Cosmic Radiation

Same as Interplanetary Space (see Section 1.3.2).

6.1.9.3 Magnetically Trapped Radiation

Based on Mariner 5 and Venera 4 data, the apparently small magnetic field of Venus would seem to preclude the existence of any significant radiation belts about the planet as compared to earth.

6.1.9.4 Thermal Radiation

Thermal radiation varies from ~ 238 W/m^2 at 200 km to ~ 9 W/m^2 at $\sim 2 \times 10^4$ km. Dark-side radiation is the same as above, although flux is subject to question due to uncertainty in planet atmosphere and surface temperatures. Thermal radiation will consist predominently of radiation from ~ 2 to 10 μm wavelength.

$$Q = FAI \quad ,$$

where

Q = the thermal radiation flux incident upon vehicle (W/m^2)

F = view factor (varies with altitude above the planet and vehicle shape)

A = the cross-sectional area of exposed spherical surface (m^2)

I = Venus thermal radiation flux (160 W/m^2).

6.1.9.5 Albedo Radiation [VI-1]

Albedo radiation varies from $\sim 3 \times 10^3$ W/m^2 at ~ 200 km to ~ 90 W/m^2 at $\sim 2 \times 10^4$ under maximum conditions (zero phase angle and normal to flux). Spectral distribution of albedo radiation is expected to approximate the solar spectrum. Albedo radiation will contribute ~ 90 percent of the total radiation from the planet upon the spacecraft.

$$Q = FASa \quad ,$$

where

Q = the incident albedo radiation flux (W/m^2)

F = the view factor

A = the cross-sectional area of exposed spherical surface (m^2)

S = solar constant at the Venus (W/m^2)

a = Venus albedo.

The thermal and albedo radiation values given in the following table were calculated with an albedo of 0.76 and a solar constant of 2676 W/m^2. More recent data have indicated the solar constant to be 2586 W/m^2 and the albedo to be 0.70.

Venus Thermal and Albedo Radiation Upon a Spherical Satellite

Altitude (km)	Thermal (W/m^2)	Albedo (W/m^2)
200	238	3000
400	208	2660
600	189	2400
1 000	152	1920
4 000	67	770
8 000	35	354
20 000	9	89

6.1.10 Meteoroid Environment

6.1.10.1 Cometary Meteoroid Flux

The flux (F_c), in number/m^2 s^2, of cometary meteoroids of mass m or greater on a randomly tumbling surface is: for $10^{-6} \leqq m \leqq 10^2$,

$$\log F_c = -14.202 - 1.213 \log m + \log \left(1 + \frac{0.469}{r}\right) + \log \frac{1}{2}\left[1 + \left(1 - \frac{1}{r^2}\right)^{1/2}\right] + \log V_c \quad .$$

For $10^{-12} \leqq m \leqq 10^{-6}$,

$$\log F_c = -14.171 - 1.584 \log m - 0.063 (\log m)^2 + \log \left(1 + \frac{0.469}{r}\right) + \log \frac{1}{2}\left[1 + \left(1 - \frac{1}{r^2}\right)^{1/2}\right] + \log V_c \quad ,$$

where r is the distance of spacecraft from the center of the planet (in units of the planet's radius).

6.1.10.2 Average Velocity of Cometary Meteoroids

The average velocity of cometary meteoroids relative to the spacecraft is 22.86×10^3 m/s.

6.1.10.3 Survival Mass [VI-4]

The survival mass for micrometeoroids can be calculated as a function of height in the atmosphere by using the following approximate expression:

$$m^{1/3} - m_\infty^{1/3} = \frac{\Lambda A \rho_m^{-2/3} v^2}{6 \xi \cos Z} \int_\infty^h \rho_a \, dh$$

(does not hold for dustballs), where

$$\text{columnar mass} = -\int_{h}^{\infty} \rho_a \, dh$$

Z = zenith angle

ρ_m = density of micrometeoroid ($3.5 > \rho_m > 0.5$ g/cm^3)

v = velocity of micrometeoroid ($v_{parabolic}$ or $v_{orbital} > v > v_{escape}$)

A = shape factor = 1.2 for sphere

$\Lambda/\xi = 10^{-11.449}$.

6.1.11 Magnetic Environment

6.1.11.1 Magnetic Field [VI-31]

From Mariner 5 data, the upper limit to the magnetic dipole moment of Venus is estimated to be within a factor of 2 of 10^{-3} times that of the earth.

6.1.12 Astrodynamic Constants [VI-32]

Distance from sun (average)	1.082×10^8 km
Eccentricity of orbit	0.0067921
Inclination of orbit to ecliptic	3 deg 23 min 39.2 s
Orbital period (sidereal)	224.70080 days
Radius (equatorial)	6050 km
Mass ratio (sun/planet)	408 522 ± 3
Flattening (dynamic)	Unknown

	Average density[3]	5.087 g/m^3
	Rotational period	242.6 days
	Gravitational parameter	3.24860×10^5 km^3/s^2

6.1.13 Additional Information

A more detailed discussion of the Venus atmosphere is given in References VI-1 and VI-29.

6.2 Surface Environment

6.2.1 Temperature

Measurements from the earth indicate a surface temperature of about 600 to 650 K. Mariner 2 yielded 700 K, and Venera 7 yielded 747 K. Mariner 2 detected a large region, slightly cooler than the rest of the disc, that possibly represents the influence of a surface temperature.

6.2.2 Features

Since no breaks large enough to reveal the surface have ever been seen in the clouds, no telescopic surface data exist. Radar studies have shown areas of enhanced surface roughness. Recent probes have revealed new information.

6.2.3 Terrain and Composition

Though the surface has never been seen by earth based telescopes, it is generally agreed that it is probably dry, dusty, rocky, and windy.

6.2.4 Dielectric Constant

Radar data indicate a value of 2 to 4 [VI-33]. Recent data by JPL [VI-34] indicate a value of 2.5 as a mean dielectric constant based on data obtained using a high resolution twin-dish interferometer radio telescope.

6.3 Satellites

None observed [VI-35].

REFERENCES

VI-1. Anon.: Models of Venus Atmosphere (1972). NASA Space Vehicle Design Criteria (Environment), NASA SP-8011, Revised September 1972.

VI-2. Ingersoll, A. P., and Leovy, C. B.: The Atmospheres of Mars and Venus. Annual Reviews of Astronomy and Astrophysics, vol. 9, 1971, pp. 147-182.

VI-3. Anon.: Planetary Explorer Phase A Report and Universal Bus Description. NASA Goddard Space Flight Center, May 1971.

VI-4. Mueller, H.: Some Results of the Flight of Mariner 10 to Venus and Mercury Orion. Vol. 32, December 1974.

VI-5. Hansen, J. E.: The Atmosphere of Venus. Proceedings of a Conference held at Goddard Institute for Space Studies, October 15-17, 1974, NASA SP-382, 1975.

VI-6. Kuiper, G. P.: "On the Nature of the Venus Clouds," Planetary Atmospheres. IAU Symposium No. 40, Springer-Verlag (New York), 1971, pp. 91-109.

VI-7. Rea, D. G.: The Composition of the Upper Clouds of Venus. Reviews of Geophysics and Space Physics, vol. 10, no. 1, February 1972, pp. 369-378.

VI-8. Hansen, J. E., and Arking, A.: Clouds of Venus: Evidence for their Nature. Science, vol. 171, February 19, 1971, pp. 669-672.

VI-9. Sagan, C., and Pollack, J. B.: On the Structure of the Venus Atmosphere. Icarus 10, 1969, pp. 274-289.

VI-10. Campbell, D. B., et al.: Venus: Topography Revealed by Radar Data. Science, vol. 175, February 4, 1972, pp. 514-516.

VI-11. Hall, R. W., and Branson, N. F. B. A.: High Resolution Radio Observations of the Planet Venus at a Wavelength of 6 cm. Monthly Notes Royal Astronomical Society, 151, 1971, pp. 185-196.

REFERENCES (Continued)

VI-12. Sinclair, A. C. E., et al.: Preliminary Report on Interferometer Observations of Venus at 11.1 cm Wavelength. Radio Science, vol. 5, 1970, pp. 347-354.

VI-13. Avduevsky, V. S., Marov, M. Ya, and Rozhdestvensky, M. K.: The Atmosphere of the Planet Venus from Data of the Soviet Space Probe Venera 4. Space Research IX, 11th Plenary Meeting of COSPAR, North-Holland Publishing Co. (Amsterdam), 1969, pp. 745-759.

VI-14. Kliore, A., and Cain, D. L.: Mariner 5 and the Radius of Venus. Journal of the Atmospheric Sciences, vol. 25, no. 4, July 1968, pp. 549-554.

VI-15. Hunten, D. M., and McElroy, M. B.: The Upper Atmosphere of Venus: The Regulus Occultation Reconsidered. Journal of Geophysical Research, vol. 73, no. 13, July 1, 1968, pp. 4446-4448.

VI-16. Avduevsky, V. S., Marov, M. Ya., and Rozhdestvensky, M. K.: A Tentative Model of the Venus Atmosphere Based on the Measurements of Veneras 5 and 6. Journal of the Atmospheric Sciences, vol. 27, no. 4, July 1970, pp. 561-568.

VI-17. Avduevsky, V. S., Marov, M. Ya., and Rozhdestvensky, M. K.: Results of Measurements Made on Venera 5 and Venera 6 Space Probes and a Model of the Venusian Atmosphere. Cosmic Research, vol. 8, no. 6, Nov.-Dec. 1970, pp. 800-808.

VI-18. Vinogradov, A. P., Surkov, U. A., and Florensky, C. P.: The Chemical Composition of the Venus Atmosphere Based on the Data of the Interplanetary Station Venera 4. Journal of the Atmospheric Sciences, vol. 25, no. 4, July 1968, pp. 535-536.

VI-19. Vinogradov, A. P., et. al.: The Chemical Composition of the Atmosphere of Venus. Planetary Atmospheres, IAU Symposium No. 40, Springer-Verlag (New York), 1971, pp. 3-16.

VI-20. Mikhnevich, V. V., and Sokolov, V. A.: A Model Atmosphere of Venus Based on the Results of Direct Temperature and Density Measurements. Cosmic Research, vol. 7, no. 2, March-April, 1969, pp. 197-208.

REFERENCES (Continued)

VI-21. Mikhnevich, V. V., and Sokolov, V. A.: Temperature and Density of the Venus Atmosphere According to Measurements Obtained by Venera 4. Space Research IX, 11th Plenary Meeting of COSPAR, North-Holland Publishing Co. (Amsterdam), 1969, pp. 730-744.

VI-22. Avduevsky, V. S., Marov, M. Ya., and Rozhdestvensky, M. K.: Results of Measurement of Parameters of the Atmosphere of Venus by the Soviet Probe Venus 4. Cosmic Research, vol. 7, no. 2, March-April 1969, pp. 209-220.

VI-23. Kliore, A., et. al.: Structure of the Atmosphere of Venus Derived from Mariner V S-Band Measurements. Space Research IX, 11th Plenary Meeting of COSPAR, North-Holland Publishing Co. (Amsterdam), 1969, pp. 712-729.

VI-24. Fjeldbo, G., Kliore, A. J., and Eshleman, V. R.: The Neutral Atmosphere of Venus as Studied with the Mariner V Radio Occultation Experiments. The Astronomical Journal, vol. 76, no. 2, March 1971, pp. 123-140.

VI-25. Fjeldbo, G., and Eshleman, V. R.: Atmosphere of Venus as Studied with the Mariner 5 Dual Radio-Frequency Occultation Experiment. Radio Science, vol. 4, no. 10, October 1969, pp. 879-897.

VI-26. Barth, C. A.: Interpretation of the Mariner 5 Lyman Alpha Measurements. Journal of Atmospheric Sciences, vol. 25, 1968, p. 564-567.

VI-27. Barth, C. A.: Exospheric Temperature of Venus from Mariner 5. Planetary Atmospheres, IAU Symposium No. 40, Springer-Verlag (New York), 1971, pp. 17-22.

VI-28. Kerzhanovich, V. V., Andreev, B. N., and Gotlib, V. M.: Investigation of the Dynamics of the Atmosphere of Venus with Automatic Interplanetary Stations Venera 5 and Venera 6. Soviet Physics-Doklady, vol. 15, no. 9, March 1971, pp. 797-799.

VI-29. Pitts, D.: A Computer Program for Calculating Model Planetary Atmospheres. NASA TN D-4292, 1968.

REFERENCES (Concluded)

VI-30. Marov, M. Ya.: Venus: A Perspective at the Beginning of Planetary Exploration. Icarus, vol. 16, no. 3, June 1972, pp. 415-461.

VI-31. Reese, David E., and Swan, R.: Venera 4 Probes Atmosphere of Venus. Ames Research Center and Office of Adv. Res. and Tech., Moffett Field, California, Science, vol. 159, January 25, 1968.

VI-32. Melbourne, W. G., Mulholland, J. D., Sjogren, W. L., and Sturms, F. M., Jr.: Constants and Related Information for Astrodynamic Constants, 1968. Technical Report 32-1306, Jet Propulsion Laboratory, July 1968.

VI-33. Mayer, Cornell H.: Radioastronomy Studies of Venus and Mars. Astronautics and Aeronautics, April 1966.

VI-34. Kliore, A., Levy, G. S., Cain, D. L., Fjeldbo, G., and Rasool, S. I.: Atmosphere and Ionosphere of Venus from the Mariner V S-Band Radio Occultation Experiment. Science, vol. 158, December 11, 1967.

VI-35. Van Flandern, T. C. and Harrington, R. S.: A Dynamical Investigation of the Conjecture that Mercury is an Escaped Satellite of Venus. Icarus, vol. 28, August 1976, pp. 435-440.

SECTION VII. MARS

(FROM NASA SP-8010 and NASA SP-8020)

7.1 Atmospheric Environment (Based on VII-3)

Recently acquired Viking data (1976) are now in the process of extensive analysis and only preliminary results are available at this time [VII-2].

The need for information on the Martian atmosphere that could be used to develop atmospheric engineering models for spacecraft design purposes was recognized in the middle 1960s [VII-3]. Continuous observation of Mars from earth, particularly by radio and radar astronomy, and the successful flyby mission of Mariner 4 in 1965 provided new information that was incorporated into improved models. Since then, knowledge of the Martian atmosphere and of the planet itself has undergone many changes. The most significant information prior to Viking came from the Mariner 6, 7, and 9 experiments. The revised Mars engineering models for the Viking Project [VII-4] were developed on the basis of new findings from Mariner 6, 7, and 9. For a discussion of engineering models, the Martian atmosphere is divided into lower and upper regions as shown in Figure VII-1. Reference VII-5 provides an overview of the impact of Mariner 9 on the knowledge of Mars as well as a useful reference chart. Reference VII-6 gives a more detailed account. The following sections briefly describe the current status of information for the parameters needed to construct model atmospheres. (Viking preliminary results are presented in References VII-7, VII-8, VII-9, VII-10, VII-11, and VII-12.)

7.1.1 Lower Atmosphere

7.1.1.1 Surface Pressure

Modern Studies of the Martian atmospheric pressure began in 1963 with the spectroscopic study of Kaplan, Munch, and Spinrad. Grandjean and Goody used the observation of carbon dioxide (CO_2) to determine the relationship between the surface pressure and the total volume fraction of CO_2. The full significance of this result was not appreciated because of the then prevailing theories that favored high values for atmospheric pressure. Goody noted that the assumption of a pure CO_2 atmosphere led to a lower limit for the surface pressure of 13 mb. Another analysis made by Belton and Hunten gave 5.5 ± 0.5 mb. Low pressure was also derived by Musman and Evans from Martian ultraviolet albedos. Musman used an albedo for the total disc obtained photoelectrically by de Vaucouleurs. With assumptions of no absorbing atmospheric constituents,

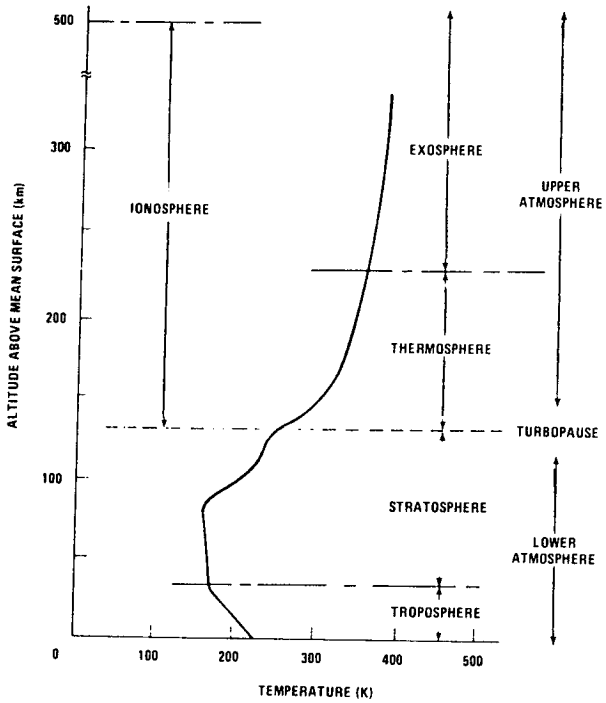

Figure VII-1. Atmospheric regions of Mars.
(For temperature profile see Fig. VII-15.)

no particles in the atmosphere that might contribute to the albedo, and a surface reflectivity of zero, Musman calculated a surface pressure of 27 mb for a pure N_2 atmosphere and 19 mb for a pure CO_2 atmosphere. On the other hand, Evans found surface pressures of 6 ± 3 mb for pure CO_2, 9 ± 4 mb for pure nitrogen (N_2), and 12 ± 6 mb for pure argon (A) atmospheres on the basis of an ultraviolet spectrum from 2400 to 3600 Å that was obtained by an Aerobee rocket [VII-3].

Through a careful examination of spectroscopic measurements, Wood concluded that the values of the surface pressure on Mars fall between 5 and 7 mb except for two measurements which yielded pressures of 4.4 mb and 8.0 mb. Wood derived a mean Martian surface pressure of 5.3 mb on the basis of spectroscopic measurements of CO_2 abundance [VII-3].

Additional information on the atmospheric pressure was obtained from Mariner 4, 6, and 7 occultation experiments in which changes in the frequency, phase, and amplitude of the S-band radio signal during passage through the atmosphere of Mars was observed immediately before and after occultation by the planet. Analysis of these effects yielded estimates of the refractivity and density of the atmosphere near the surface, the scale height in the atmosphere, and the electron density profile of the ionosphere. From these data, surface pressure was estimated in the 4.2 to 8.0 mb range [VII-3]. Preliminary Viking I surface pressure is about 7 mb at the landing site [VII-10].

Surface pressure results were derived from both ground-based observations and Mariner 9 experiments. Absorption of CO_2 in the Martian atmosphere (from which the partial pressure of CO_2 can be inferred) was measured from earth by means of a multislit spectrometer in 1969 and in 1971. These measurements, which provided moderate spatial resolution, covered about three-fourths of the circumference from 40 deg north to 20 deg south latitude in 1969 and almost all of the surface from 40 deg north to 60 deg south in 1971. The results of these measurements were in general agreement [VII-3].

An occultation experiment similar to those of Mariner 4, 6, and 7 was conducted on Mariner 9. The results were similar to the previous occultation results even though the measurements were made at a time when the entire planet was shrouded by a dust storm. This storm obscured the surface at wavelengths ranging from the ultraviolet to the infrared. Unlike earlier Mariners, Mariner 9 was placed in orbit around Mars so it provided occultation measurements over various regions. Measurements made in the equatorial regions resulted in an average surface pressure of about 4.95 mb without taking into account minimum and maximum measurements. The minimum surface pressure of approximately 2.8 mb was measured in the Phoenicis Lacus region of the Tharsis ridge area as well as in the Claritas area at approximately 34.5 deg south latitude. The highest surface pressure of 8.9 mb was measured at the bottom of the Hellas depression [VII-3].

Surface pressures at about 65 deg north latitude were considerably higher than those in the equatorial region. Pressures ranged from about 7.2 to 10.3 mb with a mean value of approximately 8.9 mb. The pressures derived from Mariner 9 occultation data are in agreement with earth-based spectroscopic results of Reference VII-3.

The difference in surface pressures shown by the spectroscopic and occultation results correlates with the topography of Mars.[1] Radar observations and spacecraft occultation experiments prior to 1969 showed that the elevation difference on Mars was about 12 km; other measurements indicated elevation variations of about 14 km. However, later topographic estimates that have been derived from occultation, radar, spectral, and optical measurements show a range of elevations from 4 km below the mean surface in Hellas depression to an altitude of 28 km on Olympus Mons as shown in Figure VII-2[2] [VII-3].

1. Besides variation with topography, seasonal variation of surface pressure by 10 to 20 percent is indicated in recent study by P.M. Woiceshyn, entitled "Global Seasonal Fluctuations on Mars," Icarus 22, July 1974.

2. Christensen, E. J.: Martian Topography Derived from Occultation, Radar, Spectral and Optical Measurements. Journal of Geophysical Research, to be published in 1975.

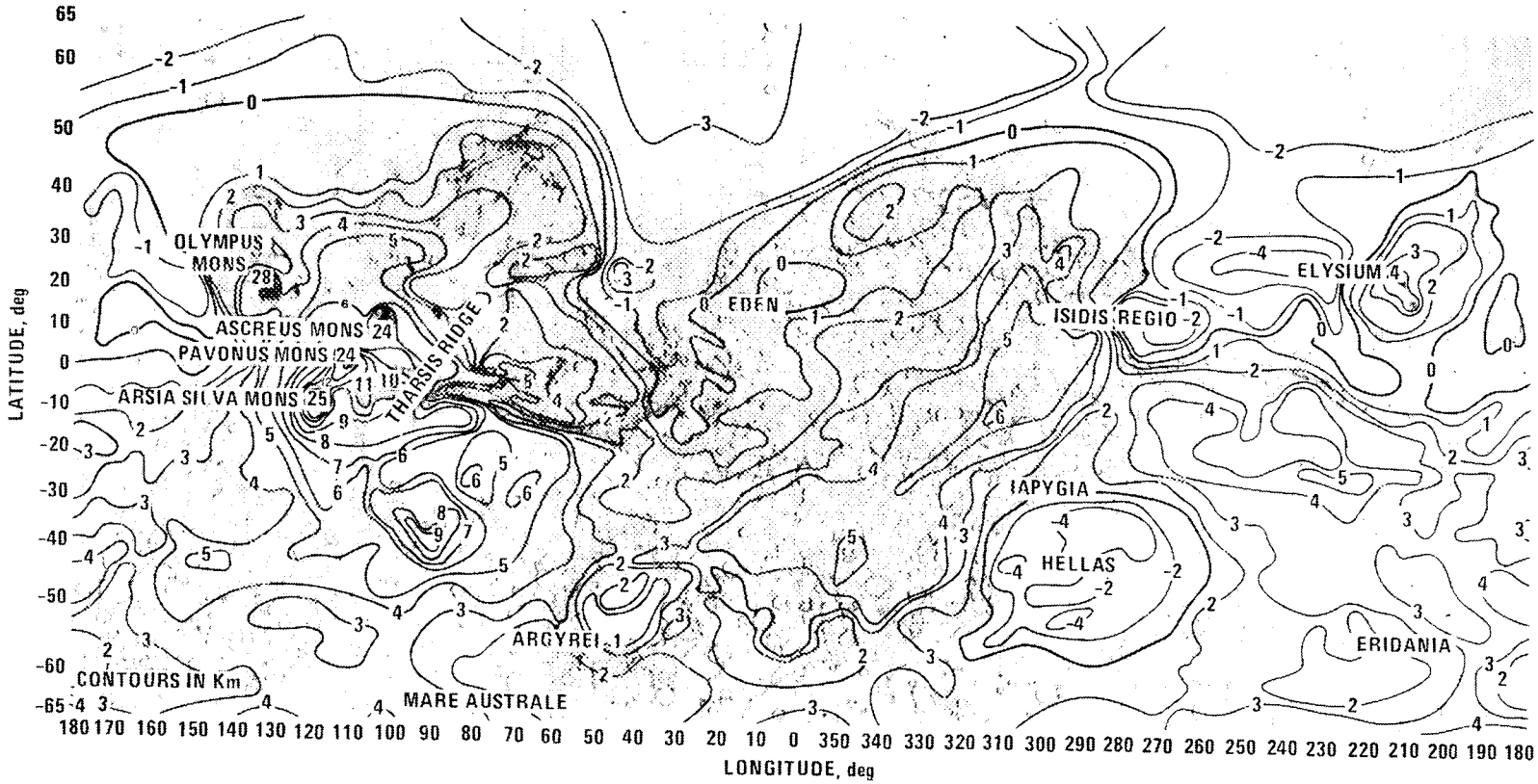

Figure VII-2. Topographic map of Mars (altitudes in km).

The surface pressure data achieved by the Mariner 9 occultation experiment strongly suggest that the physical shape of Mars is substantially more oblate than its gravitational equipotential surface and is approximated by a triaxial ellipsoid. Optical measurements of Mars indicate that the shape is an ellipsoid with an equatorial radius of 3398 ± 3 km and a polar radius of 3371 ± 4 km. Earth and Mariner 9 observations were combined to yield ellipsoid radii of 3400.12, 3394.19, and 3375.45 km.[3] The mean equatorial radius of Mars determined from combined radar data is 3394 ± 2 km [VII-3].

7.1.1.2 Composition and Molecular Mass

Present knowledge of the composition of the Martian atmosphere is based on spectroscopic observations and on theoretical deductions that certain gases are present. Additionally, the polarization and occultation measurements provide information on the total amount of gases. Table VII-1 from Reference VII-2 lists the abundances of all the observed and assumed constituents.

7.1.1.2.1 Major Constituents

Of the expected major constituents (N_2, CO_2, and A), only CO_2 has been observed spectroscopically. The amount of CO_2 reported lies within the range of 50 to 90 m-atm [VII-3], and the arithmetic mean of CO_2 abundance for the ten best measurements was 72 m-atm [VII-4]. A current value is 79 m-atm [VII-3]. On the basis of the observed spatial variations of total pressure, one would expect similar spatial variations for CO_2.

A small amount of nitrogen may be present in the Martian atmosphere even though it was not detected by the ultraviolet spectrometers on the Mariner 6, 7, and 9 spacecraft. From Mariner 6 and 7 evidence that the ionosphere of Mars contains CO_2^+ ions, Goody [VII-3] noted that the amount of nitrogen present in the Martian atmosphere must be less than 10 percent or else the ions would be OH^+ and CO^+. Dalgarno and McElroy [VII-3] estimated the maximum mole fraction of N_2 relative to CO_2 must be less than 5 percent on the basis of an analysis of dayglow data. It has been suggested [VII-4] that the presence of 1 percent nitrogen may be assumed for the purpose of calculating radio blackout phenomena.

The possibility of potassium compounds near the surface of Mars led to the long-held assumption that the Martian atmosphere contains some argon associated with the production of potassium 40 by radioactive decay.

3. D. L. Cain et al.: Approximations to the Mean Surface of Mars and Mars Atmosphere Using Mariner 9 Occultations. Chapter 37 of Mariner Mars 1971 Report Project Final Report, vol IV (Ref. 9), July 15, 1973, pp. 495-498.

TABLE VII-1. COMPOSITION OF THE MARTIAN ATMOSPHERE [VII-3]

Constituent	Abundance (cm atm)[a]
CO_2	7800
CO	5.6
O_2	10.4
H_2O	~3, variable
H_2	~0.4
O_3	$\sim 10^{-4}$
N_2	< 400
A + inert gases	< 1560
SO_2	$< 3 \times 10^{-3}$
N_2O	< 200
CH_4	< 10
C_2H_4	< 2
C_2H_6	< 1
NH_3	< 2
NO_2	$< 8 \times 10^{-4}$

a. These values give the abundance of each gas according to its thickness in cm if spread evenly over the planet. The uniform density is that for standard temperature and pressure (0°C and 760 mm Hg). 1 cm atm is equivalent to a 1 cm thickness and contains 2.69×10^{23} molecules/m^2.

The amount of argon in the Martian atmosphere is small according to Viking preliminary results [VII-10]. CO_2 is the only major constituent; inert species other than argon can account for at most 10 percent of the total atmospheric mass [VII-3, VII-13].

7.1.1.2.2 Minor Constituents

Besides water vapor and dust, minor identified constituents are CO, O_2, and O_3. Water vapor was first detected spectroscopically by Spinrad, Munch, and Kaplan. An analysis of the line intensities gave an average abundance of 14 ± 7 μm precipitable water over the entire planet. Other findings for H_2O were reported by Dollfus who gave a value of 45 μm precipitable water, the highest determination, and by Shorn et al. who estimated an abundance of 10 to 20 μm precipitable water from study of the lines of H_2O near 8200 Å with a new high-dispersion spectrograph during the 1964-65 apparition. The mean relative humidity of the Martian atmosphere may be as high as 50 percent [VII-3].

Seasonal and latitudinal variations of water vapor content have been reported by Tull who found that during the period from the middle summer to the middle autumn, the amount of precipitable water vapor reached as much as 48 μm in the northern hemisphere and 20 μm in the southern hemisphere. Schorn et al. reported that more precipitable water vapor was found in the northern hemisphere in the northern midspring and more in the southern hemisphere in the northern midsummer [VII-3].

Water vapor was identified conclusively from spectra obtained by the infrared interferometer spectroscopy (IRIS) experiment on Mariner 9. The total H_2O content was determined from a quantitative comparison of observed and synthesized spectra. This comparison indicated the abundance of water vapor at 10 to 20 μm of precipitable water. Water vapor data from the IRIS experiment are compared to earth-based observations in Figure VII-3. The data shown by the dashed lines were made concurrently with the IRIS data. Latitudinal gradients were not found to be significant from the South pole to the equator. The 1971 earth-based measurements and IRIS data are in general agreement; however, earth measurements in previous years during similar seasonal conditions indicated larger amounts of water vapor. Results from the 1.38 μm water vapor band experiment on the USSR Mars 3 indicate substantially lower water vapor amounts although the reason for an actual discrepancy is not clear [VII-3].

The average abundance of water vapor determined by IRIS was lower than values observed during previous oppositions. It is theorized that this could result from an unusually large amount of water trapped in the north polar cap (water vapor was not detected over the north polar hood) or that the large dust storm in late 1971 could have resulted in the adsorption of water vapor on the dust particles.

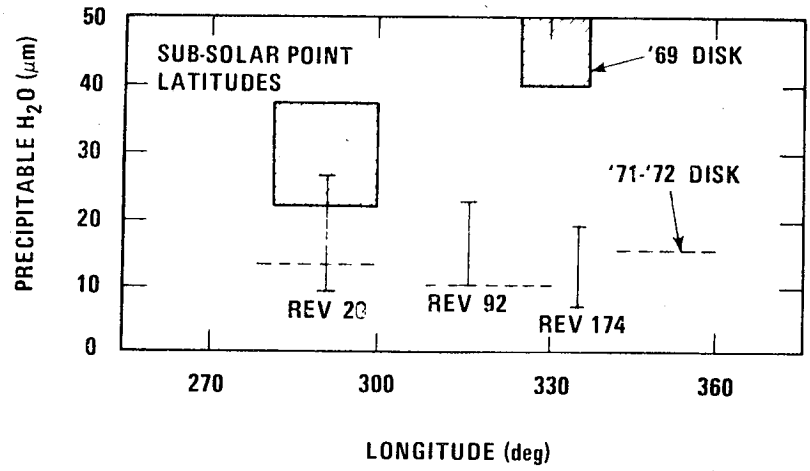

a. South subsolar point latitudes (20 to 30 deg south)

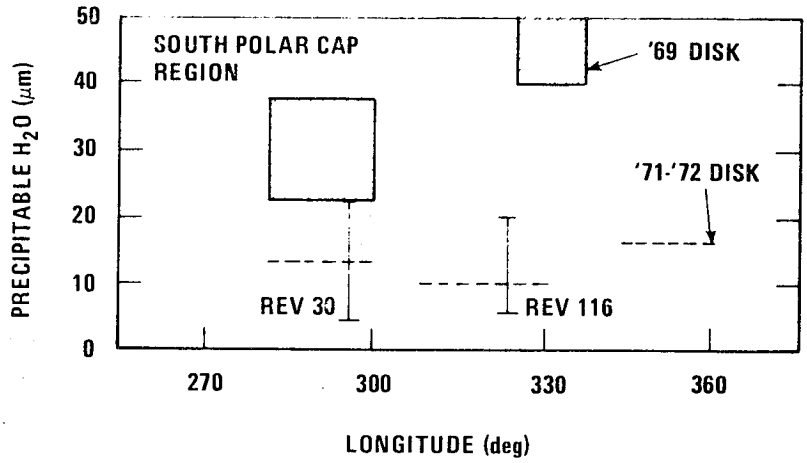

b. South polar cap region

BARKER et al.

TULL & BARKER

MARINER 9

Figure VII-3. Water vapor content of the Martian atmosphere [VII-3].

When Mariner 9 entered into orbit of Mars on November 14, 1971, the entire planet was shrouded by a dust storm. Thus, dust must be considered a likely atmospheric constituent. Comparison of Mariner 9 observations of the brightness of the dust storm with results from a simple multiple scattering theory leads to an albedo of about 0.7 for the particles. This is consistent with values for Martian surface albedo obtained from earth-based measurements. Therefore, the mean size and composition of the dust storm particles appear to be similar to those for particles on the Martian surface. The mean particle size of surface material has been estimated as between 10 and 300 μm [VII-3].

Because mineralogical characteristics determine the spectral position of absorption and transmission maxima, it is possible to infer the dust composition from Mariner 9 IRIS results. An empirical comparison of these data with laboratory transmission spectra of mineral dust indicates a SiO_2 content of 60 ± 10 percent [VII-3].

Other identified minor species of the lower Martian atmosphere are carbon monoxide (CO) detected by Kaplan et al., oxygen (O_2) observed by Carleton and Traub, and ozone (O_3) measured by Lane et al. Both CO and O_2 should be well mixed throughout the lower atmosphere of Mars. Their abundances are 5.6 cm-atm and 10.4 cm-atm, respectively [VII-3].

Ozone was observed by the Mariner 7 ultraviolet spectrometer experiment at the Martian south polar cap during its late spring season but nowhere else. Results from a similar experiment on Mariner 9 also indicated the presence of O_3 in the Martian atmosphere during the southern summer season. In the foregoing observations, ozone was detected only in the polar region north of 45 deg north, but it was subsequently detected in the southern hemisphere with the approach of the autumnal equinox. The presence of ozone appears to increase as the amount of water vapor in the atmosphere decreases [VII-3].

There are upper limits for the abundances of formaldehyde (HCHO), carbonyl sulfide (COS), ammonia (NH_3), methane (CH_4), and oxides of nitrogen such as NO_2, N_2O_4, NO, N_2O, and HNO_2. Theoretical models indicate expected densities for H_2O_2, H_2, H, OH, and HO_2 species that play a major role in the chemistry of the Martian atmosphere [VII-3].

7.1.1.2.3 Molecular Mass

From Mariner 4 occultation data, Spencer has shown for a mean temperature above the occultation point of 140 to 180 K, the allowable mean molecular weight could range from 33.1 to 50. Similarly, Hess and Pounder indicated that although the mean molecular weight estimated from the Mariner 4 data is between 33.2 and 39.2, a range of 31.2 is consistent with reliable spectroscopic data. More recently, both Mariner 6 and 7 occultation experiments indicated that the molecular weight of the Martian atmosphere is close to 44. Thus, the more recent data interpretations strongly favor a CO_2 rich atmosphere in which CO_2 accounts for at least 90 percent of the total atmospheric mass [VII-3].

7.1.1.3 Temperature

Numerous theoretical models have been developed to describe the thermal structure of the Martian atmosphere [VII-3]. These analyses are generally based on assumptions of radiative, convective, and conductive equilibrium for the Martian atmosphere and surface. One recent analysis [VII-14] also includes absorption of solar energy by a grey atmosphere such as might be caused by the global dust storm of 1971. These theoretical techniques are in general accord and demonstrate variation of temperature with latitude and season.

The vertical temperature structure of Mars has been determined from occultation experiments on Mariner 4 [VII-3], Mariner 6 and 7 [VII-3], and Mariner 9 [VII-3] and from the Mariner 9 IRIS experiment [VII-15]. Occultation results from Mariner 6 and 7 were compared to a revised model of the analysis developed by Leovy [VII-3]. Predictions by this model of the Martian atmospheric characteristics at the time of the Mariner 6 and 7 flybys were in excellent agreement with observed data. Mariner 9 IRIS results obtained during the global dust storm did not correlate well with the theoretical analyses for a dust-free atmosphere. However, Mariner 9 results were in reasonable agreement with the model of a dusty atmosphere presented by Gierasch and Goody [VII-14].

The 20 000 spectra from the Mariner 9 IRIS experiment indicated temperature variations with latitude, season, local time, topography, and secular events such as the global dust storm [VII-3]. Figure VII-4a shows variation with latitude and local time during the dust storm at altitudes of about 10 km (2 mb pressure level of the atmosphere). For the period after the dust storm, Figure VII-4b shows cooling of the atmosphere and shifting of the maximum temperature toward the subsolar point at the same altitudes. The

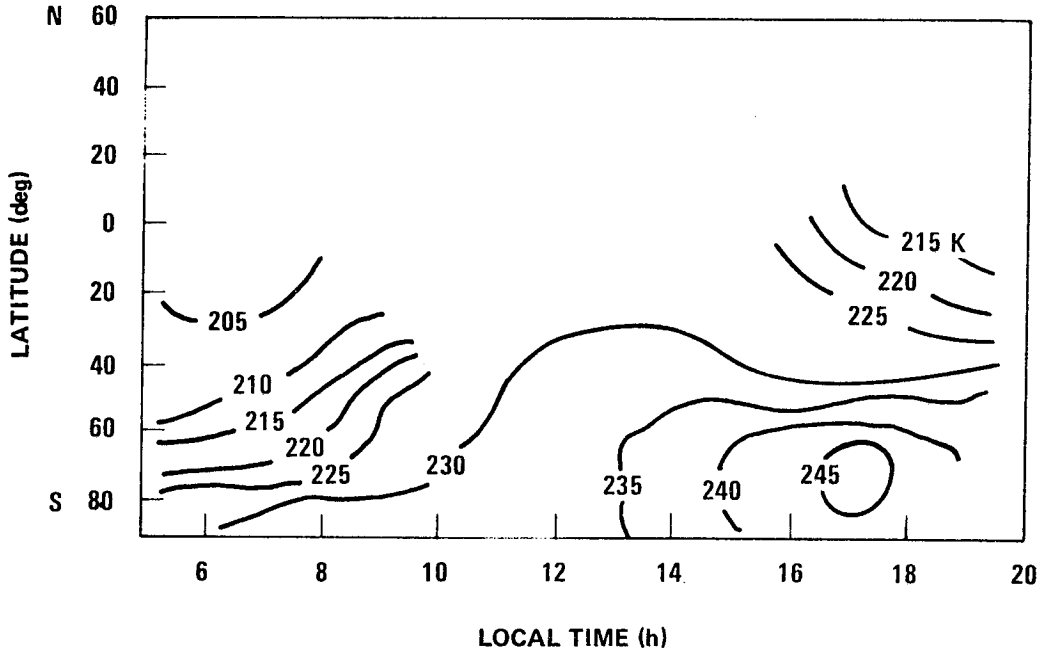

a. Revolutions 1-85 (dust storm)

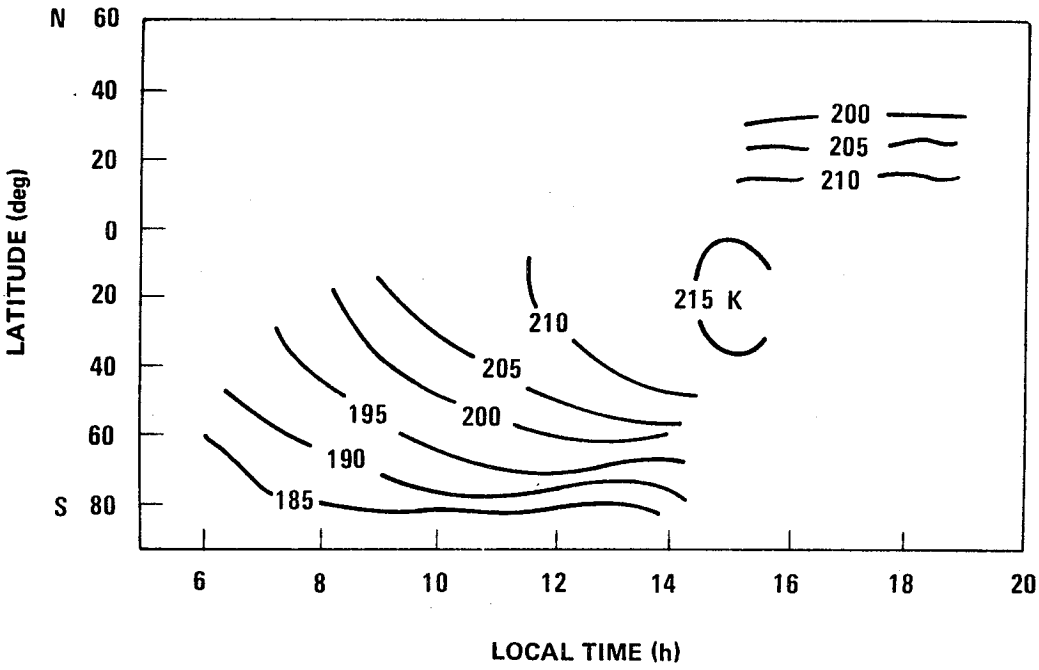

b. Revolutions 161-186 (clearing)

Figure VII-4. Variations of atmospheric temperature with latitude and local time at altitudes of about 10 km (2 mb pressure level) [VII-3].

isotherms were constructed from data averaged over 10 deg bands of latitude and 1 h intervals in Martian local time. The diurnal variations of 15 to 30 K were larger than expected from theoretical predictions.

At the surface, Figure VII-5[4] shows variation of temperature with latitude and local time during and after the dust storm [VII-3]. Maximum temperatures occurred near the subsolar point at both times with little change in the maximum.

Temperature profiles obtained from the Mariner 6 and 7 occultations are shown in Figure VII-6. The profiles are uncertain at high altitudes because of uncertainties in the motion of the spacecraft and in the refractivity of the ionosphere. These data indicate an extremely cold region in the middle atmosphere with a subadiabatic lapse rate of about 3.5 K/km. Mariner 9 occultation results were obtained during the global dust storm. Measurements at beginning of occultation were made in the equatorial region and measurements near the end at about 65 deg north latitude in the Martian early morning during midwinter. Therefore, the near-surface temperatures of 150 to 160 K obtained at the end of occultation were noticeably lower than at the beginning. Typical temperature profiles obtained from Mariner 9 IRIS are shown in Figure VII-7. The cooling of the atmosphere as the dust storm diminished is evident; however, in all cases the lapse rate remained subadiabatic [VII-3]. (Preliminary Viking I thermal mapping of the surface and atmosphere used a homogeneous thermal model based on Mariner 9 late observations [VII-9].)

7.1.1.4 Winds (Atmospheric Dynamics)

Information concerning Martian winds has been obtained from observation and theory. The observational input comes largely from the study of the motion of cloud systems in the Martian atmosphere although useful information has also been derived from analysis of temperature maps made by the IRIS instrument on Mariner 9. The theoretical work is based generally on the application of standard meteorological principles [VII-3].

Observational studies of Martian clouds have a lengthy history. Ground-based observations by Kuiper and de Vaucouleurs established the potential of the technique as a remote monitor of dynamic activity. They drew attention to a variety of interesting circulation phenomena. Their concepts have been followed in Mariner 9 experiments. The imaging experiment on this spacecraft provided superior spatial resolution and afforded an excellent opportunity for careful study of Martian meteorological phenomena [VII-3].

4. Figure VII-5 refers to the temperature on the surface. There is a large temperature drop in the first meter above the surface in the warmer parts of the day. In some temperature studies, the zero point for altitude is taken at the top boundary of this thin layer. (Preliminary Viking I results indicate the low temperature, near-surface layer might be stable, not withstanding an adverse stratification of the molecular weight [VII-9].)

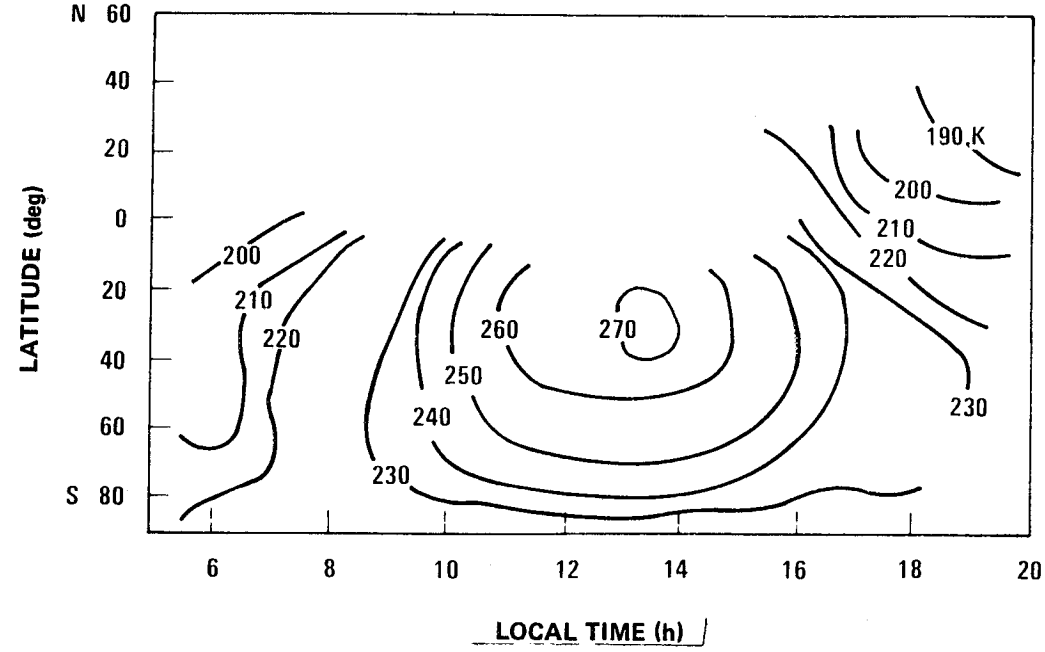

a. Revolutions 1-85 (dust storm)

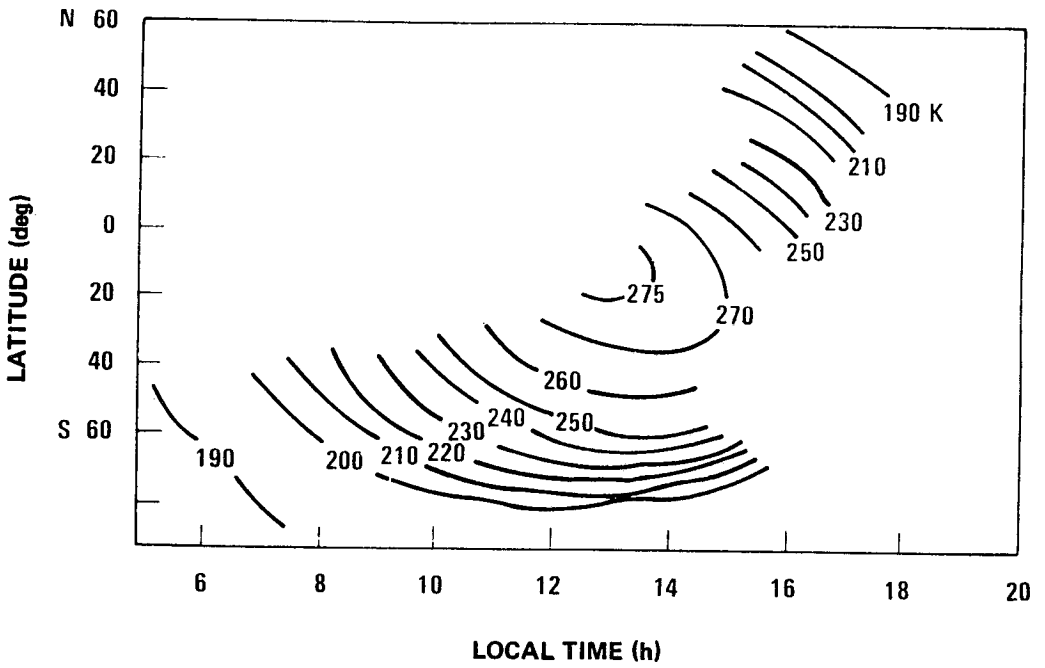

b. Revolutions 161-186 (clearing)

Figure VII-5. Variation of surface temperature with latitude and local time [VII-3].

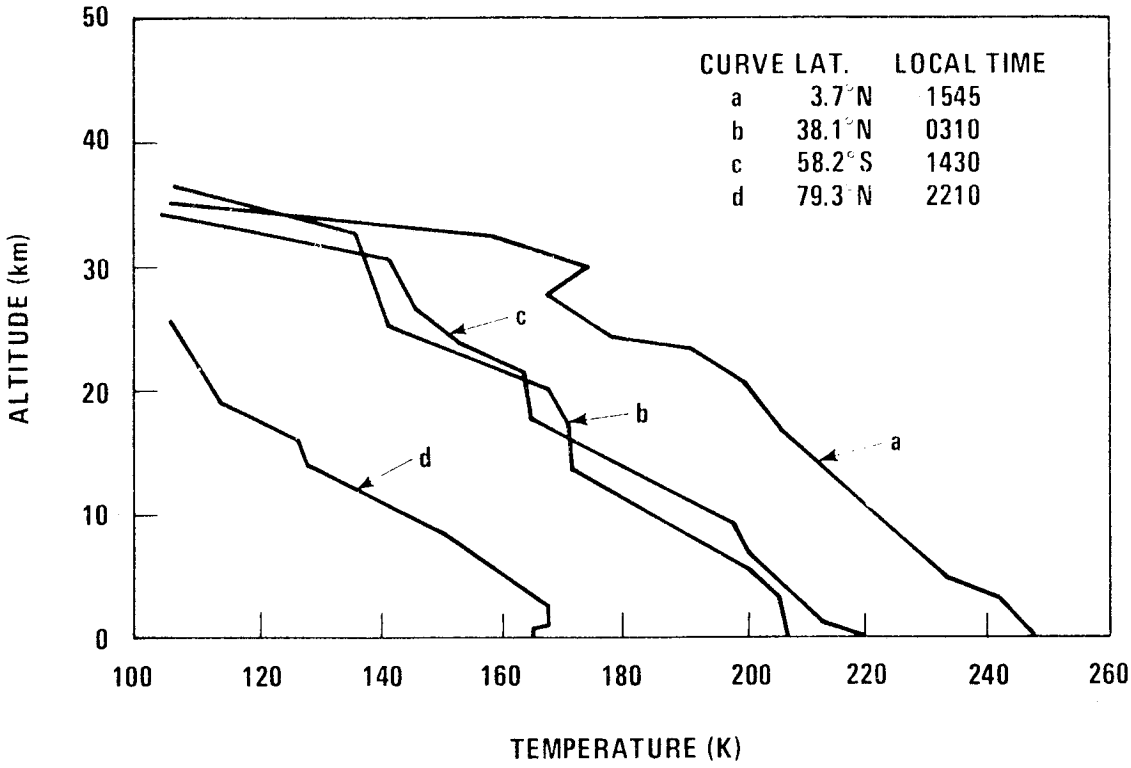

Figure VII-6. Thermal structure of lower Martian atmosphere — Mariner 6 and 7 occultation data [VII-3].

7.1.1.4.1 Mariner 9 Results

Mariner 9 arrived at Mars during a planet-wide dust storm that altered meteorological conditions drastically. Dust was lifted to altitudes above 30 km [VII-3]. This vertical extent requires strong winds and circulation; these can be attributed to alterations in the temperature structure because of dust content. The effect of dust on heating was shown by the unexpectedly high atmospheric temperatures observed by Mariner 9 experiments. These high temperatures in conjunction with their nonuniformity in horizontal directions [VII-3, VII-14] can induce vertical circulation in two ways:

a. The diurnal variation of the heating can drive a large-scale circulation capable of completely overturning the atmosphere each day.

b. If large-scale horizontal variations in dust content of the air occur, the dustier regions will be heated relative to their surroundings and will develop larger vertical velocities.

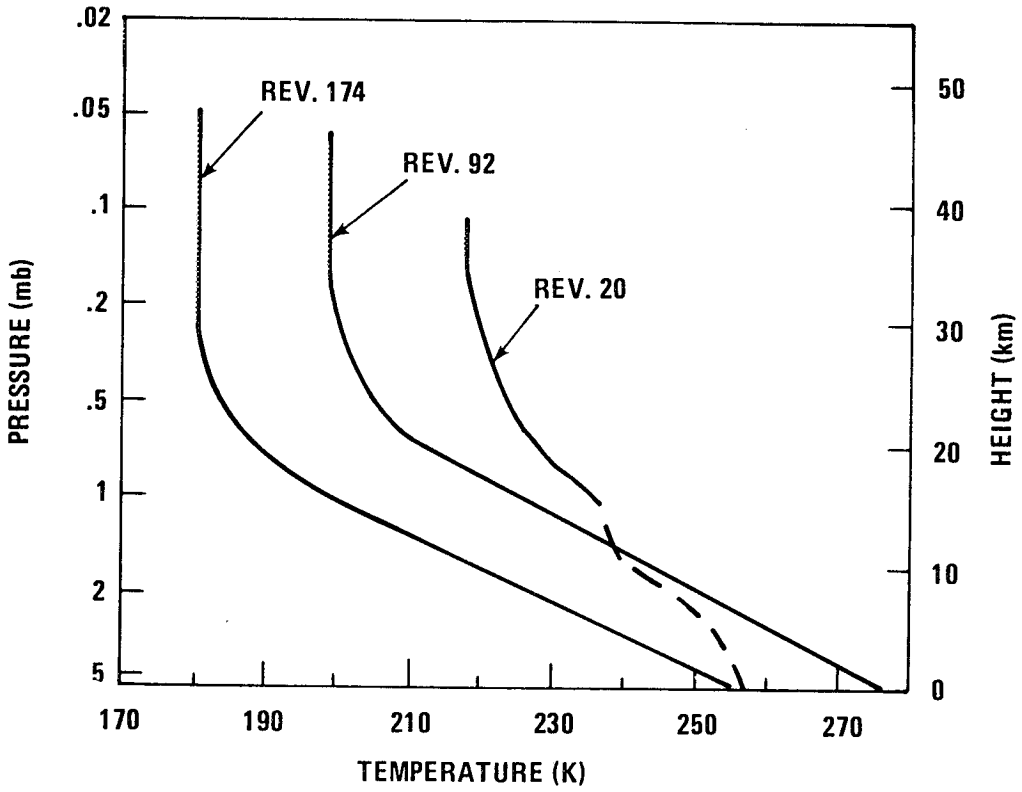

Figure VII-7. Martian temperature profiles — Mariner 9 IRIS data for revolutions 20, 92, and 174 [VII-3].

Golitsyn [VII-16] has deduced that a dust storm can result in a cyclonic vortex with thermal winds (velocity changes) of about 40 m/s. For the upper part of the atmosphere where the temperature gradient is reversed, an anticyclonic vortex should arise. Thus, the dust storm can generate strong winds that can raise new dust from the surface. Sagan [VII-17] concludes that wind velocities of 100 m/s and perhaps as high as 150 m/s are required to raise the dust to the observed atlitude.

The effect of the large observed diurnal variations in the atmospheric temperatures during the global dust storm of 1971 on tidal winds was considered and extended by Pirraglia and Conrath [VII-3]. Temperature fields derived from the Mariner 9 IRIS experiment were used as input data to solve the surface pressure tidal equation and subsequently to estimate the velocities of atmospheric winds. The derived wind fields are shown in Figures VII-8 and VII-9. The resulting diurnal winds near the surface beyond 30 deg north and south (Fig. VII-8) have amplitudes of the order of 20 m/s. These

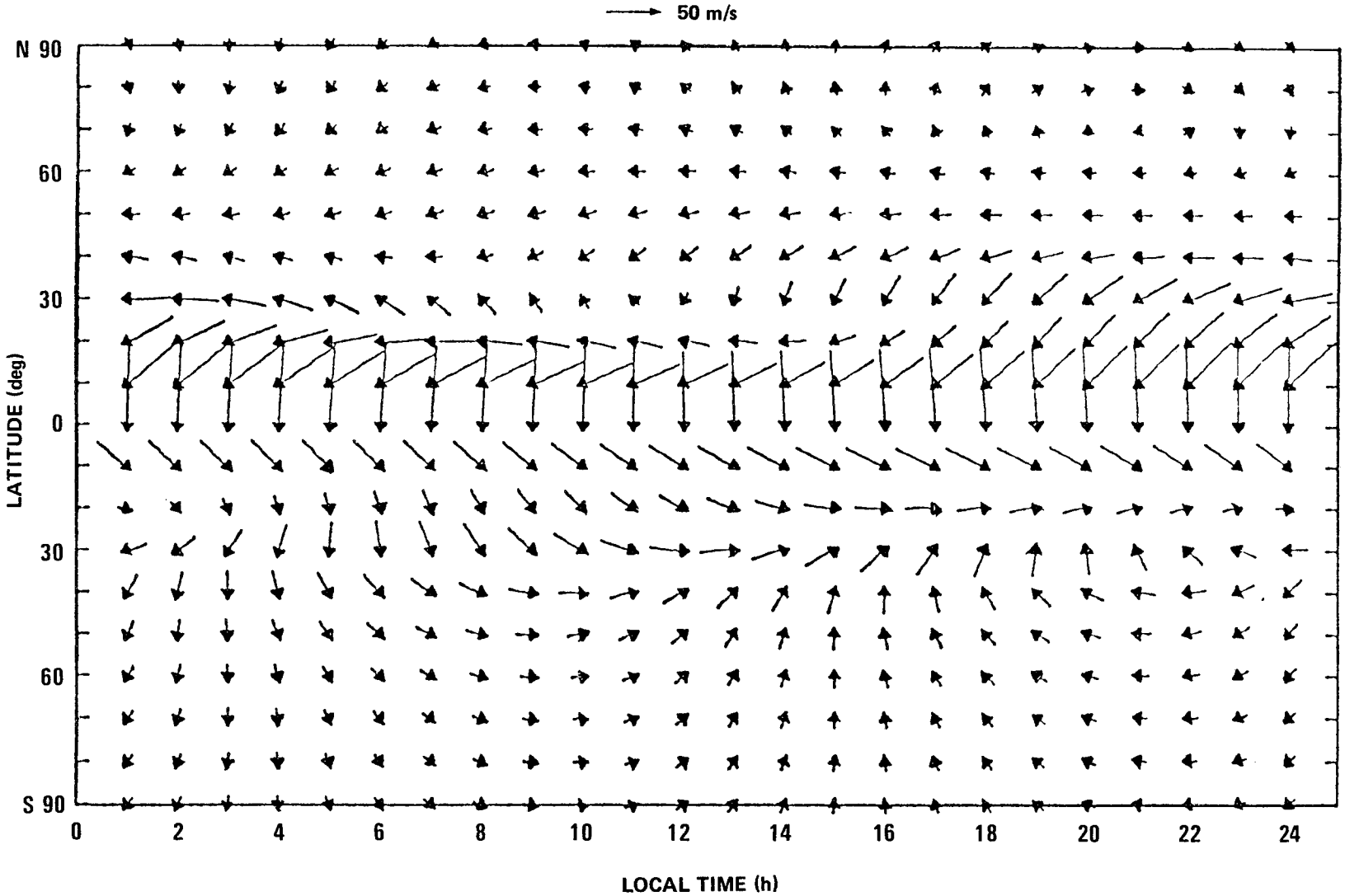

Figure VII-8. Near-surface winds during 1971 dust storm [VII-18].

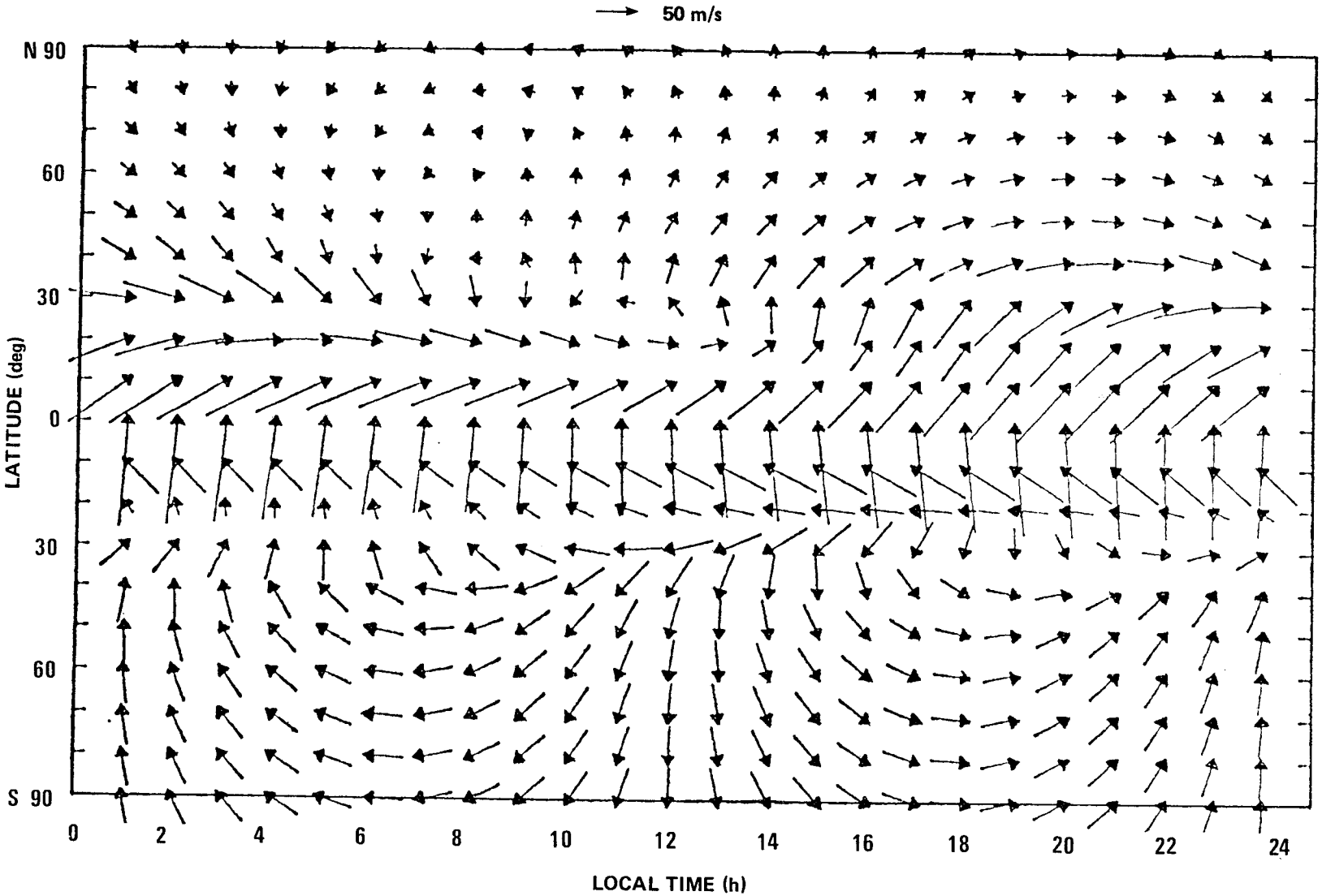

Figure VII-9. High altitude winds during 1971 dust storm [VII-18].

winds could not sustain the dust storm unless augmented by the polar symmetric fields or orographic wind fields. The 70 to 100 m/s zonally-symmetric winds in the latitude belt between 30 deg north and 30 deg south could contribute to the lifting of dust into the atmosphere.

Photographs from Mariner 9 also revealed local dust storms. In one case, the storms appear to be associated with a strong southward movement of cold air following a cold front at an apparent speed of 15 m/s. These highly convective local storms carried dust as high as 15 to 20 km.

The Mariner 9 pictures also revealed a variety of additional features of the Martian meteorology. Photographs of the clouds comprising the north polar hood (north of 45 deg north) indicated that those clouds move in a manner that is characteristic of cold fronts and associated baroclinic wave cyclones in the earth's atmosphere. Cloud bands were observed in the region between 45 and and 65 deg north during the winter season. These clouds which have 30 km wavelengths are indicative of gravity waves that are generated by flow over irregular topography. Wave orientations and positions in respect to the topography show that west-to-east winds prevail in this region. Because of the static stability of the Mars atmosphere at this time, it was inferred that a deep layer containing westerly winds with speeds of at least 55 m/s lies above the wave-generating region [VII-3].

7.1.1.4.2 Theoretical Studies

Information from earth-based Martian cloud observations was used as a direct input for the theoretical study of atmospheric circulation in which the presence of a wave-type circulation regime was found. A value of 100 m/s or more was obtained for the maximum surface wind and 13 m/s for the maximum large-scale vertical wind. The average zonal winds were about 25 m/s and average meridional winds about 1.3 m/s [VII-3].

A comprehensive theoretical investigation of general circulation on Mars by Leovy and Minta included calculations of wind velocities for the northern vernal equinox and southern summer solstice. Their results for the southern summer solstice indicate that the meridional component of mean wind has a strong circulation across the equator. This meridional flow has a speed of 10 m/s with the southerly wind at high altitude and the northerly wind near the surface. Its effective region is between 25 deg north and 30 deg south latitudes. As a result of this flow pattern, the air mass is being transferred from the diminishing polar cap to the growing polar cap. The zonal component of the mean wind at near surface is illustrated in Figure VII-10 where the

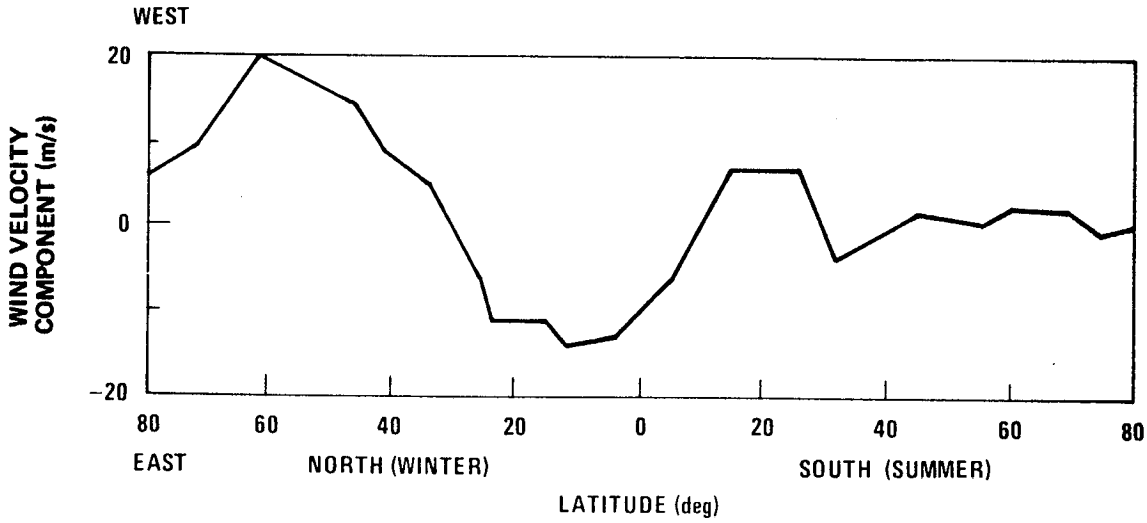

Figure VII-10. Calculated mean zonal component of wind — top of surface boundary layer at summer solstice [VII-3].

easterly and westerly winds are plotted against latitudes. The mean flow in the summer hemisphere is expected to be stable and nearly undisturbed. For the winter hemisphere, however, the mean flow becomes unstable. Leovy and Mintz also found that the maximum instantaneous near-surface wind speed occurs at 20 deg south latitude and that the average speed of the extremely strong winds at 15 km altitude at 40 deg south is about 70 m/s.

The diurnal variation in wind velocity for a clear atmosphere has been explored by Goody. Goody pointed out that the diurnal variation of wind because of temperature changes is complicated by variations in tropopause height and eddy exchange coefficient and by the unknown behavior of the atmospheric tidal energy. The magnitude of this thermally-driven diurnal change of wind is estimated to be 2 m/s. However, the diurnal fluctuation in the vertical momentum exchange can cause a diurnal variation in wind velocity as large as the zonal wind itself, which has a magnitude of 40 m/s [VII-3].

Large scale motions are known to have a significant effect on the atmospheric vertical temperature structure (e.g., References VII-19, VII-20, and VII-21). Dynamic processes including baroclinic waves, vertical oscillations such as induced by topographic relief, and vertical oscillations at altitude were studied [VII-22]. These processes were shown to modify temperature structure

predicted by radiative-convective model in such a way as to provide an explanation of the observed cold middle atmosphere that was not predicted by the less complete models [VII-3].

The vertical wind vector gradient in the Martian atmosphere has been investigated by Wood [VII-3] who took the results of wind component at two levels provided by Leovy and Mintz and assumed a linear variation of wind with height. His analysis indicated that the vertical wind vector gradient is positive from the top of the surface boundary layer to 15 km altitude and negative for the altitude region above 15 km. The magnitude of the vertical wind vector gradient has been suggested to be 6 m/s km for space vehicle design.

7.1.2 Upper Atmosphere

Measurements that pertain directly to conditions in the upper atmosphere of Mars are the electron density profiles obtained from Mariner 4, 6, 7, and 9 and the ultraviolet airglow data obtained from Mariner 6, 7, and 9 and the USSR Mars 2 and 3 and the recently acquired Viking data. Therefore, engineering models for the upper atmosphere must rely on a variety of theoretical studies and inferences derived from limited data. The range in the models, however, has been narrowed considerably by spacecraft results and is expected to be narrowed to a greater extent by the Viking results. (Preliminary Viking I results show the upper atmosphere is composed mainly of CO_2 with trace quantities of N_2, Ar, O, O_2, and CO [VII-10].)

7.1.2.1 Ionosphere

There has long been speculation that Mars has an ionosphere with a structure similar to that of earth. A scientific discussion of the upper atmosphere of Mars, however, has only been possible since the successful experiment of Mariner 4. More information has been provided by Mariner 6, 7, and 9 experiments. (Preliminary Viking I results show that at 130 km O_2^+ is the major constituent, the temperature between 140 and 200 km is about 180 ± 20 K [VII-10].)

The formation of the Martian ionosphere and interpretation of electron number density data acquired from Mariner experiments are based on earth analogy. As with the terrestrial atmosphere, the photoionization process on Mars is expected to form an ionosphere. The height and extent of the Martian ionosphere are complex functions of the season, solar activity, and time of day. In the uppermost regions of the atmosphere, the number density of the molecules is too low to produce an appreciable electron density. At lower altitudes, electron density is limited by attenuation of the ultraviolet radiation in the atmosphere and large electron recombination rates from increased density.

7.1.2.1.1 Electron Density Data

Figure VII-11 shows the distributions of electron number-density in the Martian ionosphere from Mariner 4, 6, 7 and 9 [VII-3, VII-23]. The maximum electron densities are much lower than expected at altitudes of 120 km from Mariner 4 measurements, 135 km from Mariner 6 and 7 measurements, and 135 km from Mariner 9 data. This indicates a lower atmospheric temperature than anticipated.

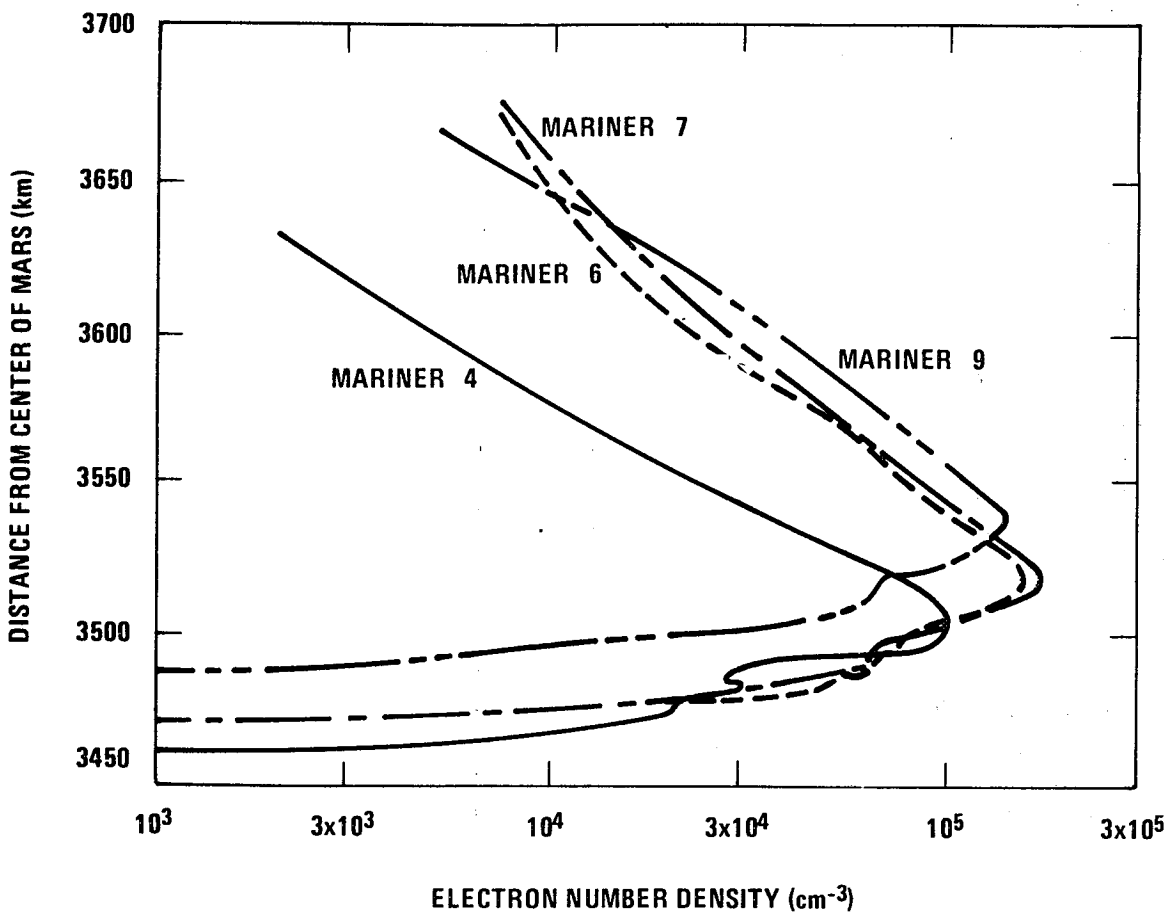

Figure VII-11. Martian ionization profiles [VII-3, VII-24].

The measured maximum electron density was 10^5 cm^{-3} from Mariner 4 when the solar activity was low and the solar zenith angle was large (67 deg). The Mariner 6 and 7 measurements gave a maximum electron density of 1.7×10^5 cm^{-3} when the solar activity was higher than in 1965. The Mariner 9 data shown are for revolution 12 at a solar zenith angle of approximately 55 deg. As the solar zenith angle decreased in subsequent revolutions, the electron maximum was observed to occur at lower altitudes and to be of greater density [VII-3].

7.1.2.1.2 Major Constituents

The major ion in the Martian ionosphere is ionized molecular oxygen, O_2^+. This has been inferred from a combination of laboratory experiments and analysis of Mariner 6 and 7 data [VII-23]. O_2^+ is generated by the reaction of atomic oxygen ions, O^+ with carbon dioxide, CO_2. Figure VII-12 is a theoretical model of the Martian ionosphere that shows the relative densities of the principal constituents at different altitudes. For a concentration of 1 percent atomic oxygen, the ratio of O_2^+ to CO_2^+ is approximately 3 to 1 [VII-25].

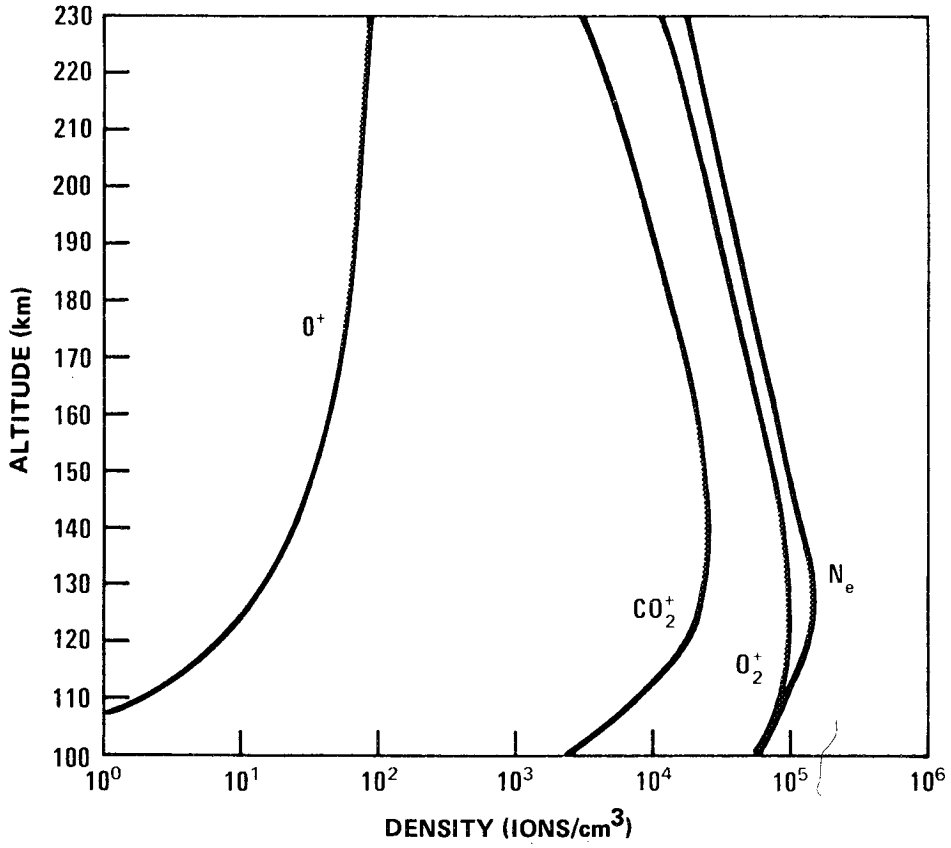

Figure VII-12. Model of Martian ionosphere components [VII-25].

Cloutier and Daniell [VII-26] considered a model in which the magnetized solar wind acted as a dynamo over the day side of the planet. In this model the distribution of currents entering the ionosphere through the plasmapause was considered carefully. The location of the plasmapause was fixed by a requirement that the total ionospheric current must be of sufficient magnitude to cancel the shock-compressed interplanetary magnetic field. This requirement led to an estimated height of 320 to 425 km for the plasmapause.

An alternate model for the outer ionosphere was discussed by Bauer and Hartle [VII-27]. They noted evidence from the USSR spacecraft Mars 2 and 3 [VII-28] for a weak intrinsic magnetic field on Mars that could be of sufficient strength to balance the dynamic pressure of the solar wind at a height of about 1000 km. The distribution of plasma inside the magnetosphere would be controlled in large measure by the convective electric field induced by the solar wind except below 300 km where chemical processes are more efficient than electrodynamically induced mass motion. A schematic illustration of the plasma flow pattern is given in Figure VII-13 [VII-27]. Bauer and Hartle estimated a plasmapause height of about 300 km.

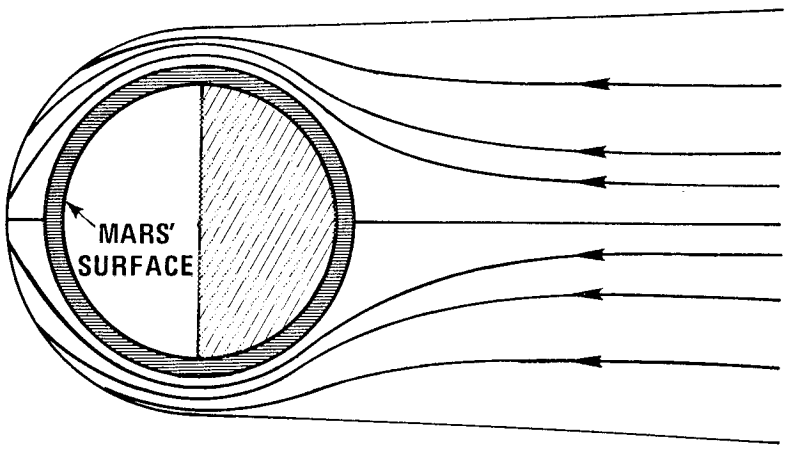

Figure VII-13. Solar wind-induced convective flow pattern for Mars [VII-27].

From the foregoing models, therefore, one could conclude that because of interaction with the solar wind, the Martian ionosphere should terminate effectively between 300 and 450 km, the predicted range of altitudes for the plasmapause. One expects also that the solar wind should induce significant departures from photochemical equilibrium in the ionosphere at high latitudes and at large solar zenith angles; there are indications in the Mariner 9 data [VII-7, VII-29] that these departures may have been observed.

7.1.2.2 Neutral Atmosphere

Mariner 6, 7, and 9 carried ultraviolet spectrometers to measure radiations emitted by atomic hydrogen and atomic oxygen [VII-25, VII-30]. The measured airglow spectrum is characteristic of an essentially pure CO_2 atmosphere. Almost all of the observed emissions were produced by the action of solar ultraviolet radiation on CO_2. Mars 2 and 3 also carried experiments to measure ultraviolet emissions of the atmosphere [VII-31]. The Mariner results showed the presence of carbon monoxide (CO), atomic carbon, atomic hydrogen, and atomic oxygen [VII-25]. The amount of atomic hydrogen at 135 km was calculated to be one part per million [VII-32] and the amount of atomic oxygen at the same altitude is about 1 percent [VII-33].

The density of atomic hydrogen at 200 km was calculated to be 3×10^4 atoms cm^{-3} [VII-32] on the basis of Mariner 6 and 7 data. The temperature at the top of the Martian thermosphere (Fig. VII-1) was determined to be 350 K from Mariner 6 and 7 data [VII-34], 325 K from Mariner 9 data [VII-35], and about 250 K from Mariner 4 data. The higher temperatures are associated with the higher values of extreme ultraviolet (EUV) radiation that occur in high-activity periods of the solar cycle.

Photodissociation of CO_2, electron-impact dissociation of CO_2, and dissociative recombination of CO_2^+ all produce atomic oxygen in the Martian upper atmosphere [VII-25]. Theoretically, it could be expected that atomic oxygen would be a dominant species; however, analysis of ionospheric profiles suggests that oxygen abundances at the ionospheric peak are less than 10 percent, which is consistent with the 1 percent result of Reference VII-33. The observed concentrations of O indicate that mixing processes must be exceedingly efficient in the upper Martian atmosphere. It may be estimated that the turbopause is located at an altitude as high as 150 km.

The major uncertainties in neutral densities of the upper atmosphere relate to the location of the turbopause and the abundance of light constituents O, N_2, CO, and He at the turbopause. Calculated densities for several known

constituents are shown in Figure VII-14, which is based on Mariner 6 and 7 observations [VII-25]. The turbopause in these models was set at 100 km. The amount of CO and O_2 in the model was based on the results of ground-based observations, that is, less than 0.1 percent for CO [VII-3] and slightly more than 0.1 percent for O_2 [VII-36]. The expected low abundance of N_2 is discussed in Paragraph 7.1.1.2. (Preliminary Viking results indicate O_2^+ is the major constituent at 130 km and CO_2 is less abundant by a factor of 9 [VII-10].)

Theoretical attempts have been made to calculate temperatures for the upper Martian atmosphere with observed values for the flux of solar ultraviolet radiation and reasonable estimates for the rates of key chemical reactions. The resulting theoretical models tend to give temperature values that are higher than values of temperatures derived from analyses of ionospheric profiles and airglow data. For example, one theoretical thermal model [VII-37] yielded an exospheric temperature of 487 K on the basis of Mariner 4 (solar flux) data (July 1965) as compared to 300 K that was derived from electron scale height. The difference was attributed to difficulties in estimating EUV heating efficiency and flux [VII-37]. An exospheric temperature of 500 K for July 1969 that was inferred from the electron scale height determined from Mariner 6 and 7 data [VII-24] can be explained by greater EUV in 1969 than in 1965. It appears that the discrepancies may be removed by inclusion of eddy transport in the theoretical models although definitive results have not yet been reported.

7.1.2.3 Clouds

Clouds have been observed from earth and have been verified by Mariner 6, 7, and 9 experiments and Viking missions to Mars, especially by television pictures. The cloud features are usually referred to as yellow, white, blue, and an ill-defined "blue haze."

The observed yellow clouds are generally considered to be associated with dust storms. Storms of local extent may become global, as observed by Mariner 9 in late 1971. The global storm of 1971 extended from the surface to as high as 30 km. Particle size has been discussed in Paragraph 7.1.2.

Stationary clouds have been observed from the earth and in Mariner 9 pictures over large calderas and other high topographical features [VII-3]. These white clouds begin to brighten in the early afternoon and continue to brighten until they disappear over the afternoon limb. These clouds have been correlated with features in the Tharsis, Olympus Mons, Elysium regions. The timing of the clouds' appearance and their relationship to very high topography indicates that they may be formed by lifting of heated air from

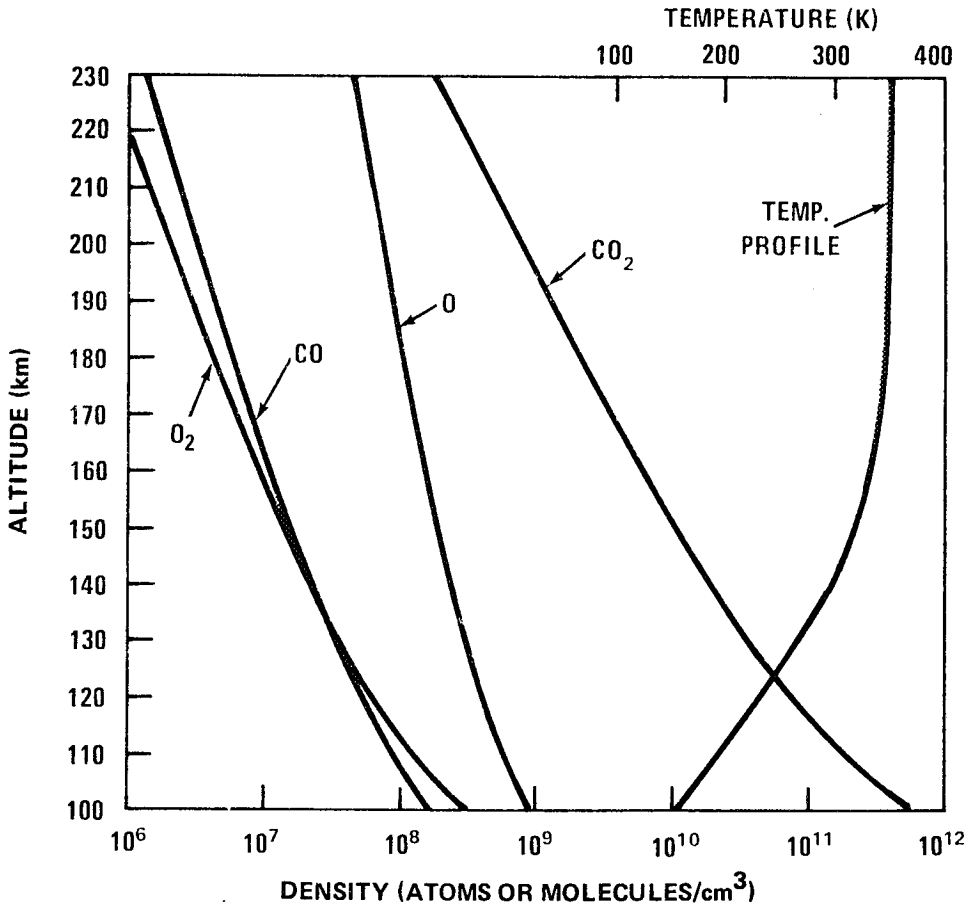

Figure VII-14. Model of Martian neutral atmosphere components [VII-25].

the surrounding lower terrain. These clouds may lie between 8 to 10 km above the surface and contain water ice [VII-38]. Water ice also has been detected in the spectrum of the north polar hood [VII-39].

Another layer of white clouds has been identified in the polar region between about 5 and 30 km [VII-40], which are generated in a wave configuration by flow over irregular topography. Topographic clouds persist north of 45 deg north during the northern late winter season. Two of the wave-cloud systems seen in Mariner 9 pictures near the periphery of the north solar hood have been seen repeatedly from earth and were detected by Mariner 6 and 7 [VII-41]. Mariner 6 and 7 measurements revealed reflection features near 4.3 μm that are characteristic of solid CO_2 [VII-42]; however, from a combination of Mariner 9 imaging and IRIS data, it has been argued that most of the clouds observed between 45 and 60 deg north are composed mostly of water ice [VII-33].

Brightness profiles and pictures from Mariner 9 indicate a cloud layer between 45 and 65 km. The layer is much bluer than the underlying dust [VII-3]. The clouds were observed near the 0.02 mb pressure level and had an estimated thickness of not more than 2 km. In the south polar region, it is suspected that water ice is the principal constituent and the clouds over the north polar hood appear to be composed of CO_2 ice, and possibly water ice. Viking data on Martian clouds is expected from the orbiter imaging results.

A "blue haze" has been observed, but its location in the atmosphere and its properties are unknown. Surface details on Mars generally are clearly seen in any light of wavelengths greater than 4500 to 4550 Å, i.e., red or yellow light. The Martian "blue haze" is a diffuse, variable phenomenon that occasionally clears and allows surface features to be observed in blue light, sometimes described as "blue clearing". The haze itself, which is probably a high-altitude layer, is not blue but extinguishes solar blue light reflected from the Martian surface although transparent to longer wavelengths of light. When the effects of observational selection are removed, some workers believe that there is some correlation of blue clearing with favorable oppositions. The evidence is not compelling, however, because blue clearings have been observed also at unfavorable oppositions or several months from opposition and on small topographical scales of Mars down to the limit of telescopic resolution. Nothing definitive concerning "blue haze" has been reported so far in preliminary Viking results.

Some authorities discount the hypothesis that the "blue haze" is produced by scattering of light by condensed particles. They suggest that the "blue haze" and its occasional clearing may result from selective absorption of light by solid particles in the atmosphere. Others have suggested that interaction of solar wind protons with the CO_2 of the atmosphere causes the "blue haze" by producing molecular ions (CO_2^+ and CO^+) that have strong absorption bands in required energies. These hypotheses are all speculative, however.

7.1.2.4 Atmospheric Models

The models were generated by the computer program described in Reference VII-43. The program was modified to include a molecular mass subroutine to handle the molecular mass variation with altitude, an extended temperature range for the calculation of the specific heat and the reduced collision integral which appears in the viscosity relationship, and the thermochemical data that allow for the inclusion of atomic oxygen and atomic hydrogen as component gases.

The basic inputs to the computer program are the temperature profile, the surface pressure, the near-surface atmospheric composition and corresponding molecular mass, the planetary radius, the acceleration of gravity

at the planet's surface, and the atmospheric density at the turbopause. The values for density, pressure, speed of sound, molecular mass, density scale height, number density, mean free path, viscosity, and pressure scale height as functions of altitude are calculated. Additional mathematical operations are required to determine the mean molecular mass values above the turbopause. All operations satisfy the hydrostatic equation and equation of state. Calculations account for the variation of gravitational acceleration with altitude throughout the atmosphere.

Models were computed for the Martian atmosphere to account for uncertainties in atmospheric parameters. Table VII-2 shows the input parameters for the engineering models of the Mars atmosphere that have been developed. The lower portion of the atmosphere was based on temperature profiles determined from spacecraft measurements. In the upper atmosphere, temperature profiles were obtained from Reference VII-44 which was based on the thermal model of Reference VII-34. The upper atmosphere temperature profiles were constrained at the lower end by density values at the turbopause and by the temperature profiles that were adopted for the lower atmosphere. The top of the upper atmosphere temperature profiles was constrained by exospheric temperatures based on spacecraft data. The temperature profiles used for the atmospheric models are shown in Figure VII-15.

The adopted temperature profiles near their minima cross the solid-vapor phase boundary for CO_2, beyond which CO_2 cannot exist as a gas. This discrepancy in the data has not been resolved in the literature. The adopted profiles represent the data that were available prior to the Viking missions.

7.1.2.5 Lower Atmosphere

Temperature profiles for the lower atmosphere have been established by spacecraft measurements (Paragraph 7.1.1.3). The mean temperature profile for the clear atmosphere is representative of Martian mid-latitudes at the mean surface level. The low temperature profile for the clear atmosphere is derived from polar region measurements given in Reference VII-45. The high temperature profile for the clear atmosphere is that of Mariner 9, revolution 174 shown in Figure VII-7. The temperature profile for the dusty atmosphere is taken from revolution 20 of Mariner 9 shown in Figure VII-7; it is representative of high temperatures encountered during a global dust storm.

Uncertainties in atmospheric surface temperature and pressure are associated with topographic differences, latitude, longitude, time of day, and season. The selected profiles encompass extremes measured by Mariner 9.

C-4

TABLE VII-2. COMPUTER INPUTS FOR MODELS OF MARS ATMOSPHERE (1974)

Parameters	Model			
	I	II	III	IV
Planetary Radius (km)	3394	3394	3394	3394
Surface Gravity (cm/s^2)	371.8	371.8	371.8	371.8
Surface Pressure (mb)	4.95	4.95	4.95	4.95
Surface Temperature (K)	207.5	182.5	255.0	255.0
Composition (% by volume)				
Below Turbopause				
CO_2	98.8	98.8	98.8	98.8
N_2	1.0	1.0	1.0	1.0
CO	0.07	0.07	0.07	0.07
O_2	0.13	0.13	0.13	0.13
At Turbopause				
CO_2	95.8	97.8	88.8	95.8
N_2	1.0	1.0	1.0	1.0
CO	0.07	0.07	0.07	0.07
O_2	0.13	0.13	0.13	0.13
O	3.00	1.00	10.00	3.00
H	0.0001	0.0001	0.0001	0.0001
Molecular Mass (g/g mole)				
Below Turbopause	43.82	43.82	43.82	43.82
At Turbopause	42.98	43.56	41.02	42.98
Density at Turbopause (g/cm^3)	1.46×10^{-12}	1.46×10^{-12}	1.46×10^{-12}	1.46×10^{-12}
Exospheric Temperature (K)	350	250	500	350

Computations were initiated at 10 km below the mean surface level to allow for topographic variation. The composition of the lower atmosphere was chosen as 98.8 percent CO_2, 1 percent N_2, 0.07 percent CO, and 0.13 percent O_2 on the basis of abundances gi en in Table VII-1.

Viking I preliminary results show total atmospheric pressure of about 7 mb at the landing site. The principal atmospheric constituents are: CO_2, 95 percent; N_2, 2 to 3 percent; Ar, 1 to 2 percent; O_2, 0.3 to 0.4 percent [VII-8].

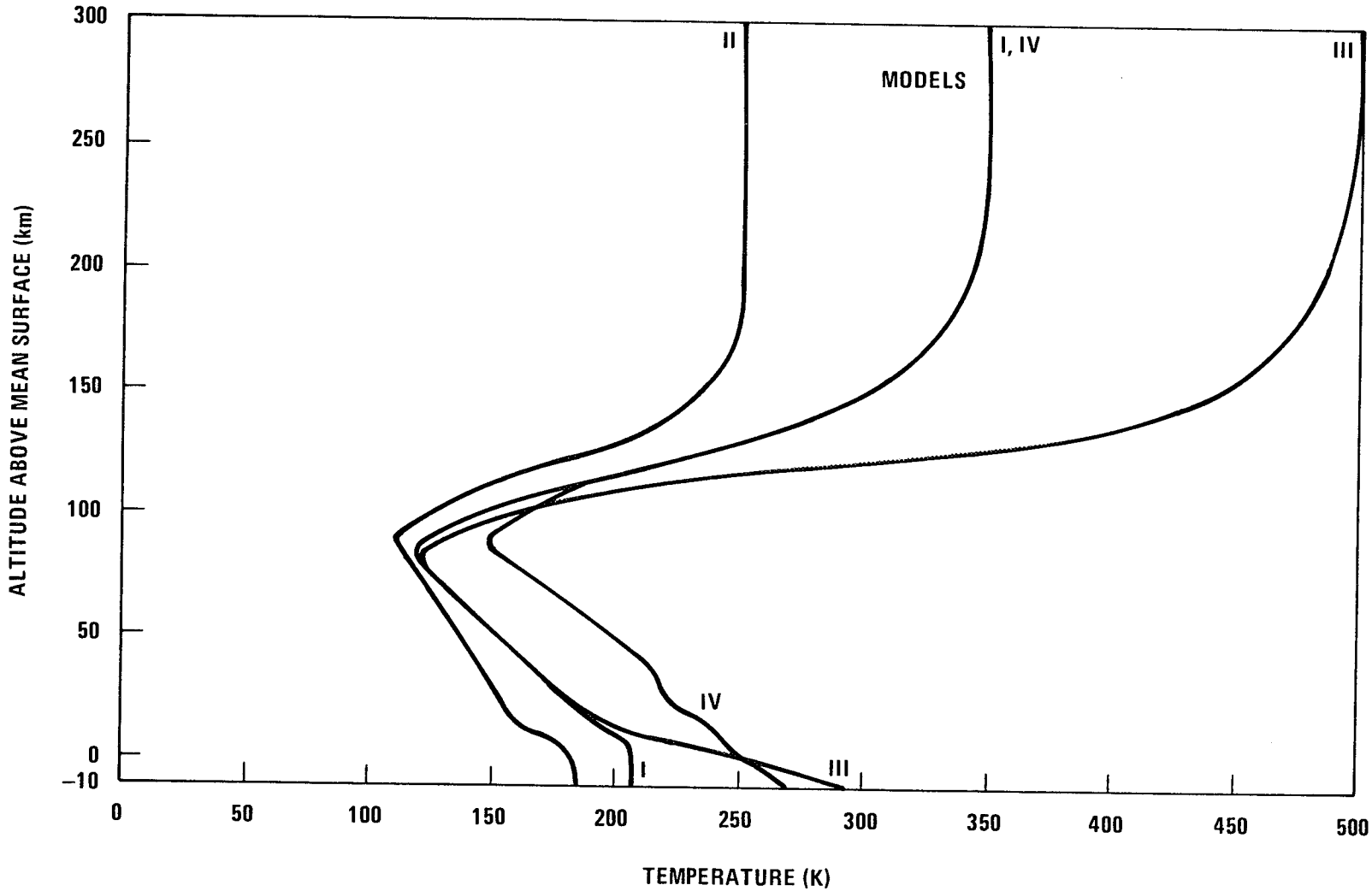

Figure VII-15. Temperature profile for models of Mars' atmosphere.

7.1.2.6 Upper Atmosphere

The lower boundary for the theoretical upper atmosphere is the turbopause. The turbopause is the altitude below which the atmospheric gases mix in constant proportions; above this altitude each constituent gas is taken to be in diffusive equilibrium, with number density decreasing with altitude at a rate that depends upon the molecular mass of the gas and the ambient atmospheric temperature. The density value at the turbopause was estimated on the basis of the composition taken for the lower atmosphere and an eddy diffusion coefficient of 1×10^8 cm^2/s. From the turbopause upward the atmospheric composition was modified by the addition of atomic oxygen O and atomic hydrogen H. The abundance of H was assumed to be the same for all models, whereas O was chosen as 1 percent to obtain a reasonable minimum density, 3 percent for the mean density, and 10 percent for a reasonable maximum density. The abundance of CO_2 was decreased according to the amount of O and H added. The models of the upper atmosphere are superposed on the lower atmosphere models at the turbopause.

The upper constraint on the upper atmosphere models is the exospheric temperature which is a function of both diurnal heating and solar cycle heating. A value of 250 K is used for a night-side atmosphere with minimum solar activity; 500 K is used for maximum solar activity and day-side exospheric temperatures; and 350 K is representative of mean conditions. The temperature profiles for the upper atmosphere for the different exospheric temperatures are shown in Figure VII-15.

7.1.2.7 Criteria

The engineering models of the Mars atmosphere presented herein should be used for mission planning and design of space vehicles that are to orbit Mars, descend through the atmosphere, maneuver in the atmosphere, land on the planetary surface, or conduct scientific investigations during a planetary flyby mission. The models should be used for all facets of space vehicle design including [see footnote to Paragraph 7.2.7.1 concerning engineering models for the Viking project]

Structure
Deceleration system
Propulsion system
Flight control system
Guidance system
Heat shield and thermal control system
Communications systems

Electronics
Power supply
Mechanical devices
Scientific experiments (equipment and measurement ranges)

The models should be regarded as approximations that are based on the best available data and which encompass current uncertainties in the atmospheric parameters. The models are by necessity relatively general in nature; they are particularly useful for preliminary design and mission tradeoff studies. In later design stages, after specific missions, orbits, and landing sites are selected, the range of atmospheric parameters can be significantly reduced by specifying geographic location of landings, orbital parameters of satellites and subsatellites, season of the Martian year, Martian local time, and predicted level of solar activity for that time. If the foregoing information is known, it may be possible to select temperature profiles from Mariner 9 data that embody the effects of variation as to spatial coordinates, topography, season, time of day, and dust storms. The Mariner 9 temperature profiles from the Infrared Interferometer Spectroscopy (IRIS) spectra were made available to the scientific community through the National Space Science Data Center, NASA Goddard Space Flight Center [VII-46].

7.1.2.8 Engineering Models of Mars Atmosphere

The engineering models of the Mars atmosphere are given in Tables VII-3 through VII-6. Model I (Table VII-3) should be considered as the nominal model. It is representative of clear atmospheric conditions at mid-latitudes in mid-spring or mid-autumn during periods of moderate solar activity. Models II through IV (Tables VII-4 through VII-6) take into account possible extremes of molecular mass, solar activity, exospheric temperature and atmospheric clarity in appropriate combinations as shown in Table VII-2. Model II (Table VII-4) presents a cold temperature model with a low density upper atmosphere. It is best applied in the polar regions, during winter, or for night-time analyses, all at periods of low solar activity. Model III (Table VII-5) presents a high temperature model of the clear atmosphere with a high density upper atmosphere. It is intended for application in equatorial regions, during summer, or for afternoon analyses, during periods of high solar activity. Model IV (Table VII-6) presents a temperature model of the atmosphere that can be considered as typical during global dust storms. Figures VII-4 and VII-5 give additional information on temperature variation with latitude, local time, and the presence of dust.

TABLE VII-3. 1974 MARS ATMOSPHERE (MODEL I) (MEAN TEMPERATURE PROFILE)[a]

Altitude (km)	Temperature (K)	Pressure (mb)	Density (g/cm^3)	Speed of Sound (m/s)	Molecular Weight	Density Scale Height (km)	Number Density (cm^{-3})	Mean Free Path (m)	Viscosity (kg/m · s) (E + 5)	Pressure Scale Height (km)
-10	207.5	1.28E+01	3.25E-05	230.	43.824	10.53	4.47E+17	3.23E-06	1.06	10.53
-8	207.5	1.06E+01	2.69E-05	230.	43.824	10.54	3.69E+17	3.91E-06	1.06	10.54
-6	207.5	8.75E+00	2.22E-05	230.	43.824	10.55	3.05E+17	4.73E-06	1.06	10.55
-4	207.5	7.24E+00	1.84E-05	230.	43.824	10.56	2.53E+17	5.71E-06	1.06	10.56
-2	207.5	5.99E+00	1.52E-05	230.	43.824	10.58	2.09E+17	6.90E-06	1.06	10.58
0	207.5	4.96E+00	1.26E-05	230.	43.824	10.59	1.73E+17	8.34E-06	1.06	10.59
2	207.5	4.11E+00	1.04E-05	230.	43.824	10.60	1.43E+17	1.01E-05	1.06	10.60
4	207.0	3.40E+00	8.66E-06	230.	43.824	10.72	1.19E+17	1.21E-05	1.05	10.59
6	206.0	2.81E+00	7.20E-06	229.	43.824	10.83	9.90E+16	1.46E-05	1.05	10.55
8	204.5	2.33E+00	6.00E-06	228.	43.824	10.90	8.24E+16	1.75E-05	1.04	10.49
10	202.0	1.92E+00	5.01E-06	227.	43.824	11.08	6.89E+16	2.10E-05	1.03	10.37
15	192.5	1.17E+00	3.21E-06	219.	43.824	10.74	4.41E+16	3.27E-05	.97	9.91
20	185.0	7.01E-01	2.00E-06	213.	43.824	10.21	2.75E+16	5.26E-05	.92	9.55
25	180.0	4.13E-01	1.21E-06	209.	43.824	9.83	1.66E+16	8.69E-05	.88	9.32
30	175.5	2.40E-01	7.21E-07	205.	43.824	9.61	9.91E+15	1.46E-04	.85	9.11
35	171.0	1.38E-01	4.25E-07	201.	43.824	9.40	5.84E+15	2.47E-04	.83	9.91
40	166.5	7.81E-02	2.47E-07	198.	43.824	9.05	3.40E+15	4.25E-04	.80	8.70
45	162.0	4.36E-02	1.42E-07	195.	43.824	8.91	1.95E+15	7.40E-04	.77	8.49
50	157.0	2.40E-02	8.06E-08	191.	43.824	8.71	1.11E+15	1.30E-03	.75	8.29
55	152.5	1.30E-02	4.49E-08	187.	43.824	8.44	6.17E+14	2.34E-03	.72	8.04
60	148.0	6.91E-03	2.46E-08	184.	43.824	8.21	3.38E+14	4.27E-03	.70	7.82
65	143.0	3.61E-03	1.33E-08	180.	43.824	8.00	1.83E+14	7.89E-03	.67	7.58
70	138.5	1.85E-03	7.04E-09	177.	43.824	7.73	9.67E+13	1.49E-02	.65	7.36
75	134.0	9.28E-04	3.65E-09	174.	43.824	7.50	5.02E+13	2.88E-02	.63	7.14
80	129.5	4.56E-04	1.86E-09	170.	43.824	7.27	2.55E+13	5.66E-02	.61	6.92
85	125.0	2.19E-04	9.22E-10	167.	43.824	7.04	1.27E+13	1.14E-01	.59	6.70
90	120.0	1.02E-04	4.49E-10	163.	43.824	6.82	6.17E+12	2.34E-01	.57	6.45
95	118.5	4.69E-05	2.09E-10	162.	43.824	6.49	2.87E+12	5.03E-01	.56	6.39
100	131.0	2.23E-05	8.99E-11	171.	43.824	6.24	1.24E+12	1.17E+00	.62	7.08
110	169.0	5.49E-06	2.02E-11	200.	43.824	7.62	2.79E+11	5.19E+00	.81	9.19
120	221.0	2.52E-06	6.31E-12	236.	43.824	9.42	8.26E+10	1.75E+01	1.11	12.09
130	254.0	1.17E-06	2.42E-12	252.	43.824	11.83	3.33E+10	4.33E+01	1.26	13.97
140	281.5	5.96E-07	1.09E-12	267.	42.864	13.61	1.53E+10	9.57E+01	1.39	15.92
150	301.5	3.26E-07	5.52E-13	277.	42.387	15.26	7.84E+09	1.87E+02	1.49	17.34
160	315.0	1.87E-07	2.98E-13	284.	41.767	16.67	4.29E+09	3.42E+02	1.55	18.49
170	324.5	1.10E-07	1.67E-13	291.	40.975	17.77	2.46E+09	5.96E+02	1.59	19.53
180	333.0	6.70E-08	9.67E-14	298.	39.966	18.63	1.46E+09	1.01E+03	1.63	20.66
190	338.0	4.18E-08	5.76E-14	305.	38.731	19.65	8.96E+08	1.64E+03	1.65	21.76
200	342.5	2.67E-08	3.50E-14	313.	37.251	20.44	5.65E+08	2.59E+03	1.67	23.06
210	345.5	1.76E-08	2.17E-14	321.	35.538	21.40	3.68E+08	3.99E+03	1.69	24.51
220	347.5	1.18E-08	1.38E-14	331.	33.625	22.42	2.47E+08	5.95E+03	1.71	25.20
230	348.5	8.18E-09	8.92E-15	342.	31.574	23.59	1.70E+08	8.63E+03	1.70	28.14
240	349.5	5.81E-09	5.89E-15	355.	29.471	24.85	1.20E+08	1.22E+04	1.71	30.40
250	350.0	4.24E-09	3.99E-15	368.	27.409	26.43	8.77E+07	1.67E+04	1.71	32.92
260	350.0	3.16E-09	2.77E-15	382.	25.473	28.31	6.55E+07	2.24E+04	1.71	35.61
270	350.0	2.41E-09	1.97E-15	396.	23.726	30.39	5.00E+07	2.94E+04	1.71	38.45
280	350.0	1.88E-09	1.43E-15	409.	22.208	32.75	3.89E+07	3.77E+04	1.71	41.30
290	350.0	1.49E-09	1.07E-15	421.	20.925	35.36	3.08E+07	4.77E+04	1.71	44.07
300	350.0	1.19E-09	8.14E-16	432.	19.872	38.14	2.47E+07	5.95E+04	1.71	46.66
310	350.0	9.67E-10	6.32E-16	442.	19.024	40.97	2.00E+07	7.33E+04	1.71	49.00
320	350.0	7.92E-10	4.99E-16	450.	18.351	43.76	1.64E+07	8.95E+04	1.71	51.07
330	350.0	6.53E-10	4.00E-16	456.	17.823	46.40	1.35E+07	1.09E+05	1.71	52.87
340	350.0	5.42E-10	3.24E-16	462.	17.412	48.84	1.12E+07	1.31E+05	1.71	54.41
350	350.0	4.52E-10	2.66E-16	466.	17.093	51.01	9.35E+06	1.57E+05	1.71	55.72
360	350.0	3.79E-10	2.19E-16	469.	16.846	52.92	7.84E+06	1.87E+05	1.71	56.84
370	350.0	3.18E-10	1.82E-16	472.	16.655	54.57	6.58E+06	2.23E+05	1.71	57.80
380	350.0	2.68E-10	1.52E-16	474.	16.516	55.99	5.54E+06	2.65E+05	1.71	58.63
390	350.0	2.26E-10	1.27E-16	476.	16.389	57.20	4.68E+06	3.14E+05	1.71	59.36
400	350.0	1.91E-10	1.07E-16	477.	16.296	58.23	3.96E+06	3.71E+05	1.71	60.02
410	350.0	1.62E-10	9.03E-17	478.	16.222	59.12	3.35E+06	4.38E+05	1.71	60.61

a. A one-or two-digit number (preceded by E and a plus or minus sign) following an entry indicates the power of ten by which that entry should be multiplied.

TABLE VII-4. 1974 MARS ATMOSPHERE (MODEL II) (LOW TEMPERATURE PROFILE)[a]

Altitude (km)	Temperature (K)	Pressure (mb)	Density (g/cm³)	Speed of Sound (m/s)	Molecular Weight	Density Scale Height (km)	Number Density (cm⁻³)	Mean Free Path (m)	Viscosity (kg/m · s) (E + 5)	Pressure Scale Height (km)
-10	185.5	1.44E+01	4.16E-05	213.	43.824	9.53	5.54E+17	2.59E-06	.92	9.41
-8	185.0	1.17E+01	3.33E-05	213.	43.824	9.52	4.57E+17	3.16E-06	.92	9.40
-6	184.5	9.43E+00	2.70E-05	212.	43.824	9.50	3.70E+17	3.90E-06	.91	9.38
-4	184.0	7.62E+00	2.18E-05	212.	43.824	9.49	3.00E+17	4.81E-06	.91	9.37
-2	183.5	6.15E+00	1.77E-05	211.	43.824	9.47	2.44E+17	5.93E-06	.90	9.35
0	182.5	4.96E+00	1.43E-05	211.	43.824	9.43	1.97E+17	7.33E-06	.90	9.31
2	182.0	4.00E+00	1.16E-05	210.	43.824	9.42	1.59E+17	9.08E-06	.91	9.30
4	181.0	3.23E+00	9.40E-06	209.	43.824	9.50	1.29E+17	1.12E-05	.89	9.26
6	179.0	2.60E+00	7.65E-06	208.	43.824	9.66	1.05E+17	1.37E-05	.88	9.17
8	177.0	2.09E+00	6.21E-06	206.	43.824	9.56	8.54E+16	1.69E-05	.86	9.07
10	173.0	1.67E+00	5.09E-06	203.	43.824	9.90	6.99E+16	2.07E-05	.84	8.88
15	163.0	9.38E-01	3.03E-06	195.	43.824	9.35	4.17E+16	3.47E-05	.78	8.39
20	156.5	5.10E-01	1.72E-06	190.	43.824	8.41	2.36E+16	6.12E-05	.74	8.08
25	154.2	2.73E-01	9.33E-07	189.	43.824	8.09	1.28E+16	1.13E-04	.73	7.99
30	151.0	1.45E-01	5.07E-07	186.	43.824	8.16	6.97E+15	2.07E-04	.71	7.84
35	148.0	7.64E-02	2.72E-07	184.	43.824	7.91	3.74E+15	3.86E-04	.70	7.71
40	145.0	3.98E-02	1.44E-07	182.	43.824	7.88	1.99E+15	7.27E-04	.68	7.57
45	142.5	2.04E-02	7.56E-08	180.	43.824	7.67	1.04E+15	1.39E-03	.67	7.47
50	139.0	1.04E-02	3.94E-08	177.	43.824	7.58	5.41E+14	2.67E-03	.65	7.30
55	136.5	5.21E-03	2.01E-08	176.	43.824	7.39	2.77E+14	5.22E-03	.64	7.19
60	133.0	2.58E-03	1.02E-08	173.	43.824	7.30	1.41E+14	1.03E-02	.63	7.03
65	130.5	1.26E-03	5.09E-09	171.	43.824	7.10	6.99E+13	2.07E-02	.61	6.92
70	127.5	6.07E-04	2.51E-09	169.	43.824	7.00	3.45E+13	4.19E-02	.60	6.78
75	124.5	2.88E-04	1.22E-09	167.	43.824	6.86	1.67E+13	8.62E-02	.59	6.64
80	121.5	1.34E-04	5.83E-10	164.	43.824	6.71	8.01E+12	1.81E-01	.57	6.50
85	118.5	6.17E-05	2.75E-10	162.	43.824	6.56	3.77E+12	3.83E-01	.56	6.35
90	115.5	2.78E-05	1.27E-10	160.	43.824	6.42	1.75E+12	8.27E-01	.55	6.21
95	112.5	1.23E-05	5.78E-11	157.	43.824	6.27	7.94E+11	1.82E+00	.53	6.07
100	110.0	5.36E-06	2.57E-11	156.	43.824	6.11	3.53E+11	4.09E+00	.52	5.95
110	132.5	1.17E-06	4.64E-12	173.	43.824	6.42	6.38E+10	2.26E+01	.62	7.21
120	167.0	3.42E-07	1.07E-12	193.	43.487	7.70	1.48E+10	9.79E+01	.8	9.21
130	202.5	1.28E-07	3.29E-13	229.	43.130	9.37	4.60E+09	3.16E+02	1.04	11.32
140	222.0	5.57E-08	1.29E-13	240.	42.525	11.20	1.82E+09	7.99E+02	1.12	12.63
150	234.0	2.60E-08	5.59E-14	248.	41.915	12.42	8.03E+08	1.81E+03	1.17	13.62
160	242.0	1.27E-08	2.59E-14	255.	40.890	13.33	3.81E+08	3.81E+03	1.21	14.51
170	247.5	6.53E-09	1.25E-14	262.	39.510	14.11	1.91E+08	7.60E+03	1.23	15.45
180	250.0	3.48E-09	6.31E-15	270.	37.699	14.90	1.01E+08	1.44E+04	1.24	16.44
190	250.0	1.93E-09	3.29E-15	278.	35.434	15.69	5.60E+07	2.59E+04	1.24	17.59
200	250.0	1.12E-09	1.77E-15	289.	32.783	16.47	3.24E+07	4.48E+04	1.24	19.12
210	250.0	6.80E-10	9.78E-16	303.	29.919	17.53	1.97E+07	7.37E+04	1.24	21.07
220	250.0	4.33E-10	5.64E-16	318.	27.091	18.94	1.25E+07	1.16E+05	1.24	23.41
230	250.0	2.89E-10	3.40E-16	334.	24.497	20.74	8.37E+06	1.74E+05	1.24	26.02
240	250.0	2.00E-10	2.15E-16	350.	22.315	22.93	5.80E+06	2.50E+05	1.24	28.72
250	250.0	1.44E-10	1.42E-16	365.	20.583	25.42	4.15E+06	3.49E+05	1.24	31.31
260	250.0	1.06E-10	9.78E-17	377.	19.270	28.06	3.06E+06	4.75E+05	1.24	33.63

a. A one or two digit number (preceded by E and a plus or minus sign) following an entry indicates the power of ten by which that entry should be multiplied.

TABLE VII-5. 1974 MARS ATMOSPHERE (MODEL III) (HIGH TEMPERATURE PROFILE)[a]

Altitude (km)	Temperature (K)	Pressure (mb)	Density (g/cm³)	Speed of Sound (m/s)	Molecular Weight	Density Scale Height (km)	Number Density (cm⁻³)	Mean Free Path (m)	Viscosity (g/cm-s)	Pressure Scale Height (km)
-10	295.0	1.02E+01	1.91E-05	350.	43.482	13.48	2.43E+17	5.75E-06	1.44E-5	1.34E+01
-8	287.5	8.87E+00	1.63E-05	346.	43.824	16.33	2.35E+17	6.46E-06	1.42	1.45E+01
-6	279.2	7.72E+00	1.46E-05	341.	43.824	15.11	2.33E+17	7.21E-06	1.39	1.43E+01
-4	271.0	6.69E+00	1.30E-05	336.	43.824	17.12	2.33E+17	8.06E-06	1.36	13.97
-2	260.5	5.77E+00	1.17E-05	331.	43.824	16.13	2.30E+17	9.01E-06	1.33	13.71
0	255.0	4.96E+00	1.02E-05	326.	43.824	15.14	2.41E+17	1.01E-05	1.32	13.44
2	245.5	4.24E+00	9.10E-06	321.	43.824	15.66	2.25E+17	1.15E-05	1.29	13.18
4	237.5	3.60E+00	7.90E-06	316.	43.824	15.27	2.17E+17	1.31E-05	1.25	12.93
6	229.0	3.05E+00	6.82E-06	310.	43.824	14.99	2.04E+17	1.49E-05	1.21	12.68
8	220.5	2.56E+00	5.82E-06	305.	43.824	14.45	2.02E+17	1.72E-05	1.18	12.43
10	213.5	2.14E+00	5.28E-06	300.	43.824	13.36	2.03E+17	1.98E-05	1.21	12.22
15	198.5	1.33E+00	3.54E-06	285.	43.824	12.39	1.87E+17	2.97E-05	1.14	11.71
20	188.0	8.07E-01	2.26E-06	275.	43.824	10.82	1.81E+17	4.64E-05	1.09	11.27
25	181.0	4.77E-01	1.39E-06	269.	43.824	9.88	1.91E+17	7.56E-05	1.09	11.07
30	175.5	2.78E-01	8.25E-07	265.	43.824	9.61	1.91E+17	1.28E-04	1.08	11.01
35	171.0	1.60E-01	4.92E-07	261.	43.824	9.40	1.75E+17	2.14E-04	1.07	10.91
40	166.5	9.04E-02	2.86E-07	258.	43.824	9.25	1.93E+17	3.67E-04	1.06	10.75
45	162.0	5.05E-02	1.64E-07	255.	43.824	8.91	2.26E+17	6.36E-04	1.05	10.46
50	157.0	2.78E-02	9.33E-08	251.	43.824	8.71	1.93E+17	1.13E-03	1.03	10.29
55	152.5	1.50E-02	5.22E-08	247.	43.824	8.44	2.14E+17	2.02E-03	1.02	10.14
60	148.0	8.00E-03	2.85E-08	244.	43.824	8.21	2.32E+17	3.69E-03	1.01	10.02
65	145.0	4.18E-03	1.54E-08	240.	43.824	8.00	2.13E+17	6.86E-03	1.00	9.87
70	138.5	2.14E-03	8.15E-09	237.	43.824	7.72	2.12E+17	1.26E-02	.987	9.74
75	134.0	1.07E-03	4.23E-09	234.	43.824	7.50	2.11E+17	2.44E-02	.977	9.62
80	129.5	5.28E-04	2.16E-09	230.	43.824	7.27	2.45E+17	4.89E-02	.961	9.48
85	127.0	2.53E-04	1.07E-09	227.	43.824	7.04	2.17E+17	9.94E-02	.947	9.35
90	126.0	1.18E-04	5.20E-10	223.	43.824	6.82	2.13E+17	2.06E-01	.938	9.23
95	123.0	5.51E-05	2.36E-10	219.	43.824	6.43	2.03E+17	4.45E-01	.919	9.03
100	140.5	2.73E-05	1.12E-10	224.	43.824	6.39	1.91E+17	9.08E-01	.944	9.06
110	196.5	9.04E-06	2.43E-11	223.	43.824	8.20	8.33E+16	4.33E+00	1.32	11.66
120	230.0	4.21E-06	7.66E-12	267.	43.824	10.50	1.96E+16	1.27E+01	1.43	13.67
130	374.0	2.43E-06	3.42E-12	299.	43.824	14.08	4.72E+16	3.07E+01	1.82	18.27
140	417.0	1.53E-06	1.94E-12	314.	43.824	18.65	2.66E+16	5.42E+01	2.02	25.07
150	442.0	1.02E-06	1.13E-12	327.	46.733	22.12	1.67E+16	9.12E+01	2.10	29.67
160	458.5	7.26E-07	7.41E-13	346.	39.955	24.31	1.12E+16	1.38E+02	2.17	29.62
170	468.5	4.99E-07	5.00E-13	354.	39.052	25.99	7.72E+15	1.97E+02	2.21	29.09
180	476.5	3.59E-07	3.44E-13	361.	38.325	27.26	5.45E+15	2.75E+02	2.24	31.07
190	482.0	2.62E-07	2.41E-13	369.	36.875	28.51	3.94E+15	3.87E+02	2.28	32.69
200	486.0	1.94E-07	1.71E-13	377.	35.637	29.66	2.92E+15	5.28E+02	2.33	33.21
210	489.0	1.46E-07	1.23E-13	385.	34.234	30.79	2.15E+15	7.06E+02	2.35	33.21
220	491.5	1.11E-07	8.94E-14	393.	32.789	31.95	1.64E+15	9.28E+02	2.35	33.17
230	493.0	8.63E-08	6.99E-14	401.	31.289	33.32	1.27E+15	1.20E+03	2.34	33.21
240	496.0	6.78E-08	5.49E-14	410.	29.775	34.41	9.92E+14	1.54E+03	2.33	33.36
250	497.5	5.40E-08	4.39E-14	417.	28.282	36.31	7.84E+14	1.94E+03	2.33	33.19
260	499.5	4.36E-08	3.52E-14	439.	26.840	38.06	6.33E+14	2.41E+03	2.34	34.15
270	500.0	3.56E-08	2.88E-14	451.	25.477	40.15	5.15E+14	2.96E+03	2.34	34.11
280	500.0	2.95E-08	1.72E-14	463.	24.213	42.60	4.27E+14	4.27E+03	2.34	37.10
290	500.0	2.46E-08	1.37E-14	474.	23.061	44.95	3.57E+14	5.07E+03	2.34	38.15
300	500.0	2.08E-08	1.10E-14	485.	22.028	47.50	3.01E+14	5.97E+03	2.34	43.27
310	500.0	1.76E-08	8.96E-15	496.	21.116	50.23	2.55E+14	6.96E+03	2.34	45.63
320	500.0	1.51E-08	7.39E-15	505.	20.321	53.11	2.13E+14	8.96E+03	2.34	47.56
330	500.0	1.30E-08	6.15E-15	514.	19.639	56.07	1.83E+14	9.08E+03	2.34	49.56
340	500.0	1.13E-08	5.17E-15	522.	19.049	59.08	1.64E+14	9.32E+03	2.34	71.85
350	500.0	9.83E-09	4.38E-15	529.	18.550	62.06	1.42E+14	1.07E+04	2.34	73.35
360	500.0	8.59E-09	3.75E-15	535.	18.130	64.98	1.21E+14	1.26E+04	2.34	75.45
370	500.0	7.54E-09	3.22E-15	540.	17.778	67.79	1.03E+14	1.48E+04	2.34	77.35
380	500.0	6.63E-09	2.79E-15	545.	17.483	70.44	9.01E+13	1.69E+04	2.34	79.08
390	500.0	5.85E-09	2.43E-15	549.	17.237	72.93	7.81E+13	1.90E+04	2.34	80.73
400	500.0	5.16E-09	2.12E-15	552.	17.032	75.22	6.82E+13	2.12E+04	2.34	82.23
410	500.0	4.59E-09	1.86E-15	555.	16.862	77.33	5.94E+13	2.29E+04	2.34	83.55
420	500.0	4.07E-09	1.64E-15	557.	16.724	79.25	5.24E+13	2.58E+04	2.34	84.79
430	500.0	3.62E-09	1.45E-15	559.	16.603	80.99	4.67E+13	3.27E+04	2.34	85.95
440	500.0	3.22E-09	1.28E-15	561.	16.515	82.57	4.16E+13	3.66E+04	2.34	87.35
450	500.0	2.87E-09	1.13E-15	562.	16.424	83.99	3.71E+13	4.11E+04	2.34	88.13
460	500.0	2.56E-09	1.01E-15	563.	16.356	85.26	3.71E+13	4.60E+04	2.34	88.91
470	500.0	2.29E-09	8.97E-16	564.	16.299	86.46	2.96E+13	5.14E+04	2.34	89.63
480	500.0	2.05E-09	8.00E-16	565.	16.252	87.53	2.63E+13	5.76E+04	2.34	90.30
490	500.0	1.83E-09	7.14E-16	565.	16.212	88.51	2.37E+13	6.42E+04	2.34	90.97
500	500.0	1.64E-09	6.38E-16	566.	16.179	89.42	2.12E+13	7.16E+04	2.34	91.60
510	500.0	1.47E-09	5.71E-16	567.	16.151	90.26	1.91E+13	7.98E+04	2.34	92.20
520	500.0	1.32E-09	5.11E-16	567.	16.127	91.05	1.71E+13	8.89E+04	2.34	92.76
530	500.0	1.18E-09	4.58E-16	567.	16.107	91.79	1.54E+13	9.90E+04	2.34	93.27
540	500.0	1.06E-09	4.11E-16	569.	16.088	92.49	1.38E+13	1.10E+05	2.34	93.45
550	500.0	9.53E-10	3.69E-16	568.	16.074	93.16	1.24E+13	1.23E+05	2.34	94.49
560	500.0	8.58E-10	3.32E-16	569.	16.061	93.81	1.12E+13	1.36E+05	2.34	95.03
570	500.0	7.72E-10	2.98E-16	569.	16.050	94.43	1.01E+13	1.51E+05	2.34	95.57
580	500.0	6.96E-10	2.68E-16	569.	16.040	95.03	9.13E+12	1.68E+05	2.34	96.11
590	500.0	6.27E-10	2.42E-16	569.	16.031	95.61	8.23E+12	1.88E+05	2.34	96.64
600	500.0	5.65E-10	2.18E-16	569.	16.023	96.18	7.33E+12	2.08E+05	2.34	97.17
610	500.0	5.09E-10	1.96E-16	569.	16.015	96.74	6.60E+12	2.28E+05	2.34	97.71
620	500.0	4.60E-10	1.77E-16	569.	16.008	97.29	5.91E+12	2.52E+05	2.34	98.22
630	500.0	4.15E-10	1.59E-16	569.	16.001	97.83	5.43E+12	2.80E+05	2.34	98.75
640	500.0	3.75E-10	1.44E-16	569.	15.995	98.37	4.91E+12	3.10E+05	2.34	99.28
650	500.0	3.39E-10	1.30E-16	570.	15.989	98.90	4.44E+12	3.43E+05	2.34	99.81
660	500.0	3.07E-10	1.18E-16	570.	15.982	99.43	3.76E+12	3.76E+05	2.34	100.35
670	500.0	2.77E-10	1.07E-16	570.	15.976	99.96	4.03E+12	4.19E+05	2.34	100.88
680	500.0	2.51E-10	9.65E-17	570.	15.970	100.48	3.64E+12	4.63E+05	2.34	101.41

a. A one or two digit number (preceded by E and a plus or minus sign) following an entry indicates the power of ten by which that entry should be multiplied.

TABLE VII-6. 1974 MARS ATMOSPHERE (MODEL IV) (TYPICAL DUSTY ATMOSPHERE TEMPERATURE PROFILE)[a]

Altitude (km)	Temperature (K)	Pressure (mb)	Density (g/cm^3)	Speed of Sound (m/s)	Molecular Weight	Density Scale Height (km)	Number Density (cm^{-3})	Mean Free Path (m)	Viscosity (kg/m · s) (E + 5)	Pressure Scale Height (km)
-10	271.0	1.05E+01	2.04E-05	259.	43.824	14.88	2.80E+17	5.16E-06	1.34	13.75
-8	268.0	9.05E+00	1.78E-05	258.	43.824	14.73	2.44E+17	5.91E-06	1.33	13.61
-6	264.5	7.80E+00	1.55E-05	256.	43.824	14.76	2.14E+17	6.76E-06	1.31	13.45
-4	261.5	6.72E+00	1.36E-05	255.	43.824	14.41	1.86E+17	7.76E-06	1.29	13.31
-2	258.0	5.78E+00	1.18E-05	253.	43.824	14.44	1.62E+17	8.90E-06	1.28	13.15
0	255.0	4.96E+00	1.02E-05	252.	43.824	14.09	1.41E+17	1.03E-05	1.26	13.01
2	252.0	4.25E+00	8.89E-06	251.	43.824	13.94	1.22E+17	1.18E-05	1.25	12.87
4	248.0	3.63E+00	7.72E-06	249.	43.824	14.13	1.06E+17	1.36E-05	1.23	12.68
6	245.0	3.10E+00	6.67E-06	248.	43.824	13.99	9.17E+16	1.56E-05	1.22	12.55
8	242.5	2.64E+00	5.74E-06	247.	43.824	13.88	7.89E+16	1.83E-05	1.21	12.43
10	241.5	2.25E+00	4.91E-06	246.	43.824	12.72	6.74E+16	2.14E-05	1.20	12.43
15	236.2	1.50E+00	3.34E-06	244.	43.824	13.00	4.59E+16	3.19E-05	1.18	12.16
20	228.1	9.87E-01	2.28E-06	241.	43.824	13.52	3.14E+16	4.60E-05	1.14	11.77
25	221.0	6.41E-01	1.53E-06	236.	43.824	12.07	2.10E+16	6.87E-05	1.11	11.44
30	218.0	4.13E-01	9.99E-07	235.	43.824	11.62	1.37E+16	1.05E-04	1.11	11.32
35	215.5	2.65E-01	6.49E-07	234.	43.824	11.52	8.91E+15	1.62E-04	1.09	11.22
40	213.5	1.70E-01	4.19E-07	233.	43.824	11.45	5.76E+15	2.51E-04	1.08	11.15
45	207.0	1.08E-01	2.74E-07	230.	43.824	11.64	3.77E+15	3.83E-04	1.05	10.84
50	202.0	6.76E-02	1.76E-07	227.	43.824	11.30	2.42E+15	5.96E-04	1.03	10.61
55	196.0	4.19E-02	1.13E-07	222.	43.824	11.02	1.55E+15	9.32E-04	.99	10.33
60	190.0	2.56E-02	7.12E-08	217.	43.824	10.72	9.73E+14	1.48E-03	.95	10.04
65	184.0	1.55E-02	4.43E-08	212.	43.824	10.41	6.09E+14	2.37E-03	.91	9.75
70	178.0	9.20E-03	2.72E-08	207.	43.824	10.11	3.74E+14	3.86E-03	.87	9.46
75	173.0	5.38E-03	1.64E-08	203.	43.824	9.74	2.35E+14	6.40E-03	.84	9.22
80	168.0	3.11E-03	9.75E-09	199.	43.824	9.49	1.34E+14	1.08E-02	.81	8.98
85	162.0	1.76E-03	5.74E-09	195.	43.824	9.28	7.89E+13	1.83E-02	.77	8.69
90	156.0	9.82E-04	3.32E-09	190.	43.824	8.97	4.56E+13	3.17E-02	.74	8.39
95	150.0	5.35E-04	1.88E-09	186.	43.824	8.65	2.59E+13	5.56E-02	.71	8.09
100	148.0	2.88E-04	1.02E-09	184.	43.824	8.18	1.41E+13	1.03E-01	.70	8.00
110	177.0	9.22E-05	2.75E-10	206.	43.824	8.32	3.77E+12	3.83E-01	.86	9.63
120	221.0	3.66E-05	8.72E-11	236.	43.824	9.75	1.20E+12	1.21E+00	1.11	12.09
130	254.0	1.69E-05	3.52E-11	252.	43.824	11.83	4.83E+11	2.99E+00	1.26	13.97
140	281.5	8.61E-06	1.61E-11	264.	43.824	13.52	2.21E+11	6.52E+00	1.39	15.57
150	301.5	4.64E-06	8.11E-12	272.	43.824	15.10	1.11E+11	1.30E+01	1.49	16.77
160	315.0	2.59E-06	4.34E-12	277.	43.824	16.39	5.96E+10	2.42E+01	1.55	17.62
170	324.5	1.48E-06	2.41E-12	281.	43.824	17.33	3.31E+10	4.36E+01	1.59	18.26
180	333.0	8.67E-07	1.34E-12	288.	42.953	18.09	1.89E+10	7.78E+01	1.63	19.22
190	338.0	5.19E-07	7.86E-13	291.	42.588	18.88	1.11E+10	1.32E+02	1.65	19.79
200	342.5	3.15E-07	4.65E-13	294.	42.113	19.38	6.67E+09	2.20E+02	1.67	20.39
210	345.5	1.95E-07	2.81E-13	297.	41.530	19.94	4.03E+09	3.65E+02	1.69	20.90
220	347.5	1.22E-07	1.71E-13	301.	40.720	20.45	2.94E+09	5.79E+02	1.70	21.54
230	348.5	7.72E-08	1.06E-13	305.	39.744	20.96	1.60E+09	9.15E+02	1.70	22.36
240	349.5	4.98E-08	6.80E-14	310.	38.548	21.43	1.03E+09	1.42E+03	1.71	23.24
250	350.0	3.27E-08	4.17E-14	316.	37.120	22.03	6.76E+08	2.17E+03	1.71	24.31
260	350.0	2.19E-08	2.66E-14	324.	35.468	22.73	4.53E+08	3.24E+03	1.71	25.59
270	350.0	1.50E-08	1.73E-14	332.	33.621	23.51	3.09E+08	4.74E+03	1.71	27.13
280	350.0	1.05E-08	1.14E-14	343.	31.639	24.48	2.17E+08	6.77E+03	1.71	28.90
290	350.0	7.50E-09	7.63E-15	354.	29.599	25.68	1.55E+08	9.45E+03	1.71	31.15
300	350.0	5.51E-09	5.22E-15	367.	27.589	27.13	1.14E+08	1.29E+04	1.71	33.61
310	350.0	4.14E-09	3.65E-15	380.	25.693	28.88	8.56E+07	1.71E+04	1.71	36.29
320	350.0	3.17E-09	2.61E-15	394.	23.964	30.92	6.56E+07	2.24E+04	1.71	39.11
330	350.0	2.48E-09	1.91E-15	407.	22.450	33.25	5.13E+07	2.86E+04	1.71	41.97
340	350.0	1.97E-09	1.43E-15	419.	21.152	35.82	4.07E+07	3.60E+04	1.71	44.77
350	350.0	1.58E-09	1.09E-15	430.	20.092	38.57	3.28E+07	4.48E+04	1.71	47.46
360	350.0	1.29E-09	8.52E-16	439.	19.232	41.40	2.67E+07	5.50E+04	1.71	49.81
370	350.0	1.06E-09	6.74E-16	448.	18.525	44.21	2.10E+07	6.69E+04	1.71	51.96
380	350.0	8.77E-10	5.42E-16	454.	17.973	46.91	1.81E+07	8.08E+04	1.71	53.84
390	350.0	7.30E-10	4.40E-16	460.	17.540	49.43	1.51E+07	9.71E+04	1.71	55.47
400	350.0	6.11E-10	3.61E-16	465.	17.201	51.70	1.27E+07	1.16E+05	1.71	56.86
410	350.0	5.14E-10	2.99E-16	469.	16.935	53.72	1.05E+07	1.38E+05	1.71	58.05
420	350.0	4.33E-10	2.49E-16	471.	16.730	55.47	8.96E+06	1.64E+05	1.71	59.08
430	350.0	3.66E-10	2.08E-16	473.	16.568	56.99	7.60E+06	1.94E+05	1.71	59.97
440	350.0	3.10E-10	1.75E-16	475.	16.441	58.30	6.42E+06	2.29E+05	1.71	60.75
450	350.0	2.63E-10	1.48E-16	477.	16.341	59.42	5.45E+06	2.69E+05	1.71	61.44
460	350.0	2.24E-10	1.25E-16	478.	16.260	60.38	4.64E+06	3.17E+05	1.71	62.07
470	350.0	1.91E-10	1.06E-16	479.	16.195	61.22	3.95E+06	3.72E+05	1.71	62.64
480	350.0	1.63E-10	9.03E-17	480.	16.140	61.96	3.37E+06	4.36E+05	1.71	63.18

a. A one-or two-digit number (preceded by E and a plus or minus sign) following an entry indicates the power of ten by which that entry should be multiplied.

All models are based on a mean planetary radius of 3394 km which corresponds to 0 km altitude in the tables. However, to encompass possible extremes of local topography as well as variations in local radius, the tables have been extended downward to -10 km which corresponds to a planetary radius of 3084 km. Thus, if a model is applied to a low area such as the Hellas region, the tables would be entered at about -4 km or if a high region such as Olympus Mons is considered, the table is entered at about 28 km (Fig. VII-2).

The four tables were terminated at altitudes where the density falls to 10^{-16} g/cm^3 because the hydrostatic equilibrium assumption upon which these models are based undoubtedly becomes invalid at greater altitudes.

7.1.3 Winds[5]

Information on Martian winds was obtained from cloud observations, studies of dust storm characteristics, and models of atmospheric circulation and tidal pressure. The following near-surface wind speeds are recommended for space vehicle design purposes.

Wind Parameter	Surface Pressure	
	4 mb	8 mb
Mean Speed (1 m above surface)	50 m/s	35 m/s
Peak Speed	145 m/s	100 m/s
Vertical Wind Vector Gradient	6 m/s • km	6 m/s • km

7.1.4 Ionosphere

Observations by Mariner 4, 6, 7, and 9 spacecraft indicate peak electron density in the Martian ionosphere to be of the order of 10^5 cm^{-3}. This density should not be large enough to affect radio communication to and from a lander on the surface. For spacecraft atmospheric entry, electron densities should not be significant even behind the bow shock wave which forms through compression of the solar wind's magnetic field against the ionosphere. The electron density profiles given in Figure VII-11 should be used in design configuration analyses.

5. Viking 1 and 2 preliminary results show a daily variation of wind gustiness at the two sites. The wind becomes gusty shortly before sunrise, as the surface boundary layer becomes convectively unstable and remains gusty until mid-afternoon. The peak observed gust was 17 m/s [VII-11].

7.1.5 Clouds

Distinct cloud layers, identified by color, have been verified by spacecraft television pictures. Cloud characteristics are summarized below.

Cloud Layer	Remarks	Altitude Above Mean Surface (km)	Composition
Yellow	Local and global dust storms	0 to 30	Surface dust; 10 to 300 μm
White-Low	High topographical features; late afternoon	8 to 10	Water ice
White-High	Wave clouds associated with irregular topography	5 to 30	Mostly water ice
Blue	Principally in polar regions	45 to 65	Water ice (south polar region); CO_2 ice and possibly water ice (north polar hood)
Blue Haze	Diffuse, variable phenomenon – usually visible; rapid changes in state – random from opacity to near transparency	Not uniform over entire atmosphere; probably high altitude	Not known; sources speculative

7.2 Surface Model

The Martian surface models and related physical, chemical, and mechanical properties presented here should be used for mission analyses and for design of landing and exploration vehicles. For the Martian atmosphere, NASA SP-8010 (Revision of 1974) provides engineering models that take into account variations in Martian time of day, season, location, and solar activity. (Viking preliminary and early results are found in References VII-7, VII-9, VII-12, VII-47, and VII-48).

7.2.1 Nominal Physical Parameters

Nominal, or average, properties of Martian physical parameters are listed in Table VII-7.

TABLE VII-7. NOMINAL MARS PHYSICAL PARAMETERS

Parameter	Nominal Value	Reference
Equatorial radius (km)	3397.2 ± 1	VII-8
Polar radius (km)	3375.5 ± 1	VII-8
Flattening (dimensionless)		
Dynamical	0.0064 ± 0.0003	VII-8
Optical	0.0057	VII-8
Mass (g)	6.418×10^{26}	VII-12
Density (g/cm^3)	3.945	VII-12
Gravitational Constant, $\mu = GM$ (km^3/s^2)	42828.32	VII-8
Gravitational Acceleration (m/s^2)	3.71	VII-12
Escape Velocity (km/s)	5.024	VII-12
Nominal Surface Pressure (mb)	4.8	VII-49
Surface Temperature (K)		
Equatorial		
Minimum	172	VII-3
Maximum	289	VII-3
Polar		
Minimum	150	VII-3
Maximum	220	VII-12
Sidereal Period of Revolution (days)	686.9804	VII-12
Sidereal Period of Rotation (h;min;s)	24;37;22.6689	VII-12
Distances from Sun (km)		
Mean (semimajor axis)	227 800 000	VII-12
Perihelion	206 500 000	VII-12
Aphelion	249 100 000	VII-12
Distance from earth (km)		
Minimum	55 810 000	VII-12
Maximum	398 900 000	VII-12
Mean Opposition	78 350 000	VII-12

7.2.2 Gravitational Field

The gravitational field potential U is expressed in terms of fourth-degree spherical harmonic expansions [VII-50, VII-51],

$$U = +\frac{GM}{r}\left\{1 - \sum_{n=2}^{4} J_n\left(\frac{R}{r}\right)^n P_{no}(\sin\theta) + \sum_{n=2}^{4}\sum_{m=1}^{4}\left(\frac{R}{r}\right)^n P_{nm}(\sin\theta)\left[C_{nm}\cos m\lambda + S_{nm}\sin m\lambda\right]\right\} ,$$

where the coefficients J_n, S_{nm} and C_{nm} are listed in Table VII-8, and where

r = radius vector to an arbitrary point

R = mean equatorial radius (corresponding to 3394 km for the coefficients in Table VII-8)

GM = gravitational constant μ in Table VII-7

P_{nm} = associated Legendre polynomials

θ = latitude

λ = longitude (deg east)

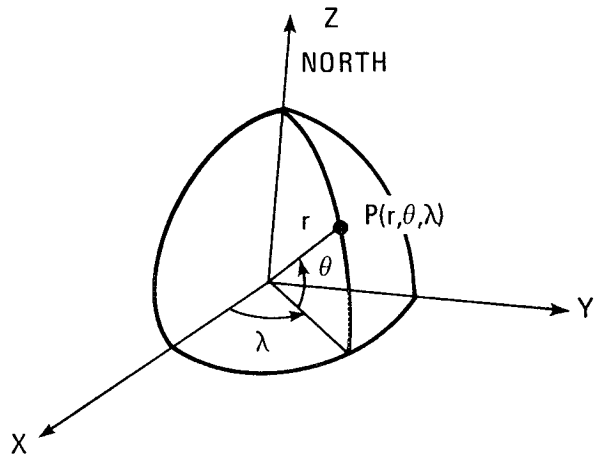

TABLE VII-8. COEFFICIENTS IN GRAVITATIONAL POTENTIAL FUNCTION

Coefficient[a]	Value (factor = 10^{-4})	Coefficient	Value (factor = 10^{-4})
J_2	19.65 ± 0.06		
J_3	0.36 ± 0.20		
J_4	- 0.29 ± 0.40		
C_{22}	-0.548 ± 0.010	S_{22}	0.31 ± 0.02
C_{31}	0.048 ± 0.040	S_{31}	0.26 ± 0.05
C_{32}	-0.055 ± 0.020	S_{32}	0.026 ± 0.020
C_{33}	0.048 ± 0.003	S_{33}	0.035 ± 0.003
C_{41}	0.025 ± 0.060	S_{41}	0.019 ± 0.070
C_{42}	-0.0063 ± 0.0100	S_{42}	-0.024 ± 0.020
C_{43}	0.0037 ± 0.0030	S_{43}	0.00015 ± 0.00200
C_{44}	-0.00023 ± 0.00070	S_{44}	-0.0025 ± 0.0010

a. The coefficients C_{21} and S_{21} are taken to be zero in the expansion [VII-52, VII-53].

The gravitational acceleration g at an arbitrary point $P(r, \lambda, \theta)$ is obtained from the partial derivative of the gravitational potential function by the equation

$$g = -\frac{\partial U}{\partial r} \quad .$$

7.2.3 Magnetic Field (Equatorial Surface)

From Mariner 4, 6, and 7 magnetometer measurements it is inferred that the equatorial surface magnetic field is less than 200 γ.

7.2.4 Terrain Properties

7.2.4.1 Morphology

Four classes of units are recognized on Mars: (1) primitive cratered terrain, (2) sparsely cratered volcanic aeolian plains, (3) circular radially symmetric volcanic constructs such as shield volcanoes, domes, and

craters, and (4) tectonic erosional units such as chaotic and channel deposits. A generalized geological map which delineates these units between the latitudes 65 deg south and 65 deg north is shown in Figure VII-16.

7.2.4.2 Elevation

Recent topographic estimates that have been derived from occultation, radar, spectral, and optical measurements show a range of elevations from 4 km below the mean surface in Hellas depression to an altitude of 28 km on Olympus Mons as shown in Figure VII-17.

Local elevation contours of selected regions having substantial relief and of geological interest are shown in Figures VII-18 (USGS, upgraded versions of the photomaps in Reference VII-54). Figure VII-18a shows Olympus Mons, the largest of the Martian shield volcanoes. The structure is approximately 600 km across and is located at 18 deg north, 134 deg west. Figure VII-18b shows Pavonis Mons (Middle Spot). It is another shield volcano located at 1 deg north, 113 deg west and is about 400 km across. Figure VII-18c shows a portion of a 4800 km long canyon system called Valles Marineris at about 8 deg south and 84 deg west.

7.2.4.3 Mean Slope and Cumulative Frequency

The variation of mean Martian slope $\bar{\alpha}$ with base length L is shown in Figure VII-19. The variation of slope α about the mean slope can be determined from the cumulative frequency function

$$N = e^{-\alpha/\bar{\alpha}} ,$$

where N represents the fraction of slopes steeper than angle α.

7.2.4.4 Power Spectral Density

Power spectral density models recommended for Mars are presented in Figure VII-20 as derived from terrestrial and lunar data.

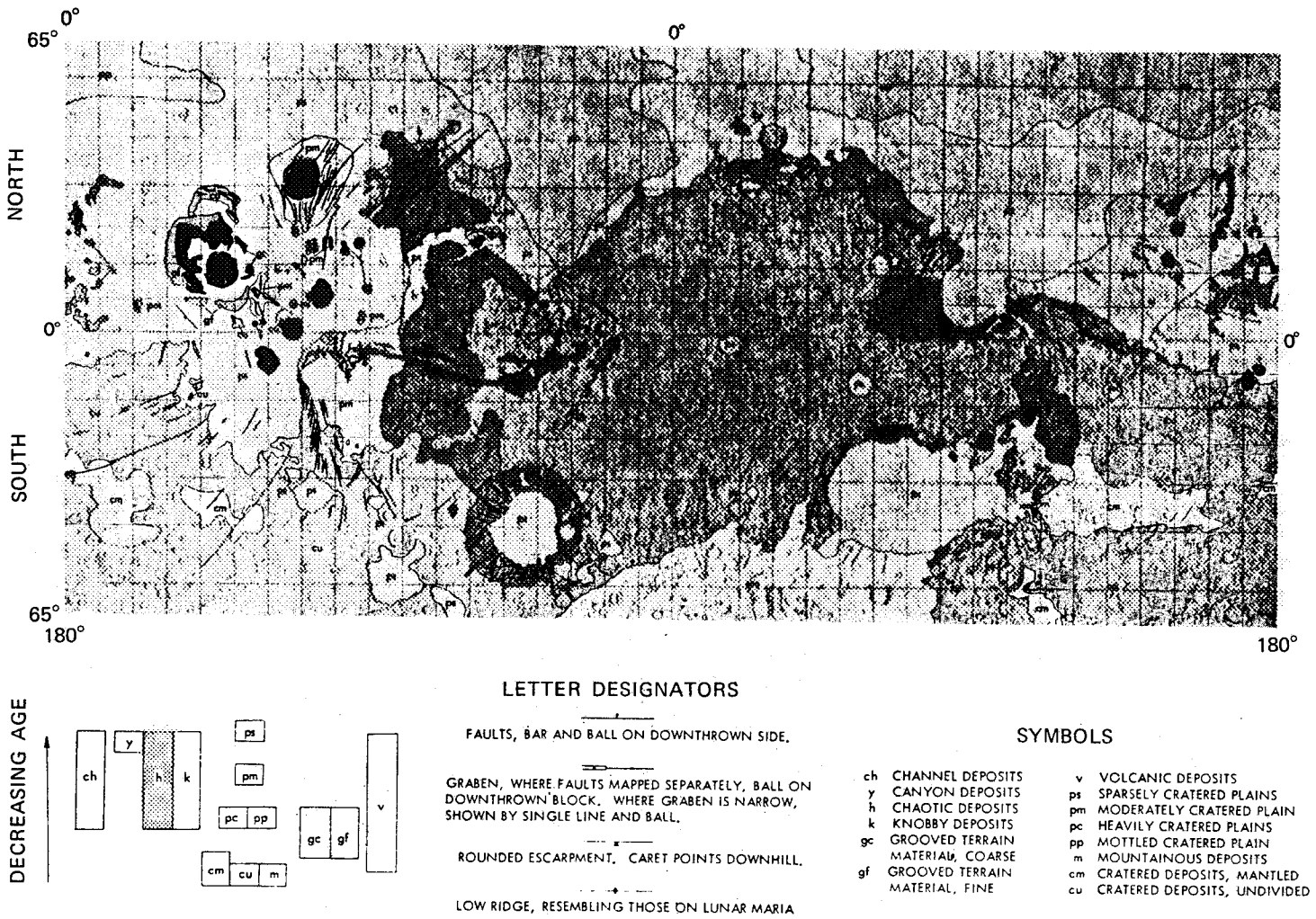

Figure VII-16. Generalized geologic map between 65 deg north and 65 deg south [VII-55].

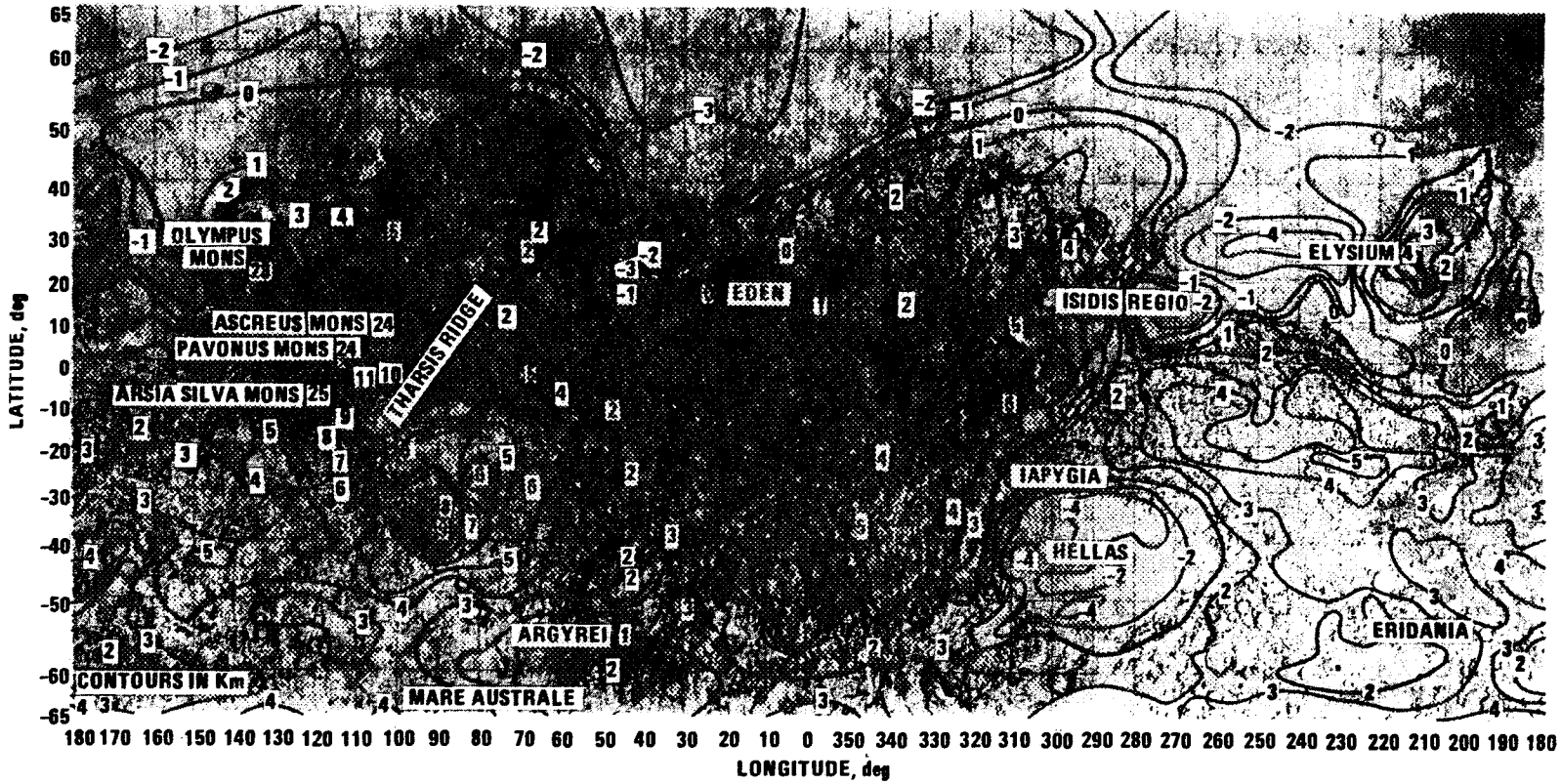

Figure VII-17. Topographic map of Mars (altitudes in km) (NASA SP-8010, Dec. 1974).

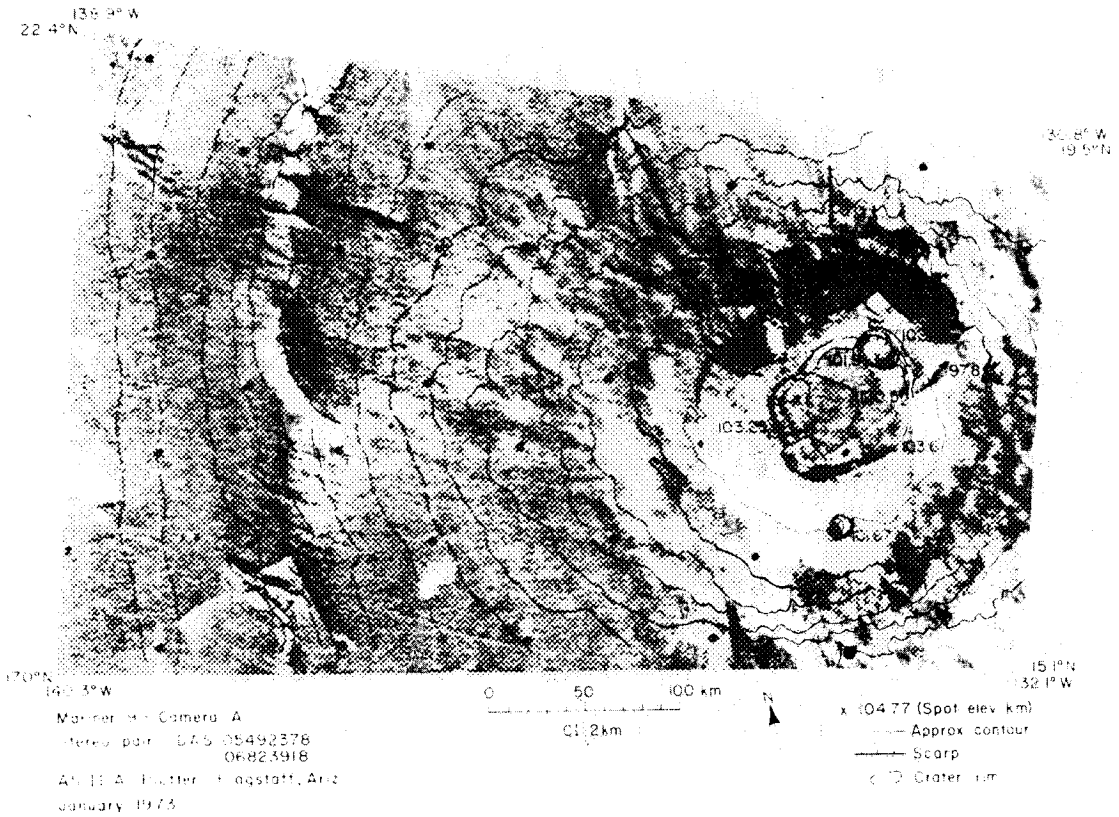

Figure VII-18a. Relative elevations at 2 km intervals of Olympus Mons from Mariner 9 camera (USGS, Flagstaff, Ariz.).

7.2.5 Craters and Blocks

7.2.5.1 Morphology

The cratered regions of the Martian surface have been subdivided into the two regions called (1) heavily cratered provinces, and (2) sparsely cratered provinces. The maximum crater frequency model presented here corresponds roughly to the saturation crater frequency distribution, whereas the nominal and minimum curves correspond approximately to the crater distributions seen in heavily and sparsely cratered provinces. A range of crater forms starts at small diameters with small bowl-shaped craters, proceeds through craters having central peaks, extends to craters having interior rings on the crater floor, and ends with the largest crater basins in which all manifestations of central mountains have disappeared [VII-55].

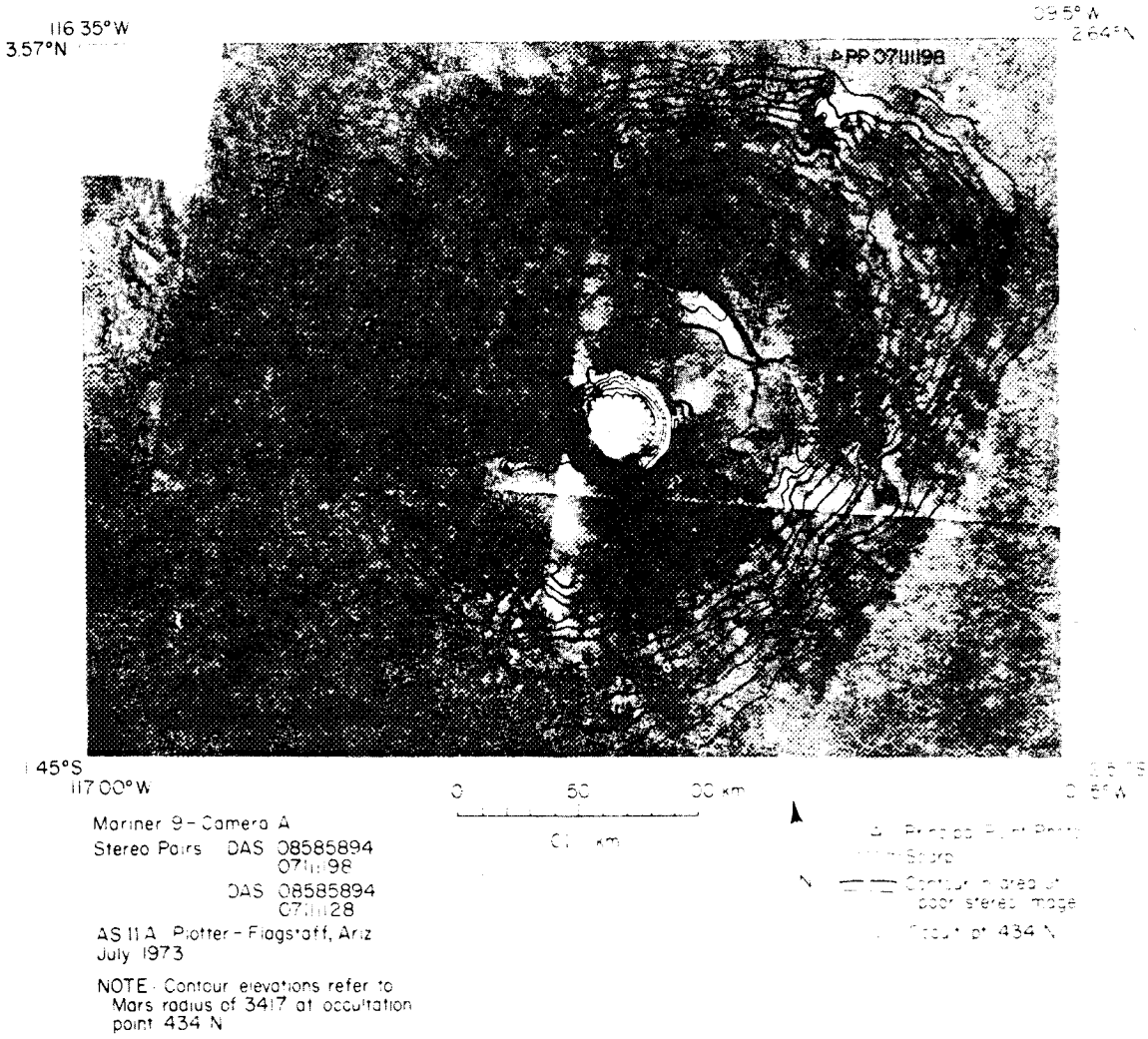

Figure VII-18b. Relative elevations at 1 km intervals of Pavonis Mons from Mariner 9 camera (USGS, Flagstaff, Ariz.).

Mariner 9 Martian photographs do not have sufficient resolution to provide block data. The models presented here are taken to be the same as those for the moon. A standard Martian block can be considered as one having a ratio of its longest dimension to its shortest dimension in the range 1:1 to 5:1. Block surfaces may be rounded or rectangular, and they may be pitted, eroded, or vesiculated. The resolution of the Viking photography is much better, and block data probably will be extensively presented in the final results of the Viking data.

Figure VII-18c. Relative elevations at 400 m intervals for Canyonlands at about 8 deg south and 84 deg west from Mariner 9 camera (USGS, Flagstaff, Ariz.).

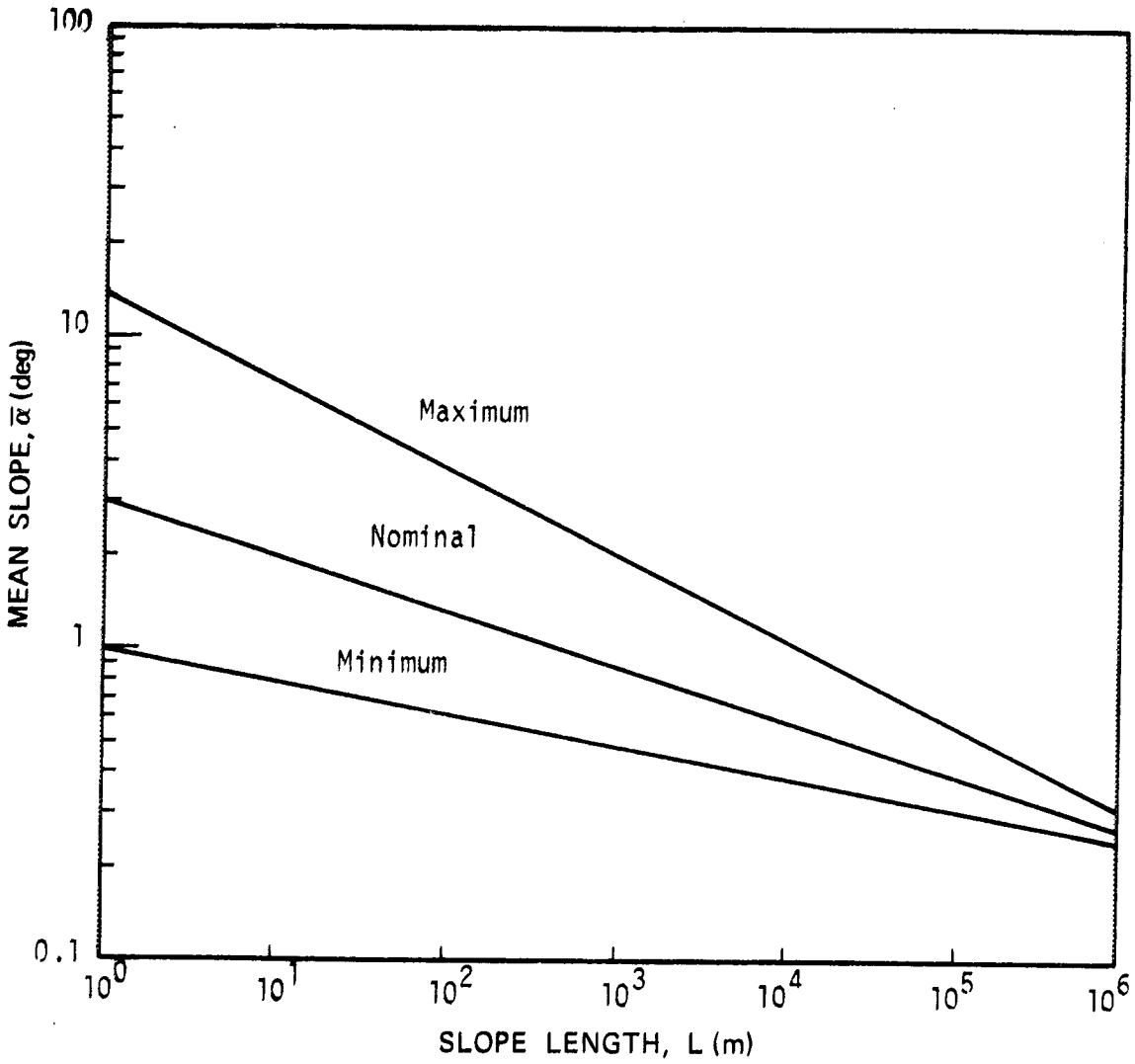

Figure VII-19. Mean surface slope [VII-56].

7.2.5.2 Frequency

Cumulative numbers of craters and blocks are shown in Figures VII-21 and VII-22.

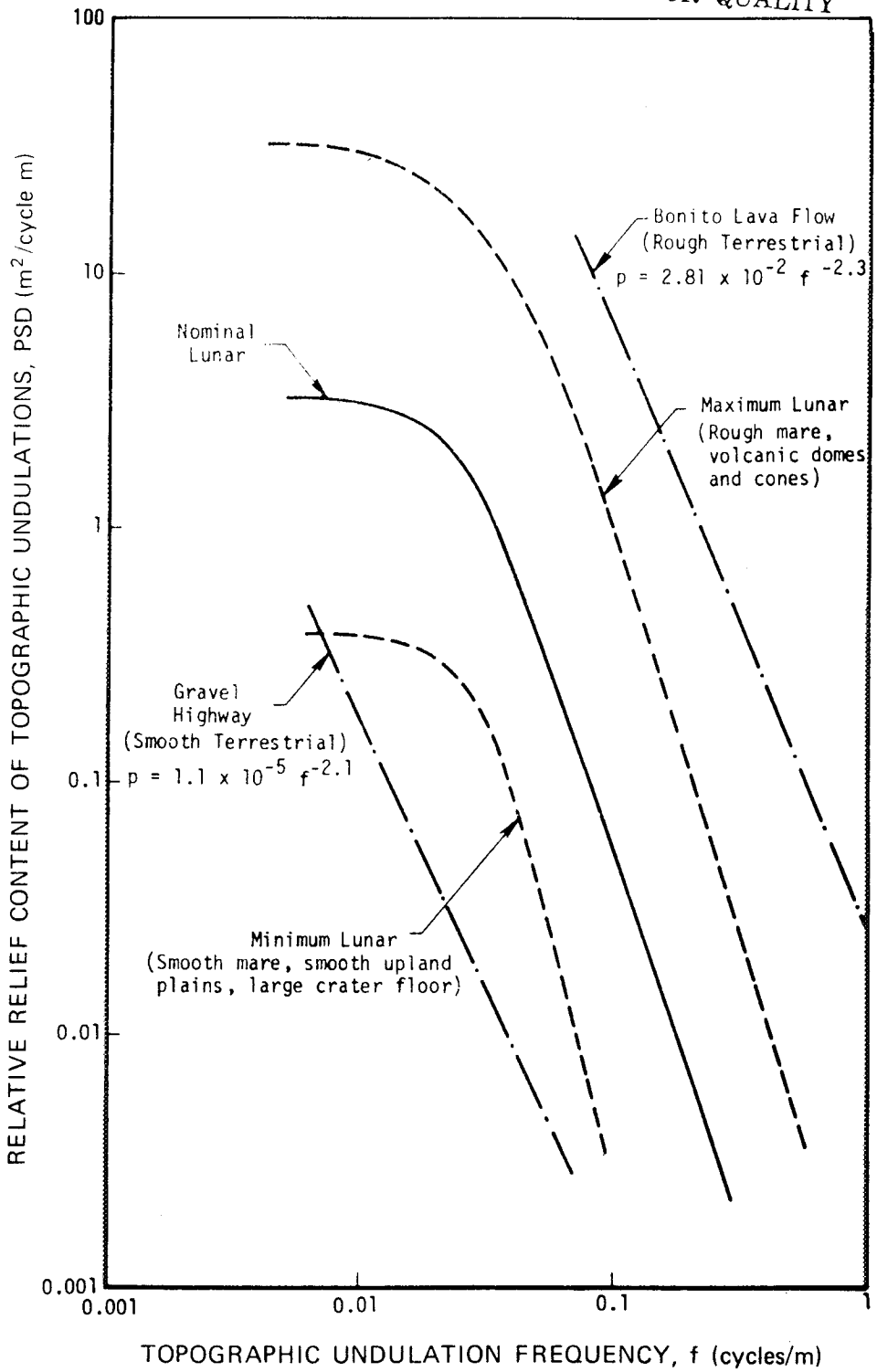

Figure VII-20. Surface roughness — power spectral density versus surface wave frequency (R. J. Pike, USGS).

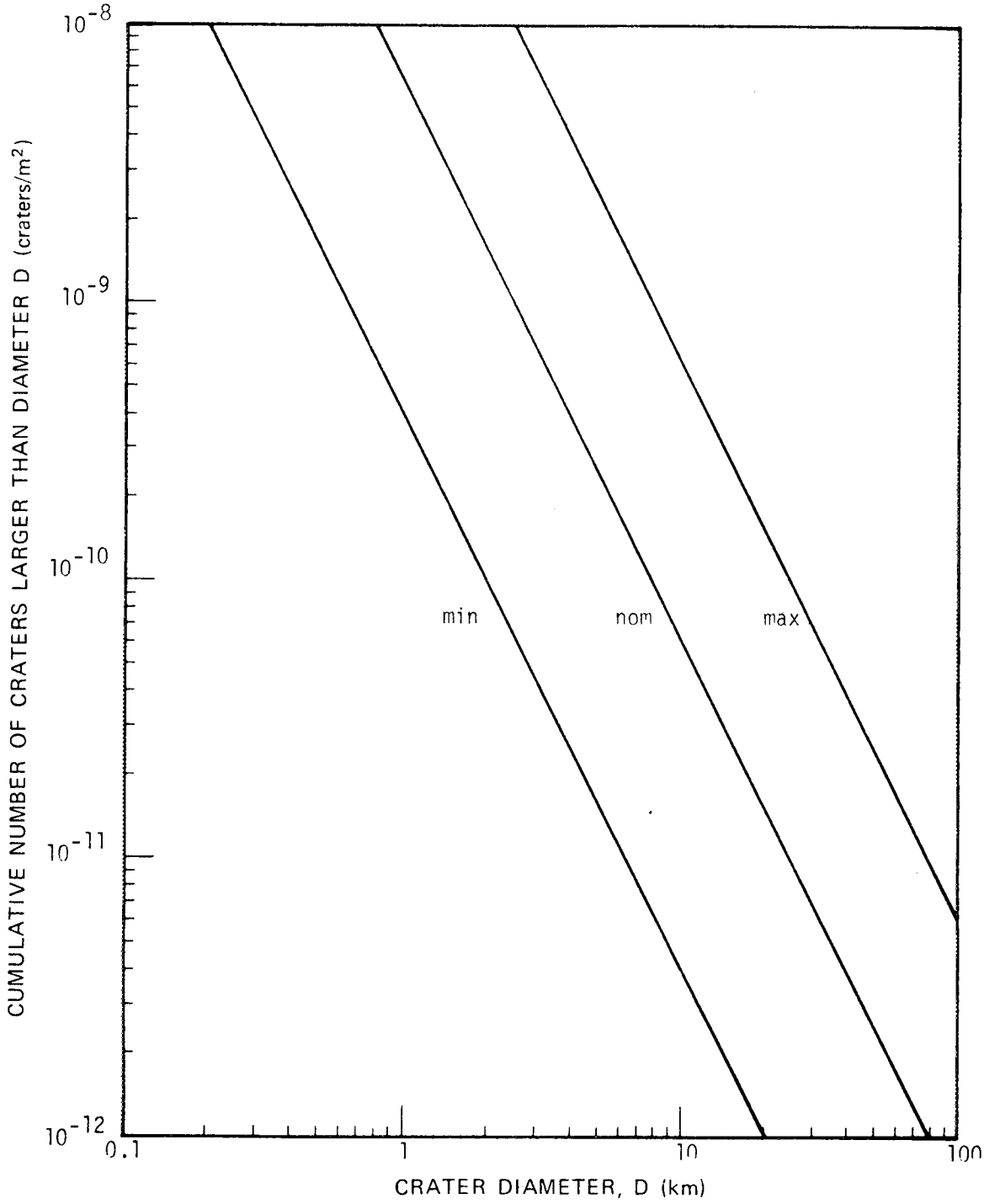

Figure VII-21. Cumulative number of craters.

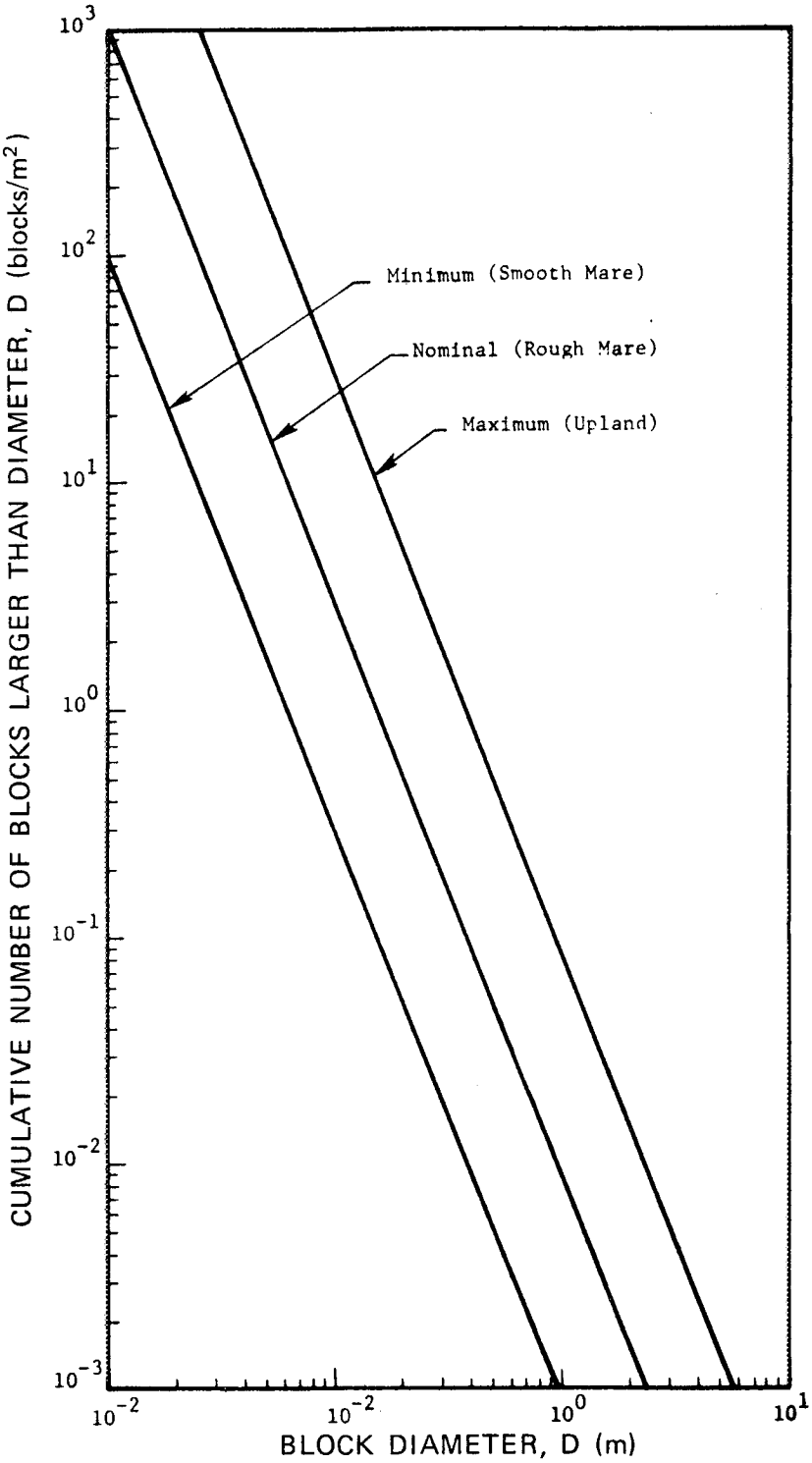

Figure VII-22. Cumulative number of blocks.

7.2.6 Soil Properties[6]

7.2.6.1 Composition

The near-surface materials of Mars can be considered to be basaltic in composition with 60 ± 10 percent SiO_2 except where there are extensive deposits of carbon dioxide. Reflectivity data indicate that the surface contains varying amounts of limonite, hematite, geothite, montmorillonite and other impurities through chemical weathering and oxidation of the basalt. Preliminary Viking 1 results show that the surface fine material consists of iron calcium, aluminum, silicon, and sulfur as main constituents. A high calcium to potassium ratio indicates the rock is not granite-like [VII-57].

7.2.6.2 Soil Models

Martian data imply the surface contains a variety of soil types just as on earth. As a result, five different models are used to encompass the possible types of Martian soils.

The nominal Martian soil is considered to be the same as the average lunar soil. The four additional soil models are: loess, dune sand, lag gravel, and hard rock. Combinations of these five models may exist; for example, a layer of loess or sand overlaying rock. Recommended values for selected soil parameters are listed in Table VII-9 for the five soil models. Cumulative particle size distributions are shown in Figure VII-23.

7.2.6.3 Soil Penetration Resistance

The penetration resistance of the lunar nominal soil ranges from about 1 to 6 $N/cm^2/cm$ [VII-58]. The lower limit of this range can be considered to be representative of Martian loess and the upper limit to be representative of dune sand.

On the basis of theories like those in Reference VII-49, estimates of the soil static bearing capacity of the soil can be made with the soil parameters listed in Table VII-9. (The static bearing capacity of the soil generally has the characteristic that a small additional load suddenly produces a large increase in penetration.)

---

6. Final Viking reports are expected to improve the properties given in Paragraph 7.2.6.

TABLE VII-9. SOIL PARAMETERS

Parameter	Soil Model				
	Nominal	Loess	Dune Sand	Lag Gravel	Rock
Bulk Density, ρ (g/cm^3)	1.35 to 1.8	0.7 to 1.6	1.4 to 1.7	1.4 to 1.7	2.7 to 3.2
Porosity (percent)	48 ± 8	56 ± 10	49 ± 5	49 ± 5	0 to 3
Cohesion (N/cm^2)	0.003 to 0.21	0 to 10	0 to 0.01	0	1000 to 5000
Angle of Internal Friction (deg)	35 to 45	25 to 41	30 to 40	30 to 40	40 to 50
Permeability (cm^2)	10^{-8} to 10^{-7}	10^{-8} to 10^{-6}	10^{-6} to 10^{-3}	10^{-3} to 10^{-1}	10^{-10}
Thermal Inertia, I (10^{-3} cal/cm^2 $s^{1/2}$ K)	1.2 to 2.0	4.5	6.0	10	20
Dielectric Constant	2.3 to 3.5	1.6 to 3.0	2.6 to 3.2	2.6 to 3.2	7.2 to 13

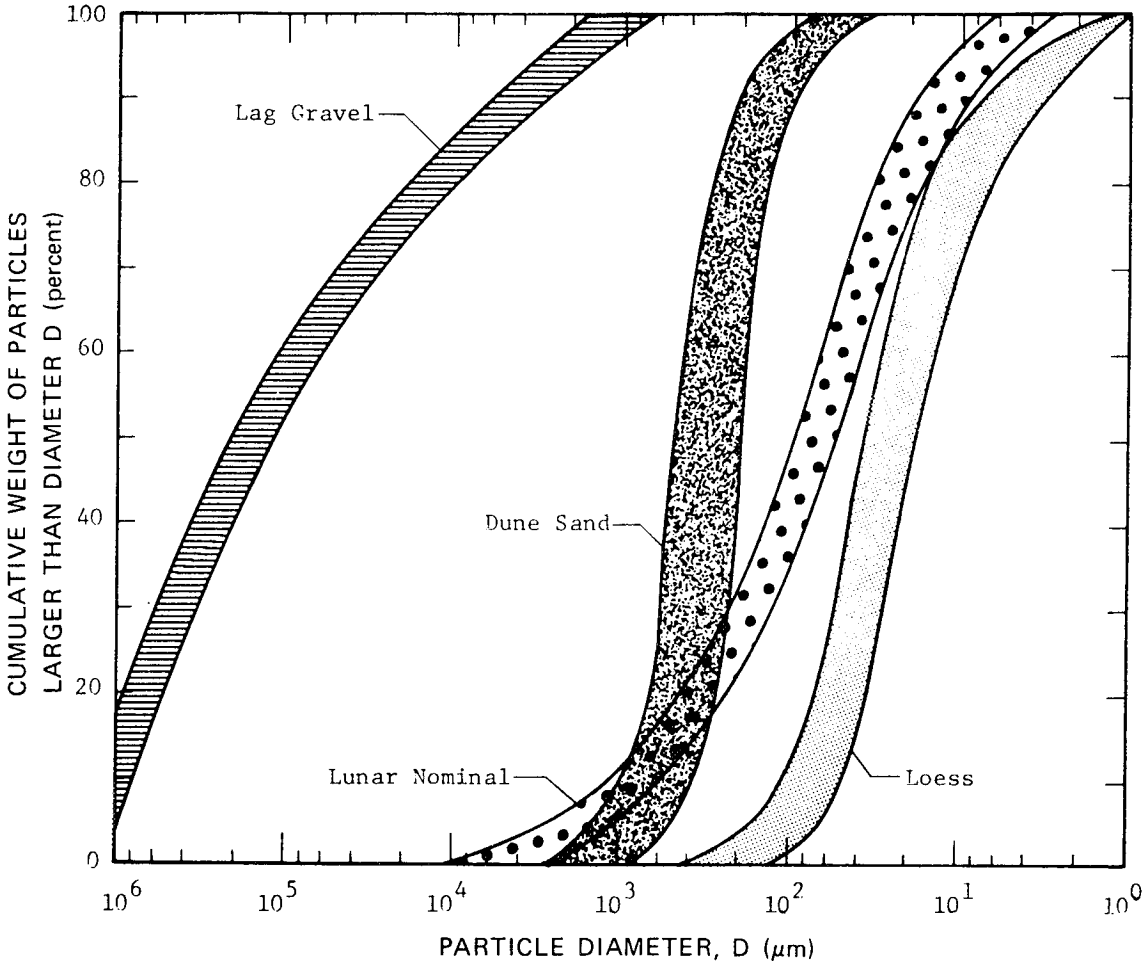

Figure VII-23. Cumulative particle distribution.

7.2.6.4 Moisture Content

Although Martian data clearly indicate the presence of water vapor in the atmosphere, it is not expected that liquid water will be common or necessarily exist on the surface. Because the average atmospheric surface pressure of about 5 or 6 mb is very near the triple point on the phase diagram for water, only a small amount of liquid water would be present. The most likely location of liquid water would be near the surface in thermally protected areas such as caves, fissures, and voids in the Martian soil.

For engineering purposes, the Martian soil should be considered to be dry except for minor amounts of moisture held by capillary tension. These small amounts may increase the soil cohesion and thereby have an influence on soil bearing capacity and on such mechanical operations as sieving or grinding of soil samples.

7.2.7 Thermal Properties

7.2.7.1 Surface Temperature

The theoretical annual variation of minimum and maximum surface temperatures over the entire planet are shown in Figures VII-24 and VII-25. The temperatures were computed from a mathematical model developed by H. H. Kieffer[10] from thermal properties and temperatures based on Martian data. No attempt was made in the development of the model to represent temperature gradients precisely at the edge of the polar cap. As a result, the large temperature changes at the polar cap boundaries are only representative of the actual temperature variation. Figures VII-24 and VII-25 correspond to an emissivity $\epsilon = 1.00$, bolometric albedo $A_{bol} = 0.25$, and thermal inertia $I = 0.0065$ cal/cm^2 s$^{1/2}$ K. The variation of minimum and maximum temperatures for other values of I, ϵ, and A_{bol} can be estimated from the diurnal variations of surface temperature shown in Figures VII-26 and VII-27.

Figure VII-26 shows the diurnal temperature variation at the equator for four values of thermal inertia for $\epsilon = 1.00$ and $A_{bol} = 0.25$ when Mars is at a zero heliocentric longitude. Figure VII-27 shows the diurnal temperature variation corresponding to the 0.0065 thermal inertia curve in Figure VII-26 when ϵ ranges between 0.90 and 1.00 and A_{bol} ranges between 0.25 and 0.35. The upper boundary corresponds to $A_{bol} = 0.25$, $\epsilon = 0.90$, while the lower boundary corresponds to $A_{bol} = 0.35$, $\epsilon = 1.00$.

Preliminary Viking 1 results using a homogeneous thermal model based on Mariner 9 late observations used $A_{bol} = 25$ and $I = 0.0065$ ca/cm^{-2} s^{-2}. Warm regions have some correlation with the areas depicted as dark regions on the Mariner 9 maps [VII-9].

7.2.7.2 Subsurface Temperature

The variation of subsurface temperature along the equator is shown in Figure VII-28 for the first 15 cm of depth. These temperatures correspond to $I = 0.0065$ cal/cm^2 S$^{1/2}$ K, $\epsilon = 1.00$, and $A_{bol} = 0.25$.

---

8. Final Viking results are expected to improve the properties given in Paragraph 7.2.7.

9. Figures VII-24 through VII-28 were developed by Hugh H. Kieffer of UCLA; this work was used in establishing engineering models for the Viking Project.

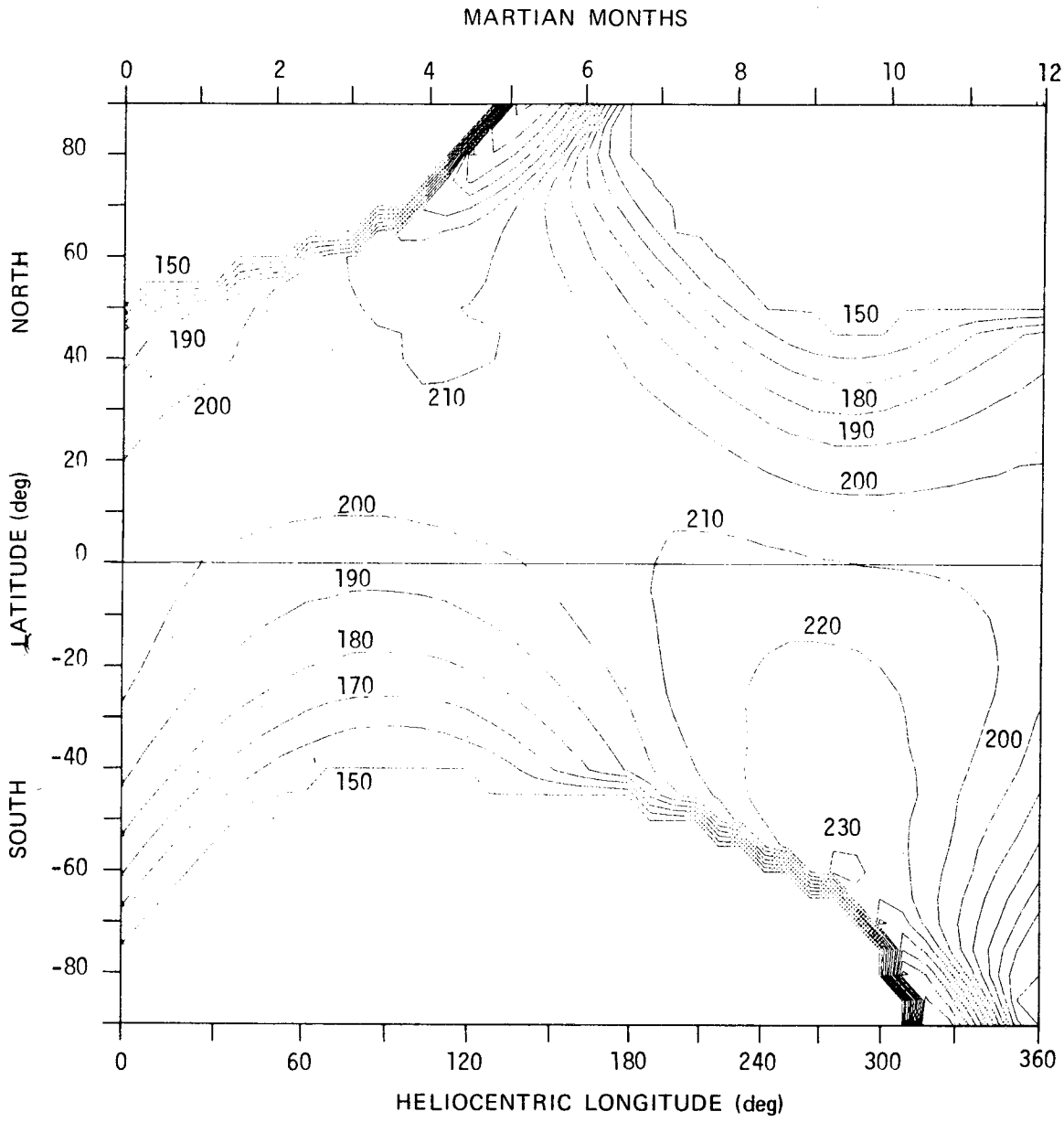

Figure VII-24. Annual variation of minimum global surface temperature in K for I = 0.0065 cal/cm^2 s$^{1/2}$ K, A_{bol} = 0.25, and ϵ = 1.00.

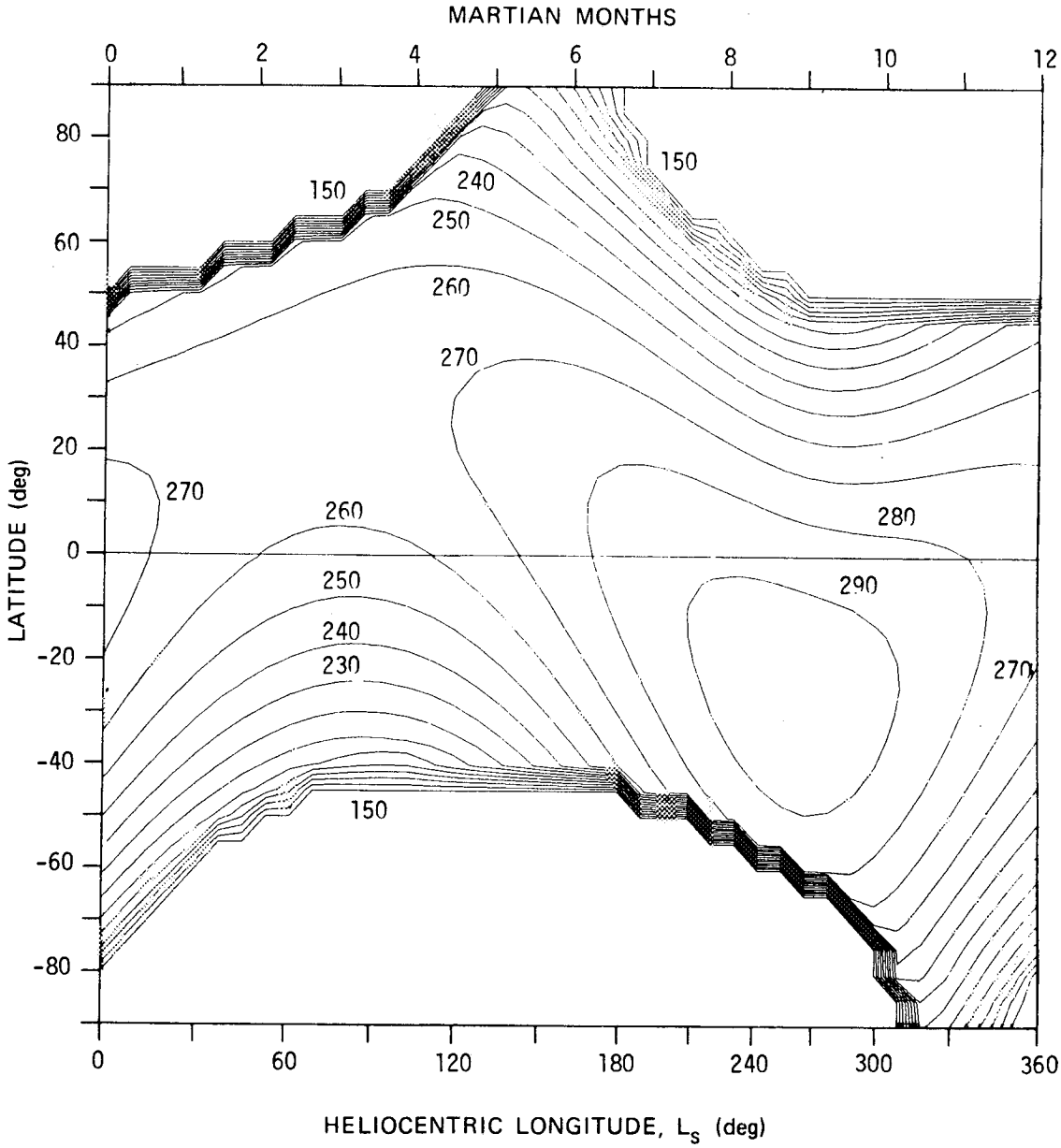

Figure VII-25. Annual variation of maximum global surface temperature in K for I = 0.0065 cal/cm^2 s$^{1/2}$ K, A_{bol} = 0.25, and ϵ = 1.00.

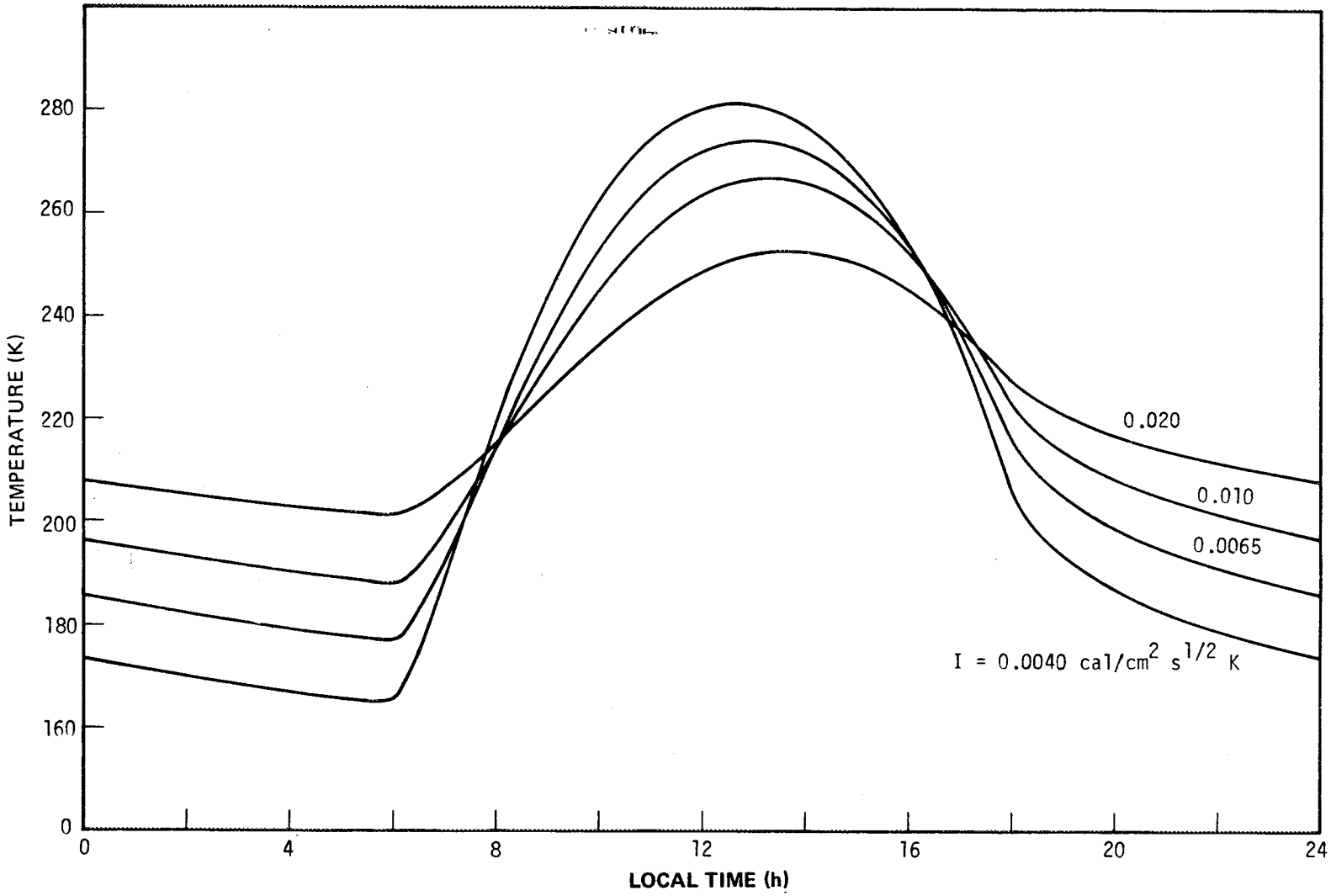

Figure VII-26. Influence of thermal inertia on equatorial surface temperature for the beginning of Northern Spring, $A_{bol} = 0.25$ and $\epsilon = 1.00$.

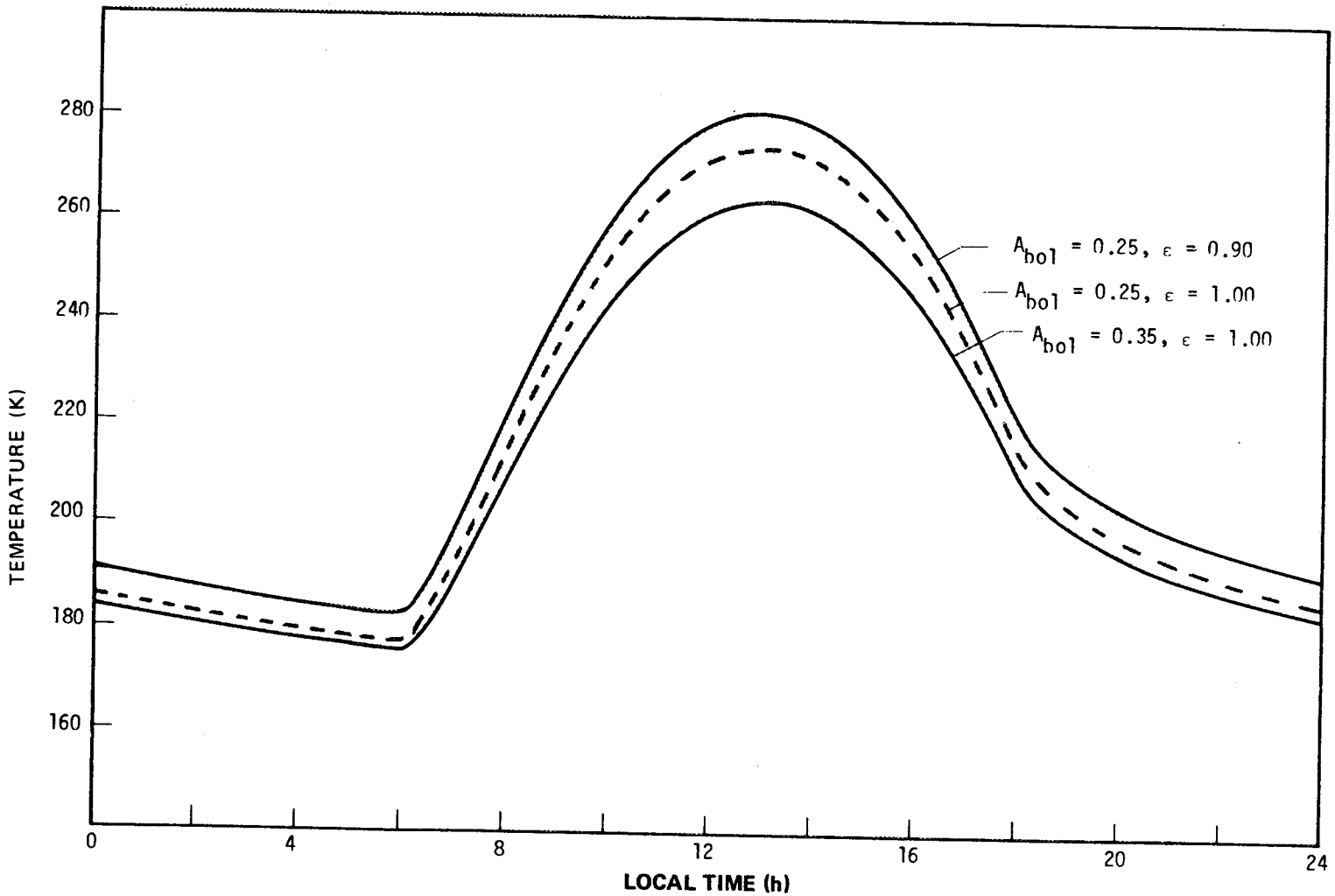

Figure VII-27. Influence of bolometric albedo and emissivity on equatorial surface temperature for the beginning of Northern Spring, thermal inertia = 0.0065 cal/cm^2 s$^{1/2}$ K.

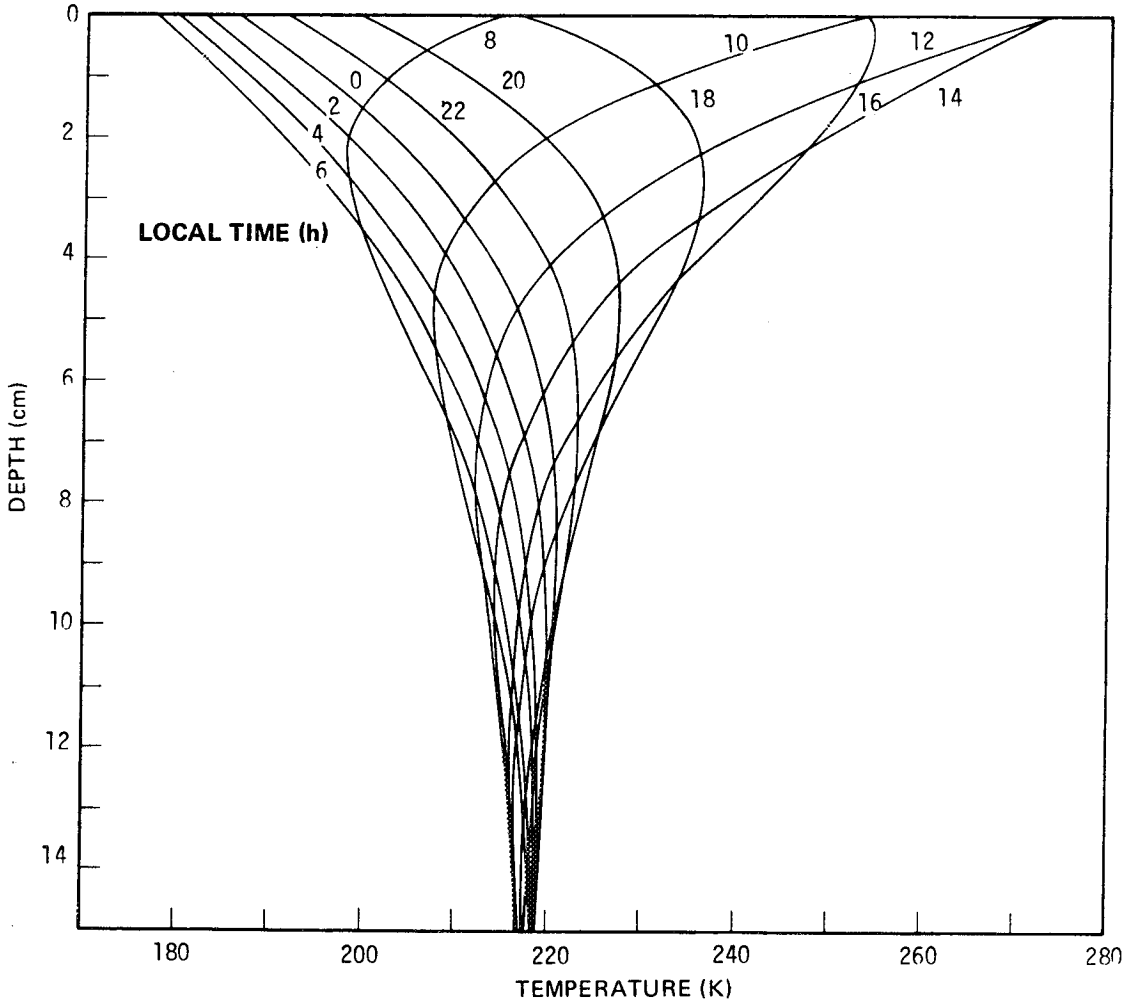

Figure VII-28. Equatorial subsurface temperature for the beginning of Northern Spring, I = 0.0065 cal/cm^2 s$^{1/2}$ K, A_{bol} = 0.25, and ϵ = 1.00.

7.2.7.3 Thermal Parameters

Recommended values for the Martian surface thermal parameters are listed in Table VII-10.

7.2.8 Electrical Properties

7.2.8.1 Dielectric Constant

Ranges for the dielectric constant, ϵ, and loss tangent, tan δ, are given in Table VII-11.

TABLE VII-10. THERMAL PARAMETERS

Parameter	Value
Thermal Conductivity, k (cal/s cm K)	2×10^{-5} to 2×10^{-4}
Specific Heat, c (cal/g K)	0.15 to 0.19
Emissivity, ϵ (dimensionless)	0.90 to 0.98
Thermal Inertia, I (10^{-3} cal/cm^2 s$^{1/2}$ K)	4 to 10
Bolometric Albedo, A_{bol} (dimensionless)	0.2 to 0.4

TABLE VII-11. ELECTRICAL PROPERTIES OF SOIL AND ROCKS

Parameter	Value	
	Soil	Rocks
Dielectric constant, ϵ	1 to 3	7 to 9
Loss tangent, tan δ	0.005 to 0.05	0.01 to 0.10

7.2.9 Optical Properties

The surface spectral radiance is expressed in Reference VII-56.

$$N_\lambda = \frac{1}{\pi} E_s \tau_\lambda(i;\gamma)\tau_\lambda(e;\gamma)\rho_o \Phi(i, e, \alpha) \quad ,$$

where

N = surface spectral radiance (W/cm^2 sr)

E_s = solar irradiance at Mars (W/cm^2)

$\tau_\lambda(i;\gamma)$ = spectral transmission of atmosphere = exp ($-\gamma$/cos i) (dimensionless)

$\tau_\lambda(e;\gamma)$ = spectral transmission of atmosphere = exp ($-\gamma$/cos e) (dimensionless)

ρ_o = surface normal spectral albedo (dimensionless)

γ = atmospheric optical thickness (dimensionless) .

The photometric function $\Phi(i, e, \alpha, \lambda)$ is given in Paragraph 7.2.9.2 in terms of the angles shown in Figure VII-29. In the figure, i and e are the angles of incidence and emergence measured between the surface normal line and the incidence and emergence rays, respectively, and α is the angle in the plane containing the incident and emitted rays (the phase plane). The great circle passing through the point N, and perpendicular to the phase plane, intercepts the phase plane at N'. The two factors $\tau_\lambda(i;\gamma)$ and $\tau_\lambda(e;\gamma)$ account for the loss of light through the atmosphere. If the point of observation is on the surface, the factor $\exp(-\gamma/\cos e)$ is set equal to unity. Observations from orbit require both factors to account for the loss in the incident and emergence light rays. Recommended values for the optical thickness γ are listed in Reference VII-56 over the wavelength range 0.25 to 0.50 μm. The values listed imply $\gamma = 0.006 \pm 0.004$ is a reasonable range for the wavelength range of validity of the photometric function given in Paragraph 7.2.9.1.

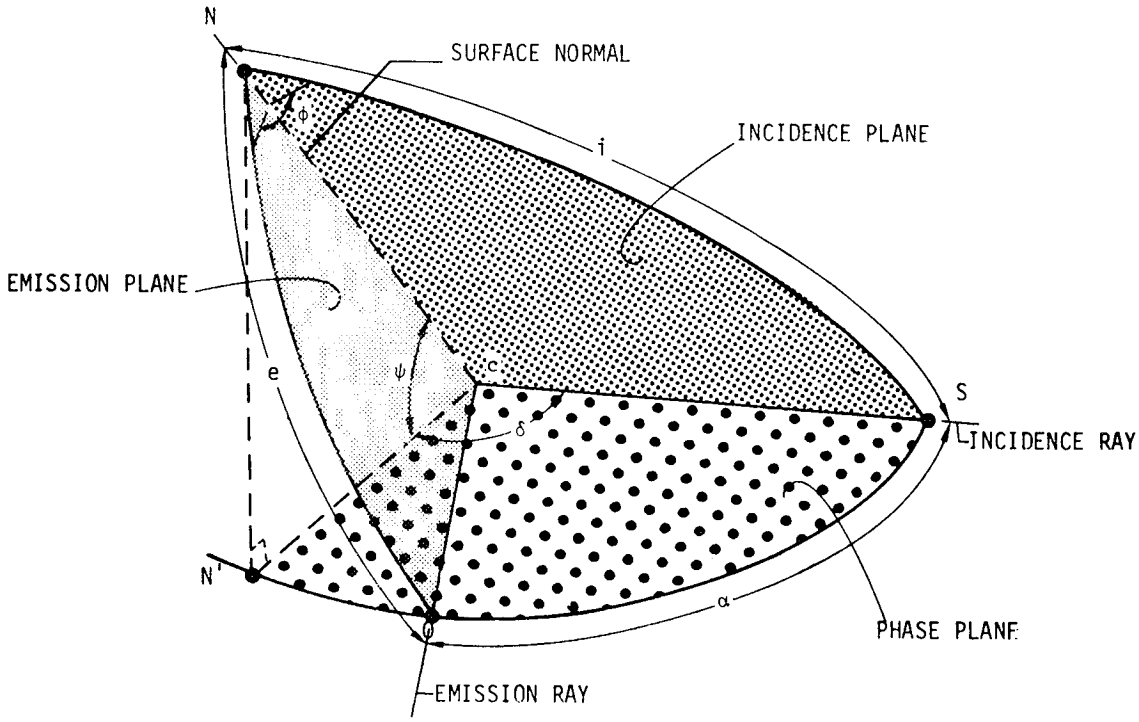

Figure VII-29. Geometrical parameters in photometric function.

7.2.9.1 Photometric Function

The photometric function (valid over the approximate range $\lambda = 0.42$ to $0.70\ \mu m$) is expressed in terms of the angles shown in Figure VII-29 as

$$\Phi(i,e,\alpha) = \frac{\cos i}{(1 + a_0 + a_1)(\cos i + \cos e)} [(1 + a_0 \cos \alpha)\, f(i,e,\alpha; a_2) + a_1(\cos i + \cos e)] ,$$

where $a_0 = 0.55$, $a_1 = 0.60$, $a_2 = 0.18$ are empirical parameters that depend on properties of the surface, and where

$$f(i,e,\alpha;a_2) = e^{\mu-\nu} + \nu \int_0^1 \exp\{\mu - \frac{\nu}{6\pi g} [3\pi(2g - 1)x + 6x \sin^{-1} x + 2(2 + x^2)(1 - x^2)^{1/2}]\}\, dx$$

in which

$$\mu = \frac{4a_2(1 + \cos \alpha)}{3 \sin \alpha}$$

$$\nu = \frac{\pi a_2(\cos i + \cos e)[\cos \delta + \cos(\alpha - \delta)]\cos \psi}{\sin \alpha \cos i \cos e}$$

$$g = \frac{(\cos i + \cos e)\cos \delta \cos(\alpha - \delta)\cos \psi}{[\cos \delta + \cos(\alpha - \delta)]\cos i \cos e}$$

$$\cos \alpha = \cos i \cos e + \sin i \sin e \cos \phi .$$

7.2.9.2 Albedo

Spectral albedo values are listed in Table VII-12 and plotted in Figure VII-30.

TABLE VII-12. ESTIMATED SURFACE NORMAL SPECTRAL ALBEDO FOR DESERT AND MARE AREAS [VII-56]

Wavelength λ (μm)	Normal Spectral Albedo, ρ_o			
	Mare		Desert	
	Dark Area	Average	Average	Bright Area
0.40	0.06	0.06	0.06	0.07
0.45	0.07	0.07	0.07	0.09
0.50	0.08	0.09	0.10	0.13
0.55	0.09	0.11	0.14	0.20
0.60	0.11	0.14	0.20	0.28
0.65	0.13	0.17	0.25	0.35
0.70	0.14	0.19	0.28	0.38
0.75	0.14	0.20	0.30	0.39
0.80	0.14	0.21	0.30	0.40
0.85	0.13	0.21	0.30	0.40
0.90	0.12	0.21	0.30	0.40
0.95	0.12	0.21	0.30	0.40
1.00	0.12	0.20	0.30	0.40

7.2.10 Meteoroid Environment

7.2.10.1 Cometary Meteoroid Flux

The flux (F_c), in number per square meter per second, of cometary meteoroids of mass m on a randomly tumbling surface is: For $10^{-6} \leqq m \leqq 10^{-2}$,

$$\log F_c = -14.851 - 1.213 \log m + \log \left(1 + \frac{0.233}{r}\right) + \log \frac{1}{2}\left[1 + \left(1 - \frac{1}{r^2}\right)^{1/2}\right] + \log V_c \quad .$$

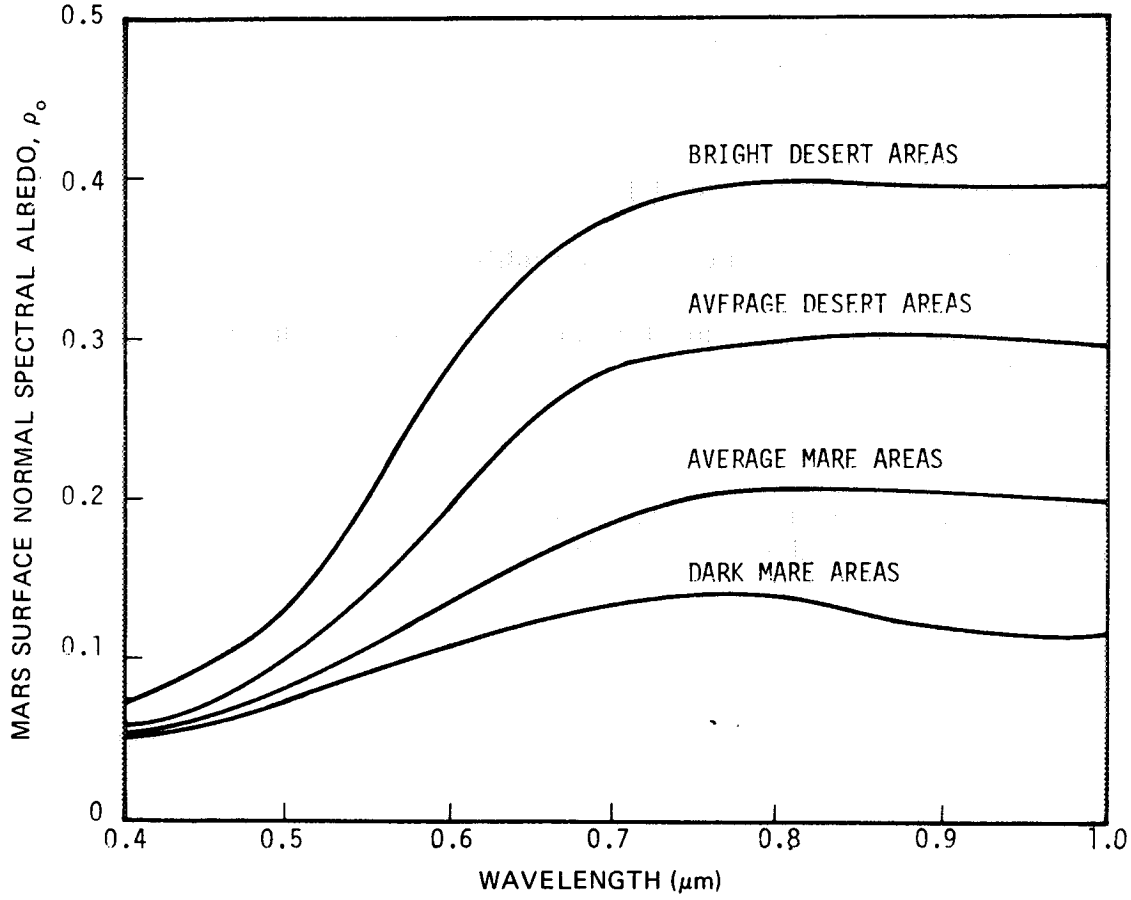

Figure VII-30. Estimates of Mars surface normal spectral albedo [VII-56].

For $10^{-12} \leqq m \leqq 10^{-6}$,

$$\log F_c = -14.820 - 1.584 \log m - 0.063 (\log m)^2 + \log \left(1 + \frac{0.233}{r}\right) + \log \frac{1}{2} \left[1 + \left(1 - \frac{1}{2}\right)^{1/2}\right] + \log V_c \quad ,$$

where

V_c = average cometary velocity relative to spacecraft in meters per second

r = distance of the spacecraft from the center of the planet (in units of the planet's radius).

7.2.10.2 Average Velocity of Cometary Meteoroids

The average velocity of cometary meteoroids relative to the spacecraft is 15.74 km/s.

7.2.10.3 Survival Mass

The survival mass for micrometeoroids can be calculated as a function of height in the atmosphere by using the following approximate expression:

$$m^{1/3} = m_{\infty}^{1/3} = \frac{\Lambda A \rho_m^{-2/3} v^2}{6 \xi \cos Z} \int_{\infty}^{h} \rho_a \, dh \quad \text{(does not hold for dustballs)}$$

where

$$\text{columnar mass} = -\int_{h}^{\infty} \rho_a \, dh$$

z = zenith angle

ρ_m = density of micrometeoroid ($3.5 > \rho_m > 0.5$ g/cm^3)

v = velocity of micrometeoroid ($v_{parabolic}$ or $v_{orbital} > v > v_{escape}$)

A = shape factor = 1.2 for sphere

$\Lambda/\xi = 10^{-11.449}$.

7.3 Satellites

Mars has two known satellites: Phobos and Deimos. Phobos, the larger of the two, has a period of rotation about one-third that of Mars. Thus, Phobos appears to be in retrograde motion as seen from the surface of Mars, though actually it is not (Phobos will rise in the west and set in the east). Deimos, very nearly a synchronous satellite, will rise in the east very slowly and almost half of its phases will be visible in one night, as seen from the surface of Mars. However, both satellites are small and will appear only as bright stars, Phobos being the brighter of the two. The results of searches for other moons disclosed no detectable satellites. However, objects less than 1.609×10^5 cm (1 mile) in diameter would not have been detected. Data for satellites of Mars are summarized in Table VII-13.

7.4 Radiation Environment

7.4.1 Galactic Cosmic Radiation

Same as Interplanetary Space (Section 1.3.1).

7.4.2 Solar Cosmic Radiation

Same as Interplanetary Space (Section 1.3.2).

7.4.3 Trapped Radiation

Mariners 4, 6, and 7 measurements did not detect any trapped radiation belts beyond 4 Martian radii, which is their limit of detection.

7.4.4 Solar Thermal Radiation

In the vicinity of Mars beyond the Martian atmosphere, the solar radiation will be assumed to have the same spectrum as that of interplanetary space. The integrated intensity will be varying from 490 to 713 W/m^2 [VII-59], depending on the sun-Mars distance at encounter. The significant difference between the Mars spectrum and that of the earth's atmosphere is that it does not have the absorption band in the ultraviolet region because of O_3 and O_2. Therefore, the solar ultraviolet from 2000 to 3000 Å can penetrate the Martian atmosphere and arrive at the Martian surface.

TABLE VII-13. DATA SUMMARY FOR SATELLITES OF MARS

Satellite	Discovery		Siderial Period of Revolution (P_{sid})		Mean Synodic Period of Revolution (P_{syn})		Orbital Mean Motion, P_{sid} (°/d)	Eccentricity (e)
	Discoverer	Date	d	mean solar time	d	mean solar time		
II Phobos	A. Hall	17 Aug. 1877	0.31891031	0 07 39 13.851	0.3190585	0 07 39 26.65	1128.84402	0.021
I Deimos	A. Hall	11 Aug. 1877	1.26244064	1 06 17 54.871	1.2647648	0 06 21 15.68	285.16192	0.002

Satellite	Apparent Distance			Mean Distance from Planet (a)			Inclination of Orbit to Planet's Equator (g)	Visual Magnitude at Mean Opposition Distance (m_{viz})	Radius, R (km)
	At Unit Distance	As Seen From Sun	At Mean Opposition	(10^{-3} AU)	(10^3 km)	In Eq. Radii of the Primary			
II Phobos	12.938	8.491	24.705	0.062725	9.384	2.747	0°57'	11.6	8
I Deimos	32.373	21.246	61.817	0.15695	23.479	6.873	1°18'	12.8	4

The average annual radiation from the surface of Mars is 103 W/m^2 which corresponds to an average surface temperature of 206°K if the albedo of Mars is 0.295. This average surface temperature is too low as compared to the result of 220 K obtained by Öpik. However, the average surface temperature will be raised to 215.6 K if the albedo of Mars is 0.159.

Objects on or near the surface of Mars will receive radiation according to their shape, orientation, and distance from the surface. For a spherically shaped object, the following equation may be used to compute the incident flux:

$$Q = FAI ,$$

where

Q = flux incident on sphere

F = view factor which depends on altitude

A = cross-sectional area of sphere

I = Mars thermal radiation flux ($103/Wm^2$).

7.4.5 Albedo Radiation

Albedo radiation varies from 241 W/m^2 at 200 km to 4 W/m^2 at 2×10^4 km under maximum conditions (zero phase angle and normal to flux) Albedo radiation will contribute about 70 percent of the total radiation from the planet upon a spacecraft if a planetary integrated albedo of 0.295 is taken. No reliable determinations of the integrated albedo of Mars are available at present; however, when separated from the total spectrum, the albedo is usually considered to be 0.159 [VII-59]. The incident albedo radiation flux, Q, can be calculated from the following equation:

$$Q = FASa ,$$

where

F = the view factor, which varies with altitude

A = cross-sectional area of exposed spherical surface

S = solar constant at Mars orbital position

a = Mars albedo.

7.4.6 Albedo

Mars traditionally has been divided into a number of areas which have been visible to the optical astronomers more or less consistently for the last century or so on the basis of albedo differences. The relative albedo range from light areas is found to be $0.18 > 0.3$, and for dark areas to be < 0.09 to 0.18. Based on these data, a contour map of the geometric albedo has been constructed.

One should remember that the geometric albedo varies with wavelength. Harris [VII-65] has tabulated the values of geometric albedo for the wavelength from 4050 to 6360 Å. If the visual albedo is defined as the albedo at 5500 Å, then it has a value of 0.159. However, the average albedo, which is defined as the ratio of the amount of solar radiation reflected over the whole spectrum to the incident radiation, has a value of 0.295.

7.4.7 Solar Constant

The solar constant is the rate at which energy is received upon a unit surface, perpendicular to the sun's direction, in free space at the Mars' mean distance from the sun. It is generally expressed in calories per square centimeter per minute or in watts per square centimeter per minute or in watts per square meter. A recent study indicates that the solar constant for Mars is

	cal/cm^2min	W/m^2
Perihelion	1.017	708.8
Average	0.836	582.8
Aphelion	0.699	487.0

These values were obtained based on the value of solar constant at 1 AU being 1.94 cal/cm^2 min.

7.5 Astrodynamic Constants

Mars Constants (Epoch 1960.0)

Distance from sun (average)	2.2794×10^8 km or 1.5236915 AU
Eccentricity of orbit	0.0933681
Inclination of orbit to ecliptic	1° 50' 59.8"
Orbital period (sidereal)	686.97971 days
Radius (equatorial)	3393.4 km
Mass ratio (sun/planet)	3 098 700 ± 100
Mass ratio (Mars/earth)	0.1074469
Flattening (dynamic)	1:190.5
Average density	3.879 g/m^3
Rotational period	24 hr 37 min 22.6689 s
Gravitational parameter	4.28284×10^4 km^3/s^2
Mean orbital velocity	24.13 km s^{-1}

REFERENCES

VII-1. Ingersol, A. P., and Leovy, C. B.: The Atmospheres of Mars and Venus. Annual Reviews of Astronomy and Astrophysics, vol. 9, 1971, pp. 147-182.

VII-2. Soffen, G. A.: Scientific Results of the Viking Missions. Science, vol. 194, 1976, pp. 1274-1276.

VII-3. Anon.: Models of Mars Atmosphere (1974). NASA Space Vehicle Design Criteria (Environment). NASA SP-8010, Revised December 1974.

VII-4. Anon.: Mars Engineering Model. NASA Langley Research Center, Viking Project Office M75-125-1, December 1970.

VII-5. Weaver, K. F.: Journey to Mars. National Geographic, vol. 143, no. 2, February 1973, pp. 231-263.

VII-6. Anon.: Mariner Mars 1971 Project Final Report; Vol. IV — Science Results. Jet Propulsion Laboratory, Technical Report 32-1550, July 15, 1973.

VII-7. Soffen, G. A., and Snyder, C. W.: The First Viking Mission to Mars. Science, vol. 193, 1976, pp. 759-765.

VII-8. Farmer, C. B. and LaPorte, D. D.: Viking: Mars Atmospheric Water Vapor Mapping Experiment — Preliminary Report of Results. Science, vol. 193, 1976, pp. 776-780.

VII-9. Kieffer, H. H., et al.: Infrared Thermal Mapping of the Martian Surface and Atmosphere: First Results. Science, vol. 193, 1976, pp. 780-785.

VII-10. Nier, A. O., et al.: Composition and Structure of the Martian Atmosphere: Preliminary Results from Viking 1. Science, vol. 193, 1976, pp. 786-788.

VII-11. Hess, S. I., et al.: Preliminary Meteorological Results on Mars from the Viking 1 Lander. Science, vol. 193, 1976, pp. 788-791.

REFERENCES (Continued)

VII-12. Anon: Viking 1 Early Results. NASA SP-408, 1976.

VII-13. Abelson, P. H.: Viking 1. Science, vol. 193, 1976.

VII-14. Gierasch, P., and Goody, R.: The Effect of Dust on the Temperature of the Martian Atmosphere. Journal of Atmospheric Sciences, vol. 29, 1972, pp. 400-402.

VII-15. Kliore, A. J., et al.: Mariner 9 S-Band Martian Occultation Experiment: Initial Results on the Atmosphere and Topography of Mars. Science, vol. 175, January 21, 1972, pp. 313-317.

VII-16. Golitsyn, G. S.: On the Martian Dust Storms. Icarus, vol. 18, 1973, pp. 113-119.

VII-17. Sagan, C.: Sandstorms and Eolian Erosion on Mars. Chapter XII of Mariner Mars 1971 Project Final Report: Vol. IV (ref. 9), July 15, 1973, pp. 171-178.

VII-18. Pirraglia, J. A., and Conrath, B. J.: Martian Tidal Pressure and Wind Fields Obtained from the Mariner 9 Infrared Spectroscopy Experiment. J. of Atmos. Sci., vol. 3, no. 2, March 1974, pp. 318-329.

VII-19. Chapman, S., and Lindzen, R. S.: Atmospheric Tides. Reidel Publishing Co., (Dordrecht, Holland), 1970.

VII-20. Lindzen, R. S.: The Application and Applicability of Terrestrial Atmospheric Tidal Theory to Venus and Mars. Journal of Atmospheric Science, vol. 27, July 1970, pp. 536-549.

VII-21. Blumsack, S. L., Gierasch, P. J., and Wessel, W. R.: An Analytical and Numerical Study of the Martian Planetary Boundary Layer over Slopes. Journal of Atmospheric Science, vol. 30, 1972, pp. 66-82.

VII-22. Blumsack, S. L., and Gierasch, P. J.: The Vertical Thermal Structure of the Martian Atmosphere: Modifications by Motions. Icarus, vol. 18, 1973, pp. 126-133.

REFERENCES (Continued)

VII-23. Fehsenfeld, F. C., Dunkin, D. B., and Ferguson, E. E.: Rate Constants for the Reaction of CO_2^+ with O, O_2 and NO; N_2^+ with O and NO; and O_2^+ with NO. Planetary Space Sciences, vol. 18, 1970, pp. 1267-1269.

VII-24. Fjeldbo, G., Kliore, A., and Seidel, B.: The Mariner 1969 Occultation Measurements of the Upper Atmosphere of Mars. Radio Science, vol. 5, 1970, pp. 381-386.

VII-25. Barth, C. A., et al.: Mariner 9 Spectrometer Experiment: Mars Airglow Spectroscopy and Variations in Lyman Alpha. Icarus, vol. 17, 1972, pp. 457-468.

VII-26. Cloutier, P. A., and Daniell, R. A., Jr.: Ionospheric Currents Induced by Solar Wind Interaction with Planetary Atmospheres. Planetary Space Sciences, vol. 21, 1973, pp. 463-474.

VII-27. Bauer, S. J., and Hartle, R. E.: On the Extent of the Martian Ionosphere. J. of Geophysical Research, vol. 78, no. 16, June 1, 1973, pp. 3169-3171.

VII-28. Dolginov, Sh. Sh., Yeroshenko, Ye. G., and Zhuzgov, L. N.: The Magnetic Field in the Very Close Neighborhood of Mars According to Data from the Mars 2 and Mars 3 Spacecraft. J. of Geophysical Research, vol. 78, 1973, pp. 4779-4786.

VII-29. Kliore, A. J., et al.: S-Band Radio Occultation Measurements of the Atmosphere and Topography of Mars with Mariner 9: Extended Mission Coverage of Polar and Intermediate Latitudes. Chapter XXXVI of Mariner Mars 1971 Project Final Report: Vol. IV (ref. 9), July 15, 1973, pp. 473-494.

VII-30. Barth, C. A., et al.: Mariner 6 and 7 Ultraviolet Spectrometer Experiment: Upper Atmosphere Data. Journal of Geophysical Research, vol. 76, 1971, pp. 2213-2227.

VII-31. Dementyeva, N. N., et al.: Preliminary Results of Measurements of UV Emissions Scattered in the Martian Upper Atmosphere. Icarus, vol. 17, 1972, pp. 475-483.

REFERENCES (Continued)

VII-32. Anderson, D. E., Jr., and Hord, C. W.: Mariner 6 and 7 Ultraviolet Spectrometer Experiment: Analysis of Hydrogen Lyman Alpha Data. Journal of Geophysics Research, vol. 76, 1971, pp. 6666-6673.

VII-33. Strickland, D. J., Thomas, G. E., and Sparks, P. R.: Mariner 6 and 7 Ultraviolet Spectrometer Experiment: Analysis of the OI 1304A and 1356A Emission. Journal of Geophysical Research, vol. 77, 1972, pp. 4052-4068.

VII-34. Stewart, A. I.: Mariner 6 and 7 Ultraviolet Spectrometer Experiment: Implications of CO_2^+, CO, and O Airglow. Journal of Geophysics Research, vol. 77, 1972, pp. 54-68.

VII-35. Stewart, A. I., et al.: Mariner 9 Ultraviolet Spectrometer Experiment: Structure of Mars' Upper Atmosphere. Icarus, vol. 17, 1972, pp. 469-474.

VII-36. Barker, E. S.: Detection of O_2 in the Martian Atmosphere with the Echelle-Coude Scanner of the 107-inch Telescope. Bull. Amer. Astron. Soc., vol. 4, 1972, pp. 371, 372.

VII-37. McElroy, M. B.: Ionization Processes in the Atmospheres of Venus and Mars. Ann. Geophy., vol. 26, no. 2, 1970, pp. 643-652.

VII-38. Curran, R. J., et al.: Mars: Mariner 9 Spectroscopic Evidence for H_2O Ice Clouds. Science, vol. 182, no. 4110, October 26, 1973, pp. 381-383.

VII-39. Pearl, J., et al.: Results from the Infrared Spectroscopy Experiment on Mariner 9. Exploration of the Planetary System, Proceedings of IAU Symposium 65, A. Woszczyk and C. Iwaniszewska, eds., D. Reidel (Dordrecht, Holland), 1974, p. 201.

VII-40. Briggs, G. A., and Leovy, C. B.: Mariner 9 Observations of the Mars North Polar Hood. Bulletin of the American Meteorological Society, vol. 55, no. 4, April 1974, pp. 278-296.

VII-41. Leovy, C. B., et al.: Mariner Mars 1969: Atmospheric Results. Journal of Geophysical Research, vol. 76, 1971, pp. 297-312.

REFERENCES (Continued)

VII-42. Herr, K. C., and Pimentel, G.: Evidence for Solid Carbon Dioxide in the Upper Atmosphere of Mars. Science, vol. 167, 1970, pp. 47-49.

VII-43. Pitts, D.: A Computer Program for Calculating Model Planetary Atmospheres. NASA TN D-4292, 1968.

VII-44. Strickland, D. J., et al.: Mariner 9 Ultraviolet Spectrometer Experiment: Mars Atomic Oxygen 1304-A Emission. Chapter XXIII of Mariner Mars 1971 Project Final Report: Vol. IV (ref. 9), July 15, 1973, pp. 355-368.

VII-45. Conrath, B., et al.: Atmospheric and Surface Properties of Mars Obtained by Infrared Spectroscopy on Mariner 9. Chapter XX of Mariner Mars 1971 Project Final Report: Vol. IV (ref. 9), July 15, 1973, pp. 299-314.

VII-46. Anon.: Mariner 9 Infrared Interferometer Spectrometer (IRIS) Reduced Data Records Documentation. NASA X-622-73-305, Goddard Space Flight Center, October 1973.

VII-47. Carr, M. H., et al.: Preliminary Results from the Viking Orbiter Imaging Experiment. Science, vol. 193, 1976, pp. 766-775.

VII-48. Mutch, T. A., et al.: The Surface of Mars: The View from the Viking 1 Lander. Science, vol. 193, 1976, pp. 791-800.

VII-49. Terzaghi, K., and Peck, R.: Soil Mechanics in Engineering Practice. J. Wiley and Sons, New York, 1967.

VII-50. Michaux, C. M., and Newburn, R. L., Jr.: Mars Scientific Model. JPL Document No. 606-1, March 1, 1972.

VII-51. Jordan, J. F., and Lorell, J.: Mariner 9, An Instrument of Dynamical Science. Presented at AAS/AIAA Astrodynamics Conference, Vail, Colorado, July 16-18, 1973.

VII-52. Hobbs, R. W., and Knapp, S. L.: Planetary Temperatures at 9.55 mm Wavelength. Icarus, vol. 14, 1971, pp. 204-209.

REFERENCES (Concluded)

VII-53. Marov, M. Ya., and Petrov. G. I.: Investigations of Mars from the Soviet Automatic Stations Mars 2 and 3. Icarus, vol. 19, 1973, pp. 163-179.

VII-54. Parkinson, T. D., and Hunten, D. M.: CO_2 Distribution on Mars. Icarus, vol. 18, 1973, pp. 29-53.

VII-55. Carr, M. H., Masursky, H., and Saunders, R. S.: A Generalized Geologic Map of Mars. JGR, vol. 78, no. 20, 1973, pp. 4031-4036.

VII-56. Anon.: Mars Engineering Model. Viking 75 Project Report M75-125-3, January 4, 1974.

VII-57. Martin, J. S., Jr., and Young, A. T.: Viking to Mars Profile of a Space Expedition. Astronautics and Aeronautics, November 1976.

VII-58. Anon.: Lunar Surface Models. NASA SP-8023, September 1973.

VII-59. Lave, E. G., and Drummon, A. J.: Solar Constant: First Direct Measurements. Science, vol. 161, 1968, pp. 888-891.

SECTION VIII. JUPITER

8.1 Atmospheric Environment

8.1.1 Definition

The atmospheric environment of Jupiter is defined as the region between the surface and 20 000 km above the surface of Jupiter.

8.1.2 Gas Properties

The variable image of the disc of Jupiter, as observed telescopically in visible light, strongly indicates an active atmosphere of sufficient thickness to obscure any features of a solid planetary surface. The presence of methane and ammonia in the absorption bands of the spectrum of Jupiter was discovered approximately 40 years ago. The occulation of σ Arietis by Jupiter was observed photoelectrically by Baum and Code in 1952, and a mean molecular weight of 3.3 was derived for their assumed stratospheric temperature of 86 K which confirmed the dominance of hydrogen and helium in Jupiter's atmosphere. The positive identification of the major component (hydrogen) was reported in 1960 and was accomplished by the spectroscopic detection of molecular hydrogen by means of its quadrupole rotation-vibration spectrum. The next step, the determination of abundances, temperatures, and pressures, for the most dense part of the atmosphere is continuing. Papers by Owens [VIII-1] and McElroy [VIII-2] summarize the abundance results from visible and infrared spectra in which absorption lines of H_2, CH_4, and NH_3 can be identified as originating in the atmosphere of Jupiter. They conclude that the abundance ratios are consistent with those of a solar mixture of elements which has evolved into simple hydrogen-bearing molecules with modification by saturation and condensation of some species, particularly NH_3 and H_2O. This conclusion is adopted herein although it must be stressed that absorption lines of He, a presumably important constituent, and minor constituents such as H_2O and Ne have not been observed in the spectra. In view of the uncertainty thereby introduced and the uncertain solar ratios of elements (particularly He), it is appropriate to consider the fractions by mass of all molecules other than H_2 uncertain by a factor of two in either direction. Atmospheric compositions and other parameters for Jovian model atmospheres are given in Table VIII-1 [VIII-3].

TABLE VIII-1. COMPOSITIONS AND OTHER PARAMETERS FOR MODEL ATMOSPHERES OF JUPITER [VIII-3].

Parameter	Cool Model	Nominal Model	Warm Model
Fractions by mass (or weight)			
H_2	0.50696	0.75348	0.87674
He	0.46000	0.23000	0.11500
CH_4	0.00857	0.00429	0.00214
NH_3	0.00219	0.00109	0.00055
H_2O	0.01601	0.00800	0.00400
Ne	0.00229	0.00115	0.00057
Others	0.00398	0.00199	0.00100
Fractions by number (or volume)			
H_2	0.68454	0.86578	0.93754
He	0.31057	0.13214	0.06149
CH_4	0.00145	0.00062	0.00028
NH_3	0.00035	0.00015	0.00007
H_2O	0.00240	0.00102	0.00048
Ne	0.00031	0.00013	0.00006
Others	0.00038	0.00016	0.00008
Mean molecular weight, u (g/mole)	2.70	2.30	2.14
Acceleration of gravity, g (cm/s^2)	2700	2500	2300
Effective temperature, T_e (K)	128	134	140
Troposphere lapse rate parameters β_o	0.222	0.236	0.259
Troposphere lapse rate parameters K_1 (K)	500	500	500
Troposphere lapse rate parameters K_2 (K)	500	295	324
Correspondence level temperature (K)	125	125	125
Correspondence level pressure (atm)	0.50	0.30	0.20
Stratosphere temperature (K)	108	113	118
Stratosphere vertical extent (scale heights)	∞	1.0	1.0
Inversion level temperature (K)	None	145	500
Inversion level pressure (atm)	None	0.0065	2×10^{-7}

The variable appearance of the planet in visible light, analogous to weather patterns on the earth is attributed to large-scale cloud features which are condensates formed in upward convecting gas. Infrared (thermal) radiation emitted in the lower atmosphere at wavelengths longer than 5 μm leads to two important conclusions: (1) Jupiter's disc is uniform within 20 percent in brightness between 8 and 14 μm, and (2) the planet radiates considerably more energy than it receives from the sun. These conclusions suggest that lower atmospheric parameters need not be specifically associated with planetary latitudes and time of day but that these variations should be included within the uncertainty specified by a single set of models [VIII-3].

8.1.2.1 Model Atmospheres [VIII-3, VIII-4, VIII-5]

The lower atmosphere of Jupiter, commencing with the observed large scale cloud features and continuing inward to an indeterminate level, is thought to be in hydrostatic equilibrium and convective to a very great depth. Lewis concludes that the three most significant condensates in the upper regions of the lower atmosphere are ammonia ice, ammonium hydrosulfide (NH_4SH), and water. Despite the pressure of the foregoing condensates, the lapse rate is nearly equal to the condensation free adiabatic value appropriate to a gas composition adapted for a model atmosphere. Another model requirement is a pressure temperature correspondence at some point. Attempts to establish such a correspondence from measurements of spectral line widths, equivalent widths, and their ratios are available but open to serious question. In particular, "cloud top reflection layer" and ammonia saturation concepts are not considered satisfactory, and on-going discussions of rotational temperatures and the associated abundance are incomplete. An alternate approach by Gillett et al. combines the 125 K temperature measured near 12 μm with the calculated opacity of the dominant absorber H_2 at that wavelength to give an abundance of 12 km-atm H_2 and a partial pressure of 0.25 atm H_2. This correspondence and the foregoing composition and lapse rate lead to a reasonable lower atmosphere model, similar to that of Owen [VIII-6], which explains many of the observed features of the reflection and emission spectra [VIII-3].

Jupiter's infrared emission suggests an effective temperature near 134 K [VIII-3]. The upper boundary of the lower atmosphere is taken as the level at which the temperature reaches 113 K with an isothermal strat stratosphere overlaying that level and extending upward at least one scale height. The upper atmosphere, as differentiated from the lower atmosphere of Jupiter, extends above the regions of significant radiation reflection,

absorption, and emission. Observational data are meager, but major conclusions are that (1) temperatures are probably near 150 K, but possible solar cycle effects may raise temperatures to as high as 500 K [VIII-3], and (2) molecular hydrogen predominates up to heights of ~ 500 km and pressures of $\sim 10^{-6}$ atm. The model atmospheres used in this document are those presented in Reference VIII-3 and follow the parameters as set forth in Tables VIII-1 through VIII-4 and Figures VIII-1 through VIII-5 for cool, nominal, and hot models.

The nominal model has been constructed with the constant values of $T_e = 134$ K, $g = 2500$ cm/s^2, and $u = 2.30$ (where T_e is the effective temperature of Jupiter, g is the local acceleration of gravity, and u is the mean molecular weight) which corresponds to the nominal composition and other quantities shown in Table VIII-1. The convective troposphere has an adiabatic lapse rate near -2 K/km, extends indefinitely downward from the tropopause boundary temperature of 113 K, and includes the correspondence level established at P = 0.30 atm and T = 125 K. Above the tropopause, an isothermal stratosphere extends upward one scale height (16.3 km). Above the stratosphere an inversion layer of constant (P/T) (dT/dP) is limited by an uppermost level at which P = 6.5 mb and T = 145 K. An isothermal region extends indefinitely upward from the latter level [VIII-7].

The limiting models are cool and warm in the sense that for a given pressure of the nominal model they provide extremes of temperature and density which are thought to bracket the range of possible Jupiter values. The values for model construction were selected as reasonable limits to the nominal values and are given in Table VIII-1. More detailed discussions of the models are available in Reference VIII-3 and the references quoted in that document. The zero altitude is set by earth analogy, at the level at which the pressure P equals 1 atm in all three models, and corresponds to the optical surface or limb of the planet near the ammonia clouds. The zero of altitude is set at 1.01325×10^{11} N/cm^2 (pressure of 1 earth atm) and corresponds to the distance from Jupiter's center of R_s, given by

$$R_s = R_J \left[1 - \epsilon (\sin \Phi)^2\right] \quad , \qquad \text{(VIII-1)}$$

where $R_J = 71\,422 \pm 2000$ km, Φ is the latitude, ϵ is the flattening, and R_s specifies the level of the optical disc of the planet (not a real liquid or solid surface).

TABLE VIII-2. VALUES AT SELECTED PRESSURES FOR NOMINAL MODEL ATMOSPHERE OF JUPITER

P (atm)	T (K)	ρ (g/cm^3)	z (km)	H_ρ (km)	H_ρ (km)	w (mg/liter)	Remarks
2.00×10^{-7}	145.0	3.86×10^{-11}	313.4	21.0	21.0		
3.00×10^{-7}	145.0	5.80×10^{-11}	304.9	21.0	21.0		
1.00×10^{-6}	145.0	1.93×10^{-10}	279.7	21.0	21.0		
3.00×10^{-6}	145.0	5.80×10^{-10}	256.6	21.0	21.0		
1.00×10^{-5}	145.0	1.93×10^{-9}	231.4	21.0	21.0		
3.00×10^{-5}	145.0	5.80×10^{-9}	208.3	21.0	21.0		
1.00×10^{-4}	145.0	1.93×10^{-8}	183.1	21.0	21.0		
3.00×10^{-4}	145.0	5.80×10^{-8}	160.0	21.0	21.0		
0.00100	145.0	1.93×10^{-7}	134.8	21.0	21.0		
0.00300	145.0	5.80×10^{-7}	111.7	21.0	21.0		
0.00650	145.0	1.26×10^{-6}	95.5	21.0	21.0		Top of inversion layer
0.0100	139.0	2.02×10^{-6}	86.7	20.1	18.3		
0.0300	124.8	6.73×10^{-6}	65.7	18.1	16.4		
0.0829	113.0	2.06×10^{-5}	48.3	16.3	16.3		Stratopause
0.100	113.0	2.48×10^{-5}	45.2	16.3	16.3		
0.225	113.0	5.59×10^{-5}	31.9	16.3	16.3		Tropopause
0.267	120.0	6.24×10^{-5}	29.1	17.4	26.8		
0.300	125.0	6.72×10^{-5}	27.0	18.0	27.9	0.00119	Correspondence level
0.350	132.0	7.44×10^{-5}	24.1	19.1	29.3	0.00583	
0.406	139.0	8.20×10^{-5}	21.2	20.1	30.8	0.0243	
0.469	146.0	9.00×10^{-5}	18.3	21.1	32.3	0.0888	NH_3 ice cloud base
1.00	189.1	1.48×10^{-4}	0.0	27.3	41.2		Zero of altitude[a]
1.27	205.0	1.74×10^{-4}	-6.9	29.7	44.4		
1.80	230.0	2.20×10^{-4}	-17.8	33.3	49.5	0.0743	
2.13	243.0	2.46×10^{-4}	-23.6	35.1	52.1	0.292	
2.41	253.0	2.68×10^{-4}	-28.0	36.6	54.2	0.758	
2.76	264.2	2.93×10^{-4}	-33.0	38.2	56.4	2.02	H_2O ice cloud base
3.00	271.3	3.10×10^{-4}	-31.2	39.2	57.8		
10.0	395.8	7.08×10^{-4}	-96.7	57.2	82.5		
30.0	550.0	1.53×10^{-3}	-168.3	79.6	112.6		
100.0	777.0	3.61×10^{-3}	-282.8	112.4	156.3		
300.0	1052.6	7.99×10^{-3}	-427.2	152.3	209.1		
1000.0	1452.9	1.93×10^{-2}	-643.7	210.1	285.4		

a. The zero of altitude is specified by equation (VIII-1).

TABLE VIII-3. VALUES OF PHYSICAL QUANTITIES AT SELECTED PRESSURES FOR COOL, DENSE MODEL ATMOSPHERE OF JUPITER

P (atm)	T (K)	ρ (g/cm^3)	z (km)	H_ρ (km)	H_ρ (km)	w (mg/liter)	Remarks
2.00×10^{-7}	108.0	6.09×10^{-11}	192.8	12.3	12.3		
3.00×10^{-7}	108.0	9.14×10^{-11}	187.8	12.3	12.3		
1.00×10^{-6}	108.0	3.05×10^{-10}	173.0	12.3	12.3		
3.00×10^{-6}	108.0	9.14×10^{-10}	159.5	12.3	12.3		
1.00×10^{-5}	108.0	3.05×10^{-9}	144.6	12.3	12.3		
3.00×10^{-5}	108.0	9.14×10^{-9}	131.1	12.3	12.3		
1.00×10^{-4}	108.0	3.05×10^{-8}	116.3	12.3	12.3		
3.00×10^{-4}	108.0	9.14×10^{-8}	102.7	12.3	12.3		
0.00100	108.0	3.05×10^{-7}	87.9	12.3	12.3		
0.00300	108.0	9.14×10^{-7}	74.3	12.3	12.3		
0.0100	108.0	3.05×10^{-6}	59.5	12.3	12.3		
0.0300	108.0	9.14×10^{-6}	46.0	12.3	12.3		
0.100	108.0	3.05×10^{-5}	31.1	12.3	12.3		
0.259	108.0	7.88×10^{-5}	19.4	12.3	12.3		Tropopause
0.300	111.6	8.84×10^{-5}	17.6	12.7	16.4		
0.500	125.0	1.32×10^{-4}	10.7	14.3	18.3		Correspondence level
0.833	140.0	1.96×10^{-4}	3.0	16.0	20.5	0.0276	
1.00	145.8	2.26×10^{-4}	0.0	16.6	21.4	0.0793	Zero of altitude[a]
1.14	150.0	2.49×10^{-4}	-2.2	17.1	22.0	0.162	
1.42	157.6	2.96×10^{-4}	-6.1	18.0	23.1	0.534	NH_3 ice cloud base
3.00	186.1	5.30×10^{-4}	-20.7	21.2	27.3		
10.0	243.1	1.35×10^{-3}	-50.0	27.7	35.6	0.406	
16.1	270.0	1.96×10^{-3}	-63.8	30.8	39.6	3.00	
22.1	290.0	2.51×10^{-3}	-74.1	33.1	42.5	10.3	
30.0	310.2	3.18×10^{-3}	-84.5	35.4	45.5	30.4	
32.3	315.4	3.37×10^{-3}	-87.2	36.0	46.3	39.2	Solution cloud base (NH_3-H_2O)
100.0	405.3	8.12×10^{-3}	-133.3	46.2	59.4		
300.0	517.2	0.0191	-190.9	59.0	75.8		
1000.0	675.7	0.0487	-272.3	77.1	99.1		

a. The zero of altitude is specified by equation (VIII-1).

TABLE VIII-4. VALUES AT SELECTED PRESSURES FOR WARM, EXTENDED MODEL ATMOSPHERE OF JUPITER

P (atm)	T (K)	ρ (g/cm^3)	z (km)	H_ρ (km)	H_ρ (km)	w (mg/liter)	Remarks
2.00×10^{-7}	500.0	1.04×10^{-11}	634.8	84.5	75.8		
3.00×10^{-7}	477.4	1.64×10^{-11}	601.3	80.7	72.4		
1.00×10^{-6}	416.1	6.27×10^{-11}	510.6	70.3	63.1		
3.00×10^{-6}	367.1	2.13×10^{-10}	438.0	62.0	55.7		
1.00×10^{-5}	320.0	8.15×10^{-10}	368.2	54.1	48.5		
3.00×10^{-5}	282.3	2.77×10^{-9}	312.4	47.7	42.8		
1.00×10^{-4}	246.1	1.06×10^{-8}	258.7	41.6	37.3		
3.00×10^{-4}	217.1	3.60×10^{-8}	215.8	36.7	32.9		
0.00100	189.2	1.38×10^{-7}	174.5	32.0	28.7		
0.00300	166.9	4.69×10^{-7}	141.5	28.2	25.3		
0.0100	145.5	1.79×10^{-6}	109.8	24.6	22.1		
0.0300	128.4	6.09×10^{-6}	84.4	21.7	19.5		
0.0627	118.0	1.39×10^{-5}	69.0	19.9	19.9		Stratopause
0.100	118.0	2.21×10^{-5}	59.7	19.9	19.9		
0.171	118.0	3.77×10^{-5}	49.1	19.9	19.9		Tropopause
0.179	120.0	3.88×10^{-5}	48.2	20.3	31.8	0.000340	
0.200	125.0	4.17×10^{-5}	45.8	21.1	33.0	0.00119	Correspondence level
0.223	130.0	4.47×10^{-5}	43.5	22.0	34.3	0.00378	
0.248	135.0	4.78×10^{-5}	41.1	22.8	35.5	0.0110	
0.270	139.2	5.05×10^{-5}	39.2	23.5	36.6	0.0253	NH_3 ice cloud base
0.300	144.6	5.41×10^{-5}	36.6	24.4	37.9		
0.756	200.0	9.85×10^{-5}	9.9	33.8	51.7	0.00550	
0.871	210.0	1.08×10^{-4}	5.0	35.5	54.7	0.0180	
1.00	220.2	1.18×10^{-4}	0.0	37.2	56.6	0.0537	Zero of altitude[a]
1.06	225.0	1.23×10^{-4}	-2.4	38.0	57.8	0.0867	
1.21	235.0	1.34×10^{-4}	-7.3	39.7	60.2	0.221	
1.36	244.7	1.45×10^{-4}	-12.1	41.3	62.6	0.505	H_2O ice cloud base
3.00	318.6	2.45×10^{-4}	-49.5	53.8	80.4		
10.0	470.2	5.55×10^{-4}	-128.9	79.4	116.2		
30.0	661.4	1.18×10^{-3}	-233.0	111.8	160.9		
100.0	949.0	2.72×10^{-3}	-395.2	160.4	227.4		
300.0	1306.2	5.98×10^{-2}	-602.9	220.7	309.5		
1000.0	1837.3	1.42×10^{-2}	-919.9	310.5	413.3		

a. The zero of altitude is specified by equation (VIII-1).

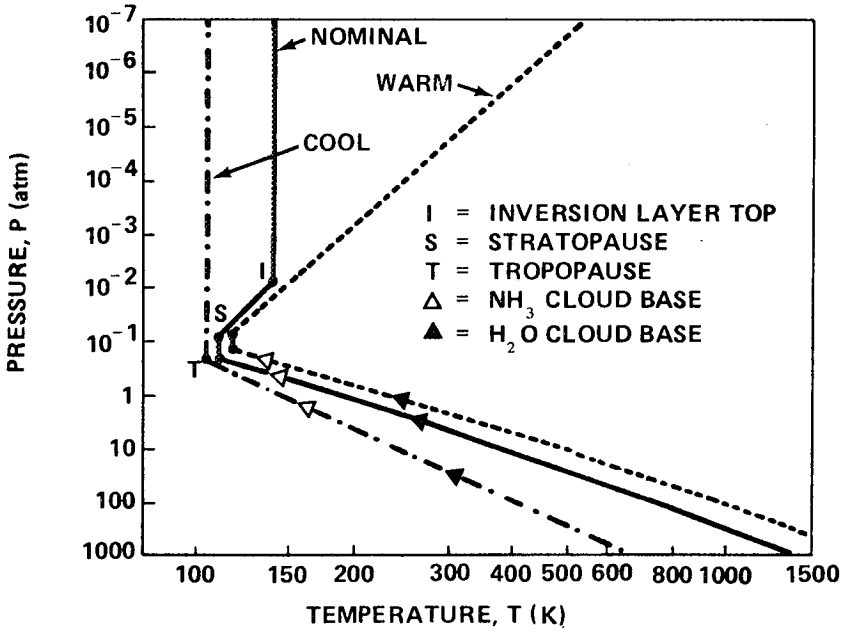

Figure VIII-1. Pressure versus temperature for the Jupiter model atmospheres [VIII-3].

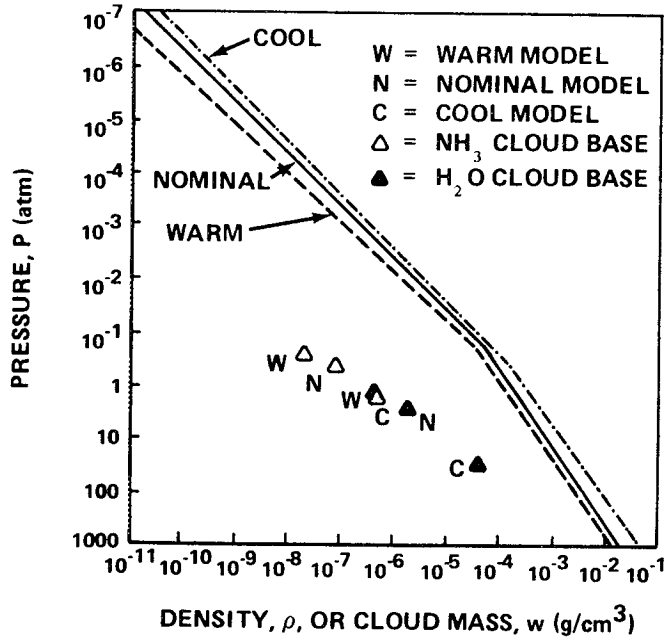

Figure VIII-2. Pressure versus density and cloud masses at cloud bases for the Jupiter model atmospheres [VIII-3].

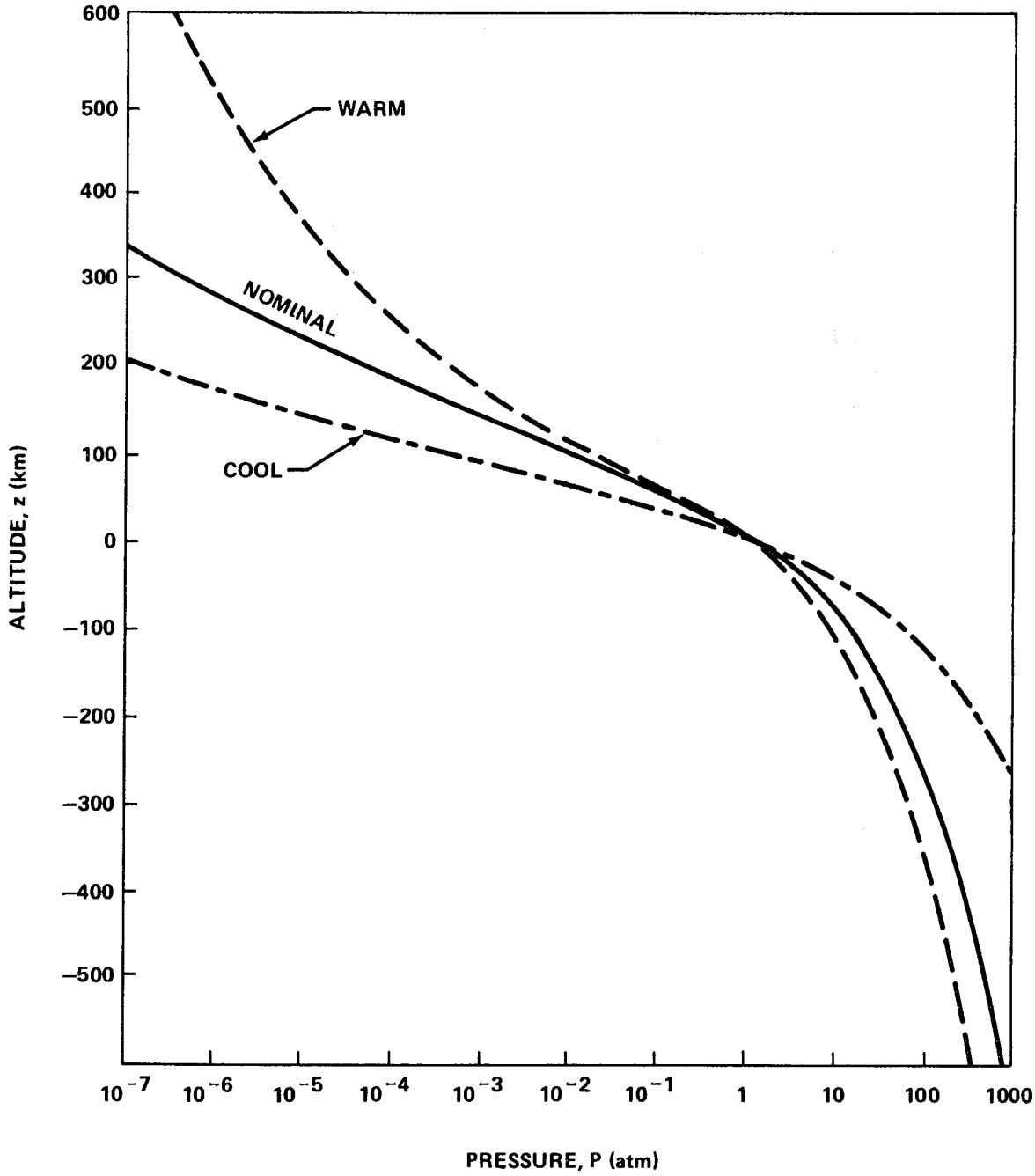

Figure VIII-3. Pressure versus altitude for the Jupiter model atmospheres [VIII-3].

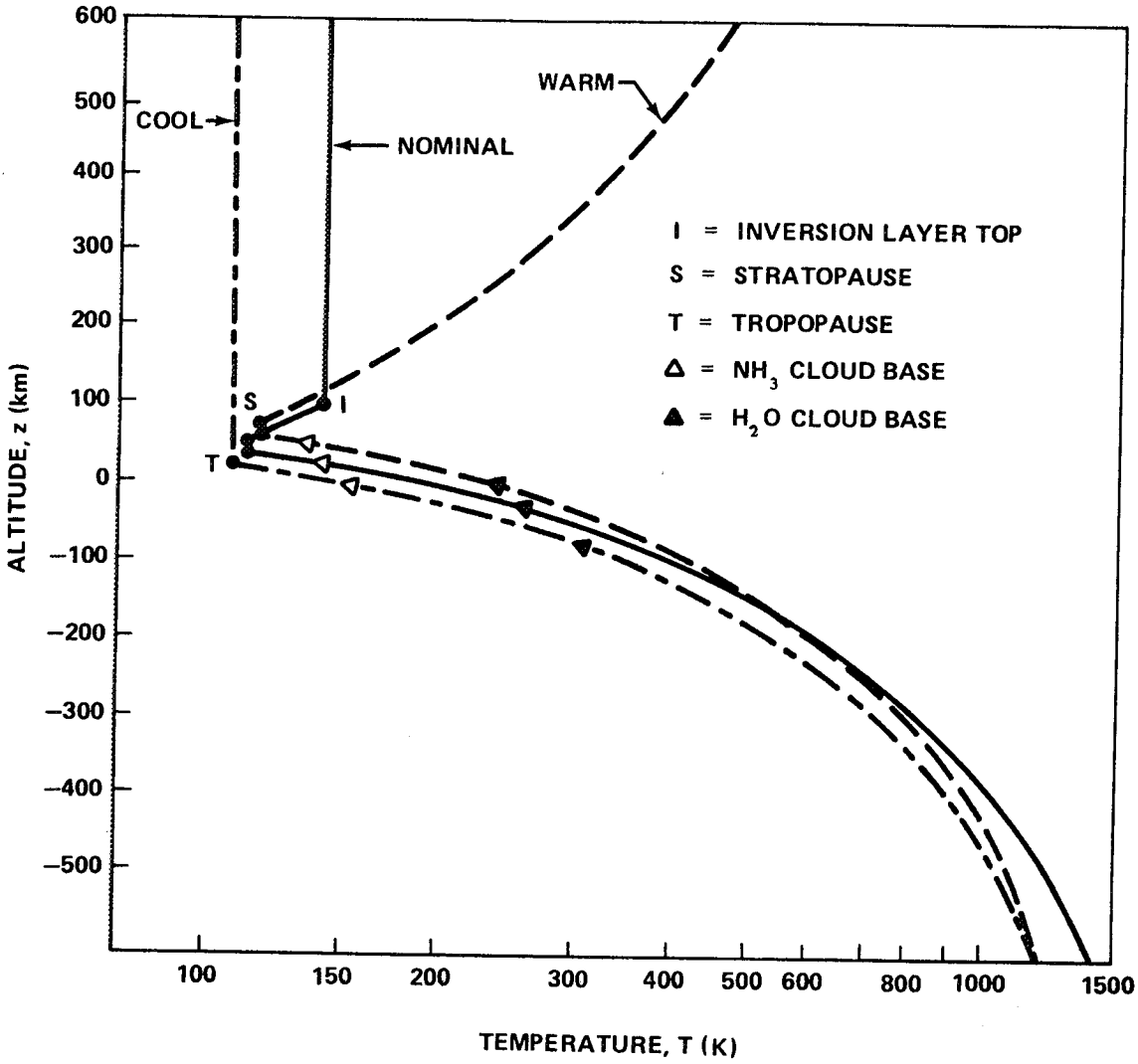

Figure VIII-4. Temperature versus altitude for the Jupiter model atmospheres [VIII-3].

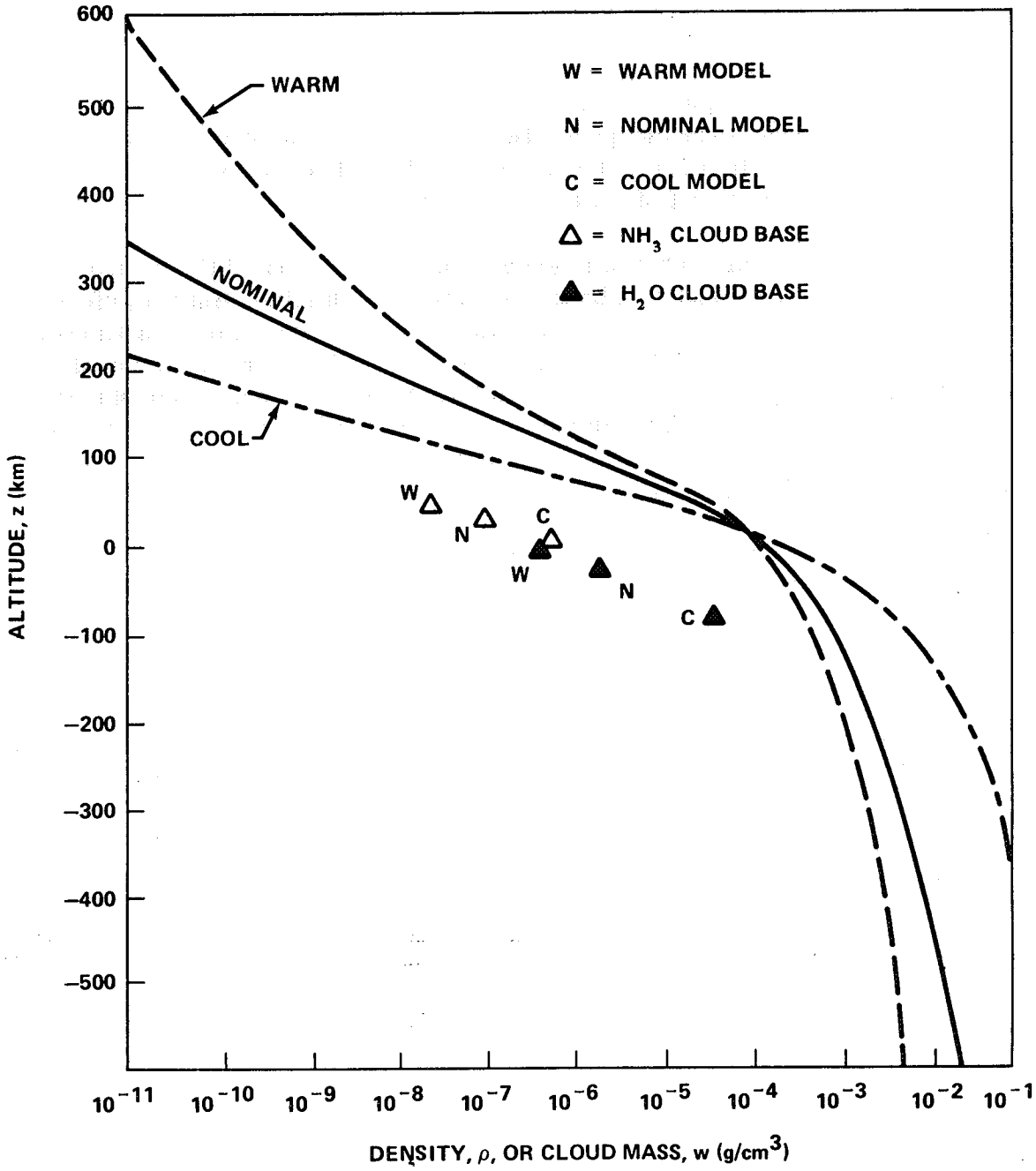

Figure VIII-5. Density versus altitude and cloud masses at cloud bases for the Jupiter model atmospheres [VIII-3].

8.1.3 Ionosphere

There are two approaches to the description of Jupiter's ionosphere. The first is theoretical in which considerations such as photoionization and solar UV flux values (useful in understanding the earth's ionosphere) are applied to Jupiter. The other approach is based on inferences from the HF bursts to which various generation mechanisms and requirements are applied. Within the rather large uncertainties inherent in the two approaches, agreement is quite satisfactory.

The theoretical approach is exemplified by the work of Gross and Rasool. Their results are supported by those derived by Shimizu, Hunten [VIII-8], Henry and McElroy, and Capone and Barrow which consider similar processes in less detail. In Reference VIII-3, solar ultraviolet radiation at wavelengths of the order of 1000 Å is responsible for the photoionization of molecular and atomic hydrogen down to those altitudes at which it is fully absorbed. Secondary reactions, e.g., recombination, occur such that the equilibrium abundances of the species recombination, occur such that the equilibrium abundances of the species H_2^+, He, H, H^+, and e^- (listed roughly in order of decreasing concentration) are significant near the maximum of charged particle density, approximately 10^6 electrons/cm^3 and 10^6 protons/cm^3. The local gas pressure at that maximum is approximately 3×10^{-5} N/cm^2; atmospheric models suggest that this level occurs within the altitude range $z_0 = 250 \pm 150$ km (Paragraph 8.1.2.1). Below this altitude the electron density becomes negligible within several kilometers, whereas upward the electron density it decreases roughly exponentially with a scale height of approximately 100 km. According to the same authors, the ionospheric temperature ranges from 100 to 200 K [VIII-3].

Numerous arguments from mechanisms of HF burst generation have yielded electron density values independent of the foregoing considerations. Smith et al. [VIII-9] suggest that a maximum electron number density of the order of 10^7 cm^{-3} may be required to cause reflection of the HF bursts at the ionosphere. Investigations by Northrop and Birmingham [VIII-10] and Papadopoulos and Lerche [VIII-11] use various HF burst mechanisms to derive values within one or two orders of magnitude of the preceding density.

The presence in the earth's ionosphere of several distinct layers of electron and ion concentration suggest that a one-layer model is probably too simplistic for Jupiter. For this reason and on the basis of the foregoing derived values, it is appropriate to adopt a peak number density of 10^6 cm^{-3} for electrons and protons and to estimate the uncertainty as an order of magnitude in either direction.

8.1.4 Clouds

The color, size, and shape of the visible atmospheric layers of Jupiter are constantly changing as winds and clouds alter the various features observed. Beyond approximately ± 50 deg latitude are the two polar regions which are dark and featureless at the resolution and wavelengths observed from the earth. At lower latitudes the planet has stripes parallel to the equator, classified as zones and belts. As usually observed from the earth in visible light, the zones are bright and the belts dark. Their latitudes and relative and absolute brightnesses vary with longitude, time, and wavelength of observation; i.e., color effects are important. The semipermanent, well-documented, generally uniform belts and zones are occasionally divided by thin bands also parallel to the equator and sometimes are blemished by light or dark spots whose motions in latitude and longitude have provided information on planetary rotation and atmospheric currents. These spots have characteristic horizontal dimensions ranging from 1000 to 10 000 km and lifetimes ranging from a few hours to weeks. Their resolution is marginal from earth observations so that very little is known about their actual properties. The spots are comparable in size and possibly in nature to major weather systems in the earth's atmosphere.

One much larger feature has existed for at least three centuries, namely the Great Red Spot. In a presentation of recent observational results, Solberg [VIII-12] reports that the Red Spot usually contrasts sharply with its surroundings in light of wavelengths $\lambda < 5000$ Å (very dark). Its oval shape extends horizontally about 13 000 km in latitude and 40 000 km in longitude, and its area varies by about 50 percent. The latitude of its center is usually within 3 of 22 deg south. Its longitude oscillates with an amplitude near 0.8 and a period near 90 days, and drifts with respect to longitude system II[1] at a rate of several degrees/year. The Red Spot's nature and how it retains its integrity are enigmatic although Hide has developed the Taylor column hypothesis in which relatively uniform, stagnant fluid overlies some topographical feature in the rotating fluid which forms Jupiter's deep atmosphere [VIII-3].

Theories of cloud formation and structure have been applied to the vertical distribution of condensates in Jupiter's lower atmosphere (Paragraph 8.1.2). Techniques based on the analysis of Lewis [VIII-13] have

1. The artificial Jupiter longitude measurement system in which the meridian at 96.58 is directed toward the earth at 0^h Universal Time on 14 July 1897 and has prograde rotation with angular velocity of 870.27 deg/day. It is applied to the analysis of optical observations at mid-latitudes.

been applied to the models given in Paragraph 8.1.2.1 with numerical data for the condensates of ammonia and water from the International Critical Tables and Lange [VIII-3]. Some of the cloud properties are given in Tables VIII-2, VIII-3, and VIII-4 and Figures VIII-1, VIII-2, VIII-4, and VIII-5. Cloud altitudes, masses, and compositions, primarily H_2O and NH_3 ices with a dilute NH_3-H_2O solution replacing H_2O in the cool model, show broad ranges which may be exceeded in the real atmosphere for any of the following reasons: (1) additional condensates, particularly NH_4SH and NH_4Cl, may form clouds of their own or contaminate the ones considered leading to nonuniform cloud structure and color [VIII-13], (2) convection may carry the condensates to other altitudes, and (3) in downward convecting regions (cooler than upward-moving ones at a given pressure), condensates are likely to be present so there is a reasonable basis for equating downward convecting regions with Jupiter's dark belts. Lastly, by earth analogy, it would not be surprising if storms were occasionally present in regions of high cloud activity, leading to rain, hail, snow, thunder, and lightning within the lower atmosphere.

8.1.5 Atmospheric Motions, Rotation Rate, and Winds

Atmospheric motions are roughly classified as rotation and winds. Vertical motions, motions at polar latitudes, motions above the tropopause, and motions on scales less than 1000 km are inferred from assumptions and theories. Probably the most significant rotation period given for Jupiter is that obtained from radio observations:

$$T_o = 9^h 55^{min} 29.^s 73 \neq 0.^s 04 \quad .$$

Rotation periods derived from visible features on the planetary disc are averaged and give two distinct periods as follows: Latitudes with ±10 deg of equator

$$T_1 = 9^h\ 50^{min}\ 30.^s 003 \quad .$$

Latitudes other than those mentioned previously:

$$T_2 = 9^h\ 55^{min}\ 40.^s 632 \quad .$$

In accord with Chapman's concept of the horizontal surface motions on Jupiter [VIII-14], it is appropriate to define winds as any motions differing from solid body planetary rotation (assumed to have a period equal to that for Jupiter's radio sources). At latitudes within 50 deg of the equator, visual and photographic observations of the positions of spots and features on the Jupiter disc imply horizontal winds on scales larger than 1000 km that are zonal, i.e., parallel to the equator, and apparently unceasing. According to Chapman [VIII-14], the major winds can be described by (1) a westerly equatorial current between latitudes ±10 deg of average speed near 100 m/s, corresponding to the fast system I^2 rotation period T_1, with local winds up to 10 m/s in any direction with respect to the prevailing wind, (2) local winds between latitudes of 10 and 50 deg north and up to 10 m/s in any direction with a frequent westerly current (the north temperature current) of speeds up to 100 m/s within 10 deg of latitude 25 deg north, (3) local winds between latitudes 10 and 50 deg south up to 20 m/s of which the most prominent and persistent (the circulating current) has an easterly component near 20 deg south and a westerly component near 25 deg south, and (4) a wind having counterclockwise vorticity near the edges of the Great Red Spot of speeds near 10 m/s. Additional details of the winds may be inferred from the observational analysis of Peek and the theoretical analyses of Hide and Ingersoll and Cuzzi. Winds have not been observed on a smaller scale, at latitudes beyond ±50 deg, or moving in vertical directions, but a reasonable assumption is that such winds the characteristic speed of 10 m/s holds. The limits in height and depth to which these winds might extend are unknown, but a reasonable assumption is that the horizontal winds may occur everywhere in the atmosphere, whereas the vertical ones are confined to the troposphere (Paragraph 8.1.4). The literature contains no estimate of the magnitude of wind shear [VIII-3].

8.1.6 Radiation Environment [VIII-3]

Three distinct categories of radiation are known to emanate from Jupiter: (1) the centimeter region, (2) the decimeter region, and (3) the decameter range.

Radio emission from Jupiter at wavelengths of a few centimeters is undoubtedly thermal in origin. The 3 cm region is somewhat higher than

---

2. Ibid.

the infrared temperature, but this can be accounted for if the radio frequency emission at 3 cm is from regions below the tops of the ammonia clouds.

The radiation from Jupiter in the decimeter wavelength region is mainly nonthermal in character. It is, however, emitted continuously, although the intensity exhibits long-term variations. It has been proposed that this radiation is emitted by electrons of high energy spiraling around the lines of force of the Jovian magnetic field. The electrons trapped are similar to the outer Van Allen zone in the earth's magnetic field. It appears that this is synchrotron radiation from relativistic electrons with energies in the range of 5 to 10 MeV.

In the decameter range, emission is of the noise-storm type; i.e., it occurs in bursts of a 1 or 2 s duration emitted in groups lasting 5 to 10 min and continuing intermittently over a period of a few hours. This radiation is circularly polarized and exhibits very complex intensity variations. The probability of this occurrence is inversely related to the sunspot number. Indications exist that occasionally there is strong emission from Jupiter a few days after a strong solar flare. There is also definite correlation of the Jovian longitude at which emission is strongest with the rotation of the planet. As yet, there is no satisfactory explanation of Jupiter's decameter radiation.

8.1.6.1 Electromagnetic Radiation [VIII-3]

8.1.6.1.1 Solar Radiation

Near Jupiter the sun is the dominant source of light which may be direct, reflected, or scattered. NASA SP-8005 [VIII-15] summarizes the direct solar spectrum at 1 AU and specifies P_λ, the power per unit area and per unit wavelength interval for wavelengths between 50 Å and 100 cm. The values from Reference VIII-15 and standard relationships for intensity and flux lead to the formulas given for the sun in Table VIII-5.

Above the tropopause (here the tropopause at altitude $z = 35 \pm 15$ km is the appropriate limit), the formulas in Table VIII-5 specify the ranges of intensities, fluxes, and temperatures associated with the electromagnetic radiation environment under conditions of maximum illumination. Under partial illumination, total shadowing, or eclipse, the values for intensities and fluxes range down to zero from the maximum illumination conditions of Table VIII-5, and temperatures range down to 3 K. The wavelength of interest determines which of the radiation sources listed in Table VIII-5 should be considered. Figure VIII-6 shows the geometric albedo p and

TABLE VIII-5. ELECTROMAGNETIC RADIATION PARAMETERS NEAR JUPITER WITH MAXIMUM ILLUMINATION

Parameters	Direct Sunlight[a]	Reflected Sunlight[a]	Thermal Radiation[b]	Synchrotron UHF Radiation[c]
Wavelength	$1\ \text{Å} < \lambda < 100$ cm	$1\ \text{Å} < \lambda < 10\ \mu$m	$1\ \mu\text{m} < \lambda < 100$ cm	$1\text{ cm} < \lambda < 100$ cm
Intensity Power/area wavelength solid angle	$i_\lambda = \frac{P_\lambda}{(0.000068\ \text{sterad})}$	$i_\lambda = \frac{pP_\lambda}{(90 \pm 10}$	$i_\lambda = B_\lambda(T_{BD})$	
Power/area frequency solid angel			$i_\nu = B_\nu(T_{BD})$	$i_\nu = 2kT_{BS}/\lambda^2$
Flux Power/area wavelength	$F_\lambda = \frac{P_\lambda}{r^2}$	$F_\lambda = \frac{pH_\lambda}{(27 \pm 3)\ (R/R_j)^2}$	$F_\lambda = \frac{\pi B_\lambda(T_{BD})}{(R/R_j)^2}$	
Power/area frequency			$F_\nu = \frac{\pi B_\nu(T_{BD})}{(R/R_j)^2}$	$F_\nu = \frac{(5 \pm 2) \times 10^8}{4 + (R/R_j)^2}$ FU
Integrated flux Power/area	$F = \frac{(1.353 \pm 0.021) \times 10^6}{r^2}\ \left(\frac{\text{erg}}{\text{cm}^2\text{s}}\right)$	$F = \frac{(1.4 \pm 0.2) \times 10^4}{(R/R_j)^2}\ \left(\frac{\text{erg}}{\text{cm}^2\text{s}}\right)$	$F = \frac{(1.8 \pm 0.3) \times 10^4}{(R/R_j)^2}\ \left(\frac{\text{erg}}{\text{cm}^2\text{s}}\right)$	$F = \frac{(15 \pm 7) \times 10^{-6}}{4 + (R/R_j)^2}\ \left(\frac{\text{erg}}{\text{cm}^2\text{s}}\right)$
Brightness Temperature			T_{BD}	$T_{BS} = \frac{D\lambda^2}{R_j}\ (0.30 \pm 0.15)$ K
Effective Temperature	5800 ± 15 K		$T_c = 134 \pm 6$ K	

a. Solar irradiance from NASA SP-8005 [VIII-15], solar distance r in AU only, and geometric albedo p from Figure VIII-6.

b. Brightness temperature T_{BD} from Figure VIII-6 and Planck functions B_λ (T) and B_ν(T) from Allen [VIII-3] or elsewhere.

c. Use λ in cm only and estimate D/R_j from Figure VIII-7 with D being the approximate pathlength of line of sight through the volume. Radiation is up to 30 percent linearly polarized.

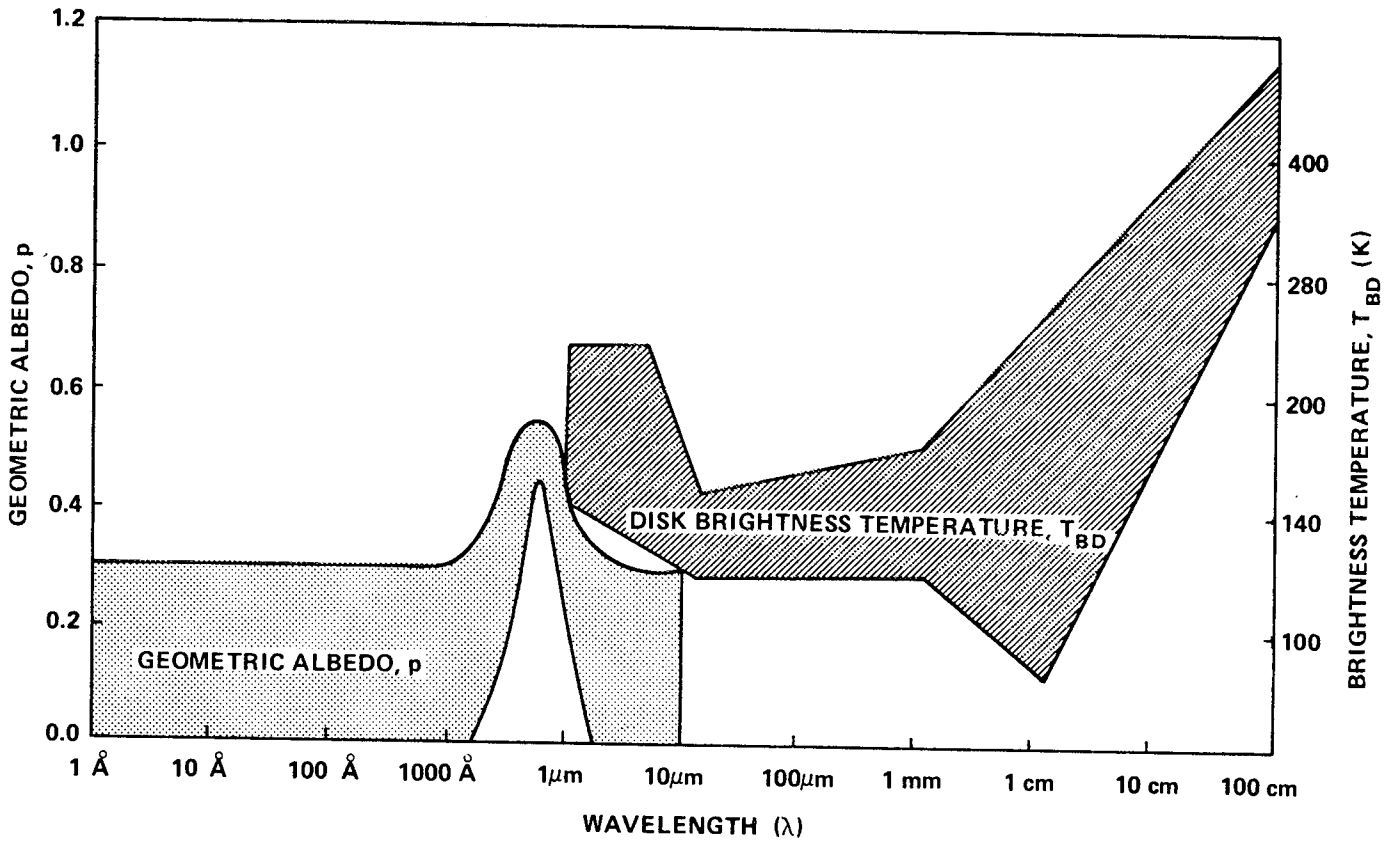

Figure VIII-6. Ranges of geometric albedo and disk brightness temperature as functions of wavelength [VIII-3].

brightness temperature T_{BD} as functions of the wavelength. In Table VIII-5, the quantity D is the approximate pathlength of the line of sight through the schematic synchrotron emission volume shown in Figure VIII-7.

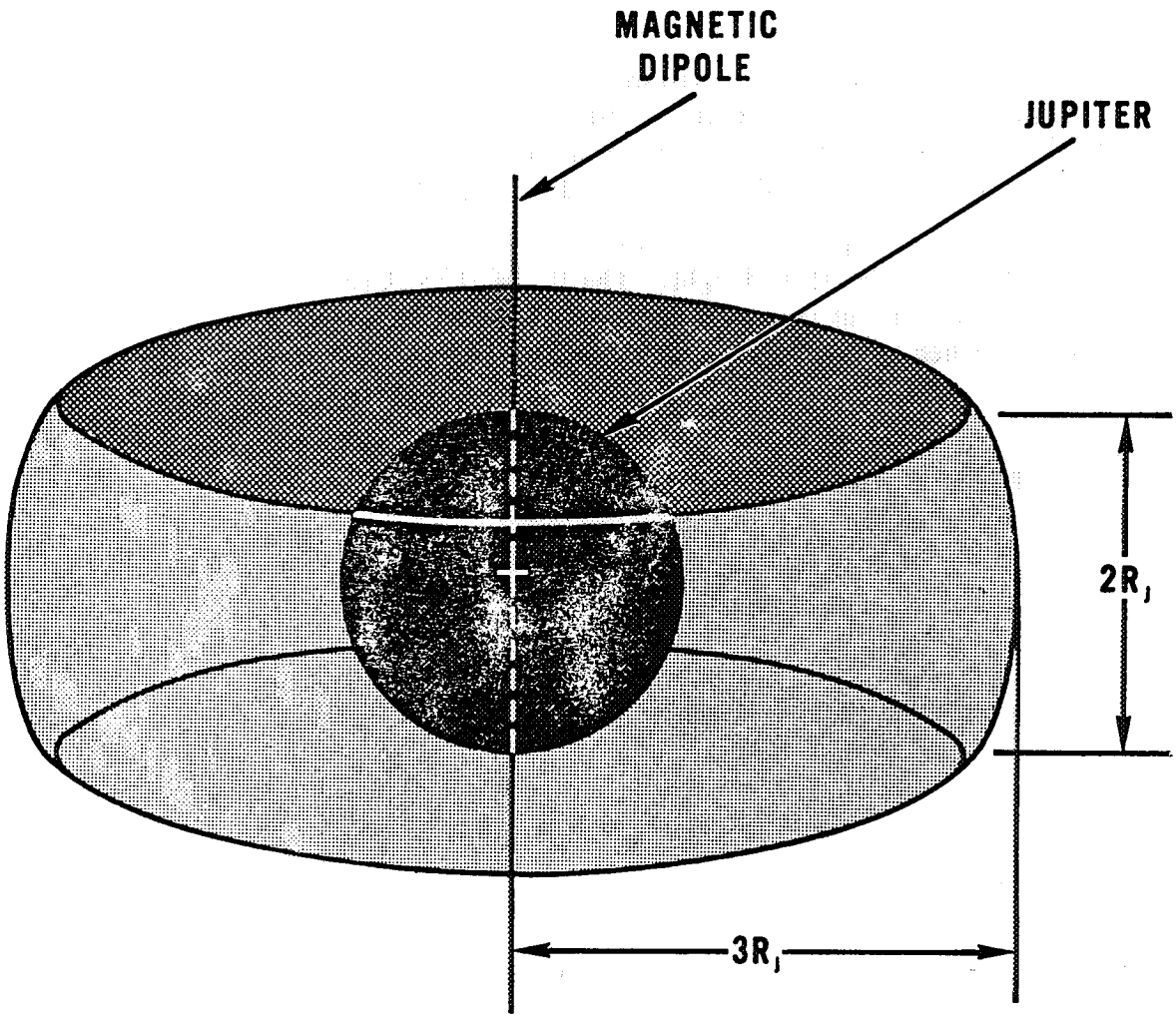

Figure VIII-7. Schematic volume for the calculation of the brightness temperature, T_{BS}, of Jupiter's synchrotron emission source [VIII-3].

In addition, Jupiter's satellites and the other planets constitute light sources, but their fluxes near Jupiter are minor compared to the sources listed in Table VIII-5. Their positions are published annually in the American Ephemeris and Nautical Almanac [VIII-16], and their visual magnitudes and and colors are specified by

$$m_v = (m_0 \pm 0.3) + 5 \log r\ \Delta + (0.03 \pm 0.02)\alpha \qquad \text{(VIII-2)}$$

and the parameters in Table VIII-6 where α is in degrees, and r and Δ in AU. The radiation from stars and other non-solar-system objects is identical to that beyond the earth's atmosphere.

Below the tropopause, i.e, altitudes $z < 35 \pm 15$ km, the maximum contributions of the sun and the synchrotron source are identical to those specified in Table VIII-5 which uses the geometric albedo p and brightness temperature T_{BD} given in Figure VIII-6. The reflected sunlight intensity and flux in Table VIII-5 are appropriate but must be considered omnidirectional to account for the maximum scattered light. The thermal radiation is specified by Table VIII-7. In addition, sporadic lightning may require that light-sensitive surfaces be covered when local meteorological conditions are stormy.

TABLE VIII-6. MAGNITUDES AND COLORS FOR SATELLITES OF JUPITER AND PLANETS

	m_o	U-B	B-V
Jupiter V (Amalthea)	6.3	—	—
I (Io)	- 1.90	1.30	1.17
II (Europa)	- 1.53	0.52	0.87
III (Ganymede)	- 2.16	0.50	0.83
IV (Callisto)	- 1.20	0.55	0.86
VI-XII	$\geq$ 7.0	—	—
Mercury	- 0.36	—	0.93
Venus	- 4.29	0.50	0.82
Earth	- 3.87	—	0.2

TABLE VIII-6. (Concluded)

	m_o	U-B	B-V
Mars	- 1.52	0.58	1.36
Jupiter	- 9.25	0.48	0.83
Saturn	- 8.88	0.58	1.04
Uranus	- 7.19	0.28	0.56
Neptune	- 6.87	0.21	0.41
Pluto	- 1.01	0.27	0.80

TABLE VIII-7. THERMAL RADIATION PARAMETERS BELOW THE TROPOPAUSE IN JUPITER'S ATMOSPHERE

Wavelength	$1\mu m < \lambda < 100$ cm
Intensities	$\begin{cases} I_\lambda = B_\lambda(t) \\ I_\nu = B_\nu(t) \end{cases}$
Fluxes	$\begin{cases} F_\lambda = \pi B_\lambda(t) \\ F_\nu = \pi B_\nu(t) \end{cases}$
Integrated Fluxes	$F = \begin{cases} (1.8 \pm 0.3) \times 10^4 \left(\frac{erg}{cm^2 s}\right) & \text{for } T < 134 \text{ K} \\ \left(\frac{T}{134}\right)^4 (1.8 \pm 0.3) \times 10^4 \left(\frac{erg}{cm^2 s}\right) & \text{for } T > 134 \text{ K} \end{cases}$
Brightness Temperature	t = larger of T and T_{BD}

Radiation and its effects at wavelengths shorter than 1 Å (γ-rays) should be ignored. The power emitted sporadically in the HF bursts near Jupiter ranges up to 4×10^{16} erg/s at wavelengths longer than 7.5 m; intensities at wavelengths longer than 1 m are unknown but probably high compared to communications intensities.

8.1.6.1.2 Jupiter Reflected Radiation [VIII-3]

The solar radiation reflected from Jupiter (or its clouds) has been observed only at phase angles less than 12 deg and is conventionally described in terms of astronomical magnitudes, colors, and albedos. The definition of geometric albedo p leads to formulae for the intensity and flux of Jupiter-reflected radiation observed at zero phase angle and jovicentric distance R,

$$I_\lambda = \frac{p P_\lambda}{\pi r^2} \qquad \text{(VIII-3)}$$

and

$$F_\lambda = \frac{p P_\lambda}{r^2 (R/R_j)^2} \quad , \qquad \text{(VIII-4)}$$

where r^2 evaluated for Jupiter in $(AU)^2$ has the value 27 ±3. For other observable phase angles (<12 deg), these quantities are smaller than the results of equation (VIII-3). Therefore, it can be inferred that the zero phase angle formulas constitute correct upper limits at all phase angles.

Photoelectric measurements of the geometric albedo p for Jupiter at wavelengths between 2000 Å and 1.5 μm are summarized in Table VIII-8. Limiting values from Table VIII-8 are shown in Figure VIII-8, and although the data are restricted to one decade in wavelength, the albedo is apparently decreasing as both ends of the observed range are approached. Thus, a range of values for p between 0 and 0.3 at unobserved wavelengths in addition to the range from Table VIII-8 is adopted herein. Table VIII-8 also lists the result of a photoelectric determination of the bolometric albedo p_b. That value and its substitution in the following expression for the integrated reflected flux are adopted here,

TABLE VIII-8. OBSERVED GEOMETRIC ALBEDOS FOR JUPITER

Wavelength[a] (Å)	Geometric Albedo (p)
1730	0.2 ±0.15
2100	0.2 ±0.15
2800	0.23 ±0.1
3530 (U)	0.31 ±0.05
4480 (B)	0.42 ±0.05
5540 (V)	0.50 ±0.05
6900 (R)	0.47 ±0.05
8200 (I)	0.35 ±0.05
10 635	0.31 ±0.1
15 000	0.15 ±0.1
Bolometric Albedo	$P_b = 0.28 \pm 0.03$

a. Letters specify pass bands in the conventional magnitude system.

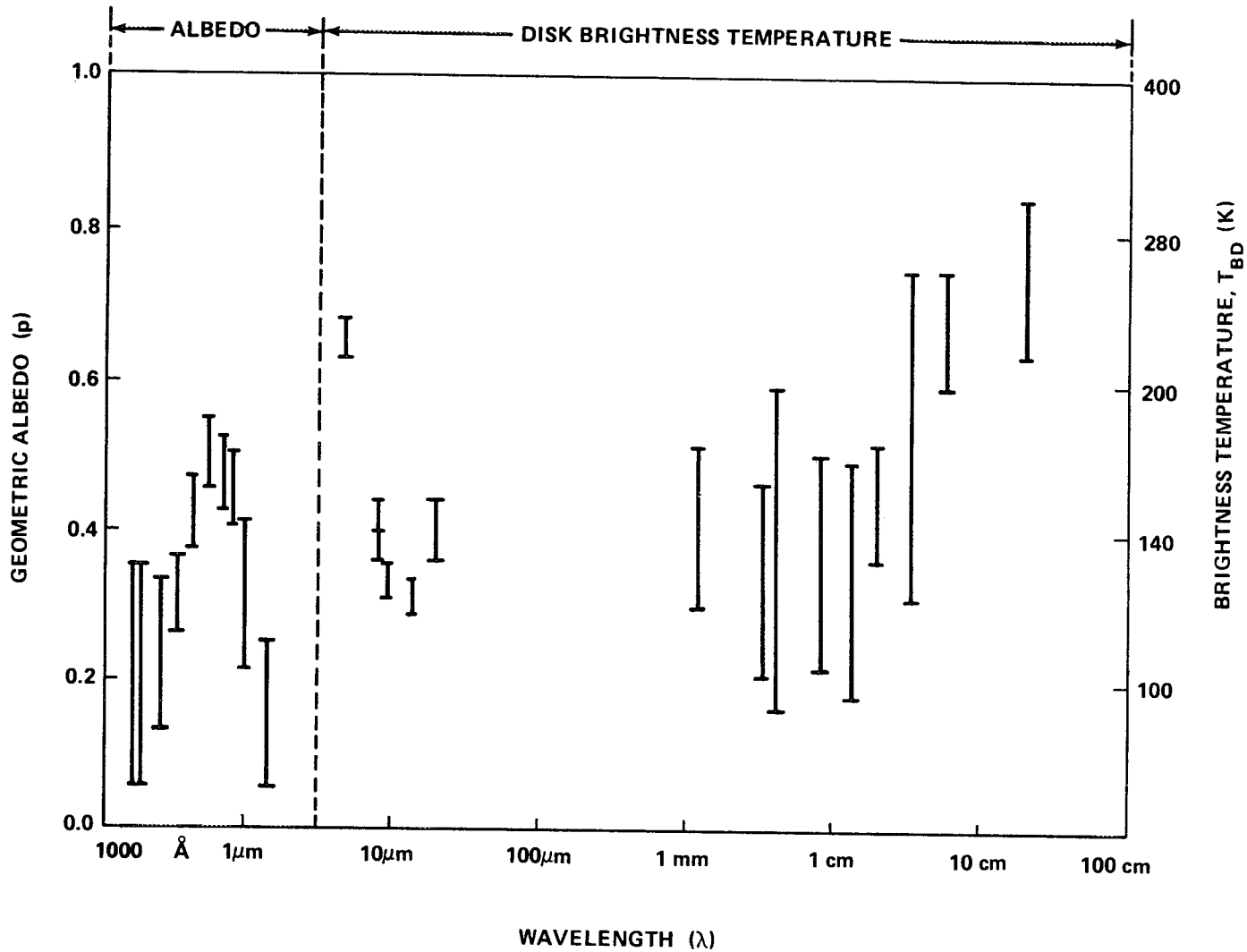

Figure VIII-8. Typical values of geometric albedo p and disk brightness temperature T_{BD}, taken from Table VIII-8. (The temperature scale is logarithmic.)

$$F = \frac{p_b \bar{S}}{r^2 (R/R_j)^2} \qquad \text{(VIII-5)}$$

8.1.7 Meteoroid Environment

No direct evidence exists of meteoroidal debris in the environment of Jupiter. Traditionally, the meteoroid environment near a planet has been inferred from the presumed gravitational enhancement of the nearby interplanetary cometary debris [VIII-17]. Although such an enhancement is definitely to be expected, the uncertainties involved in the evaluation of the interplanetary debris distribution and the enhancement characteristics in the case of Jupiter amount to several orders of magnitude.

Another reasonable approach is to consider Jupiter's irregular satellites (Table VIII-9, J VI through XII) as the observable, large body end of a meteoroid distribution analogous to that expected in the asteroid belt. Such an approach assumes that the smaller satellites of Jupiter have individual properties and a mass distribution comparable to those of the asteroids, an assumption which is neither confirmed nor denied by the meager satellite data available.

The masses M_n in grams and radii R_n in cm for J V through XII presented in Table VIII-9 are derived from the relationships

$$\log M_n = 26 \pm 1 - 0.6\, m_o$$

and

$$\log R_n = 8.3 \pm 0.3 - 0.2\, m_o$$

TABLE VIII-9. PROPERTIES OF JUPITER'S SATELLITES

Satellite	Orbital Period (days)	Range of Distance from Jupiter (radii of Jupiter, R_j)	Maximum Jovicentric Latitude (deg)	Orbital Speed (km/s)	Radius, R_n (km)	Mass, M_n (g)
V (Amalthea)	0.498	2.539 ±0.08	0.4	26	$100 \times 2^{\pm 1}$	$10^{22} \pm 1$
I (Io)	1.76914	5.905	0	17	1800 ±160	$(7.2 \pm 0.6 \times 10^{25}$
II (Europa)	3.55118	9.396	0	14	1550 ±100	$(4.7 \pm 0.1) \times 10^{25}$
III (Ganymede)	7.15455	14.99	0	11	2600 ±400	$(15.5 \pm 0.2) \times 10^{25}$
IV (Callisto)	16.68902	26.36	0	8	2400 ±400	$(9.6 \pm 0.8) \times 10^{25}$
VI	251	161 ±25	29	3	$70 \times 2^{\pm 1}$	$10^{21.5 \pm 1}$
VII	260	164 ±23	28	3	$10 \times 2^{\pm 1}$	$10^{19 \pm 1}$
X	253	164 ±23	29	3	$7 \times 2^{\pm 1}$	$10^{18 \pm 1}$
VIII	737	300 ±200	33	2	$8 \times 2^{\pm 1}$	$10^{19 \pm 1}$
IX	758	330 ±120	23	2	$7 \times 2^{\pm 1}$	$10^{18.5 \pm 1}$
XI	692	313 ±63	18	2	$7 \times 2^{\pm 1}$	$10^{18.5 \pm 1}$
XII	631	290 ±50	34	2	$7 \times 2^{\pm 1}$	$10^{18.5 \pm 1}$

which are reasonable for asteroids of absolute magnitude m_o, mass density 3.5 g/cm^3, and visual albedo 0.2. If the positions of the outer seven satellites are distributed uniformly within a volume centered on Jupiter of radius $500R_j$[3] and at latitudes within ±30 deg, the number per unit volume N_M of particles of mass $M \geq 10^{18.5}$ g is $10^{-31\pm1}$ m^{-3}. This is almost identical to the peak spatial density at this mass in the asteroid belt [VIII-17]. Application of a crude mass distribution similar to that in Reference VIII-17 gives

$$\log N_M = 31 \pm 1 - (0.8 \pm 0.1)(\log M - 18.5).$$

Equation requires N_M in particles/m^3 and applies for $10^{-9} \leq M \leq 10^{20}$ g within the foregoing given volume near Jupiter.

Omnidirectional fluxes of particles may be computed by multiplying N_M by v/4 where the speed v of the particles relative to a spacecraft (with speed v_s) is approximately $v = [v_s^2 + (R_j/R)\ (40\text{km/s})^2]^{\frac{1}{2}}$.[4] The particle density is $3.5 \times 2^{\pm1}$ g/cm^3. Lack of relevant data makes it impossible to decide whether such a distribution dominates anticipated cometary debris of lower density, but it is recommended that cometary debris be neglected on the basis of the small fluxes suggested in References VIII-3 and VIII-17.

8.1.8 Magnetic Environment

8.1.8.1 Magnetic Field

Pioneer 10 data indicate that Jupiter's magnetic dipole moment M = 4.0 (71422 km)^3 gauss is tilted 11 deg to Jupiter's rotational axis to give a field strength of ~4 gauss at 1 radii. The longitude of the northern hemisphere

---

3. The inner boundary for meteoroids could be $100R_j$ because of sweeping action by the satellites and gravitational forces. However, an inner boundary of $1R_j$ is assumed herein.

4. The average particle velocity relative to Jupiter is taken here as the orbital velocity (40 km/s at $R/R_j = 1$) which is distinct from the escape velocity given in Reference VIII-17.

north-seeking pole is 222 deg. The offset dipole is displaced from the center of Jupiter by 0.11 R_j in the direction of latitude 16 deg and longitude 176 deg [VII-9].

Recent Pioneer 10 measurements are included in References VII-9, VII-18, and VII-19. Recent Jupiter synchrotron radiation at 10.4 cm is given in Reference VIII-10.

8.1.8.2 Magnetosphere

Jupiter's magnetosphere is the region within which Jupiter's own magnetic field and charged particles dominate. In the solar direction the magnetosphere boundary is conventionally fixed by equating the solar wind and planetary magnetic field pressures and consists of both a shock front (at which the solar wind velocity decreases abruptly) and a magnetopause (limiting Jupiter's regular magnetic field). The result is 50 ± 20 R_j which includes most estimates of the distance of the sunward boundary from Jupiter [VIII-18, VIII-3]. This distance is adopted here as the minimum radius of the magnetosphere. In other directions, additional complex features, including distortion by Jupiter's rotation and a more distant magnetosphere boundary, are expected by analogy with the earth. In the antisolar direction the length of Jupiter's magnetospheric tail is greater than 100 R_j [VIII-3, VIII-18, VIII-20, VIII-21].

8.1.9 Charged Particle Environment

A thorough description of the Jupiter electron and proton radiation environment and their effects on spacecraft is given in Reference VIII-22. Available data from the Pioneer 10 encounter of Jupiter are compared with pre-encounter models of the Jupiter radiation belts. These data depict the electron and proton environment out to 16 Jovian radii.

8.1.9.1 Galactic Cosmic Rays

Near the earth, galactic cosmic ray intensities are modulated by the interplanetary magnetic field. In general, it is expected that this modulation reduces the intensities more severely at lower energies, closer to the sun, and during intervals of greater solar activity. Quantitative predictions of the intensities near Jupiter have not been made, however. Jupiter's own magnetic field may reduce the intensities further, particularly at low energies and latitudes. Thus the approach adopted is to specify the fluxes in the energy range observed (0.1 to 10^{10} GeV) as between zero and a spectrum extrapolated from the highest energies observed for the most

abundant particle kinds at times near minimum solar activity. This spectrum can be approximated by the following expression for the flux of particles with kinetic energy greater than E:

$$\Phi_E = A\ (E + m_o c^2)^{-1.5} \quad ,$$

where $m_o c^2$ is the rest energy of the particle and E is the particle kinetic energy in GeV (per nucleon for alpha-particles). The summary given by Haffner [VIII-20] specifies the coefficient $A \approx 10\ cm^{-2}\ s^{-1}$ for protons and $A \approx 1\ cm^{-2}\ s^{-1}$ for alpha-particles; Fanselow specifies $A \simeq 0.2\ cm^{-2}\ s^{-1}$ for electrons [VIII-3].

8.1.9.2 Solar Particle Events

Protons and alpha-particles of energy greater than 1 MeV are emitted sporadically by the sun and have been detected by ground-based and spacecraft-borne instrumentation. Their fluxes near the earth vary over several orders of magnitude in time, have both directional and isotropic components, and frequently can be identified with specific solar flares. The recent theoretical model by Englade [VIII-23] cites the important references which treat the complex processes involved. This literature shows that neither the probability of occurrence of an event nor the variation of the particle fluxes with solar distance can be reliably estimated at this time [VIII-3].

8.1.9.3 Solar Wind

Properties of the solar wind are summarized by Hundhausen. On the basis of observations from Mariner spacecraft at 0.8 to 1.5 AU from the sun, protons and electrons during quiet solar conditions have concentrations of approximately $5r^{-2}\ cm^{-3}$ (for r in AU) and are streaming radially away from the sun at speeds near 320 km/s. Increases in solar activity are accompanied by temporary increases up to factors of 10 in the concentration and 3 in the speed. The applicable theory suggests that the extrapolation of these conditions on the basis of heliocentric distance r to the orbit of Jupiter is justified. The interaction of the solar wind with Jupiter's magnetic field is responsible for the formation of the outer boundary of Jupiter's magnetosphere.

8.1.10 Astrodynamic Constants

8.1.10.1 Jupiter Constant [VIII-3]

Distance from sun	$r = 5.20 \pm 0.25$ AU
Period of revolution about sun	$T = 11.862$ years
Mass of planet, excluding satellites	$M_j = (1.899 \pm 0.002) \times 10^{30}$ g
Equatorial radius	$R_j = 71422 \pm 200$ km
Mean density	$\bar{\rho} = 1.32 \pm 0.01$ g/cm^3
Flattening (dynamical)	$\epsilon = 0.0645 \pm 0.0008$
Period of rotation	$T_o = 9^h\ 55^m\ 29.^s73 \pm 0.^s04$
Rotational angular velocity	$\omega_o = (1.758531 \pm 0.000002) \times 10^{-4}$ rad/s
Angular momentum	$C\omega_o = (4.3 \pm 0.2) \times 10^{45}$ g-cm^2/s
Celestial coordinates of North Pole	$\alpha_R = 17^h52^m\ 0.^s84 + 0.^s247\ (t-1919.0)$
	$\delta_R = +64°\ 33'34''\ 6 - 0.60''\ (t-1910.0)$
Moment of inertia about rotational axis	$C = (2.4 \pm 0.1) \times 10^{49}$ g-cm^2
Moment of inertia about equatorial axes	$A = (2.25 \pm 0.1) \times 10^{49}$ g-cm^2
Gravitational parameter	1.267076×10^8 km^3/s^2

8.1.10.2 Gravitational Potential [VIII-3, VIII-24]

The gravitational potential function can be expressed as

$$\Phi\ (R, \theta) = \frac{GM}{R}\left[1 - J_2 (R_E/R)^2\, P_2^{\,o} - J_4\ (R_E/R)^4\, P_4^{\,o}\right] ,$$

and the radial acceleration of gravity as

$$Z = -\frac{\partial \Phi}{\partial R} = \frac{GM}{R^2}\left[1 - 3J_2 (R_E/R)^2\, P_2^{\,o} - 5J_4\ (R_E/R)^4\, P_4^{\,o}\right]$$

where

R_E = equatorial radius

$GM = 1.267076 \times 10^8\ km^3/s^2$

$J_2 = 1.471 \times 10^{-2}$

$J_4 = -6.75 \times 10^{-4}$

$P_2^{\,o} = 3/2 \sin^2 \phi - 1/2$ (ϕ = latitude)

$P_4^{\,o} = 4.375 \sin^4 \phi - 3.75 \sin^2 \phi + 0.375$

R = distance from the center of Jupiter (km).

For many practical purposes the above gravitational model should be sufficiently accurate for a simple model. However, if a more accurate gravitational model is needed or desired, Nulls model in Reference VIII-25 is recommended.

8.1.11 Additional Information

The physical properties of the planet Jupiter are discussed in detail in References VIII-3 and VIII-26.

8.2 Surface Environment

The interior of Jupiter is that portion of the planet below the atmospheric altitudes at which radiation of various wavelengths escapes. The only compositions capable of retaining the low mean density of Jupiter at the pressures required by its high gravity consist primarily of hydrogen and possibly

include helium and other elements listed in Table VIII-1. Theoretical models of the interior have been constructed by DeMarcus and refined by Peeble; thermal effects are included in Reference VIII-3. The models suggest the following probable conclusions:

a. The planet is fluid either everywhere or throughout much of its bulk with the metallic phase of hydrogen being likely in the central regions; a small, heavy-element core is not excluded.

b. The pressure,density, and temperature increase in moving inward; the rate of increase is uncertain because the equation of state is poorly known. The temperature reaches values near the center of the order of magnitude of 10^4 K.

c. Energy is released to the exterior due to cooling and gravitational contraction.

d. The energy is transported by convection in most layers of the planet, and electron conduction is significant elsewhere.

e. Convection in the rotating, conducting fluid hydrogen interior is responsible for the maintenance of the planetary magnetic field. (The magnetohydrodynamic processes involved are not well understood.)

f. Although phase transitions may occur even in the probable chemically homogeneous interior, they do not constitute a rigid, solid surface at any level but are characterized by density and viscosity graduation over a radial distance scale of kilometers or greater. Therefore, the atmosphere is considered to be an extension of the interior rather than a distinct entity. (For later information, see Reference VIII-27.)

8.3 Satellites

Four categories of known satellites of Jupiter are listed in Table VIII-9 which specifies some of their properties. Additional photometric data for the Galilean satellites are given in Paragraph 8.1.7.1.1. Detailed ephemerides may be found in the American Ephemeris and Nautical Almanac [VIII-16] and the references specified there [VIII-28, VIII-29].

REFERENCES

VIII-1. Owen, T.: The Atmosphere of Jupiter. Science, vol. 167, no. 3926, 1970, p. 1675.

VIII-2. McElroy, M. B.: Atmospheric Composition of the Jovian Planets. J. of the Atmospheric Sciences, vol. 26, no. 5, 1969, p. 798.

VIII-3. Anon.: The Planet Jupiter (1970). NASA SP-8069, December 1971.

VIII-4. Owen, T.: The Composition of Planetary Atmospheres. Physics of the Solar System, Chapter 7, NASA SP-300, 1972.

VIII-5. Hunten, D. M.: Lower Atmospheres of the Planet. Physics of the Solar System, Chapter 6, NASA SP-300, 1972.

VIII-6. Owen, T.: The Spectra of Jupiter and Saturn in the Photographic Infrared. Icarus, vol. 10, no. 3, 1969, p. 355.

VIII-7. Eshleman, Von R.: Jupiter's Atmosphere: Problems and Potential of Radio Occultation. Science, vol. 189, no. 4206, September 12, 1975, p. 876.

VIII-8. Hunten, D. M.: The Upper Atmosphere of Jupiter. J. of the Atmospheric Sciences, vol. 26, no. 5, 1969, p. 826.

VIII-9. Smith, E. J., Davis, L. Jr., Jones, D. E., Coleman, P. J., Jr., Colburn, D. S., Dyal, P., Sonett, C. P., and Frandsen, A. M. A.: The Planetary Magnetic Field and Magnetosphere of Jupiter: Pioneer 10. Journal of Geophysical Research, vol. 79, no. 25, September 1, 1974, p. 3501.

VIII-10. Northrop, T. G., and Birmingham, T. J.: The Magnetosphere of Jupiter as Observed with Pioneer 10; 3. Jovian Synchrotron Radiation at 10.4 cm as Deduced from Observed Electron Fluxes. Journal of Geophysical Research, vol. 79, no. 25, September 1, 1974, p. 3583.

VIII-11. Papadopoulos, K., and Lerche, I.: Collective Bremsstrahlung from Relativistic Electrons as a Possible Mechanism in Radio Sources. Astrophys. J., vol. 158, no. 3, 1969, p. 981.

REFERENCES (Continued)

VIII-12. Solberg, H. G., Jr.: Jupiter's Red Spot in 1967-68. Icarus, vol. 10, no. 3, 1969, p. 412.

VIII-13. Lewis, J. S.: The Clouds of Jupiter and the NH_3-H_2O and NH_3-H_2S Systems. Icarus, vol. 10, no. 3, 1969, p. 365.

VIII-14. Chapman, C. R.: Jupiter's Zonal Winds: Variation with Latitude. J. of the Atmospheric Sciences, vol. 26, no. 5, 1969, p. 986.

VIII-15. Anon.: Solar Electromagnetic Radiation. NASA SP-8005, Revised May 1971.

VIII-16. The American Ephemeris and Nautical Almanac. U.S. Government Printing Office, Washington, D.C.

VIII-17. Anon.: Meteoroid Environment Model-1970 (Interplanetary and Planetary). NASA SP-8038, June 1970.

VIII-18. Van Allen, J. A., Baker, D. N., Randall, B. A., and Sentman, D. D.: The Magnetosphere of Jupiter as Observed with Pioneer 10; 1. Instrument and Principal Findings. Journal of Geophysical Research, vol. 79, no. 25, September 1, 1974, p. 3559.

VIII-19. Northrop, T. G., Goertz, C. K., and Thomsen, M. F.: The Magnetosphere of Jupiter as Observed with Pioneer 10; 2. Nonrigid Rotation of the Magnetodisc. Journal of Geophysical Research, vol. 79, no. 25, September 1, 1974, p. 3579.

VIII-20. Haffner, J. W.: The Magnetospheres of Jupiter and Saturn. AIAA Paper No. 1971, pp. 71-30.

VIII-21. Busse, F. H.: Generation of Planetary Magnetism by Convection. Physics of the Earth and Planetary Interiors, vol. 12, no. 4, September 1976, pp. 350-358.

VIII-22. Parker, R. H.: Jupiter's Radiation Belts and Their Effects on Spacecraft. JPL Technical Memorandum 33-708, October 15, 1974.

VIII-23. Englade, R. C.: A Computational Model for Solar Flare Particle Propagation. University of Chicago, July 1970.

REFERENCES (Concluded

VIII-24. Sjogren, W. L.: Gravity Fields . . . . Jovian, Martian, Cytherean, Mercurian, and Lunar Mass Distributions. IEEE Transactions on Geoscience Electronics, vol. GE-14, July 1976.

VIII-25. Null, G. W.: Gravity Field of Jupiter and Its Satellites from Pioneer 10 and Pioneer 11 Tracking Data. Astronomical Journal, vol. 81, December 1976, p. 1153.

VIII-26. Michaux, C. M.: Handbook of the Physical Properties of the Planet Jupiter. NASA SP-3031, 1967.

VIII-27. Smouchowski, R.: Interior Structure of Giant Planets. Physics of the Solar System, Chapter 8, NASA SP-300, 1972.

VIII-28. Gross, S. T.: Galilean Satellites and Jovian Energetic Particles. Science, vol. 190, November 1975, pp. 564-566.

VIII-29. Dollfus, A.: Optical Polarimetry of the Galilean Satellites of Jupiter. Icarus, vol. 25, July 1975, pp. 416-431.

BIBLIOGRAPHY

Bender, M. L.: Infrared Radiometer for the Pioneer 10 and 11 Missions to Jupiter. Applied Optics, vol. 13, November 1974, pp. 2623-2628.

Potter, H. E.: Near-Infrared Spectra of Jupiter, Saturn and Uranus. NASA SP-3086, 1974.

SECTION IX. SATURN

9.1 General

Saturn resembles Jupiter in many respects: the large size, the color bands, and the large number of satellites. Saturn ranks second to Jupiter in size and number of satellites, and has the lowest mean density and greatest oblateness of any planet in the solar system. The combination of a large radius and small density produces a gravitational force on the surface slightly greater than that of the earth [IX-2].

9.2 Composition of the Atmosphere

The atmosphere of Saturn has been estimated from spectroscopic observations to consist of CH_4, NH_3, O_3, and SO_2. Hydrogen and helium have not been detected spectroscopically; however, it is reasonable to believe that they may be present. Neon and argon probably exist also. Measured infrared radiometer temperature of Saturn at the top of the ammonia clouds is about 125 K, while microwave radiation at a wavelength of 3.4 cm shows 106 $\pm$ 21 K. The blackbody temperature as calculated from the solar radiation is 107 K. Since methane can solidify at these temperatures, it is possible that there may be methane clouds of the cirrus type below the ammonia clouds [IX-2].

9.3 Radiation

Some indications exist that Saturn emits synchrotron radiation in the decimeter wavelength region resulting from the relativistic electrons trapped in the radiation belt, or belts, surrounding the planet. This synchrotron radiation implies that Saturn has a magnetic field that is being generated by a dynamo mechanism resulting from the rotating planet and its liquid core. The radiation, however, has been noted to exhibit a plane of polarization that is perpendicular to the equator rather than parallel to it. This tends to imply that the magnetic axis of the planet is at right angles to the axis of rotation. However, some indications exist that the rings of Saturn may be removing electrons that are in the equatorial region of the radiation belts, thus creating this particular type of field. The visual albedo has been estimated to be 0.76 [IX-1, IX-2].

9.4 Astrodynamic Constants (Epoch 1960.0) [IX-2]

Distance from sun (average)	1.42699×10^9 km
Eccentricity of orbit	0.0556818
Inclination of orbit to ecliptic	2°29'23.7"
Orbital period (sidereal)	10759.205 days
Radius (equatorial)	60 401.0 km
Mass ratio (sun/planet)	3499.2 ± 0.4
Flattening (dynamic)	1:10.21
Average density	0.679 g/m^3
Rotational period	10 hr 14 min
Gravitational parameter	3.792651×10^7 km^3/s^2

9.5 Telescopic Appearance

Saturn, as seen through the telescope, is similar to Jupiter in that the general appearance and albedo are about the same. Both planets have satellites (they appear to be flattened) and exhibit bands parallel to the equator. The brightest band on Saturn is the equatorial band, which is yellowish in color. A greenish band surrounds the poles and is less distinct than the band on Jupiter. These bands are somewhat variable with respect to their intensities as well as to latitude in location and dimension. Occasionally, signs of activity exist in the atmosphere, and clouds or bright spots are seen in the equatorial zone. There does not seem to be a permanent feature as the Red Spot on Jupiter. The period of rotation at the equator is 10 h and 14 min. Although the period of rotation at the poles is considered to be longer than at the equator, it is not exactly known. The most striking feature is the rings which vary in width caused by the equatorial plane being inclined at a large angle to the orbital plane and the plane of the ecliptic. The rings are discussed in the following paragraph.[IX-2].

9.6 Rings

Saturn has three concentric rings in the plane of the equator, designated A, B, and C. The diameter of the entire ring system is 274 000 km. The A ring has an outer diameter of 274 000 km and a width of approximately 16 000 km. This ring is separated from the B ring by a gap of approximately 4000 km. The B or bright ring has a width of 26 000 km. The C or inner ring, called the Crepe, is about 21 000 km in width. Measurements have indicated the thickness of the rings is not more than 16 to 19 km and could be even less. These measurements were made during the time that the rings appear to be edgewise when viewed from the earth. The mass of these rings is not known, but based on observations of perturbations in the orbits of the satellites of Saturn which would be caused by these rings, their mass is then indicated to be as an upper limit somewhat less than the mass of the moon. Infrared spectra suggest that the rings are composed of particles of ice or solid ammonia [IX-1].

9.7 Satellites

Table IX-1 is a summary of data for the satellites of Saturn. Titan is the only satellite in the solar system to have an atmosphere recognized by Kuiper in his spectroscopic studies.

TABLE IX-1. DATA SUMMARY FOR SATELLITES OF SATURN

Satellite		Discovery		Siderial Period of Revolution (P_{sid})		Mean Synodic Period of Revolution P_{syn}		Orbital Mean Motion n_{sid} (°/d)	Eccentricity (e)
		Discoverer	Date	d	Mean Solar Time	d	Mean Solar Time		
VII	Mimas	W. Herschel	18 Sept. 1789	0.942 421 9	0 22 37 05.25	0.942 505	0 22 37 12.4	381.994 519	0.020 1
VI	Enceladus	W. Herschel	29 Aug. 1789	1.370 217 8	1 08 53 06.82	1.370 392	1 08 53 21.9	262.731 954	0.004 44
V	Tethys	J. D. Cassini	21 March 1684	1.887 802 5	1 21 18 26.14	1.888 134	1 21 18 54.8	190.697 915	0.000 0
IV	Dione	J. D. Cassini	21 March 1684	2.736 915 9	2 17 41 09.53	2.737 612	2 17 42 09.7	131.534 915	0.002 21
III	Rhea	J. D. Cassini	23 Dec. 1672	4.517 502 6	4 12 25 12.23	4.519 400	4 12 27 56.2	79.690 048	0.000 98
I	Titan	C. Huyghens	25 March 1655	15.945 452	15 22 41 27.1	15.969 04	15 23 15 25	22.576 971	0.028 9
VIII	Hyperion	G. P. Bond	16 Sept. 1848	21.276 665	21 06 38 23.9	21.318 82	21 07 39 06	16.919 945	0.104
II	Iapetus	J. D. Cassini	25 Oct. 1671	79.330 82	79 07 56 23	79.920 09	79 22 04 56	4.537 959	0.028 28
IX	Phoebe	W. H. Pickering	16 Aug. 1898	550.441 6	550 10 35 54	523.651 6	523 15 38 18	-0.654 02	0.163 26
X	Janus	A. Dollfus	1 Jan. 1967		17.975 hr				

Satellite		Apparent Distance			Mean Distance from Planet (a)			Inclination of Orbit to Planet's Equator (R)	Visual Magnitude at Mean Opposition Distance ($^{m}_{vis}$)	Radius R (km)	Mass M (Primary=1)	Visual Albedo (A_{vis})
		At Unit Distance	As Seen From Sun	At Mean Opposition	(10^{-3} AU)	(10^{3} km)	In Eq. Radii of the Primary					
VII	Mimas	255.89	26.826	29.968	1.240 6	185.59	3.067	1 31.0	12.1	250	1:14 960 000	0.29
VI	Enceladus	328.29	34.416	38.447	1.591 6	238.10	3.935	0 01.4	11.77	300	1: 7 900 000	0.32
V	Tethys	406.40	42.605	47.594	1.970 3	294.75	4.872	1 05.56	10.27	500	1: 876 400	0.49
IV	Dione	520.51	54.567	60.958	2.523 5	377.51	6.240	0 01.40	10.44	500	1: 548 000	0.55
III	Rhea	726.89	76.203	85.127	3.524 1	527.20	8.714	0 20.49	9.76	800	1: 250 000	0.48
I	Titan	1 684.35	176.578	197.257	8.166 0	1 221.62	20.191	0 20.00	8.39	2400	1: 4 147	0.12
VIII	Hyperion	2 044.4	214.32	239.42	9.911 5	1 482.8	24.51	0 25.34	14.16	200	1: 5 000 000	
II	Iapetus	4 908.6	514.59	574.86	23.797 6	3 360.1	58.84	14 43	11.03 (10.1-11.9)	600		
IX	Phoebe	17 861.0	1 872.45	2 091.74	86.592 6	12 954	214.11	150	14.5	120		
X	Janus					~97.09				~175		

REFERENCES

IX-1. Palluconi, F. D., and Pettengill, G. H.: The Rings of Saturn. NASA SP-343, 1973.

IX-2. Anon: The Planet Saturn (1970). NASA SP-8091, June 1972.

SECTION X. URANUS

10.1 General

Uranus, when viewed through the telescope, exhibits a greenish color. This planet is unusual in that its equator is inclined at nearly right angles to the plane of the ecliptic. At certain times a whitish equatorial zone and bands, similar to Jupiter and Saturn but somewhat fainter, can be observed.

The atmosphere of this planet, based on spectroscopic data, is composed of large proportions of methane. In addition, some bands of molecular hydrogen have been detected. Other atmospheric constituents which have not been identified may be ammonia, helium, neon, and argon.

10.2 Astrodynamic Constants [X-1]

Distance from sun (mean)	19.1819 A.U.
Eccentricity of orbit	0.0472095
Inclination of orbit to ecliptic	0° 46' 23.3''
Orbital period (sidereal)	30 685.5 days
Radius (equatorial)	27 000 ± 1000 km
Mass ratio of Uranus and satellites	$8.72 \pm 0.08 \times 10^{25}$ kg
Optical flattening	0.03 ± 0.02
Average density	1.1 ± 0.1 g/cm^3
Rotational period	10.8 h ± 1 h
Gravitational parameter	$5.82 \pm 0.05 \times 10^6$ km^3/s^2

10.3 Satellites

Uranus has five satellites. The nearest satellite to Uranus, Miranda, or V, was not discovered until 1948 by Kuiper. Tabular data for the satellites are shown in Table X-1.

TABLE X-1. DATE SUMMARY FOR SATELLITES OF URANUS [X-2]

Satellite	Discovery		Siderial Period of Revolution (P_{sid})		Mean Synodic Period of Revolution (P_{syn})		Orbital Mean Motion, N_{sid} (°/d)	Eccentricity (e)
	Discoverer	Date	d	Mean Solar Time	d	Mean Solar Time		
V Miranda	G. P. Kuiper	1 March 1948	1.414	1 09 56	1.414	1 09 56	254.6	0.005
III Ariel	W. Lassell	24 Oct. 1851	2.520 383	2 12 29 21.1	2.520 60	2 12 29 40	142.835 43	0.002 8
IV Umbriel	W. Lassell	24 Oct. 1851	4.144 183	4 03 27 37.4	4.144 73	4 03 28 25	86.868 75	0.003 5
I Titania	W. Herschel	11 Jan. 1787	8.705 876	8 16 56 27.7	8.708 33	8 17 00 00	41.351 38	0.002 4
II Oberon	W. Herschel	11 Jan. 1787	13.463 262	13 11 07 05.8	13.469 17	13 11 15 36	26.739 43	0.000 7

Satellite	Apparent Distance (arc-sec)			Mean Distance from Planet (a)			Inclination of Orbit to Planet's Equator (g)	Visual Magnitude at Mean Opposition Distance (Mvis)	Radius, R (km)	Mass, M (Primary=1)	Visual Albedo (A_{vis})
	At Unit Distance	As Seen From Sun	At Mean Opposition	(10^{-3} AU)	(10^3 km)	In Eq. Radii of the Primary					
I Miranda	179.9	9.38	9.89	0.872	130.5	5.25	0	16.5	80	1: 1 000 000	
III Ariel	264.43	13.785	14.544	1.282 0	191.78	7.72	0	14.4	300	1: 70 000	
IV Umbriel	368.38	19.205	20.261	1.786 0	267.18	10.75	0	15.3	200	1: 170 000	
I Titania	604.42	31.510	33.243	2.930 3	438.37	17.64	0	14.01	500	1: 20 000	
II Oberon	808.29	42.138	44.456	3.918 7	586.23	23.59	0	14.20	400	1: 34 000	

REFERENCES

X-1. Anon: The Planets Uranus, Neptune, and Pluto (1971). NASA Space Vehicle Design Criteria (Environment), NASA SP-8012, November 1972.

X-2. Smith, R. E.: Space and Planetary Environment Criteria Guidelines for Use in Space Vehicle Development (1971 Revision). NASA TM X-64627, November 15, 1971.

SECTION XI. NEPTUNE

11.1 General

Neptune appears as a small greenish disk when viewed through the telescope. The location of this planet was predicted by Adams in England in 1846 and Leverrir in France independently in the same year. Galle, in 1846, the German astronomer, used these position data and discovered Neptune.

The atmosphere of Neptune as indicated by spectroscopic studies is chiefly methane. Neptune has the largest amount of methane detected for any planet [XI-1]. Hydrogen has also been identified spectroscopically. Although other gases have not been identified, they may be helium, neon, or argon.

11.2 Astrodynamic Constants [XI-2]

Distance from sun (average)	30.3 A.U.
Eccentricity of orbit	0.0085747
Inclination of orbit to ecliptic	1° 46' 21.8''
Orbital period (sidereal)	60 189.5 days
Radius (equatorial)	25 200 ± 200 km
Mass of Neptune and satellites	$1.03 \pm 0.01 \times 10^{26}$ kg
Optical flattening	0.02 ± 0.02
Average density	1.57 ± 0.04 g/cm^3
Rotational period	16 h ± 2 h
Gravitational parameter	$6.87 \pm 0.07 \times 10^6$ km^3/s^2

11.3 Satellites

Tabulated data for satellites are given in Table XI-1.

TABLE XI-1. DATA SUMMARY FOR SATELLITES OF NEPTUNE [XI-3]

Satellite	Discovery		Siderial Period of Revolution ($^{P}_{sid}$)		Mean Synodic Period of Revolution ($^{P}_{syn}$)		Orbital Mean Motion N_{sid} (°/d)	Eccentricity (e)
	Discoverer	Date	d	Mean Solar Time	d	Mean Solar Time		
I Triton	W. Lassell	10 Oct. 1846	5.876 833	5 21 02 38.4	5.876 452	5 21 03.25	-61.257 48	0.000 0
II Nereid	G. P. Kuiper	10 May 1949	359.881	359 21 09	361.315	361 07 34	1.000 33	0.749 34

Satellite	Apparent Distance (arc-sec)			Mean Distance from Planet (a)			Inclination of Orbit to Planet's Equator (g)	Visual Magnitude at Mean Opposition Distance ($^{M}_{vis}$)	Radius, R (km)	Mass, M (Primary=1)	Visual Albedo (A_{vis})
	At Unit Distance	As Seen From Sun	At Mean Opposition	(10^{-3} AU)	(10^{3} km)	In Eq. Radii of the Primary					
I Triton	489.82	16.296	16.857	2.374 7	355.25	14.21	159 57	13.55	2 100	1: 757	0.21
II Nereid	7 668.86	255.137	263.917	37.179 7	5 562.03	222.48	27 48.4	18.7	150	1: 3 000 000	

REFERENCES

XI-1. Guinan, E. F.; Shaw, J. S.: The Diameter and Structure of the Atmosphere of Neptune from the Occultation of BD -17° 4388. American Astronomical Soc., Bull., vol. 2, no. 2, 1970, pp. 195-196 (abstract).

XI-2. Anon: The Planets Uranus, Neptune, and Pluto (1971). NASA Space Vehicle Design Criteria (Environment), NASA SP-8103, November 1972.

XI-3. Smith, R. E.: Space and Planetary Environment Criteria Guidelines for Use in Space Vehicle Development (1971 Revision). NASA TM X-64627, November 15, 1971.

SECTION XII. PLUTO

12.1 General

The planet Pluto is the farthest known planet from the sun. Orbital data, brightness, and color give some indication of its characteristics. Astronomers began to search for this planet when the perturbations noted in the orbit motion of Uranus could not be explained even after the influence of Neptune had been considered. Around 1914, Percival Lowell and W. H. Pickering agreed that some other body was causing this perturbation. Both men searched for the object, but it was not discovered until 1930 by C. Tombaugh. Pluto has the most highly eccentric orbit of any planet in our solar system, and at the perihelion, it orbits inside the orbit of Neptune. This planet is so far away from the sun that the sun would appear as a star in the distance. The spherical blackbody average temperature for Pluto has been estimated to be 40 K.

12.2 Astrodynamic Constants (Epoch 1960.0) [XII-1]

Distance from sun	31.7 to 30.2 A.U.
Eccentricity of orbit[1]	0.2486438
Inclination of orbit to ecliptic[1]	17.° 144
Orbital period (sidereal)[1]	90737.2
Radius (equatorial)	$5700 \times 1.2^{\pm 1}$ km
Mass of Pluto	$(5.7 \times 1.7^{\pm 1}) \times 10^{23}$ kg
Flattening (dynamic)	Unknown
Average density	$5.9 \times 3^{\pm 1}$ g/cm^3
Rotational period	6.387 ± 0.001 days
Gravitational parameter	$(3.8 \times 1.7^{\pm 1}) \times 10^4$ km^3/s^2

REFERENCE

XII-1. Anon: The Planets Uranus, Neptune, and Pluto (1971). NASA Space Vehicle Design Criteria (Environment), NASA SP-8703, November 1972.

APPENDIX A. SOLAR CYCLE PREDICTION TECHNIQUE

Current analyses have shown that properties of the natural atmospheric environment are dependent upon solar activity. This appendix provides a brief description of the method that is currently used at the Marshall Space Flight Center to predict future levels of solar activity.

In 1949, Lincoln and McNish [A-1] suggested that the prediction of a future solar cycle, based on the mean approximation of all past solar cycles, could be improved by adding to the mean a correction proportional to the departure of the earlier values of the cycle from the mean cycle. However, this technique was not recommended for making predictions longer than 1 year in the future.

Using data from two additional solar cycles, Lockheed [A-2] modified the Lincoln-McNish technique so that the Zürich-smoothed sunspot number could be predicted for 10 years in advance, and at quarterly rather than yearly intervals. Recently, another version of the original technique has been programmed that permits evaluation at quarterly, monthly, or 27 day intervals. This allows us to make predictions for shorter intervals and also to incorporate more recent data into the predictions.

The time within each cycle is measured from the minimum which defines the beginning of a cycle. The data are arranged in matrix form; each row consists of a solar cycle and each column consists of the jth year after the origin of the cycle. A mean cycle is determined by averaging each jth point of all cycles. The deviation of each jth point in all cycles from the mean at that point is computed. The products of the deviation columns are summed, and the matrix inversion technique is used to calculate prediction coefficients.

An updated prediction of future solar activity parameters is tabulated from time to time by the Space Sciences Laboratory of Marshall Space Flight Center. Table A-1 contains an example of such a prediction based on the data available in December 1971.

The following paragraphs are a mathematical description, in terms of input and output, of the sunspot prediction program currently in use at the Marshall Space Flight Center.

TABLE A-1. PREDICTION OF SUNSPOT NUMBERS, SOLAR FLUX AND GEOMAGNETIC INDEX (USING DATA AVAILABLE IN DECEMBER 1971) — AN EXAMPLE

Time	Sunspots		10.7 cm Flux		K_P	
	Nominal	Percentile (95.)	Nominal	Percentile (95.)	Nominal	Percentile (95.)
1971.583	59.80	66.06	109.33	114.50	2.20	3.02
1971.833	54.16	64.86	104.68	113.51	2.20	3.02
1972.083	51.20	63.49	102.24	112.38	2.20	3.02
1972.333	47.91	60.69	99.53	110.07	2.20	3.02
1972.583	42.82	57.54	95.33	107.47	2.20	3.02
1972.833	39.36	55.85	92.47	106.08	2.20	3.02
1973.083	35.08	53.23	88.94	103.91	2.20	3.02
1973.333	31.67	49.97	86.13	101.22	2.20	3.02
1973.583	29.27	46.97	85.56	98.75	2.20	3.02
1973.833	25.65	42.18	83.39	94.79	2.20	3.02
1974.083	22.48	38.02	81.49	91.37	2.20	3.02
1974.333	19.68	35.46	79.81	89.26	1.80	3.02
1974.583	17.91	34.22	78.74	88.23	1.80	3.02
1974.833	15.64	31.72	77.38	86.17	1.80	3.02
1975.083	14.86	31.21	76.91	85.75	1.80	3.02
1975.333	15.23	36.09	77.14	89.78	1.80	3.02
1975.583	16.17	45.90	77.70	97.87	1.80	3.02
1975.833	18.96	60.34	79.38	109.78	1.80	3.02
1976.083	22.68	74.61	81.61	122.14	2.20	3.54
1976.333	28.11	89.84	84.87	136.88	2.20	3.54
1976.583	34.22	103.73	88.23	150.31	2.20	3.54
1976.833	42.18	117.74	94.80	163.86	2.20	3.54
1977.083	50.48	130.40	101.65	176.09	2.20	3.54
1977.333	57.47	138.11	107.42	183.55	2.20	3.54
1977.583	64.16	145.60	112.93	190.80	2.20	3.54
1977.833	70.28	150.08	117.96	195.13	2.20	3.54
1978.083	78.27	161.31	125.68	205.99	2.20	3.54
1978.333	83.94	169.93	131.17	214.32	2.80	3.54
1978.583	89.02	173.29	136.08	217.57	2.80	3.54
1978.833	92.16	173.89	139.12	218.15	2.80	3.54
1979.083	92.65	170.06	139.59	214.45	2.80	3.54
1979.333	94.35	168.14	141.23	212.59	2.80	3.54
1979.583	93.56	164.21	140.47	208.80	2.80	3.54
1979.833	92.58	160.20	139.53	204.91	2.80	3.54
1980.083	89.10	149.08	136.16	194.16	2.80	3.54
1980.333	84.57	139.32	131.78	184.73	2.80	3.54
1980.583	83.17	133.44	130.43	179.04	2.80	3.54
1980.833	80.11	123.88	127.46	169.79	2.20	3.54
1981.083	77.60	117.20	125.03	163.33	2.20	3.54
1981.333	74.50	109.56	122.04	155.94	2.20	3.54
1981.583	68.97	99.99	116.90	146.69	2.20	3.54
1981.833	63.62	92.16	112.49	139.12	2.20	3.54
1982.083	59.11	85.88	108.76	133.04	2.20	3.54
1982.333	55.26	79.80	105.59	127.16	2.20	3.54
1982.583	51.70	76.12	102.66	123.61	2.20	3.02
1982.833	46.99	71.76	98.77	119.39	2.20	3.02
1983.083	42.94	66.62	95.43	114.43	2.20	3.02
1983.333	40.17	63.70	93.14	112.55	2.20	3.02
1983.583	37.16	60.05	90.66	109.54	2.20	3.02
1983.833	35.23	56.77	89.06	106.84	2.20	3.02
1984.083	32.91	57.16	87.15	107.15	2.20	3.02
1984.333	29.27	53.41	85.56	104.06	2.20	3.02
1984.583	26.71	54.89	84.03	105.28	2.20	3.02
1984.833	24.92	59.08	82.95	108.74	2.20	3.02
1985.083	23.43	62.42	82.06	110.36	2.20	3.02
1985.333	22.97	65.29	81.78	113.13	2.20	3.02
1985.583	22.82	67.84	81.69	115.61	2.20	3.02
1985.833	23.14	70.39	81.88	118.07	2.20	3.02
1986.083	24.12	72.91	82.47	120.51	2.20	3.54

A.1 Input Data

The input to the program includes the Zürich smooth sunspot numbers for cycles 1 through 20 and as many values in the 21st cycle as are available. These values were obtained by the Zürich smoothing method described in the following equation:

$$R_\ell = \frac{1}{12}\left[\sum_{k=\ell-5}^{\ell+5} R_k + \frac{R_{\ell-6} + R_{\ell+6}}{2}\right],$$

where R_ℓ is the Zürich-smoothed sunspot at the ℓ th month and R_k is the monthly relative sunspot number for the kth month (see Fig. A-2).

The smoothed sunspot numbers, R_{ij}, were obtained for the first month in each cycle and at 3 month intervals thereafter for 12 years. The month and year which currently define the first point in each cycle are defined below. For recent predictions a selected set of the past 20 cycles was used.

Cycle No.	First Month	Cycle No.	First Month
1	Mar. 1755	11	Mar. 1867
2	May 1766	12	Dec. 1878
3	June 1775	13	Feb. 1890
4	Sept. 1784	14	Jan. 1902
5	Apr. 1798	15	Aug. 1913
6	July 1810	16	July 1923
7	Apr. 1823	17	Sept. 1933
8	Nov. 1833	18	Feb. 1944
9	July 1843	19	Apr. 1954
10	Dec. 1855	20	Oct. 1964

These data defining the beginning of the cycle were obtained from Reference A-3.

A.2 Computational Procedure

Let R_{ij} denote the smoothed Zürich sunspot number for the ith cycle and the jth time point within the cycle. For the initial point within the cycle, j = 1 and the jth time points is j - 1 quarters later in time. The mean value for any given point within the cycle is given by

$$\bar{R}_j = \frac{1}{n - n_o} \sum_{i=n_o}^{n-1} R_{ij} \quad ,$$

where n is the subscript denoting the current cycle and n_o is the subscript for the first cycle to be used in the regression model. The deviations, ΔR_{ij}, from this mean are

$$\Delta R_{ij} = R_{ij} - \bar{R}_j \quad .$$

The first point to be predicted within the nth cycle will be denoted by the subscript m. The first known value in the nth cycle to be used in the prediction will be designated by the subscript m_o. The sunspot numbers, $R_{n,\, m_o}$, $R_{n\, m_o+1} \cdots R_{n\, m-1}$ will be used to predict $R_{n\, m}$, $R_{n\, m+1}$, $\cdots$, R_{nM}, where M denotes the last sunspot value to be predicted. The following matrix notation will simplify the description of the procedure:

$$a_{jk} = \sum_{i=n_o}^{n-1} \Delta R_{ij}\, \Delta R_{ik} \quad .$$

$$A = \left\| a_{jk} \right\| , \qquad j,k = m_o,\ m_o + 1,\ \ldots,\ m - 1$$

$$B = \left\| a_{jk} \right\| , \qquad j = m_o,\ m_o + 1,\ \ldots,\ m - 1$$
$$k = m,\ m + 1,\ \ldots,\ M$$

$$m_o = \begin{cases} 1 , & m \leqq 8 \\ m - 8, & m > 8 \end{cases} .$$

The predicted values are defined by the following $1 \times (M - m + 1)$ matrix:

$$R_p = \left[R_{nm} \quad R_{n\,m+1} \quad \cdots \quad R_{nM} \right]$$

$$\bar{R} = \left[\bar{R}_m \quad \bar{R}_{m+1} \quad \cdots \quad \bar{R}_M \right]$$

$$\Delta R = \left[\Delta R_{nm} \quad \Delta R_{n\,m+1} \quad \cdots \quad \Delta R_{n\,M} \right] ,$$

where

$$R_p = \bar{R} + \Delta R .$$

The values in the nth cycle that are to be used in the prediction are included in the following $1 \times (m - m_o)$ matrix:

$$\Delta R_o = \left[\Delta R_{n\,m_o} \quad \Delta R_{n\,m_o + 1} \quad \cdots \quad \Delta R_{n\,m-1} \right] .$$

The matrix of predicted values is then described by the following equation:

$$R_p = \bar{R} + \Delta R_o A^{-1} B ,$$

where

$$A\,A^{-1} = I \quad .$$

The current MSFC prediction routine actually predicts Zürich smoothed sunspot numbers. The 10.7 cm solar flux is obtained from the following equations: If $RZ \geqq 70$,

$$F = 50 + 0.967\,RZ.$$

If $30 \leqq RZ < 70$,

$$F = 60 + 0.825\,RZ.$$

If $RZ < 30$,

$$F = 68 + 0.6\,RZ.$$

The term RZ is the Zürich-smoothed relative sunspot numbers and F is the 10.7-cm solar flux. The geomagnetic index, Kp, is obtained from the following equations: If $F \geqq 130$,

$$Kp = 2.8.$$

If $80 \leqq F < 130$,

$$Kp = 2.2.$$

If $F < 80$,

$$Kp = 1.8.$$

A.3 Computer Output Example

The computer printout of this program contains predicted nominal and $+2\,\sigma$ values and $-2\,\sigma$ values for (1) sunspot numbers, (2) 10.7 cm solar flux, and (3) Kp, 3-hour geomagnetic index for the remainder of cycles 20 through 21 as shown in Table A-1. Figure A-1 is a graph of the long-range prediction of the quarterly smoothed sunspots showing the 50- and 95-percentile values.

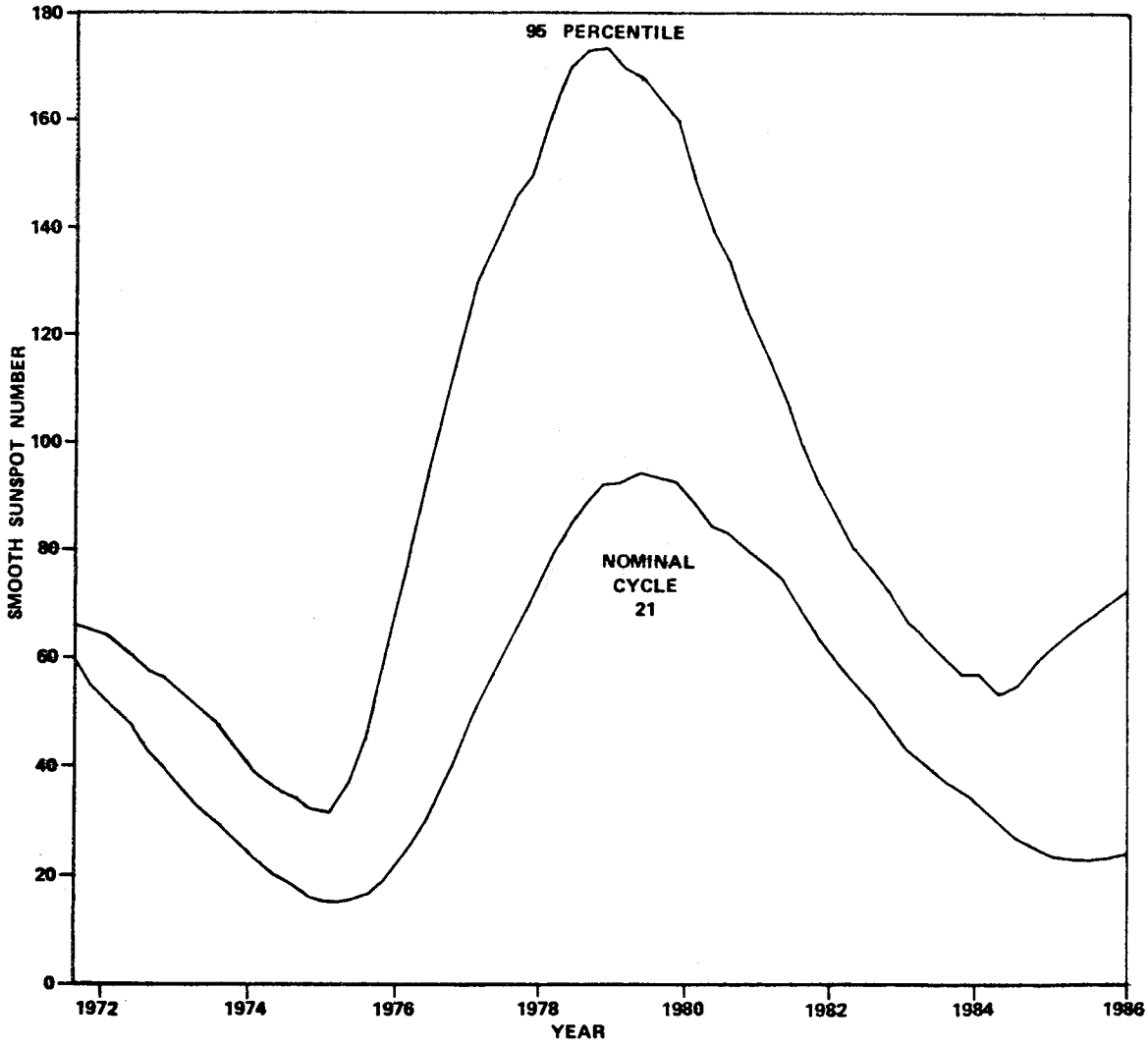

Figure A-1. Prediction of sunspot numbers (using data available in July 1974) — an example.

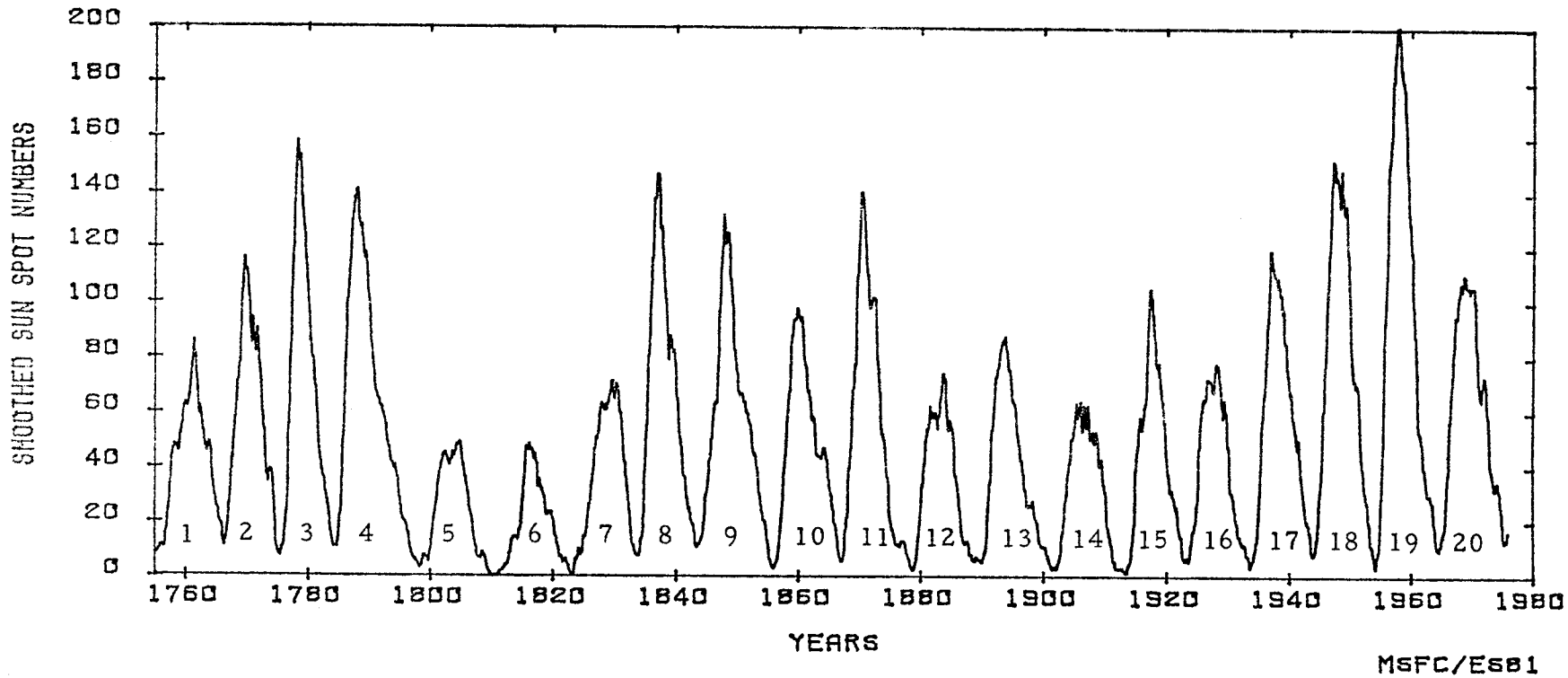

ZURICH SUNSPOT NUMBER (WOLF NUMBER)

$R = K(10g + S)$

- S = NO. OF SPOTS
- g = NO. OF GROUPS
- K = OBSERVATORY CONSTANT

ZURICH SMOOTHED SUNSPOT NUMBER

$$\bar{R}_Z = \left(R_{-6} + R_{+6} + 2\sum_{i=-5}^{+5} R_i\right)/24$$

Figure A-2. Solar cycle history.

REFERENCES

A-1. McNish, A. G., and Lincoln, J. V.: Prediction of Sunspot Numbers. Transactions, American Geophysical Union, vol. 30, no. 5, October 1949.

A-2. Boykin, E. P., and Richards, T. J.: Application of the Lincoln-McNish Technique to the Prediction of the Remainder of the Twentieth Sunspot Cycle. Lockheed Missiles and Space Company, Technical Memorandum 54/30-89, Huntsville, Alabama, March 1966.

A-3. Waldmeier, M.: The Sunspot Activity in the Years 1610-1960. Zurich Schulthess and Company, Switzerland, 1961.

APPENDIX B. NEUTRAL ATMOSPHERE MODELS

B.1 Density Variations and Models

Since the advent of the first orbiting satellite in 1957, significant advances have been made in our knowledge of the earth's upper atmosphere. The accepted model of the earth's upper atmosphere at that time was one in which the temperature, pressure, density, and composition varied only with height. Predictions of future sightings (orbital positions) of the first satellites using this invariant atmosphere soon showed that the model was in error. Subsequently, several periodic variations in the density, temperature, and composition of the upper atmosphere have been identified. They are classified as:

a. Variations with the solar cycle ~11 year.

b. Variations with the daily change in activity on the solar disc.

c. The diurnal variation.

d. Variations with geomagnetic activity.

e. The semiannual variation.

f. Seasonal-latitudinal variations of the lower thermosphere.

g. Seasonal-latitudinal variations of helium at all altitudes.

h. Rapid density fluctuations probably connected with tidal and gravity waves.

The first seven have some regularity and can be modeled with varying degrees of accuracy. Since temperature plays a minor role in comparison with density, current models have been developed to represent, insofar as practical and possible, the variability of the ambient mass density rather than the temperature. The models are based on temperature profiles (Fig. B-1) [B-1] which have been adjusted so as to produce the density values derived from the analyses of satellite orbital decay data.

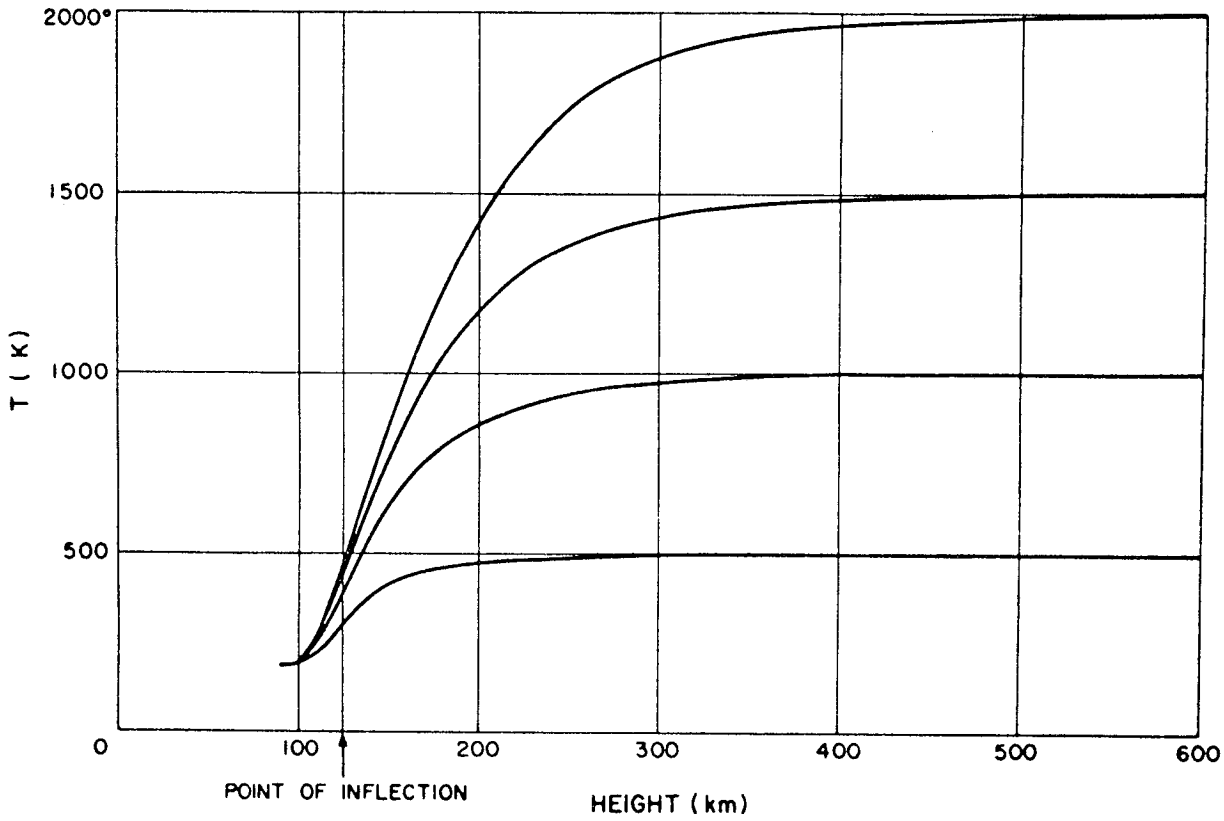

Figure B-1. Four temperature profiles from the present models [B-1].

B.1.1 Variations with Solar Activity

The ultraviolet solar radiation that heats and causes compositional changes (Fig. B-2) [B-1] in the earth's upper atmosphere consists of two components, one related to active regions on the solar disc and the other to the disc itself. The active-region component varies from day to day while the disc component varies more slowly, presumably with the longer periodicities in the solar activity; i.e., the ~11 year solar cycle. The atmosphere has been observed to react in a different manner to each of these two components. Jacchia and Slowey have found that the disc component of the solar radiation is, for all practical purposes, linearly related to the 10.7 cm solar flux smoothed over three solar rotations (81 days).

The effect of solar activity on atmospheric density is shown in Figures B-3 and B-4 after Jacchia [B-1]. When the short-period oscillations which are caused by the diurnal variation are removed, there is essentially an 11 year variation that parallels the smoothed 10.7 cm solar flux data.

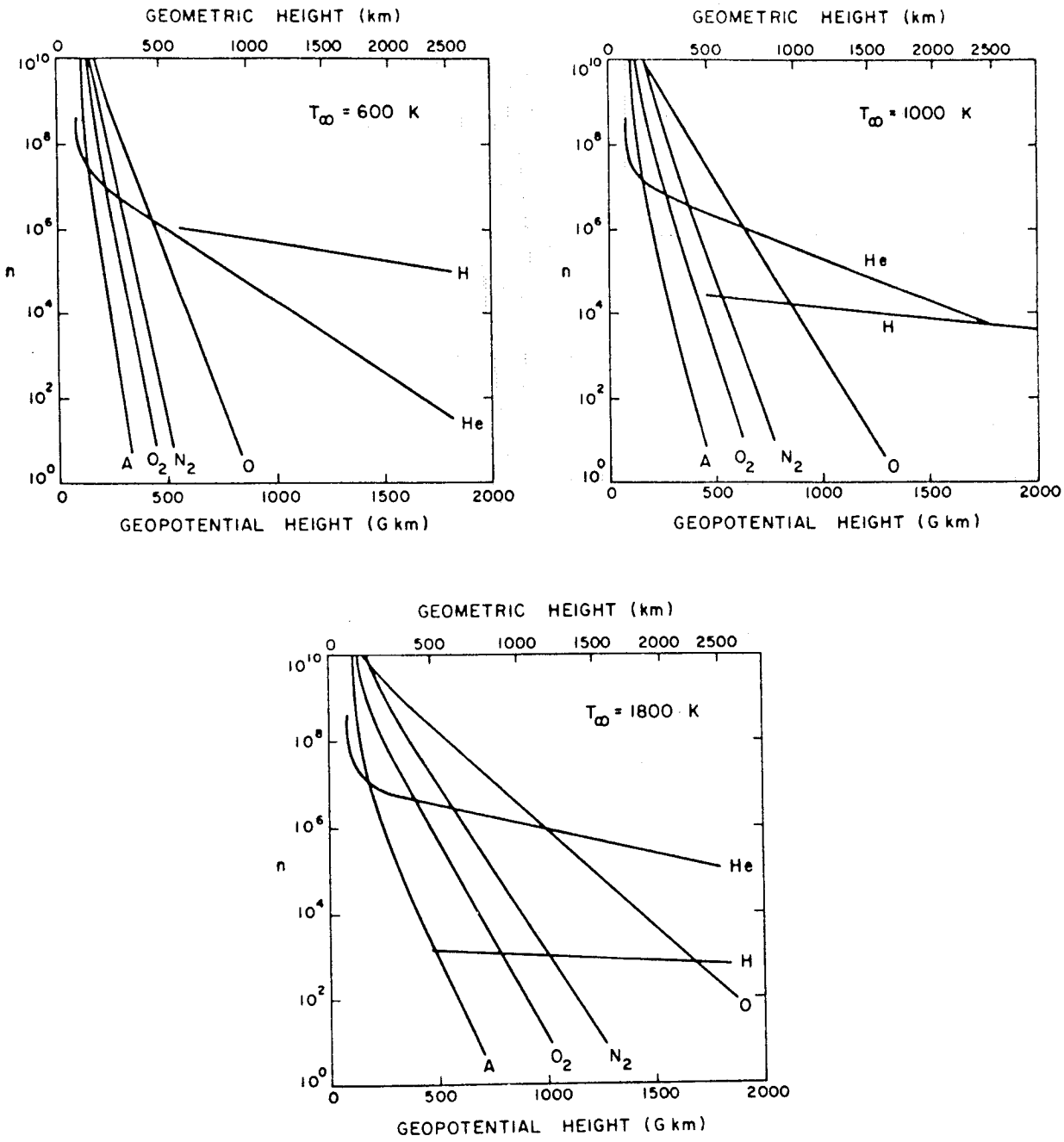

Figure B-2. Atmospheric composition for three values of the exospheric temperature [B-1]. (Number densities (n) are plotted against geopotential height. The corresponding geometric heights are marked at the top of the diagrams.)

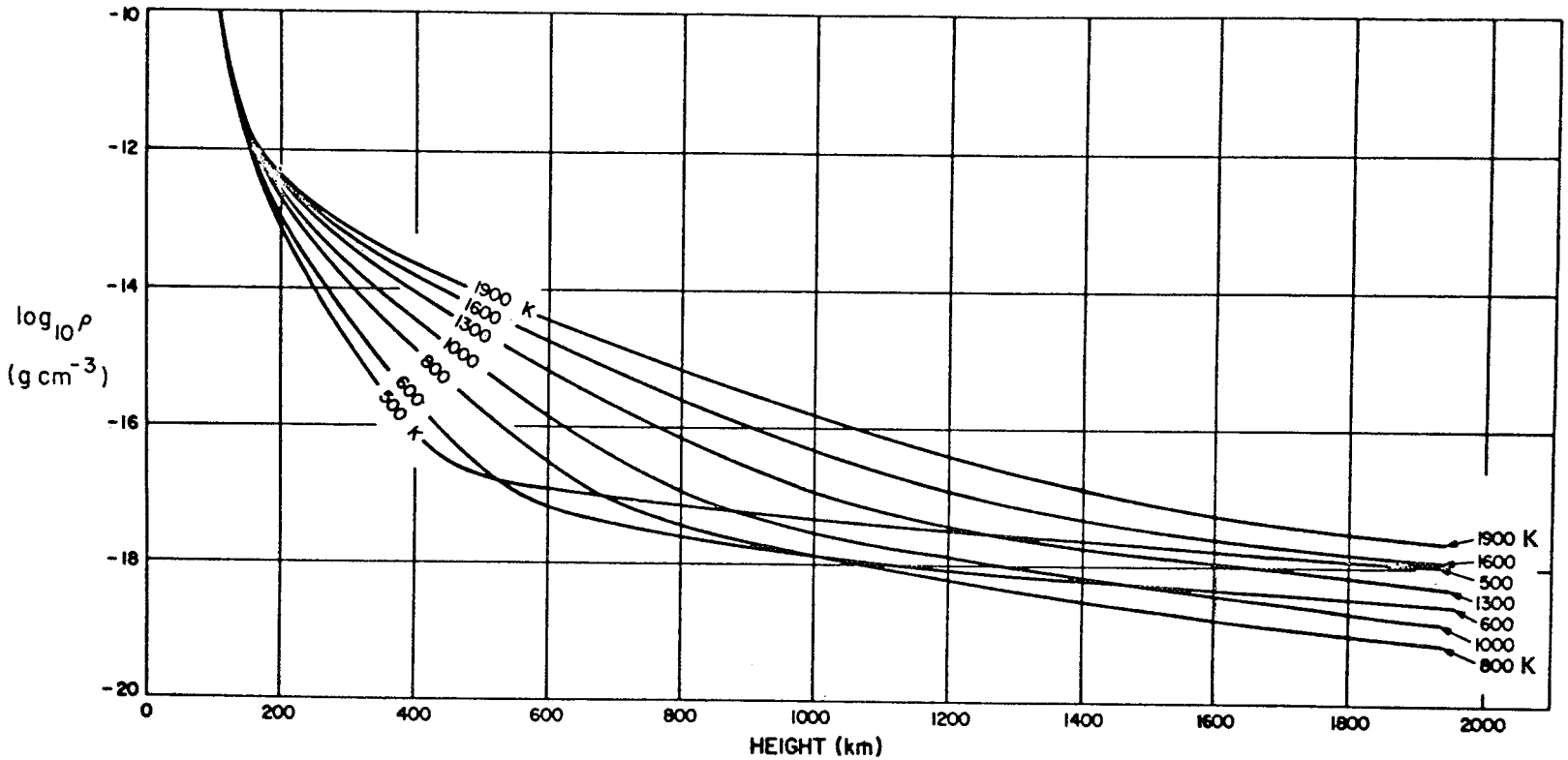

Figure B-3. Density profiles for seven values of the exospheric temperature [B-1].

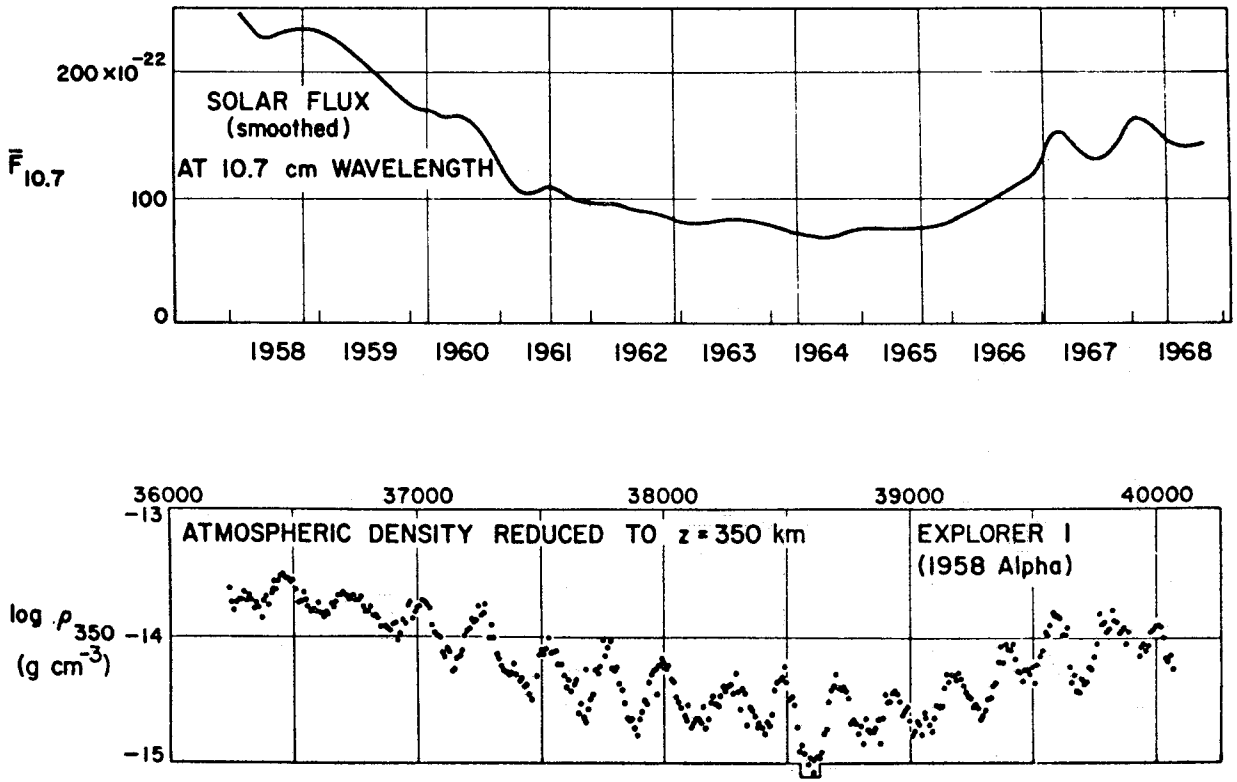

Figure B-4. Ten day means of the densities obtained from the drag of the Explorer 1 satellite compared with variations in the 10.7 cm solar flux [B-1]. [M.J.D. is the Modified Julian Day (J.D. minus 2 400 000.5).]

Figure B-5, after Jacchia [B-1], shows some of the variations in greater detail. The variations with a 27 day period are caused by the sun's rotation — the active-region component. The semiannual variation can also be seen.

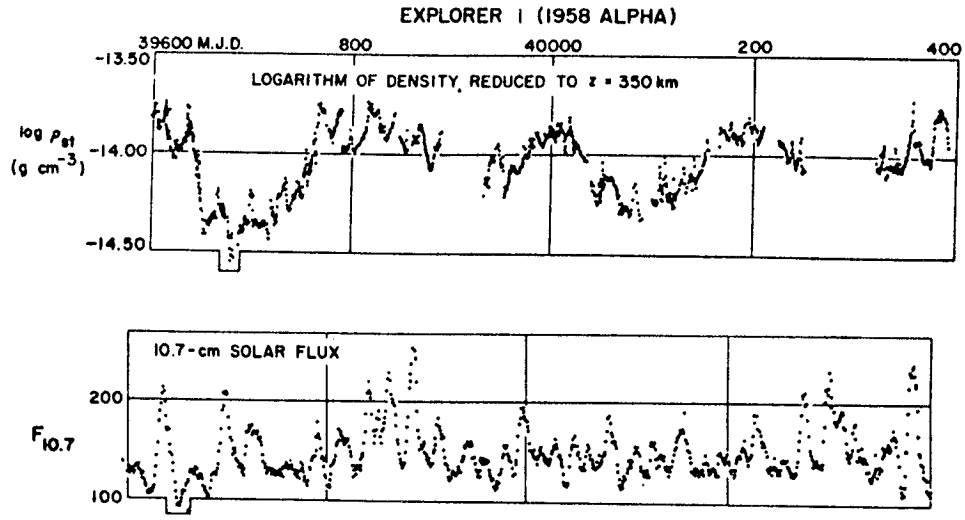

Figure B-5. Densities obtained from the drag of the Explorer 1 satellite compared with variations in the 10.7 cm solar flux.

B.1.2 The Diurnal Variation

Analyses of satellite orbital decay histories have shown that upper atmospheric densities reach a maximum around 2 p.m. local solar time at a latitude approximately equal to that of the subsolar point while the minimum occurs between 3 and 4 a.m. at about the same latitude in the opposite hemisphere. Consistency between temperature and density cannot be achieved on a diurnal basis in a static model; therefore, the temperature profile has been used as a parameter so that observed density values can be reproduced by the models. The temperature distribution needed to achieve this required reproduction of the observed density values is depicted on a global scale in Figure B-6 [B-1]. Even though the global temperature distribution is an artifact developed solely for use in the density and composition models, some experimental results are in good agreement [B-2, B-3, B-4, B-5]. Thomson-scatter temperature measurements [B-6, B-7, B-8], as shown in Figure B-7 [B-1], generally show that the temperature maximum occurs between 3 and 5 p.m. rather than near 2 p.m. This controversy has not been resolved at this time; however, it appears as if there is a phase lag between the density maximum and the temperature maximum which cannot be included in the current atmospheric models.

EXOSPHERIC TEMPERATURE DISTRIBUTION AT THE EQUINOXES

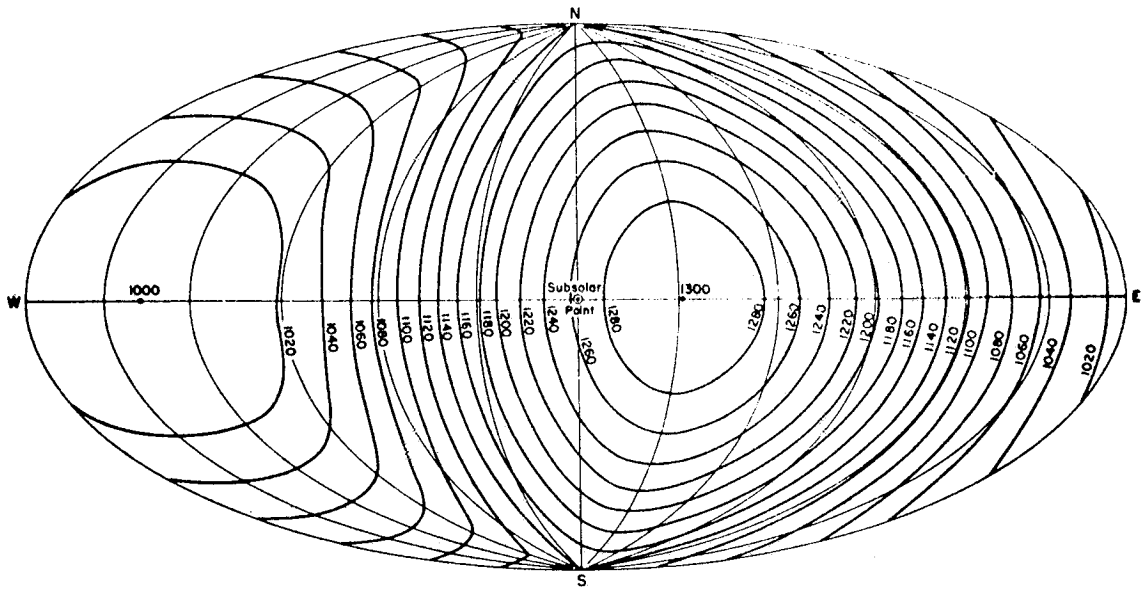

EXOSPHERIC TEMPERATURE DISTRIBUTION AT NORTHERN SUMMER SOLSTICE

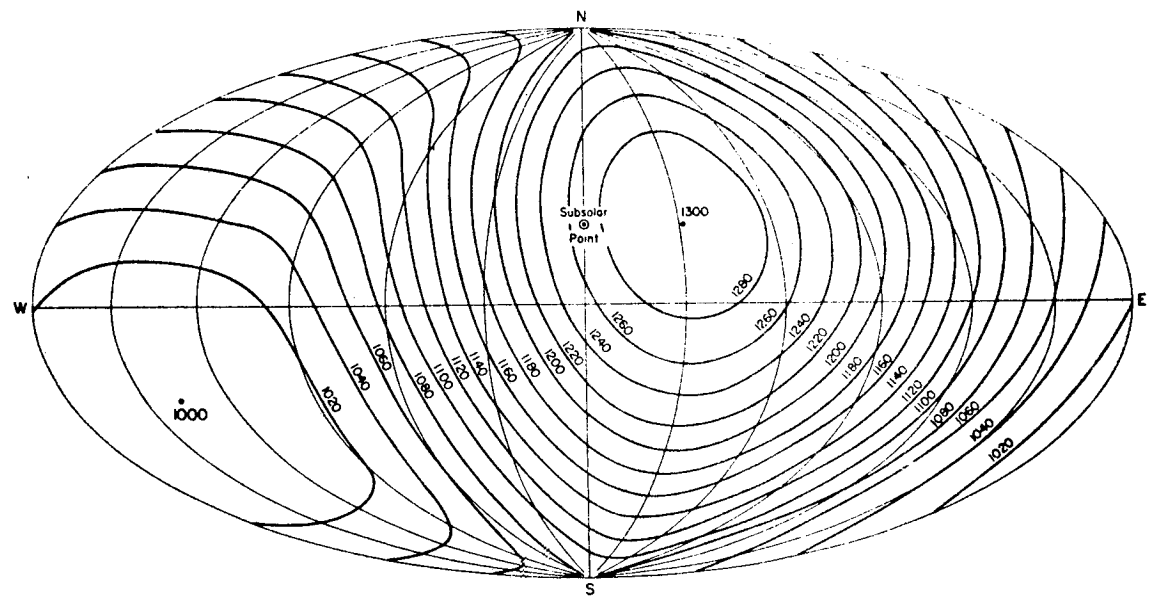

Figure B-6. Exospheric isotherms (K) above the globe, for the case when the minimum temperature is 1000 K [B-1].

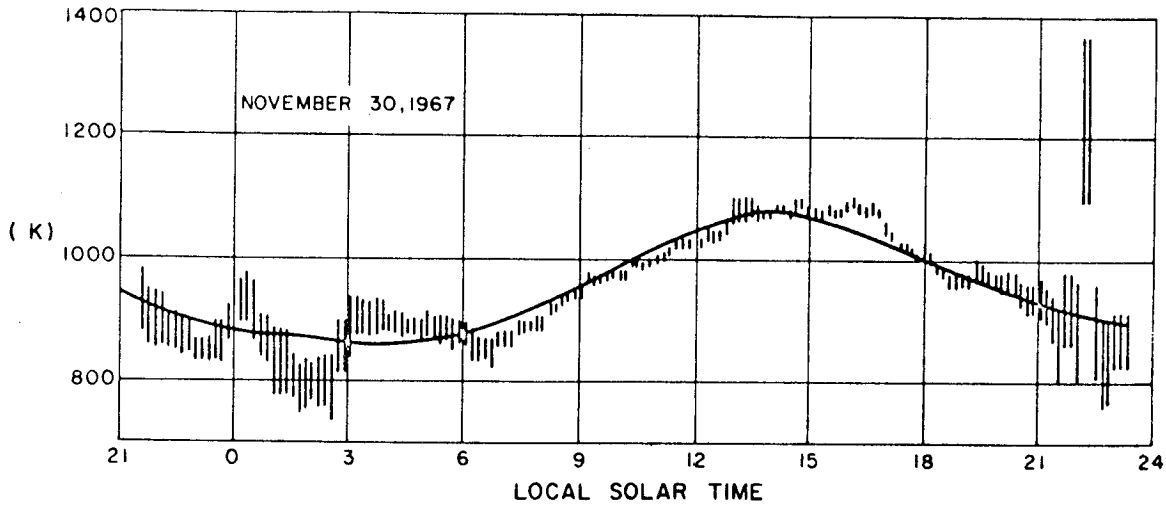

Figure B-7. Atmospheric temperatures obtained on November 30, 1967, by Carru and Waldteufel [B-7] by use of Thomson-scatter techniques, compared with temperatures predicted by the present models for a height of 300 km (solid line).

B.1.3 The Semiannual Variation

No satisfactory explanation has been found for this variation. It was initially assumed that this density variation could be linked with a temperature variation; however, data from analyses of more recently orbited satellites showed that the original assumption was in error. The amplitude of this density variation is strongly height-dependent and variable from year to year, with a primary minimum in July and principal maximum in October; however, it does not appear to be related to solar activity. Figure B-8 [B-1] shows the semiannual variation as derived from the orbital decay analysis of Explorer 32.

B.1.4 Variations with Geomagnetic Activity

Analyses of orbital decay histories can give only a blurred picture of the complex reaction of the upper atmosphere to geomagnetic disturbances (Fig. B-9) [B-1]. Blamont and Luton [B-9] and DeVries [B-10] have shown that the upper atmosphere first reacts in the auroral zones with the energy subsequently propagating toward the equator apparently in the form of wave-like perturbations. It appears as if the atmosphere reacts with a zero time delay in the auroral zones with the geomagnetic storm effects showing up in the

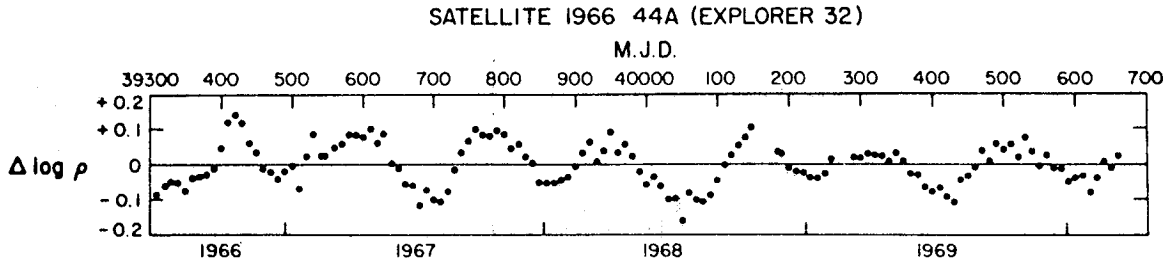

Figure B-8. The semiannual density variation as derived from drag analysis on Satellite 1966 44 A (Explorer 32). [All other variations have been suppressed by using the appropriate equations. M.J.D. is the Modified Julian Day (J.D. minus 2 400 000.5).]

equatorial zone about 6 to 9 hours later. It is very difficult to adequately include this effect in a static model. The current models calculate the density variations on the basis of a global increase in exospheric temperature. Observations [B-9, B-10] have shown that this is not the case; however, for satellite lifetime prediction calculations, an assumed global temperature increase is acceptable. For some calculations, such as control dynamics analyses, control moment gyro analyses and aerodynamic torques, instantaneous temperature (and therefore density), increases for short time periods and specific locations may be required. These studies may require special applications of the models.

B.1.5 Seasonal-Latitudinal Variations of the Lower Thermosphere

Presently accepted models assume constant temperature and density values at 90 km to prevent the models from becoming too complex even though large temperature and somewhat smaller density variations are known to exist. Current models therefore are constructed with a seasonal-latitudinal density variation which varies in the vertical from 0 at 90 km to a maximum at 110 and back to zero at 170 km. In the horizontal, the maximum occurs on December 27 at the North Pole and on June 25 at the South Pole. These variations are included as additions to the mass densities calculated as a function of the exospheric temperature used in the model. These variations are small and because they occur solely below 170 km altitude they will have little effect on orbital lifetime prediction calculations.

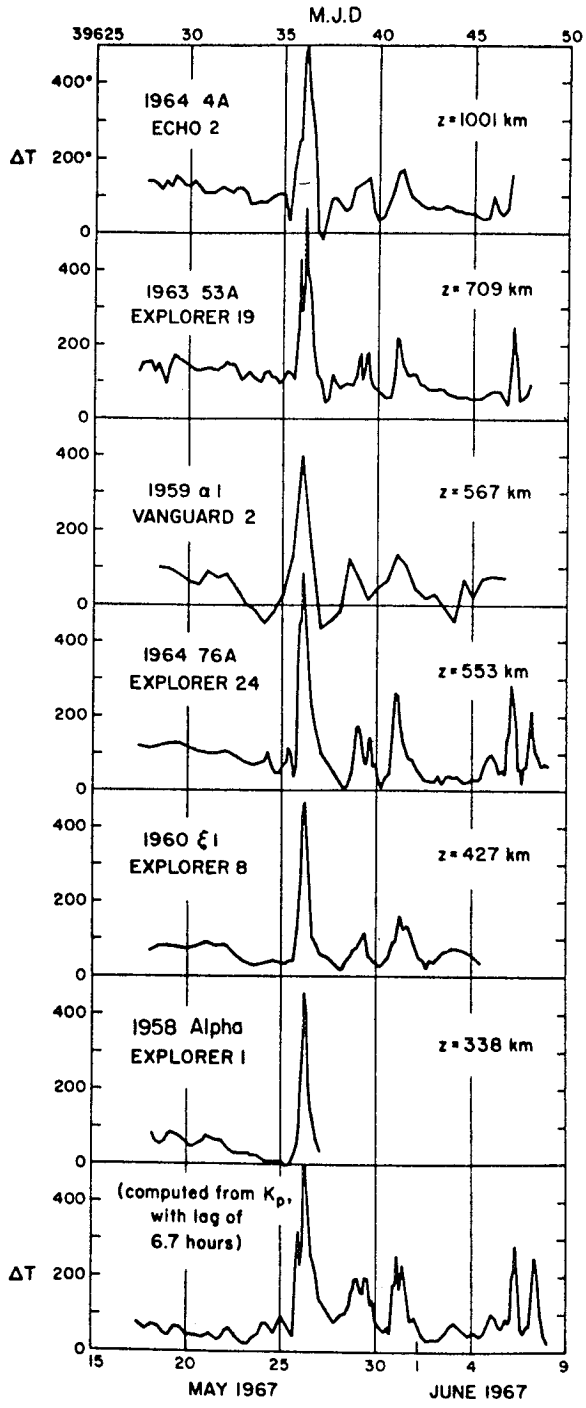

Figure B-9. The geomagnetic effect as derived from the drag of six satellites in May and June 1967. [The plotted ΔTs are temperature residuals from the models when all variations except the geomagnetic effect have been taken into account. M.J.D. is the Modified Julian Day (J.D. minus 2 400 000.5).]

B.1.6 Seasonal-Latitudinal Variations of Helium

Experimental results have shown a strong increase of helium above the winter pole. The mechanism for this migration is unclear; however, empirical equations which describe the phenomenon are included in the models. These variations influence the computed densities only at heights above approximately 600 km (Fig. B-10).

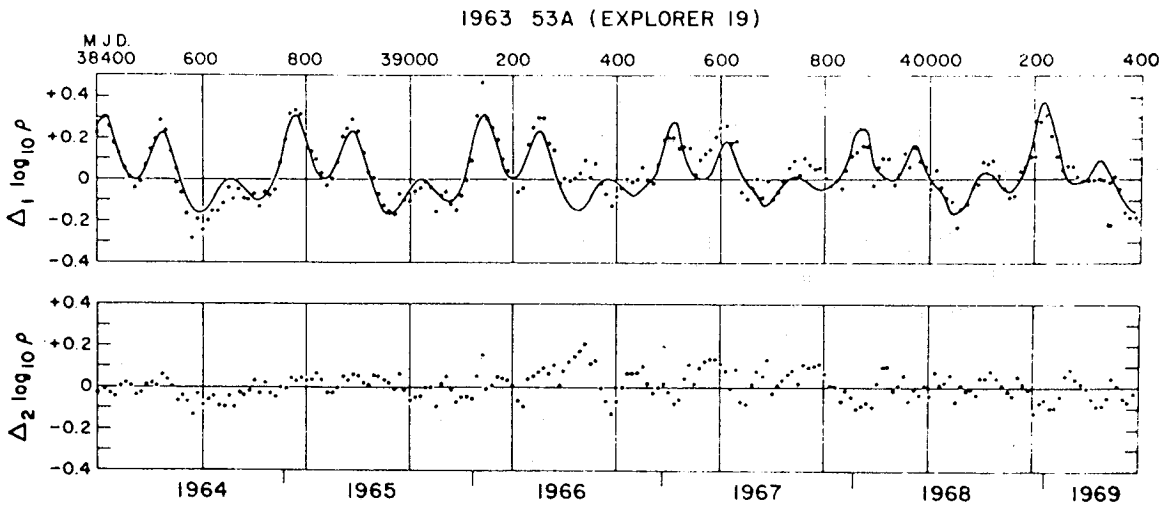

Figure B-10. Observed and computed density variations caused by the helium migration, as derived from the drag on Satellite 1963 53A (Explorer 19). [The data points in $\Delta_1 \log \rho$ are density residuals from the model when all variations except the helium variation are suppressed. $\Delta_2 \log \rho$ is the difference O-C in $\Delta_1 \log \rho$. M.J.D. is the Modified Julian Day (J.D. minus 2 400 000.5).]

B.1.7 Density Waves

Ambient density waves have been detected throughout the upper atmosphere in the height range from 140 to at least 510 km [B-4, B-10]. In addition, traveling ionospheric disturbances (TIDs) have long been thought of as manifestations of internal gravity waves. The waves appear to be more prevalent at the higher latitudes near the auroral zone; however, TIDs have been observed at all latitudes. Their vertical wavelengths apparently increase with altitude. Density increases on the order of 100 percent have been observed

to occur over short distances [B-10]. The waves apparently propagate from either south to north or north to south with maximum horizontal wavelengths on the order of 500 to 700 km. Although current models do not include variations associated with internally propagating waves, users should be cautioned that they have been observed.

B.2 Applications

Requirements exist for models of the earth's neutral upper atmosphere which will:

a. When used in lifetime prediction calculations, make predictions of lifetimes for satellites with orbital altitudes between ~ 180 and 2500 km within reasonable limits.

b. Contain the short period fluctuations observed in upper atmospheric density which may influence the design and operation of reaction control systems (RCS), thrust augmented control systems (TACS), control moment gyroscopes (CMG), rendezvous and docking systems, etc.

c. Provide continuous values of atmospheric parameters from orbital altitudes down to about 25 km altitude for use in evaluating thermal protection systems (TPS), control and guidance systems, etc., during reentry of space vehicle (e.g., the Shuttle), and in accomplishing orbital debris analyses.

d. Provide data on the composition and thermal structure of the upper atmosphere and its temporal and spatial variability for use in interpreting and analyzing results of scientific and technical investigations; e.g., contamination surrounding the Skylab.

e. Provide data on the variability of the neutral atmosphere at mesopause heights for use in aerobraking maneuver studies.

B.3 Criteria

a. The Global Reference Atmosphere [B-13,14] model will be used in conjunction with the MSFC Lifetime Prediction Computer Routine for calculating orbital lifetime. Data from the monthly Solar Activity memorandum prepared and distributed by the Space Sciences Laboratory will be used as inputs to the model. This model is a combination of the 4-D Model Atmosphere, the Groves Model, and the Jacchia 1970 [B-11] Atmosphere model. It provides continuous density, temperature and composition data from the surface to 2500 km for

analyses requiring these data. Copies of the computer program for this model are available upon request to the Space Sciences Laboratory, MSFC. A computerized simplified version of the Jacchia 1970 atmosphere model is available upon request from the Space Sciences Laboratory.

b. Personnel performing analyses requiring knowledge of any small scale, short time period fluctuations in atmospheric parameters such as those perturbations associated with internally propagating waves should contact the Space Sciences Laboratory, MSFC for model data to be used in each specific analysis.

REFERENCES

B-1. Jacchia, L. G.: Revised Static Models of the Thermosphere and Exosphere with Empirical Temperature Profiles. Smithsonian Astrophysical Obs., Special Report 332, May 5, 1972.

B-2. Taeusch, D. R., Niemann, H. B., Carignan, G. R., Smith, R. E., and Ballance, J. O.: Space Research 8. A. P. Mitra, L. G. Jacchia, and W. S. Newman, eds., North Holland Publishing Co., Amsterdam, 1968, pp. 930-939.

B-3. Reber, C. A., and Nicolet, M.: Planet Space Science, vol. 13, 1965, pp. 617-646.

B-4. Newton, G. P.: Journal of Geophysical Research, vol. 74, 1969, pp. 6409-6414.

B-5. Hall, L. A., Chagnon, G. W., and Hinteregger, H. E.: Journal of Geophysical Research, vol. 72, 1967, pp. 3425-3427.

B-6. Carru, H., Petit, M., and Waldteufel, P.: Planet Space Science, vol. 15, 1967, pp. 944-945.

B-7. Carru, H., and Waldteufel, P.: Ann de Geophys, vol. 25, 1969, pp. 485-494.

B-8. McClure, J. P.: Journal of Geophysical Research, vol. 74, 1969, pp. 279-291.

B-9. Blamont, J. E., and Luton, J. M.: Space Research, vol. 11, Akademie-Verlag, Berlin, 1971.

B-10. DeVries, L. L.: Experimental Evidence in Support of Joule Heating Associated with Geomagnetic Activity. NASA TM X-64568, MSFC, February 10, 1971.

B-11. Jacchia, L. G.: Smithsonian Astrophysical Observatory Special Report No. 313. 1970, pp. 87.

B-12. Groves, G. V.: Environmental Research Papers, No. 368, AFCRL-71-0410, Bedford, Mass., 1971.

REFERENCES (Concluded)

B-13. Justus, C. G., Woodrum, A. W., Roper, R. G., and Smith O. E.: Four-D Global Reference Atmosphere: Technical Description: Part I, NASA TM X-64871, Sept. 1974.

B-14. Justus, C. G., Woodrum, A. W. Roper, R. G., and Smith, O. E.: Four-D Global Reference Atmosphere: Users Manual and Programmers Manual: Part II, NASA TM X-64872, Sept. 1974.

APPENDIX C. A PRELIMINARY SUMMARY OF THE MSFC PLANETARY ATMOSPHERE COMPUTER PROGRAM

C.1 Summary

The MSFC Planetary Atmosphere Computer Program contains the exact equations and most refined techniques necessary to the development of models of planetary atmospheres. All of the atmospheric parameters that are essential to spacecraft design studies and aerospace operations are output in tabular form for levels of geopotential height and geometric altitude from the surface to the altitude where the planetary atmosphere is the same as interplanetary space.

C.2 Purpose

This appendix briefly outlines the computation procedure used in the Planetary Atmosphere Computer Program developed by the MSFC Computation Data Systems Laboratory for the B5500 computer.

C.3 Basic Data

In developing a model atmosphere, it is necessary to establish certain basic data so that various parameters that define the model may be computed. It has been found that the most refined models may be developed if these basic data consist of kinetic temperature and molecular weight versus geopotential height profiles and a surface pressure.

C.4 Computational Procedure

A. Input Data

1. Kinetic temperature at geopotential height levels.
2. Molecular weight at geopotential height levels.
3. Surface pressure.
4. Surface kinetic temperature.

5. Surface molecular weight.

6. Surface gravity.

7. Planet radius.

8. Universal gas constant.

9. Sutherland's constant.

10. Boltzman's constant.

11. Avogadro's number.

12. Effective collision diameter of mean air particle.

13. Ratio of specific heats.

B. Computations at Geopotential Height Levels

1. Kinetic temperature lapse rates

$$L_K = \frac{dT_k}{dH} = \frac{(T_K)_n - (T_K)_{n+1}}{H_{n+1} - H_n} \qquad \text{(C-1)}$$

where n is the input levels in geopotential kilometers.

2. Molecular weight lapse rates

$$J = \frac{dM}{dH} = \frac{M_n - M_{n+1}}{H_{n+1} - H_n} \qquad \text{(C-2)}$$

where n is the input levels in geopotential kilometers.

3. Kinetic temperatures

Kinetic temperatures are computed for each km from 1 to 1000 km geopotential height from the surface temperature (T_o) and the computed lapse rate (L_K) .

4. Molecular weight

Molecular weight values are computed for each km from 1 to 1000 km geopotential height from the surface molecular weight (M_o) and computed molecular weight lapse rate (J).

5. Molecular temperatures

Molecular temperatures are computed for each km from 0 to 1000 km geopotential height.

$$(T_M)_j = \frac{(T_K)_j M_o}{M_j} \quad . \tag{C-3}$$

6. Molecular temperature lapse rate

$$(L_M)_{j-1 \text{ to } j} = \frac{(T_M)_{j-1} - (T_M)_j}{H_j - H_{j-1}} \tag{C-4}$$

$j = 1, 2, 3, \ldots, 999, 1000$ — $(T_M)_{j-1} = (T_M)_o$ for first computation.

7. Atmospheric pressure (discussed later in this appendix)

a. If $L_M \neq 0$,

$$P_j = P_{j-1} \left[\frac{(T_M)_{j-1}}{(T_M)_j} \right]^{\frac{M_o G_o}{R^* (L_M)_{j-1 \text{ to } j}}} \tag{C-5}$$

where $P_{j-1} = P_o$ for first computation.

b. If $L_M = 0$,

$$P_j = P_{j-1} \exp\left[\frac{M_o G_o (H_j - H_{j-1})}{R^* (T_M)_j} \right] \quad . \tag{C-6}$$

C. Computations for Each km from 0 to 1000 km Geometric Altitude

1. Geometric altitude

$$Z_i = \frac{RH_i}{R - H_i} \quad . \qquad \text{(C-7)}$$

2. Atmospheric pressure

Using pressure values (P_j) computed at geopotential height levels by equations (C-5) and (C-6), atmospheric pressures are interpolated logarithmically for each kilometer of geometric altitude and denoted as $(P)_i$.

3. Kinetic temperature

Using kinetic temperatures $(T_K)_j$ computed at geopotential height levels, kinetic temperatures are interpolated for each km of geometric altitude and denoted as $(T_K)_i$.

4. Molecular weight

Molecular weight values are similarly interpolated for each kilometer of geometric altitude and denoted by M_i.

5. Molecular temperature

$$(T_M)_i = \frac{(T_K)_i M_o}{M_i} \quad . \qquad \text{(C-8)}$$

6. Atmospheric density

$$\rho_i = \frac{M_o P_i}{R^*(T_M)_i} \quad . \qquad \text{(C-9)}$$

7. Gravity

$$G_i = G_o \left[\frac{R}{R + (Z)_i} \right]^2 \quad (C-10)$$

8. Pressure scale height

$$SH_P = \frac{R^* (T_M)_i}{M_o G_i} \quad (C-11)$$

9. Density scale height

$$SH_d = \frac{(SH_P)_i}{1 + \frac{R^*}{M_o G_i} (dT_M/dZ)_i} \quad (C-12)$$

where

$$(dT_M/dZ)_i = \frac{(T_M)_{i-1} - (T_M)_{i+1}}{Z_{i+1} - Z_{i-1}} \quad (C-13)$$

10. Number density

$$(ND)_i = \frac{M_o NP_i}{R^* M_i (T_M)_i} \quad (C-14)$$

11. Most probable air-particle speed

$$PS_P = \left[2 \frac{R^*}{M_o} (T_M)_i \right]^{1/2} \quad (C-15)$$

12. Mean air-particle speed

$$PS_M = \left[\frac{8}{\pi} \frac{R^*}{M_o} (T_M)_i \right]^{1/2} \quad (C-16)$$

13. Atmospheric mean free path

$$(MFP)_i = \frac{R^*(M)_i \quad T_{M\,i}}{\sqrt{2}\,\pi\,N\,\sigma^2\,M_o\,(P)_i} \quad . \qquad (C\text{-}17)$$

14. Collision frequency

$$(CF)_i = \frac{(PS_M)_i}{(MFP)_i} \quad . \qquad (C\text{-}18)$$

15. Speed of sound

$$(C_s)_i = \left[\gamma \frac{R^*}{M_o} \quad T_{M\,i}\right]^{1/2} \quad . \qquad (C\text{-}19)$$

16. Coefficient of viscosity

$$(CV)_i = \frac{(T_K)_i^{3/2}}{(T_K)_i + S} \quad . \qquad (C\text{-}20)$$

D. Output

The various computer parameters are printed in tabular form for kilometer increments of both geopotential height and geometric altitude. The program is designed so that the printing interval may be varied at the discretion of the operator. For example, parameters may be printed for each kilometer in the lower atmosphere, then for each 10 km over a defined altitude region, and then for each 100 km in the upper atmosphere.

C.5 Computer Program Accuracy and Versatility

Accuracy and versatility have been emphasized in the development of this computer program. Atmospheric pressures are computed from the exact hydrostatic equation without constant molecular weight or isothermal temperature assumptions. This pressure computation technique has been found to be more accurate than those approximation techniques which assume that the

molecular weight is constant and that the temperature is isothermal over the computation interval. The computation interval is considered as 1 km in this report, but the computer program is designed so that the size of this interval is input and may be varied. It should be noted, however, that the size of the computation interval does not influence the accuracy when the exact pressure equation is used.

To maintain a high degree of versatility in the application of this computer program, all constants that are descriptive of an individual planet are input. The program may be used in the development of the atmosphere of any planet including the earth. The program is designed to allow computations from the planet's surface to interplanetary space altitude levels, which generally occurs between 10 000 and 20 000 km.

APPENDIX D. GLOSSARY

Adhesion — Normal component of attractive molecular force-per-unit-area between unlike substances.

Adiabatic — Characteristic of processes in which heat is not transferred across system boundaries; in an atmosphere such a system is a hypothetically rising or falling parcel of gas, and the adiabatic requirement must be satisfied when the parcel reaches equilibrium with the local pressure, temperature, and density.

Angle of Internal Friction (ϕ) — If the ratio of tangential to normal external stress exceeds $\tan \phi$, slippage within the material occurs.

Angstrom (Å) — A unit used to express the wavelength of light ($1Å = 10^{-10}$ m).

Annual — Refers to the variation of a parameter during one revolution of the planet (yearly variation).

Anorthosite — Igneous rock, primarily plagioclase; on earth crystallized at relatively high pressures below the surface.

Aphelion — That point in an orbit farthest from the sun.

Apoapsis — That point in an orbit farthest from the center of attraction.

Astronomical Unit (AU) — The semimajor axis of the earth's orbit about the sun approximately; Gurnette and Woolley provide a more precise definition; a modern value cited by Melbourne et al. is $1 \text{ AU} = 1.49597893 \times 10^8 \pm 5$ km.

Bandwidth — The range of frequencies (or wavelengths) within which electromagnetic radiation is emitted or detected; the power or response distributions need not be uniform within this range.

Basalt — Dark gray igneous rock, primarily plagioclase, pyroxene, ilmenite, and magnetite; on earth crystallized rapidly at relative low pressures.

Blackbody — An ideal body which is in complete thermodynamic equilibrium with its surroundings and radiates energy according to Planck's law.

Bolometric — Characteristic of an infinite bandwidth, and including electromagnetic radiation at all frequencies (or wavelengths) and polarizations.

Bolometric albedo — The bond albedo weighted over wavelengths by the solar flux.

Bond albedo — A measure of the reflectivity of a planet. It is the ratio of the total amount of sunlight reflected from the body in all directions to the amount falling upon the body.

Brightness Temperature — The temperature at which a blackbody would radiate an intensity of electromagnetic radiation identical to that of the source for the bandwidth and polarization considered.

Chronocentric — Referenced to the center of Saturn.

Chronographic — Referenced to a line parallel to the direction of the zenith at Saturn.

Cohesion — Normal component of attractive molecular force per unit area between like substances.

Color — For a given light source, the difference in magnitude for two bandwidths centered on different wavelengths.

Decametric — Characteristic of electromagnetic radiation at those radio wavelengths between 10 and 100 m; used here to cover a broader range extending, perhaps, to 7 m.

Decimetric — Characteristic of electromagnetic radiation at those microwave wavelengths between 10 and 100 cm; used here synonymously with UHF to cover a broader range extending, perhaps, to 1 cm.

Declination — The celestial coordinate equal to the angle (north taken positive) between the direction of the item considered and the plane of the earth's equator; the precession of the latter implies a slow variation of the declination even of fixed directions.

Dielectric Constant — The ratio of the permittivity (ϵ) of a material to a free space value (ϵ_0); this ratio is normally referred to as the relative or effective dielectric constant.

Disk Brightness Temperature (T_D) — The resulting brightness temperature when all radiation (excluding background sources) from a region surround-

ing an object is associated with the disk of that object; for Saturn the disk brightness temperature may include a contribution from the rings (thermal) and/or radiation belts (non-thermal).

Diurnal — Refers to the variation of a parameter during one rotation of the planet (daily variation).

Elevation Angle (B_o, B_{ob}, B_R, $B_\odot$) — The angular distance of a (intersecting) line above a plane; the Saturn equatorial (ring) plane is used exclusively.

Effective Temperature (T_e) — The temperature at which a blackbody would radiate a bolometric intensity of electromagnetic radiation identical to that of the source.

Elongation — For a planetary satellite system, the configuration of planet and satellite which presents the largest angular displacement between the two as seen from the earth.

Flattening (ϵ) — The positive difference between unity and the ratio of the polar to the equatorial diameter of a planetary disk (optical), or the value for the same quantity which would be derived on the basis of hydrodynamic theory and the gravitational potential inferred from observed satellite motions.

Flattening (f) — A measure of the shape of a planet. Flattening is the difference between the mean equatorial diameter and polar diameter divided by the mean equatorial diameter.

Flux of Electromagnetic Radiation (F, F_ν, or F_λ) — The power per unit area crossing an imaginary plane surface from one side to the other, either per unit bandwidth or integrated over all frequencies.

Flux of Charged Particles (ϕ_E) — The number of particles per unit area and per unit time crossing an imaginary plane surface with positive or negative (but not both) velocity components perpendicular to the surface.

Geometric Albedo [$p(\lambda)$] — The ratio of the reflected flux (power per unit detector area) from an astronomical object (observed at distance Δ, zero phase angle, and zero optical depth) to the quotient of the solar power intercepted by the object divided by $\pi\Delta^2$, in the bandwidth considered. Here the flux, the power, and Δ must be expressed in consistent units; and Δ must be large compared to the dimensions of the object.

Heliocentric — Referenced to the center of the sun.

Heliocentric Longitude — The angle to the planet as measured from the point in orbit where the sun is in the zenith and moving northward, i.e., the beginning of spring in the Northern Hemisphere.

Hermocentric — Referenced to the center of Mercury.

Igneous — Formed by solidification from a molten or partially molten state.

Ilmenite — A black mineral composed of an oxide of iron and titanium ($FeTiO_3$).

Integrated Flux — Flux of electromagnetic radiation integrated over all wavelengths or frequencies.

Intensity (I_ν or I_λ) — The flux of electromagnetic radiation per unit solid angle of the source for a defining imaginary surface whose normal intersects the source; intensity is independent of the source-surface separation.

Ionosphere — The atmospheric layer which includes the major maxima of electron and ion concentration.

Isophote — A line of equal or constant brightness.

Lambert Surface — A surface which emits luminance flux at a rate proportional to the cosine of the angle between the surface normal and the direction of observation.

Loss Tangent — The capacity of a material to transmit an electromagnetic wave; transmission distance increases with a decreasing value of loss tangent.

Luminance Longitude — The angle of observation projected onto the phase plane.

Magnetopause — The outer boundary of the magnetosphere, where a planet's field interacts with external magnetic field and charged particle environments, particularly the solar wind.

Magnetosphere — The region surrounding a planet in which the local magnetic field is dominated by planet-associated fields rather than by external environments.

Magnitude (m, m_o) — Five-halves times the common logarithm (base ten) of the ratio of the power received per unit area within some bandwidth for a standard object to that for an astronomical object. The base of this logarithmic scale is $x = 2.512$ so that an increase of one magnitude corresponds to a decrease in power by a factor x^{-1} or an increase in distance by a factor $x^{1/2}$. Apparent magnitudes (m) are those observed. Absolute magnitudes (m_o) are those for which absorption and scattering effects have been removed and observation is assumed to occur in a standard geometrical configuration. For solar system objects, the standard configuration is sun-object distance $r = 1$ AU, object-observer distance $\Delta = 1$ AU, and phase angle $\alpha = 0$.

Megahertz (MHz) — The frequency unit 10^6 cycles per second.

Millibar (mb) — A unit of atmospheric pressure (1 bar = 10^6 dynes/cm^2).

Normal Albedo — The brightness of the surface divided by the brightness of a Lambert surface (white screen) when observer and illuminator are located along the same normal vector.

Optical Thickness (τ) — A parameter related to absorption and scattering of electromagnetic radiation; the ratio of the intensity of a source after (absorption and scattering) to that before is exp ($-\tau$).

Perihelion — That point in an orbit closest to the sun.

Phase Angle (Ψ) — The angle sun-object observer.

Phase Function [$\phi(\alpha)$] — The ratio of the brightness at any phase angle α to the brightness at the phase angle ($\alpha = 0$).

Phonon — The particle used in describing sound or vibration phenomena in matter; somewhat analogous to photon which can be defined as a particle used in describing electromagnetic radiation phenomena.

Photoclinometry — The process of relating the measured brightness seen in a photograph to the viewing and lighting geometry, and the surface photometric function to obtain slope information.

Photometric Function — The function relating reflectance properties of the surface to the viewing direction, solar illumination direction, and surface orientation.

Photometric Passband — The range of wavelengths or frequencies within which electromagnetic radiation is detected. The response of a given device is rarely uniform within its passband. Photometric passbands may be narrow or broad, and a number of photometric systems designated by letters such as U, B, V, etc., are in general use. See Newburn and Gulkis (1971), TR 32-1529, JPL, and the references therein for a discussion of photometric systems.

Pitch Angle — The angle between the particle velocity vector and the external magnetic field vector evaluated at the position of the particle.

Plagioclase — Mineral of the feldspar family, composed of silicates of aluminum and sodium or calcium ($NaAlSi_3O_8$ or $CaAl_2Si_2O_8$).

Plasma — A gas in which the concentration of charged particles has non-negligible effects on the properties of the gas.

Polarized Light — A light beam in which the waves are all vibrating in a single plane.

Porosity — Ratio of the unoccupied volume to total volume.

Power Spectral Density — The Fourier transform of the autocorrelation function of the surface elevation.

Prograde — The sense of rotation or revolution common in the solar system in which the motion is counter-clockwise as viewed from the north.

Pyroxene — A complex mineral composed of silicates of iron, magnesium, aluminum, and sodium or calcium.

Radiance Factor — Ratio of observed radiance of a point on the surface to the radiance of a white screen placed normal to the incident solar rays.

Rayleigh Scattering — Scattering of electromagnetic radiation by particles whose characteristic size is small compared to the wavelength λ; in this case, the scattering center may be approximated by an oscillating electric dipole whose scattering cross-section and opacity are proportional to λ^{-4}.

Relief — Total vertical rise of a surface feature, e.g., bottom of crater to top of rim.

Resonance — Orbital resonance occurs when the ratio of the orbital frequency to the rotational frequency equals the ratio of two integers; for Mercury this ratio is 2/3 and results in periodic repetition of a given geometric configuration.

Revolution — The orbital motion of a planet around the sun.

Right Ascension — The celestial coordinate equal to the angle (east taken positive) between the projection on the plane of the earth's equator of the direction of the item considered and that of the vernal equinox; the precession of the earth's rotation axis implies a slow variation of the right ascension even of fixed directions.

Rim Height — Height of crater rim above local surface plane.

Rotation — The turning of a planet on its axis.

Scale Height (H_p, H_ρ) — a measure of the vertical gradient of a quantity x, e.g., pressure, electron concentration, such that if $H = x(dx/dz)^{-1}$ is constant with altitude z, the quantity x changes by a factor e within the altitude interval H.

Seeing — A term used by astronomers to describe the visual appearance of a star or planet as affected by atmospheric conditions.

Sidereal — Located with respect to the stars.

Solar Constant — The amount of radiant energy received from the sun at the upper limits of the planet's atmosphere per unit time and unit surface area. (The solar "constant" actually varies slightly with time. Values quoted are estimates of the average value over the time interval of interest.)

Steradian — Solid angle subtended at the center of a sphere by an area on the surface equal to the square of the radius of the sphere. (The total solid angle about a point is 4π steradians).

Stratosphere — The atmospheric layer directly above the troposphere within which the temperature is constant or increases with altitude.

Subsolar Point — The point on a planet where the sun is at the zenith.

Terminator — The line that separates the illuminated and unilluminated portions of a planet.

Thermal Conductivity (K) — Rate of heat energy transfer per unit time, area, and temperature gradient; specific to the material and depending on temperature if radiative energy transport is important.

Thermal Inertia — The quantity $(K_\rho C)^{1/2}$ where $(K_\rho C)$ is proportional to the natural unit of time for temperature variations within a material for contact (phonon) conduction.

Thermal Parameter — The inverse of the thermal inertia.

Trapped Radiation — Energetic charged particles whose trajectories in a planetary magnetic field are bounded in space; a particle travels nearly along the field line, "mirrors" at equal north and south magnetic latitudes, and drifts in longitude.

Triple Point — A point on the pressure-temperature phase diagram of a substance in which solid, liquid, and vapor phases may all three co-exist in equilibrium with one another.

Tropopause — The upper boundary of the troposphere and the lower boundary of the stratosphere, characterized by a near-discontinuity in the temperature gradient.

Troposphere — The atmospheric layer within which major weather phenomena occur, characterized by decreasing temperature with altitude.

Ultra High Frequency (UHF) — Characteristic of electromagnetic radiation at those microwave frequencies between 300 and 3000 MHz, used here synonymously with decimetric to cover a broader range extending perhaps to 30 000 MHz.

Vernal Equinox — The direction from the center of the earth to the center of the sun at the time when the latter lies in the plane of the earth's equator in March of each year.

Zenith — The direction opposite to that of the local acceleration of gravity (including the centrifugal terms) and perpendicular to the local horizon.

Zenith Angle (Z) — Angular distance from the zenith at the observer's position. (The zenith is the direction above and perpendicular to the local horizon.)

APPENDIX E

GENERAL BIBLIOGRAPHY

1. Anon.: Models of Mars' Atmosphere (1974), NASA SP-8010, December 1974.

2. Anon.: Models of Venus Atmosphere (1972), NASA SP-8011, September 1972.

3. Anon.: Surface Models of Mars (1975), NASA SP-8020, September 1975.

4. Anon.: The Earth's Ionosphere, NASA SP-8049, March 1971.

5. Champion, K. S. W.: Dynamics and Structure of the Quiet Thermosphere, AFCRL-TR-74-0318, Air Force Surveys in Geophysics, No. 280, July 1974.

6. Chappell, C. R.: Recent Satellite Measurements of the Morphology and Dynamics of the Plasmasphere, Reviews of Geophysics and Space Physics, Volume 10, Number 4, November 1972.

7. Chiu, Y. T.: An Improved Phenomenological Model of Ionospheric Density, REPORT SAMSO-TR-75-94, March 1975.

8. Hansen, J. E., Editor: The Atmosphere of Venus, NASA SP-382, 1975.

9. Swider, W.: The D- and E-Regions, AFCRL-TR-74-0493, Environmental Research Papers, No. 488, September 1974.

10. Conference on the Atmosphere of Venus, Journal of the Atmospheric Sciences, Vol. 32, No. 6, June 1975 (all articles).

11. SNS-NUS-932 "Worldwide Environmental Summary. Part I. Demographic, Soils and Meteorologic Data," NUS Corporation, June, 1972.

12. Slade, David H., Editor. Meteorology and Atomic Energy, 1968. July 1968.

APPENDIX F

INDEX

B

C

D

E

F

G

H

I

M

N

O

P

Q

R